frontiers | Research Topics

Increasing penetration of renewable sources in power systems: Opportunities and challenges

Edited by
Xue Lyu, Minghao Wang, Siqi Bu, Tao Liu and Jiajia Yang

Published in
Frontiers in Energy Research

ISSN 1664-8714
ISBN 978-2-83252-199-1
DOI 10.3389/978-2-83252-199-1

About Frontiers

Frontiers is more than just an open access publisher of scholarly articles: it is a pioneering approach to the world of academia, radically improving the way scholarly research is managed. The grand vision of Frontiers is a world where all people have an equal opportunity to seek, share and generate knowledge. Frontiers provides immediate and permanent online open access to all its publications, but this alone is not enough to realize our grand goals.

Frontiers journal series

The Frontiers journal series is a multi-tier and interdisciplinary set of open-access, online journals, promising a paradigm shift from the current review, selection and dissemination processes in academic publishing. All Frontiers journals are driven by researchers for researchers; therefore, they constitute a service to the scholarly community. At the same time, the *Frontiers journal series* operates on a revolutionary invention, the tiered publishing system, initially addressing specific communities of scholars, and gradually climbing up to broader public understanding, thus serving the interests of the lay society, too.

Dedication to quality

Each Frontiers article is a landmark of the highest quality, thanks to genuinely collaborative interactions between authors and review editors, who include some of the world's best academicians. Research must be certified by peers before entering a stream of knowledge that may eventually reach the public - and shape society; therefore, Frontiers only applies the most rigorous and unbiased reviews. Frontiers revolutionizes research publishing by freely delivering the most outstanding research, evaluated with no bias from both the academic and social point of view. By applying the most advanced information technologies, Frontiers is catapulting scholarly publishing into a new generation.

What are Frontiers Research Topics?

Frontiers Research Topics are very popular trademarks of the *Frontiers journals series*: they are collections of at least ten articles, all centered on a particular subject. With their unique mix of varied contributions from Original Research to Review Articles, Frontiers Research Topics unify the most influential researchers, the latest key findings and historical advances in a hot research area.

Find out more on how to host your own Frontiers Research Topic or contribute to one as an author by contacting the Frontiers editorial office: frontiersin.org/about/contact

Increasing penetration of renewable sources in power systems: Opportunities and challenges

Topic editors

Xue Lyu — Pacific Northwest National Laboratory (DOE), United States
Minghao Wang — Hong Kong Polytechnic University, Hong Kong, SAR China
Siqi Bu — Hong Kong Polytechnic University, Hong Kong, SAR China
Tao Liu — The University of Hong Kong, Hong Kong, SAR China
Jiajia Yang — University of New South Wales, Australia

Citation

Lyu, X., Wang, M., Bu, S., Liu, T., Yang, J., eds. (2023). *Increasing penetration of renewable sources in power systems: Opportunities and challenges*. Lausanne: Frontiers Media SA. doi: 10.3389/978-2-83252-199-1

Table of contents

frontiers | Frontiers in Energy Research

BRIEF RESEARCH REPORT
published: 23 May 2022
doi: 10.3389/fenrg.2022.920654

Over-Voltage Regulation of Distribution Networks by Coordinated Operation of PV Inverters and Demand Side Management Program

Seyed Saeid Heidari Yazdi[1], *Tohid Rahimi*[2], *Saeideh Khadem Haghighian*[3], *Gevork B. Gharehpetian*[4] *and Mehdi Bagheri*[1]*

[1]Department of Electrical and Computer Engineering, School of Engineering and Digital Sciences, Nazarbayev University, Nursultan, Kazakhstan, [2]Department of Electronics, Carleton University, Ottawa, ON, Canada, [3]Electrical Engineering Department, California State University, Long Beach, CA, United States, [4]Electrical Engineering Department, Amirkabir University of Technology, Tehran, Iran

The increase of Photovoltaics (PV) units' penetration factor in the power grids might create overvoltage over the network buses. The active power curtailment (APC) and the reactive power provision methods use inverters to regulate their output active and reactive powers for high PV-penetrated grids. However, the mentioned solutions would reduce the maximum injectable active solar power to the grid, not financially acceptable. Continuous employment of the maximum apparent power capacity of the inverters will practically decrease the inverters' lifetime, require special design considerations, and make the control system complex. To overcome those issues, a feasible solution would be increasing the load consumption within the time intervals in which the grid faces the over-voltage problem. In this research, the demand response (DR) program is employed. Load shifting techniques are exerted to move a portion of loads from the peak hours to when further power consumption is expected for voltage level reduction purposes. A new long-term strategy based on the coordinated operation of the PV inverters and load shifting techniques is proposed to resolve the over-voltage issue in the network. Consequently, the PV inverter's contribution to voltage control is reduced; a new sight of DR potential is implemented, and also the under-voltage level in peak times is decreased significantly.

Keywords: PV inverters, active power curtailment (APC), over-voltage, demand reposed (DR), high penetrance

OPEN ACCESS

Edited by:
Minghao Wang,
Hong Kong Polytechnic University,
Hong Kong SAR, China

Reviewed by:
Jianqiang Luo,
Guangdong University of Technology, China
Yong Li,
Hunan University, China

***Correspondence:**
Mehdi Bagheri
mehdi.bagheri@nu.edu.kz

Specialty section:
This article was submitted to Smart Grids, a section of the journal Frontiers in Energy Research

Received: *14 April 2022*
Accepted: *05 May 2022*
Published: *23 May 2022*

Citation:
Heidari Yazdi SS, Rahimi T, Khadem Haghighian S, Gharehpetian GB and Bagheri M (2022) Over-Voltage Regulation of Distribution Networks by Coordinated Operation of PV Inverters and Demand Side Management Program. Front. Energy Res. 10:920654. doi: 10.3389/fenrg.2022.920654

INTRODUCTION

Over recent decades, the aim was to install more PV units, especially PV farms, to address the global warming issue and come up with clean energy. The PV electricity generation cost has been considerably reduced, and the PV units have been employed in a wide range of applications (Wongsaichua et al., 2004). However, the high penetration factor of the PV systems leads to critical challenges in power quality (e.g., over-voltage) (Yang et al., 2020).

In high PV-penetrated power systems, the PV generators may cause to flow reverse current in grids' lines, and then nodal overvoltage might appear. Researchers have used two general techniques, namely the active power curtailment (APC) and reactive power control of PV inverters, to mitigate the overvoltage challenge. Application of the APC techniques (which reduce the solar power generation) and reactive power consumption by the inverters can decrease the nodal voltages

down to the acceptable ranges. Many significant efforts have been performed to address the over-voltage issue emerging from high active power injection from renewable sources (Yeh et al., 2012; Kryonidis et al., 2016; Molina-García et al., 2016; Li et al., 2017; Ciocia et al., 2018;; Singhal et al., 2018; Couraud et al., 2019; Fatama et al., 2020; Joseph et al., 2020). A study by (Singhal et al., 2018), has focused on implementing an adaptive volt/Var control system for the PV inverters to resolve the steady-state voltage deviation and improve the system's response to external faults. In work done by (Ciocia et al., 2018), three different approaches have been recommended and practiced to utilize the voltage control devices and employ a static voltage controller (SVC) instead of a On-Load Tap Changer (OLTC). The authors of (Kryonidis et al., 2016) have proposed a decentralized control strategy to minimize the power losses and provide a fast response in the voltage regulation. Researchers have tried to earn revenue from the participation of the PV inverters in the ancillary services market (Karbouj et al., 2020). A three-level control system consisting of power, voltage, and current control loops has been recommended by (Molina-García et al., 2016) for the PV inverters to overcome the over-voltage issues and the power flow convergence problems. Also, a modified voltage-reactive power curve and a power flow routine have been presented to prevent time-consuming calculations for determining the nodes' voltage and lines' current. The utilization of a transformer with tap changing capability, switched capacitor banks, and distributed generation units have also been discussed by (Joseph et al., 2020) to improve the voltage quality. However, this method will reduce the transformer's lifetime and requires expensive switched capacitors. The over-voltage and under-voltage challenges are expected in high PV-penetrated power systems under cloudy conditions. Therefore, solutions have been proposed by (Li et al., 2017) to mitigate those challenges by regulating the active and reactive power values of the PV inverters. Unbalanced grid voltage conditions can be mitigated by the coordinated operation of distributed inverters and other power quality devices to improve voltage unbalance condition (Peng et al., 2020).

A precise analysis of the literature shows that the APC techniques and reactive power control of PV inverters have been commonly practiced to overcome the over-voltage issue in different conditions. However, relying on those methods will reduce the voltage control freedom. Furthermore, they will initiate other technical problems for the PV inverters and impose a more economic burden on the owners. The reactive power injection/absorption by PV inverters will increase the required Volt-Ampere (VA) of the inverters. Therefore, the size of the inverters would be increased, advanced cooling systems would be required, and investment costs would be increased. In addition, injection of the reactive power through the inverters may potentially decrease their lifetime because of the implied current stresses (Anurag et al., 2015). Employing APC techniques would lead to solar power spillage and would reduce the financial benefits. Also, the network operators should pay a penalty cost to the PV units' owners for their contribution to the voltage regulation. Therefore, it is essential to reduce the PV inverter's contributions to improve voltage quality issues.

This study proposes a new technique considering DR program to address the discussed challenges. This letter's main contribution is proposing simultaneous and coordinated employment of the DR programs and reactive/active power regulation of the PV inverters to improve the voltage quality of the network. Nevertheless, DR techniques have been employed by researchers (Aghaei et al., 2016; Dong et al., 2017; Yao et al., 2019; Antonopoulos et al., 2020; Barik and Das 2020; Li et al., 2020; Xie et al., 2020) to cover different objectives such as voltage stability, short-term voltage stability, and long/short term voltage quality. All mentioned works have been implemented without considering Distributed Generators (DGs) and PV units' contribution to the voltage support. Also, Electric Vehicles (EVs) have been considered additional tools to improve the voltage quality (Prabawa and Choi, 2021; Dutta et al., 2021; Pournazarian et al., 2019). However, EVs can mainly address dynamic voltage deviations quickly, while utility operators prefer to adopt a long-term voltage control strategy. The literature has not yet studied the DR potential for reducing the PV system's contribution to voltage control. To be more precise, the aim is to overcome the over-voltage issues of distribution networks by proposing a coordinated operation of DR of loads and APC and reactive power regulation of PV farms. The effective performance of the proposed methodology is examined over the IEEE 33 bus distributed network.

The proposed strategy is introduced in **section 2**. The criteria, fitness functions, and the case study with its characteristics are presented in **section 3**. To assess the proposed strategy, simulations are conducted and their results are discussed in **Section 4**. Finally, **section 5** is dedicated to highlighting the main conclusion.

THE PROPOSED STRATEGY

The derivation steps of the proposed methodology are shown in **Figure 1**. In **Figure 1A**, the over-voltage issue is clear around noontime due to high PV power generation. In consequence, a real power curtailment has been applied to the PV farm inverters, and reactive power compensation has been applied to mitigate the over-voltage issue, see **Figure 1B**. Different reactive control methods can also be applied over the PV inverters during the over-voltage conditions, such as adjusting the reactive power considering IEEE 1547–2018. A relatively high APC level has been applied, and the PV inverters have regulated their reactive power generation to mitigate the over-voltage issue.

The main challenges of the contribution of PV inverters in voltage control without employing a suitable DR program can be inferred from **Figure 1B**. In more detail:

- Increasing the reactive power generation of inverters will increase the required VA rates for the PV inverters, and then investment costs would be increased.
- The clipped active power, which is indicated by P1, is very significant; considerable financial losses would be incurred because of employing APC methods.

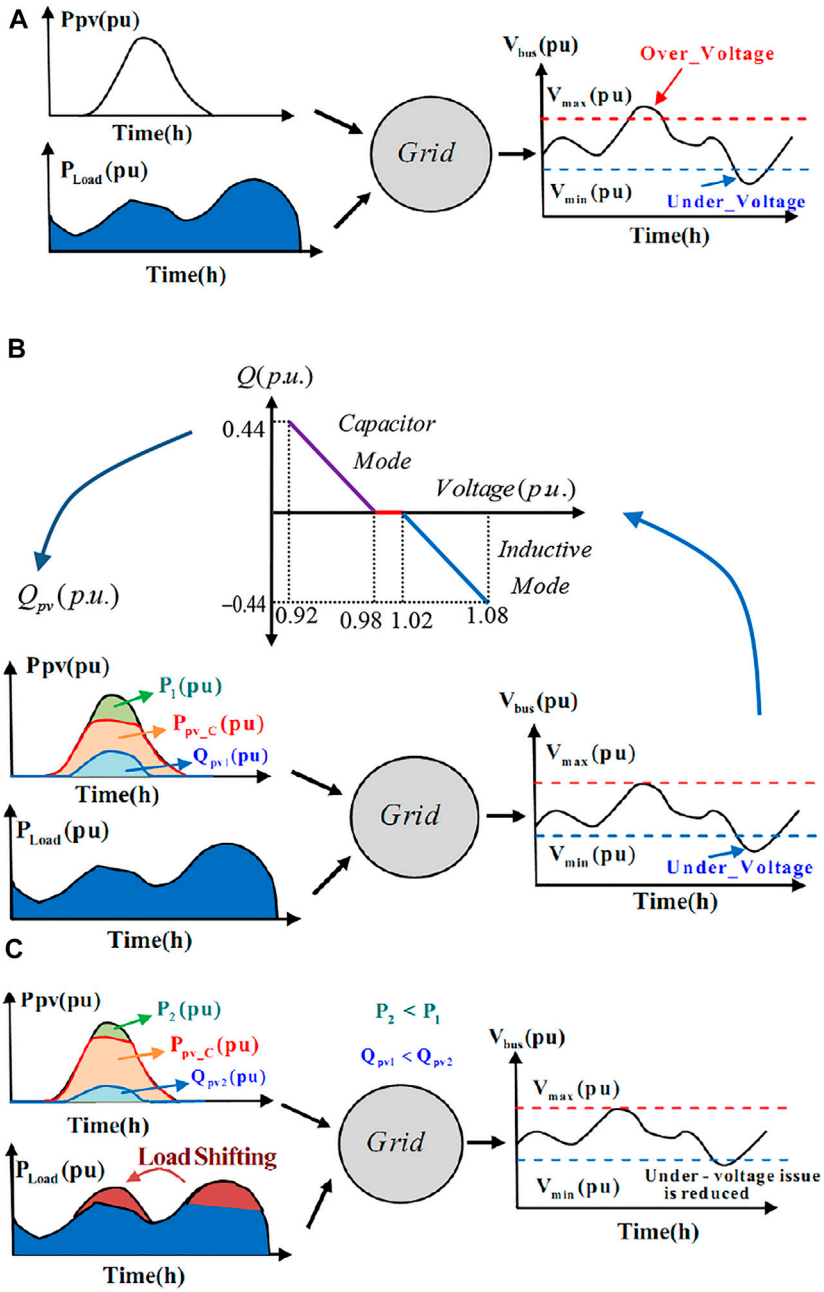

FIGURE 1 | The derivation steps of the proposed methodology: **(A)** Without voltage support by PV inverters and without implementing the DR program, **(B)** conventional voltage support by PV inverters and without implementing the DR program, and **(C)** the proposed strategy for coordinated operation of PV inverters and DR program.

In the proposed technique, shifting load from the peak times to times in which the PV farm injects high power to the grid (in our case: around noon time) would be an effective approach. It is assumed that the customers allow the network operator to shift a certain percentage of their power consumption from peak times to off-peak times using DR programs. Hence, **Figure 1C** shows the voltage profile of the grid employing the coordinated operation of PV inverters and DR programs where the over-voltage issue is eliminated. The load-shifting (LSH) technique is selected to implement the DR program. As a result, the PV inverters' levels of active power curtailment and reactive power generation are reduced. Another advantage would be decreasing the under-voltage issue during peak times which this support is highlighted in **Figure 1C**.

Considering the discussion above, reactive power support by inverters is still needed in power grids, but its level can be significantly reduced. In this context, a regulation loop should be implemented in the control software of the PV inverters to

$$\begin{cases} \alpha_p = \dfrac{Idr(t_p)}{Load_b(t_p)} & p \in t_{peak} \\ \alpha_{ik} = \dfrac{Idr(t_i)}{Load_b(t_i)} & i \in t_{non-peak} \end{cases} \quad (1)$$

$$Load(t_p) = (1+\alpha_p) \times Load_b(t_p) \quad (2)$$

$$Load(t_i) = (1+\alpha_i) \times Load_b(t_i) \quad (3)$$

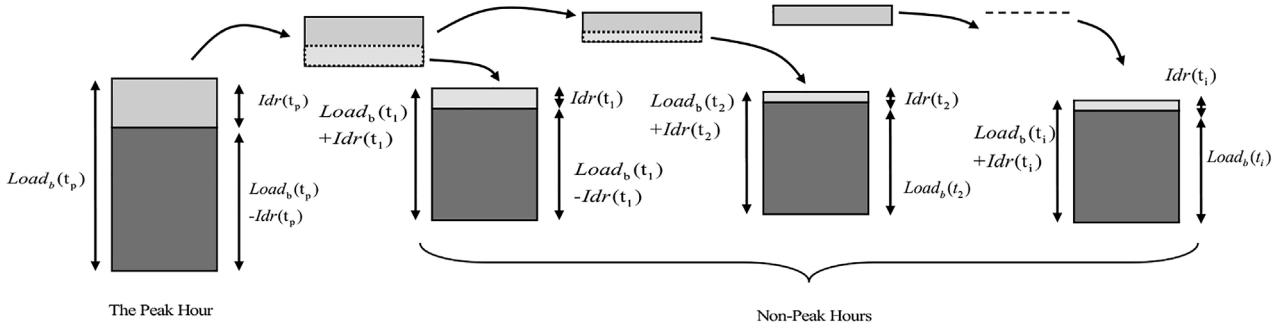

FIGURE 2 | The concept of the LSH technique.

regulate its reactive power (Q) as a function of grid conditions [voltage level (V)]. The IEEE Std. 1,547 has defined the required Q-V function for the PV inverters, see **Figure 1B**.

In this part, the DR concept is discussed. Nowadays, loads' behavior can be predicted with high accuracy. In DR programs, customers contribute voluntarily, contract-based and mandatory-based in some emergency conditions in power consumption patterns. Therefore, there is little concern about unpredictability and uncontrollability from users' perspectives. **Figure 2** clearly shows the DR concept and **Eqs 1–3** try to express this concept. It is assumed that customers allow the network operator to be able to shift certain percentages of their power consumption from peak times to non-peak times. The final load at each time after participation in DR programs may be more or less than the base load. **Figure 2**; **Eqs 1–3**, $Load\,(t_p)$ and $Load\,(t_i)$ indicate the final load in the peak and non-peak times, respectively. $Load_b\,(t_i)$ and $Load_b\,(t_p)$ are the base-load in non-peak and peak times, respectively. Idr (tp) indicates the shifted load from a peak time to other off-peak times. On the other hand, Idr (ti) factor shows the consumer participation level in absorbing Idr (tp) at *i*th off-peak time. The loads' values after running the DR program at peak times and off-peak times could be obtained *via* 2) and 3).

$$\begin{cases} \alpha_p = \dfrac{Idr\left(t_p\right)}{Load_b\left(t_p\right)} p \in t_{peak} \\ \alpha_{ik} = \dfrac{Idr\,(t_i)}{Load_b\,(t_i)} i \in t_{non-peak} \end{cases} \quad (1)$$

$$Load\left(t_p\right) = \left(1 + \alpha_p\right) \times Load_b\left(t_p\right) \quad (2)$$

$$Load\,(t_i) = (1 + \alpha_i) \times Load_b\,(t_i) \quad (3)$$

IMPLEMENTATION OF THE PROPOSED STRATEGY

This section aims to clarify the implementation process of the proposed strategy. As discussed in this paper, the contribution of PV units in voltage control means owners of PV farms would lose some revenue due to applying the APC technique, which must be compensated by the grid owner. On the hand, the owner of the grid must pay PV unit owners for their contribution to reactive power control as an ancillary service. To reduce the mentioned costs, it is proposed to employ DR programs in this research. Shifting the loads from peak times to off-peak times is an incentive program and induces costs. However, by implementing optimum schedules, an optimum solution can be found in which the total penalty cost allocated to the owner of the grid would be the lowest. In general, different fitness functions, optimization algorithms, scenarios, and load profiles can be considered to examine the performance of the proposed strategy. But, this study tries to simply implement the proposed strategy. In this context, three fitness functions are first defined.

The costs of the contribution of the PV inverters in voltage regulation can be expressed as:

$$RC = \sum_{t=1}^{t=t_{end}} \left|Q_t^{PV}\right| \times C_{q-t} \quad (4)$$

$$AC = \sum_{t=1}^{t=t_{end}} \left|P_t^{PV}\right| \times C_{P-t} \quad (5)$$

where, Q_t^{PV} and P_t^{PV} are the exchanged reactive and active power by a PV inverter. The allocated per unit reactive and active power costs for each time interval are indicated by Cq-t and CP-t,

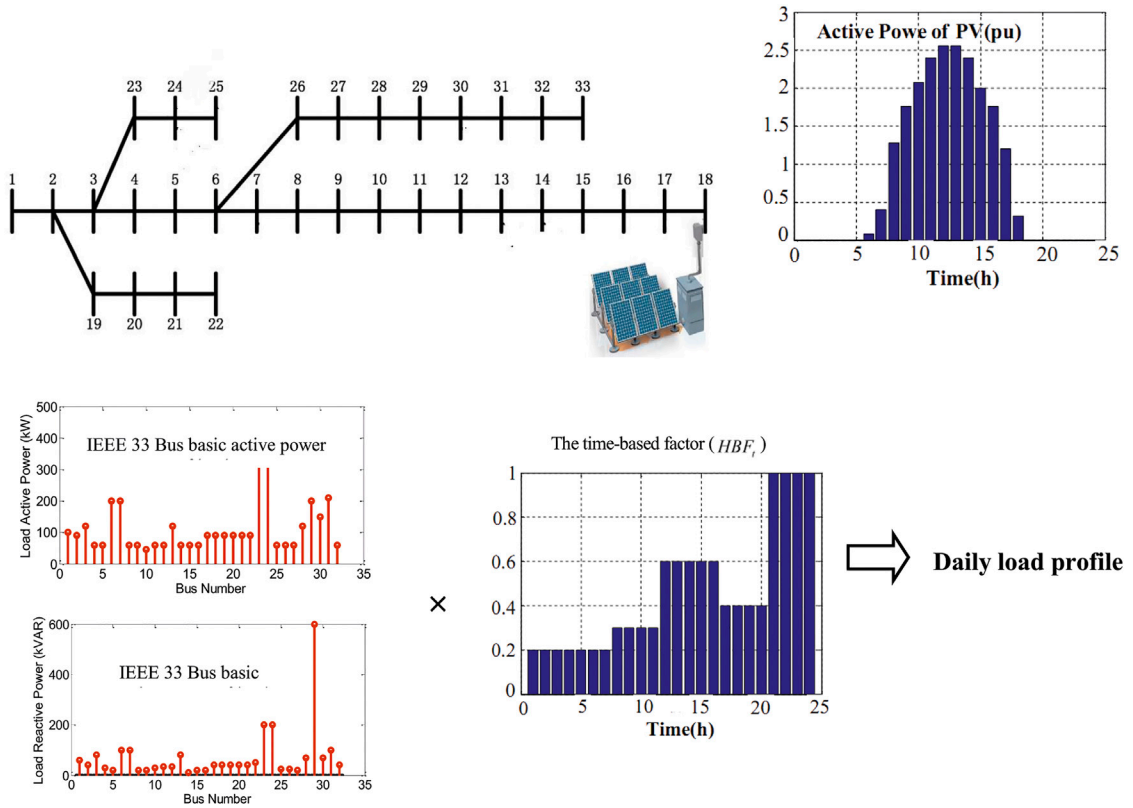

FIGURE 3 | Single line diagram of IEEE 33 bus distribution network.

respectively. A penalty cost is also expressed by **(6)** to consider the cost of load shifting from peak time to off-peak times. It is assumed that the load change after applying the DR program is ΔP (t). Thus, the allocated penalty cost can be obtained as,

$$C_{DR} = \sum_{y=1}^{t=t_{end}} \Delta P(t) \times C_{PL-t} \tag{6}$$

where CPL-h is the daily price of electricity determined by the distribution network owner for each time interval. In this step, a multi-objective optimization problem is indicated. One of the techniques to simplify multiple objective problems is aggregating all objectives in one expression by assigning a certain weight factor to each objective:

$$FT = \omega_1 RC + \omega_2 AC + \omega_3 C_{DR} \tag{7}$$

where, ωi is the weighted factor for the *i*th fitness function It is worthy of mentioning that, concerning the operator's aims and priorities, certain weight factors can be defined to realize the power quality requirement and maximize the operator's profit simultaneously.

CASE STUDY

The IEEE 33-bus, as a test platform, is selected to evaluate the proposed technique. This system is a Medium Voltage (MV) distribution and a suitable network for grid-connected large-scale PV farms. It has a radial feature to enlarge the effect of high PV penetration. The single-line diagram of the case study is illustrated in **Figure 3**. Since the MW sized and GW sized and grid-connected PV units have been developed around the world (Trindade et al., 2016), it is assumed that the large-scale PV farm is connected to the proposed network. In particular, a PV farm is connected to bus#18 to highlight the operational effect of the PV farm on the over-voltage phenomenon. To simplify the analyses, all the parameters are expressed in Per Unit (p.u.) format for load flow studies, the load types are P-Q, while the PV farm is modeled as a load with the capability to inject and absorb reactive power.

The basic active and reactive power of the loads is reported in the literature (Yuvaraj et al., 2021). However, the load profile is not reported for different time intervals of a day. Thus, a time-based factor (HBFt) should be applied to the base-load data to create a daily load profile. This factor will be changed over a day, see **Figure 3**, to model the load profile during peak and off-peak times. However, different scenarios considering load and power generation profiles can also be considered. The active ($P^L_{i,t}$) and reactive ($Q^L_{i,t}$) powers of *i*th bus at *t*th time interval are calculated as,

$$P^L_{i,t} = P^L_{i,base} \times HBF_t \tag{8}$$

$$Q^L_{i,t} = Q^L_{i,base} \times HBF_t \tag{9}$$

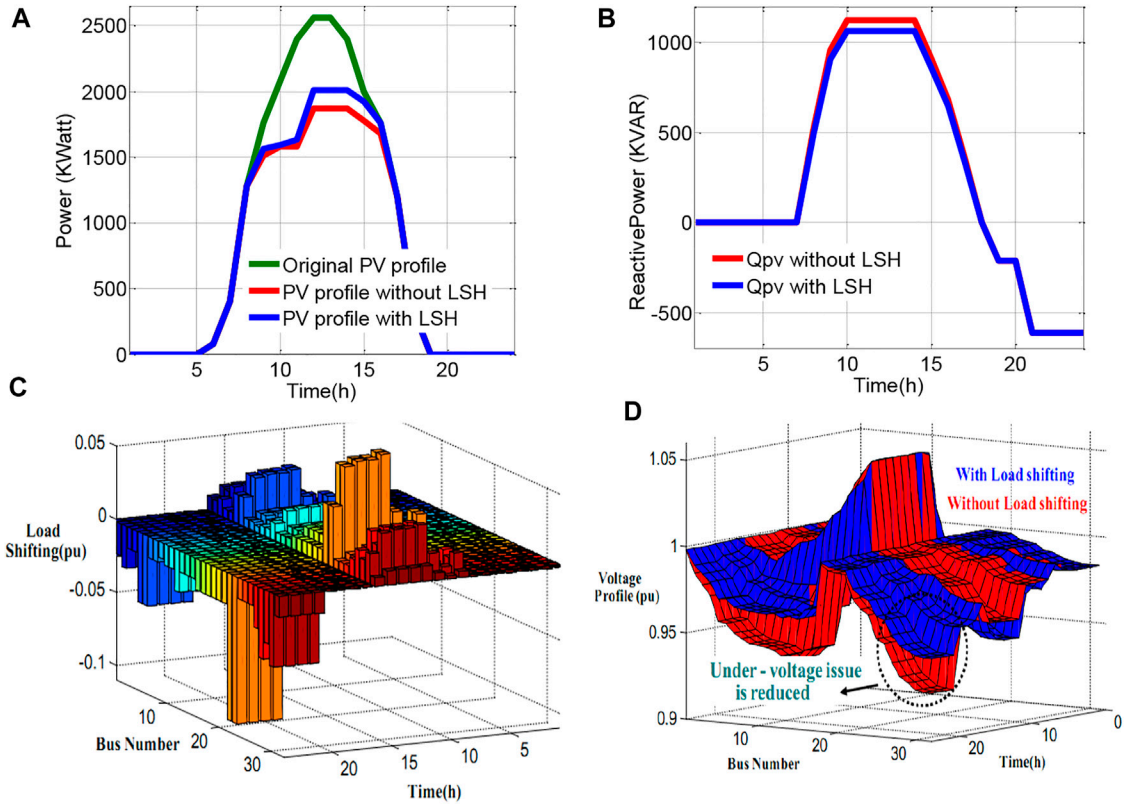

FIGURE 4 | Profiles of output power with and without load LSH method: **(A)** active power generation and **(B)** reactive power compensation, **(C)** Demand profile variation after performing the LSH method, and **(D)** Comparison of voltage profile concerning different voltage control strategies.

where, $P^{L}_{i,base}$ and $Q^{L}_{i,base}$ are the base active and reactive powers.

As demonstrated in **Figure 3**, a large-scale PV farm is connected to the grid. **Figure 3** also illustrates the forecasted average power generation of the large-scale PV farm for the day ahead.

RESULTS AND DISCUSSION

To assess the proposed methodology's effectiveness, the case study and its characteristics during a day are modeled and simulated in the MATLAB software environment. The power flow technique is based on the matrix lines-nodes concept, which is discussed in detail by (Sotkiewicz and Vignolo, 2006). In each step of the MATLAB code, the loads and generation data are called, the reactive power is adjusted, the voltage of nodes is checked, and PV power generation is reduced in the case of over-voltage happening; this process repeats until the requirements of stopping criteria met.

It should mention that the optimization algorithm, load and generation profiles, and the studied test system are selected to highlight this paper's goals. Different scenarios considering load and power generation profiles can be considered by researchers.

The simulation results are provided in **Figure 4**. Note that, due to eliminating the slack bus in power flow, the remaining bus numbers are 32 buses. Therefore, the *n*th bus in voltage profile figures is that of (n+1)th bus over the examined network. The active power profiles of the PV farms in different scenarios are also shown in **Figure 4A**. The APC level by applying the LSH method is lower than that in the case of LSH absent. Therefore, employing the LSH method can increase the benefits of the PV owners by selling more active power. Moreover, the contribution of the PV farm in consuming reactive power is reduced, which will decrease the inverter power loss and consequently increase the inverter's lifetime. Considering the employed Q support, see **Figure 1**, the PV unit should consume the reactive power around noon times to reduce the over-voltage issue. On the other hand, the PV unit is responsible for injecting reactive power into the grid to support the profile voltage during the night with respect to the IEEE 1547–2018 standard. The mentioned contribution of the PV unit in Q support is illustrated in **Figure 4B**.

The demand profile variation of all the grid buses after implementing the LSH method is also provided in **Figure 4C**, where the most demand variations occur during noontime. In addition, the demand reduction occurs during hours 8 p.m. to 12 a.m. for all the buses. The resultant voltage profile is shown in **Figure 4D**. The voltage value during the day and for all buses remains under 1.05 p. u. Correspondingly, the under-voltage issue is reduced during peak times.

CONCLUSION

A novel strategy to coordinate the PV units' active and reactive power controllers and the demand response program is proposed. The proposed strategy mitigated the challenges of the contribution of PV inverters in voltage control. Those challenges consist of high mandatory APC levels and the increased cost and stresses of the PV inverters in reactive power generation. The high contribution of PV units in the voltage control is not cost-effective and may impose complexity in the design and control of inverters. The proposed strategy solved the over-voltage issue and the mentioned challenges by proposing a method for coordinated operation of the PV inverters (considering their active and reactive power exchange) and DR program. Three fitness functions were introduced and integrated into a fitness function. The DR program coordinated the PV unit's operation to minimize the final fitness function simultaneously and solve the over-voltage issue. The proposed strategy's effectiveness has been verified successfully on the IEEE 33 bus grid test.

DATA AVAILABILITY STATEMENT

The original contributions presented in the study are included in the article/Supplementary Material, further inquiries can be directed to the corresponding author.

AUTHOR CONTRIBUTIONS

All authors listed have made a substantial, direct, and intellectual contribution to the work and approved it for publication.

FUNDING

This work was supported by the Collaborative Research Project (CRP) grant, Nazarbayev University (Project no. 021220CRP0322).

REFERENCES

Aghaei, J., Alizadeh, M. I., Abdollahi, A., and Barani, M. (2016). Allocation of Demand Response Resources: toward an Effective Contribution to Power System Voltage Stability. *IET Gener. Transm. & Distrib.* 10 (16), 4169–4177. doi:10.1049/iet-gtd.2016.0680

Antonopoulos, I., Robu, V., Couraud, B., Kirli, D., Norbu, S., Kiprakis, A., et al. (2020). Artificial Intelligence and Machine Learning Approaches to Energy Demand-Side Response: A Systematic Review. *Renew. Sustain. Energy Rev.* 130, 109899. doi:10.1016/j.rser.2020.109899

Anurag, A., Yang, Y., and Blaabjerg, F. (2015). Thermal Performance and Reliability Analysis of Single-phase PV Inverters with Reactive Power Injection outside Feed-In Operating Hours. *IEEE J. Emerg. Sel. Top. Power Electron.* 3 (4), 870–880. doi:10.1109/jestpe.2015.2428432

Barik, A. K., and Das, D. C. (2020). Coordinated Regulation of Voltage and Load Frequency in Demand Response Supported Biorenewable Cogeneration-based Isolated Hybrid Microgrid with Quasi-oppositional Selfish Herd Optimisation. *Int. Trans. Electr. Energy Syst.* 30 (1), e12176. doi:10.1002/2050-7038.12176

Ciocia, A., Boicea, V. A., Chicco, G., Di Leo, P., Mazza, A., Pons, E., et al. (2018). Voltage Control in Low-Voltage Grids Using Distributed Photovoltaic Converters and Centralized Devices. *IEEE Trans. Industry Appl.* 55 (1), 225–237.

Couraud, B., Kumar, P., Robu, V., Jenkins, D., Norbu, S., Flynn, D., et al. (2019). "December. Assessment of Decentralized Reactive Power Control Strategies for Low Voltage PV Inverters," in 2019 8th International Conference on Power Systems (ICPS), Jaipur, India, 20-22 Dec. 2019 (IEEE), 1–6.

Dong, Y., Xie, X., Shi, W., Zhou, B., and Jiang, Q. (2017). Demand-response-based Distributed Preventive Control to Improve Short-Term Voltage Stability. *IEEE Trans. Smart Grid* 9 (5), 4785–4795.

Dutta, A., Ganguly, S., and Kumar, C. (2021). Coordinated Volt/Var Control of PV and EV Interfaced Active Distribution Networks Based on Dual-Stage Model Predictive Control. *IEEE Syst. J.* 2021, 1–10. doi:10.1109/jsyst.2021.3110509

Fatama, A. Z., Khan, M. A., Kurukuru, V. B., Haque, A., and Blaabjerg, F. (2020). Coordinated Reactive Power Strategy Using Static Synchronous Compensator for Photovoltaic Inverters. *Int. Trans. Electr. Energy Syst.* 30 (6), e12393. doi:10.1002/2050-7038.12393

Joseph, A., Smedley, K., and Mehraeen, S. (2020). Secure High DER Penetration Power Distribution via Autonomously Coordinated Volt/VAR Control. *IEEE Trans. Power Deliv.* 35 (5), 2272–2284. doi:10.1109/tpwrd.2020.2965107

Karbouj, H., Rather, Z. H., and Pal, B. C. (2020). Adaptive Voltage Control for Large Scale Solar PV Power Plant Considering Real Life Factors. *IEEE Trans. Sustain. Energy* 12 (2), 990–998.

Kryonidis, G. C., Demoulias, C. S., and Papagiannis, G. K. (2016). A Nearly Decentralized Voltage Regulation Algorithm for Loss Minimization in Radial MV Networks with High DG Penetration. *IEEE Trans. Sustain. Energy* 7 (4), 1430–1439. doi:10.1109/tste.2016.2556009

Li, H., Azzouz, M. A., and Hamad, A. A. (2020). Cooperative Voltage Control in MV Distribution Networks with Electric Vehicle Charging Stations and Photovoltaic DGs. *IEEE Syst. J.* 15 (2), 2989–3000.

Li, J., Xu, Z., Zhao, J., and Wan, C. (2017). A Coordinated Dispatch Model for Distribution Network Considering PV Ramp. *IEEE Trans. Power Syst.* 33 (1), 1107–1109.

Molina-García, Á., Mastromauro, R. A., García-Sánchez, T., Pugliese, S., Liserre, M., and Stasi, S. (2016). Reactive Power Flow Control for PV Inverters Voltage Support in LV Distribution Networks. *IEEE Trans. Smart Grid* 8 (1), 447–456.

Peng, Y., Li, Y., Lee, K. Y., Tan, Y., Cao, Y., Wen, M., et al. (2020). Coordinated Control Strategy of PMSG and Cascaded H-Bridge STATCOM in Dispersed Wind Farm for Suppressing Unbalanced Grid Voltage. *IEEE Trans. Sustain. Energy* 12 (1), 349–359.

Photovoltaics, D. G., and Storage, E. (2018). *IEEE Standard for Interconnection and Interoperability of Distributed Energy Resources with Associated Electric Power Systems Interfaces*. IEEE Std, 1547–2018.

Pournazarian, B., Karimyan, P., Gharehpetian, G. B., Abedi, M., and Pouresmaeil, E. (2019). Smart Participation of PHEVs in Controlling Voltage and Frequency of Island Microgrids. *Int. J. Electr. Power & Energy Syst.* 110, 510–522. doi:10.1016/j.ijepes.2019.03.036

Prabawa, P., and Choi, D.-H. (2021). Hierarchical Volt-VAR Optimization Framework Considering Voltage Control of Smart Electric Vehicle Charging Stations under Uncertainty. *IEEE Access* 9, 123398–123413. doi:10.1109/access.2021.3109621

Singhal, A., Ajjarapu, V., Fuller, J., and Hansen, J. (2018). Real-time Local Volt/var Control under External Disturbances with High PV Penetration. *IEEE Trans. Smart Grid* 10 (4), 3849–3859.

Sotkiewicz, P. M., and Vignolo, J. M. (2006). Allocation of Fixed Costs in Distribution Networks with Distributed Generation. *IEEE Trans. Power Syst.* 21 (2), 639–652. doi:10.1109/tpwrs.2006.873112

Trindade, F. C., Ferreira, T. S., Lopes, M. G., and Freitas, W. (2016). Mitigation of Fast Voltage Variations during Cloud Transients in Distribution Systems with PV Solar Farms. *IEEE Trans. Power Deliv.* 32 (2), 921–932. doi:10.1109/TPWRD.2016.2562922

Wongsaichua, W., Lee, W. J., Oraintara, S., Kwan, C., and Zhang, F. (2004). "October. Integrated High Speed Intelligent Utility Tie Unit for Disbursed/renewable Generation Facilities," in Conference Record of the 2004 IEEE Industry Applications Conference, 2004. 39th IAS Annual Meeting, 2051–2056.3

Xie, Q., Hui, H., Ding, Y., Ye, C., Lin, Z., Wang, P., et al. (2020). Use of Demand Response for Voltage Regulation in Power Distribution Systems with Flexible Resources. *IET Gener. Transm. & Distrib.* 14 (5), 883–892. doi:10.1049/iet-gtd.2019.1170

Yang, Y., Yeh, H. G., and Tran, K. H. (2020). Cooperative Volt-Ampere Reactive Control for a PV-Enabled Distribution Network with Abnormally High Power Loads. *IEEE Syst. J.* 15 (4), 5714–5723.

Yao, M., Molzahn, D. K., and Mathieu, J. L. (2019). An Optimal Power-Flow Approach to Improve Power System Voltage Stability Using Demand Response. *IEEE Trans. Control Netw. Syst.* 6 (3), 1015–1025. doi:10.1109/tcns.2019.2910455

Yeh, H.-G., Gayme, D. F., and Low, S. H. (2012). Adaptive VAR Control for Distribution Circuits with Photovoltaic Generators. *IEEE Trans. Power Syst.* 27 (3), 1656–1663. doi:10.1109/tpwrs.2012.2183151

Yuvaraj, T., Devabalaji, K. R., Srinivasan, S., Prabaharan, N., Hariharan, R., Haes Alhelou, H., et al. (2021). Comparative Analysis of Various Compensating Devices in Energy Trading Radial Distribution System for Voltage Regulation and Loss Mitigation Using Blockchain Technology and Bat Algorithm. *Energy Rep.* 7, 8312–8321. doi:10.1016/j.egyr.2021.08.184

Conflict of Interest: The authors declare that the research was conducted in the absence of any commercial or financial relationships that could be construed as a potential conflict of interest.

Publisher's Note: All claims expressed in this article are solely those of the authors and do not necessarily represent those of their affiliated organizations, or those of the publisher, the editors and the reviewers. Any product that may be evaluated in this article, or claim that may be made by its manufacturer, is not guaranteed or endorsed by the publisher.

frontiers | Frontiers in Energy Research

ORIGINAL RESEARCH
published: 15 June 2022
doi: 10.3389/fenrg.2022.935484

Research on Energy Management Strategy of Pure Electric Vacuum Vehicle Based on Fuzzy Control

Yujie Wang[1], *Yu Lei*[1], *Licheng Zhang*[2] *and Shengshi Zhong*[3]*

[1]School of International Education, Wuhan University of Technology, Wuhan, China, [2]School of Automation, Wuhan University of Technology, Wuhan Road Rover Intelligent Technology Co., Ltd., Wuhan, China, [3]Liuzhou Wuling Automobile Industry Co., Ltd., Liuzhou, China

The current pure electric vacuum vehicle is equipped with main and auxiliary motors, and the two motors work independently without affecting each other. The traditional auxiliary motor usually operates with constant power while the main motor is only responsible for the vehicle driving. The lack of cooperation between the two motors results in high energy consumption. Therefore, formulating a reasonable strategy for the two motors has a significant effect on the performance of the vacuum vehicle. This paper takes a pure electric vacuum vehicle as an example to propose an energy management strategy based on fuzzy control. First, for the working motor, a fuzzy controller is designed by taking the vehicle speed and acceleration as input and motor speed and torque as output. Therefore, the vacuum vehicle can automatically adjust the operating power of the cleaning system according to the real-time road conditions; the driving motor control strategy adopts a closed-loop control strategy that combines driver input and vehicle state parameter feedback based on considering the operating motor. Finally, the effectiveness of the strategy is verified by simulation. The results show that the energy-saving control strategy effectively reduces the power consumption per 100 km and increases the driving range, which is of great significance to the development and design of the vacuum vehicle.

Keywords: pure electric vacuum vehicle, energy management strategy, fuzzy control, control strategy, energy-saving

OPEN ACCESS

Edited by:
Xue Lyu,
University of Wisconsin-Madison, United States

Reviewed by:
Zhaowei Chen,
Chongqing Jiaotong University, China
Rongchao Jiang,
Qingdao University, China

***Correspondence:**
Shengshi Zhong
zhongshengshi@wuling.com.cn

Specialty section:
This article was submitted to Smart Grids, a section of the journal Frontiers in Energy Research

Received: *04 May 2022*
Accepted: *24 May 2022*
Published: *15 June 2022*

Citation:
Wang Y, Lei Y, Zhang L and Zhong S (2022) Research on Energy Management Strategy of Pure Electric Vacuum Vehicle Based on Fuzzy Control. Front. Energy Res. 10:935484. doi: 10.3389/fenrg.2022.935484

1 INTRODUCTION

As the country pays more and more attention to environmental issues, the traditional working methods of road sanitation workers can no longer meet the current needs. As a road cleaning vehicle, the vacuum cleaner effectively relieves the pressure on sanitation and plays an important role in improving the environment. However, compared to the developed countries, domestic vacuum vehicles have some disadvantages, such as noise, and have more power consumption (Zhang, 2020). Different from the pure electric vehicle driven by dual motors (Ruan and Song, 2019; Wu et al., 2019; Wu and Zhang, 2021), for the research object of this article, the main motor is equipped to drive the car, and the auxiliary motor provides power for the bodywork system (Yang, 2016), so a reasonable strategy is developed for the two motors. It has a great effect on the working performance of the vacuum vehicle.

Lee (Lee et al., 2019), Wang (Wang et al., 2021), Kant (Kant et al., 2021) et al. have optimized the structure of the motor to make its performance more prominent, and the focus of this paper is mainly on the control strategy. The drive motor in this paper is similar to the traditional car, and the research

TABLE 1 | Vehicle and motor parameters.

Project		Parameter	Project	Parameter
Vehicle Parameter	Vehicle size	7160 × 2200 × 2750 mm	Wheelbase	3800 mm
	Curb weight	6575 kg	Total mass	8275 kg
	Rolling radius	0.406 m	Air resistance coefficient	0.35
	Frontal Area	6.05 m^2	Rolling resistance coefficient	0.012
Battery	Capacity	90 A/h	Nominal voltage	381.7 V
Driving motor		Rated power	50 kW	
		Rated torque	280 Nm	
		Rated speed	1600 r/min	
Working motor		Rated power	30 kW	
		Rated torque	100 Nm	
		Rated speed	2950 r/min	

strategies to reduce energy consumption mainly focus on the drive control strategy, the regenerative braking energy feedback strategy, and the power limiting strategy (Zhang, 2014). At the same time, different scholars have applied different control methods to achieve the ideal effect. Luo et al. select the corresponding drive mode to give appropriate torque compensation according to the driver's operation intention and improves the power and economy of pure electric vehicles (Luo and Niu, 2020). Ye et al. use a fuzzy control method to determine the ratio of mechanical braking force and regenerative braking force according to different braking intensities to formulate energy recovery control strategies (Ye et al., 2021). Justo et al. proposed a control strategy to predict torque using the fuzzy model of the permanent magnet synchronous motor of an electric vehicle, and the control is simple (Justo et al., 2017). At the same time, the energy management strategy based on fuzzy rules can realize the power distribution of the power system by setting the logic threshold, thereby improving the economy of the vehicle (Guo et al., 2021).

The working motor is only used in some special vehicles, and scholars have not studied it much, Dong constructed a torque control model of the multi-motor power system of an electric sweeper based on a fuzzy control strategy (Dong, 2019). Wang et al. developed and validate an efficiency model for electronically commutated motor fan systems (Wang et al., 2020). Long established the mathematical model of the control relationship of the hydraulic motor tracking servo motor, and the PID parameter setting combined control algorithm is adopted (Long et al., 2018). Shao designed a digital throttle control scheme for the speed of the disc brush motor using a fuzzy control algorithm so that the speed of the disc brush can be adjusted automatically, but the power consumption is not taken into consideration (Shao, 2005).

In addition, the research on multi-motor systems mainly considers the torque distribution between motors (Zhai et al., 2016; Liu et al., 2019), which provides certain ideas for multi-motor power systems. However, in general, there are few studies on energy-saving strategies for multi-motor commercial vehicles with large energy consumption. In this paper, for a certain pure electric vacuum vehicle, comprehensively considering SOC, vehicle speed, operating conditions, etc. an energy-saving strategy for pure electric vacuum vehicle based on fuzzy control is established. The torque output of the two motors is controlled separately, and the Simulink-Cruise joint simulation model verifies the economics of the strategy.

2 OBJECT DESCRIPTION

Pure electric vacuum vehicles use batteries as power sources to drive motors to realize the vehicle's walking and operating functions. Therefore, they can be divided into two parts: the driving system and the working system. According to the needs of vacuum vehicles, they can be equipped with single or dual motors. The research object of this paper is a dual-motor arrangement type. The main motor (that is, the driving motor) drives the vacuum vehicle to travel, and the auxiliary motor (that is, the working motor) provides power for the working device. The block diagram is shown in **Figure 1**. The vehicle and motor parameters of the research vehicle are shown in **Table 1**.

3 MODEL ESTABLISHMENT

3.1 Driving Model

During the driving process, the vehicle is affected by driving resistance, slope resistance, air resistance, and acceleration resistance. The required torque of the driving motor can be calculated by the dynamic equation of the driving system:

$$\frac{Ti_g i_0 \eta_t}{r} = mgf\cos\alpha + mg\sin\alpha + \frac{C_d A u^2}{21.15} + \delta m\frac{du}{dt} \quad (1)$$

where, T is the required torque, i_g is the transmission ratio, i_0 is the main transmission ratio of the differential box, η_t is the transmission efficiency, r is the wheel rolling radius, m is the mass of the vehicle, g is the acceleration of gravity, f is the rolling resistance coefficient and α is the slope angle. C_d is the coefficient of air resistance, A is the windward area, u is the vehicle speed, and δ is the conversion coefficient of the rotating mass.

3.2 Operating Model

In the operating system, the auxiliary motor mainly provides power for the fan and hydraulic components. The fan generates negative pressure and uses the force generated by the pressure to

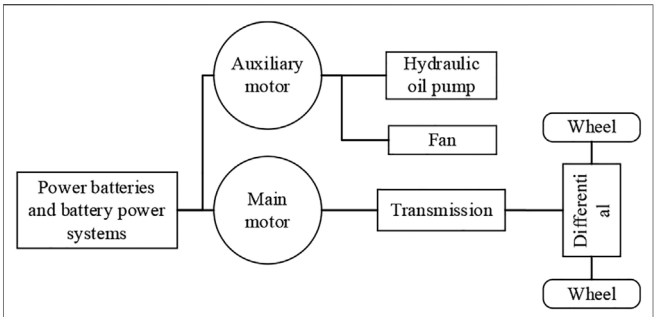

FIGURE 1 | Block diagram of the main and auxiliary motor drive modes.

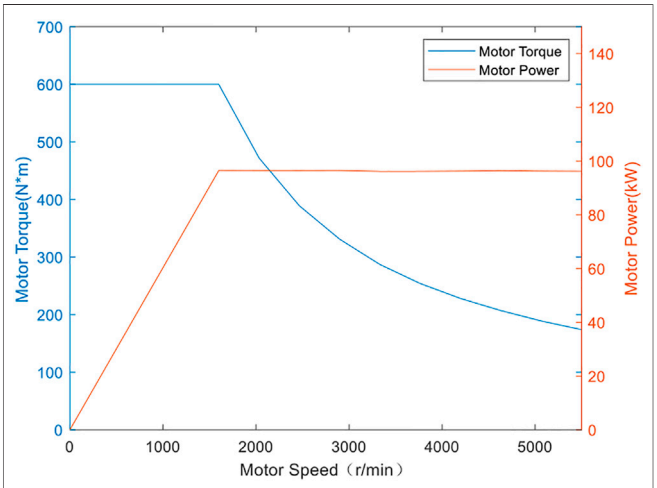

FIGURE 2 | External characteristic diagram of the motor.

suck in garbage and dust. The hydraulic components are used to achieve the lifting and moving of the suction cup (Zhang, 2019). Since the power consumed by hydraulic components is much lower than the fan. It is ignored and only the power consumed by the fan is taken into consideration.

The needed torque of the working motor is:

$$T_{fan} = \frac{9550QP \times 130\%}{n_f n_t \rho} \tag{2}$$

Where, Q is the air volume, P is the air pressure, η_f is the working motor efficiency, n_t is the working motor speed, and ρ is the force rate.

3.3 Motor Model

The motor has complex structure and varies methods to establish its model with different complexity. In this case, the model is part of the vehicle, the performance of the components inside the motor is ignored. Thus, a simplified model with the torque and power characteristics is established (Tian et al., 2020). When the motor speed is less than the base speed, the motor works in the constant torque region, and the output power increases with the increase of the speed. When the motor speed is greater than the

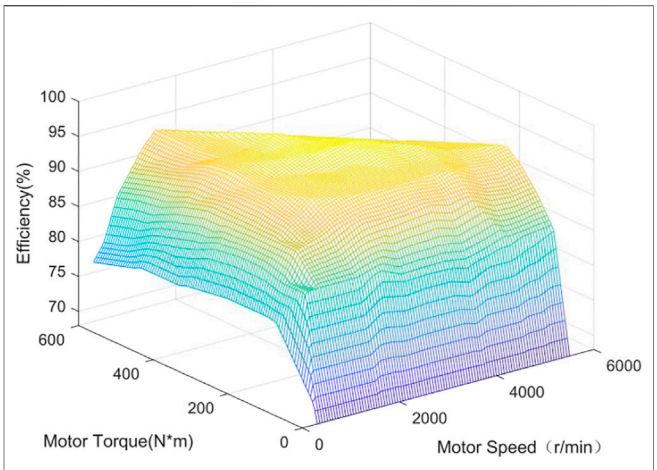

FIGURE 3 | MAP diagram of motor efficiency.

base speed, the motor works in the constant power area, and the output torque decreases as the speed increases. The motor's operating characteristics are shown as the following equation.

$$P_m = \frac{T_m n}{9550}\eta_m \tag{3}$$

Where, P_m is the motor output power, T_m is the motor output torque, n is the motor speed, and η_m is the motor efficiency.

The operating characteristic of the electrical motor is shown in **Figure 2**. The motor efficiency changes with the output speed and torque. The efficiency map of the driving motor is shown in **Figure 3**.

4 ENERGY MANAGEMENT STRATEGY

4.1 Working Strategy

For traditional road vacuum vehicles, when the vacuum suction system is operating, it will clean the road garbage with constant power. Since the amount of garbage on the road does not always remain in a large state, the bodywork system of the vacuum vehicle always working at the same power will inevitably cause unnecessary energy loss (Li, 2020).

At the same time, during the operation of the electric vacuum vehicle, the relationship between the rotation speed, torque, and vehicle speed of the working motor is non-linear, which makes it impossible for us to establish an accurate mathematical model of the operation system. Therefore, a fuzzy controller is designed. It allows the vacuum vehicle to automatically adjust the operating power of the auxiliary motor according to the real-time road conditions, to achieve the goal of energy-saving.

During the operation, the driver adjusts the speed of the vehicle based on the garbage and dust on the road. At the same time, the cleaning efficiency decreases with the increase of the vehicle speed (Li et al., 2019), so when the driver recognizes that there is a lot of garbage on the road, he often reduces the vehicle speed and improves the cleaning degree. With the change of the vehicle speed, the rotation speed and torque of the working

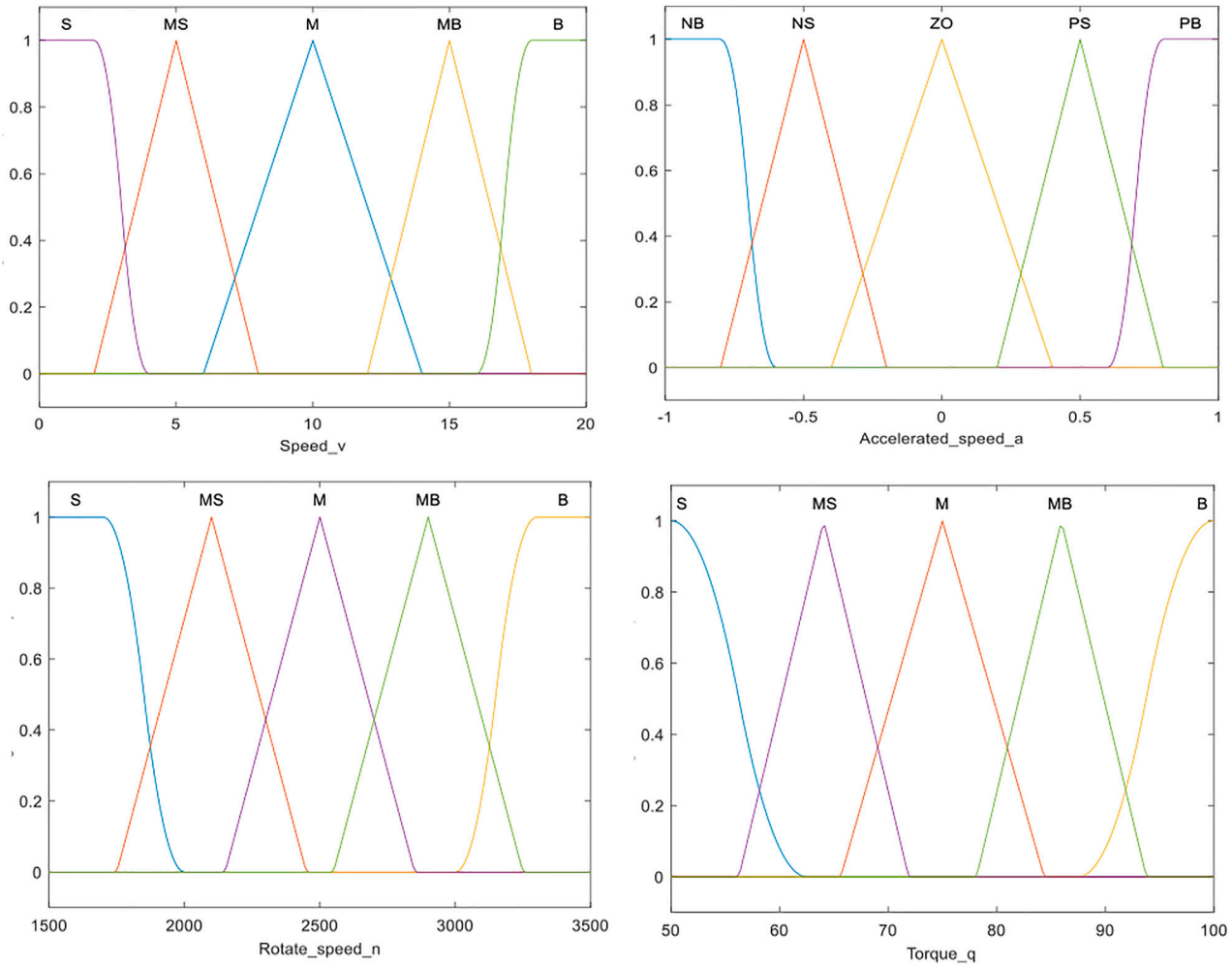

FIGURE 4 | Membership function of input and output variables.

motor also varies. Therefore, this paper selects the vehicle speed v and acceleration a as the input, and the rotation speed of the working motor n, Torque q is the output, and a two-dimensional fuzzy controller is designed.

In the fuzzy control module, the fuzzy subsets, domains, and membership functions of input and output variables are defined. The explanation is as follows: The domain of the vehicle speed during the operation of the vacuum vehicle is set as (0, 20) km/h, and the fuzzy subset is taken as (S, MS, M, MB, B), which indicate that the vehicle speed is at low speed, low-to-medium speed, medium speed, medium-to-high-speed, and high-speed state respectively, the domain of the vacuum vehicle acceleration a is determined as (−1,1) m/s^2, and its fuzzy subset is taken as: (NB, NS, ZO, PS, PB). It represents the acceleration is negatively large, negatively small, zero, positively small, and positively large. For output, the fuzzy domain of the operating motor speed n is determined to be (1500, 3500) r/min, use (S, MS, M, MB, B) to correspond to low speed, medium-low speed, medium speed, medium high speed, high-speed, The fuzzy domain of torque q is (50, 100) Nm, (S, MS, M, MB, B) indicates that the working motor is in the state of the small, medium-small, medium, medium-large, and large torque, respectively.

The membership function is often formulated based on experience. This article refers to some related literature (Cui et al., 2019; Luo et al., 2021). At the same time, according to the simulation analysis and theory, the membership function is adjusted to make it adapt to the energy control strategy. The membership degrees of input and output variables are shown in **Figure 4**:

The corresponding fuzzy rules follow the following principles:

1) Under the premise of ensuring the cleaning efficiency, when the vehicle speed increases and the acceleration is relatively large, cleaning the road with the same garbage level requires greater power of the working motor, and the speed and torque of the working motor should be increased;
2) When the vehicle decelerates and the acceleration is small, it is less difficult to vacuum. To reduce energy consumption, the rotation speed and torque of the working motor should be reduced accordingly.

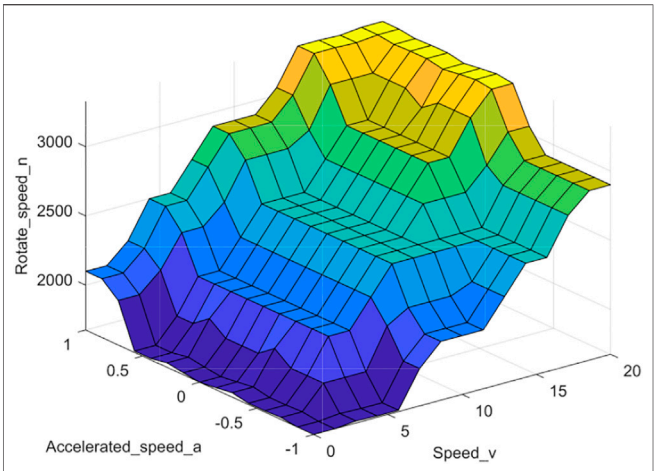

FIGURE 5 | Fuzzy control reasoning surface.

Based on the above rules, the fuzzy logic rules expressed by if-then sentences are established, and the inference surface of fuzzy control deduced is shown in **Figure 5**.

4.2 Driving Strategy

The driving strategy should meets the drivers' intention while maintain the motor works in the relatively high efficiency region. The proper driving strategy could extend the mileage of the electric vehicle (Asher et al., 2019). The drive motor torque control strategy proposed in this paper adopts a closed-loop control strategy that combines driver input and feedback of the vehicle state parameter. It does not only reflect the driver's actual driving intentions but also considers the current vehicle system state. **Figure 6** illustrates the torque control architecture. Among them, the output torque is defined as:

$$T = T_{eco} + T_{com} \tag{4}$$

$$T_{com} = \begin{cases} 0, T_{eco} > T_{act} \\ \Delta T, T_{eco} < T_{act} \end{cases} \tag{5}$$

Where, T_{eco} is the economic torque, T_{com} is the compensation torque, and T_{act} is the actual torque.

4.2.1 Economic Torque MAP

During the operation of the vacuum vehicle, the driver obtains different required motor torques by controlling the position of the accelerator pedal. The operating characteristics of the motor can well meet the vehicle's high torque at low speed and high power demand at high speed. To make the torque output corresponding to different accelerator pedal position more uniform, this paper will adopt the following interval division:

$$T_e = \begin{cases} LT_{\max}, & n \le n_e \\ \dfrac{9550 LT_{\max} n_e}{n}, & n > n_e \end{cases} \tag{6}$$

Where, T_e is the target demand torque, L is the torque load factor, $T_{\max}$ is the peak torque of the motor, n_e is the base speed, and n is the current speed of the motor.

It can be seen from **Figure 3** that the working efficiency is the highest when the motor speed n is within the range of 1700–4500 rpm, and the accelerator pedal position S is set as 40–80%. The relationship between them is shown in **Table 2**. According to **Eq. 7**, the relationship between the vehicle speed and rotation speed of the motor is established.

$$n = \frac{i_g i_0 u}{0.377 r} \tag{7}$$

Where, i_g is the transmission ratio, i_0 is the main reducer transmission ratio, u is the vehicle speed and r is the wheel rolling radius.

In this case, the corresponding vehicle speed is around 34 km/h-91 km/h. Assuming that the vehicle is driving at a constant speed on the road without any slope, ignoring the gradient

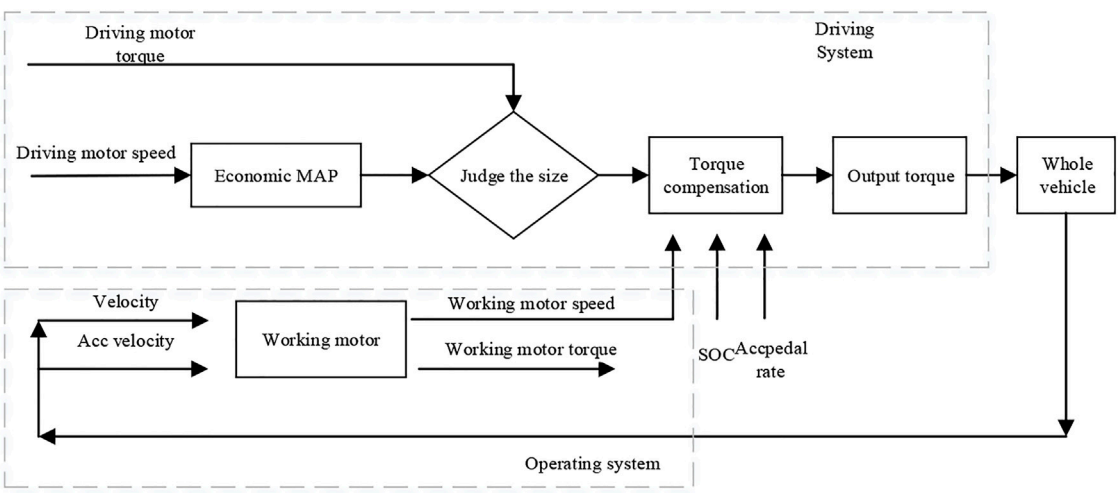

FIGURE 6 | Torque control architecture.

TABLE 2 | The relationship between motor speed *n* and accelerator pedal opening S.

***n* (rpm)**	**1700**	**2400**	**3100**	**3800**	**4500**
S (%)	40	50	60	70	80

TABLE 3 | Relationship between speed *n* and torque load factor L.

n	**1700**	**2400**	**3100**	**3800**	**4500**
S	40%	50%	60%	70%	80%
Tneed	50.4	57.2	66.2	77.6	91.2
Tpmax	561.7	398	308	251.3	212.2
L	0.09	0.144	0.216	0.308	0.4309

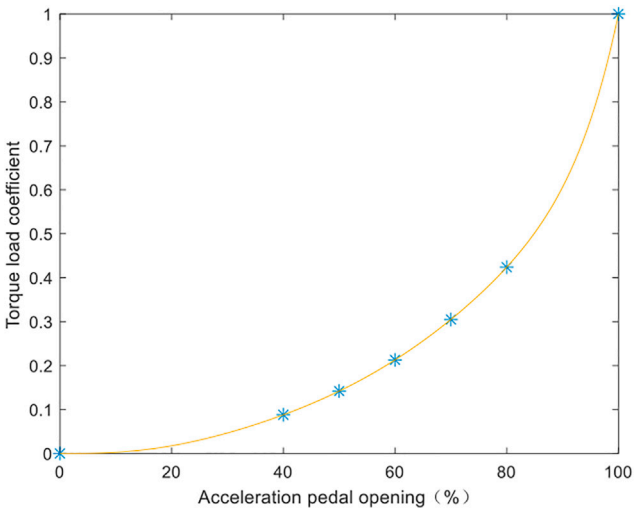

FIGURE 7 | Relationship between accelerator pedal opening S and torque load coefficient L.

resistance and acceleration resistance, the following formula can be obtained:

$$T_{need} = \left(mgf + \frac{C_d A u^2}{21.15} \right) \frac{u}{3600\eta_t} \frac{9550}{n} \tag{8}$$

Where, T_{need} is the demand torque.

Define the torque load factor L. The relationship between the speed and torque load coefficients obtained is shown in **Table 3**.

$$L = \frac{T_{need}}{T_{p\max}} \tag{9}$$

Where, $T_{p\max}$ is the maximum torque, which can be obtained from **Figure 2**.

Using the curve for fitting, the relationship between the accelerator pedal position S and the torque load coefficient L is shown in **Figure 7**.

It can be seen from **Figure 7**, that when the accelerator pedal opening is small, the corresponding torque load coefficient is small and at the same time torque difference is small, this makes the maneuverability of the vehicle better. It is conducive to the long-term stable driving of the pure electric vacuum vehicle. When the accelerator pedal opening is increased, the torque difference increases and the motor demand torque response is more sensitive. The final economic torque MAP is shown in **Figure 8**.

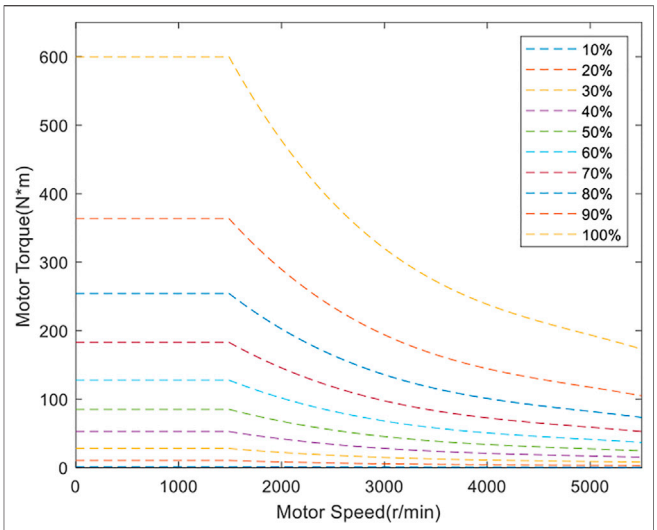

FIGURE 8 | Economic torque MAP.

4.2.2 Compensation Torque

From **Formula 5**, when the economic torque found by the actual speed is less than the actual torque, a compensation torque is set, otherwise, the compensation torque is 0. In this paper, a compensation torque fuzzy controller is designed to obtain the value of ΔT.

The acceleration pedal change rate, operating motor speed, and battery SOC were selected as input variables to calculate the compensation torque increment by fuzzy reasoning.

The fuzzy subsets of SOC are defined as: (S, M, B), representing low, medium, and high respectively; The input range of operating motor speed is defined as 1500–3500 r/min, and (S, M, B) is used to correspond to low, medium and high-speed states. The input of acceleration pedal opening change rate is defined as −1 ~ 1, and it is defined as (S, MS, M, MB, B) in the case of slow to urgent.

In the operation process, when the SOC is high, the operating motor speed is low, and the acceleration pedal opening change rate is large, it reflects that the driver has a high-power driving demand, and relatively high compensation torque is given. When the SOC is low, the operating motor speed is high, the acceleration pedal change rate is small, the driver's power demand is relatively low and the compensation torque is small.

At the same time, considering that the sudden change of torque during the driving process of the vehicle will cause a greater impact, which will affect the ride comfort, it is necessary to consider the limit of the impact degree when determining the compensation torque increment (Wan, 2016), the expression of the impact degree:

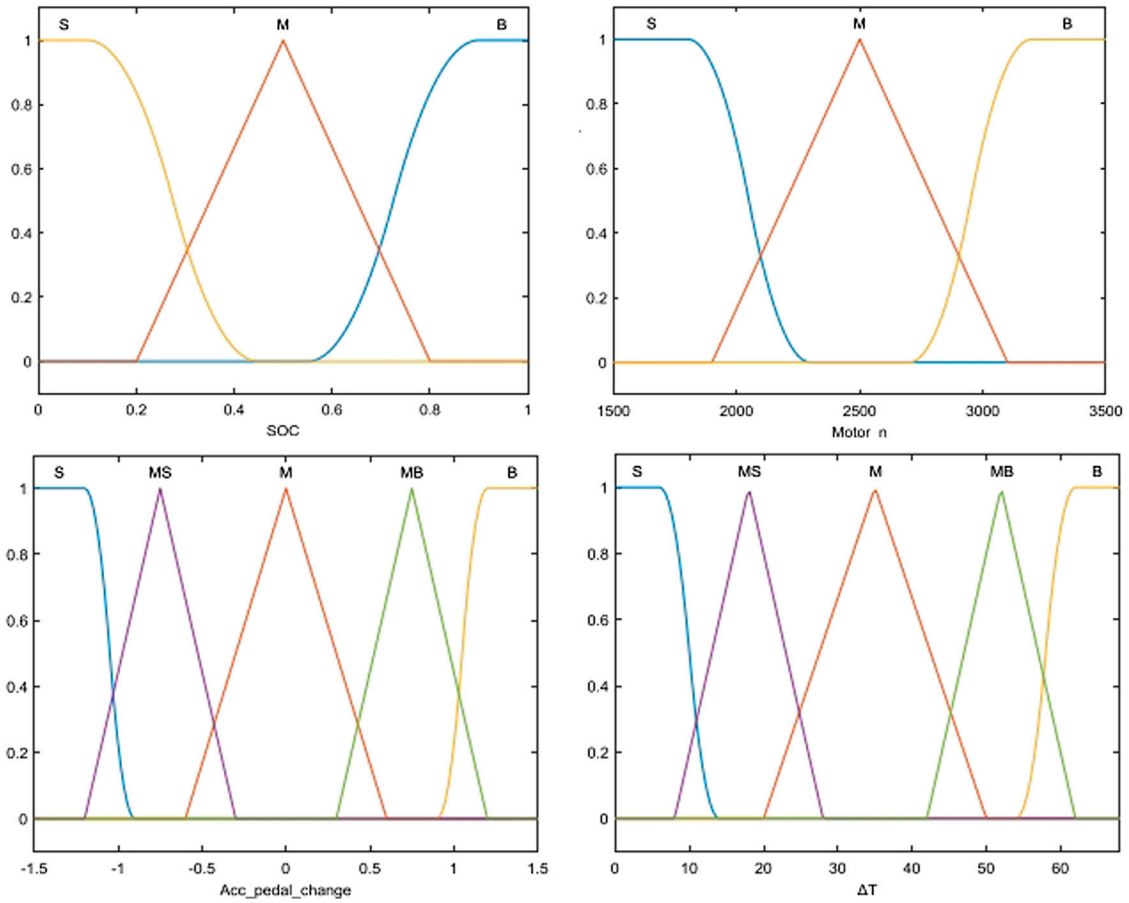

FIGURE 9 | Membership function of input and output variables.

TABLE 4 | Torque compensation fuzzy rules.

SOC	Operating motor speed	Acceleration pedal opening change rate (%)				
		S	MS	M	MB	B
B	S	MS	M	MB	B	B
	M	MS	MS	M	MB	B
	B	S	S	MS	M	MB
	S	MS	M	MB	B	B
M	M	S	MS	MS	M	MB
	B	S	MS	M	M	MB
	S	MS	MS	M	MB	B
S	M	S	S	MS	M	MB
	B	S	S	MS	M	MB

$$j = \frac{d^2u}{dt^2} \approx \frac{1}{m}\left(\frac{i\eta_t}{r}\frac{dT}{dt}\right) \tag{10}$$

Where, j is the impact received while driving, also called the rate of change in acceleration, η_t is the transmission efficiency.

From **Formula 10**, it can be obtained that the impact degree of the vehicle during driving is proportional to the rate of change of torque. The German shock degree standard stipulates $j \leq 10\,\mathrm{m/s^3}$, substituting the vehicle parameters and taking a 10% margin, the maximum value of the compensation torque ΔT is 60.1 Nm. The membership degrees of input and output variables are shown in **Figure 9**. The fuzzy rules of torque compensation are shown in **Table 4**.

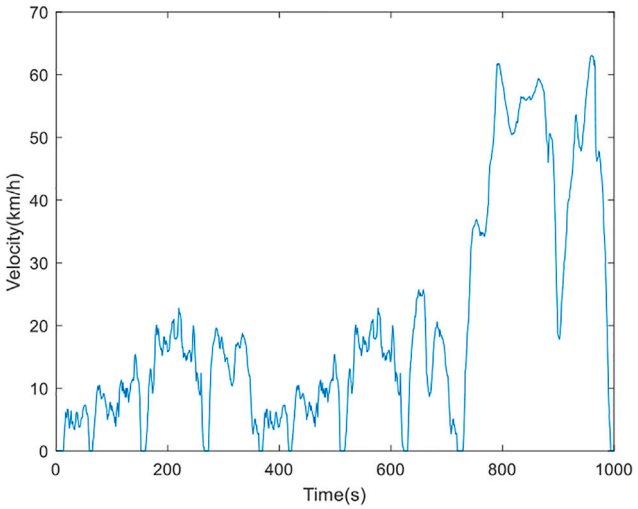

FIGURE 10 | Road spectrum diagram of vacuum vehicle.

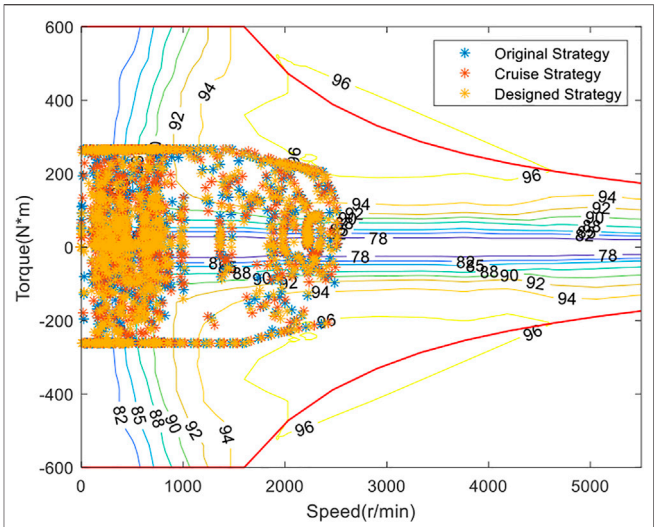

FIGURE 12 | Distribution of working efficiency points of the drive motor.

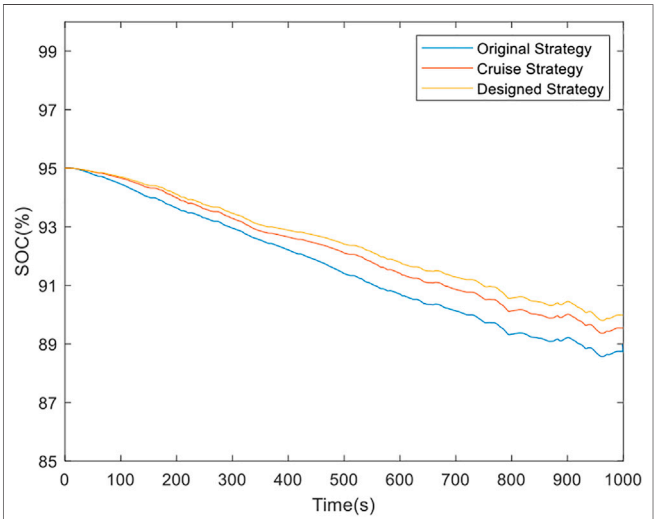

FIGURE 11 | SOC trend changes.

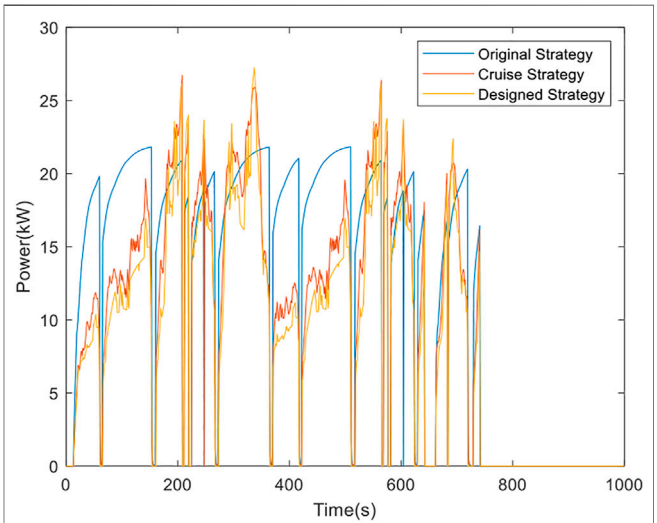

FIGURE 13 | Comparison of power consumption of operating motor.

5 JOINT SIMULATION AND SIMULATION RESULT ANALYSIS

This paper uses a pure electric vacuum vehicle as the research object to verify the effectiveness and superiority of the strategy. AVL Cruise software is used to build a vehicle model, and the energy-saving control model analyzed is built in MATLAB/Simulink software. In the simulation process, the performance of the original strategy, design strategy, and CRUISE strategy are compared. The original strategy refers to the strategy that the bodywork system works with the same power and there is no vehicle state feedback during driving. The CRUISE strategy refers to the strategy that comes with the CRUISE software and uses a linear method to adjust the power of the bodywork. The results were analyzed by co-simulation.

5.1 Establishment of Operating Conditions

Setting the condition is an important step in AVL CRUISE software simulation. The operating conditions of pure electric vacuum vehicles include working conditions and transition conditions, in which the working conditions account for more than 75% (Ma et al., 2018). Referring to the establishment process of NEDC, Tang et al. constructed a typical working condition of a sweeping vehicle (Tang, 2020). In this paper, part of the working conditions spectrum of CHTC is selected as the reference for transition conditions. Where, CHTC condition is the driving condition for Chinese automobiles used by the commercial vehicles with a total mass greater than 5500 kg. It includes the urban cycle (342 s), suburban cycle (988 s), and high-speed cycle (470 s). And the working conditions of vacuum vehicles in a

TABLE 5 | Comparison of energy consumption per 100 km and driving range.

Condition	Strategy	Energy consumption per 100 km (kWh/100 km)	Driving range (km)
Vacuum vehicle operating condition	Original Strategy	88.35	60.941
	Cruise Strategy	75.65	71.012
	Designed Strategy	70.09	76.772

certain area are combined to build the spectrum of the operating condition as shown in **Figure 10**.

5.2 Simulation Analysis

In the case of a vacuum vehicle running in AVL CRUISE software, **Figure 11** shows the comparison of SOC change trends under three strategies. The SOC decreases at a lower rate when energy-saving strategies are initiated. The original strategy has the minimum SOC at the end of the simulation.

Figure 12 shows the distribution of the working efficiency points of the driving motor. According to the simulation results, although the control strategy requires the motor to work in the optimal region, the driving motor must meet the requirements of high-speed transition, while the vacuum vehicle has been operating in the low-speed zone for a long time, most of the working points are in the range of 78–88%. The proportion of efficiency points in the high-efficiency area of motors with energy management strategies has increased compared with the original strategies.

Figure 13 is a comparison diagram of the power consumption of the working motor. It can be seen that the energy-saving strategy based on fuzzy control can automatically adjust the working power of the bodywork system. Compared with the other two strategies, the power consumption is smaller to achieve the effect of energy-saving. At the same time, it can be seen from the figure that the working motor of the vacuum vehicle is turned on under the working condition, and after the 750s, it is the transition condition, and the working motor does not work.

The energy consumption per 100 km and the driving range obtained in the AVL CRUISE with the three strategies are compared in **Table 5**.

According to the simulation results under the constructed vacuum vehicle operating conditions, the energy consumption per 100 km of the vehicle is reduced from 88.35 kWh/100 km in the original strategy and 75.65 kWh/100 km in the Cruise strategy to 70.09 kWh/100 km in the design strategy. With a lower energy consumption, the charging and discharging time of the battery can be decreased, which means its life cycle can be extended.

Overall, the energy management strategy of the vacuum vehicle established in this paper reduces the power consumption per 100 km by 20.66%, and the driving range increases by 20.62%. In summary, the energy-saving strategy of electric vacuum vehicles based on fuzzy control proposed in this paper can effectively benefit the battery life cycle, reduce battery energy consumption and increase driving range.

6 CONCLUSION

To reduce the energy consumption of pure electric vacuum vehicles during operation, an energy management strategy based on fuzzy control is proposed. To verify the feasibility and superiority of the proposed control strategy, a vehicle dynamics model was established by AVL CRUISE and evaluated on the Simulink/CRUISE co-simulation platform. The conclusions of the study are as follows:

1) Based on the current road condition and vehicle status, the proposed fuzzy controller succeeds in managing the rotation speed and torque of the operating motor in a relatively high-efficiency region.
2) According to the simulation, compared with the original strategic control, the energy-saving strategy proposed in this paper reduces the economic performance index (power consumption per 100 km) by 20.66% and extends the driving range by 20.62%.

Since the energy consumption of the hydraulic system and mechanical lifting system is much lower than the motors, they are ignored. Therefore, the accuracy of the established model can be further improved by considering these factors in the next stage. Hence, the superiority of the proposed control strategy can be enhanced.

DATA AVAILABILITY STATEMENT

The raw data supporting the conclusions of this article will be made available by the authors, without undue reservation.

AUTHOR CONTRIBUTIONS

YW contributes to the writting of the manuscript, SZ provides the idea of this paper. YL and LZ help YW to finish this work.

FUNDING

This study was funded by the Innovative Research Team Development Program of Ministry of Education of China (IRT_17R83), and the 111 Project (B17034) of China.

REFERENCES

Asher, Z. D., Patil, A. A., Wifvat, V. T., Frank, A., Samuelsen, S., Samuelsen, S., et al. (2019). Identification and Review of the Research Gaps Preventing a Realization of Optimal Energy Management Strategies in Vehicles. *SAE Int. J. Alt. Power.* 8 (2), 133–149. doi:10.4271/08-08-02-0009

Cui, P., Ding, A., Shen, Y., and Wang, Y.-X. (2019). "Hybrid Fuel Cell/Battery Power System Energy Management by Using Fuzzy Logic Control for Vehicle Application," in 2019 IEEE 3rd International Conference on Green Energy and Applications (ICGEA), Taiyuan, China, 16-18 March 2019. doi:10.1109/ICGEA.2019.8880770

Dong, J. (2019). *Research on Energy-Saving Strategy of Multi-Motor Power System of Electric Sweeper*. Shanxi, China: Taiyuan University of Science and Technology. Available at: https://kns.cnki.net/KCMS/detail/detail.aspx?dbname=CMFD202101&filename=1019613483.nh.

Guo, C., Cao, D., Qiao, Y., Yang, Z., Chang, Z., Zhao, D., et al. (2021). Energy Management Strategy of Extended-Range Electric Bus Based on Model Predictive Control. *SAE Int. J. Commer. Veh.* 14 (2), 229–238. doi:10.4271/02-14-02-0018

Justo, J. J., Mwasilu, F., Kim, E.-K., Kim, J., Choi, H. H., and Jung, J.-W. (2017). Fuzzy Model Predictive Direct Torque Control of IPMSMs for Electric Vehicle Applications. *IEEE/ASME Trans. Mechatron.* 22 (4), 1542–1553. doi:10.1109/tmech.2017.2665670

Kant, K., Kirtley, J. L., Iyer, L. V., and Schlager, G. (2021). Finite Element Simulation-Based Design Optimization of Permanent Magnet Motors Considering Drive Cycle. *SAE Int. J. Alt. Power.* 7 (2), 157–165. doi:10.4271/14-10-02-0012

Lee, J. G., Yeo, H. K., Jung, H. K., Kim, T. K., and Ro, J. S. (2019). Electromagnetic and Thermal Analysis and Design of a Novel→structured Surface→mounted Permanent Magnet Motor with High→power→density. *IET Electr. Power Appl.* 13, 472–478. doi:10.1049/iet-epa.2018.5322

Li, J. H. (2020). *Research on Energy-Saving Strategy of Pavement Garbage Identification and Top-Loading System of a Certain Type of Sweeper*. Jilin, China: Jilin University. Available at: https://kns.cnki.net/KCMS/detail/detail.aspx?dbname=CMFD202002&filename=1020644024.nh.

Li, Y. J., Zhang, Y. P., Zhu, Y. D., and Huang, L. L. (2019). Analysis of the Influence of Working Parameters of Suction Sweepers on Cleaning Efficiency. *Mech. Eng. Automation* 48 (06), 19–20+23.

Liu, J., Zhong, H., Wang, L., and Chen, H. (2019). *A Novel Torque Distribution Strategy for Distributed-Drive Electric Vehicle Considering Energy Saving and Brake Stability*. SAE Technical Paper 2019-01-0334. doi:10.4271/2019-01-0334

Long, Z.-M., Guan, B.-J., Chen, S.-Y., Chen, G.-J., and Guo, S.-Q. (2018). "Modeling and Simulation of Hydraulic Motor Tracking Servo Motor Driving Load," in 2018 International Conference on Smart Grid and Electrical Automation (ICSGEA), Changsha, China, 9-10 June 2018. doi:10.1109/icsgea.2018.00037

Luo, R., and Niu, Z. G. (2020). Drive Control Strategy of Pure Electric Vehicle Based on Pattern Recognition. *Mech. Des. Manuf.* 58, 37–41. doi:10.19356/j.cnki.1001-3997.2020.11.010

Luo, X., Deng, B., and Gan, W. (2021). Research on Fuzzy Control Strategy and Genetic Algorithm Optimization for Parallel Hybrid Electric Vehicle. *J. Phys. Conf. Ser.* 1986, 012106. doi:10.1088/1742-6596/1986/1/012106

Ma, C. S., Wang, K., and Ji, Q. X. (2018). Simulation Research on Power System of Pure Electric Sweeper Based on ADVISOR. *Equip. Manuf. Technol.* 2018 (09), 228–230.

Ruan, J., and Song, Q. (2019). A Novel Dual-Motor Two-Speed Direct Drive Battery Electric Vehicle Drivetrain. *IEEE Access* 7, 54330–54342. doi:10.1109/access.2019.2912994

Shao, Z. G. (2005). *Design of Electric Control System of Sweeper and Research on Speed Control of Disc Brush*. Nanjing, China: Nanjing University of Science and Technology. Available at: https://kns.cnki.net/KCMS/detail/detail.aspx?dbname=CMFD0506&filename=2005117818.nh.

Tang, Z. C. (2020). *Establishment and Model Characterization of Typical Operating Conditions of Sweepers Based on Visual Perception*. Jilin, China: Jilin University. Available at: https://kns.cnki.net/KCMS/detail/detail.aspx?dbname=CMFD202002&filename=1020644090.nh.

Tian, Z., Yang, B., Peng, D., Liu, Z., and Tan, G. (2020). *Pre-Curve Braking Planning of Battery Electric Vehicle Based on Vehicle Infrastructure Cooperative System*. Nanjing, China: WCX SAE World Congress Experience. SAE Technical Paper 2020-01-1643. doi:10.4271/2020-01-1643

Wan, H. T. (2016). *Research on Drive Control Strategy of Pure Electric Vehicle*. Beijing, China: Beijing Institute of Technology. Available at: https://kns.cnki.net/KCMS/detail/detail.aspx?dbname=CMFD201801&filename=1018812602.nh.

Wang, H. Y., Jiang, Z. L., Chao, P. B., Xiong, D. F., and Dai, Y. (2021). Analysis and Optimization of Stator Iron Loss of Permanent Magnet Synchronous Motor for Vehicles. *Mot. Control Appl.* 63 (09), 96–102+109.

Wang, Z., Han, Z., Ding, L., and Wang, G. (2020). Development of an Efficiency Model for Electronically Commutated Motor Fan Systems in Air Handling Units. *Sci. Technol. Built Environ.* 27, 329–340. doi:10.1080/23744731.2020.1797443

Wu, B., and Zhang, S. (2021). Energy Management Strategy for Dual-Motor Two-Speed Transmission Electric Vehicles Based on Dynamic Programming Algorithm Optimization. *SAE Int. J. Elec. Veh.* 10 (1), 19–31. doi:10.4271/14-10-01-0002

Wu, C.-Y., Liu, H.-J., Cheng, C.-Y., Hu, J.-S., and Tsai, M.-C. (2019). "Efficiency Regulation Algorithm for Dual-Motor Drive Electric Vehicles," in 2019 IEEE Vehicle Power Propulsion Conference (VPPC), Hanoi, Vietnam, 14-17 Oct. 2019. doi:10.1109/vppc46532.2019.8952469

Yang, M. H. (2016). *Research on Overall Design and Dust Collection System of Pure Electric Vacuum Sweeper*. Shandong, China: Shandong University of Technology. Available at: https://kns.cnki.net/KCMS/detail/detail.aspx?dbname=CMFD201701&filename=1016230841.nh.

Ye, M., Tan, G., Lei, F., Chen, K., Feng, J., and Zhao, F. a. (2021). *Research on Parallel Regenerative Braking Control of the Electric Commercial Vehicle Based on Fuzzy Logic*. Wuhan, China: WCX SAE World Congress Experience. SAE Technical Paper 2021-01-0119. doi:10.4271/2021-01-0119

Zhai, L., Sun, T., and Wang, J. (2016). Electronic Stability Control Based on Motor Driving and Braking Torque Distribution for a Four In-Wheel Motor Drive Electric Vehicle. *IEEE Trans. Veh. Technol.* 65 (6), 4726–4739. doi:10.1109/tvt.2016.2526663

Zhang, D. B. (2020). Development Status and Future Trends of New Energy Sweepers in My Country. *Automot. Pract. Technol.* 45 (03), 27–29. doi:10.16638/j.cnki.1671-7988.2020.03.010

Zhang, P. Z. (2014). *Research on Drive Control and Energy Management Strategy of Pure Electric Car*. Jilin, China: Jilin University. Available at: https://kns.cnki.net/KCMS/detail/detail.aspx?dbname=CMFD201702&filename=1016123924.nh.

Zhang, T. J. (2019). *Design and Simulation of Hydraulic System of Wet Road Sweeper*. Shandong, China: Shandong University. Available at: https://kns.cnki.net/KCMS/detail/detail.aspx?dbname=CMFD201902&filename=1019077654.nh.

Conflict of Interest: Author LZ was employed by the company Wuhan Road Rover Intelligent Technology Co., Ltd. Author SZ was employed by the company Liuzhou Wuling Automobile Industry Co., Ltd.

The remaining authors declare that the research was conducted in the absence of any commercial or financial relationships that could be construed as a potential conflict of interest.

frontiers | Frontiers in Energy Research

ORIGINAL RESEARCH
published: 20 June 2022
doi: 10.3389/fenrg.2022.911872

A Transition Mechanism for the Participation of Renewable Energy Generation Companies in Competitive Electricity Spot Markets

Kun Wang[1], Hui Deng[2], Jiajia Yang[1], Chengwei Xu[2], Ziqing Zhou[2], Fushuan Wen[3] and Donglian Qi[3]*

[1]College of Electrical Engineering, Zhejiang University, Hangzhou, China, [2]State Grid Zhejiang Electric Power Co., Ltd. Research Institute, Hangzhou, China, [3]Hainan Institute, Zhejiang University, Sanya, China

Under the China's 'dual carbon' national goal–reaching peak carbon emissions by 2030 and achieving carbon neutrality by 2060, one of the key issues in China is how to smoothly transit from a fixed-price mode to a competitive market pricing mode for renewable energy generation companies. Aiming at minimizing governmental subsidies and maximizing the fairness among renewable energy generation companies, a multi-agent three-layer transition mechanism with the transactions of green certificates considered is proposed in this paper. Through adjusting subsidy policies, the developed transition mechanism can stimulate the renewable energy generation companies to gradually participate in the competitive electricity spot market. Specifically, a multi-market multi-agent transaction framework in the transition mechanism is first established. Then, in order to derive the important parameters of the transition mechanism, a method that decouples the electricity market and the green certificate market is designed. Finally, the feasibility and efficiency of the proposed transition mechanism are demonstrated through numerical examples.

Keywords: carbon neutral, renewable energy generation, electricity spot market, tradable green certificate, contract coverage

OPEN ACCESS

Edited by:
Xue Lyu,
University of Wisconsin-Madison, United States

Reviewed by:
S. N. Singh,
Indian Institute of Technology Kanpur, India
Qin Wang,
Electric Power Research Institute (EPRI), United States
Weijia Liu,
National Renewable Energy Laboratory (DOE), United States

****Correspondence:***
Fushuan Wen
wenfs@hotmail.com

Specialty section:
This article was submitted to Smart Grids, a section of the journal Frontiers in Energy Research

Received: *03 April 2022*
Accepted: *24 May 2022*
Published: *20 June 2022*

Citation:
Wang K, Deng H, Yang J, Xu C, Zhou Z, Wen F and Qi D (2022) A Transition Mechanism for the Participation of Renewable Energy Generation Companies in Competitive Electricity Spot Markets. Front. Energy Res. 10:911872. doi: 10.3389/fenrg.2022.911872

1 INTRODUCTION

The Renewable Energy Sources (RESs) in China have been developing rapidly with the goal of reaching peak carbon emissions by 2030 and achieving carbon neutrality by 2060 (The State Council Information Office of the People's Republic of China, 2020). By the end of 2020, the total installed capacity of RES-based generation in China reached 530 million kW, accounting for 25.5% of the total generation installed capacity. The rapid development of RESs also results in the large amount of subsidies to RES investors. In order to mitigate financial burdens on the government due to RES subsidies, the energy administrative authorities have been continuously lowering the benchmark electricity prices for photovoltaic and wind power generation. In June 2021, the National Development and Reform Commission issued a relevant document (National Development and Reform Commission of China, 2020), stipulating that the central government would no longer subsidize the newly registered centralized photovoltaic power plants, industrial and commercial distributed photovoltaic projects, and newly approved onshore wind power projects in 2021. This will help to alleviate the financial burden, but it may lead to a sharp decline in the growth rate of RES installations.

In order to alleviate the financial burden of subsidy while promoting the development of renewable energy generation, mature electricity markets have taken a number of measures. The German Ministry of Energy adopted the policy of feed-in premium in 2014, which guide RESs to participate in the competition in the electricity spot market (Schallenberg-Rodriguez and Haas, 2012). It is a transitional way for RESs to gradually shift from full acquisition to full competition (Gawel and Purkus, 2013). In contrast, the United States uses the renewable energy quota system to promote the development of RESs (Barbose et al., 2016; Luo, 2016). At present, more than 30 states in the United States have established a renewable energy quota system, which is conducive to encouraging RESs to adjust its own output according to market supply and demand, and reduce the pressure on system operation. The United Kingdom has implemented a policy of renewable obligation (RO) since 2002, which is similar to a quota system (García-Alvarez et al., 2017). Since the implementation of the RO policy, the RESs has developed rapidly in United Kingdom, and the average annual growth rate of power generation has reached 12%. In addition, both the United States and the United Kingdom allow RES units to participate in the electricity spot market (Kilinc-Ata, 2016).

Overall, the combination of "financial contract + spot market" and quota system is often adopted in practical electricity markets around the world (Ren et al., 2022), in which RES units participate in the electricity spot market equally with other types of generation units, and the risks of spot market prices are hedged by signing Contracts For Difference (CFD) between power supply companies and RES generation companies. Meanwhile, the establishment of a marketplace for Tradable Green Certificates (TGCs) is also deployed as an important measure to encourage the development of RES generation. The fixed-price procurement of RES generation as a subsidy for RES generation can be gradually replaced by governmental compensations to TGC transactions. This will not only help mitigate the governmental financial burdens but also promote the participation of RES generation units in competitive electricity spot markets, which is align with the requirements of sustainable development.

Currently, there is still no effective market mechanism to support the participation of RES generation units in electricity spot markets in China. On the one hand, the income of RES-based generation companies cannot be guaranteed after the participation, which will damage the confidence of RES-based generation investors, and is not conducive to the long-term RES generation development. On the other hand, the participation of RES generation units in the electricity spot market may increase the market volatility and lead to severe fluctuations in spot market prices (Xu et al., 2020; Yang et al., 2020). Therefore, the participation of RES generation units in electricity spot markets requires an effective transition mechanism.

Some publications are availabe on the participation mechanism/mode of RES generation units in electricity spot markets. Specifically, the impacts of RESs on electricity spot market due to the uncertainty are examined from both theoretical and empirical perspectives in (Li and Xu, 2021; Zhao et al., 2021). An electricity market transition model considering is proposed in (Shinde et al., 2021) to represent a possible requirement to undertake system balancing with increasing amounts of Intermittent RESs. A bilateral transaction model based on the Bayesian game is proposed in (Kong et al., 2021) to calculate the Bayes-Nash equilibrium point of the electricity spot market with high penetration RESs, thereby evaluating the smoothness of the participation of RESs in the electricity spot market. It is pointed out in (Gu, 2020) that the government-authorized contract system needs to be adopted collaboratively to ensure the accommodation of RES generation and external electricity, and the percentage of electricity covered by government-authorized contracts should be adjusted reasonably to achieve a smooth transition to the competitive market is proposed. A transition mechanism for the market participation of RESs based generation units, which can gradually guide the transition of RES generation units to the electricity spot market by adjusting the percentage of electricity covered by medium- and long-term contracts is proposed in (Dai and Chen, 2020). However, the specific method for determining the percentage of electricity is not given.

In addition, none of the above publications considers the impacts of TGC transactions on the spot electricity market participation of RES generation units. Since 2017, a green certificate voluntary subscription market has been in operation in China, laying the foundation for the implementation of the mandatory quota system. As an important measure to support the quota system, TGC trading has a positive effect on reducing the burdens on government financial subsidies and restructuring the revenue of renewable energy generation. A system dynamic model is established, and case studies are conducted in (Zhang et al., 2021; Zhu et al., 2022), pointing out that compared with fixed price purchases, the development efficiency and economic benefits of RES generation units under the quota system are higher. A study that analyzes the overall framework, core elements and supporting measures of the quota system in recent years together with China's current national conditions, and puts forward a dual-track system of "fixed electricity price + quota system" is established in (Jiang et al., 2020). Another study that shows the role of the penalty mechanism of the quota system and points out that setting a reasonable penalty can support the market mechanism to improve the income of RES generation units, thereby reducing the financial burden of subsidies on the government is proposed in (Zhang et al., 2017).

In order for the sustainable development of renewable energy generation and the relief of the government financial burdens, it is of great significance to explore and study the transition mechanism for RES units to participate in the electricity spot market. To fill this knowledge gap, the main contributions of this paper are summarized as follows:

1) A new transition mechanism is proposed to reduce the financial burden of governmental subsidies and guide the participation of RES units in the electricity spot market.
2) A multi-agent three-layer optimal decision-making model is established to calculate the contract coverage ratio (CCR). CCR denotes the percentage of electricity traded *via* CFDs over the total on-grid electricity and is an important parameter in the transition mechanism. The method for determining the CCR of RES units is proposed to maximize the income of generators while taking into

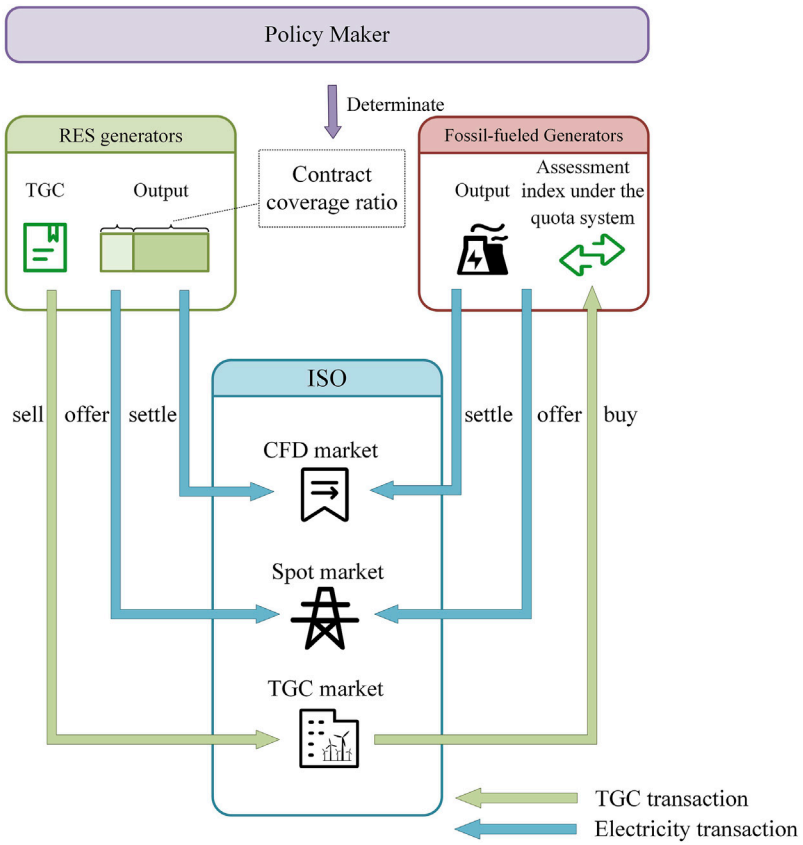

FIGURE 1 | Framework of market transactions considering RES unit participation.

account the clearing results of the electricity spot market and the green certificate market.

3) Extensive numerical experiments using practical electricity market data are conducted to demonstrate the feasibility and efficiency of the proposed transition mechanism and solving methods. Both short-term and medium-long-term simulations are carried out in the experiments.

The rest of paper is organized as follows: **Section 2** introduces the established transition mechanism for RES units to participate in the electricity spot market. **Section 3** presents the method for determining the CCR. Extensive numerical experiments are employed to illustrate the proposed model in **Section 4**, and the simulation results are also analyzed. Finally, the paper is concluded in **Section 5**.

2 TRANSITION MECHANISM FOR THE PARTICIPATION OF RENEWABLE ENERGY GENERATORS IN THE ELECTRICITY SPOT MARKET

How to balance the financial burdens of government subsidies and the incentives for renewable energy development is an important issue in the electricity market reform. In the early stage of market development, RES generators face difficulties due to their weak market competitiveness, immature technologies, and recovery of investment costs, thus government financial subsidies are needed (Upton and Snyder, 2017). During this period, the government can sign CFDs with the RES generators to ensure their income and encourage their continued development. With the continuous progress of the electricity market reform, the number of RES generation companies is increasing, and the total amount of government subsidies will be increasing accordingly. In order to avoid such a situation, it is necessary to gradually reduce the CFDs for RES units, and guide RES units to participate in the electricity spot market. Meanwhile, through cooperation with the TGC market, the subsidies for RES units can be gradually shifted from government financial subsidies to TGC transaction subsidies (Ma et al., 2017), so as to encourage RES companies to carry out technological innovation while ensuring the consumption of green electricity. The market transaction framework of the proposed transition mechanism is shown in **Figure 1**.

In the above framework, the income of RES units is divided into three parts, namely the income from CFDs, the income of selling electricity in the spot market, and the income of selling TGCs. According to existing policy (National Development and Reform Commission of China, 2020), depending on the number

TABLE 1 | Comparison of the two types of RES units.

RES units	Project registered time	CFD price	Number of TGCs issued
Type I	Before 2021	Including the governmental premium subsidy, which is higher than the local benchmark price of coal-fired power generation	Issued for electricity traded in the spot market
Type II	In and after 2021	Local benchmark price of coal-fired power generation	Issued for all of the RES output

of issued TGCs and the price of CFDs, the calculation rules for RES units with different registered times are different, as shown in **Table 1**. Therefore, this paper categorizes RES units into two types.

The RES units in type I are those which was put into operation before 2021, and their CFD price is higher than the local benchmark price of coal-fired power generation. For these RES units, the government will subsidize for the generation output covered in the CFDs, and TGCs will be issued only for the electricity traded in the spot market. It means that only the RES generations traded in the spot market are compensated through the TGC market.

The RES units in type II are those to be put into operation after 2021, whose contract purchase price is specified as the benchmark price of local coal-fired power generation, and the CFDs of such RES units do not receive governmental subsidies. For these RES units, TGCs are issued for the electricity in both the CFDs and the spot market, thus the RES generations traded in both the CFDs and the spot market are compensated.

The CCR of RES units in the proposed transition mechanism is defined as the percentage of electricity traded *via* CFDs over the total on-grid electricity, as shown in **Eq. 1**.

$$\gamma_F = Q_F^c / \left(Q_F^c + Q_F^{sp}\right) \tag{1}$$

where γ_F is the CCR (%); Q_F^c is the electricity covered by CFDs (MWh); Q_F^{sp} is the amount of electricity allowed to be traded in the electricity spot market (MWh).

The CCR stipulates the share of RES generations entering the spot market, and also determines the amount of government financial subsidies. The CCR is a key parameter and should be determined carefully considering the system reliability requirements, the reform process of the power market and other factors. The determination of CFD coverage is also related to the revenue of RES units and the number of TGCs issued, and may affect the market strategies of fossil-fueled generation units in the spot market and TGC market. Therefore, designing an innovative method for determining the contract coverage is the key to a smooth transition of the reform.

It should be noted that the continuous development of renewable energy generation will greatly increase the uncertainty of the power system. Correspondingly, the demand for ancillary market will also increase. This will inevitably have an impact on the clearing results of the electricity spot market and the market strategies of fossil-fueled generation units. But the situation discussed in this paper is in the early stage of RES development. In other words, the impact of participation of RESs in the electricity spot market on ancillary market is not fatal. Notably, the focus of this paper is on the participation of RES in electricity energy markets, and the extension of the proposed mechanism to the ancillary market will be systematically studied in our future work.

3 MATHEMATICAL FORMULATIONS OF PROPOSED TRANSITION MECHANISM

The ratio of RES electricity generations covered by CFD contracts directly affects the amount of government financial subsidies and the income of RES units, and it is closely related to the clearing results of the spot market and the TGC market. In the transition mechanism, a three-layer optimization model is established, where the objective is to maximize the revenues for both RES units and fossil-fueled units while taking into account the outcomes of the spot market and the TGC market. The method for solving the optimal CCR is also presented.

Figure 2 illustrates the structure of decision-making model in the proposed transition mechanism. Specifically, the input parameters of the three-layer model include the predicted generation output, typical load curve, elasticity of load demand, generation constraints, network constraints, fuel costs of fossil-fueled units, and assessment weights of the quota system. In the upper-level model, the research object is the policymaker, the decision variable is the contract coverage of RES units, and the objective function is to minimize government financial subsidies and to maximize the fairness of subsidies. The contract coverage obtained in the upper model is passed to the middle-level model. The middle-level model includes the clearing models of both the electricity spot market and the green certificate market, which are managed by the Independent System Operator (ISO). The middle-level model feeds back the market clearing results to the upper model *via* simulations of the electricity spot market and the green certificate market. The lower-level model formulates the bidding strategies of RES and fossil-fueled units aiming at maximizing their income, and the optimal bidding results will be fed back to the middle-level model to complete the simulation of market operation.

3.1 Upper-Level: Decision-Making Model for Policymaker

The decision-making model for policymaker is to solve the CCR. The CCR not only determines the amount of financial subsidies, but also affects the fairness among RES units. Therefore, the upper-level model adopts a multi-objective optimization method

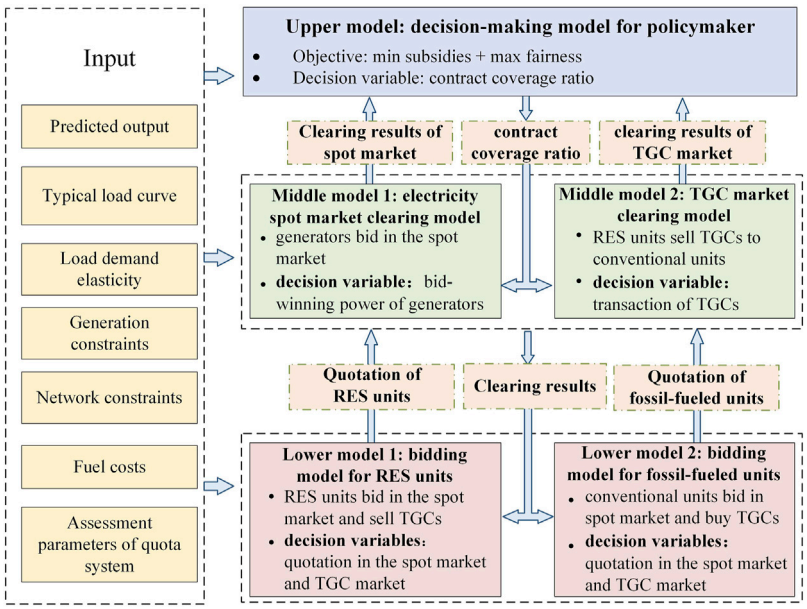

FIGURE 2 | Illustration of the three-layer optimization model for determining the CCR.

to minimize government financial subsidies while maximizing the fairness. In this section, photovoltaic (PV) generators and wind turbines are taken as examples to elaborate details of the upper-level model.

3.1.1 Objective Function

3.1.1.1 Government Financial Subsidies

Alleviating the financial burdens of governmental subsidies is the first objective of this model, which is measured by the premium CFDs for RES units. It is modeled here that the difference between the CFD price and the spot market price is the premium value of government subsidies. Therefore, the objective function based on the amount of government financial subsidies can be expressed as follows.

$$\min f_{p1} = \sum_{t=1}^{T} \left(P_{pI}^{c} - P_{t}^{sp} \right) \cdot Q_{pI,t}^{en} \cdot \gamma_{p} \tag{2}$$

where f_{p1} is the amount of government financial subsidy to the photovoltaic generation; P_t^{sp} is the spot market price during the trading period t; P_{pI}^{c} and $Q_{pI,t}^{en}$ are the CFD price of the type I photovoltaic generators and the predicted output during the trading period t, respectively; γ_p is the photovoltaic contract coverage in the decision-making period T. As mentioned earlier, based on existing policies, the government only subsidizes the type-I RES generation units. For the type-II units, the government financial subsidy is 0.

3.1.1.2 Fairness in the Benefits Among Renewable Energy Sources Generation Units

The fairness of the governmental subsidy is crucial for the policymaker. While maximizing the overall benefit of RES units, it is necessary to ensure that each unit can benefit from the transition mechanism as much as possible. Therefore, another goal of the upper-level model is to maximize the fairness of income among the same type of units. The concept of unit power generation profit as defined in **Eq. 3** is introduced to measure the fairness.

$$K_{pi,t_d} = \frac{\sum_{t=1}^{t_d} \left[P_{pi}^{c} Q_{pi,t}^{en} \gamma_p + P_t^{sp} Q_{pi,t}^{en} \left(1 - \gamma_p \right) + P_t^{gr} Q_{pi,t}^{gr} \right] - \varpi_{pi} C_p}{\sum_{t=1}^{t_d} Q_{pi,t}^{en}} \tag{3}$$

where K_{pi,t_d} is the unit power generation profit of the i^{th} photovoltaic generator in trading period t_d; t_d is the time period for calculating the unit power generation profit, which can avoid the problem that the denominator of **Eq. 3** is 0 when there is no photovoltaic output at night, usually takes $t_d = 24$; P_{pi}^{c} is the CFD price of the i^{th} photovoltaic generator; $Q_{pi,t}^{en}$ and $Q_{pi,t}^{gr}$ are the predicted output of the i^{th} photovoltaic generator and the amount of electricity traded in the TGC market in the trading period t, respectively; C_p is the levelized cost of photovoltaic generation; ϖ_{pi} is the efficiency coefficient of the i^{th} photovoltaic generator, which is assessed by professional organizations. When the power generation efficiency is higher than the average level, $\varpi_{pi} > 1$.

To ensure that the RES units of the same type have the smallest variance in the unit power generation profit in all trading periods, the objective function to measure the fairness of the RES profit can be expressed by **Eq. 4**.

$$\min f_{p2} = \sum_{i=1}^{N_p} \sum_{t_d=1}^{T} \left(K_{pi,t_d} - \frac{1}{N_p} \sum_{i=1}^{N_p} K_{pi,t_d} \right)^2 \tag{4}$$

where f_{p2} is the fairness coefficient of photovoltaic generators, i.e., the sum of squared difference of the unit power generation profit of each unit in each trading period; N_p is the number of photovoltaic generators. The unit power generation profit obtained by the same type of RES units in a certain trading period through CFDs, the spot market, and the TGC market is used as an indicator to measure the fairness, which reflects the equal treatment of the same type of units.

Similarly, the objective functions for wind turbines can be formulated by **Eqs. 5**, **6**.

$$\min f_{w1} = \sum_{t=1}^{T} \left(P_{wI}^{c} - P_{t}^{sp}\right) \cdot Q_{wI,t}^{en} \cdot \gamma_{w} \tag{5}$$

$$\min f_{w2} = \sum_{i=1}^{N_w} \sum_{t_d=1}^{T} \left(K_{wi,t_d} - \frac{1}{N_w} \sum_{i=1}^{N_w} K_{wi,t_d} \right)^2 \tag{6}$$

where f_{w1} and f_{w2} are the amount of government financial subsidy and fairness coefficient of the wind turbines, respectively; P_{wI}^{c} and $Q_{wI,t}^{en}$ are the CFD price and the predicted output of wind turbines during the trading period t; γ_w is the contract coverage of the wind turbines in the decision-making period T; N_w is the number of wind turbines; K_{wi,t_d} is the unit power generation profit of the i^{th} wind turbine in trading period t_d, as calculated in **Eq. 7**.

$$K_{wi,t_d} = \frac{\sum_{t=1}^{t_d} \left[P_{wi}^{c} Q_{wi,t}^{en} \gamma_w + P_t^{sp} Q_{wi,t}^{en} \left(1 - \gamma_w\right) + P_t^{gr} Q_{wi,t}^{gr} \right] - \varpi_{wi} C_w}{\sum_{t=1}^{t_d} Q_{wi,t}^{en}} \tag{7}$$

where P_{wi}^{c} is the CFD price of the i^{th} wind turbine; $Q_{wi,t}^{en}$ and $Q_{wi,t}^{gr}$ are the predicted output of the i^{th} wind turbine and the amount of electricity traded in the TGC market in the trading period t, respectively; C_w is the levelized cost of wind power generation; ϖ_{wi} is the efficiency coefficient of the i^{th} wind turbine.

3.1.2 Constraints and Solution

The output constraints of RES generators are included in the upper-level decision-making model, as shown in **Eqs. 8**, **9**.

$$\gamma_{p\min} \le \gamma_p \le \gamma_{p\max} \tag{8}$$

$$\gamma_{w\min} \le \gamma_w \le \gamma_{w\max} \tag{9}$$

where $\gamma_{p\ min}$ and $\gamma_{p\ max}$ are the upper and lower limits of the CCR of photovoltaic generators; $\gamma_{w\ min}$ and $\gamma_{w\ max}$ are the upper and lower limits of the CCR of wind turbines.

With the above objective functions and constraints, a multi-objective optimization model is obtained for solving the CCR of photovoltaic generators and wind turbines. The original objective functions are first normalized to [0,1] to get rid of the influence of dimension and order. Then the weighting factors are added as in **Eq. 10**.

$$\min f\left(\gamma_p, \gamma_w\right) = \sum_{i=1}^{2} \left(a_{pi} \frac{f_{pi} - f_{pi,\min}}{f_{pi,\max} - f_{pi,\min}} + a_{wi} \frac{f_{wi} - f_{wi,\min}}{f_{wi,\max} - f_{wi,\min}} \right) \tag{10}$$

where a_{pi} and a_{wi} are the weighting factors of each part of the objective function. They are determined according to factors such as power supply reliability, environmental benefits, policy support for RES development, financial subsidy burdens during this period, etc.

3.2 Middle-Level: Market Clearing Model

3.2.1 Electricity Spot Market Clearing Model

The clearing results of the electricity spot market are required when calculating the CCR. Therefore, the electricity spot market clearing model is the first middle-level model to provide market data for decision-making in the upper-level model. Participants in the spot market can be divided into fossil-fueled generation units and renewable energy units. For a trading session t, the spot market clearing model is given as follows.

$$\min \sum_{i=1}^{N_F} r_{Fi,t}^{sp} p_{Fi,t}^{sp} + \sum_{j=1}^{N_G} r_{Gj,t}^{sp} p_{Gj,t}^{sp} \tag{11}$$

$$s.t. \sum_{i=1}^{N_F} p_{Fi,t}^{sp} + \sum_{j=1}^{N_G} p_{Gj,t}^{sp} = \sum_{k=1}^{N_D} p_{Dk,t} \tag{12}$$

$$p_{Fi,t\min}^{sp} \le p_{Fi,t}^{sp} \le p_{Fi,t\max}^{sp} \qquad \forall i \in [1, N_F] \tag{13}$$

$$p_{Gj,t\min}^{sp} \le p_{Gj,t}^{sp} \le p_{Gj,t\max}^{sp} \qquad \forall j \in [1, N_G] \tag{14}$$

$$\sum_{i=1}^{N_F} p_{Fi,t}^{sp} \rho_{l,i} + \sum_{j=1}^{N_G} p_{Gj,t}^{sp} \rho_{l,j} + \sum_{k=1}^{N_D} p_{Dk,t} \rho_{l,k} \le P_l^{\max} \forall l \in [1,\ N_l] \tag{15}$$

$$\sum_{j=1}^{N_G} r_{j,t}^{reserve\_+} \ge R_t^{reserve\_+} \tag{16}$$

$$\sum_{j=1}^{N_G} r_{j,t}^{reserve\_-} \ge R_t^{reserve\_-} \tag{17}$$

where $p_{Dk,t}$ is the power demand of the k^{th} load in clearing period t; $r_{Fi,t}^{sp}$ and $r_{Gj,t}^{sp}$ are the market quotations of the i^{th} RES unit and the j^{th} fossil-fueled generation unit, respectively; $p_{Fi,t}^{sp}$ and $p_{Gj,t}^{sp}$ are the bid-winning power of the i^{th} RES unit and the j^{th} fossil-fueled generation unit, respectively; $\rho_{l,i}$, $\rho_{l,j}$, and $\rho_{l,k}$ are the power transmission distribution factors of the RES unit i, fossil-fueled generation unit j, and load k, respectively; P_l^{max} represents the transmission capacity of line l; N_F, N_G and N_l are number of RES units, fossil-fueled generation units, and lines, respectively; $r_{j,t}^{reserve\_+}$ and $r_{j,t}^{reserve\_-}$ represent the positive spinning reserve and the negative spinning reserve provided by the j^{th} fossil-fueled generation unit, respectively; $R_t^{reserve\_+}$ and $R_t^{reserve\_-}$ represent the positive spinning reserve requirement and the negative spinning reserve requirement of the system, respectively; $p_{Gj,t\ max}^{sp}$ and $p_{Gj,t\ min}^{sp}$ are the upper and lower limits of the bid-winning power of the fossil-fueled generation unit; $p_{Fi,t\ max}^{sp}$ and $p_{Fi,t\ min}^{sp}$ are the upper and lower limits of the bid-winning power of the RES units.

For both the type I and type II RES units, $p_{Fi,t\ max}^{sp}$ is the generation output minus the power covered by CFDs, as shown in **Eq. 18**.

$$p_{Fi,t\max}^{sp} = \frac{Q_{Fi,t}^{en}\left(1 - \gamma\right)}{t} \tag{18}$$

where $Q_{Fi,t}^{en}$ is the predicted output of the RES unit in trading period t; γ is the CCR corresponding to the RES unit, $\gamma \equiv [\gamma_p, \gamma_w]$.

3.2.2 Green Certificate Market Clearing Model

The TGC market clearing model is the other middle-level model. During a decision cycle, the TGC market clearing process is repeated. After a market clearing, the winning participants can conduct transactions, and the participants who have not reached a transaction will requote and enter the next market clearing process. Since the clearing results of the spot market and the TGC market affect each other, it is assumed that the clearing cycle of the TGC market is consistent with the spot market. For a trading session t, the TGC market clearing model is shown in **Eqs. 19–22**.

$$\max \sum_{i=1}^{N_F} r_{Fi,t}^{gr} q_{Fi,t}^{gr} - \sum_{j=1}^{N_G} r_{Gj,t}^{gr} q_{Gj,t}^{gr} \tag{19}$$

$$s.t. \sum_{i=1}^{N_F} q_{Fi,t}^{gr} = \sum_{j=1}^{N_G} q_{Gj,t}^{gr} \tag{20}$$

$$0 \le q_{Fi,t}^{gr} \le q_{Fi,t\max}^{gr} \quad \forall i \in [1, N_F] \tag{21}$$

$$0 \le q_{Gj,t}^{gr} \le q_{Gj,t\max}^{gr} \quad \forall j \in [1, N_G] \tag{22}$$

where $r_{Fi,t}^{gr}$ / $r_{Gj,t}^{gr}$ is the market quotation of the i^{th} RES/ j^{th} fossil-fueled generation unit; $q_{Fi,t}^{gr}$ and $q_{Fi,t\ max}^{gr}$ are the number and the upper limit of TGCs offered by RES generation unit, respectively; $q_{Gj,t}^{gr}$ and $q_{Gj,t\ max}^{gr}$ are the number and the upper limit of TGCs bid by the fossil-fueled generation unit, respectively. $q_{Fi,t}^{gr}$ and $q_{Fi,t\ max}^{gr}$ corresponds to the output of RES unit $Q_{Fi,t}^{gr}$ and $Q_{Fi,t\ max}^{gr}$. For type I and type II RES units, the upper limits on electricity corresponding to the number of winning TGCs are different, as shown in **Eq. 23**.

$$\begin{aligned} Q_{FI\max}^{gr} &= Q_{FI}^{en} \cdot (1-\gamma) \\ Q_{FII\max}^{gr} &= Q_{FII}^{en} \end{aligned} \tag{23}$$

where $Q_{FI\ max}^{gr}$ and $Q_{FII\ max}^{gr}$ represent the upper limits on electricity corresponding to the number of winning TGCs for the type I and type II RES units, respectively; Q_{FI}^{en} and Q_{FII}^{en} represent the predicted output of the type I and type II RES units, respectively. **Eq. 23** corresponds to the definitions of the two types of RES units.

3.3 Lower-Level: Bidding Model of Participants

3.3.1 Bidding Model for Renewable Energy Units

RES units participate in both the electricity spot market and the TGC market, so their income is made up of two parts as shown in **Eq. 24**.

$$\max E_{Fi,t} = E_{Fi,t}^{sp}\left(r_{Fi,t}^{sp}\right) + E_{Fi,t}^{gr}\left(r_{Fi,t}^{gr}\right) \tag{24}$$

where $E_{Fi,t}$ is the total revenue of the i^{th} RES unit at time t; $E_{Fi,t}^{sp}$ and $E_{Fi,t}^{gr}$ are the spot market revenue and TGC market revenue of the i^{th} RES unit at time t, respectively.

The constraints in the bidding model of RES generation units are shown in **Eqs. 25–27**.

$$r_{Fi,t\min}^{sp} \le r_{Fi,t}^{sp} \le r_{Fi,t\max}^{sp} \tag{25}$$

$$r_{Fi,t\min}^{gr} \le r_{Fi,t}^{gr} \le r_{Fi,t\max}^{gr} \tag{26}$$

$$p_{Fi,t\min} \le p_{Fi,t} \le p_{Fi,t\max} \tag{27}$$

where **Eq. 25** and **Eq. 26** are bidding price constraints, and **Eq. 27** is the biding output constraint. $r_{Fi,t\ max}^{sp}$ / $r_{Fi,t\ min}^{sp}$ and $r_{Fi,t\ max}^{gr}$ / $r_{Fi,t\ min}^{gr}$ are the maximum/minimum bidding prices of the i^{th} RES unit at time t in the electricity spot market and TGC market; $p_{Fi,t\ max}$ and $p_{Fi,t\ min}$ are the maximum and minimum output of the i^{th} RES unit at time t, respectively.

Since the marginal cost of RES units is nearly zero, their market strategies in the spot market is always bidding the lowest price, so that they can win the bid as much as possible. In the TGC market, the market strategies is affected by the historical clearing results in the TGC market and the spot market as well as the CCR. It is important to point out that changes in contract coverage will only affect the number of TGCs issued for the type-I RES generation units (i.e., the subsidized units). Therefore, in the early stage of market reform when the type-I RES generation units accounting for a larger proportion of the total generation, the CCR has larger impacts on the supply and demand relationship in the TGC market. As the electricity marketization reform progresses, the proportion of the type-II RES generation units (i.e., the unsubsidized units) will increase, and the CCR will have less impacts on the TGC market clearing results.

Notably, RESs are usually coupled with energy storage resources (ESRs). Since this paper discusses the situation in the early stage of RES participation in electricity markets, the penalty mechanism for the generation output deviations of RES units is not considered in this paper. The forecasting results of RES generation outputs could be more accurate if ESRs are modeled, but the attained conclusions will remain unchanged. It is implicitly assumed that the predicted generation outputs of RES units could be accurate enough, even without ESRs installed.

3.3.2 Bidding Model for Fossil-Fueled Generation Units

When fossil-fueled generation units participate in the spot market, they need to purchase TGCs in the TGC market, so their income is also divided into two parts, as shown in **Eq. 28**.

$$\max E_{Gj,t} = E_{Gj,t}^{sp}\left(r_{Gj,t}^{sp}\right) + E_{Gj,t}^{gr}\left(r_{Gj,t}^{gr}\right) \tag{28}$$

where $E_{Gj,t}$ is the total revenue of the j^{th} fossil-fueled generation unit at time t; $E_{Gj,t}^{sp}$ and $E_{Gj,t}^{gr}$ are the spot market revenue and TGC market revenue of the j^{th} fossil-fueled generation unit at time t, respectively. $E_{Gj,t}^{gr}$ is usually negative.

The constraints of the bidding model for fossil-fueled generation units are shown in **Eqs. 29–31**. Among them, **Eqs. 29**, **30** are the bidding constraints, and **Eq. 31** is the output constraints.

$$r_{Gj,t\min}^{sp} \le r_{Gj,t}^{sp} \le r_{Gj,t\max}^{sp} \tag{29}$$

$$r_{Gj,t\min}^{gr} \le r_{Gj,t}^{gr} \le r_{Gj,t\max}^{gr} \tag{30}$$

$$p_{Gj,t\min} \le p_{Gj,t} \le p_{Gj,t\max} \tag{31}$$

where **Eq. 29** and **Eq. 30** are the bidding price constraints, and **Eq. 31** is the bidding output constraint. $r_{Gj,t\ max}^{sp}$ / $r_{Gj,t\ min}^{sp}$ and

$r^{gr}_{Gj,t\ max}$, / $r^{gr}_{Gj,t\ min}$ are the maximum/minimum bidding prices of the j^{th} fossil-fueled generation unit at time t in the electricity spot market and TGC market; $p_{Gj,t\ max}$ and $p_{Gj,t\ min}$ are the maximum and minimum output of the j^{th} fossil-fueled generation unit at time t, respectively.

In the spot market, the market strategies of fossil-fueled generation units not only depends on its production conditions, fuel prices and other factors, but also is affected by the TGC market clearing results. When the TGC market clearing price is high and fossil-fueled units cannot buy enough TGCs, their risk of being punished for not meeting the quota will increase, so they will tend to reduce the value of offering prices.

In the TGC market, the market strategies of fossil-fueled generation units (i.e., TGC buyers) is affected by the clearing results of the spot market. If the clearing electricity in the spot market is low, or the clearing price is low, the incentive of purchasing TGCs will drop. In the long run, the market strategies of fossil-fueled units is also affected by factors such as the approaching assessment date and the overall trend of TGC prices throughout the assessment cycle.

3.4 Reformulation and Solution

Mathematical reformulations are conducted to solve the proposed three-layer model. Since the lower-level model is a linear programming problem, the Karush-Kuhn-Tucker (KKT) condition is a necessary and sufficient condition of optimality. Therefore, the two bidding models in the lower layer can be replaced with their KKT conditions and incorporated into the middle-level model, thereby transforming the original three-layer model into a two-layer optimization model. Given **Eq. 24** and **Eq. 28**, the Lagrangian functions of the bidding model for renewable energy based generation units and the bidding model for fossil-fueled generation units are formulated as follows.

$$\Gamma_{Fi,t} = -E^{sp}_{Fi,t}\left(r^{sp}_{Fi,t}\right) - E^{gr}_{Fi,t}\left(r^{gr}_{Fi,t}\right) \tag{32}$$

$$\Gamma_{Gj,t} = -E^{sp}_{Gj,t}\left(r^{sp}_{Gj,t}\right) - E^{gr}_{Gj,t}\left(r^{gr}_{Gj,t}\right) \tag{33}$$

Thus, the KKT conditions of the lower-level model are derived as **Eqs. 34–37**.

$$\frac{\partial \Gamma_{Fi,t}}{\partial r^{sp}_{Fi,t}} = \pi^{sp}_{Fi,t} \tag{34}$$

$$\frac{\partial \Gamma_{Fi,t}}{\partial r^{gr}_{Fi,t}} = \pi^{gr}_{Fi,t} \tag{35}$$

$$\frac{\partial \Gamma_{Gj,t}}{\partial r^{sp}_{Gj,t}} = \pi^{sp}_{Gj,t} \tag{36}$$

$$\frac{\partial \Gamma_{Gj,t}}{\partial r^{gr}_{Gj,t}} = \pi^{gr}_{Gj,t} \tag{37}$$

Based on the above KKT conditions, the lower-level model is transformed into linear constraints and incorporated into the middle-level optimization model.

Similarly, since the two market clearing models in the middle layer are both linear programming problems, the middle-level model can also be replaced with its KKT condition, thereby transforming the original problem into a single-level optimization model. After substituting **Eqs. 34–37** into **Eqs. 11–17** and **Eqs. 19–22**, the Lagrangian functions of the spot market clearing model and the TGC market clearing model are constructed as below.

$$\begin{aligned}\Gamma^{sp} = &\sum_{t=1}^{T}\left(\sum_{i=1}^{N_F} r^{sp}_{Fi,t}p^{sp}_{Fi,t} + \sum_{j=1}^{N_G} r^{sp}_{Gj,t}p^{sp}_{Gj,t}\right) + \sum_{t=1}^{T}\sum_{i=1}^{N_F}\pi^{sp}_{Fi,t}\\ &+ \sum_{t=1}^{T}\sum_{j=1}^{N_G}\pi^{sp}_{Gj,t} + \sum_{t=1}^{T}\lambda^{sp}_{t}\left(\sum_{i=1}^{N_F} p^{sp}_{Fi,t} + \sum_{j=1}^{N_G} p^{sp}_{Gj,t} - \sum_{k=1}^{N_D} p_{Dk,t}\right)\\ &- \sum_{t=1}^{T}\sum_{i=1}^{N_F}\widehat{\mu}^{sp}_{Fi,t}\left(p^{sp}_{Fi,t\max} - p^{sp}_{Fi,t}\right) - \sum_{t=1}^{T}\sum_{i=1}^{N_F}\breve{\mu}^{sp}_{Fi,t}\left(p^{sp}_{Fi,t} - p^{sp}_{Fi,t\min}\right)\\ &- \sum_{t=1}^{T}\sum_{j=1}^{N_G}\widehat{\mu}^{sp}_{Gj,t}\left(p^{sp}_{Gj,t\max} - p^{sp}_{Gj,t}\right) - \sum_{t=1}^{T}\sum_{j=1}^{N_G}\breve{\mu}^{sp}_{Gj,t}\left(p^{sp}_{Gj,t} - p^{sp}_{Gj,t\min}\right)\\ &- \sum_{t=1}^{T}\sum_{l=1}^{N_l}\nu_{l,t}\left(P^{\max}_{l} - \sum_{i=1}^{N_F} p^{sp}_{Fi,t}\rho_{l,i} - \sum_{j=1}^{N_G} p^{sp}_{Gj,t}\rho_{l,j} - \sum_{k=1}^{N_D} p_{Dk,t}\rho_{l,k}\right)\end{aligned} \tag{38}$$

$$\begin{aligned}\Gamma^{gr} = &\sum_{t=1}^{T}\left(-\sum_{i=1}^{N_F} r^{gr}_{Fi,t}q^{gr}_{Fi,t} + \sum_{j=1}^{N_G} r^{gr}_{Gj,t}q^{gr}_{Gj,t}\right) + \sum_{t=1}^{T}\sum_{i=1}^{N_F}\pi^{gr}_{Fi,t}\\ &+ \sum_{t=1}^{T}\sum_{j=1}^{N_G}\pi^{gr}_{Gj,t} + \sum_{t=1}^{T}\lambda^{gr}_{t}\left(\sum_{i=1}^{N_F} q^{gr}_{Fi,t} - \sum_{j=1}^{N_G} q^{gr}_{Gj,t}\right)\\ &- \sum_{t=1}^{T}\sum_{i=1}^{N_F}\widehat{\mu}^{gr}_{Fi,t}\left(q^{gr}_{Fi,t\max} - q^{gr}_{Fi,t}\right) - \sum_{t=1}^{T}\sum_{i=1}^{N_F}\breve{\mu}^{gr}_{Fi,t}q^{gr}_{Fi,t}\\ &- \sum_{t=1}^{T}\sum_{j=1}^{N_G}\widehat{\mu}^{gr}_{Gj,t}\left(q^{gr}_{Gj,t\max} - q^{gr}_{Gj,t}\right) - \sum_{t=1}^{T}\sum_{j=1}^{N_G}\breve{\mu}^{gr}_{Gj,t}q^{gr}_{Gj,t}\end{aligned} \tag{39}$$

Therefore, the KKT conditions of the electricity spot market clearing model and the TGC market clearing model can be expressed by **Eqs. 40–60**.

3.4.1 Equality Constraints

$$\frac{\partial \Gamma^{sp}}{\partial p^{sp}_{Fi,t}} = r^{sp}_{Fi,t} + \lambda^{sp}_{t} + \widehat{\mu}^{sp}_{Fi,t} - \breve{\mu}^{sp}_{Fi,t} + \nu_{l,t}\rho_{l,i} + \frac{\partial \pi^{sp}_{Fi,t}}{\partial p^{sp}_{Fi,t}} = 0 \tag{40}$$

$$\frac{\partial \Gamma^{sp}}{\partial p^{sp}_{Gj,t}} = r^{sp}_{Gj,t} + \lambda^{sp}_{t} + \widehat{\mu}^{sp}_{Gj,t} - \breve{\mu}^{sp}_{Gj,t} + \nu_{l,t}\rho_{l,j} + \frac{\partial \pi^{sp}_{Gj,t}}{\partial p^{sp}_{Gj,t}} = 0 \tag{41}$$

$$\frac{\partial \Gamma^{gr}}{\partial q^{gr}_{Fi,t}} = -r^{gr}_{Fi,t} + \lambda^{gr}_{t} + \widehat{\mu}^{gr}_{Fi,t} - \breve{\mu}^{gr}_{Fi,t} + \frac{\partial \pi^{gr}_{Fi,t}}{\partial q^{gr}_{Fi,t}} = 0 \tag{42}$$

$$\frac{\partial \Gamma^{gr}}{\partial q^{gr}_{Gj,t}} = r^{gr}_{Gj,t} - \lambda^{gr}_{t} + \widehat{\mu}^{gr}_{Gj,t} - \breve{\mu}^{gr}_{Gj,t} + \frac{\partial \pi^{gr}_{Gj,t}}{\partial q^{gr}_{Gj,t}} = 0 \tag{43}$$

$$\frac{\partial \Gamma^{sp}}{\partial \lambda^{sp}_{t}} = \sum_{i=1}^{N_F} p^{sp}_{Fi,t} + \sum_{j=1}^{N_G} p^{sp}_{Gj,t} - \sum_{k=1}^{N_D} p_{Dk,t} = 0 \tag{44}$$

$$\frac{\partial \Gamma^{gr}}{\partial \lambda^{gr}_{t}} = \sum_{i=1}^{N_F} q^{gr}_{Fi,t} - \sum_{j=1}^{N_G} q^{gr}_{Gj,t} = 0 \tag{45}$$

$$\pi^{sp}_{Fi,t} = \pi^{sp}_{Gj,t} = \pi^{gr}_{Fi,t} = \pi^{gr}_{Gj,t} = 0 \tag{46}$$

3.4.2 Inequality Constraints

$$p^{sp}_{Fi,t\,\min} \le p^{sp}_{Fi,t} \le p^{sp}_{Fi,t\,\max} \quad \forall i \in [1, N_F], \forall t \in [1, T] \tag{47}$$

$$p^{sp}_{Gj,t\,\min} \le p^{sp}_{Gj,t} \le p^{sp}_{Gj,t\,\max} \quad \forall j \in [1, N_G], \forall t \in [1, T] \tag{48}$$

$$\sum_{i=1}^{N_F} p^{sp}_{Fi,t}\rho_{l,i} + \sum_{j=1}^{N_G} p^{sp}_{Gj,t}\rho_{l,j} + \sum_{k=1}^{N_D} p_{Dk,t}\rho_{l,k} \le P^{\max}_{l} \quad \forall l \in [1,\ N_l], \forall t \in [1, T] \tag{49}$$

$$0 \le q^{gr}_{Fi,t} \le q^{gr}_{Fi,t\,\max} \quad \forall i \in [1, N_F], \forall t \in [1, T] \tag{50}$$

$$0 \le q^{gr}_{Gj,t} \le q^{gr}_{Gj,t\,\max} \quad \forall j \in [1, N_G], \forall t \in [1, T] \tag{51}$$

3.4.3 Dual Complementary Constraints

$$0 \le \widehat{\mu}^{sp}_{Fi,t} \perp \left(p^{sp}_{Fi,t\,\max} - p^{sp}_{Fi,t}\right) \ge 0 \quad \forall i \in [1, N_F], \forall t \in [1, T] \tag{52}$$

$$0 \le \breve{\mu}^{sp}_{Fi,t} \perp \left(p^{sp}_{Fi,t} - p^{sp}_{Fi,t\,\min}\right) \ge 0 \quad \forall i \in [1, N_F], \forall t \in [1, T] \tag{53}$$

$$0 \le \widehat{\mu}^{sp}_{Gj,t} \perp \left(p^{sp}_{Gj,t\,\max} - p^{sp}_{Gj,t}\right) \ge 0 \quad \forall j \in [1, N_G], \forall t \in [1, T] \tag{54}$$

$$0 \le \breve{\mu}^{sp}_{Gj,t} \perp \left(p^{sp}_{Gj,t} - p^{sp}_{Gj,t\,\min}\right) \ge 0 \quad \forall j \in [1, N_G], \forall t \in [1, T] \tag{55}$$

$$0 \le \nu_{l,t} \perp \left(P^{\max}_{l} - \sum_{i=1}^{N_F} p^{sp}_{Fi,t}\rho_{l,i} - \sum_{j=1}^{N_G} p^{sp}_{Gj,t}\rho_{l,j} - \sum_{k=1}^{N_D} p_{Dk,t}\rho_{l,k}\right) \ge 0 \quad \forall l \in [1, N_l], \forall t \in [1, T] \tag{56}$$

$$0 \le \widehat{\mu}^{gr}_{Fi,t} \perp \left(q^{gr}_{Fi,t\,\max} - q^{gr}_{Fi,t}\right) \ge 0 \quad \forall i \in [1, N_F], \forall t \in [1, T] \tag{57}$$

$$0 \le \widehat{\mu}^{gr}_{Gj,t} \perp \left(q^{gr}_{Gj,t\,\max} - q^{gr}_{Gj,t}\right) \ge 0 \quad \forall j \in [1, N_G], \forall t \in [1, T] \tag{58}$$

$$0 \le \breve{\mu}^{gr}_{Fi,t} \perp q^{gr}_{Fi,t} \ge 0 \quad \forall i \in [1, N_F], \forall t \in [1, T] \tag{59}$$

$$0 \le \breve{\mu}^{gr}_{Gj,t} \perp q^{gr}_{Gj,t} \ge 0 \quad \forall j \in [1, N_G], \forall t \in [1, T] \tag{60}$$

where $0 \le x \perp y \ge 0$ means that at most one of the scalars x and y can be strictly greater than 0.

For the dual complementary constraints in **Eqs. 52–60**, the big M method can be used to convert them into linear constraints. For example, a binary variable τ is introduced to transform **Eq. 52** into **Eq. 61** and **Eq. 62**.

$$0 \le \widehat{\mu}^{sp}_{Fi,t} \le M\tau^{sp}_{Fi,t} \quad \forall i \in [1, N_F], \forall t \in [1, T] \tag{61}$$

$$0 \le \left(p^{sp}_{Fi,t\,\max} - p^{sp}_{Fi,t}\right) \le M\left(1 - \tau^{sp}_{Fi,t}\right) \quad \forall i \in [1, N_F], \forall t \in [1, T] \tag{62}$$

where M is a sufficiently large positive number.

With the above KKT conditions, the middle- and lower-level models are transformed into linear constraints and incorporated into the upper-level optimization model. At this point, the three-layer optimization model to determine the contract coverage of RES units has been transformed into a Mixed-Integer Linear Programming (MILP) problem, which can be solved by the GUROBI solver in MATLAB, and finally obtain the optimal CCR for RES generation units.

4 NUMERICAL EXAMPLES AND RESULTS

4.1 Data Specifications

Numerical experiments are performed using the real-world data of the electricity market in a province of eastern China. It is assumed that the RES units begin to participate in the electricity spot market in 2020. The fossil-fueled generation units are coal-fired units, and the RES units include photovoltaics and wind turbines. The parameters of each unit in 2020 are shown in **Table 2**. The RES units in 2020 all belonged to type I; the number of type-II units started increasing from 2021, and the annual growth rate is set according to governmental policies (The State Council Information Office of the People's Republic of China, 2020). The CFD price for the type-II RES units is the same as for coal-fired units. The RES output is predicted based on the historical data, and the annual load demand curve is obtained based on the load curve of that province in 2020. The responsibility weight of the quota system for coal-fired units is set according to governmental policies (National Development and Reform Commission and National Energy Administration Commission, 2021). The lower and upper limits of the clearing price in the spot market are set to −200 yuan/MWh and 1000 yuan/MWh respectively, and the lower and upper limits of the clearing price in the TGC market are set to 0 yuan/MWh and 800 yuan/MWh respectively.

In this experiment, the CCR in the peak period, flat period, and valley period of each day for photovoltaic generators and wind turbines will be determined, respectively. Furthermore, the comprehensive CCR is introduced to reflect the overall CCR of RES units, which is a weighted average of the contract coverage at different times, as shown in **Eq. 63**.

$$\gamma_c = \frac{\gamma_p Q^{en}_{F,p} + \gamma_a Q^{en}_{F,a} + \gamma_b Q^{en}_{F,b}}{Q^{en}_{F,p} + Q^{en}_{F,a} + Q^{en}_{F,b}} \tag{63}$$

where γ_c is the comprehensive CCR; γ_p, γ_a, and γ_b are the CCR of RES generation units in the peak, flat, and valley periods, respectively; $Q^{en}_{F,p}$, $Q^{en}_{F,a}$, and $Q^{en}_{F,b}$ are the generation outputs of RES generation units during the peak, flat and valley periods, respectively.

4.2 Analysis of Short-Term Simulation Results

The changes in CCR in 2020 are simulated by adjusting the weighting factors of the decision-making model, as shown in **Figure 3** and **Figure 4**. Changes in policy, load supply, and demand are simulated by changing the ratio of a_{p2}/a_{p1} and a_{w2}/a_{w1}. The decrease of a_{p2}/a_{p1} and a_{w2}/a_{w1} indicates that the determination of CCR is more inclined to ease the financial burden of the government, and the increase indicates that it is more inclined to the fairness of the RES units. Affected by the epidemic, the load demand is at a low level from January to April in 2020. At this time, the clearing price of the spot market is relatively low. In order to protect the interests of RES units and promote their development, a_{p2}/a_{p1} and a_{w2}/a_{w1} should increase. From June to September, the load demand is at a high level, the spot market clearing price is relatively high. In addition, due to

TABLE 2 | Parameter settings of generation units in 2020.

Generator type	Number of units	Total installed capacity (MW)	CFD price (yuan/MWh)
Coal-fired	18	8428	380
Photovoltaics	10	945	590
Wind turbines	6	760	570
Total	34	10133	/

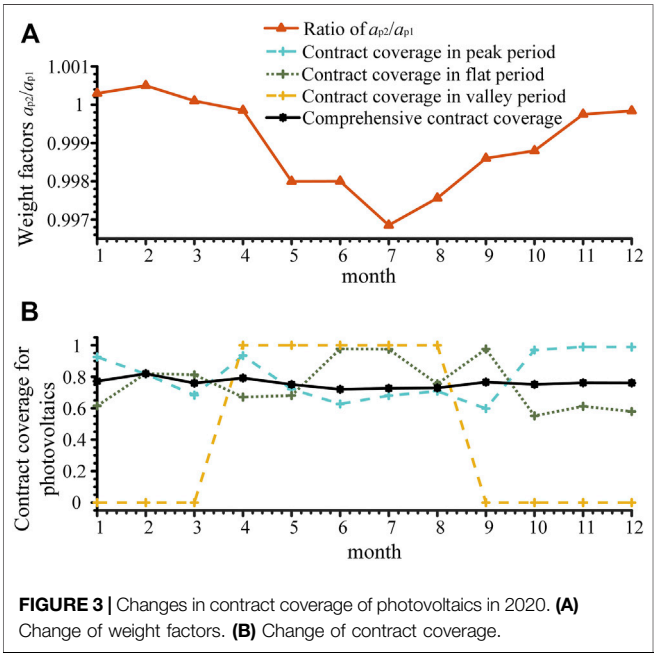

FIGURE 3 | Changes in contract coverage of photovoltaics in 2020. **(A)** Change of weight factors. **(B)** Change of contract coverage.

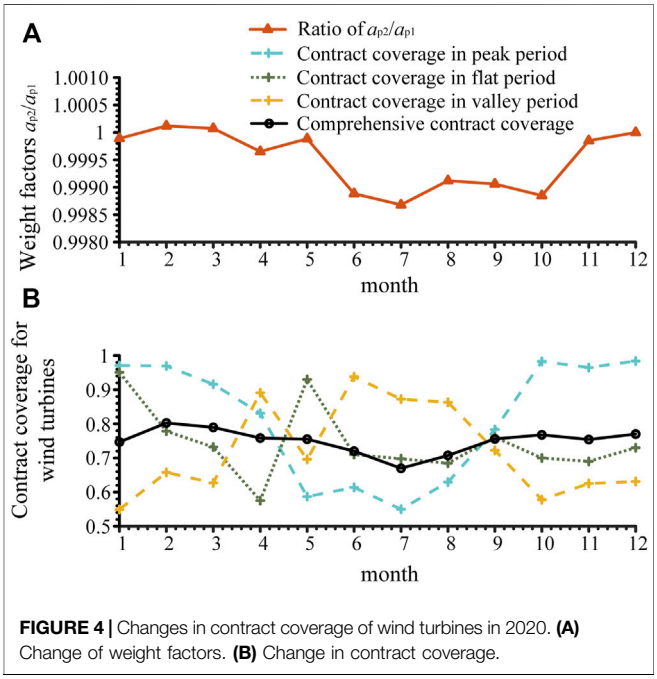

FIGURE 4 | Changes in contract coverage of wind turbines in 2020. **(A)** Change of weight factors. **(B)** Change in contract coverage.

seasonal factors, the output of RES units increases, meaning that RES units can earn more from the spot market and the TGC market, so a_{p2}/a_{p1} and a_{w2}/a_{w1} should be reduced to ease the government's financial burden.

It can be seen in **Figure 3** and **Figure 4** that the comprehensive CCR of photovoltaics and wind turbines is consistent with the trend of the weighting factors. This indicates that the CCR can achieve the expected effect by adjusting the weighting factors. Specifically, at the beginning of the year, the contract coverage of RES units remains at a high level since the winter is the peak period, and then it decreases significantly in the summer. This allows RES units to maintain a high level of income through high-coverage CFDs in winter. When the spot market price is higher in summer, the CCR of RES generations is low and thus the remaining RES outputs can opt to participate in the spot market. This is consistent with the intention of setting the weighting factors. The output of photovoltaics mainly concentrates in the middle of the load, so it needs to be maintained at a high level to ensure the income. The output of wind turbines in each load period fluctuates greatly due to the uncertainty of wind power, so its CCR varies more. The contract coverage of photovoltaics in the load valley period is extreme, because the output of photovoltaics in the valley period is extremely small, whose impact on the objective function is limited.

The results of income and fairness coefficients for RES units are compared between proposed method and the fixed contract coverage method, as shown in **Table 3**. For the income analysis, fixing the CCR will increase the government's financial subsidy but reduce the income of RES units in the spot market and the TGC market. For the fairness analysis, the fairness coefficient of fixing the contract coverage is relatively large, meaning that the variance of unit power generation income among the RES units is too high. Further analysis shows that fixing the annual CCR is a solution to the proposed model, but not the optimal solution. The decision-making cycle of optimal contract coverage should be determined according to the changes of generation output and load demand, while considering the policy formulation and the implementation of RES units.

4.3 Analysis of Medium and Long-term Results

Based on the "14th Five-Year Plan", the "carbon peaking" goal in 2030, and the outline of the long-term goal in 2035 (The State Council Information Office of the People's Republic of China, 2020; National Development and Reform Commission of China, 2021), the simulation of RES unit participation in the spot market from 2020 to 2035 is carried out, as shown in **Figure 5**.

TABLE 3 | Comparisons between the results attained by the proposed method and the fixed contract coverage.

Unit type	CFD income (yuan)		Spot market income (yuan)		TGC market income (yuan)		Fairness coefficient	
	Proposed method	Fixed contract coverage	Proposed method	Fixed contract coverage	Proposed method	Fixed contract coverage	Proposed method	Fixed contract coverage
Photovoltaics	514318 k	568199 k	89089 k	57802 k	61488 k	38382 k	184.7	418.1
Wind turbines	672275 k	765772 k	126694 k	76212 k	85649 k	51911 k	340.3	610.4

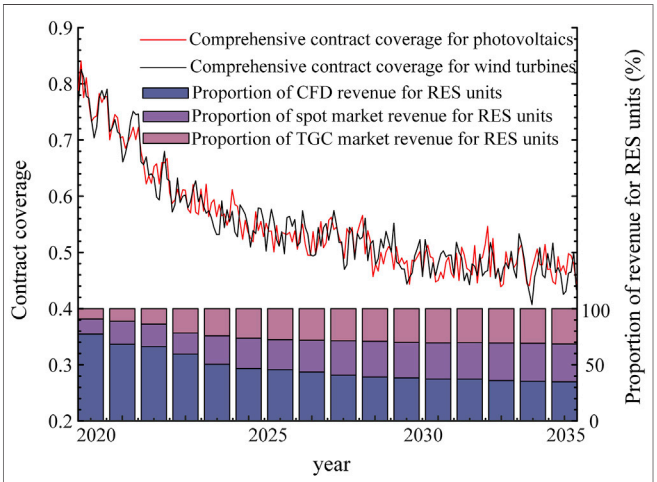

FIGURE 5 | Changes in contract coverage and revenue share of RES generation units from 2020 to 2035.

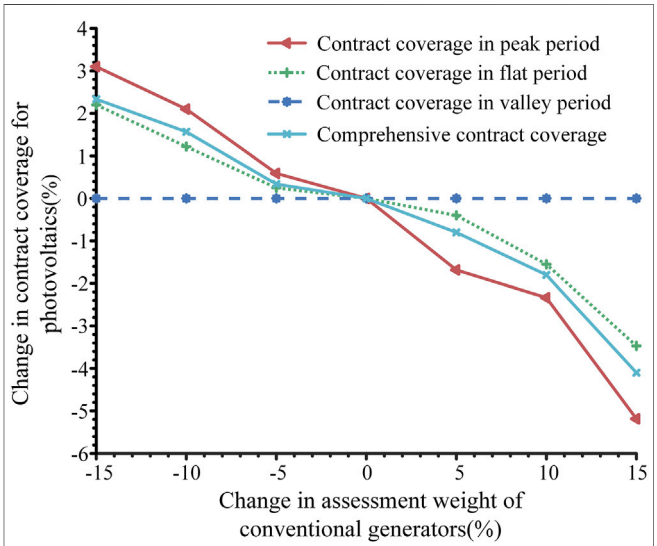

FIGURE 6 | Changes in CCR for photovoltaics under different assessment weights of the quota system.

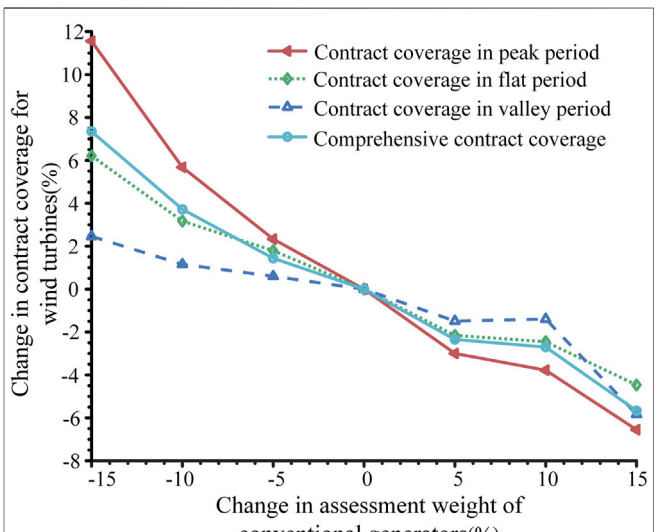

FIGURE 7 | Changes in CCR of wind turbines under different assessment weights of the quota system.

As can be seen from **Figure 5**, during the transition of electricity market reform, due to the continuous development of renewable energy generation technology, government subsidies decrease, and the CCR of RES units and the proportion of CFD revenue also decrease. The proportion of spot market revenue and TGC market revenue increase, indicating that RES units gradually adapt to the spot market during the transition, and the subsidy for RES units changes smoothly from the financial subsidy to TGC subsidy. As the number of type II RES units increases year by year, the impact of contract coverage on the spot market and TGC market gradually decreases. In this example, to 2035, the revenue composition of RES units is relatively fixed, the change in contract coverage tends to be stable, and the curve only fluctuates with changes in load demand and generation output. When RES units have completed the transition phase to participate in the spot market, the determination of the contract coverage can be further adjusted according to the development and policies of renewable energy.

4.4 Sensitivity Analysis of Contract Coverage

Sensitivity analysis is carried out for the contract coverage against market boundary conditions including the assessment weights of the quota system and system load demand.

Firstly, the changes in CCR for RES units under different assessment weights of the quota system for fossil-fueled units are studied. Taking the simulation data in July 2025 as an example, the results are shown in **Figure 6** and **Figure 7**. It can be found that with the increasing of the assessment weights, the CCR of RES units shows a downward trend. The reason is that when the assessment

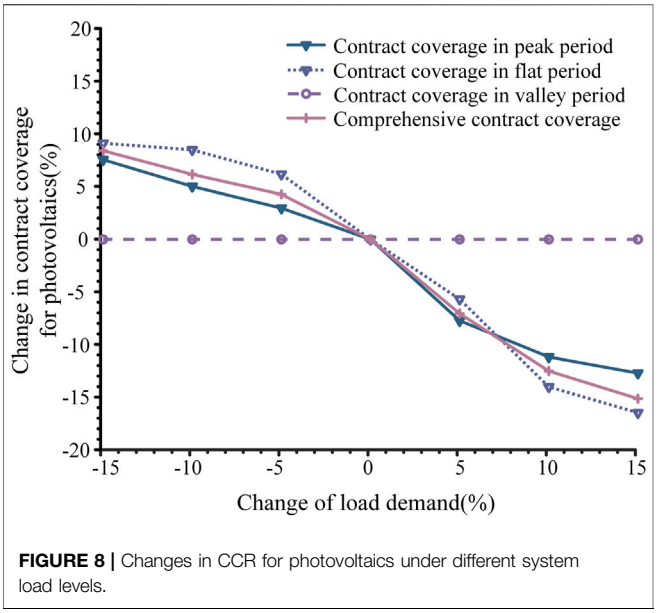

FIGURE 8 | Changes in CCR for photovoltaics under different system load levels.

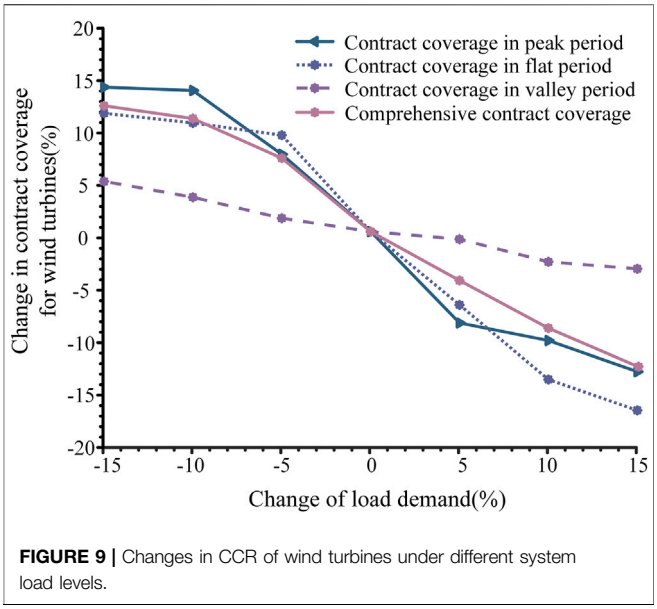

FIGURE 9 | Changes in CCR of wind turbines under different system load levels.

weights of the quota system for fossil-fueled units increase, their demand for TGC increases, which then leads to an increase in the clearing price of the TGC market. Under the same weighting factors, the reduction in government subsidy burdens caused by the decrease in contract coverage does not come at the expense of a sharp decline in the RES generator revenue, because the number of TGCs sold by type I RES units increases, making the RES generator revenue from TGC market increase. As fossil-fueled units have a greater demand for TGC during peak load periods, the contract coverage decreases the most during peak periods. Changing the market strategies of fossil-fueled units in the TGC market can effectively make up for the difference in the degree of decline of RES units in peak, flat and valley periods. Due to the output uncertainties of RES units and the approaching deadline for assessment, this difference cannot be eliminated. However, it is worth noting that due to the small output of photovoltaics during the valley period, the CCR does not change when adjusting the assessment weights.

Secondly, the changes in CCR for RES units under different load levels are examined. Taking the simulation data in July 2025 as an example, the results are shown in **Figure 8** and **Figure 9**. The results show that the contract coverage shows a downward trend as the load demand increases. The reason is that the increase in load will lead to an increase in the spot market price. Under the same weighting factors, the reduction in government subsidy caused by the decrease in contract coverage does not come at the expense of a sharp drop in the revenue of RES units, because the spot market revenue of RES units increases. Similar to when adjusting the assessment weights, adjusting the load demand does not change the CCR for photovoltaics during valley periods.

Figures 6–9 shows that the changes in the assessment weights of the quota system and the system load level change the supply-demand relationship in the TGC market and the spot market, respectively. When the market demand exceeds the supply, the contract coverage for RES unit tends to decline.

5 CONCLUSION

How to realize the smooth transition from a fixed-price transaction mode to a full participation in the electricity spot market is an important issue for RES generation in the electricity market reform procedure of China. In this paper, a transition mechanism for RES units to participate in the electricity spot market considering the TGC market is presented. In this transition mechanism, the adjustment of CFD coverage for RES units is a key part of the design. By modeling the decision-making of various agents participating in the electricity spot market, a three-layer optimization model for solving the CCR is proposed, which provides a scientific basis for adjusting the CCR during the transition period. Extensive numerical experiments are conducted to manifest the feasibility and efficiency of proposed models and algorithms. The impact of the transition mechanism on the RES development is analyzed from the perspectives of short-term and medium-/long-term. The sensitivity analysis of CCR against the assessment weights and system load level shows that when the market demand exceeds supply, the CCR of RES units tends to decline.

DATA AVAILABILITY STATEMENT

The original contributions presented in the study are included in the article/supplementary material, further inquiries can be directed to the corresponding author.

AUTHOR CONTRIBUTIONS

KW, HD, and CX conceptualized the study. HD, JY, and CX performed the analysis. KW, JY, CX, and DQ

performed investigations. HD and ZZ acquired resources. HD, CX, and ZZ acquired funding. KW wrote the original draft. JY, CX, and FW reviewed and edited the manuscript. All authors agreed to be accountable for the content of the work.

REFERENCES

Barbose, G., Wiser, R., Heeter, J., Mai, T., Bird, L., Bolinger, M., et al. (2016). A Retrospective Analysis of Benefits and Impacts of U.S. Renewable Portfolio Standards. *Energy Policy* 96, 645–660. doi:10.1016/j.enpol.2016.06.035

Dai, J., and Chen, H. (2020). Research on Transition Mechanism of Renewable Energy's Participation in Electricity Spot Market. *Zhejiang Electr. Power* 39 (12), 78–84.

García-Alvarez, M. T., Cabeza-García, L., and Soares, I. (2017). Analysis of the Promotion of Onshore Wind Energy in the EU: Feed-In Tariff or Renewable Portfolio Standard? *Renew. Energy* 111, 256–264. doi:10.1016/j.renene.2017.03.067

Gawel, E., and Purkus, A. (2013). Promoting the Market and System Integration of Renewable Energies through Premium Schemes-A Case Study of the German Market Premium. *Energy Policy* 61, 599–609. doi:10.1016/j.enpol.2013.06.117

Gu, F. (2020). Make Good Use of the Government Authorized Contract System to Promote the Construction of Electricity Spot Market. *Chin. power Enterp. Manag.* (16), 36–39.

Jiang, Y., Cao, H., Yang, L., Fei, F., Li, J., and Lin, Z. (2020). Mechanism Design and Impact Analysis of Renewable Portfolio Standard. *Automation Electr. Power Syst.* 44 (7), 187–199.

Kilinc-Ata, N. (2016). The Evaluation of Renewable Energy Policies across EU Countries and US States: An Econometric Approach. *Energy Sustain. Dev.* 31, 83–90. doi:10.1016/j.esd.2015.12.006

Kong, P., Yang, L., Hu, Z., Lin, X., and Wang, B. (2021). "Bilateral Transaction of Bayesian Game in Reformed Electricity Spot Market," in *2021 11th International Conference on Power and Energy Systems (ICPES) (IEEE)*. doi:10.1109/icpes53652.2021.9683848

Li, F., and Xu, P. (2021). "Zonal Reserve Evaluation and Optimization Method in Electricity Spot Market for Power System Integrated with Wind Generation," in *2021 IEEE Sustainable Power and Energy Conference (iSPEC) (IEEE)*.

Luo, C. (2016). Evolution and Trends in Global Supportive Renewable Energy Policies. *Sino-Global Energy* 21 (9), 20–27.

Ma, Z., Zhong, H., Tan, Z., Xia, Q., and Wang, Y. (2017). Incenting Demand and Supply of Renewable Energy with Renewable Portfolio Standard: Mechanism Design of National Renewable Energy Market. *Automation Electr. Power Syst.* 41 (24), 90–96.

National Development and Reform Commission and National Energy Administration Commission (2021). Notice on the 2021 Renewable Energy Power Consumption Responsibility Weight and Related Matters [Online]. Available: http://www.gov.cn/zhengce/zhengceku/2021-05/26/content_5612441.htm (Accessed February 22, 2022 2022).

National Development and Reform Commission of China (2020). Notice on Matters Concerning the 2021 Renewable Energy Feed-In Tariff Policy [Online]. Available: http://www.gov.cn/zhengce/zhengceku/2021-06/11/content_5617297.htm (Accessed Mar 24, 2022 2022).

National Development and Reform Commission of China (2021). The 14th Five-Year Plan for National Economic and Social Development of the People's Republic of China and Outline of the Vision for 2035 [Online]. Available: http://www.gov.cn/xinwen/2021-03/13/content_5592681.htm (Accessed Mar 24, 2022 2022).

Ren, X., Zhu, L., Xie, D., and Ye, B. (2022). Discussion on Key Issues of Renewable Energy Participation in the Electricity Spot Market and its Application on A Case Study. *Mod. Electr. Power* 1 (2), 203–211.

Schallenberg-Rodriguez, J., and Haas, R. (2012). Fixed Feed-In Tariff versus Premium: A Review of the Current Spanish System. *Renew. Sustain. Energy Rev.* 16 (1), 293–305. doi:10.1016/j.rser.2011.07.155

Shinde, P., Hesamzadeh, M. R., Date, P., and Bunn, D. W. (2021). Optimal Dispatch in a Balancing Market with Intermittent Renewable Generation. *IEEE Trans. Power Syst.* 36 (2), 865–878. doi:10.1109/tpwrs.2020.3014515

The State Council Information Office of the People's Republic of China (2020). *Energy In China's New Era* [Online]. Available: http://www.scio.gov.cn/ztk/dtzt/42313/44537/index.htm (Accessed Mar. 24, 2022 2022).

Upton, G. B., and Snyder, B. F. (2017). Funding Renewable Energy: An Analysis of Renewable Portfolio Standards. *Energy Econ.* 66, 205–216. doi:10.1016/j.eneco.2017.06.003

Xu, C., Wen, F., and Palu, I. (2020). Electricity Market Regulation: Global Status, Development Trend, and Prospect in China. *Energy Convers. Econ.* 1 (3), 151–170. doi:10.1049/enc2.12020

Yang, J., Dong, Z. Y., Wen, F., Chen, G., and Qiao, Y. (2020). A Decentralized Distribution Market Mechanism Considering Renewable Generation Units with Zero Marginal Costs. *IEEE Trans. Smart Grid* 11 (2), 1724–1736. doi:10.1109/TSG.2019.2942616

Zhang, L., Chen, C., Wang, Q., and Zhou, D. (2021). The Impact of Feed-In Tariff Reduction and Renewable Portfolio Standard on the Development of Distributed Photovoltaic Generation in China. *Energy* 232, 120933. doi:10.1016/j.energy.2021.120933

Zhang, Y., Zhao, X., Zuo, Y., Ren, L., and Wang, L. (2017). The Development of the Renewable Energy Power Industry under Feed-In Tariff and Renewable Portfolio Standard: A Case Study of China's Photovoltaic Power Industry. *Sustainability* 9 (4), 532. doi:10.3390/su9040532

Zhao, Y., Chen, F., Li, Z., Zhu, M., and Li, K. (2021). "Correlation Analysis between Transaction Price and Wind Power Generation Based on Copula Function," in *2021 IEEE 2nd International Conference on Information Technology, Big Data and Artificial Intelligence (ICIBA) (IEEE)*. doi:10.1109/iciba52610.2021.9688290

Zhu, C., Fan, R., Luo, M., Zhang, Y., and Qin, M. (2022). "Simulating Policy Interventions for Different Quota Targets of Renewable Portfolio Standard: A Combination of Evolutionary Game and System Dynamics Approach," in *Sustainable Production and Consumption*. doi:10.1016/j.spc.2022.01.029

FUNDING

This study received funding from the Science and Technology Program of State Grid Zhejiang Electric Power Co., Ltd. (No. B311DS21000A).

Conflict of Interest: Authors HD, CX, and ZZ were employed by the company State Grid Zhejiang Electric Power Co., Ltd., Research Institute.

The remaining authors declare that the research was conducted in the absence of any commercial or financial relationships that could be construed as a potential conflict of interest.

Publisher's Note: All claims expressed in this article are solely those of the authors and do not necessarily represent those of their affiliated organizations, or those of the publisher, the editors and the reviewers. Any product that may be evaluated in this article, or claim that may be made by its manufacturer, is not guaranteed or endorsed by the publisher.

frontiers | Frontiers in Energy Research

TYPE Original Research
PUBLISHED 18 July 2022
DOI 10.3389/fenrg.2022.965669

OPEN ACCESS

EDITED BY
Jiajia Yang,
University of New South Wales, Australia

REVIEWED BY
Luhao Wang,
University of Jinan, China
Jinyu Wang,
Xi'an Jiaotong University, China
Yumin Zhang,
Shandong University of Science and Technology, China

*CORRESPONDENCE
Hua Wei,
weihua@gxu.edu.cn

SPECIALTY SECTION
This article was submitted to Smart Grids,
a section of the journal
Frontiers in Energy Research

RECEIVED 10 June 2022
ACCEPTED 29 June 2022
PUBLISHED 18 July 2022

CITATION
Ji Y and Wei H (2022), An approximate dynamic programming method for unit-based small hydropower scheduling. *Front. Energy Res.* 10:965669. doi: 10.3389/fenrg.2022.965669

An approximate dynamic programming method for unit-based small hydropower scheduling

Yueyang Ji and Hua Wei*

School of Electrical Engineering, Guangxi University, Nanning, China

Hydropower will become an important power source of China's power grids oriented to carbon neutral. In order to fully exploit the potential of water resources and achieve low-carbon operation, this paper proposes an approximate dynamic programming (ADP) algorithm for the unit-based short-term small hydropower scheduling (STSHS) framework considering the hydro unit commitment, which can accurately capture the physical and operational characteristics of individual units. Both the non-convex and non-linearization characteristics of the original STSHS model are retained without any linearization to accurately describe the hydropower production function and head effect, especially the dependence between the net head and the water volume in the reservoir, thereby avoiding loss of the actual optimal solution due to the large error introduced by the linearization process. An approximate value function of the original problem is formulated via the searching table model and approximate policy value iteration process to address the "curse of dimensionally" in traditional dynamic programming, which provides an approximate optimal strategy for the STSHS by considering both algorithm accuracy and computational efficiency. The model is then tested with a real-world instance of a hydropower plant with three identical units to demonstrate the effectiveness of the proposed method.

KEYWORDS

water, small hydropower scheduling, hydropower unit commitment, approximate dynamic programming, renewable energy sources

1 Introduction

With the high proportion of renewable energy penetration in power system, hydropower is of great significance for achieving the "dual carbon" national goal as a clean energy source with almost zero carbon emissions. Different from other countries' energy structure, China has the richest hydropower resources in the world, which can be a natural advantage to reduce the carbon dioxide emissions in daily operation of power grid. Short-term hydropower scheduling (STHS), which aims to determine the optimal hydropower generation strategy for each hydroelectric unit during a time horizon from several minutes or hours to 1 day, plays an essential role in the daily or shorter

operation of power systems to maximize the utilization of the potential hydropower resources. STHS problems are generally formulated for hydropower plants, i.e., aggregating all the hydroelectric units in a plant and taking them as one equivalent unit to significantly reduce the size of the STHS problem (Zhao et al., 2021). However, these equivalent models neglect the detailed characterization of the properties of the hydroelectric units and thus are not suitable for the STSHS problem, which requires a more accurate and detailed representation of the nonlinear hydropower production function (HPF) and head effect of each unit (Guisández and Pérez-Díaz, 2021; Diniz and Maceira, 2008). Therefore, the representation of more details, such as exact unit commitment and nonconvex HPF, is needed to express the operating characteristics of small hydropower in unit-based ("unit-based" refers to "regarding each hydro-turbine generator unit in a plant as an independent entity") STSHS more accurately.

STHS considering hydro unit commitment (HUC) is a combinatorial, non-convex and non-linear optimization problem (Catalão et al., 2010; Postolov and Iliev, 2022; Wang et al., 2022). The STHS problem has been extensively investigated by researchers in recent years (Chen et al., 2016). For an aggregated hydropower plant and a single hydropower unit, the interior-point method (IPM) can effectively address non-linear constraints in the STHS, but it cannot solve STHS problems with 0–1 binary variables (Apostolopoulou and McCulloch, 2019; Cheng et al., 2022). Mixed-integer linear programming (MILP) is one of the most widespread methods for STHS problems considering HUCs due to its modelling flexibility, simple and efficient software environment, and global search capability (Guedes et al., 2017). In (Cheng et al., 2016), a MILP model for HUC is developed, and the unit performance curves are discretized into a set of piecewise curves based on a discretized net head such that the head effect can be modelled. In (Zhao et al., 2021), a MILP-based HUC framework is proposed to solve the irregular forbidden zone-related constraints for very large hydropower plants. In (Guisández and Pérez-Díaz, 2021), five MILP formulations for piecewise linearization of the HPF equation are discussed: the traditional method based on a single concave piecewise-linear flow-power function (Conejo et al., 2002; Kong et al., 2020), the rectangle method (Borghetti et al., 2008; D'Ambrosio et al., 2010), the logarithmic independent branching 6-stencil method (Huchette and Vielma, 2017), the quadrilateral method (Keller and Karl, 2017), and the parallelogram method (PAR) (Guisández and Pérez-Díaz, 2021). The above-mentioned linearization methods can mitigate the computational burden, and the errors caused by linearization can be accepted in the economic dispatch of large hydropower stations with high head-power dependency and large installed capacity (Shi et al., 2017; Zhang et al., 2021). However, in the STHS of small hydropower plants, the operating net head of hydroelectric units is generally low, and the water volume of reservoirs and the installed capacity of hydro plants are generally small; therefore, the head effect is obvious. The effects of linearization errors in both the net head and the output can be ignored only if the breakpoints are sufficiently dense in the piecewise linearization process (Skjelbred et al., 2020). Nevertheless, with an increase in the density of breakpoints, the advantage of MILP in improving the solution efficiency is often lost with the sharp increase in the time cost.

To solve the above-mentioned large-scale, discrete non-convex and non-linear optimization problem of the unit-based STSHS (Marchand et al., 2018), dynamic programming (DP) has been applied effectively in the hydro scheduling field due to its superior performance in handling discrete variables and non-convex and non-linear constraints in STSHS problems (Morillo et al., 2020). DP decomposes a multi-stage decision problem into a number of single-stage sub-problems and can obtain the global optimal solution in most cases. However, DP is difficult to solve even for medium-sized scheduling problems because the computational burden increases exponentially with the dimensionality of the state space. To alleviate the problem of the curse of dimensionality, several variants of DP have been proposed in recent years. In (Flamm et al., 2021), a two-stage dual dynamic programming method is proposed to reconstruct the nonlinear problem; the approach is notable for its calculation accuracy and solving efficiency. In (Feng et al., 2017), an orthogonal discrete differential dynamic programming (ODDDP) method is introduced. The orthogonal experimental design can select some small but representative state combinations, thereby alleviating the curse of dimensionality. Although these improved DP methods have achieved various degrees of success in terms of alleviating the curse of dimensionality, the computational burden may still be intolerable when the problem scale reaches a certain degree. In addition, to ensure computational efficiency, the nonlinear expression of HPF in the literature is usually not sufficiently accurate, and the impacts of power generation on the water head are also not considered, so it is not suitable for STSHS. Thus, there is an urgent need to develop new efficient algorithms to improve the computational efficiency and convergence accuracy for STSHS.

Approximate dynamic programming (ADP) is an important and powerful artificial intelligence optimal method (Zeng et al., 2019) that has attracted considerable attention in the fields of power system scheduling (Lin et al., 2019; Zhu et al., 2019; Lin et al., 2020; Zhu et al., 2020). The theory of ADP was proposed by Powell W.B. (Powell, 2011), and its core idea is to avoid the traversal of all states to reduce the computational burden of value function approximation (VFA) while ensuring approximate accuracy. ADP has been successfully applied to power system optimization. In (Xue et al., 2022), an ADP algorithm proposed for the real-time schedule of an integrated heat and power system established the mapping relationship between the battery and heat storage tank to approximate the value function through a

table function model, thereby achieving the approximation of the optimal value function by traversing discrete values with fewer state variables. In (Shuai et al., 2019), an ADP algorithm based on a piecewise-linear approximation strategy was employed to address the fluctuations in renewable energy generation and electricity prices in the real-time dispatching of microgrids. In (Shuai et al., 2020), a hybrid approximate dynamic programming method was proposed by combining model predictive control and ADP. The model was then applied to the real-time scheduling of gas-electricity integrated energy systems, successfully addressing the tight coupling between time periods caused by the material balance equation of natural gas systems. ADP inherits all the advantages of DP and can efficiently address discrete or continuous, linear or nonlinear, deterministic or stochastic problems (Qiu et al., 2020). However, to the best of our knowledge, few published studies have been conducted on solving the unit-based STSHS framework, especially when the HUC problem is non-convex and the HPF is a bivariate quadratic equation.

This paper formulates the unit-based STSHS optimization problem considering HUC as a mixed-integer nonlinear programming (MINLP) model, which includes the constraints that can describe the HPF and head effect of hydroelectric units accurately. We propose the ADP algorithm to solve the STSHS model without any approximation treatment of the nonlinear constraints.

The contributions of this paper are summarized as follows:

1) An ADP algorithm is proposed to solve the STSHS model. The intractable MINLP problem is reformulated into a solvable NLP problem by decomposing the multi-period optimization into multiple single-period optimizations for the sake of computational tractability. The non-linear expression of HPF and the head effect is retained to ensure the optimality of the schedule strategy.
2) A table function model is developed to establish the mapping relationship between the discrete states of the water volume of the reservoir and the value function; by such means, the high-dimensional state variables are aggregated to approximate the value function, and the optimal value function is approximated by the value iteration method. Thus, schedule strategy optimality and a computationally efficient policy are achieved.
3) A state space compression strategy, according to the operation characteristics of small hydropower plants, is proposed for the consideration of both the effectiveness and optimization ability. This compression strategy can remove the redundant states from the search space by analyzing the variation in available water in each period, which does not reduce the number of discrete states. This strategy not only ensures the optimization ability but also greatly reduces the scale of the problem and further improves the computational efficiency.

The rest of this paper is organized as follows: Section 2 describes the STSHS framework, including the start-up and shutdown of each hydro unit. Section 3 proposes the ADP algorithm for the HUC, which is the main contribution of this paper. In Section 4, we test the proposed ADP algorithm on a realistic instance of a hydropower station with three identical units to verify the effectiveness of our method. Finally, Section 5 presents conclusions.

2 Description of short-term small hydropower scheduling framework considering hydro unit commitment

2.1 Objective function

The objective of the optimal operation of the STSHS is to find the maximum power generation of all the small hydropower units in the entire scheduling horizon, which can be expressed as

$$\max F_p = \sum_{t=1}^{T}\sum_{i=1}^{m} d_{i,t} \cdot p_{i,t} \cdot \Delta t \tag{1}$$

The output power $p_{i,t}$ is defined by the HPF, and it can generally be expressed as

$$p_{i,t} = G \cdot \eta_{i,t}^{\mathrm{Gen}}\left(p_{i,t}\right) \cdot \eta_{i,t}^{\mathrm{Turb}}\left(h_{i,t}, q_{i,t}\right) \cdot h_{i,t} \cdot q_{i,t} \tag{2}$$

The hydro turbine efficiency $\eta_{i,t}^{\mathrm{Turb}}$ is associated with converting the water head potential energy in the reservoir into mechanical energy in the hydro turbine; therefore, it primarily depends on the water head and turbine flow. $\eta_{i,t}^{\mathrm{Turb}}$ decreases as turbine flow increases after reaching the optimum efficiency point. Similarly, the hydropower generation efficiency $\eta_{i,t}^{\mathrm{Gen}}$ is related to the conversion of mechanical energy into electrical energy in the generator, which is usually higher than 95%, and it increases monotonically as the output power of the generator increases.

Since the mathematical expression of the hydro unit efficiency function is considerably complicated, a fixed constant is typically used to replace the efficiency function irrespective of the characteristics of the HPF, which will lead to larger errors. To describe the input–output relationship of the efficiency function implicitly in the HPF more accurately, this paper conducts a polynomial fitting of the water head and water flow in the HPF based on the Hill diagram of the hydropower unit (Zhang et al., 2021; Zhao et al., 2021), which can be expressed as

$$p_{i,t} = a_i h_{i,t}^2 + b_i q_{i,t}^2 + c_i h_{i,t} q_{i,t} + d_i h_{i,t} + e_i q_{i,t} + f_i \tag{3}$$

where a_i, b_i, c_i, d_i, e_i and f_i are the quadratic fitting coefficients of the HPF, which models the relationship between the power output of hydroelectric unit i and the water discharge and net head.

2.2 Constraints

The STSHS problem is subject to a variety of constraints, including water balance, water level, water head, and other operating limits.

2.2.1 Water balance constraint

The volume change of the reservoir is affected by the inflow, water discharge and spillage of the reservoir. The water balance equation is denoted as

$$r_{t+1} = r_t - \left(\sum_{i=1}^{m} q_{i,t} + s_t - j_t\right)\Delta t \tag{4}$$

2.2.2 Water volume constraints

As the water volume of the reservoir at the end of the last period is the initial volume of the next dispatch horizon, to ensure the normal operation of the reservoir in the next dispatch horizon, the water volume of the reservoir at the beginning and the end of the dispatch horizon should be restricted as

$$\begin{cases} r_0 = r^{\text{init}} \\ r_T = r^{\text{final}} \end{cases} \tag{5}$$

2.2.3 Limit constraints of water volume

$$r^{\min} \le r_t \le r^{\max} \tag{6}$$

2.2.4 Net head balance constraint

$$h_t = h_t^{\text{up}} - h_t^{\text{dw}} \tag{7}$$

2.2.5 Net head effect constraints

The head effect has a direct impact on the unit's efficiency and operating limits, which is the crucial part of the formulation of the STSHS problem. For a fixed-head hydropower plant, the net head is relatively high; thus, the effect of water level changes in the forebay and tailrace caused by power generation can be ignored. However, for a low-head hydropower plant, the changes in the water levels of the forebay and tailrace have relatively obvious impacts on the net head. Therefore, the relationship between the forebay level and the water volume, as well as the tailrace level and the outflow, can be expressed as

$$h_t^{\text{up}} = a^{\text{up}} r_t^2 + b^{\text{up}} r_t + c^{\text{up}} \tag{8}$$

$$h_t^{\text{dw}} = a^{\text{dw}} \left(\sum_{i=1}^{m} q_{i,t} + s_t\right)^2 + b^{\text{dw}} \left(\sum_{i=1}^{m} q_{i,t} + s_t\right) + c^{\text{dw}} \tag{9}$$

where a^{up}, b^{up} and c^{up} are the fitting coefficients of the relationship between the forebay level and water volume. a^{dw}, b^{dw} and c^{dw} are the fitting coefficients of the relationship between the tailrace level and the total outflow of the hydropower plant, respectively.

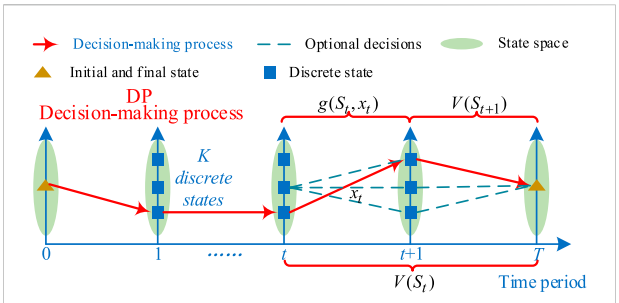

FIGURE 1
Diagram of ADP solution.

2.2.6 Limits of net head

$$h^{\min} \le h_t \le h^{\max} \tag{10}$$

2.2.7 Output limits

$$d_{i,t} p_i^{\min} \le p_{i,t} \le d_{i,t} p_i^{\max} \tag{11}$$

2.2.8 Constraints of water discharge

$$d_{i,t} q_i^{\min} \le q_{i,t} \le d_{i,t} q_i^{\max} \tag{12}$$

3 Approximate dynamic programming

3.1 Process of approximate dynamic programming

ADP is an excellent method proposed by Powell to solve the curse of dimensionality problem of dynamic programming (Xue et al., 2022). A diagram of the use of ADP to solve the STSHS problem is illustrated in Figure 1, in which the system state S_t includes the reservoir volume of the water head and the on/off status of the unit. The decision variables x_t include the allocation of power generation flow, water spillage, and the start-up/shutdown action of units during each period. S_{t+1} is the state vector of the next period after decision x_t is executed in state S_t. $g(S_t, x_t)$ denotes the benefit generated by reaching state S_{t+1} after executing x_t. The value function $V(S_t)$ reflects the influence of the current state on the revenue from period t to T, that is, the maximum power generation during $[t, T]$.

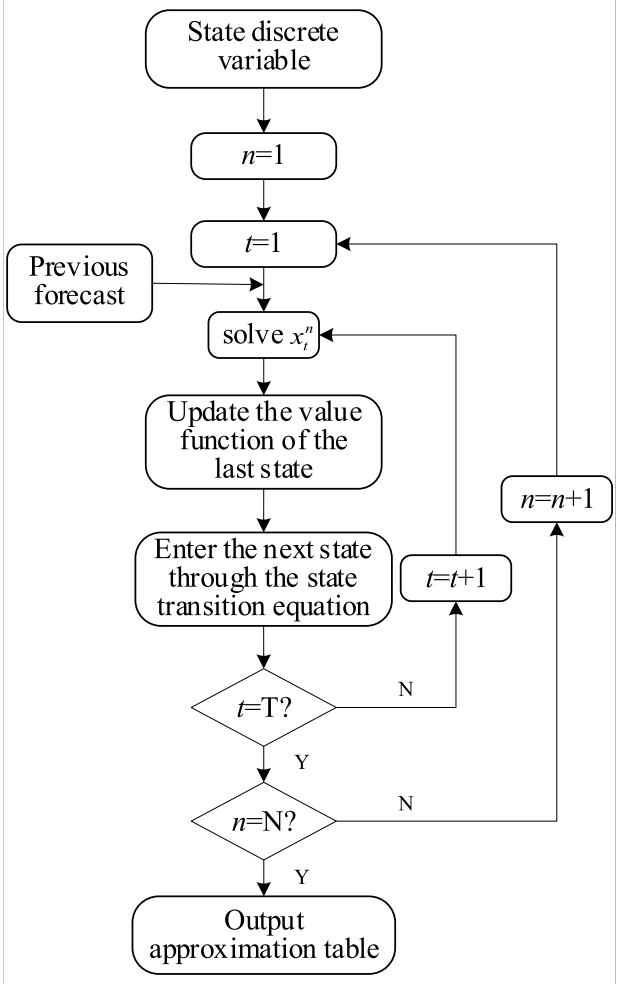

FIGURE 2
Iteration flow chart of the approximate value table.

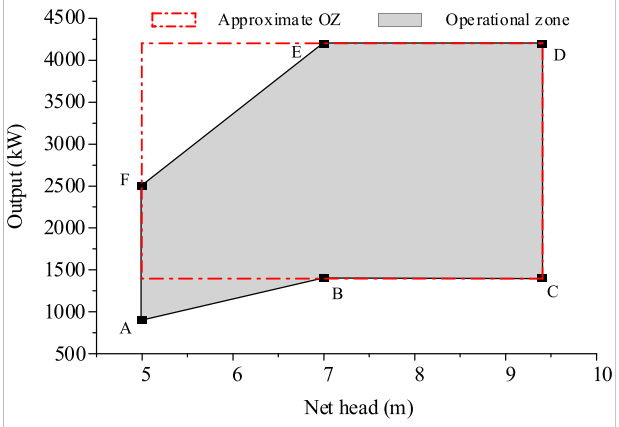

FIGURE 3
The operational zone of small hydropower units.

According to the optimality principle, the above T stage maximum profit problem can be transformed into T single-period decision-making problems with the Bellman equation so that the optimal solution can be obtained via step-by-step recursion, which can be expressed as

$$V(S_t) = \max\left[g(S_t, x_t) + V(S_{t+1})\right] \tag{13}$$

The solution of the Bellman equation is based on the calculation of the value functions of all states in the state space. However, current computer technology is still insufficient to traverse the combination of the enormous state space and decision space. The key idea of ADP is to use the approximate value function $\tilde{V}_k(S_{t+1})$ instead of $V_k(S_{t+1})$ and to approximate the optimal value function in an iterative manner, thereby avoiding direct calculation of the value function.

The basic process of value function iteration is as follows:

First, set the initial value of the approximate value function of each state. Then, calculate the approximate value function from period 0 to period T; the optimal solution of this iteration is determined based on the rule that the function value of the last period is optimal. Next, proceed to the next iteration according to the updated approximation function. In this way, the approximate value function is gradually approximated to the optimal value function through the iterative process. In each iteration, instead of traversing the entire state space to calculate the value function, only a small number of states participate in the calculation in each period, so the computational complexity no longer increases exponentially with an increase in the number of state variables and the total number of periods, thereby overcoming the curse of dimensionality.

The value function approximation (VFA) methods commonly used in ADP include table function approximation, piecewise linear function approximation and neural network approximation, among which table function approximation is a basic but very effective method that can accurately approximate the complex non-linear value function in hydro economic dispatch. Hence, the look-up table model is applied to approximate the value function, and the value iteration method is employed to solve the Bellman equation.

3.2 Lookup table for the short-term small hydropower scheduling problem

The optimization strategy based on the look-up table establishes a mapping relationship between the discretized system state variables and the sum of the power generation of each time period. The table function is used to approximate the real value function, and by means of variable decoupling between time periods, the original MINLP problem can be decomposed into multiple NLP sub-problems containing only continuous variables to reduce the difficulty of solving.

TABLE 1 Parameters of hydro units.

Parameter	Value	Parameter	Value	Parameter	Value	Parameter	Value
r^{max} (Mm^3)	14.4	q^{min} (m^3/s)	14	c_p	10.0971	br	0.0042
r^{min} (Mm^3)	13.4	p^{max} (kW)	4200	d_p	78.0492	cr	21.4179
h^{max} (m)	9.4	p^{min} (kW)	1,400	e_p	9.4814	aq	−1.2228e-7
h^{min} (m)	5.0	a_p	−8.4886	f_p	−427.0754	bq	0.0023
q^{max} (m^3/s)	52	b_p	−0.1963	a_r	−3.1084e-7	cq	20.88

The continuous variables in the state variables are discretized as

$$\Delta S_i = \left(S_i^{\max} - S_i^{\min}\right)/\left(K_i - 1\right) \tag{14}$$

where ΔS_i represents the discretization step size of the continuous variable. $S_i^{\max}$ and $S_i^{\min}$ are the upper and lower limits of the variable, respectively. K_i is the number of discrete variables. In this paper, the water volume of the reservoir is discretized into K_r states, and the on/off status of m units is 2^m, so the size of the state space is $M = 2^m \times K_r$. After the process of discretization, we can initialize an empty value table to measure the value of being in a state, and the size of the table is $M \times T$.

3.3 Approximate value iteration

The value iteration of ADP forms a value function sequence by continuously updating the value table to approximate the optimal value function. In each iteration, the decision is determined by the estimated value of the current value function and the state variable, which can be expressed as

$$x_t^k = \arg\max\left\{g_t\left(S_t, x_t\right) + \gamma \tilde{V}_t^{k-1}\left(G\left(S_t\right)\right)\right\} \tag{15}$$

where $\gamma \in (0, 1)$ is the decay factor. When γ is 0, the value function focuses on only the immediate benefits after the decision is made in the current period, and the algorithm becomes a short-sighted myopic algorithm. When γ approaches 1, the algorithm pays more attention to the benefits in the future period, which is more conducive to obtaining the optimal value table of the whole period. $G\left(S_t\right) = \{r_t, d_{1,t}, \ldots, d_{m,t}\}$ is the aggregated state variable.

After completing the decision for each period, the observed value $\hat{v}_t^k$ of the value function of the current state is calculated as

$$\hat{v}_t^k = \min\left\{g_t\left(S_t, x_t\right) + \tilde{V}_t^{k-1}\left(G\left(S_t\right)\right)\right\} \tag{16}$$

Then, the value function of the previous period is updated as

$$\tilde{V}_{t-\Delta t}^k\left(G\left(S_{t-\Delta t}^k\right)\right) = \alpha^k \hat{v}_t^k + \left(1 - \alpha^k\right)\tilde{V}_{t-\Delta t}^{k-1}\left(G\left(S_{t-\Delta t}^k\right)\right) \tag{17}$$

where $\alpha^k \in (0, 1)$ is the step size in the k-th value iteration.

In the process of value iteration, only the value function corresponding to the state accessed in each period is updated. In other words, in the approximate value table, only the cells corresponding to the current reservoir volume and the unit on/off status are updated. In each iteration, the corresponding elements accessed in the table function are updated in a forward manner step by step until a converged approximation table is obtained. The iterative process for updating the value table is shown in Figure 2.

3.4 Compression of state space

In the above ADP algorithm, for each time period t, all discrete states are traversed when solving 15) to select the optimal decision-making action, which makes the solution process highly time-consuming. Therefore, to reduce the computational burden caused by the increase in discrete states, considering the operation mode of determining electricity-by-water of small hydropower, we compress the existing state space to further reduce the solution time.

First, the forecasting information of water inflow is developed to compress the search space of discrete states of water volume. For period t of the k-th iteration, the total available water volume $q_{k,t}^{\text{avl}}$ can be defined as

$$q_{k,t}^{\text{avl}} = j_t \cdot \Delta t - \left(r_{k,t+1} - r_{k,t}\right) \tag{18}$$

To ensure $q_{k,t}^{\text{avl}} > 0$, the upper bound of the search space of the water volume $r_{k,t+1}$ in the next period should not exceed $j_t \cdot \Delta t + r_{k,t}$. In addition, to avoid unreasonable water abandonment, the total available water should not exceed the upper limit of the power generation flow of the units; that is, the lower bound of the search space of the water volume $r_{k,t+1}$ in the next period should not be lower than $j_t \cdot \Delta t + r_{k,t} - \sum_{i=1}^{m} q_i^{\max}$. Therefore, the search space for discrete states of water volume can be restricted to:

$$\begin{cases} r_{k,t+1}^{\min} = j_t \cdot \Delta t + r_{k,t} - \sum_{i=1}^{m} q_i^{\max} \\ r_{k,t+1}^{\max} = j_t \cdot \Delta t + r_{k,t} \end{cases} \tag{19}$$

Similar strategies can be used to compress the on/off status of units in the search space. For period t in the k-th

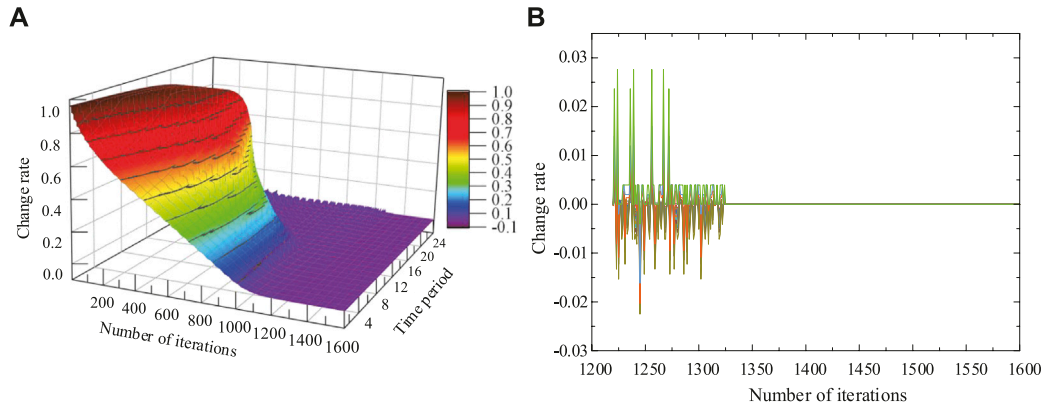

FIGURE 4
Approximate value function iteration process. **(A)** Full view; **(B)** Front view of iterations after 1200.

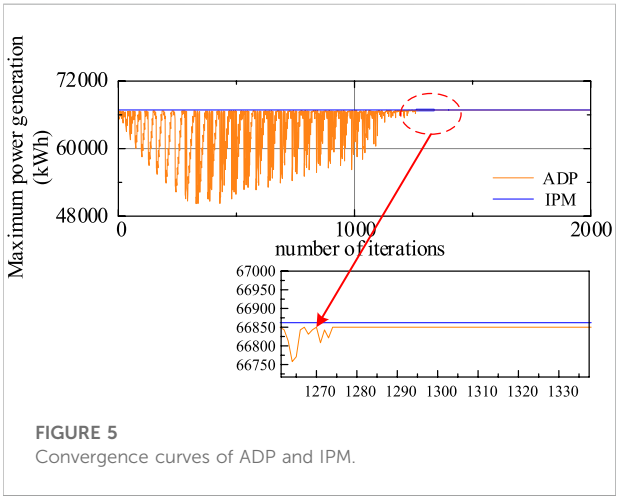

FIGURE 5
Convergence curves of ADP and IPM.

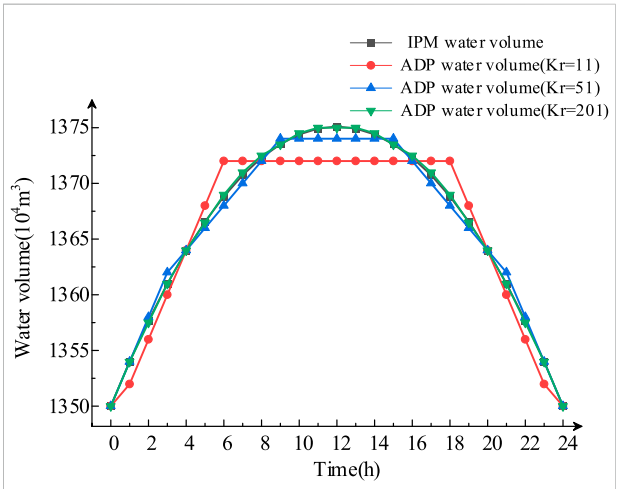

FIGURE 6
Changes in the water volume under different numbers of discrete points.

iteration, if the difference between the total available water in this period and the previous period satisfies $\Delta q_{k,t}^{\mathrm{avl}} = q_{k,t}^{\mathrm{avl}} - q_{k,t-1}^{\mathrm{avl}} > 0$, unnecessary traversal of the state that requires a shutdown action to reach should be avoided. For instance, if the current unit status is [1,100], then [0100] and [1,000] should be eliminated in the decision space during this period. In contrast, if the available water volume is reduced compared with that in the previous period, the statuses that require a start-up action to reach should be avoided. Therefore, [1,110], [1,101] and [1,111] should be excluded from the search space.

The scale of the problem is greatly reduced by adopting the above compression processing strategy of the search space. For the hydro units of the identical model, their output characteristics are exactly the same. For the objective of maximum power generation, the exchange of on/off status between units will not affect the optimization results, so the optional states can be further compressed. For example, for the same four hydro units, assuming that the state in a certain period is [1,100], regardless of the trend of available water, the five statuses [1,010], [1,001], [0110], [0101] and [0011] in the state space can be represented by the original state [1,100], so these five states can be eliminated from the search space. When the number of units of the same model increases, the proposed strategy makes the state space no longer grow exponentially but increase linearly, further reducing the decision space, thereby greatly reducing the computational burden.

TABLE 2 Comparison of IPM and ADP optimization results.

Period	Output power of IPM (kW)	Output power of ADP(K_r = 11) (kW)	Output power of ADP(K_r = 51) (kW)	Output power of ADP(K_r = 201) (kW)
1	1984.11	2,388.43	1986.91	1986.91
2	2058.92	1988.53	1990.15	2092.03
3	2,133.12	1991.77	1993.40	2095.03
4	2,206.78	1995.01	2,400.42	2,199.37
5	2,279.93	1998.25	2,402.42	2,302.68
6	2,352.36	2001.48	2,404.41	2,305.06
7	2,424.07	2,802.11	2,406.40	2,407.40
8	2,495.10	2,802.11	2,408.39	2,508.58
9	2,565.46	2,802.11	2,410.38	2,608.53
10	2,635.03	2,802.11	2,804.47	2,609.62
11	2,703.86	2,802.11	2,804.47	2,708.32
12	2,771.94	2,802.11	2,804.47	2,805.66
13	2,839.26	2,802.11	2,804.47	2,805.66
14	2,905.75	2,802.11	2,804.47	2,901.55
15	2,971.22	2,802.11	2,804.47	2,995.93
16	3,036.01	2,802.11	3,182.63	2,994.66
17	3,099.71	2,802.11	3,179.89	3,087.41
18	3,162.50	2,802.11	3,177.14	3,178.52
19	3,224.32	3,543.71	3,174.40	3,267.89
20	3,285.15	3,537.47	3,171.65	3,264.34
21	3,344.98	3,531.22	3,168.90	3,351.80
22	3,403.76	3,524.96	3,528.09	3,437.40
23	3,461.44	3,518.69	3,521.83	3,432.08
24	3,518.01	3,152.37	3,515.56	3,515.56
Total energy (kWh)	66,862.79	66,797.21	66,849.81	66,861.98
Error	--	0.0981%	0.0194%	0.0012%

3.5 Description of non-convex operational zone in approximate dynamic programming process

The operational zone (OZ) of small hydropower units is usually a non-convex polygon region, as shown in Figure 3.

The boundaries of the irregularly shaped OZ vary with the net head and have several inflection points, such as points B and E, as illustrated in Figure 3, which makes the OZ a non-convex region. The mathematical representation of the irregularly shaped OZ can be derived as follows:

$$\begin{cases} k_i^{AB}\left(h_{i,t}-h_i^A\right)+p_i^A \le p_{i,t} \le k_i^{FE}\left(h_{i,t}-h_i^F\right)+p_i^F, h_i^A \le h_{i,t} \le h_i^B \\ p_i^B \le p_{i,t} \le p_i^E, h_i^B \le h_{i,t} \le h_i^C \end{cases} \tag{20}$$

where h_i^A, h_i^B, h_i^C and h_i^F represent the net head of points A, B, C and F, respectively. p_i^A, p_i^E and p_i^F indicate the unit output of points A, E and F, respectively. k_i^{AB} and k_i^{FE} denote the slopes of $\overrightarrow{AB}$ and $\overrightarrow{FE}$, respectively. If we employ a regularly shaped rectangle to approximate OZ, such as the red dotted box shown in Figure 3, the approximate OZ would not only raise the lower limit of unit output under the lower net head but also reduce the final generation. However, it will fail to ensure the safety of unit operation when the water discharge is large. Generally, such a non-convex region cannot be perfectly represented with linear constraints in programming models unless additional 0–1 variables are introduced.

Under the ADP framework proposed in this paper, the irregularly shaped OZ can be perfectly expressed. In each single-period optimization process, the variation in water volume is a constant. As a result, the optimal result of water discharge for each unit is obtained before solving the single-period sub-problem, which means the net head has already been pre-designated. Thus, the upper and lower boundaries of the OZ can be dynamically updated as the net head changes.

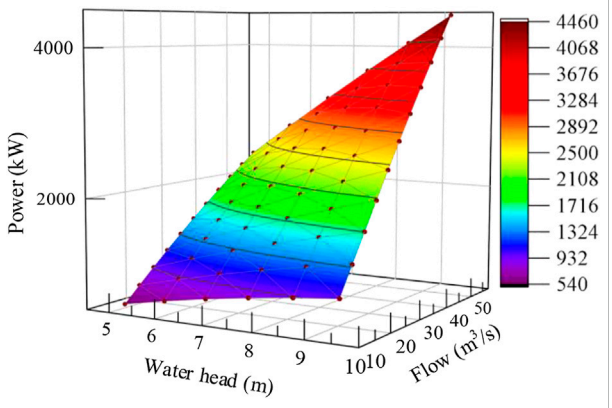

FIGURE 7
Approximate output surface using the PAR method (M_h = 6, M_q = 11)

of RAM. The scheduling period is 24 h, and the time resolution is 1 h.

4.1 Iterative process of the approximate value function

To express the dynamic approximation process of the value function, we define the change rate of the approximation function as follows:

$$\eta\left(\tilde{V}_{k,t}\right) = \left(\tilde{V}_{k,t} - \tilde{V}_{opt,t}\right) / \left(\tilde{V}_{0,t} - \tilde{V}_{opt,t}\right) \times 100\% \quad (21)$$

The indicator $\eta(\tilde{V}_{k,t})$ reflects the differences in the value function of each period compared with the optimal value function in the k-th iteration. The change in this difference represents the adjustment of the state of the ADP algorithm in the iterative process to achieve the maximum power

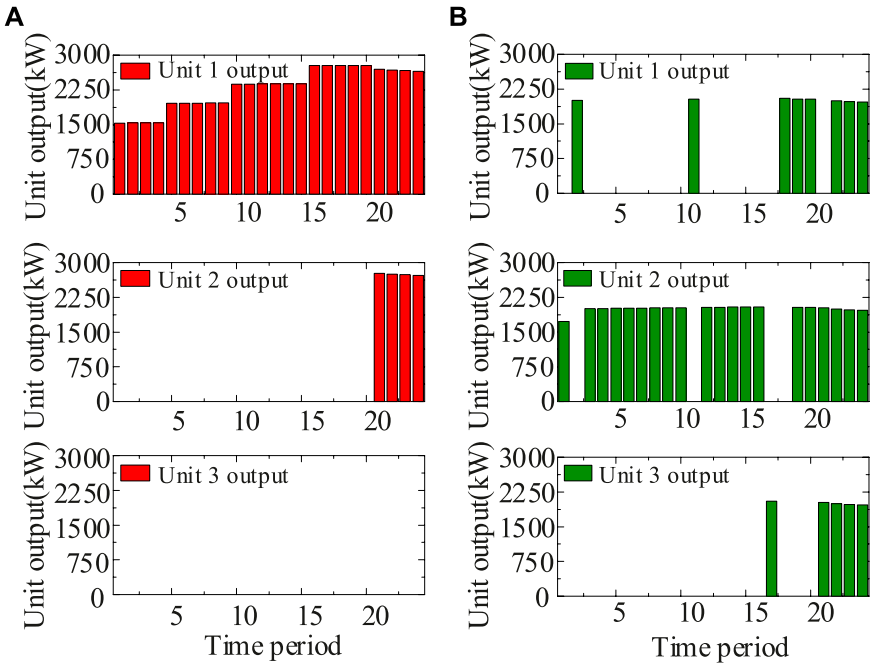

FIGURE 8
Comparison of unit output between ADP and PAR-MILP. **(A)** ADP; **(B)** MILP.

4 Case studies

A small hydropower plant in southern China is adopted as a test system to verify the effectiveness of the proposed formulation and methodology. The parameters of each unit are illustrated in Table 1. All simulations are implemented with MATLAB R2021a using a PC with a 3.6 GHz AMD R7 4700G processor and 16 GB

generation. For instance, if the initial value function $\tilde{V}_{0,t}$ of period t is greater than the optimal value function $\tilde{V}_{opt,t}$, and $\eta(\tilde{V}_{k,t}) > 0$ in the k-th iteration, then there is $\tilde{V}_{k,t} > \tilde{V}_{opt,t}$, indicating that the value function of the state during the current period is better than the optimal value function. However, due to the significant impact on the state of t+1 and subsequent periods, which restricts future power generation, it is

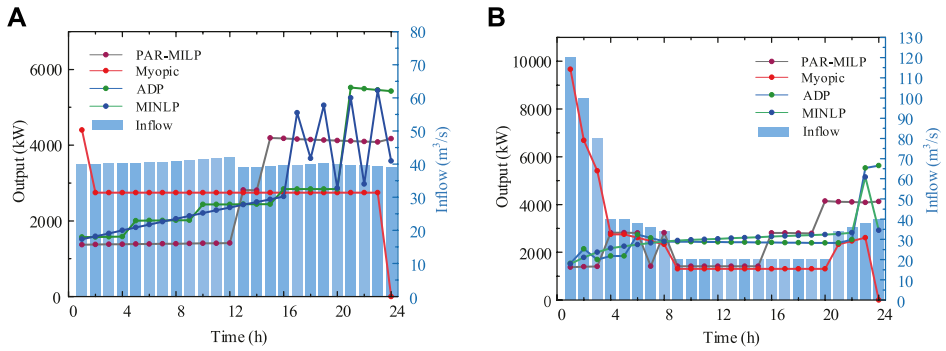

FIGURE 9
Comparison of the output of each method under different inflows. **(A)** Case 1: Relatively smooth inflow; **(B)** Case 2: Inflow with a significant drop.

TABLE 3 Comparison of optimization results of each method.

	Algorithms	ADP(K_r = 21)	Myopic	PAR-MILP	MINLP
Case 1	Generation (kWh)	67,205.43	64,860.89	63,740.5	67,071.40
	Time (s)	2,129.8	209.4	7,685.2	43,200
Case 2	Generation (kWh)	61,910.67	57,591.58	58,545.69	61,989.52
	Time (s)	1,589.6	41.4	3,687.1	2,800

discarded in the subsequent iteration process. In contrast, if $\eta(\tilde{V}_{k,t}) < 0$, then $\tilde{V}_{k,t} < \tilde{V}_{opt,t}$, indicating that the approximation of the value function in the current period is inferior to the optimal value function. Therefore, a better strategy will be sought in the subsequent iteration process.

Figure 4A shows the change rate of the approximate value function of the three units in 24 time periods with the ADP iteration process, and the change rate convergence curve for each time period is shown in Figure 4B. Figure 4 shows that $\eta(\tilde{V}_{k,t})$ oscillates positively and negatively with the value iteration process and finally converges to 0, indicating that the algorithm gradually updates the strategy in the iterative process and approaches the optimal value function to achieve the goal of maximum power generation.

4.2 Optimization results of single-unit short-term small hydropower scheduling

To clarify the approximation process of the power generation obtained by the proposed ADP algorithm to the optimal solution, the discrete state number *Kr* of the water volume is taken as 51, and the single-unit optimization convergence curve of the ADP algorithm is obtained as depicted in Figure 5. The ADP algorithm converges to the optimal generation of 66,849.81 kWh when the number of iterations reaches 1,325, which is only 0.0194% different from the optimal result of 66,862.79 kWh obtained by IPM, thereby demonstrating the optimality of the proposed ADP algorithm in solving the STSHS.

To illustrate the influence of *Kr* on the approximation of the optimal solution of the non-linear problem by the ADP algorithm, the number of discrete states *Kr* of water volume is taken as 11, 51, and 201, and the optimization results of single-unit STSHS by ADP and IPM are compared, as shown in Figure 6. As *Kr* increases, the water volume of ADP gradually approaches the optimal water volume of IPM. When *Kr* is 201, the water volume curve of ADP almost overlaps with that of IPM, which indicates that the decision made by ADP in each period will gradually approach the optimal as the number of discrete points of water volume increases.

To further illustrate the performance of the ADP algorithm, Table 2 lists the unit output of the IPM and ADP algorithms in all 24 time periods. Table 2 shows that as the number of discrete states of water volume increases, the approximate solution obtained by ADP gradually approaches the optimal solution obtained by IPM. When *Kr* = 11, the error compared to the maximum power generation of IPM is reduced to 0.0982%, which can fully meet the needs of engineering applications. When *Kr* is increased to 201, the error compared to the maximum power generation of IPM is only 0.0012%. The above results show that

TABLE 4 Comparison of optimization results before and after space compression.

Period	Output power without state compression (kW)			Output power with state compression (kW)		
	Unit 1	Unit 2	Unit 3	Unit 1	Unit 2	Unit 3
1	0.00	1784.41	0.00	1784.41	0.00	0.00
2	0.00	1788.02	0.00	1788.02	0.00	0.00
3	0.00	1791.62	0.00	1791.62	0.00	0.00
4	0.00	1795.21	0.00	1795.21	0.00	0.00
5	0.00	1798.79	0.00	1798.79	0.00	0.00
6	0.00	1802.37	0.00	1802.37	0.00	0.00
7	0.00	1805.93	0.00	1805.93	0.00	0.00
8	0.00	1809.49	0.00	1809.49	0.00	0.00
9	0.00	1813.04	0.00	1813.04	0.00	0.00
10	0.00	2,835.36	0.00	2,835.36	0.00	0.00
11	0.00	2,835.36	0.00	2,835.36	0.00	0.00
12	0.00	2,835.36	0.00	2,835.36	0.00	0.00
13	0.00	2,835.36	0.00	2,835.36	0.00	0.00
14	0.00	2,835.36	0.00	2,835.36	0.00	0.00
15	0.00	2,835.36	0.00	2,835.36	0.00	0.00
16	0.00	2,835.36	0.00	2,835.36	0.00	0.00
17	0.00	2,835.36	0.00	2,835.36	0.00	0.00
18	0.00	2,835.36	0.00	2,835.36	0.00	0.00
19	0.00	2,835.36	0.00	2,835.36	0.00	0.00
20	0.00	2,835.36	0.00	2,835.36	0.00	0.00
21	0.00	2,835.36	0.00	2,835.36	0.00	0.00
22	0.00	2,850.36	2,850.36	2,850.36	2,850.36	0.00
23	0.00	2,832.07	2,832.07	2,832.07	2,832.07	0.00
24	2,813.69	2,813.69	0.00	2,813.69	2,813.69	0.00
Total energy (kWh)	67,205.43			67,205.43		
n	464			464		
t(s)	4422.8			2,129.8		

TABLE 5 Comparison of ADP optimization results with different value table sizes.

Value table size	K_r = 21	K_r = 51	K_r = 101
Generated energy(kWh)	67,205.43	67,254.17	67,262.80
Number of iterations	464	1,325	2,628
Time consuming (s)	2,129.8	11,764.1	47,941.7

for the STSHS problem, the error between the solution of the ADP algorithm and the optimal solution is extremely small, and the quality of the solution can be significantly improved by increasing the number of discrete states, further indicating that the proposed algorithm has superior convergence performance and practical engineering value.

4.3 Optimization results of multiple-unit short-term small hydropower scheduling

When the STSHS model includes 0–1 variables representing the on/off status of the units, it cannot be solved by IPM. With the maturity of the solving technology of the MILP problem, the MILP model of the STSHS problem can be achieved via piecewise linearization and then using a commercial solver to obtain the optimal solution. In this paper, PAR is used to perform piecewise linearization of the HPF function (3). The number of discrete points of net head M_h = 6, the number of discrete points of water discharge M_q = 11, and the obtained approximate output surface is shown in Figure 7.

For the STSHS problem involving three units, the state discrete number K_r of the water volume is set to 51, and the

unit output optimization results obtained using ADP and PAR-MILP are shown in Figure 8.

Figure 8 shows that the units start and stop frequently in the MILP results. One reason is that the output characteristics of the three hydropower units are the same. The second reason is that, ignoring the start-up and shutdown costs of small-capacity hydropower units, if the inflow is small, the reservoir tends to store water to raise the net head, and the amount of water available for power generation is limited, resulting in an unnecessary start and stop. In comparison, the optimization results of unit commitment obtained via ADP are more stable and reasonable, among which unit 3 is not even turned on during the whole scheduling period. The reason is that in the ADP algorithm, the search space for the unit commitment decision is compressed, and the redundant on/off state is eliminated from the decision space. As a result, a relatively smooth unit commitment scheme can be obtained without applying additional constraints, such as unit start/stop costs.

Next, to further verify that the ADP algorithm proposed in this paper more easily achieves a satisfactory trade-off between solving efficiency and solution optimality compared with other algorithms, we compare the optimization results of MILP, MINLP and myopic methods with ADP. The Gurobi 9.1.2 commercial solver is used for MILP, and the LINGO commercial solver is used for MINLP. The results of the power outputs of each method under different reservoir inflows are shown in Figure 9, and the time consumption and total generation results are shown in Table 3.

As shown in Figure 9 and Table 3, regardless of the inflow changes, the generation results of ADP and MINLP are extremely close and larger than those of other methods because they completely retain the nonlinearity of HPF and the head effect. Although the myopic algorithm also completely retains the original non-linearity, due to its short-sighted characteristics, the impacts of the current strategy on the subsequent period cannot be considered in the decision-making process, and the power generation obtained is the lowest. Especially after rainfall, when the water inflow gradually decreases, the disadvantages of the myopic algorithm become more obvious. As shown in Figure 9B, myopic tends to maximize the water discharge during each time period, ignoring the reduction of net head in the next time period, which causes the total generation to be 7.5% less than that of the ADP method. Using commercial solvers directly to solve MINLP problems can also produce high-quality solutions, which are only 0.2% different from the ADP results, but the time consumption is 20 times greater than that of ADP. Although PAR-MILP approximates the nonlinear HPF surface by piecewise approximation, the energy generation optimization result is not substantially different from that of ADP, but the corresponding time cost is still much higher than that of ADP. The comparison results indicate that the solution quality of ADP is remarkable among the four algorithms on the premise of ensuring the optimization accuracy level within 0.2%. In terms of computational efficiency, ADP is superior to MILP and MINLP.

4.4 Effect of state space compression

To further illustrate the effect of the proposed state space compression strategy in improving the efficiency of ADP, the number of discrete states K_r of the water volume is set to 21, and the optimization results before and after state space compression are obtained, as shown in Table 4, where n is the number of ADP iterations and t is the time consumption of ADP.

Table 4 shows that the optimal power generation obtained by the ADP algorithm before and after state space compression is the same, indicating that the states eliminated by the proposed compression strategy are redundant states that do not need to be traversed and will not affect the algorithm's optimization ability. In addition, the execution time of ADP after state compression is reduced by 51.84%, which demonstrates that the proposed compression strategy significantly improves the solution efficiency and is suitable for cases with multiple hydropower units, showing its potential practicability and validity for solving the STSHS problem.

4.5 The effect of value table size on approximate dynamic programming optimization results

To clarify the relationship between the approximate accuracy of ADP and the size of the value table, we set the discrete number K_r of the water volume to 21, 51, and 101, which means that the adjacent state intervals of the water volume are 50,000 m^3, 20,000 m^3, and 10,000 m^3, respectively. To ensure that the reservoir can reach the maximum water storage capacity, the initial volume of the reservoir is set to 13.4 million m^3. The simulation results of ADP with different values are shown in Table 5.

Table 5 shows that as the size of the value table increases, the power generation gradually increases, indicating that the quality of the solution also improves. In addition, the number of iterations and solution time increase linearly with the size of the value table. A possible explanation for this is that as the number of discrete states increases, the value table must be updated more often to better approximate the value function, so the number of iterations required to converge increases. In addition, since the state of the water volume is more discrete, in the ADP algorithm, more sub-problems must be solved in each period and in each iteration to make the optimal decision, resulting in an increase in the time consumption of each iteration. Therefore, when using ADP to solve the STSHS problem with unit commitment, a trade-off should be made

between approximation accuracy and calculation time according to engineering requirements.

5 Conclusion

An ADP solution algorithm is proposed for the problem of short-term economic dispatch of small hydropower. The mapping relationship between the discrete state of the water volume and the value function is established through the table function model. Furthermore, the state space is compressed, and the MINLP problem is transformed into multiple NLP sub-problems to reduce the model complexity.

A comparison with the IPM optimization results shows that ADP and IPM tend to produce the same solution in the case of single-unit operation, which proves that the proposed ADP method can obtain high-quality solutions.

For the case of multi-unit optimal scheduling, comparison with the results of myopic, MILP and MINLP shows that ADP obtains better power generation results than myopic and MILP because it retains the nonlinearity of the original model. In addition, the solution time required to make MINLP obtain the same level of optimization results as ADP will obviously exceed that of ADP. This verifies that the proposed method can consider both the quality of the solution and the computational efficiency in solving the non-convex nonlinear SHED problem.

The results of ADP optimization with space compression show that the proposed space compression strategy can effectively reduce the number of candidate decision-making actions in the iterative process and significantly improve the solution efficiency.

Simulation results with different table sizes show that the proposed algorithm can achieve a balance between optimality and solution efficiency by setting the discrete number of water volumes.

Data availability statement

The original contributions presented in the study are included in the article/supplementary material, further inquiries can be directed to the corresponding author.

Author contributions

YJ: Software; Formal analysis; Investigation; Writing-Original Draft; Data Curation; Visualization. HW: Conceptualization; Methodology; Resources; Data Curation; Writing-Review & Editing Supervision; Funding acquisition.

Funding

This work was supported by the National Natural Science Foundation of China (No. 51967002) and in part by the Guangxi Special Fund for Innovation-Driven Development (AA19254034).

Conflict of interest

The authors declare that the research was conducted in the absence of any commercial or financial relationships that could be construed as a potential conflict of interest.

Publisher's note

All claims expressed in this article are solely those of the authors and do not necessarily represent those of their affiliated organizations, or those of the publisher, the editors and the reviewers. Any product that may be evaluated in this article, or claim that may be made by its manufacturer, is not guaranteed or endorsed by the publisher.

References

Apostolopoulou, D., and Mcculloch, M. (2019). Optimal short-term operation of a cascaded hydro-solar hybrid system: A case study in Kenya. *IEEE Trans. Sustain. Energ.* 10 (4), 1878–1889. doi:10.1109/TSTE.2018.2874810

Borghetti, A., D'Ambrosio, C., Lodi, A., and Martello, S. (2008). An MILP approach for short-term hydro scheduling and unit commitment with head-dependent reservoir. *IEEE Trans. Power Syst.* 23 (3), 1115–1124. doi:10.1109/TPWRS.2008.926704

Catalão, J., Pousinho, H., and Mendes, V. M. F. (2010). Mixed-integer nonlinear approach for the optimal scheduling of a head-dependent hydro chain. *Electr. Power Syst. Res.* 80 (8), 935–942. doi:10.1016/j.epsr.2009.12.015

Chen, Y., Liu, F., Liu, B., Wei, W., and Mei, S. (2016). An efficient MILP approximation for the hydro-thermal unit commitment. *IEEE Trans. Power Syst.* 31 (4), 3318–3319. doi:10.1109/TPWRS.2015.2479397

Cheng, C., Wang, J., and Wu, X. (2016). Hydro unit commitment with a head-sensitive reservoir and multiple vibration zones using MILP. *IEEE Trans. Power Syst.* 31 (6), 4842–4852. doi:10.1109/TPWRS.2016.2522469

Cheng, X., Feng, S., Zheng, H., Wang, J., and Liu, S. (2022). A hierarchical model in short-term hydro scheduling with unit commitment and head-dependency. *Energy* 251, 123908. doi:10.1016/j.energy.2022.123908

Conejo, A., Arroyo, J., Contreras, J., and Villamor, F. (2002). Self-scheduling of a hydro producer in a pool-based electricity market. *IEEE Trans. Power Syst.* 17 (4), 1265–1272. doi:10.1109/TPWRS.2002.804951

D'Ambrosio, C., Lodi, A., and Martello, S. (2010). Piecewise linear approximation of functions of two variables in MILP models. *Operations Res. Lett.* 38 (1), 39–46. doi:10.1016/j.orl.2009.09.005

Diniz, A., and Maceira, M. (2008). A four-dimensional model of hydro generation for the short-term hydrothermal dispatch problem considering head and spillage effects. *IEEE Trans. Power Syst.* 23 (3), 1298–1308. doi:10.1109/TPWRS.2008.922253

Feng, Z., Niu, W., Cheng, C., and Liao, S. (2017). Hydropower system operation optimization by discrete differential dynamic programming based on orthogonal experiment design. *Energy* 126, 720–732. doi:10.1016/j.energy.2017.03.069

Flamm, B., Eichler, A., Warrington, J., and Lygeros, J. (2021). Two-stage dual dynamic programming with application to nonlinear hydro scheduling. *IEEE Trans. Control Syst. Technol.* 29 (1), 96–107. doi:10.1109/TCST.2019.2961645

Guedes, L., de Mendonca Maia, P., Lisboa, A., Vieira, D., and Saldanha, R. (2017). A unit commitment algorithm and a compact MILP model for short-term hydro-power generation scheduling. *IEEE Trans. Power Syst.* 32 (5), 3381–3390. doi:10.1109/TPWRS.2016.2641390

Guisández, I., and Pérez-Díaz, J. (2021). Mixed integer linear programming formulations for the hydro production function in a unit-based short-term scheduling problem. *Int. J. Electr. Power & Energy Syst.* 128, 106747. doi:10.1016/j.ijepes.2020.106747

Huchette, J., and Vielma, J. (2017). Nonconvex piecewise linear functions: Advanced formulations and simple modeling tools. Available at: https://arxiv.org/pdf/1708.00050v3.pdf (Accessed July 19, 2020).

Keller, M., and Karl, H. (2017). Response-time-optimized service deployment: MILP formulations of piece-wise linear functions approximating bivariate mixed-integer functions. *IEEE Trans. Netw. Serv. Manage.* 14 (1), 121–135. doi:10.1109/TNSM.2016.2611590

Kong, J., Skjelbred, H., and Fosso, O. (2020). An overview on formulations and optimization methods for the unit-based short-term hydro scheduling problem. *Electr. Power Syst. Res.* 178, 106027. doi:10.1016/j.epsr.2019.106027

Lin, S., Fan, G., Jian, G., and Liu, M. (2020). Stochastic economic dispatch of power system with multiple wind farms and pumped-storage hydro stations using approximate dynamic programming. *IET Renew. Power Gener.* 14 (13), 2507–2516. doi:10.1049/iet-rpg.2019.1282

Lin, S., Wang, Y., Liu, M., Fan, G., Yang, Z., Li, Q., et al. (2019). Stochastic optimal dispatch of PV/wind/diesel/battery microgrids using state-space approximate dynamic programming. *IET Gener. Transm. &amp. Distrib.* 13 (15), 3409–3420. doi:10.1049/iet-gtd.2018.5840

Marchand, A., Gendreau, M., Blais, M., and Emiel, G. (2018). Fast near-optimal heuristic for the short-term hydro-generation planning problem. *IEEE Trans. Power Syst.* 33 (1), 227–235. doi:10.1109/TPWRS.2017.2696438

Morillo, J., Zéphyr, L., Pérez, J., Lindsay Anderson, C., and Cadena, Á. (2020). Risk-averse stochastic dual dynamic programming approach for the operation of a hydro-dominated power system in the presence of wind uncertainty. *Int. J. Electr. Power & Energy Syst.* 115, 105469. doi:10.1016/j.ijepes.2019.105469

Postolov, B., and Iliev, A. (2022). New metaheuristic methodology for solving security constrained hydrothermal unit commitment based on adaptive genetic algorithm. *Int. J. Electr. Power & Energy Syst.* 134, 107163. doi:10.1016/j.ijepes.2021.107163

Powell, W. (2011). *Approximate dynamic programming: Solving the curses of dimensionality*. Hoboken, NJ: John Wiley & Sons, Inc. Press.

Qiu, Y., Lin, J., Liu, F., Song, Y., Chen, G., Ding, L., et al. (2020). Stochastic online generation control of cascaded run-of-the-river hydropower for mitigating solar power volatility. *IEEE Trans. Power Syst.* 35 (6), 4709–4722. doi:10.1109/TPWRS.2020.2991229

Shi, L., Wang, R., and Yao, L. Z. (2017). Modelling and solutions of coordinated economic dispatch with wind–hydro–thermal complex power source structure. *IET Renew. Power Gener.* 11 (3), 262–270. doi:10.1049/iet-rpg.2016.0429

Shuai, H., Ai, X., Fang, J., Ding, T., Chen, Z., Wen, J., et al. (2020). Real-time optimization of the integrated gas and power systems using hybrid approximate dynamic programming. *Int. J. Electr. Power & Energy Syst.* 118, 105776. doi:10.1016/j.ijepes.2019.105776

Shuai, H., Fang, J., Ai, X., Tang, Y., Wen, J., He, H., et al. (2019). Stochastic optimization of economic dispatch for microgrid based on approximate dynamic programming. *IEEE Trans. Smart Grid* 10 (3), 2440–2452. doi:10.1109/TSG.2018.2798039

Skjelbred, H. I., Kong, J., and Fosso, O. (2020). Dynamic incorporation of nonlinearity into MILP formulation for short-term hydro scheduling. *Int. J. Electr. Power & Energy Syst.* 116, 105530. doi:10.1016/j.ijepes.2019.105530

Wang, J., Zheng, H., Feng, S., Chen, C., Liu, S., Wang, Y., et al. (2022). Comparison of efficient procedures for hydropower unit commitment. *Energy Rep.* 8, 2472–2479. doi:10.1016/j.egyr.2022.01.184

Xue, X., Ai, X., Fang, J., Yao, W., and Wen, J. (2022). Real-time schedule of integrated heat and power system: A multi-dimensional stochastic approximate dynamic programming approach. *Int. J. Electr. Power & Energy Syst.* 134, 107427. doi:10.1016/j.ijepes.2021.107427

Zeng, P., Li, H., He, H., and Li, S. (2019). Dynamic energy management of a microgrid using approximate dynamic programming and deep recurrent neural network learning. *IEEE Trans. Smart Grid* 10 (4), 4435–4445. doi:10.1109/TSG.2018.2859821

Zhang, Y., An, X., and Wang, C. (2021). Data-driven two-stage stochastic optimization model for short-term hydro-thermal-wind coordination scheduling based on the dynamic extreme scenario set. *Sustain. Energy Grids Netw.* 27, 100489. doi:10.1016/j.segan.2021.100489

Zhao, Z., Cheng, C., Liao, S., Li, Y., and Lu, Q. (2021). A MILP based framework for the hydro unit commitment considering irregular forbidden zone related constraints. *IEEE Trans. Power Syst.* 36 (3), 1819–1832. doi:10.1109/TPWRS.2020.3028480

Zhu, J., Mo, X., Zhu, T., Guo, Y., Luo, T., Liu, M., et al. (2019). Real-time stochastic operation strategy of a microgrid using approximate dynamic programming-based spatiotemporal decomposition approach. *IET Renew. Power Gener.* 13 (16), 3061–3070. doi:10.1049/iet-rpg.2019.0536

Zhu, J., Wang, C., Guo, Y., Luo, T., Mo, X., Xia, Y., et al. (2020). Approximate dynamic programming-based decentralised robust optimisation approach for multi-area economic dispatch considering wind power uncertainty. *IET Renew. Power Gener.* 14 (13), 2376–2385. doi:10.1049/iet-rpg.2019.0794

Nomenclature

Sets and indices

i index of hydro units

M set of units

t index of periods

T set of time periods

Parameters

$\mathbf{h_{i,t}}$ net head of reservoir at period t

$\mathbf{h^{max}}$ maximum net head of the reservoir (m)

$\mathbf{h^{min}}$ minimum net head of the reservoir (m)

p*max *i maximum production of unit *i* (kW)

p*min *i minimum production of unit *i* (kW)

q*max *i maximum water discharge of unit *i* (m^3/s)

q*min *i minimum water discharge of unit *i* (m^3/s)

r^{final} water volume of the reservoir at the end of the last period (m^3)

r^{init} water volume of the reservoir at the beginning of the initial period (m^3)

r^{max} maximum water volume of the reservoir (m^3)

r^{min} minimum water volume of the reservoir (m3)

Δt length of each time period (h)

Variables

$d_{i,t}$ binary variable, which is equal to 1 if hydro unit *i* is online at period *t* and 0 otherwise

h_t net head of reservoir at period *t*

h*dw *t tailrace level of the reservoir at period *t* (m)

h*up *t forebay level of the reservoir in period *t* (m)

j_t inflow of reservoir at period *t* (m^3/s)

$p_{i,t}$ power output of hydro unit *i* at period *t*

$q_{i,t}$ water discharge of unit *i* at period *t*

r_t water volume of the reservoir at period *t* (m^3)

s_t total reservoir spillage in period *t* (m^3/s)

frontiers | Frontiers in Energy Research

TYPE Original Research
PUBLISHED 22 July 2022
DOI 10.3389/fenrg.2022.977077

OPEN ACCESS

EDITED BY
Minghao Wang,
Hong Kong Polytechnic University,
Hong Kong SAR, China

REVIEWED BY
Xing Zhao,
University of York, United Kingdom
Chao Gong,
University of Alberta, Canada

*CORRESPONDENCE
Shu Xiong,
xiongshuok@163.com

SPECIALTY SECTION
This article was submitted to Smart Grids,
a section of the journal
Frontiers in Energy Research

RECEIVED 24 June 2022
ACCEPTED 04 July 2022
PUBLISHED 22 July 2022

CITATION
Xiong S, Yang Y and Pan J (2022), A new dual-ferrite–assisted hybrid reluctance machine with two-stage excitation for starter generator application.
Front. Energy Res. 10:977077.
doi: 10.3389/fenrg.2022.977077

A new dual-ferrite–assisted hybrid reluctance machine with two-stage excitation for starter generator application

Shu Xiong[1,2]*, Yucui Yang[1,2] and Jian Pan[1,2]

[1]School of Physics and Electronics Electrical Engineering, Huaiyin Normal University, Huai'an, China, [2]Jiangsu Province Key Construction Laboratory of Modern Measurement Technology and Intelligent System, Huai'an, China

Reluctance machines with DC field coil in stator are a competitive candidate for starter generation application, due to the elimination of rare-earth permanent magnet (PM), robust structures, and controllable excitation. However, due to the poor excitation ability of DC field coils, the torque density is disadvantageous. Moreover, with the increase in the DC field current, it is exposed to the risk of extra DC saturation in stator teeth. As a consequence, the torque density and efficiency are both constrained. To solve the aforementioned problems, based on the comprehensive consideration of production cost and torque performance, this study proposed a novel type of hybrid reluctance machine with dual-ferrite–assisted in stator slots. The inner-layer ferrite PM is magnetized tangentially, which can effectively achieve the DC-saturation–relieving effect, while the outer-layer ferrite PM is magnetized radially to increase the machine torque density through the flux modulation effect. Based on finite element analysis, the machine torque density and efficiency can be improved by 20 and 5%, respectively. Furthermore, to simplify the excitation system of the DC terminal, a two-stage excitation method is proposed by splitting some turns of armature winding to feed DC field winding with passive rectifier. No power switching devices are needed for the excitation system in this way, making the system highly robust. The effectiveness of the proposed design is verified by time-stepping finite element analysis.

KEYWORDS

dual-ferrite magnets, DC-saturation-relieving, hybrid reluctance machine, starter generator application, two-stage excitation

Introduction

Due to high torque density and high efficiency, the rare-earth permanent magnet (PM) machines have been widely used in electrical vehicles and wind power generation systems (Zhu and Howe, 2007; Chau et al., 2008; Pellegrino et al., 2012; Sarlioglu and Morris, 2015; Zhao et al., 2018; Gong et al., 2019; Zhao et al., 2020a; Zhao et al., 2021; Zhao et al., 2022a), which enables the increasing penetration of renewable energy into traditional power systems, driving to a carbon-free future. However, the rare-earth PM is a non-renewable resource and its supply status is unstable with a relatively high price, which is desired to be reduced in electrical machine systems (Polinder et al., 2006; Fasolo et al., 2014; Niu et al., 2019). The switched reluctance motor (SRM) is a potential non-PM solution (Polinder et al., 2006; Niu et al., 2019), but the core of SRM can only operate in the first quadrant of the BH curve, thus torque density is poorer than that of the PM machine. In addition, the torque ripple is serious due to its half-cycle conducting principle.

A doubly-fed doubly salient machine (DF-DSM) has a similar stator and rotor structure with SRM. The difference is that the space of the stator slot is shared by DC coils and AC coils. This allows DF-DSM to operate in a whole electric period and be driven by a universal inverter (Fasolo et al., 2014; Zhao et al., 2020b; Zhao et al., 2022b). Nevertheless, its torque ripple is severe due to rich even-order flux harmonics and asymmetric magnetic circuits between phases. To address this issue, another structure named as variable flux reluctance machine (VFRM) is proposed, which can be designed with more flexible slot pole combinations (Xue et al., 2010). In particular, with the design of odd rotor pole pair, the even-order harmonics in flux linkage can be canceled, and symmetrical magnetic circuits between phases are obtained. Therefore, lower cogging torque and small torque ripple can be acquired (Takeno et al., 2012; Hu et al., 2020). Unfortunately, the torque density of VFRM is still lower than that of SRM and quite lower than that of PM machines. Two reasons behind this are, on one hand, the excitation ability of DC field coils is much poor compared to rare-earth PMs. On the other hand, DC field windings produce a DC flux bias in the stator core, making it prone to magnetic saturation. This problem is severe under heavy load conditions, which degrades torque performance and increases core loss. To solve this issue, tangential PMs can be embedded in slots to create an opposite magnetic bias against that of DC field winding (Liu and Zhu, 2013; Lee et al., 2014; Liu and Zhu, 2014; Wang et al., 2016; Zhu et al., 2016; Ullah et al., 2019; Zhao et al., 2019; Zhao et al., 2020c), hence weakening the magnetic saturation in the stator core.

This study proposed a new hybrid reluctance machine (HRM) using dual-ferrite magnets in stator slots. The inner-layer ferrite PMs are used to release the saturation of the

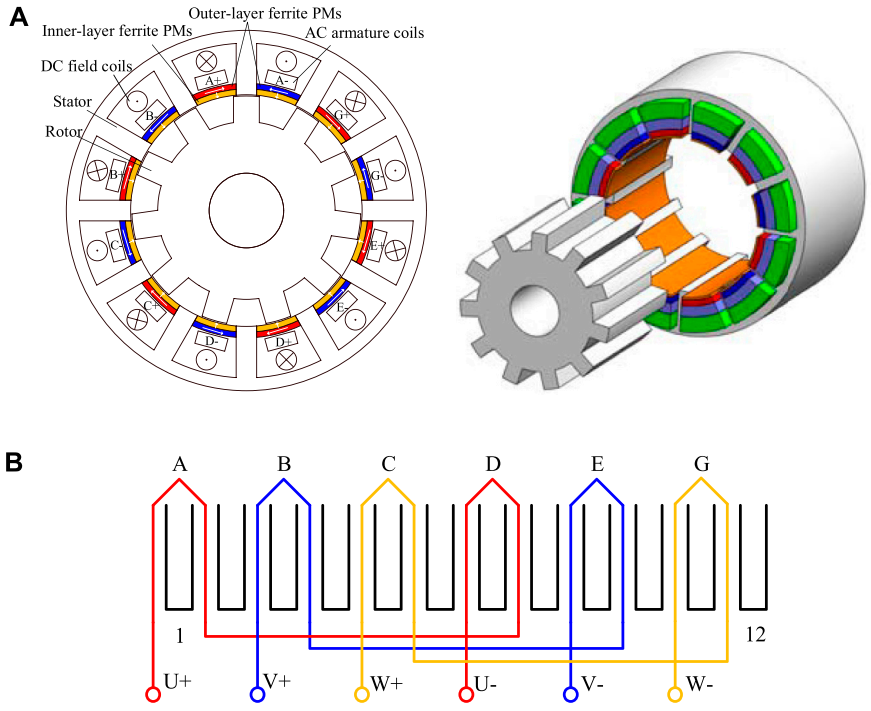

FIGURE 1
(A) Structure of the proposed HRM. **(B)** Armature winding connection.

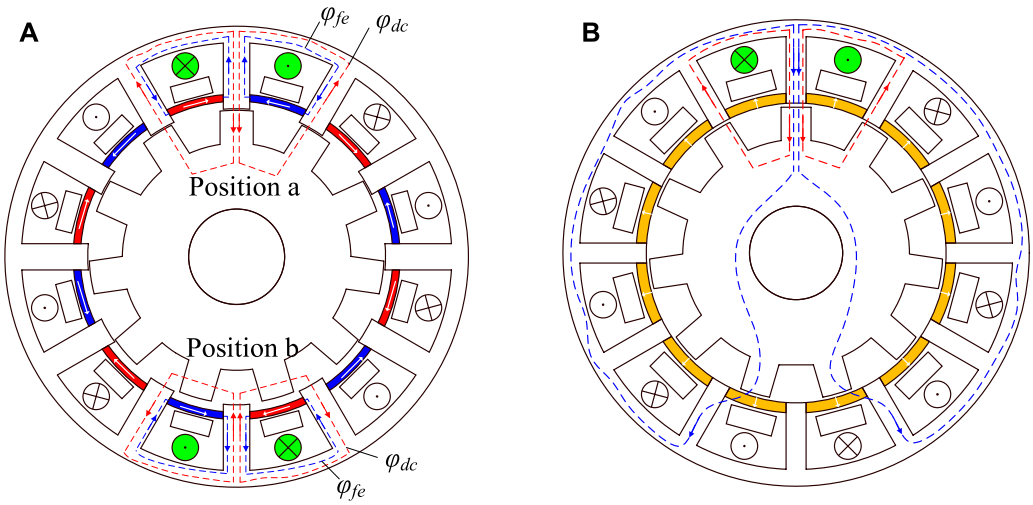

FIGURE 2
Flux linkage distribution. **(A)** Inner-layer ferrite PMs and DC field coils. **(B)** Outer-layer ferrite PMs and DC field coils. The flux linkage excited by DC field winding can be expanded by Fourier series.

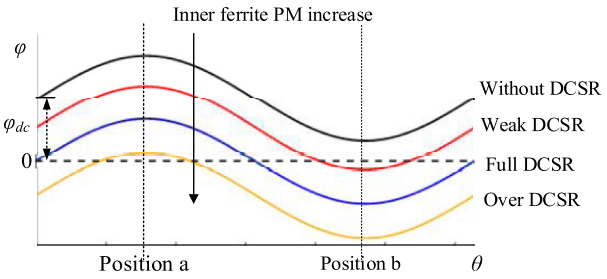

FIGURE 3
Schematic coil flux with the increase in inner-layer ferrite PMs.

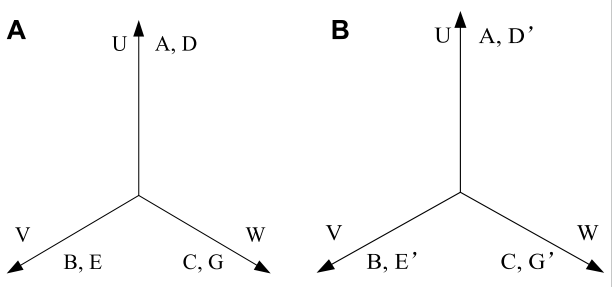

FIGURE 4
Winding configuration. **(A)** 12/10 and 12/14. **(B)** 12/11 and 12/13.

TABLE 1 Dominant harmonics excited by outer-layer ferrite PMs.

	$i = 1, j = 0$	$i = 1, j = 1$	
$v_{i,j}$	0	$n_s + n_r$	$\lvert n_s - n_r \rvert$
$PPN_{i,j}$	n_s	$\frac{n_r}{n_s+n_r}\omega_r$	$\frac{n_r}{n_s-n_r}\omega_r$

magnetic circuit due to extra DC bias generated by DC field winding. The outer-layer ferrite PMs contribute to the effective flux linkage and torque boost effect through the flux modulation effect. In this way, the proposed HRM can achieve improved torque density and efficiency at the same time compared to the traditional non-PM design. The cost increase due to ferrite magnets is acceptable as well. Moreover, to simplify the excitation system of the DC current terminal, a two-stage excitation method is proposed by splitting some turns of armature winding to feed DC field winding with passive rectifier. No power switching devices are needed for the excitation system in this way, making the system highly robust. The rest of the study is arranged as follows. In Section 2, the configuration and principle of the proposed HRM are introduced. In Section 3, different pole pair combinations are compared through finite element analysis, including magnetic field distribution, cogging torque, and back electromotive force. In Section 4, the electromagnetic performance of the optimal design is analyzed, with emphasis on the effect of dual-layer ferrite PMs on the magnetic saturation and torque generation. In Section 5, the feasibility of a power device free two-stage excitation system is verified by field-circuit co-simulation, proving its potential for stater generator applications. Some conclusions are drawn in Section 6.

TABLE 2 Design parameters for the proposed machine.

Symbol	Parameter	Unit	Value
d_{so}	Outer diameter of stator	mm	130
dsi	Inner diameter of stator	mm	90
dro	Outer diameter of rotor	mm	89
dri	Inner diameter of stator	mm	60
hry	Height of rotor yoke	mm	20
hsy	Height of stator yoke	mm	5
h1	Height of outer-layer ferrite PMs	mm	Variable
h2	Height of inner-layer ferrite PMs	mm	Variable
Δ	Air-gap length	mm	0.5
L	Stack length	mm	80
w_s	Width of stator teeth	mm	6
w_r	Width of rotor salient pole	mm	9
	Turns of each DC coil		80
	Turns of each AC coil		80
	Slot factor		0.79
	Rated speed	rpm	2,500
	Rated current density	A/mm^2	10

The proposed hybrid reluctance machine

The structure of the proposed dual-ferrite–assisted HRM is shown in Figure 1. It uses a doubly salient structure. There are two sets of windings in the stator, namely, DC field winding and AC armature winding. The AC armature winding uses a single-layer concentrated connection, thus the winding ends are short and good isolation can be achieved. The rotor consists of an iron core only, providing good mechanical robustness. Dual-ferrite PMs are introduced in stator slots and play different roles in the electromagnetic characteristics of the proposed HRM. Extra pole shoes can be designed to enable the placement of slot PMs and make sure the mechanical strength requirement. Considering the winding ends are usually the hotpots in an electrical machine system. The ferrite magnets are likely to be exposed to the demagnetization risk. Some advanced natural/water/oil cooling methods can be used to bring down the temperature rise and thus ensure the working environment of magnets. As shown in Figure 2A, the inner ferrite PMs are tangentially magnetized to generate a magnetic bias opposite to that of DC field windings, and in this way, the saturation of the magnetic circuit can be reduced, namely, DC-saturation–relieving (DCSR) effect in this study. It is worth noting that the inner-layer ferrite PMs only adjust the offset of the flux linkage and have little influence on the phase angle. The outer-layer radially magnetized ferrite PMs will create extra flux that overlaps with that of DC field winding, as shown in Figure 2B, and thus boost torque density. The working principle of dual-layer ferrites is expanded as follows:

TABLE 3 Major parameters and specifications.

Ferrite PM	Material remanence coercive force	Y30H 0.4 T 300 kA/m
Steel	Material saturated flux density mass density	MG19_24 1.8 T 7,650 kg/m^3

$$\varphi_{coil} = \varphi_{dc} + \sum \varphi_n \sin(n\omega t + \theta_n), \quad n = 1, 2, 3 \ldots, \tag{1}$$

where φ_{dc} is the DC flux bias, φ_n is the magnitude of the nth flux harmonics, ω is the electrical angle velocity, t is the time, and θ_n is the initial phase angle. φ_{dc} can be further described using permeance and magnetomotive force model as follows:

$$\varphi_{dc} = N_{dc} i_{dc} \Lambda_{ave} \theta_s d_{so} l, \tag{2}$$

where N_{dc} is the turns of DC coils, i_{dc} is the current of DC coils, Λ_{ave} is the average permeance, θ_s is the arc of stator teeth, d_{so} is the outer diameter of stator, and l is the stack length.

As shown, the DC flux bias in the stator core is determined by the magnetomotive force of DC field winding and average rotor permeance. To avoid the flux saturation in the stator teeth, inner-layer ferrite PMs are introduced to achieve the DCSR effect. As shown in Figure 3, without DCSR, the phase flux linkage has a bias with φ_{dc}. With the help of the constant flux generated by inner-layer ferrite PMs, the DC flux bias can be regulated. With the increase in inner-layer ferrite PMs, the DC flux bias can be adjusted to zero, which can be named as the full DCSR effect. However, the overuse of ferrite PMs may produce a negative offset for the phase flux as well, namely, an over DCSR effect, and meanwhile reduce the slot space area for windings Hence, the proper amount of ferrite is a very important parameter, and the optimal usage of inner-layer ferrite PMs can be designed by.

$$h = \frac{H_c \Lambda_s \theta_s d_{so} l}{\varphi_{dc}}, \tag{3}$$

where h is the height of the inner-layer ferrite PMs, H_c is the coercivity of ferrite PMs, Λ_s is the average permeance of inner-layer ferrite PM magnetic circuit, θ_s is the arc of stator teeth, d_{so} is the diameter of the stator teeth, and l is the stack length.

The outer-layer ferrite PMs and the adjacent stator tooth form the magnetic poles, and the ferrite PM field is modulated by rotor salient poles. At the same time, the redundant air-gap harmonics are excited to boost the torque generation. The rotational speed $v_{i,j}$ and the pole pair number $PPN_{i,j}$ can be expressed as:

$$\begin{cases} v_{i,j} = \dfrac{jn_r}{in_s + jn_r}\omega_r, \\ PPN_{i,j} = \left|in_s \pm jn_r\right|, \end{cases} \quad i = 1, 3, 5 \ldots, \; j = 0, 1, 2, 3 \ldots, \tag{4}$$

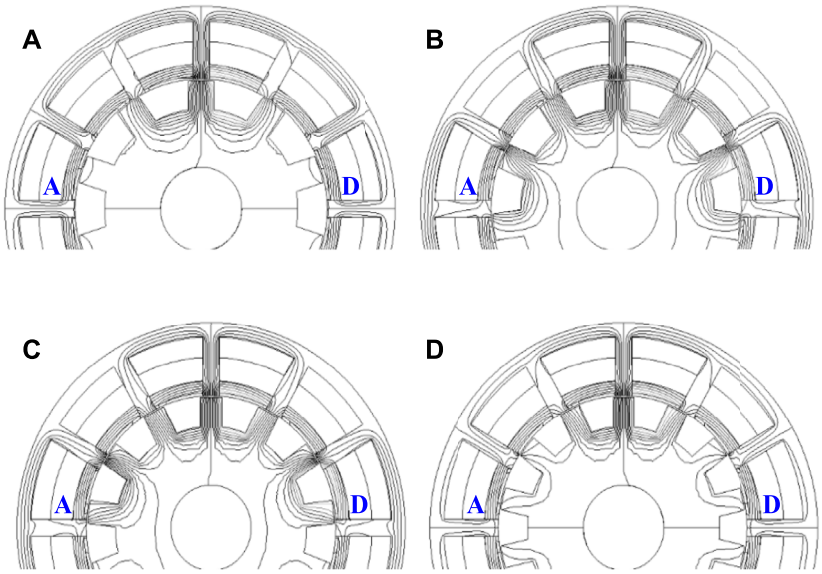

FIGURE 5
Flux distribution generated by DC field coils and dual-layer ferrite PMs **(A)** 12/10. **(B)** 12/11. **(C)** 12/13. **(D)** 12/14.

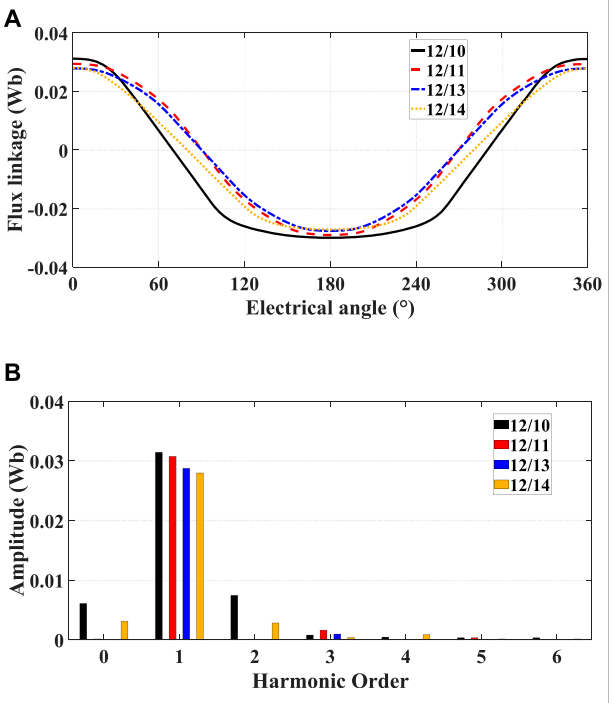

FIGURE 6
(A) Phase flux linkage waveforms. **(B)** Harmonic distribution.

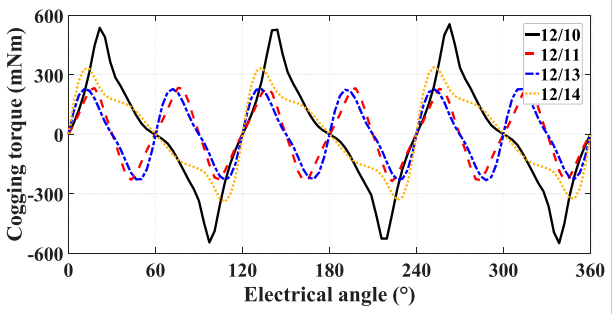

FIGURE 7
Cogging torque waveforms.

where n_s is the PPN of outer-layer ferrite PMs. n_r is the pole pair number of rotor poles andω_r is the rotor mechanical angular velocity. The dominant components of air-gap harmonics after the modulation are summarized in Table 1.

When $i = 1$, $j = 0$, the rotational speed is 0, thus there are no effective flux linkage and electromagnetic torque produced. When $i = 1$, $j = 1$, two dominant harmonics of outer-layer ferrite PMs are generated after rotor modulation, and their rotating directions are opposite. To transmit the maximum electromagnetic torque with ferrite PMs harmonics, the pole pair number of AC armature winding can be designed by.

$$n_a = |n_s - n_r|. \tag{5}$$

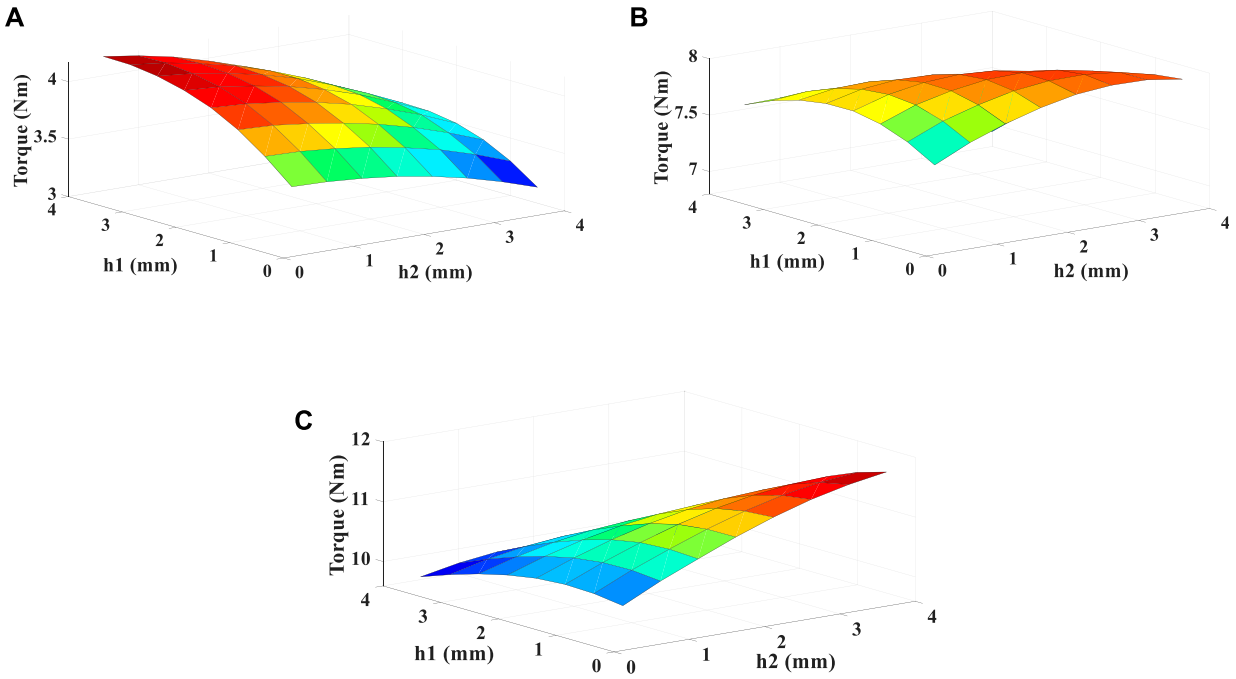

FIGURE 8
Average torque with variable usage of dual-ferrite PMs under different current densities **(A)** 5 A/mm2. **(B)** 10 A/mm2. **(C)** 15 A/mm2.

The electromagnetic torque produced by outer-layer ferrite PMs can be defined as:

$$T = \frac{3}{2} krln_r \frac{B_p}{G_r} NI, \tag{6}$$

where k is the fundamental winding factor, r is the air-gap radius, l is the stack length, B_p is the amplitude of harmonic flux density, and NI is the winding ampere turns.

Design considerations

In the proposed HRM, the magnetic circuits between phases are entirely symmetrical. Four slot pole combinations of 12/10, 12/11, 12/13, and 12/14 are selected to be analyzed in this study. Since the proposed HRM should use a single-layer concentrated connection, the vector diagram of winding connection for each design is presented in Figure 4. In 12/10 and 12/14 cases, the armature coils in opposite positions are positively cascaded as they have the same phase of flux linkage, while the phase flux of 12/11 and 12/13 cases in opposite positions is delayed by the half electrical period, and hence they are negatively cascaded. The detailed design parameters and the specifications of major machine materials are presented in Tables 2, 3,.

The flux distributions of the proposed HRM with four pole pair combinations are illustrated in Figure 5, with a DC field current of 5A. It is clear to see that the flux linkage circulates into a loop according to the wounded stator tooth, aligned rotor tooth, and the adjacent stator teeth. As shown in Figure 5, the phase U is composed of coil A and coil D, the flux of phase U of 12/10 and 12/14 can be derived by using Fourier series as:

$$\varphi_U = 2\varphi_{dc} + 2\sum \varphi_n \sin(n\omega t + \theta_n), \quad n = 1, 2, 3 \ldots \tag{7}$$

For 12/11 and 12/13, the coil A and coil D are negatively connected, and then the flux of phase U can be rewritten as:

$$\varphi_U = \sum \varphi_n \sin(n\omega t + \theta_n) + \sum \varphi_n \sin(n\omega t + n\pi + \theta_n),$$

$$n = 1, 2, 3 \ldots \tag{8}$$

$$\varphi_U = 2\sum \varphi_n \sin(n\omega t + \theta_n), \qquad n = 1, 3, 5 \ldots \tag{9}$$

As demonstrated by equation (10), in 12/11 and 12/13 cases, the DC flux bias and all even-order harmonics are canceled in the combined phase. As the flux linkage and its harmonic orders are compared in Figure 6, the 12/11 and 12/13 cases can acquire more symmetrical flux linkage without any even-order harmonics. In addition, the fundamental components of flux linkage of 12/10 and 12/11 cases are larger than the others. As shown in Figure 7, the cogging torques of 12/11 and 12/13 are quite smaller than those of 12/10 and 12/14. This is because a smaller or least common

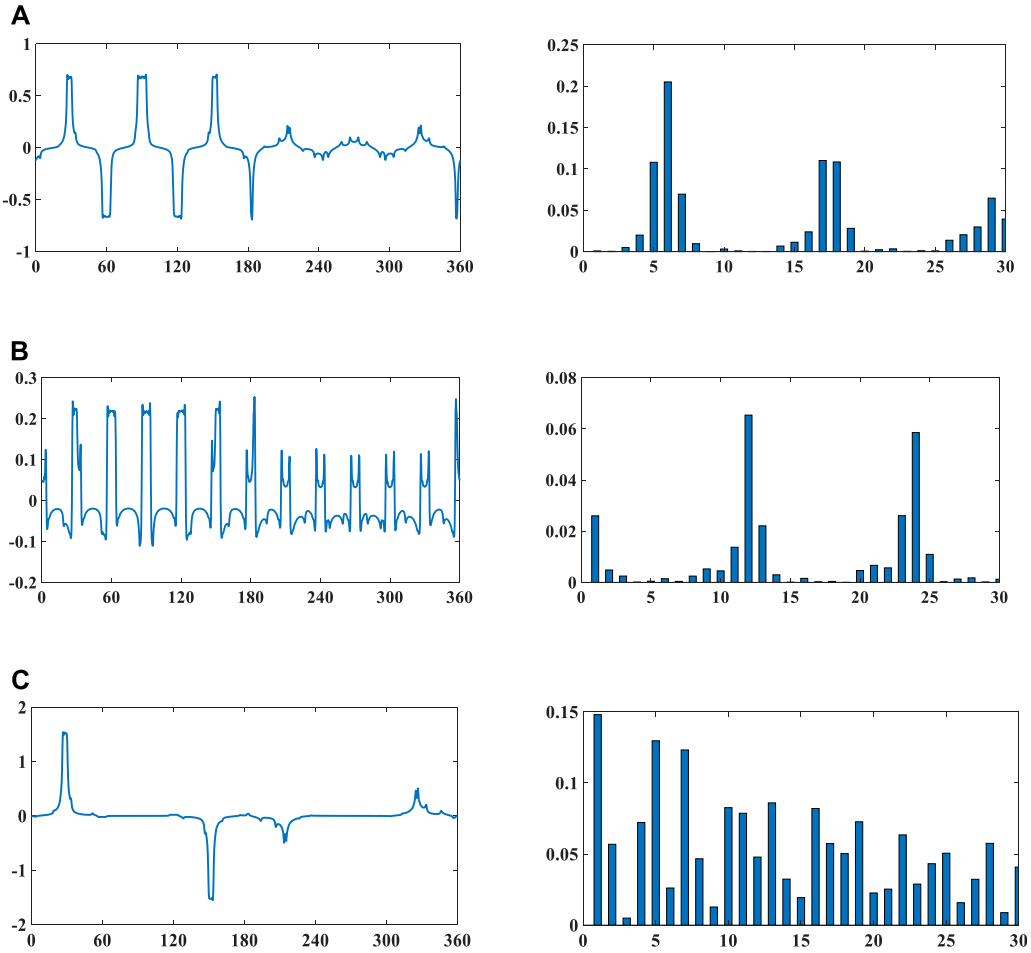

FIGURE 9
Flux density in the air gap and its harmonic distribution. **(A)** Only DC 5A. **(B)** Only outer-layer ferrite PMs. **(C)** Only AC armature current 5A.

multiple of the stator teeth number and rotor pole pair may cause bigger cogging torque. Based on the aforementioned analysis, the 12/11 case is a suitable pole pair combination for the proposed dual-ferrite HRM.

The usage of dual-layer ferrite PMs is a key parameter for the proposed HRM. On one side, the over usage of ferrite PMs may occupy the space of DC coils and AC coils, which leads to a decrease in the torque density. On the other side, insufficient ferrite PMs cannot produce enough flux modulation and DCSR effect. Under different current densities, the suitable usage of dual-layer ferrite magnets is analyzed and the results are given in Figure 8. Under low current densities, the outer-layer ferrite PM plays a significant role, as shown in Figure 8A. With the increase in outer-layer ferrite PMs, the average torque increases distinctly. By contrast, the inner-layer ferrite magnets are less important since flux saturation is not serious under low current density. As shown in Figure 8C, the inner-layer ferrite PMs start to show their effect. With the increase in the usage, the average torque increases significantly. Figure 8B describes the combined effect of dual-layer ferrite PMs. With the increase in dual-layer ferrite PMs, the average torque increases first and then shows a downward trend, proving that the overuse of ferrite PMs may cause a negative effect on torque generation. Consequently, the usage of ferrite magnets is designed as 4 mm for inner-layer ferrite and 1 mm for outer-layer ferrite to achieve the maximum average torque at a rated current density of 15 A/mm^2.

Electromagnetic performance

Figure 9 presents the harmonics excited by the DC field coils, outer-layer ferrite PMs, and AC armature coils, respectively. According to the flux modulation effect, if the harmonics excited by DC coils and outer-layer ferrite PMs have the same rotational speed and the same pole pair number as AC

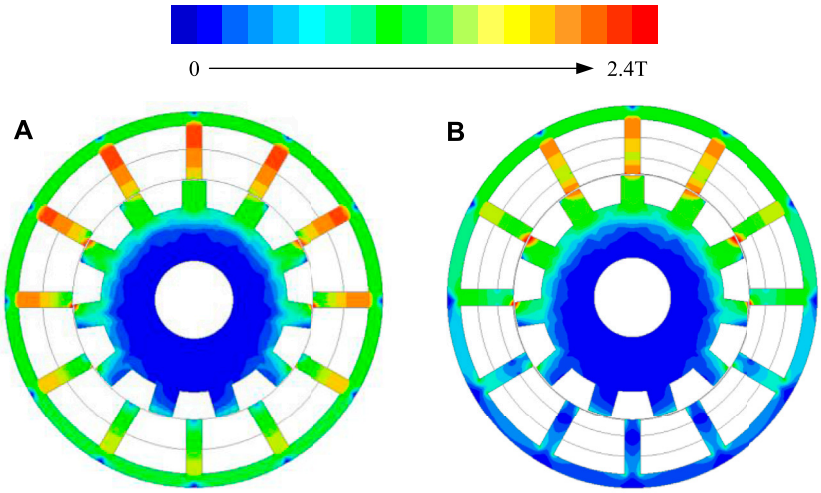

FIGURE 10
Magnetic field distribution at different excitation statuses. **(A)** DC field current only. **(B)** DC field current and dual-ferrite PMs.

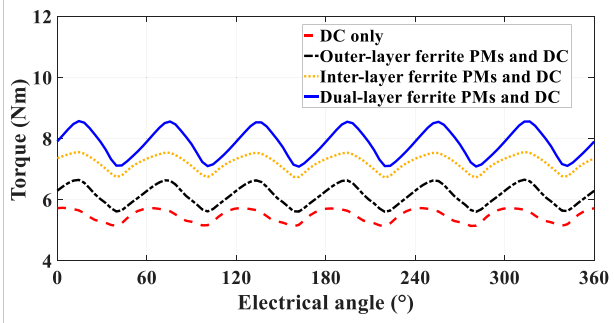

FIGURE 11
Steady torque curves at different excitation statuses.

harmonics, the torque density can be improved. Figure 9A shows the air-gap flux density with only DC field excitation, and its harmonics distribution obtained by the fast Fourier transform (FFT). Figure 9B shows the flux density of outer-layer ferrite PMs and its FFT of the main harmonic components. The orders of dominant harmonic components of two excitation sources are quite different. When compared the redundant harmonics excited by armature excitation using a single-layer concentrated winding connection as shown in Figure 9C, it can be concluded that both DC excitation and outer-layer ferrite excitation contribute to torque density improvement effectively.

When the proposed HRM is excited by DC coils only, the magnetic circuit distribution under the no-load condition is shown in Figure 10A. The magnetic circuit in the stator teeth is severely saturated, which will seriously affect the torque performance and efficiency. With the help of inner-layer ferrite PMs, the magnetic circuit saturation in the stator slots and teeth is effectively released by the DCSR effect, which is shown in Figure 10B. Meanwhile, as shown in Figure 11, compared with the torque performance excited by the DC field current only, the torque density of the proposed dual-ferrite–assisted HRM has been improved by more than 20%. Also, the efficiency can be increased by 5% due to core loss mitigation, as indicated in the simulation data in Table 4.

TABLE 4 Power, loss, and efficiency.

Parameter	Unit	With DC only	With dual-layer ferrite PMs
Rated power	W	1,387	1831
Copper loss	W	180	143
Core loss	W	99	101
Eddy current loss	W	-	40
Rated efficiency	-	79.9%	84.5%

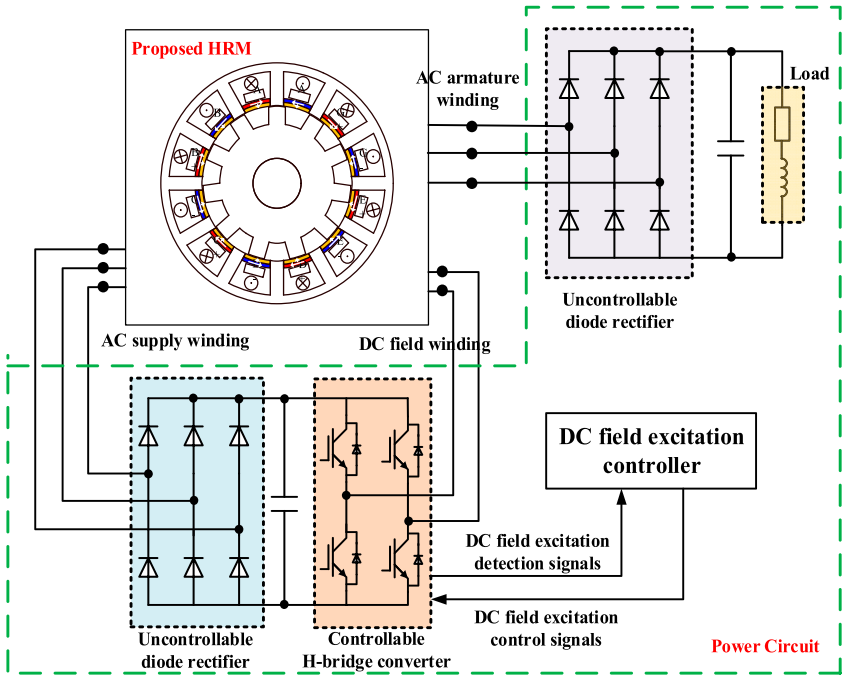

FIGURE 12
Two-stage excitation system for the proposed HRM.

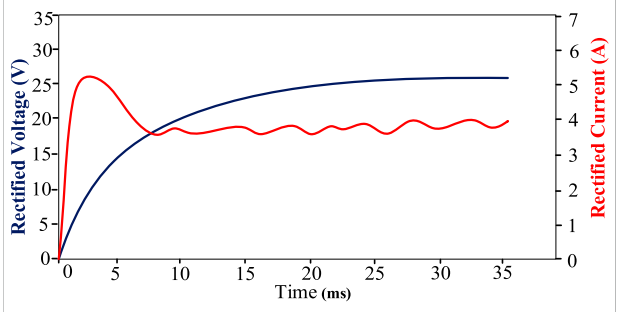

FIGURE 13
Rectified voltage and current in the DC field terminal.

Two-stage excitation system

Figure 12 presents the two-stage excitation system for the proposed HRM, based on the field-circuit co-simulation (combined with the finite element electromagnetic field analysis and circuit transition analysis). The key is to split a few turns of the AC armature winding to function as an AC supply winding to feed the DC field winding through the passive diode rectifier. In this way, the extra exaction circuit for the DC field terminal can be eliminated, including the switching devices and related control systems, thereby making the system highly robust. This two-stage excitation system is an ideal solution for stable generation mode as a stater generator candidate. Figure 13 shows the simulation results of the rectified current and voltage excitation in the DC field terminal through the AC supply winding and diode rectifier. It is observed that the DC field voltage and current excitation can naturally achieve a stable value after a certain time, which verifies the system effectiveness.

Conclusion

A novel dual-ferrite–assisted HRM is proposed in this study. The key is to apply the inner-layer ferrite PM to achieve the DCSR effect and the outer-layer ferrite PM to help modulate the air-gap flux and thus increase the torque

density. Four pole pair combinations of the proposed machine are compared in terms of flux harmonics and cogging torque, and the optimal case is selected for further analysis. The effect of ferrite PM usage on torque generation is evaluated. The combined effects of dual-layer ferrite PMs are verified by FEA, which reveals that, with the flux modulation effect and DCSR effect, the torque density and efficiency can be increased by 20 and 5%, respectively. Furthermore, the two-stage excitation system is verified by field-circuit co-simulation, which verifies that the proposed solution is very suitable for a stater generator application with enhanced electromagnetics performance at the starting mode and simplified power circuit at the generation mode.

Data availability statement

The original contributions presented in the study are included in the article/Supplementary Materials; further inquiries can be directed to the corresponding author.

Author contributions

Writing—original draft preparation and supervision: SX. Writing—review and editing: YY. Writing—review and editing: JP.

Conflict of interest

The authors declare that the research was conducted in the absence of any commercial or financial relationships that could be construed as a potential conflict of interest.

Publisher's note

References

Chau, K. T., Chan, C. C., and Liu, C. (2008). Overview of permanent-magnet brushless drives for electric and hybrid electric vehicles. *IEEE Trans. Ind. Electron.* 55 (6), 2246–2257. doi:10.1109/tie.2008.918403

Fasolo, A., Alberti, L., and Bianchi, N. (2014). Performance comparison between switching-flux and IPM machines with rare-earth and ferrite PMs. *IEEE Trans. Ind. Appl.* 50 (6), 3708–3716. doi:10.1109/tia.2014.2319592

Gong, C., Hu, Y., Gao, J., Wang, Y., and Yan, L. (2019). An improved delay-suppressed sliding-mode observer for sensorless vector-controlled PMSM. *IEEE Trans. Ind. Electron.* 67 (7), 5913–5923. doi:10.1109/tie.2019.2952824

Hu, Y., Xiao, L., Pan, C., Li, J., and Wang, C. (2020). Multidomain analysis and nth-order synchronous reference vector adaptive control of the doubly salient motor. *IEEE Trans. Power Electron.* 35 (9), 9563–9573. doi:10.1109/tpel.2020.2970459

Lee, C. H. T., Chau, K. T., Liu, C., Ching, T. W., and Li, F. (2014). Mechanical offset for torque ripple reduction for magnetless double-stator doubly salient machine. *IEEE Trans. Magn.* 50 (11), 1–4. doi:10.1109/tmag.2014.2320964

Liu, X., and Zhu, Z. Q. (2013). Comparative study of novel variable flux reluctance machines with doubly fed doubly salient machines. *IEEE Trans. Magn.* 49 (7), 3838–3841. doi:10.1109/tmag.2013.2242047

Liu, X., and Zhu, Z. Q. (2014). Stator/rotor Pole combinations and winding configurations of variable flux reluctance machines. *IEEE Trans. Ind. Appl.* 50 (6), 3675–3684. doi:10.1109/tia.2014.2315505

Niu, S., Sheng, T., Zhao, X., and Zhang, X. (2019). Operation principle and torque component quantification of short-pitched flux-bidirectional-modulation machine. *IEEE Access* 7, 136676–136685. doi:10.1109/access.2019.2942482

Pellegrino, G., Vagati, A., Guglielmi, P., and Boazzo, B. (2012). Performance comparison between surface-mounted and interior PM motor drives for electric vehicle application. *IEEE Trans. Ind. Electron.* 59 (2), 803–811. doi:10.1109/tie.2011.2151825

Polinder, H., van der Pijl, F. F. A., de Vilder, G. J., and Tavner, P. J. (2006). Comparison of direct drive and geared generator concepts for wind turbines. *IEEE Trans. Energy Convers.* 21 (3), 725–733. doi:10.1109/tec.2006.875476

Sarlioglu, B., and Morris, C. T. (2015). More electric aircraft: Review, challenges, and opportunities for commercial transport aircraft. *IEEE Trans. Transp. Electrific.* 1 (1), 54–64. doi:10.1109/tte.2015.2426499

Takeno, M., Chiba, A., Hoshi, N., Ogasawara, S., Takemoto, M., Rahman, M. A., et al. (2012). Test results and torque improvement of the 50-kW switched reluctance motor designed for hybrid electric vehicles. *IEEE Trans. Ind. Appl.* 48 (4), 1327–1334. doi:10.1109/tia.2012.2199952

Ullah, S., McDonald, S. P., Martin, R., Benarous, M., and Atkinson, G. J. (2019). A permanent magnet assist, segmented rotor, switched reluctance drive for fault tolerant aerospace applications. *IEEE Trans. Ind. Appl.* 55 (1), 298–305. Jan.-Feb. 2019. doi:10.1109/tia.2018.2864718

Wang, Y., Zhang, Z., Liang, R., Yuan, W., and Yan, Y. (2016). Torque density improvement of doubly salient electromagnetic machine with asymmetric current control. *IEEE Trans. Ind. Electron.* 63 (12), 7434–7443. doi:10.1109/tie.2016.2594761

Xue, X. D., Cheng, K. W. E., Ng, T. W., and Cheung, N. C. (2010). Multi-objective optimization design of in-wheel switched reluctance motors in electric vehicles. *IEEE Trans. Ind. Electron.* 57 (9), 2980–2987. doi:10.1109/tie.2010.2051390

Zhao, X., Jiang, J., Niu, S., and Wang, Q. (2022). Slot-PM-assisted hybrid reluctance generator with self-excited DC source for stand-alone wind power generation. *IEEE Trans. Magn.* 58 (2), 1–6. doi:10.1109/tmag.2021.3081585

Zhao, X., Niu, S., and Fu, W. (2019). A new modular relieving-DC-saturation vernier reluctance machine excited by zero-sequence current for electric vehicle. *IEEE Trans. Magn.* 55 (7), 1–5. doi:10.1109/tmag.2018.2887271

Zhao, X., Niu, S., and Fu, W. (2018). Design of a novel parallel-hybrid-excited dual-PM machine based on armature harmonics diversity for electric vehicle propulsion. *IEEE Trans. Ind. Electron.* 66 (6), 4209–4219. doi:10.1109/tie.2018.2863211

Zhao, X., Niu, S., and Fu, W. (2020). Sensitivity analysis and design optimization of a new hybrid-excited dual-PM generator with relieving-DC-saturation structure for stand-alone wind power generation. *IEEE Trans. Magn.* 56 (1), 1–5. doi:10.1109/tmag.2019.2951078

Zhao, X., Niu, S., Zhang, X., and Fu, W. (2020). A new relieving-DC-saturation hybrid excitation vernier machine for HEV starter generator application. *IEEE Trans. Ind. Electron.* 67 (8), 6342–6353. doi:10.1109/tie.2019.2939966

Zhao, X., Niu, S., Zhang, X., and Fu, W. (2020). Design of a new relieving-DC-saturation hybrid reluctance machine for fault-tolerant in-wheel direct drive. *IEEE Trans. Ind. Electron.* 67 (11), 9571–9581. doi:10.1109/tie.2019.2955418

Zhao, X., Niu, S., Zhang, X., and Fu, W. (2021). Flux-modulated relieving-DC-saturation hybrid reluctance machine with synthetic slot-PM excitation for electric vehicle in-wheel propulsion. *IEEE Trans. Ind. Electron.* 68 (7), 6075–6086. doi:10.1109/tie.2020.2996140

Zhao, X., Wang, S., Niu, S., Fu, W., and Zhang, X. (2022). A novel high-order-harmonic winding design method for vernier reluctance machine with DC coils across two stator teeth. *IEEE Trans. Ind. Electron.* 69 (8), 7696–7707. doi:10.1109/tie.2021.3104589

Zhu, Z. Q., and Howe, D. (2007). Electrical machines and drives for electric, hybrid, and fuel cell vehicles. *Proc. IEEE* 95 (4), 746–765. doi:10.1109/jproc.2006.892482

Zhu, Z. Q., Lee, B., and Liu, X. (2016). Integrated field and armature current control strategy for variable flux reluctance machine using open winding. *IEEE Trans. Ind. Appl.* 52 (2), 1. doi:10.1109/tia.2015.2490041

frontiers | Frontiers in Energy Research

TYPE Original Research
PUBLISHED 04 August 2022
DOI 10.3389/fenrg.2022.969676

OPEN ACCESS

EDITED BY
Jiajia Yang,
University of New South Wales, Australia

REVIEWED BY
Jin Zhu,
Chinese Academy of Sciences (CAS), China
Liye Zhang,
Shandong University of Science and Technology, China
Sen Zhan,
Chongqing Jiaotong University, China

*CORRESPONDENCE
Peipei Wang,
wpp2003@whut.edu.cn

SPECIALTY SECTION
This article was submitted to Smart Grids,
a section of the journal
Frontiers in Energy Research

RECEIVED 15 June 2022
ACCEPTED 05 July 2022
PUBLISHED 04 August 2022

CITATION
Wang Y, Lei Y and Wang P (2022), Integrated stability control for a vehicle in the vehicle-to-grid system on low adhesion coefficient road.
Front. Energy Res. 10:969676.
doi: 10.3389/fenrg.2022.969676

Integrated stability control for a vehicle in the vehicle-to-grid system on low adhesion coefficient road

Yujie Wang[1], Yu Lei[2] and Peipei Wang[2]*

[1]School of International Education, Wuhan University of Technology, Hubei, China, [2]School of Automation, Wuhan University of Technology, Hubei, China

For the vehicle-to-grid system, the dynamic performance of the vehicle in the transportation system is quite crucial. The stability of the vehicle is the basis of the whole system. Compared to the traditional vehicle, the vehicle with a torque distribution system allows the vehicle to have a better dynamic performance. The torque distribution method has attracted a lot of attention from researchers. Most of the current work focuses on the vehicle on the concrete road. To improve the vehicle lateral stability in the critical work condition, the nonlinear reference model and vehicle dynamic model with 8 degrees of freedom are established based on the vehicle dynamic theory. An integrated active front steering (AFS) and direct yaw control (DYC) controller are designed based on LQR (Linear quadratic regulator) and vehicle stability phase portrait. To evaluate the performance of the vehicle on the road with a relatively low adhesion coefficient. The double lane-change and fishhook maneuver are chosen as the work condition. The steering angle, wheel torque, vehicle routine, phase portrait track, and yaw rate are calculated and compared. The simulation result validates the effectiveness of the proposed integrated AFS and DYC control method. The stability of the vehicle on the low adhesion coefficient road can lay a good foundation of the vehicle-to-grid system.

KEYWORDS

vehicle-to-grid, integrated stability control, low adhesion coefficient road, linear quadratic regulator, vehicle dynamic

Introduction

The Electric vehicle (EV) shows a promising future due to its advantage in energy conservation and environment protection. The EV with wheel motors has superior performance in advanced chassis control algorithms because of its simplified chassis and independent driving torque. The independent driving torque on the vehicle wheels allows the vehicle to have a better ability on torque vectoring (TV) control. The TV control can improve the dynamic performance of the vehicle according to the driver's attention without significantly damaging its speed.

Normally, the TV or differential braking control (DBC) is integrated with the traditional steering system to improve vehicle performance (Soares et al., 2018) (Chen

et al., 2017). Based on the coordination of active front steering (AFS), direct yaw control (DYC), and TV control, an integrated control algorithm is provided to maintain the vehicle stability during extreme work conditions (Aouadj et al., 2020); (Li et al., 2019). Besides lateral stability, some researchers also consider roll stability, the TV control is combined with the AFS to enhance the yaw and roll stability of a coach (Zheng et al., 2018). Usually, the torque control distribution algorithm is made up of 2 or 3 layers (Khalfaoui et al., 2018). The stability judgment, slip rate calculation, torque allocation, and steering angle are determined in the upper layer, while the lower layer conducts the torque inverting. The plane phase method can represent the nonlinear characteristics, therefore, it is widely used in vehicle stability judgment. The plane phase method can be classified according to the state variable used in the plane phase, including sideslip angle-sideslip angular velocity (Inagaki et al., 1994), yaw rate-sideslip angle (Ono et al., 1998), and front-rear tire sideslip angle (Bobier and Gerdes, 2013). Different torque control algorithms, such as fuzzy control (Boada et al., 2005), PID (Liu et al., 2019), LQR (Linear quadratic regulator) (Dai et al., 2019), MPC (Model predictive control) (Zhang and Wu, 2016), and sliding-mode control (Truong et al., 2013) are initiated to allocate the needed torque during the steering process. For the torque distribution process, even distribution, generalized inverse matrix, and least square are the commonly used algorithms (Xu et al., 2019).

Plenty of works have been done in this area, most of the current research focuses on vehicles running on the regular road with an adhesion coefficient of around 0.8. With a lower adhesion coefficient, lower friction force can be provided by the road surface, thus, the easier the vehicle runs out of control. To deal with the critical situation of the passenger car, an 8 DOFs vehicle and 2 DOFs reference model are established and validated by the result of Carsim. According to the stability phase portrait and LQR method, an integrated AFS and DYC controller is designed. The effectiveness of the controller is proved by the simulation of two critical maneuvers on low friction adhesion road. The results show the overall improvement of the vehicle's lateral stability.

Vehicle dynamic model

To investigate the differential torque steering control algorithms, the vehicle dynamic model is established based on the vehicle dynamic theory. For an operating vehicle, lots of freedom exists in the whole system, the simplification must be done based on the researchers' focus. Normally, a 2 DOF model is established as the reference model and the multiple DOF model such as the 8, 10, or 14 DOF model is established to verify the torque distribution algorithms (Jaafari and Shirazi, 2016); (Goodarzi et al., 2011). In this case, 2 and 8 DOF vehicle dynamic models are built. Since the 8 DOF model is much more complicated than the 2 DOF model, the 8 DOF model is introduced first. The 8 DOF model is combined with the vehicle body, wheel, motor, and tire model.

Vehicle body model

For the vehicle dynamic model, the 4 out of 8 DOFs are for the vehicle body and the remaining 4 DOFs are for the wheel rotations. The 4 DOFs for the vehicle body model are the motion of longitudinal, lateral, yaw, and roll (Figure 1). The four motions can be identified as Eqs 1–4, the symbol and vehicle parameters used in these equations are shown in Table 1.

$$m\left(\dot{v}_x - v_y\gamma\right) + m_s h_s \gamma\dot{\phi} = \sum_{i=1}^{4} F_{xi} - \frac{1}{2}C_d A\rho v_x^2 - mgf \tag{1}$$

$$m\left(\dot{v}_y + v_x\gamma\right) - m_s h_s\ddot{\phi} = \sum_{i=1}^{4} F_{yi} \tag{2}$$

$$I_x\ddot{\phi} - m_s h_s\left(\dot{v}_y + \gamma v_x\right) - I_{xz}\dot{\gamma} = m_s g h_s\phi - \left(K_f + K_r\right)\phi - \left(C_f + C_r\right)\dot{\phi} \tag{3}$$

$$I_z\dot{\gamma} - I_{xz}\ddot{\phi} = M + \left(F_{y1} + F_{y2}\right)L_f - \left(F_{y3} + F_{y4}\right)L_r \tag{4}$$

$$M = \frac{L_w}{2}\left(F_{x2} + F_{x4} - F_{x1} - F_{x3}\right) \tag{5}$$

Where, v_x and v_y are the longitudinal and lateral speed of the vehicle, γ means the yaw rate, ϕ is the roll angle, F_{xi} and F_{yi} are the longitudinal and lateral force of the four wheels in the coordinate system based on the vehicle body, $i = 1, 2, 3, 4$, θ is steering angle. The force on the wheels, F_{xi} and F_{yi}, can be gained by the wheel force in the coordinate system based on the wheel itself, F_{xwi} and F_{ywi}.

$$\begin{bmatrix} F_{xi} \\ F_{yi} \end{bmatrix} = \begin{bmatrix} \cos\theta_i & -\sin\theta_i \\ \sin\theta_i & \cos\theta_i \end{bmatrix} \begin{bmatrix} F_{xwi} \\ F_{ywi} \end{bmatrix} \tag{6}$$

In this case, only the front axle is the steering axle, therefore, $\theta_1 = \theta_2 = \theta$, $\theta_3 = \theta_4 = 0$.

Wheel model

The rotation motion of the four wheels is taken into consideration in the wheel dynamic model. The dynamic of each wheel can be demonstrated as follows:

$$I_w\dot{\omega}_i = T_i - F_{xi}R_w \tag{7}$$

Where, T_i means the driving torque of the wheel. The slip rate of the wheel, s_i, can be acquired by Eq. 8.

$$s_i = \frac{\omega_i R_w - v_{wi}}{\max\left(\omega_i R_w, v_{wi}\right)} \tag{8}$$

Where, v_{wi} is the speed of the wheel. For the wheels on the steering axle, the speed of the left and right wheel, v_{w1} and, v_{w2} can be expressed as:

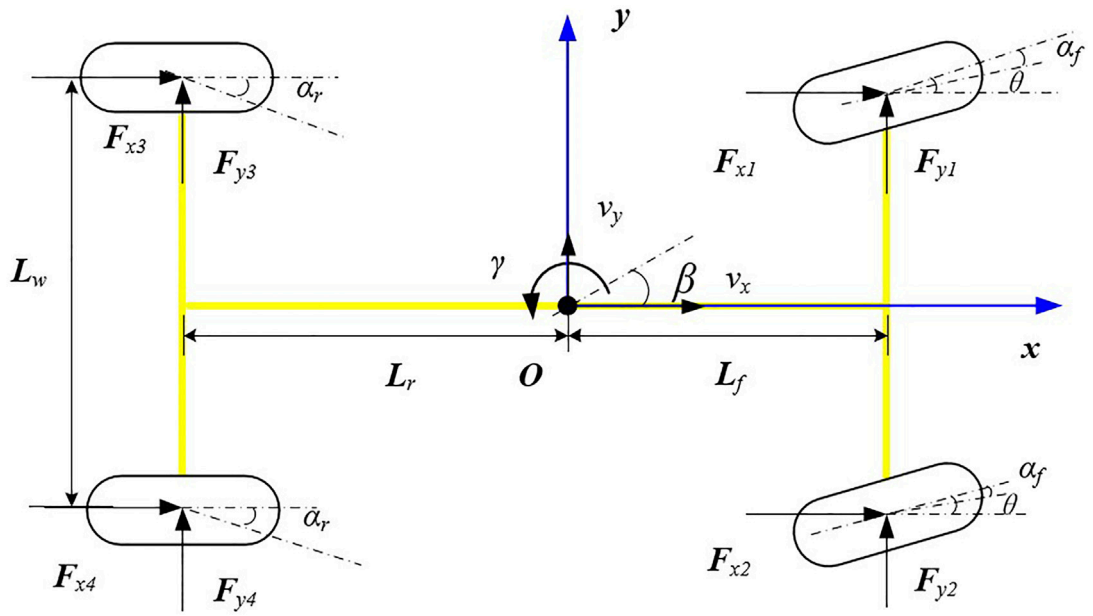

FIGURE 1
Diagram of the 8DOF model.

TABLE 1 Vehicle parameters.

Parameter	Symbol	Value	Unit
Vehicle mass	m	1704.70	kg
Sprung mass	m_s	1527	kg
Vehicle area	A	2.1	m^2
Roll inertial of the vehicle	I_x	744.0	$kg·m^2$
Yaw inertial of the vehicle	I_z	3048.1	$kg·m^2$
product of inertia of x, z axis	I_{xz}	21.09	$kg·m^2$
Height of the sprung mass	h_s	0.55	m
Distance between the vehicle gravity left to the front axle	L_f	1.035	m
Distance between the vehicle gravity left to the rear axle	L_r	1.675	m
Distance between the wheels	L_w	1.39	m
Rolling stiffness of the front axle	K_f	4728	$Nm·rad^{-1}$
Rolling stiffness of the rear axle	K_r	3731	$Nm·rad^{-1}$
Rolling damper of the front axle	C_f	2823	$Nms·rad^{-1}$
Rolling damper of the rear axle	C_r	2653	$Nms·rad^{-1}$
Wheel radius	R_w	0.313	m
Inertial of wheel	I_w	2.5	$kg·m^2$
Air drag coefficient	C_d	3.2	—
Rolling resistance coefficient	f	0.002	—

$$\begin{cases} v_{w1} = \left(v_x - \dfrac{L_w}{2}\gamma\right)\cos\theta + \left(v_y + L_f\gamma\right)\sin\theta \\ v_{w2} = \left(v_x + \dfrac{L_w}{2}\gamma\right)\cos\theta + \left(v_y + L_f\gamma\right)\sin\theta \end{cases} \tag{9}$$

For the wheels on the rear, the speed of the left and right wheel, v_{w3} and, v_{w4} can be expressed as:

$$\begin{cases} v_{w3} = \left(v_x - \dfrac{L_w}{2}\gamma\right) \\ v_{w4} = \left(v_x + \dfrac{L_w}{2}\gamma\right) \end{cases} \tag{10}$$

Motor model

For the EV, as the driving unit, the motor is quite critical for the vehicle dynamic model. There are kinds of methods to establish the motor model (Adam, 2013). In this case, the torque distribution algorithm is the concern of our work. The mechanism inside the motor is not the priority. Thus, the model is built with a simple method that can represent the torque characteristic of the motor.

The motor model calculates the maximum torque in the current rotation speed, based on the dynamic response characteristic simulated by the first-order inertial response unit, the output torque of the motor, T, can be acquired.

$$T = \frac{1}{1+\tau_t}\max\left(T_{m\max}, T_d\right) \tag{11}$$

Where, τ_t is the constant time in a first-order system, $T_{m\max}$ means the maximum output of the motor in the current rotation speed, T_d represents the demand torque form the vehicle control unit.

Tire model

The tire system contacts the vehicle to the road surface, all of the vibration and forces are translated by it. To present the characteristic of the tire accurately, lots of work have been done to establish the tire model, the Fila tire model, UA tire model, Gim tire model, Dugoff tire model, HRSI tire model, Uni-Tire model, Magic Formula tire model (MF tire) are widely used in the vehicle dynamic model. In this case, two tire models are used, MF tire and brush tire.

For the MF tire model, its parameters are fit from the analysis of the test. It can be expressed as (Pacejka and Besselink, 1997):

$$Y(X) = D\sin\left[C\arctan\{BX - E(BX - \arctan(BX))\}\right] \tag{12}$$

When Y is the longitudinal force, F_x, the variable, X is the slip rate of the wheel, s. When Y is the lateral force, F_y, the corresponding variable, X, is the sideslip angle the wheel, α. The

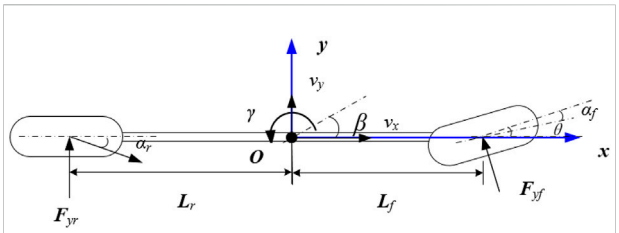

FIGURE 2
2 DOF reference model.

B, C, D, E are parameters fitted based on the test on different road types, wheel load, camber angle, temperature, inflation, and tread wear. Some of them are related to the tire load F_z, which can be gained by:

$$\begin{cases} F_{z1} = \dfrac{mgL_r}{2\left(L_f+L_r\right)} - \dfrac{ma_xh_s}{2\left(L_f+L_r\right)} + \dfrac{mK_f}{K_f+K_r}\left(\dfrac{a_yh+gh_s\phi}{L_w}\right) \\ F_{z2} = \dfrac{mgL_r}{2\left(L_f+L_r\right)} - \dfrac{ma_xh_s}{2\left(L_f+L_r\right)} - \dfrac{mK_f}{K_f+K_r}\left(\dfrac{a_yh+gh_s\phi}{L_w}\right) \\ F_{z3} = \dfrac{mgL_f}{2\left(L_f+L_r\right)} + \dfrac{ma_xh_s}{2\left(L_f+L_r\right)} + \dfrac{mK_r}{K_f+K_r}\left(\dfrac{a_yh+gh_s\phi}{L_w}\right) \\ F_{z4} = \dfrac{mgL_f}{2\left(L_f+L_r\right)} - \dfrac{ma_xh_s}{2\left(L_f+L_r\right)} - \dfrac{mK_r}{K_f+K_r}\left(\dfrac{a_yh+gh_s\phi}{L_w}\right) \end{cases} \tag{13}$$

In which, the longitudinal acceleration $a_x = \dot{v}_x - \omega v_y$, lateral acceleration, $a_y = \dot{v}_y + \omega v_x$.

For the later force of the tire, F_y, on the road with the adhesion coefficient, μ, can be determined by Eq. 14.

$$F_y = \mu D_y \sin\left[\left(\frac{5}{4} - \frac{\mu}{4}\right)C_y \arctan\left\{(2-\mu)B_y\alpha - E_y\left((2-\mu)B_y\alpha - \arctan\left((2-\mu)B_y\alpha\right)\right)\right\}\right] \tag{14}$$

2 DOF reference model

The 2DOF model (shown in Figure 2), also known as the single-track model or bicycle model, is a classic model to analyze the lateral stability of a vehicle. In this model, only the degree of lateral and yaw motion is taken into consideration, the tire sideslip angle of one axle is the same.

The 2 DOF model can be built based on the simplification of Eqs 2, 4. The simplified equations to describe the lateral and yaw motion of the vehicle are Eqs 15, 16:

$$m\left(\dot{v}_y + v_x\gamma_r\right) = F_{yf}\cos\theta + F_{yr} \tag{15}$$

$$I_z\dot{\gamma} = F_{yf}\cos\theta L_f - F_{yr}L_r \tag{16}$$

The relationship between the lateral force and tire sideslip angle is nonlinear. A nonlinear tire model is necessary to calculate the lateral force. A brush tire model variant of the Fiala nonlinear brush model, assuming one coefficient of friction and parabolic force distribution, as described by Pacejka (Pacejka, 2012). In the brush model, the lateral force, F_{yi}, can be expressed as:

$$F_{yi} = \frac{C_{\alpha i} f(\xi_i) \tan \alpha_i}{\xi_i (1 + \lambda_i)} \tag{17}$$

$$f(\xi_i) = \begin{cases} \xi_i - \frac{\xi_i^2}{3\mu F_{zi}} + \frac{\xi_i^3}{27\mu^2 F_{zi}^2} & |\xi_i| < 3\mu F_{zi} \\ \mu F_{zi} & |\xi_i| \geq 3\mu F_{zi} \end{cases} \tag{18}$$

$$\xi_i = \sqrt{C_{xi}^2 \left(\frac{\lambda_i}{1 + \lambda_i}\right)^2 + C_{\alpha i}^2 \left(\frac{\tan \alpha_i}{1 + \lambda_i}\right)^2} \tag{19}$$

$$\lambda_i = \frac{R_\omega \omega_i - v_x}{\max(R_\omega \omega_i, v_x)} \tag{20}$$

The footnote, i, stands front f and rear r, respectively. The normal force of the front and rear axle, F_{zf} and F_{zr}, can be defined as:

$$\begin{cases} F_{zf} = \frac{mgL_r}{(L_f + L_r)} \\ F_{zr} = \frac{mgL_f}{(L_f + L_r)} \end{cases} \tag{21}$$

α_{sl} is the sideslip angle corresponding to the full saturation of the tire force.

$$\alpha_{sl} = \arctan \frac{3\mu F_z}{C_\alpha} \tag{22}$$

α_f and α_r are the sideslip angle of the front and rear tires, respectively.

$$\begin{cases} \alpha_f = \frac{v_y + L_f \gamma}{v_x} \\ \alpha_r = \frac{v_y - L_r \gamma}{v_x} \end{cases} \tag{23}$$

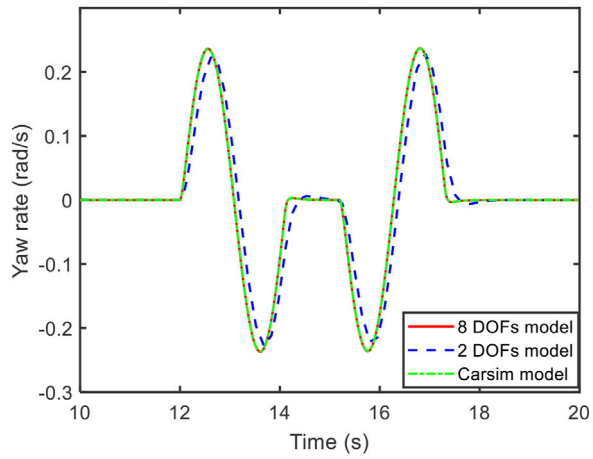

FIGURE 3
Comparison of yaw rate.

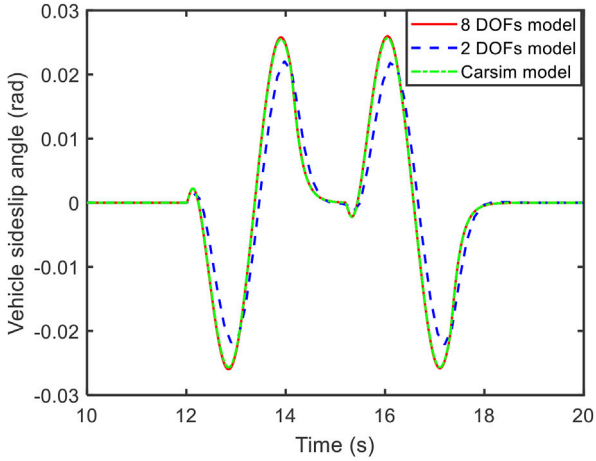

FIGURE 4
Comparison of vehicle sideslip angle.

Model validation

To investigate the vehicle dynamics control algorithm, the accuracy and efficiency of the model should be taken into consideration. The model should be able to reflect the vehicle dynamics but not too complicated. Normally, the vehicle field test result or results are simulated by commercial platforms, such as Adams/Car and Carsim. In this case, Carsim is chosen to validate the established model.

The severe double lane-change maneuver is one of the most common conditions to verify the accuracy of models. It is a dynamic process consisting of rapidly driving a car from its original lane to another parallel lane and returning to the initial lane. During the process, the vehicle should not exceed the lane boundaries. It is widely used in vehicle stability assessment because its result is repeatable and discriminatory. In this case, the double lane-change maneuver on the high adhesion road with the speed of 80 km/h is chosen to verify the established models.

The vehicle yaw rate, sideslip angle, and trajectory of the established models and Carsim model in the double-lane change condition on the road with the adhesion of 0.3 are compared in Figures 3–5.

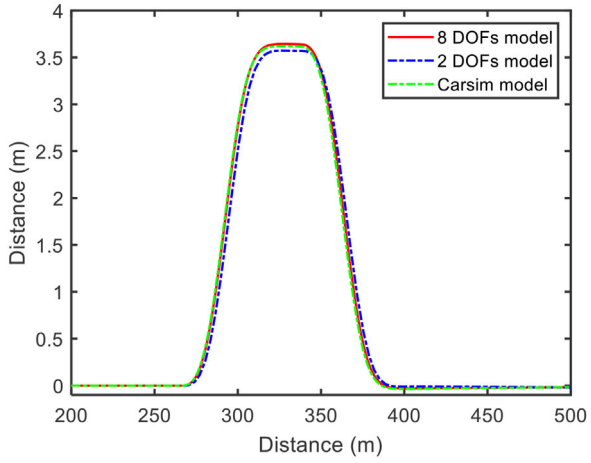

FIGURE 5
Comparison of vehicle trajectory.

TABLE 2 MAPE of the established models.

Output	8 DOFs model (%)	2 DOFs model (%)
Yaw rate	1.36	3.66
Vehicle sideslip angle	1.91	5.71
Vehicle trajectory	2.44	4.29

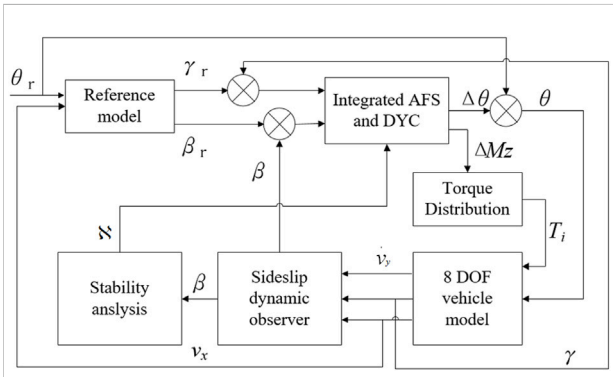

FIGURE 6
Structure of control strategy.

According to the comparison in Figures 3–5, the output of the established 8 DOFs and 2 DOFs models is close to the Carsim. Taking the result of Carsim as the baseline, the MAPE (mean absolute percentage error) is listed in Table 2.

The MAPE of the 8 DOFs model is lower than the 2DOFs model. The MAPE of the 2 DOFs model stays at a relatively low level, the maximum MAPE is lower than 6%. Therefore, these two models can be used in further analysis.

Design of control system

The structure of the proposed control strategy is shown in Figure 6. The reference model is a 2 DOF model with a nonlinear brush tire. The main goal of the control system is to make the actual yaw rate, γ, to follow the ideal yaw rate, γ_r, generated by the reference model and maintain the vehicle sideslip angle, β, in a certain range to prevent the vehicle from spinning. According to the comparison of the ideal and actual yaw rate and vehicle sideslip angle, the controller generates the active steering angle, $\Delta\theta$, and yaw moment, ΔM_z. The yaw moment is converted to driving torque on the four wheel motors.

Integrated AFS and DYC controller

Based on Eqs 14–17, the state-space function of the 2 DOF model can be expressed as:

$$\dot{x}(t) = \mathrm{A}x(t) + \mathrm{B}_1 y(t) + \mathrm{B}_2 u(t) \tag{24}$$

$$x(t) = \begin{bmatrix} \beta_r & \gamma_r \end{bmatrix}^T \tag{25}$$

$$A = \begin{bmatrix} \frac{2(k_f + k_r)}{mv_x} & -1 + \frac{2(L_r k_r - L_f k_f)}{mv_x^2} \\ \frac{2(L_r k_r - L_f k_f)}{I_z} & \frac{2(L_f^2 k_f + L_r^2 k)_r}{v_x} \end{bmatrix} \tag{26}$$

$$\mathrm{B}_1 = \begin{bmatrix} -\frac{2k_f}{mv_x} & -\frac{2L_f k_f}{I_z} \end{bmatrix}^T \tag{27}$$

$$y(t) = \theta \tag{28}$$

$$\mathrm{B}_2 = \begin{bmatrix} \frac{2k_f}{mv_x} & 0 \\ \frac{2L_f k_f}{I_z} & \frac{1}{I_z} \end{bmatrix} \tag{29}$$

$$u(t) = \begin{bmatrix} \Delta\theta & \Delta M_z \end{bmatrix}^T \tag{30}$$

The lateral stiffness of the front tire can be gained based on Eqs 16, 22.

$$\begin{cases} k_f = \frac{F_{yf}}{\alpha_f} \\ k_r = \frac{F_{yr}}{\alpha_r} \end{cases} \tag{31}$$

According to the 2 DOFs model, the ideal vehicle yaw rate and sideslip angle can be gained. The active steering angle and torque are acquired according to the optimal solution of equation (24). It can be expressed as:

$$J = \int_0^\infty \left[x(t)^T Q x(t) + u(t)^T R u(t) \right] dt \tag{32}$$

Where, matrix Q and R are symmetric positive definite weighting matrix. The optimal controller $u(t)$ can be written as:

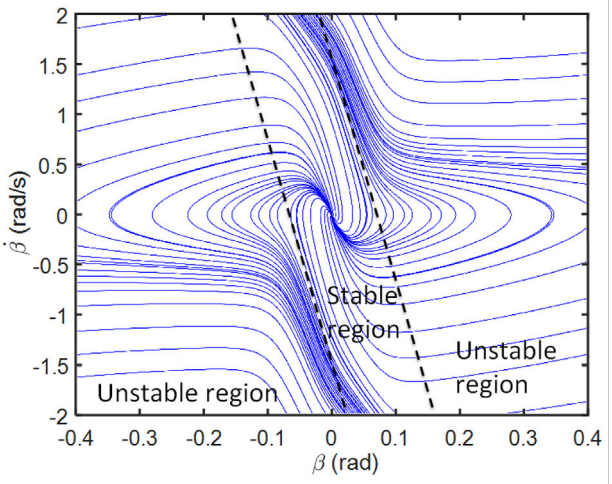

FIGURE 7
Stable region in the sideslip angle and angular velocity phase portrait.

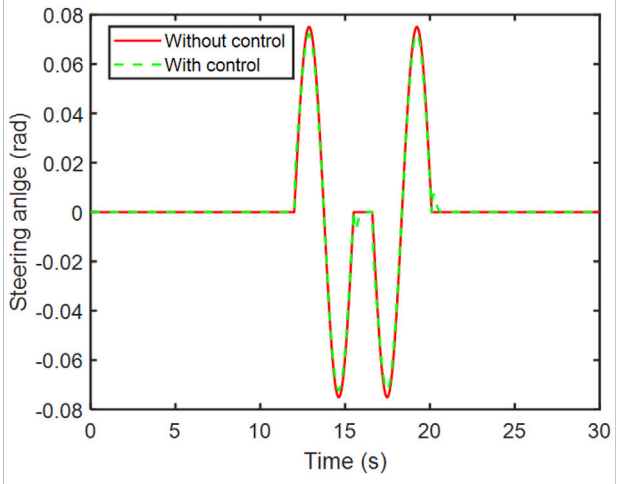

FIGURE 8
Comparison of steering angle.

$$u(t) = -R^{-1}B^{T}Px(t) = -Kx(t) \tag{33}$$

The matrix meets the Riccati equation.

$$PA + A^{T}P - PBR^{-1}B^{T}P + Q = 0 \tag{34}$$

Coordination of AFS and DYC

Once the steering angle and yaw moment are gained, the control task should be determined. According to Aouadj's work, the steering angle will always be taken as the input, the yaw moment will be initiated only when the vehicle is in a dangerous condition (Aouadj et al., 2020). In this case, the $\dot{\beta} - \beta$ phase portrait is used to determine the stability state of the vehicle, as shown in Figure 7.

As shown in Figure 7, the phase portrait is divided into three parts, one stable region, and two unstable regions. The boundary of the stable and stable region can be described by Eq. 35 (He et al., 2006):

$$\aleph = \left|a\dot{\beta} + b\beta\right|, \aleph < 1 \tag{35}$$

The parameter a and b are acquired based on the $\dot{\beta} - \beta$ phase portrait boundary (dash lines in Figure 4).

$$\dot{\beta} = \frac{a_y}{v_x} - \gamma \tag{36}$$

Simulation and discussion

There are some classical work conditions to access the vehicle's lateral stability, such as steady steering, snake steering, fishhook, and double lane change. Among them, the double lane-change and

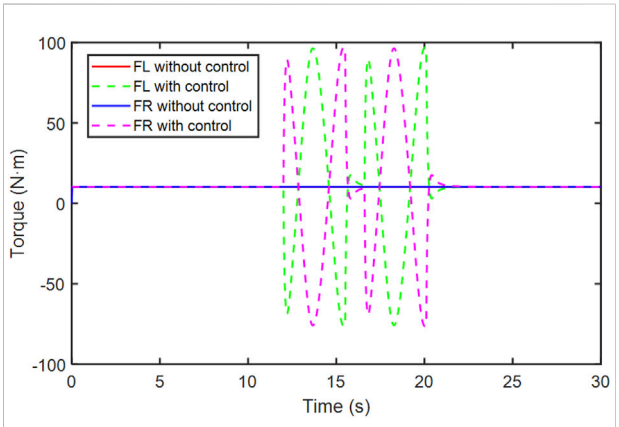

FIGURE 9
Comparison of front wheel torque.

fishhook are the most critical conditions. Therefore, they are chosen to compare the lateral stability performance with two different torque control algorithms. The double lane-change is initiated based on the regulation in ISO-3888-1–2018 (ANSI, 2018)(Passenger cars-Test track for a severe lane-change maneuver: Part 1 double-lane change), the fishhook test is based on Laboratory test procedure for dynamic rollover, the fishhook maneuver test procedure (New car assessment program, NCAP).

Double lane-change

Normally, the recommended speed on the snow or ice road is within 30 km/h. However, some drivers run the vehicle at a

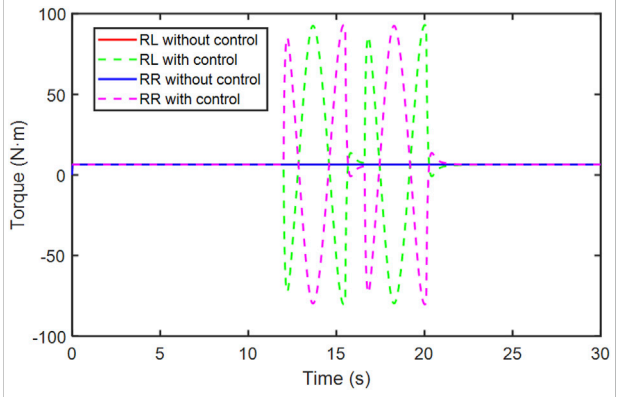

FIGURE 10
Comparison of rear wheel torque.

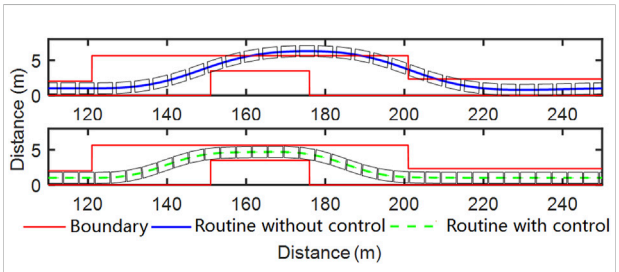

FIGURE 11
Comparison of double lane-change routine.

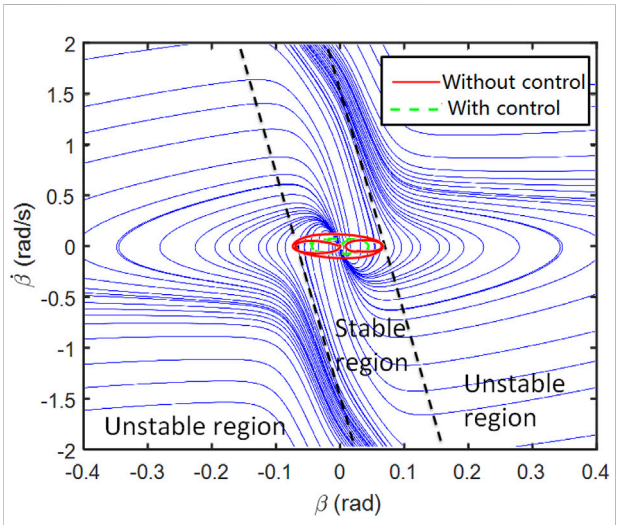

FIGURE 12
Comparison of the phase portrait.

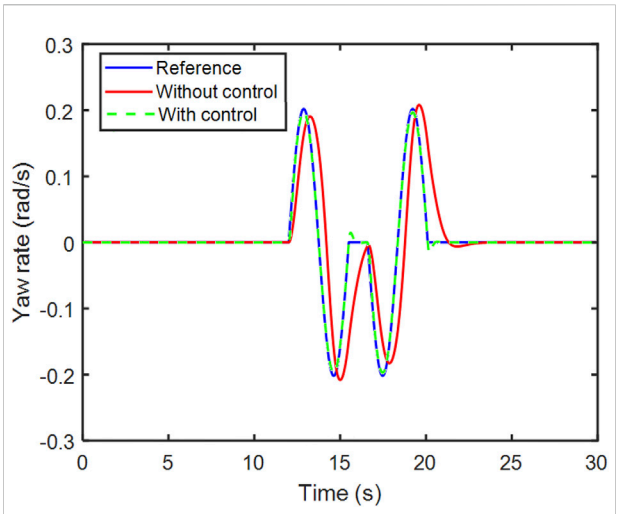

FIGURE 13
Comparison of yaw rate.

higher speed based on their experience. Therefore, the speed of 36 km/h is chosen to initiate the simulation.

The steering angle and torque of each wheel are shown in Figures 8–10, respectively.

In Figure 8, the steering angle with and without control is compared. Without control, the steering angle is the same as the reference. With the controller, the steering angle is different from the reference, the maximum gap is 0.002 rad.

According to the comparison in Figures 9, 10, with the control algorithm, the torque varies to maintain the stability of the vehicle. The left and right wheel torque of the same axle have the opposite variation trend.

The vehicle routine, phase portrait, and yaw rate are calculated and compared in Figures 11–13.

In Figure 11, the red line represents the lane boundary regulated in ISO 3888:2018. The box means the vehicle, the blue and green dash line is the vehicle routine without and with the control method. Without control, the vehicle fails to pass the double lane-change test. The maximum offset distance is 1.41 m. With the control algorithm, the vehicle can finish the test without exceeding the boundaries.

In Figure 12, it is clear that the envelope with control is smaller than the envelope without control. The envelope without exceeds the stable boundaries a bit, which means the vehicle is at the edge of stable and unstable. With the controller, both of the vehicle sideslip angle and angular velocity are maintained in a lower range.

Figure 13 shows the yaw rate variation of the reference model, without and with control. With control, the maximum

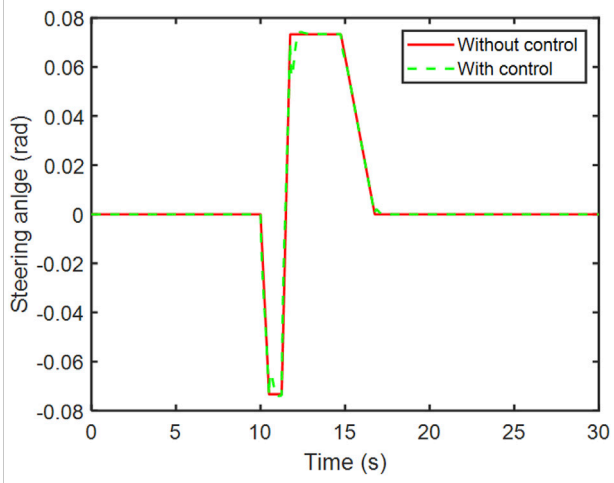

FIGURE 14
Steering angle variation during the fishhook maneuver.

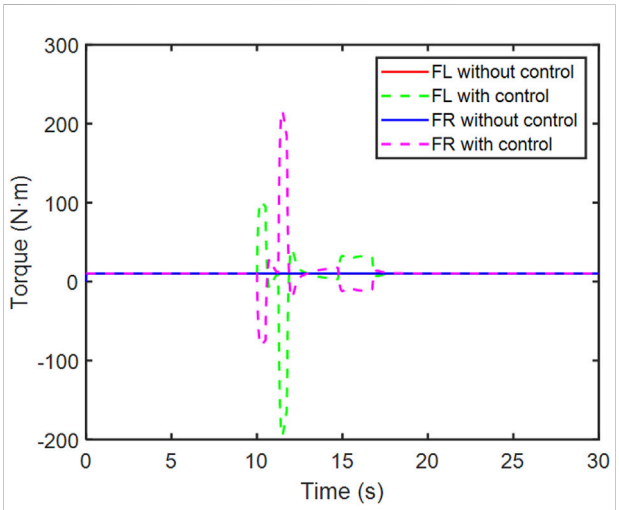

FIGURE 15
Comparison of front wheel torque.

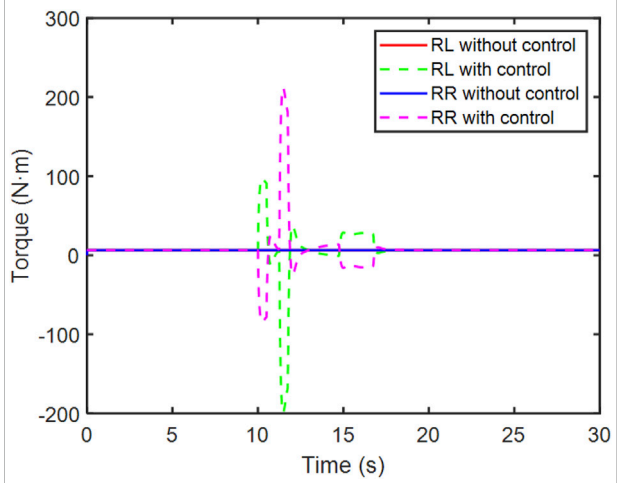

FIGURE 16
Comparison of rear wheel torque.

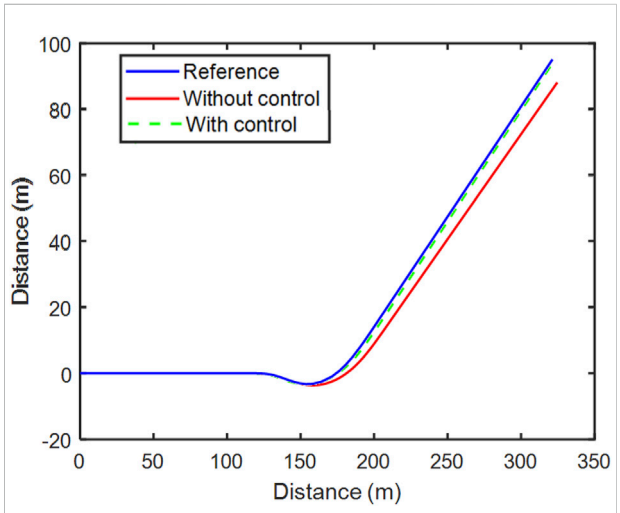

FIGURE 17
Comparison of double lane-change routine.

error of the reference model is 0.01 rad/s. Without control, the actual vehicle yaw rate is lag behind the reference model with approximately 0.5 s, the maximum error is 0.1 rad/s if the effect of the time delay is eliminated.

Fishhook maneuver

Fishhook maneuver is the test procedure of the New Car Assessment Program (NCAP) used by the National Highway Traffic Safety Administration (NHSTA) to evaluate light vehicle dynamic rollover maneuver. This test procedure is also used by the researchers to evaluate the lateral stability (Jin et al., 2017). According to the test procedure, the steering angle variation during the process is shown in Figure 14 (without control).

With the controller, the AFS makes the steering angle varies from the reference angle. The gap occurs at the sudden change of the steering angle, the maximum gap is 0.016 rad.

During the fishhook maneuver, the toque of the wheels is shown in Figures 15, 16.

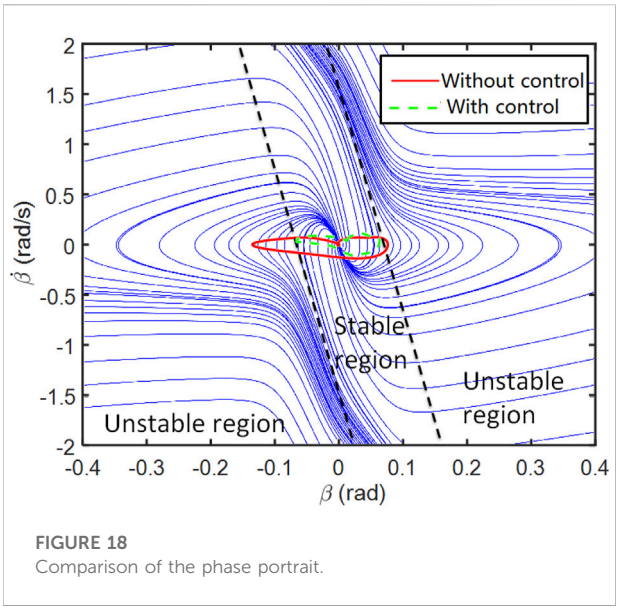

FIGURE 18
Comparison of the phase portrait.

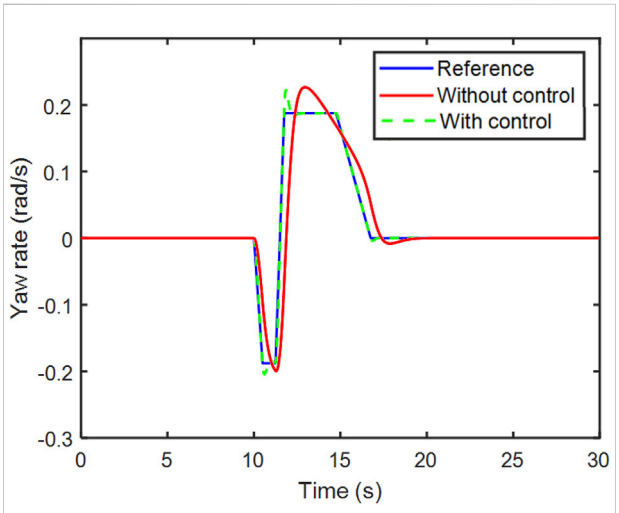

FIGURE 19
Comparison of yaw rate.

The vehicle routine, phase portrait, and yaw rate during the fishhook maneuver are calculated and compared in Figures 17–19.

Figure 17 illustrates the vehicle track of the reference model, with and without the control algorithm. With the integrated control, the gap between the reference model and the 8 DOF model is relatively small. The difference between the track of the model without control and the reference model occurs at the beginning of the steering and gets bigger with time.

Figure 18 demonstrates the difference of the phase portrait track. The track of the model without control exceeds the boundary of stable boundaries. The variation range of the vehicle sideslip angle is much higher than the vehicle sideslip angular velocity. With the help of control method, the AFS and DYC are coordinated and the track stays in the stable region.

In Figure 19, the yaw rate of the three models is compared. The yaw rate of the reference model varies strictly with the steering input. The yaw rate of the model with control is close to the yaw rate of the reference model, except for the two inflection points 10.5 and 11.75 s, the error between the model with control and reference model gets bigger. The maximum error is 0.03 rad/s. For the yaw rate of the model without control, it takes more time to eliminate the gap to the reference model, the maximum error is 0.03 rad/s. However, the mean error is bigger than the model with control.

Conclusion

The goal of this study is to design an integrated vehicle dynamics controller to enhance the vehicle lateral stability. To deal with the critical condition on a low adhesion coefficient road, a 2 DOF nonlinear reference model and 8 DOFs model are built and validated by Carsim. The integrated AFS and DYC controller is designed. Based on the dynamic analysis, the effectiveness of the provided algorithm in two typical conditions is proved by the 8 DOFs model.

Without the control method, the vehicle fails to pass the double lane-change test at the speed of 36 km/h on the road with a low adhesion coefficient of 0.3. The track on the $\dot{\beta} - \beta$ phase portrait exceeds the stable region in both the double lane-change and fishhook maneuvers. With the integrated controller, the vehicle yaw rate, the routine can follow the reference model with a much smaller error, and the track on the $\dot{\beta} - \beta$ phase portrait stays in the stable region, which means the vehicle stability is enhanced.

According to the comparison of lateral stability indicators of double lane-change and fishhook maneuver, the goal is achieved, the lateral stability and path tracking ability of the vehicle on the low adhesion road is improved. The improvement of the vehicle safety and path tracking ability lays a good foundation for the whole vehicle-to-grid system.

Data availability statement

The raw data supporting the conclusion of this article will be made available by the authors, without undue reservation.

Author contributions

YW is responisble for the simulation and writting of this paper. YL provides the assistance of the simulation and vehicle parameters. PW provides the original idea and funding.

Funding

This study was funded by the Innovative Research Team Development Program of Ministry of Education of China (IRT_17R83), and the 111 Project (B17034) of China.

Conflict of interest

The authors declare that the research was conducted in the absence of any commercial or financial relationships that could be construed as a potential conflict of interest.

Publisher's note

References

Adam, A. A. (2013). Accurate modeling of PMSM for differential mode current and differential torque calculation." in International Conference on Computing, Khartoum, August 26, 2009. IEEE.

ANSI (2018). *Passenger cars-test track for a severe lane-change maneuver: obstacle avoidance-Part 1: Double lane-change*. ISO 3888-1:2018 (E).

Aouadj, N., Hartani, K., and Fatiha, M. (2020). New integrated vehicle dynamics control system based on the coordination of active front steering, direct yaw control, and electric differential for improvements in vehicle handling and stability. *SAE Int. J. Veh. Dyn. Stab. NVH* 4, 119–133. doi:10.4271/10-04-02-0009

Boada, B. L., Boada, M. J. L., and Díaz, V. (2005). Fuzzy-logic applied to yaw moment control for vehicle stability. *Veh. Syst. Dyn.* 43 (10), 753–770. doi:10.1080/00423110500128984

Bobier, C. G., and Gerdes, J. C. (2013). Staying within the nullcline boundary for vehicle envelope control using a sliding surface. *Veh. Syst. Dyn.* 51 (2), 199–217. doi:10.1080/00423114.2012.720377

Chen, T., Xu, X., Li, Y., Wang, W., and Chen, L. (2017). *Speed-dependent coordinated control of differential and assisted steering for in-wheel motor driven electric vehicles*. Proceedings of the Institution of Mechanical Engineers Part D Journal of Automobile Engineering.095440701772818

Dai, Y., Yu, L., Song, J., and Zhao, W. (2019). *The differential braking steering control of special purpose flat-bed electric vehicle*. Detroit: WCX SAE World Congress Experience.

Goodarzi, A., Soltani, A., and Esmailzadeh, E. (2011). Active variable wheelbase as an innovative approach in vehicle dynamic control." in ASME 2011 International Design Engineering Technical Conferences and Computers and Information in Engineering Conference, Khartoum, August 26, 2009.

He, J., Crolla, D. A., Levesley, M. C., and Manning, W. J. (2006). Coordination of active steering, driveline, and braking for integrated vehicle dynamics control. *Proc. Institution Mech. Eng. Part D J. Automob. Eng.* 220 (D10), 1401–1420. doi:10.1243/09544070jauto265

Inagaki, S., Kushiro, I., and Yamamoto, M. (1994). Analysis on vehicle stability in critical cornering using phase-plane method. *JSAE Rev.* 16 (21), 216.

Jaafari, S., and Shirazi, K. H. (2016). A comparison on optimal torque vectoring strategies in overall performance enhancement of a passenger car. *Proc. Institution Mech. Eng. Part K J. Multi-body Dyn.* 1464419315627113, 469–488. doi:10.1177/1464419315627113

Jin, X., Yu, Z., Yin, G., and Wang, J. (2017). Improving vehicle handling stability based on combined afs and dyc system *via* robust takagi-sugeno fuzzy control. *IEEE Trans. Intell. Transp. Syst.* 19, 2696–2707. doi:10.1109/tits.2017.2754140

Khalfaoui, M., Hartani, K., Merah, A., and Aouadj, N. (2018). Development of shared steering torque system of electric vehicles in presence of driver behaviour estimation. *Int. J. Veh. Aut. Syst.* 14 (1), 18. doi:10.1504/ijvas.2018.093100

Li, S., Zhao, J., Yang, S., and Fan, H. (2019). Research on a coordinated cornering brake control of three-axle heavy vehicles based on hardware-in-loop test. *IET Intell. Transp. Syst.* 13 (5), 905–914. doi:10.1049/iet-its.2018.5406

Liu, Z., Pei, X., Chen, Z., Yang, B., and Guo, X. (2019). *Differential speed steering control for four-wheel distributed electric vehicle*. Detroit: WCX SAE World Congress Experience.

Ono, E., Hosoe, S., Tuan, H. D., and Doi, S. (1998). Bifurcation in vehicle dynamics and robust front wheel steering control. *IEEE Trans. Control Syst. Technol.* 6 (3), 412–420. doi:10.1109/87.668041

Pacejka, H. B., and Besselink, I. J. M. (1997). Magic Formula tyre model with transient properties. *Veh. Syst. Dyn.* 27 (S1), 234–249. doi:10.1080/00423119708969658

Pacejka, H. B. (2012). *Tire and vehicle dynamics*. Third Edition. Oxford. xiii-xvi.

Soares, N., Martins, A. G., Carvalho, A. L., Caldeira, C., Du, C., Castanheira, E., et al. (2018). The challenging paradigm of interrelated energy systems towards a more sustainable future. *Renew. Sustain. Energy Rev.* 95 (NOV), 171–193. doi:10.1016/j.rser.2018.07.023

Truong, T., Tomaske, V., and Winfried, D. (2013). Active front steering system using adaptive sliding mode control." in Chinese control and decision conference, Khartoum, August 26, 2009.

Xu, K., Luo, Y., Yang, Y., and Xu, G. (2019). Review on state perception and control for distributed drive electric vehicles. *J. Mech. Eng.* 55 (22), 60. doi:10.3901/JME.2019.22.060

Zhang, L., and Wu, G. (2016). *Combination of front steering and differential braking control for the path tracking of autonomous vehicle*. WCX SAE World Congress Experience.

Zheng, H., Wang, L., and Zhang, J. (2018). Comparison of active front wheel steering and differential braking for yaw/roll stability enhancement of a coach. *SAE Int. J. Veh. Dyn. Stab. NVH* 2 (4)–283. doi:10.4271/2018-01-0820

frontiers | Frontiers in Energy Research

TYPE Original Research
PUBLISHED 09 August 2022
DOI 10.3389/fenrg.2022.948308

OPEN ACCESS

EDITED BY
Hao Yu,
Tianjin University, China

REVIEWED BY
Astitva Kumar,
Delhi Technological University, India
Lv Chaoxian,
China University of Mining and Technology, China

*CORRESPONDENCE
Guowen Kuang,
gkuang@szpt.edu.cn

SPECIALTY SECTION
This article was submitted to Smart Grids, a section of the journal Frontiers in Energy Research

RECEIVED 19 May 2022
ACCEPTED 27 June 2022
PUBLISHED 09 August 2022

CITATION
Zhang R, Li G, Bu S, Kuang G, He W, Zhu Y and Aziz S (2022), A hybrid deep learning model with error correction for photovoltaic power forecasting. *Front. Energy Res.* 10:948308. doi: 10.3389/fenrg.2022.948308

A hybrid deep learning model with error correction for photovoltaic power forecasting

Rongquan Zhang[1,2], Gangqiang Li[3], Siqi Bu[4], Guowen Kuang[2]*, Wei He[5], Yuxiang Zhu[3] and Saddam Aziz[4]

[1]College of Transportation, Nanchang JiaoTong Institute, Nanchang, China, [2]Institute of Applied Artificial Intelligence of the Guangdong-Hong Kong-Macao Greater Bay Area, Shenzhen Polytechnic, Shenzhen, China, [3]Henan Provincial Key Laboratory of Smart Lighting, College of Computer and Artificial Intelligence, Huanghuai University, Zhumadian, China, [4]Department of Electrical Engineering, Hong Kong Polytechnic University, Kowloon, Hong Kong SAR, China, [5]School of Electrical and Information Engineering, Hunan Institute of Technology, Hengyang, China

The penetration of photovoltaic (PV) power into modern power systems brings enormous economic and environmental benefits due to its cleanness and inexhaustibility. Therefore, accurate PV power forecasting is a pressing and rigid demand to reduce the negative impact of its randomness and intermittency on modern power systems. In this paper, we explore the application of deep learning based hybrid technologies for ultra-short-term PV power forecasting consisting of a feature engineering module, a deep learning-based point prediction module, and an error correction module. The isolated forest based feature preprocessing module is used to detect the outliers in the original data. The non-pooling convolutional neural network (NPCNN), as the deep learning based point prediction module, is developed and trained using the processed data to identify non-linear features. The historical forecasting errors between the forecasting and actual PV data are further constructed and trained to correct the forecasting errors, by using an error correction module based on a hybrid of wavelet transform (WT) and k-nearest neighbor (KNN). In the simulations, the proposed method is extensively evaluated on actual PV data in Limburg, Belgium. Experimental results show that the proposed hybrid model is beneficial for improving the performance of PV power forecasting compared with the benchmark methods.

KEYWORDS

photovoltaic (PV) power, deep learning, non-pooling convolutional neural network (NPCNN), error correction, photovoltaic power forecasting

1 Introduction

Recently, photovoltaic (PV) power generation has been rapidly developed worldwide due to its cleanness and inexhaustibility (Al-Dahidi et al., 2019). However, the typical uncertainty and high volatility of PV power pose a big challenge to the stable operation and economic dispatch of the modern power system (Nguyen et al., 2020). Inevitably, the volatility of PV power directly aggravates the oscillatory instability of power system,

thereby increasing the reserve capacity for the auxiliary service market (Bu et al., 2019). The uncertainty of PV power also increases the economic dispatch cost of the modern power system, which deviates from the principle for maximizing the welfare of market members (Singla et al., 2021). Facing these challenges, it is imperative to use advanced predictive models to mitigate these negative impacts of PV power generation access on the entire power system.

So far, much of the literature about PV power forecasting has been performed, which can fall into physical methods, statistical methods, machine learning methods, and hybrid methods (Wang et al., 2020b). Physical methods are based on numerical weather prediction and PV cell physical principles, which simulate the energy conversion process of PV power generation, usually including Hottel and ASHRAE (Mayer and Gróf, 2021). Although the physical methods do not require historical PV power data, but they rely on the accurate physical model and massive inputs, such as solar radiation intensity, battery temperature, battery angle, solar incident angle, aging, dust, inverter efficiency, *etc* (Perez et al., 2010; Inman et al., 2013). Since it is difficult for physical methods to obtain sufficient inputs and identify the principle of PV power generation, thus resulting in poor interference ability and computational complexity. Unlike the physical methods, statistical methods do not require the principle of PV power generation, and have the advantages of simple model, fast speed and convenience. The statistical methods aim to establish the mapping relationship between historical and predicted PV power time series data by using linear fitting, e.g., autoregressive moving average (ARMA) (Chang et al., 1984), regression analysis (Cleveland and Devlin, 1988), Spatio-temporal correlation (Pillow et al., 2008), and generalized autoregressive conditionally heteroskedastic (GARCH) (Chen et al., 2019). However, statistical models often rely on historical data and require strongly correlated features, making it difficult to fit strong fluctuations and high-dimensionality of PV power data.

Generally speaking, machine learning methods can be roughly divided into shallow learning and deep learning methods. Shallow learning methods are mainly designed into smaller network structures to extract nonlinear features by using error minimization principles and certain optimization algorithms. Due to their remarkable capacity in learning nonlinear features, shallow learning methods have been widely used in PV power generation forecasting compared to physical methods and statistical methods. Commonly-used shallow learning methods include decision tree (DT) (Massucco et al., 2019), k-nearest neighbor (KNN) (Peterson, 2009), multilayer perceptron (Kumar et al., 2019), back-propagation neural networks (BPNN) (Mellit et al., 2013), radial basis function neural network (RBFNN) (Madhiarasan, 2020), support vector regression (SVR) (De Giorgi et al., 2016), and extreme learning machine (ELM) (Bouzgou and Gueymard, 2017). In addition, ensemble learning, as a kind of shallow learning, has received extensive attention in recent years. Common ensemble learning includes extreme gradient boosting (XGBoost) (Li et al., 2022), ensemble trees (Alaraj et al., 2021), random forest (RF) (Kumar and Thenmozhi, 2006), LGBM (Wang Y et al., 2020), and CatBoost (Prokhorenkova et al., 2018). In(Li et al., 2022), the authors propose a prediction model of solar irradiance based on XGBoost. In (Alaraj et al., 2021), the ensemble trees based machine learning approach considering various meteorological parameters is proposed for PV power forecasting. However, with the development of big data technology and intelligence optimization theories in recent years, the drawback of shallow learning models will be prone to the curse of dimensionality and under-fitting, which makes it difficult to forecast PV power data in a big data era (Soares et al., 2016). Therefore, one more effective way is needed to address the drawback in shallow learning models.

Deep learning, one of the most promising artificial intelligence techniques, is easier to implement feature extraction tasks, has been successfully applied in different fields with powerful learning capabilities compared to shallow learning models (Bai et al., 2021; Xie et al., 2021). Common deep learning models usually include deep neural network (DNN) (Kuremoto et al., 2014), deep belief network (DBN) (Zhang et al., 2021), recurrent neural network (RNN) (Li et al., 2019), long short-term memory (LSTM) (Liu B. et al., 2020), and convolutional neural network (CNN) (Wang et al., 2017), *etc*. Experimental results in (Wang et al., 2017; Chang and Lu, 2018; Li et al., 2019) show that the forecasting accuracy of deep learning based models is superior to that of other shallow learning-based methods. However, PV power forecasting based on deep learning models is not always perfect, because it extremely depends on the selection of hyperparameters and network structure (Hajirahimi and Khashei, 2019a). Meanwhile, the improvement for model bias and variance in a given dataset can also be a challenging task, since the training results of deep learning may exhibit a small model bias, which often leads to more significant model variance (Geman et al., 1992). The deviation between the predicted and true values for the training model is known as model bias, and the generalization ability in the training unseen dataset is known as model variance. To solve these problems, hybrid methods focus on combining different methods to disassemble different prediction tasks from the main task for the improvement of both model bias and variance compared to deep learning models (de Oliveira et al., 2021).

Hybrid forecasting methods can generally be divided into three steps: point prediction, bias prediction, and combine forecast results. Different hybrid methods are widely used in many applications, such as traffic (Katris and Daskalaki, 2015), health (Chakraborty et al., 2019), finance (Hajirahimi and

Khashei, 2019b), and electric energy system forecasting (Wu and Shahidehpour, 2010). For example, the authors in (de Mattos Neto et al., 2020) propose a hybrid method based on a nonlinear combination of the linear and nonlinear models for monthly wind speed forecasting, and use a data-driven intelligent model to find the appropriate combination method, aiming to maximize the forecasting performance. In (Wu et al., 2014), five types of shallow learning models to predict the short-time PV power data are developed as the first step using the historical PV power and NWP data, and genetic algorithms are used to determine their combinational models as the second step. Forecasting results reported in (Wu and Shahidehpour, 2010; Wu et al., 2014; de Mattos Neto et al., 2020) show the competitive performance of the hybrid methods is better than shallow learning models and statistical models. In these literatures, it is common to use statistical methods or shallow learning models as the first and second steps. To the authors' knowledge, deep learning-based hybrid methods for PV power forecasting in previous studies have received little attention. As reported in (Zhang et al., 2020; de Oliveira et al., 2021), the model selection at each step of the hybrid forecasting method can have a large impact on forecasting performance. However, the deep learning model significantly improves the PV power prediction performance compared to other benchmark models. Thus, the deep learning-based hybrid forecasting PV power method that takes advantage of the methodological advantages at each step becomes more meaningful.

Therefore, a new deep-learning-based hybrid model is proposed for ultra-short-term PV power forecasting. Compared with existing literature on similar topics, the main contributions of this work are as follows:

- In order to accurately predict PV power and its practical application value, a hybrid model based on a feature engineering module, a deep learning-based point prediction module, and an error correction module are proposed for the first time.
- To exploit the maximum feature training potential of the point prediction module during feature training, a new feature engineering module based on isolation forest is proposed.
- In order to efficiently extract features and minimize the network structure, the non-pooling convolutional neural network (NPCNN) based point prediction module, is originally developed.
- The residuals between the predicted and actual PV power are initially trained by using an error correction module (ECM) based on wavelet transform (WT) and KNN, which helps to reduce the error of the point prediction module while considering time efficiency.

Ourpreliminary numerical results demonstrate that the proposed hybrid deep learning based forecasting model is beneficial to improve the prediction accuracy of PV power. The rest of this paper is organized as follows. In **Section 2**, we analysis the historical data of PV power and describe the proposed hybrid framework for PV power forecasting. **Section 3** introduces each module of proposed method in detail, i.e., outlier detection in feature engineering, deep learning based point prediction model, WT+KNN for error correction. Experiment results are reported and discussed in **Section 4**, and we conclude this work in **Section 5**.

2 The proposed hybrid framework for PV power forecasting

2.1 Overview of the hybrid framework

The hybrid model proposed in this paper for PV power forecasting consists of a feature engineering module, a point prediction module and an error correction module. An overview of the proposed hybrid framework is described in **Figure 1**. It is worth noting that PV power forecasting methods can be divided into direct prediction and indirect prediction according to the input properties of the forecasting model (Wang et al., 2017). In the indirect prediction method, meteorological parameters such as solar radiation intensity, battery temperature, and wind speed are associated with the PV power forecasting model to improve its prediction accuracy. In the direct method, the input of the PV power prediction model is the historical power data. The proposed hybrid model for ultra-short-time in this paper is designed as a direct prediction method. There are three main reasons for this. *1*) The external explanatory variables (meteorological parameters) for ultra-short-term PV power forecasting fluctuate less than short-term/long-term PV power forecasting, so meteorological parameters have less impact on ultra-short-term PV power forecasting. *2*) Ultra-short-term PV power forecasting has high requirements for the real-time transmission of meteorological parameters, which may be difficult to obtain in time and high purchase cost in practical engineering applications. *3*) Since the workload of feature selection is reduced, the PV power prediction model is made simpler and more convenient. In addition, to train the point prediction module and the error correction module, the raw PV power dataset is grouped into three parts: a training dataset, a validation dataset, and a testing dataset. First, feature engineering module is used to process invalid/bad data points in the raw PV power data, such as outliers or missing values. Then, the point prediction module uses the data processed by feature engineering module to further accurately predict the PV power points. Error results based on point prediction module are sent to the error correction module for error prediction. Finally, we reconstruct the forecasting results by combining the results of the point prediction module and

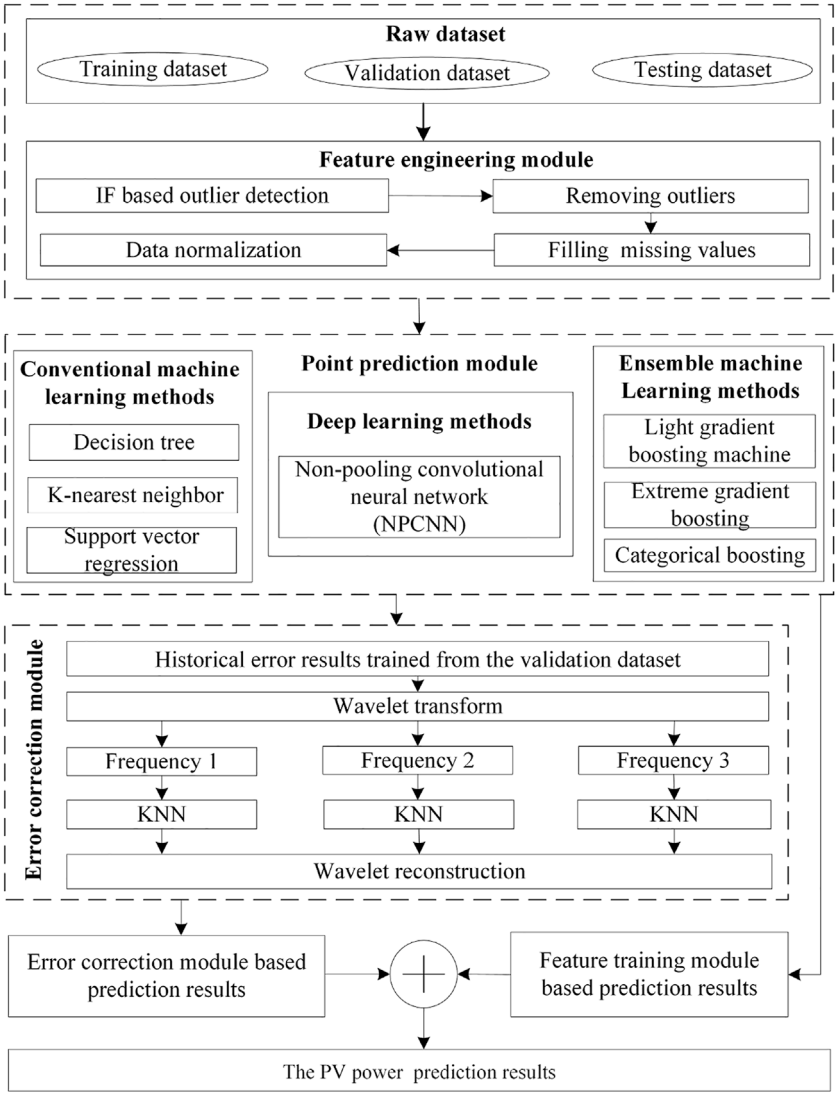

FIGURE 1
The proposed hybrid framework for PV power forecasting.

error module. The proposed forecasting framework in this paper is inspired by conventional hybrid forecasting models (Wu and Shahidehpour, 2010; de Mattos Neto et al., 2020). Comparatively, the proposed hybrid framework for PV power forecasting has at least three advantages. The first is that the feature engineering module is considered for the proposed hybrid model to further exploit the potential of the feature mining of NPCNN. The second advantage is that NPCNN can effectively extract features of PV power data by reducing the non-pooling operations of CNN. The last advantage is that the WT is taken into account in the error correction module of the prediction framework to better capture the trend of prediction deviation. Next, we analyze and discuss the role of these modules in the proposed hybrid model in detail.

2.2 Feature engineering module

Feature engineering aims to construct valuable training samples to maximize the potential of feature extraction and facilitate the training of point prediction modules. In general, raw PV power datasets may have invalid/bad data points due to PV power generation equipment failures or communication delays. It is necessary to deal with these outliers to reduce the overfitting of the feature training model to these values (Wang et al., 2020a). **Figure 2** plots the real-time measured PV power for a historical day, wherein the black dots represent the raw PV power data, and the red line represents the corrected PV power curve. It is obvious that there are some missing values and outlier values in the raw PV power compared to the corrected

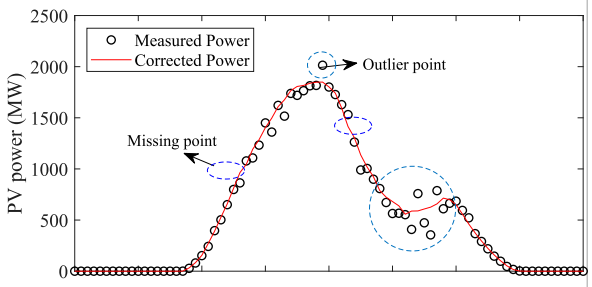

FIGURE 2
The real-time measured PV power.

curve. Moreover, if these bad power points cannot be eliminated, the training of the point prediction module suffers from data jumps and irregularities, leading to performance degradation (Wang et al., 2020a). Therefore, the raw PV generation data must be pre-processed by the feature learning module to better achieve the potential of the point prediction module. In this paper, the feature engineering module, based on IF and linear interpolation, is used to detect these outliers and fill missing values, respectively. In addition, we perform normalization on the raw PV power data to ensure parameter optimization of the point prediction module, as neural network training requires a suitable format for feature learning.

2.3 Point prediction module

The PV power forecasting based on point prediction module is shown in **Figure 3**. The input window of the point prediction module moves smoothly over the PV power sequence with time t, e.g., the inputs is $\{x_{t-3},x_{t-2},x_{t-1},x_t\}$, which corresponds to the predicted output $\tilde{x}_{t+1}$. As depict in **Figure 1**, the point prediction module can be conventional machine learning models, ensemble machine learning models, or deep learning models, such as

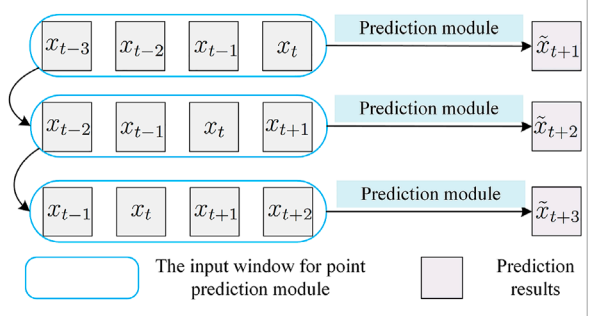

FIGURE 3
PV power forecasting based on point prediction module.

DT, KNN, SVR, XGBoost, categorical boosting (CatBoost), light gradient boosting machine (LGBM), and CNN. In general, to accurately predict PV power generation, the network structure of the point prediction module needs to be designed considering the number of features and nonlinearity of PV power generation data. Specially, CNNs, as a class of deep learning architectures, have been applied in the field of time series forecasting and achieved good performance. Since there are few relevant features for ultra-short-term PV generation prediction, they are not sufficient to support the pooling operation of conventional CNN model. In view of this, NPCNN without pooling operation is used to further extract features and learn the strong nonlinearity of the PV data in this paper. It needs to be noted that NPCNN is suitable for processing seasonal time-series data with trends, and can reduce the negative impact of pooling layers (Liu S. et al., 2020). Furthermore, The NPCNN-based point prediction module is trained based on the training dataset, and the input of NPCNN will be processed by the feature engineering module first.

2.4 Error correction module

Although different advanced forecasting methods have been proposed to reduce the model bias, they always exist more significant model variance (Geman et al., 1992). To address this issue, an error correction module based on WT and KNN is proposed in this paper to reduce the model variance of the point prediction module. Here, WT is used to decompose the raw forecasting error series into sub-frequency sequences with better contours, while KNN is used to extract the features of each frequency sequence. There are two main reasons for this: First, since the original prediction error sequence may contain nonlinear and spiky dynamic features, WT-based signal decomposition can be used to reduce their impact on the prediction performance. Each sub-frequency sequence needs to be trained by an error correction method, and KNN can quickly extract the nonlinear features of each sub-frequency sequence while losing as little prediction as possible (Saâdaoui and Rabbouch, 2019). Meanwhile, the inputs of the error correction module (ECM) should also be considered with the validation dataset errors, except for correlated features obtained from the point prediction module, as shown in **Figure 1**.

3 Description of the deep learning based hybrid model

3.1 Outlier detection in feature engineering

Isolation forest (IF) in (Liu et al., 2008; Ahmed et al., 2019) is an efficient unsupervised anomaly detection algorithm.

Compared with traditional anomaly detection methods, such as the mean-square error method and quartile method, IF provides an abnormal probability for each sample instead of judging the exception directly. IF can be divided into five processes: *1*) Several features randomly from the training dataset are selected as the feature space; *2*) A value is randomly selected in the feature space as the each node of the tree; *3*) Different trees are combined as the isolated forest; *4*) The distance between the root and leaf node of each tree are calculated as its score; *5*) If the score is low, it is an outlier. The score-based IF can be expressed as below,

$$S(x,n) = 2^{-\frac{E(h(x))}{c(n)}} \tag{1}$$

where $E(h(x))$ denotes the average length of sample x from a set of isolation trees. $c(n)$ represents the average path length with n samples obtained from a binary search tree, as below,

$$c(n) = \begin{cases} 2H(n-1) - 2(n-1)/n, & n > 2 \\ 1, & n = 2 \\ 0, & n < 2 \end{cases} \tag{2}$$

where $H(i) = \ln(i) + 0.5772156649(\text{Euler}'\text{s constant})$, which is the harmonic function. Once the scores for each sample x are solved, lower values (outliers) can manually be excluded based on the abnormal proportional coefficient ξ.

3.2 Deep learning based point prediction model

Considering that the features of time-series historical PV power data are highly uncorrelated, we proposes a two-dimensional (2D) NPCNN (no pooling layer) model as a point prediction module for PV power prediction. In this paper, the NPCNN model consists of one input layer, two conventional layers, one fully connected layer, and one output layer, as presented in **Figure 4**. Each layer are summarized as follows:

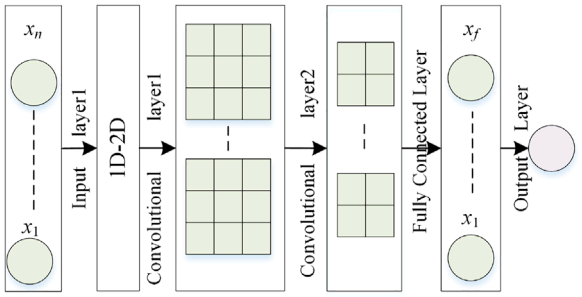

FIGURE 4
The structure of NPCNN.

- Input layer provides the input parameters of NPCNN. The historical PV power data and time attributes are combined to generate a one-dimensional time series vector, which is transformed into a two-dimensional correlation feature matrix through correlation analysis and dimensional transformation (Zhang et al., 2020).
- Convolutional layer contains several convolution kernels to generate new feature maps, which convolves the network weight with the receptive field of the feature map of the previous layer, and uses the activation function to form the feature map of the next convolutional layer (Yamashita et al., 2018).
- Fully connected layer is often used for high-level inference, which maps the features processed by the convolution layers to the output layer (Desai and Makwana, 2021).
- Output layer is the final outputs of the NPCNN.

The network parameters of NPCNN, such as weights and biases, are trained and optimized in mini-batch form using the gradient descent method based on the backpropagation algorithm to improve the forecasting performance of PV power. Meanwhile, the root-mean-square-propagation method (RMSProp) is introduced to optimize the error function of NPCNN due to its faster convergence and high accuracy (Zhang et al., 2020). Here, the mean squared error between the predicted value and the actual value is used as the loss function *Loss*, as follows,

$$Loss = \frac{1}{M} \sum_{m \in M} \sum_{d \in D} \left(r_d^m - p_d^m \right)^2 \tag{3}$$

where M and D denote the mini-batch size and the output vector size for a training sample. r_d^m and p_d^m represent the actual value and the predicted value for the dth output vector of the mth sample in mini-batch.

3.3 WT+KNN for error correction

The raw PV power forecast error data may contain peak characteristics and nonlinearities in the form of fluctuations, which can affect the PV power forecast accuracy. Both high-frequency and low-frequency signals are included in PV forecast error data (Ahmed et al., 2019). The former is due to changes in the uncertainty of the input data, and the latter is due to model over-fitting. The WT can be used to decompose the behavior of these frequencies for prediction. Therefore, the raw forecast error series based on wavelet decomposition can be described as follows,

$$Wavelet(p,q) = 2^{-(p/2)} \sum_{t=0}^{T-1} g(t)\, \phi\left[\left(t - q2^p \right) / 2^p \right] \tag{4}$$

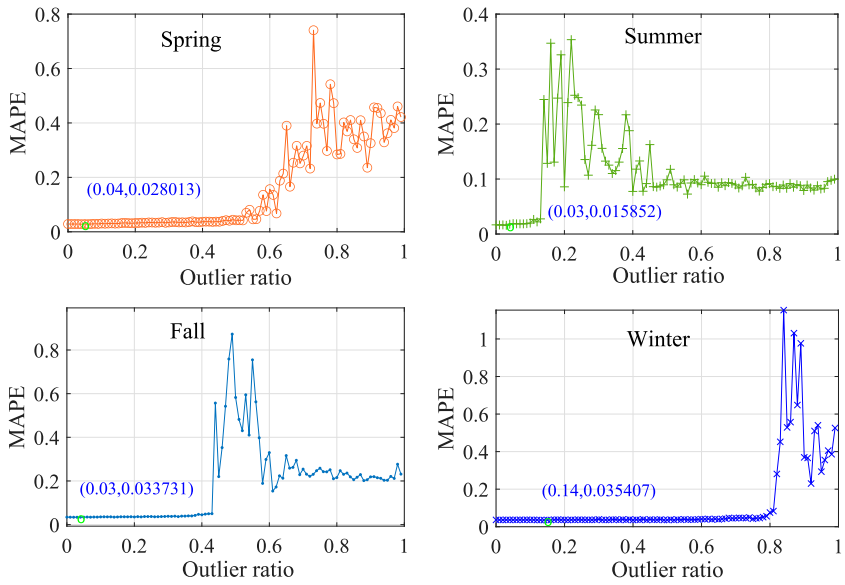

FIGURE 5
The MAPE results of IF in different outlier ratios.

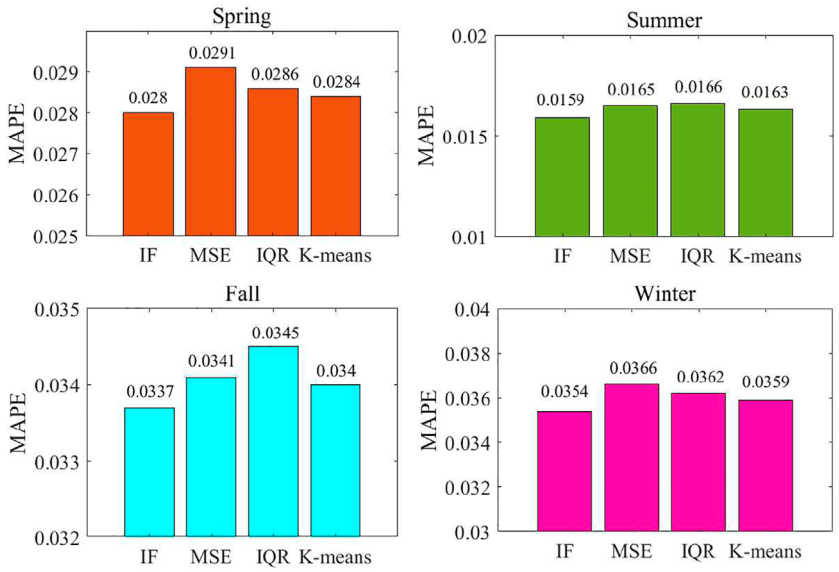

FIGURE 6
The MAPE results for different outlier detection methods.

where p and q are a scaling variable and a translation variable, respectively. $g(t)$ denotes the signal decomposed by the wavelet. Daubechies function is used as the mother wavelet function $\phi(\cdot)$ in this paper.

After the prediction error sequence is decomposed by WT, the KNN algorithm is designed to quickly extract forecast error features of different frequencies due to the ability to solve fast predictions. Each frequency error prediction based on KNN can be divided into three steps: *1*) Euclidean distance is used to measure the similarity of all features in the validation and test dataset in the forecasting error sequence for each frequency; *2*) Choose the k value based on the prediction error of the validation

TABLE 1 Statistical results of daily MAPE result for the effect of ECM in various seasons.

Season	Methods	Min	Max	Average	Variance (E)
Spring	ECM	0.0172	0.0414	0.0280	7.63–5
	Without ECM	0.0172	0.0512	0.0304	1.39–4
Summer	ECM	0.0070	0.0317	0.0158	9.54–5
	Without ECM	0.0070	0.0364	0.0189	1.24–4
Fall	ECM	0.0231	0.0546	0.0337	1.57–4
	Without ECM	0.0212	0.0555	0.0354	1.84–4
Winter	ECM	0.0200	0.0766	0.0354	4.32–4
	Without ECM	0.0202	0.0844	0.0370	5.36–4

dataset; *3*) A moving average value is performed by combining the k-nearest Euclidean distance values of the training and test sets.

3.4 Data normalization and performance criterion

In the feature learning process, due to the different dimensions of the collected data, the non-standardized features may affect the parameter optimization of the model. Therefore, data normalization is required to be performed out on these features, as follows,

$$\hat{x}_t = \frac{x_t - x_{min}}{x_{max} - x_{min}} \tag{5}$$

where x_t is the original PV power data, and $x_{\max}$ and $x_{\min}$ are the maximum and minimum values of the PV power data.

Three metrics, including mean absolute percentage error (MAPE), mean absolute error (MAE), and root mean square error (RMSE), are typically employed to evaluate the performance of forecasting models (Wang et al., 2017), as follows,

$$\mathrm{MAE} = \frac{1}{T}\sum_{t\in T}|r_t - p_t| \tag{6}$$

$$\mathrm{RMSE} = \sqrt{\frac{1}{T}\sum_{t\in T}(r_t - p_t)^2} \tag{7}$$

$$\mathrm{MAPE} = \frac{1}{T}\sum_{t\in T}\frac{|r_t - p_t|}{r_t} \times 100\% \tag{8}$$

wherein T is the number of the predicted value, r_t is the real value at the moment of t, and p_t is the predicted value at the moment of t. It is worth noting that the forecasting model has higher accuracy when MAE, RMSE, and MAPE are smaller.

3.5 Main prediction steps of the proposed hybrid model

Due to the chaotic nature of the weather system, PV power data always exhibits volatility, variability and randomness. These characteristics will affect the prediction accuracy of PV power, which is greatly detrimental to the economic optimization and stable operation of the modern power system. Therefore, in order to mitigate the impact of these characteristics on prediction accuracy, this paper presents a new hybrid model for ultra-short-term PV power forecasting consisting of a feature engineering module, a deep learning-based point prediction module, and an error correction module. The main steps of the proposed hybrid model are presented as follows: *1*) Historical PV power data are collected and divided into training datasets, validation datasets and test datasets according to different seasons. *2*) IF method are applied to detect outliers in training and testing datasets. Then, these outliers are removed from the corresponding datasets, and these vacancies are filled by applying linear interpolation. *3*) Convert all data to values between 0 and 1 using the data normalization method. *4*) The loss function of NPCNN is constructed, and the model parameters are trained using the training dataset and the RMSProp back-propagation method. *5*) The NPCNN error results of the validation set are sent to the error correction module, and these errors are decomposed into high and low frequency signals through wavelet transform, while the error trend of each signal is quickly learned using KNN. *6*) The error correction prediction results are obtained by wavelet reconstruction, and its results are combined with the prediction results of the NPCNN model to obtain the final PV power prediction data. *7*) Calculate the prediction metrics of the proposed hybrid model using the prediction results from the test datasets. The main steps of the proposed hybrid model for PV power forecasting are graphically presented in **Figure 1**.

4 Numerical results and analysis

4.1 Experimental settings

The proposed PV power prediction model based on IF, NPCNN and ECM is evaluated using historical PV power data from Limburg, Belgium. This data range from June 2019 to May 2021 at a resolution of 15 min, and can be freely obtained from the website (Elia, 2021). The PV power data is divided into a training dataset, a validation dataset, and a testing dataset, and each dataset corresponds to four parts: spring, summer, fall and winter, because the solar irradiance and the physical information of PV cell power generation vary greatly in different seasons (Wang et al., 2020a). For these data sets, the monitored capacity

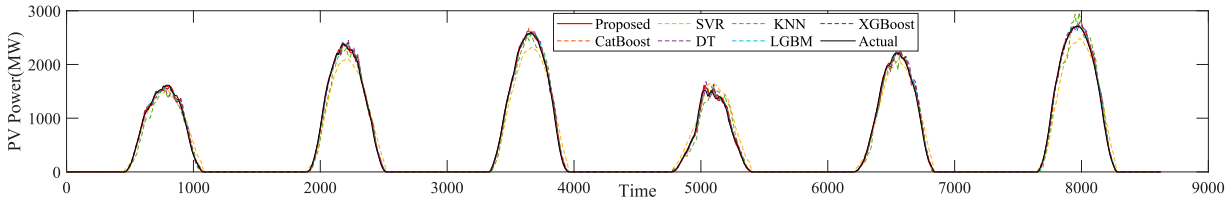

FIGURE 7
15-minutes-ahead forecasting results in spring.

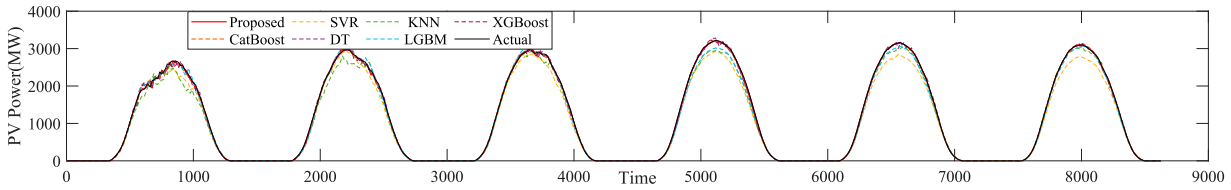

FIGURE 8
15-minutes-ahead forecasting results in summer.

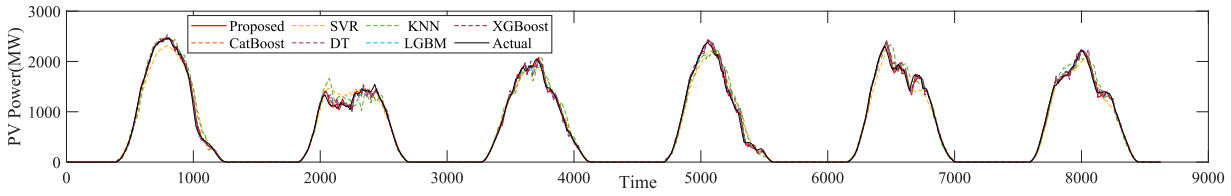

FIGURE 9
15-minutes-ahead forecasting results in fall.

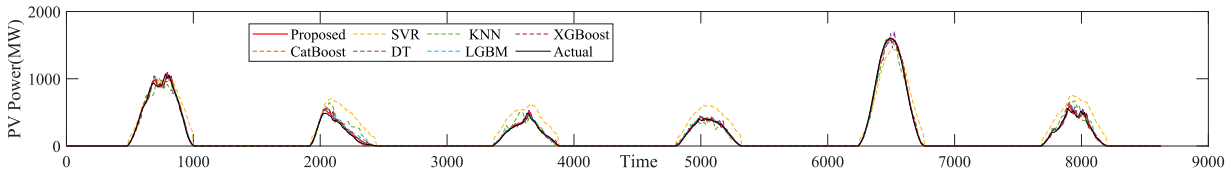

FIGURE 10
15-minutes-ahead forecasting results in winter.

is 4037.14 MW, and the minimum output power is 0 MW. The NPCNN forecasting model using the training dataset is well-trained to extract the nonlinear features, and the error correction model using the validation dataset is well-trained to reduce the forecasting error between predicted and actual PV power data. The testing dataset is adopted to evaluate the forecasting performance of the PV power prediction model. In addition, CatBoost (Prokhorenkova et al., 2018), KNN (Peterson, 2009), DT (Massucco et al., 2019), SVR (De Giorgi et al., 2016), XGBoost (Zheng et al., 2017), and LGBM (Wang Y et al., 2020) are used as the benchmark methods, which are simulated on the Python platform.

TABLE 2 The seasonal 15-min ahead forecasting results for various contrast models.

Season	Error	Proposed	CatBoost	SVR	DT	KNN	LGBM	XGBoost
Spring	MAE	11.54	20.24	70.28	21.40	45.85	19.12	19.17
	RMSE	23.69	40.52	125.37	44.86	87.12	37.29	38.26
	MAPE	0.0280	0.0446	0.2533	0.0559	0.0818	0.0449	0.0427
Summer	MAE	9.82	17.55	93.46	22.29	61.75	44.04	18.47
	RMSE	22.99	31.73	146.36	39.39	110.14	72.72	33.37
	MAPE	0.0158	0.0256	0.0659	0.0343	0.0537	0.0369	0.0340
Fall	MAE	21.74	25.99	58.18	32.99	59.31	25.58	25.43
	RMSE	42.01	50.62	102.82	60.70	108.09	49.27	49.39
	MAPE	0.0337	0.0364	0.1009	0.0502	0.0767	0.0369	0.0365
Winter	MAE	7.33	9.13	58.82	11.66	52.67	9.89	8.94
	RMSE	17.65	21.07	109.67	27.79	79.67	22.53	20.51
	MAPE	0.0351	0.0417	0.594	0.0566	0.1056	0.0552	0.0477
Average	MAE	12.61	18.23	70.19	22.09	54.90	24.66	18.00
	RMSE	26.59	35.99	121.06	43.19	96.26	45.45	35.38
	MAPE	0.028	0.037	0.254	0.049	0.079	0.043	0.040

4.2 IF based outlier detection

In order to verify the feasibility and effectiveness of IF based anomaly detection in feature engineering module, we evaluate the impact of IF on the forecasting performance of the proposed model. IF based outlier detection method is executed and analyzed using the testing dataset of 15-min ahead forecasting scenario. Three comparison algorithms, namely mean square error method (MSE), the interquartile range method (IQR), and K-means clustering method (K-means), are considered to verify the validity of outlier detection based on IF. For a fair comparison, other prediction procedures are consistent with the proposed model except for the IF based outlier detection method. The 15-min-ahead MAPE results of IF based anomaly detection method under different outlier ratios are shown in Figure 5. The mark points on the line in Figure 5 indicate the minimum values in the MAPE results with various outlier ratios in different seasons. It can be seen from Figure 5 that the optimal predicted performance in the four different seasons corresponds to the optimal anomaly ratios at 0.04, 0.03, 0.03, and 0.14, respectively. The optimal anomaly ratios in four seasons are all greater than 0, which means that IF is effective for improving forecast accuracy in different seasons. In addition, the outlier ratio corresponding to the smallest MAPE values in summer and autumn is smaller than in spring and winter. This is because the fluctuation of solar irradiance in summer and autumn is stronger than that in winter and spring, the original features during model training need to be preserved to reduce underfitting.

In Figure 6, we present the MAPE statistical results of different outlier detection methods in different seasons. For IF method, the MAPE values in the four seasons are 0.028, 0.0159, 0.0337, and 0.0354, respectively, with an average of 0.0452. Compared with the MSE, IQR, and K-means methods,

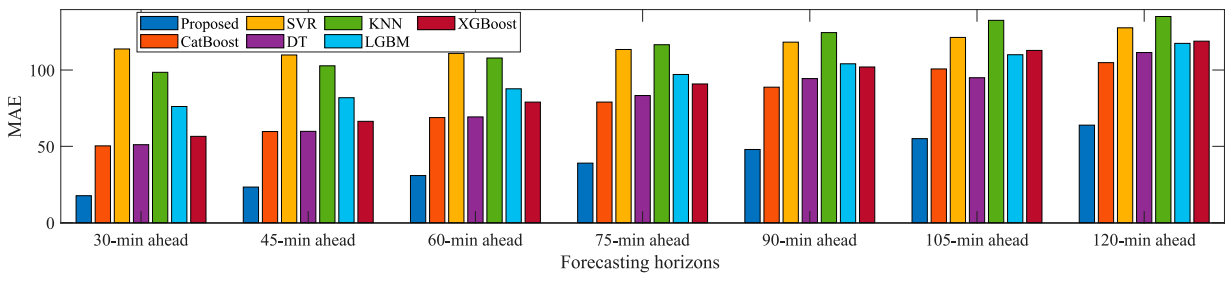

FIGURE 11
The MAE statistics for different forecasting horizons in summer.

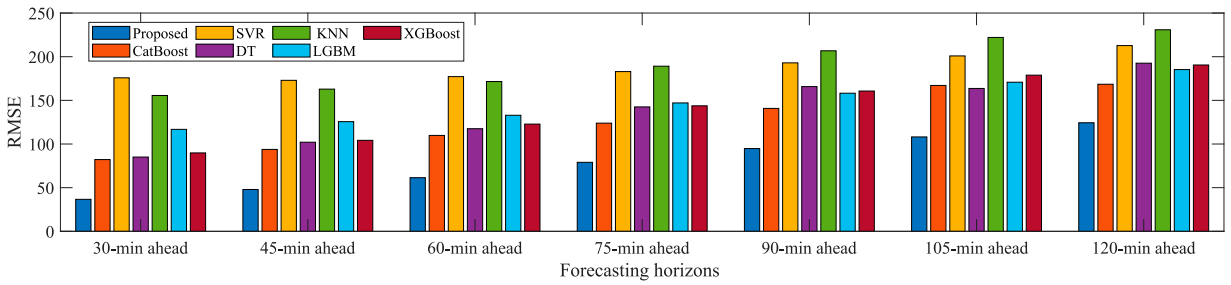

FIGURE 12
The RMSE statistics for different forecasting horizons in summer.

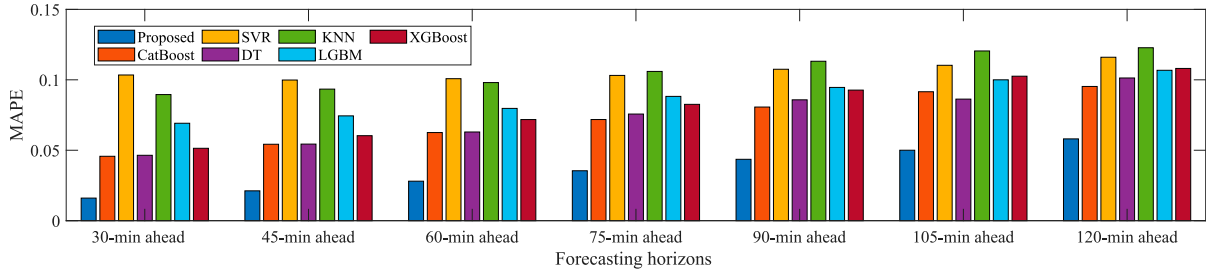

FIGURE 13
The MAPE statistics for different forecasting horizons in summer.

the average MAPE results of IF are reduced by 2.84, 2.50, and 1.40%, respectively. From these results, IF method exhibits high forecasting capability in different seasons compared with the three benchmarks. This is because IF without making any prior assumptions can efficiently process high-dimensional continuous data.

4.3 ECM based post-prediction correction

To further illustrate the advantages of ECM, we evaluate the impact of ECM-based prediction post-correction on forecasting performance. The proposed model with/without ECM is also executed and analyzed using the testing dataset of 15-min ahead forecasting scenario. The MAPE results in different seasons are statistically presented in **Table 1**. It can be seen that the MAPE results of the proposed model with ECM in spring vary from a minimum value of 0.0172 to a maximum of 0.0414 with an average of 0.0280 and a variance of 7.63E−5. While, the MAPE results of the proposed model without ECM in spring vary from a minimum value of 0.0172 to a maximum of 0.0512 with an average of 0.0304 and a variance of 1.39E−4. Compared to the benchmark method without ECM, the mean and variance of the MAPE results for the proposed model in spring have been reduced by 8.5 and 81.6%, respectively. Similarly, compared with the benchmark method without ECM, the mean of the MAPE results for the proposed model in the other three seasons have been reduced by 19.2, 5.0, and 4.6%, respectively. The variance of the MAPE results for the proposed model in the other three seasons have been reduced by 30.2, 9.2, and 24.0%, respectively. Apparently, these statistical results demonstrate that the proposed model with ECM in various seasons shows better forecasting performance and more stability.

4.4 15-minutes ahead prediction performance

Then, the 15-min ahead forecast results for different seasons are graphically displayed to demonstrate the forecasting capability of the proposed model. To comprehensively test the forecasting performance of the proposed model based on IF, NPCNN and ECM, CatBoost, SVR, DT, KNN, LGBM and XGBoost are selected as benchmark methods for performance comparison. **Figures 7–10** shows the forecasting results of the six benchmarks and the proposed model in different seasons. In **Figures 7–10**, the predicted power of the proposed model and actual power curves are red and black lines, respectively, and the predicted power curves of other benchmarks are dashed

lines. It can be seen that the power curves have obvious seasonal variation, which is mainly caused by ambient air temperature and solar radiation. Figure 8 has a higher PV power, and the curve will be relatively smoother compared with Figure 10. Likewise, the PV power curves in Figure 7 and Figure 9 also show better characteristics than those in Figure 10 (Winter). From Figures 7–10, the proposed model has strong prediction capabilities and outperforms other benchmarks, and its predicted value is basically consistent with actual PV power. Furthermore, CatBoost, LGBM, and XGBoost perform better than SVR, DT, and KNN models because the ensemble learning network is easier to handle nonlinear relationships than commonly-used shallow learning models.

Table 2 shows the MAE, RMSE, and MAPE metrics in 15-min ahead. It can be seen from Table 2 that the MAPE value of the proposed model varies from 0.0158 to 0.0337, with an average of 0.0282. While the average MAPE values of other six benchmarks are 0.0371, 0.2535, 0.0493, 0.0794, 0.0435, and 0.0402, respectively. Compared with CatBoost, SVR, DT, KNN, LGBM, and XGBoost, the average MAPE value of the proposed model is decreased by 0.009, 0.226, 0.021, 0.051, 0.015, and 0.012, respectively. Similarly, compared with CatBoost, SVR, DT, KNN, LGBM, and XGBoost, the average MAE value of the proposed model is reduced by 5.62, 57.58, 9.48, 42.29, 12.05, and 5.39, respectively. And compared with CatBoost, SVR, DT, KNN, LGBM, and XGBoost, the average RMSE value of the proposed model is reduced by 9.40, 94.47, 16.60, 69.67, 18.86, and 8.79, respectively. Apparently, these results show that the results of the proposed model perform best in terms of the MAPE, MAE, and RMSE, followed by XGBoost, CatBoost, LGBM, DT, KNN, and SVR. This means that the predicted value of the proposed model is closer to the actual value than other comparative models. The reason may be that the proposed model, apart from outlier detection and error correction methods, uses NPCNN to identify changing trends and non-linear relationship of PV data. The poor performance of the SVR model is mainly caused by the abnormal distribution of the kernel and worsened by the low feature extraction ability. Therefore, we can conclude from these analysis results that the proposed model has the best forecasting performance on 15-min ahead forecasting tasks in different seasons.

4.5 Multi-step ahead prediction performance

Furthermore, to fully verify the comprehensive prediction performance of the proposed model, simulation experiments are performed under different forecasting horizons in summer. The forecasting horizons range from 30 min ahead to 2 h ahead with 15-min intervals. The training/validation/test dataset in each forecasting horizons is acquired by time interval sampling of the original PV power data series. The average MAE, RMSE, and MAPE results over different forecasting horizons in summer are presented in Figures 11–13, respectively. It can be seen that the MAE, RMSE and MAPE indexes of the proposed model usually increase with the longer prediction horizon. This is because the lower feature correlation reduced by the longer forecasting horizon will increase the uncertainty of PV power forecasting. Obviously, at all prediction horizons, the proposed model has the smallest MAE, RMSE, and MAPE metrics, which outperforms other benchmarks and can provide excellent forecasting performance. From these results, the proposed model has more stable and robust performance compared to the benchmark methods. It is appropriate to conclude that the proposed hybrid model exhibits good generalization properties for PV power forecasting.

5 Conclusion

In this paper, a new hybrid model based on a feature engineering module, a point prediction module, and an error correction module is firstly proposed for the ultra-short-term PV power forecasting. In the proposed model, IF is used to detect outliers for PV power data, NPCNN is used to extract the nonlinear features of processed PV power data, and WT+KNN is used to reduce the model variance. The proposed hybrid model has been verified on actual PV power data from the PV plant in Limberg. It has been demonstrated in the case studies that the IF-based anomaly detection and ECM-based post-prediction correction methods are significantly helpful in practical PV power forecasting. Moreover, the proposed hybrid model has been compared with six benchmark methods based on CatBoost, KNN, DT, SVR, XGBoost, and LGBM in different seasons and forecasting horizons. Experimental results have also proved that the proposed model has a more stable and excellent performance than the benchmark methods. Therefore, the proposed hybrid model for PV power forecasting has a high potential for future application in electric energy systems.

Data availability statement

The original contributions presented in the study are included in the article/Supplementary Material, further inquiries can be directed to the corresponding author.

Author contributions

Conceptualization, RZ, GL, and SB; methodology and formal analysis, RZ and GL; software, simulation and validation, RZ; writing–original draft preparation, RZ, GL, and WH;

writing–review and editing, GK, WH, YZ, SA, and SB; visualization, GL and SB; funding acquisition, GL, GK, WH, YZ, and SB. All authors have read and agreed to the published version of the manuscript.

Funding

This work was supported in part by the Scientific Research Startup Fund for Shenzhen High-Caliber Personnel of SZPT, No.6021310030K, in part by the National Science Foundation of China under Grants 61973177, in part by the Natural Science Foundation of Henan Province of China under Grant 212102210516 and 222102210279, and in part by the Natural Science Foundation of Hunan Province under Grant 2021JJ50082.

Conflict of interest

The authors declare that the research was conducted in the absence of any commercial or financial relationships that could be construed as a potential conflict of interest.

Publisher's note

References

Ahmed, S., Lee, Y., Hyun, S.-H., and Koo, I. (2019). Unsupervised machine learning-based detection of covert data integrity assault in smart grid networks utilizing isolation forest. *IEEE Trans. Inform. Forensic Secur.* 14, 2765–2777. doi:10.1109/tifs.2019.2902822

Alaraj, M., Kumar, A., Alsaidan, I., Rizwan, M., and Jamil, M. (2021). Energy production forecasting from solar photovoltaic plants based on meteorological parameters for qassim region, Saudi Arabia. *IEEE Access* 9, 83241–83251. doi:10.1109/ACCESS.2021.3087345

Al-Dahidi, S., Ayadi, O., Adeeb, J., and Louzazni, M. (2019). Assessment of artificial neural networks learning algorithms and training datasets for solar photovoltaic power production prediction. *Front. Energy Res.* 7, 130. doi:10.3389/fenrg.2019.00130

Bai, X., Wang, X., Liu, X., Liu, Q., Song, J., Sebe, N., et al. (2021). Explainable deep learning for efficient and robust pattern recognition: a survey of recent developments. *Pattern Recognit.* 120, 108102. doi:10.1016/j.patcog.2021.108102

Bouzgou, H., and Gueymard, C. A. (2017). Minimum redundancy - maximum relevance with extreme learning machines for global solar radiation forecasting: toward an optimized dimensionality reduction for solar time series. *Sol. Energy* 158, 595–609. doi:10.1016/j.solener.2017.10.035

Bu, S., Wen, J., and Li, F. (2019). A generic framework for analytical probabilistic assessment of frequency stability in modern power system operational planning. *IEEE Trans. Power Syst.* 34, 3973–3976. doi:10.1109/TPWRS.2019.2924149

Chakraborty, T., Chattopadhyay, S., and Ghosh, I. (2019). Forecasting dengue epidemics using a hybrid methodology. *Phys. A Stat. Mech. Appl.* 527, 121266. doi:10.1016/j.physa.2019.121266

Chang, G. W., and Lu, H.-J. (2018). Integrating gray data preprocessor and deep belief network for day-ahead pv power output forecast. *IEEE Trans. Sustain. Energy* 11, 185–194. doi:10.1109/TSTE.2018.2888548

Chang, T. J., Kavvas, M. L., and Delleur, J. W. (1984). Modeling of sequences of wet and dry days by binary discrete autoregressive moving average processes. *J. Clim. Appl. Meteor.* 23, 1367–1378. doi:10.1175/1520-0450(1984)023<1367:mosowa>2.0.co;2

Chen, H., Zhang, J., Tao, Y., and Tan, F. (2019). Asymmetric garch type models for asymmetric volatility characteristics analysis and wind power forecasting. *Prot. Control Mod. Power Syst.* 4, 1–11. doi:10.1186/s41601-019-0146-0

Cleveland, W. S., and Devlin, S. J. (1988). Locally weighted regression: an approach to regression analysis by local fitting. *J. Am. Stat. Assoc.* 83, 596–610. doi:10.1080/01621459.1988.10478639

De Giorgi, M. G., Malvoni, M., and Congedo, P. M. (2016). Comparison of strategies for multi-step ahead photovoltaic power forecasting models based on hybrid group method of data handling networks and least square support vector machine. *Energy* 107, 360–373. doi:10.1016/j.energy.2016.04.020

de Mattos Neto, P. S. G., de Oliveira, J. F. L., de Oliveira Santos Junior, D. S., Siqueira, H. V., Da Nobrega Marinho, M. H., and Madeiro, F. (2020). A hybrid nonlinear combination system for monthly wind speed forecasting. *IEEE Access* 8, 191365–191377. doi:10.1109/access.2020.3032070

de Oliveira, J. F., Silva, E. G., and de Mattos Neto, P. S. (2021). A hybrid system based on dynamic selection for time series forecasting. *IEEE Trans. Neural Netw. Learn. Syst.* 1–13. doi:10.1109/TNNLS.2021.3051384

Desai, J., and Makwana, V. (2021). A novel out of step relaying algorithm based on wavelet transform and a deep learning machine model. *Prot. Control Mod. Power Syst.* 6, 1–12. doi:10.1186/s41601-021-00221-y

Elia (2021). Solar power generation. [Dataset]. Available at: https://www.elia.be/en/grid-data/power-generation/solar-pv-power-generation-data (Accessed December 31, 2021).

Geman, S., Bienenstock, E., and Doursat, R. (1992). Neural networks and the bias/variance dilemma. *Neural Comput.* 4, 1–58. doi:10.1162/neco.1992.4.1.1

Hajirahimi, Z., and Khashei, M. (2019a). Hybrid structures in time series modeling and forecasting: a review. *Eng. Appl. Artif. Intell.* 86, 83–106. doi:10.1016/j.engappai.2019.08.018

Hajirahimi, Z., and Khashei, M. (2019b). Weighted sequential hybrid approaches for time series forecasting. *Phys. A Stat. Mech. Appl.* 531, 121717. doi:10.1016/j.physa.2019.121717

Inman, R. H., Pedro, H. T. C., and Coimbra, C. F. M. (2013). Solar forecasting methods for renewable energy integration. *Prog. Energy Combust. Sci.* 39, 535–576. doi:10.1016/j.pecs.2013.06.002

Katris, C., and Daskalaki, S. (2015). Comparing forecasting approaches for internet traffic. *Expert Syst. Appl.* 42, 8172–8183. doi:10.1016/j.eswa.2015.06.029

Kumar, M., and Thenmozhi, M. (2006). "Forecasting stock index movement: A comparison of support vector machines and random forest," in Indian Institute of Capital Markets 9th Capital Markets Conference Paper.

Kumar, A., Rizwan, M., and Nangia, U. (2019). A hybrid intelligent approach for solar photovoltaic power forecasting: impact of aerosol data. *Arab. J. Sci. Eng.* 45, 1715–1732. doi:10.1007/s13369-019-04183-0

Kuremoto, T., Kimura, S., Kobayashi, K., and Obayashi, M. (2014). Time series forecasting using a deep belief network with restricted Boltzmann machines. *Neurocomputing* 137, 47–56. doi:10.1016/j.neucom.2013.03.047

Li, G., Wang, H., Zhang, S., Xin, J., and Liu, H. (2019). Recurrent neural networks based photovoltaic power forecasting approach. *Energies* 12, 2538. doi:10.3390/en12132538

Li, X., Ma, L., Chen, P., Xu, H., Xing, Q., Yan, J., et al. (2022). Probabilistic solar irradiance forecasting based on xgboost. *Energy Rep.* 8, 1087–1095. doi:10.1016/j.egyr.2022.02.251

Liu, F. T., Ting, K. M., and Zhou, Z.-H. (2008). "Isolation forest," in 2008 Eighth IEEE International Conference on Data Mining, Pisa, Italy, December 15–19, 2008. (IEEE), 413–422. doi:10.1109/icdm.2008.17

Liu, B., Chen, J., Wang, H., and Wang, Q. (2020a). Renewable energy and material supply risks: a predictive analysis based on an lstm model. *Front. Energy Res.* 8, 163. doi:10.3389/fenrg.2020.00163

Liu, S., Ji, H., and Wang, M. C. (2020b). Nonpooling convolutional neural network forecasting for seasonal time series with trends. *IEEE Trans. Neural Netw. Learn. Syst.* 31, 2879–2888. doi:10.1109/TNNLS.2019.2934110

Madhiarasan, M. (2020). Accurate prediction of different forecast horizons wind speed using a recursive radial basis function neural network. *Prot. Control Mod. Power Syst.* 5, 1–9. doi:10.1186/s41601-020-00166-8

Massucco, S., Mosaico, G., Saviozzi, M., and Silvestro, F. (2019). A hybrid technique for day-ahead pv generation forecasting using clear-sky models or ensemble of artificial neural networks according to a decision tree approach. *Energies* 12, 1298. doi:10.3390/en12071298

Mayer, M. J., and Gróf, G. (2021). Extensive comparison of physical models for photovoltaic power forecasting. *Appl. Energy* 283, 116239. doi:10.1016/j.apenergy.2020.116239

Mellit, A., Sağlam, S., and Kalogirou, S. A. (2013). Artificial neural network-based model for estimating the produced power of a photovoltaic module. *Renew. Energy* 60, 71–78. doi:10.1016/j.renene.2013.04.011

Nguyen, B. N., Nguyen, V. T., Duong, M. Q., Le, K. H., Nguyen, H. H., and Doan, A. T. (2020). Propose a mppt algorithm based on thevenin equivalent circuit for improving photovoltaic system operation. *Front. Energy Res.* 8, 14. doi:10.3389/fenrg.2020.00014

Perez, R., Kivalov, S., Schlemmer, J., Hemker, K., Renné, D., and Hoff, T. E. (2010). Validation of short and medium term operational solar radiation forecasts in the US. *Sol. Energy* 84, 2161–2172. doi:10.1016/j.solener.2010.08.014

Peterson, L. (2009). K-nearest neighbor. *Scholarpedia* 4, 1883. doi:10.4249/scholarpedia.1883

Pillow, J. W., Shlens, J., Paninski, L., Sher, A., Litke, A. M., Chichilnisky, E. J., et al. (2008). Spatio-temporal correlations and visual signalling in a complete neuronal population. *Nature* 454, 995–999. doi:10.1038/nature07140

Prokhorenkova, L. O., Gusev, G., Vorobev, A., Dorogush, A. V., and Gulin, A. (2018). "Catboost: unbiased boosting with categorical features," in Advances in Neural Information Processing Systems, NeurIPS 2018, Montréal, Canada, December 3-8, 2018, 6639–6649.

Saâdaoui, F., and Rabbouch, H. (2019). A wavelet-based hybrid neural network for short-term electricity prices forecasting. *Artif. Intell. Rev.* 52, 649–669. doi:10.1007/s10462-019-09702-x

Singla, P., Duhan, M., and Saroha, S. (2021). A comprehensive review and analysis of solar forecasting techniques. *Front. Energy* 16, 1–37. doi:10.1007/s11708-021-0722-7

Soares, J., Borges, N., Fotouhi Ghazvini, M. A., Vale, Z., and de Moura Oliveira, P. B. (2016). Scenario generation for electric vehicles' uncertain behavior in a smart city environment. *Energy* 111, 664–675. doi:10.1016/j.energy.2016.06.011

Wang, H., Yi, H., Peng, J., Wang, G., Liu, Y., Jiang, H., et al. (2017). Deterministic and probabilistic forecasting of photovoltaic power based on deep convolutional neural network. *Energy Convers. Manag.* 153, 409–422. doi:10.1016/j.enconman.2017.10.008

Wang, H., Cai, R., Zhou, B., Aziz, S., Qin, B., Voropai, N., et al. (2020a). Solar irradiance forecasting based on direct explainable neural network. *Energy Convers. Manag.* 226, 113487. doi:10.1016/j.enconman.2020.113487

Wang, H., Liu, Y., Zhou, B., Li, C., Cao, G., Voropai, N., et al. (2020b). Taxonomy research of artificial intelligence for deterministic solar power forecasting. *Energy Convers. Manag.* 214, 112909. doi:10.1016/j.enconman.2020.112909

Wang Y, Y., Chen, J., Chen, X., Zeng, X., Kong, Y., Sun, S., et al. (2020). Short-term load forecasting for industrial customers based on tcn-lightgbm. *IEEE Trans. Power Syst.* 36, 1984–1997. doi:10.1109/TPWRS.2020.3028133

Wu, L., and Shahidehpour, M. (2010). A hybrid model for day-ahead price forecasting. *IEEE Trans. Power Syst.* 25, 1519–1530. doi:10.1109/tpwrs.2009.2039948

Wu, Y.-K., Chen, C.-R., and Abdul Rahman, H. (2014). A novel hybrid model for short-term forecasting in pv power generation. *Int. J. Photoenergy* 2014, 569249. doi:10.1155/2014/569249

Xie, H., Qin, Z., Li, G. Y., and Juang, B.-H. (2021). Deep learning enabled semantic communication systems. *IEEE Trans. Signal Process.* 69, 2663–2675. doi:10.1109/tsp.2021.3071210

Yamashita, R., Nishio, M., Do, R. K. G., and Togashi, K. (2018). Convolutional neural networks: an overview and application in radiology. *Insights Imaging* 9, 611–629. doi:10.1007/s13244-018-0639-9

Zhang, R., Li, G., and Ma, Z. (2020). A deep learning based hybrid framework for day-ahead electricity price forecasting. *IEEE Access* 8, 143423–143436. doi:10.1109/access.2020.3014241

Zhang, R., Aziz, S., Farooq, M. U., Hasan, K. N., Mohammed, N., Ahmad, S., et al. (2021). A wind energy supplier bidding strategy using combined ega-inspired hpsoifa optimizer and deep learning predictor. *Energies* 14, 3059. doi:10.3390/en14113059

Zheng, H., Yuan, J., and Chen, L. (2017). Short-term load forecasting using EMD-LSTM neural networks with a xgboost algorithm for feature importance evaluation. *Energies* 10, 1168. doi:10.3390/en10081168

frontiers | Frontiers in Energy Research

TYPE Original Research
PUBLISHED 11 August 2022
DOI 10.3389/fenrg.2022.962524

OPEN ACCESS

EDITED BY
Siqi Bu,
Hong Kong Polytechnic University,
Hong Kong SAR, China

REVIEWED BY
Jianwu Zeng,
Minnesota State University,
United States
Dong Chen,
Scottish and Southern Energy,
United Kingdom

*CORRESPONDENCE
Connor Duggan,
cduggan11@qub.ac.uk
Xueqin Amy Liu,
x.liu@qub.ac.uk

SPECIALTY SECTION
This article was submitted to Smart Grids,
a section of the journal
Frontiers in Energy Research

RECEIVED 06 June 2022
ACCEPTED 04 July 2022
PUBLISHED 11 August 2022

CITATION
Duggan C, Liu XA, Best R, Brogan P and Morrow J (2022), Active power control from wind farms for damping very low-frequency oscillations.
Front. Energy Res. 10:962524.
doi: 10.3389/fenrg.2022.962524

Active power control from wind farms for damping very low-frequency oscillations

Connor Duggan*, Xueqin Amy Liu*, Robert Best, Paul Brogan and John Morrow

School of Electronics, Electrical Engineering and Computer Science, Queen's University Belfast, Belfast, United Kingdom

Timely remote activation of frequency response, provided by converter-based generation, can improve the damping of very low-frequency (VLF) oscillations. The research presented is based on both power system models and actual data from phasor measurement units (PMU) on the Irish power system. The performance of active power control (APC) is investigated, and variations in wind speed, droop, time lag and resource capacity demonstrate their effectiveness at damping wide-spectrum VLF modes. PMU data that captures the activation and deactivation of APC at wind farms is presented and analyzed; it demonstrates how APC control effectively dampens VLF modes on the Irish system. These observations are supported by sensitivity analysis carried out a power system model in DIgSILENT PowerFactory. These results demonstrate the improvement in VLF mode stability that APC can provide at wind generation. It is demonstrated that minimal amounts of generation curtailment and modest droop settings are sufficient to see substantial VLF mode damping. Index Terms—Active Power Control, Oscillation damping, Very Low-Frequency Oscillations, PMU.

KEYWORDS

active power control, oscillation damping, very low-frequency oscillations, PMU, wind farm

1 Introduction

The increasing penetration of renewables and displacement of fossil-fuel-based synchronous generation pose challenges to the security of supply, increasing the likelihood and severity of extreme power system events (National Grid, 2019). Converter Interfaced Generation (CIG) has displaced the synchronous inertia and frequency regulation historically provided by governor controlled synchronous generators (Milano et al., 2018). The reduction in inertia and frequency regulation caused by high share of CIG increases the severity of the rate of change of frequency and frequency deviation, following a generation load imbalance. If the rate of change of frequency and frequency deviation exceeds certain parameters, fines may be levied on power system operators, generators, or service providers, as they can result in catastrophic cascade tripping.

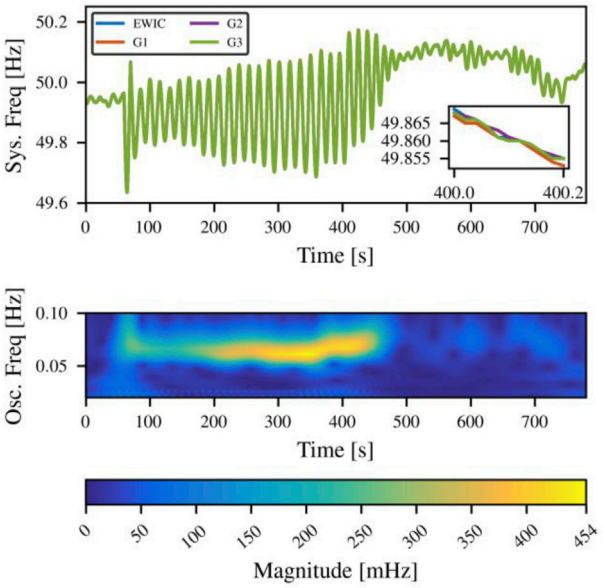

FIGURE 1
(A) 454 mHz VLFO showing system frequency measurements from four PMU locations on Ireland's power grid **(B)** Continuous Wavelet Transfrom (CWT) of system frequency shown in **(A)**.

Another challenge is very low-frequency oscillations (VLFOs), first observed on isolated or low inertia power systems. On these systems, renewable generation displaces synchronous generation, reduces power system inertia, and alters inertia distribution. These oscillations were noted on smaller islanded systems, such as Ireland (Wall et al., 2020), (Wall et al., 2019), before being observed on the much larger, islanded Great Britain power system (Clark et al., 2016) and the geographically large Australian power system (AEMO, 2017). Historically VLFOs have been observed on power systems with a high concentration of hydro generation, such as Colombia (Arango and Sanchez, 2010), where VLFO arose from hydro governor parameters.

VLFO can be a background characteristic in power system frequency, causing limited damage that may be classified as wear and tear. However, in recent years on the Irish power system, VLFO has occasionally, suddenly, and unexpectedly grown to peak-to-peak magnitudes in the region of 450 mHz (Wall et al., 2020) and have persisted for minutes as shown in Figure 1. The sustained oscillations could cause increased probability of equipment failure, degraded power quality and potentially uncontrolled cascading blackout (Wall et al., 2020). These events have threatened system security and required emergency control center intervention to suppress, with associated market costs.

The problem of displacement of governor control systems, coupled with a greater need for more sensitive governor control due to the integration of more stochastic generation, contributes to the increase in the severity and occurrence of VLFOS. Hence, new frequency response services, such as the dynamic frequency regulation in Great Britain (Homan and Brown, 2021), will be required to manage VLFOs. This paper demonstrates the effect of varying performance factors, such as droop, delay, and capacity, on VLFO damping.

VLFOs commonly occur between 0.01-0.1 Hz and are often related to governor frequency dynamics. VLFOs have a lower oscillation frequency when compared to 'low frequency' electromechanical oscillation modes, usually 0.1–2 Hz (Clark et al., 2016). VLFO, in contrast to electromechanical oscillations, are also observed to have similar magnitude and phase across large geographical areas and often entire power systems. This similar mode shape characteristic has been referred to as a coherent mode shape (Xie et al., 2018).

VLFOs are easily detected and monitored with Phasor Measurement Units (PMU) due to the very low frequency and long period; VLFOs are therefore visually evident to control centers with modern monitoring infrastructure. Although the relative changes in phase are small across a network and difficult to interpret visually, it has been demonstrated that variation in voltage phase angle between PMU monitored locations can indicate the source region (Clark et al., 2016).

2 Literature review

Previous mechanism analysis has attributed VLFOs to negatively damped governors (Chen et al., 2017), backlash (De Marco et al., 2018) and time delays (Duggan et al., 2021) within governor control systems. Several mitigation measures have been proposed to increase the damping of the VLFOs. Since governor control systems provide the most substantial interaction with the VLF mode, a method has been proposed to optimize governor parameters to increase the damping of the VLF mode in hydro governor control systems (Chen et al., 2018). In Colombia (Arango and Sanchez, 2010), the authors found that the integral component of a PI controller within a hydro based governor was the most prominent participating feature with the VLF mode. Another common approach for VLF damping is using multi-band power system stabilizers tuned with particular attention to VLF mode damping (Grondin et al., 2000). While damping a VLF mode with CIG or another technology may not remove the oscillation source, it reduces the oscillation's severity, buys time, and potentially prevents operational parameters from being infringed or cascade tripping.

In (Xie et al., 2020) the authors proposed a wide area control strategy based on distributed CIG resources to damp VLF and electromechanical modes. (Zhu et al., 2018) analytically derives how battery energy storage systems placed at generator buses can damp a target oscillation mode of choice. (Chen et al., 2017)

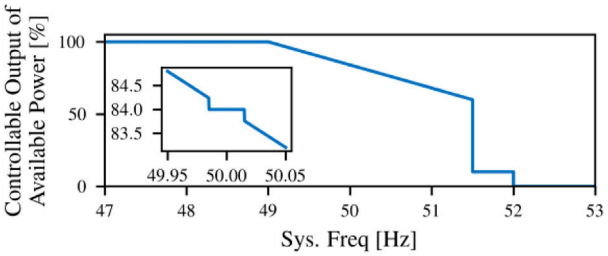

FIGURE 2
Power-Frequency response curve of APC in Ireland with 15 mHz deadband.

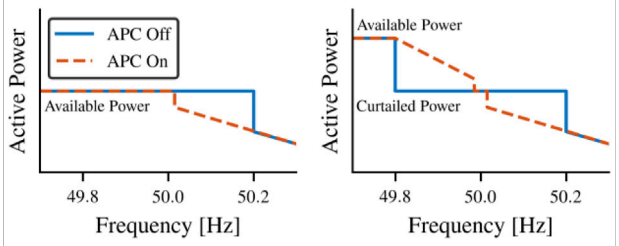

FIGURE 3
Droop curves for APC **(A)** first column shows uncurtailed wind **(B)** second column shows wind when it is curtailed.

outlines an emergency control procedure where the governor frequency response is switched off at governors that provided a salient negative dissipating energy response, calculated through the well-known energy flow theory for oscillation location in power systems (Chen et al., 2013).

Renewable generation such as wind and solar can provide damping of VLFO if power export can be curtailed. (Wilches-Bernal et al., 2016) investigates the small-signal impact that curtailing type-3 wind turbines have on primary frequency response and VLFOs. Many authors (Singh et al., 2015; Lin Zhou et al., 2017; Saadatmand et al., 2021) have studied non-synchronous generation such as wind and solar for damping electromechanical oscillations. (Wilches-Bernal et al., 2016) provides a comprehensive survey using the Western Electricity Coordinating Councils (WECC) model for small-signal stability of electromechanical oscillations. Frequency response from wind farms was investigated in (Ruttledge and Flynn, 2012), (Mele et al., 2020), they outline frequency response on Ireland's power system. A data-based system study using power system metric data and longitudinal power system frequency data found Active Power Control (APC) activation highly correlated with a reduced magnitude in VLFOs (Wall et al., 2020) on the Irish power system. Narrowing the deadband, as shown in Figure 2 from 200 to 15 mHz at the APC controls increases the frequency response interaction at wind farms and subsequently provides power out of phase with the measured bus frequency. APC control actively dissipates oscillation energy and reduces oscillation magnitude (Xie et al., 2020).

This paper is organized as follows: Section 3 presents background on APC control and the WECC models used for dynamic analysis. In Section 4, the performance and effectiveness of APC for damping VLFOs is presented, concerning wind speed, time-lag, droop setting, and amount of APC enabled wind. In Section 5 a case study employing PMU data from Ireland's power system demonstrates the real impact of APC on VLFO magnitude.

The contributions of this paper are based on small-signal and time domain simulations in DIgSILENT PowerFactory, including generalized VLFO events observed in the Irish power system. The contributions of this paper include validation of 1) a comprehensive method for VLFO damping; 2) damping VLF mode amplitude during a recreated frequency oscillation; 3) damping provided by APC at wind sites and the associated reduction in VLF mode magnitude; and sensitivity analysis of APC parameters for VLFO damping.

3 Background

APC is primarily used to provide an additional fast-acting reserve for over-frequency events on Ireland's power system. During an over frequency event, wind farms with an active APC system will ramp down their generation. Dangerous over frequency events occur in Ireland when a trip occurs on a high voltage direct current interconnection while exporting power to Great Britain.

APC can only provide a positive power response during under-frequency events if the CIG operates below its maximum potential power output, as shown in Figure 3. This is available when the system operator has curtailed generation and is an expense to the asset owner, power system operator and ultimately the consumer and the environment. It appears that curtailment is automatically implemented once APC is initiated at wind farms on the Irish power system.

The wind farms that can provide APC in Ireland are divided into six groups of approximately equal capacity (SEMO, 2020). Each of these groups can be turned on and off separately by the control center. Usually, three of the six APC groups are available for activation at any one point in time, spreading the potential impact of lost revenue due to curtailment. The "odd" APC groups (1,3 and 5) can be utilized on odd weeks, and groups (2, four and 6) can be utilized on even weeks. Curtailment for APC control is not constantly in operation but is implemented when the TSO deems it is necessary for system stability.

Figure 4 shows the dynamic response of the Irelands power system following the loss of 460 MW when EWIC was exporting power to Great Britain. This loss of load represented 12% of total

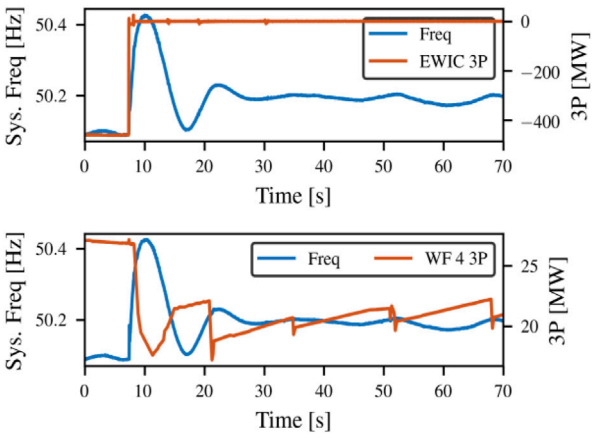

FIGURE 4
High frequency event on the Ireland's power system following the loss -460 MW on the HVDC interconnector **(A)** Presents the loss of 460 MW of load and the resulting frequency deviation **(B)** Presents the dynamics response from a wind farm reducing its power output.

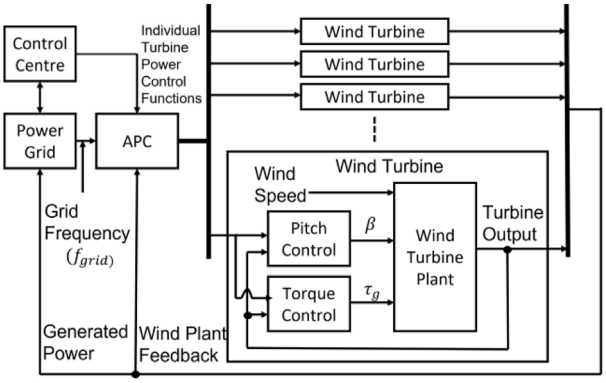

FIGURE 5
Active power control of wind power plants modelling.

system demand, and the high frequency event triggered the APC control at the wind farms in Figure 4B, reducing its output in response to the event.

Shown in Figure 5. is the overall design of the control system for active power control for a wind farm participating in frequency response. The APC control behaves as a single unit and controls the active power production. The APC will default to wind following mode, where the objective is maximum power export, as dictated by wind speed. The control center at the TSO can send power setpoints to the wind farm, remotely reducing power output by a specified fraction below maximum power output. In the simulations in this investigation, a value of 85% of the maximum available generation was employed.

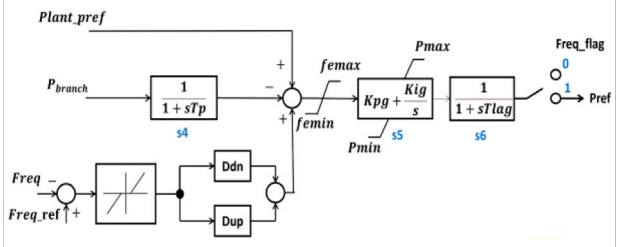

FIGURE 6
APC for plant controller configuration for REPC_A (Ellis et al., 2012)

3.1 Dynamic modelling

3.1.1 System Generation Generic Model representation

The lack of access to comprehensive and generic dynamic models has been a problem when studying power system dynamics and stability from the beginning of renewable power plant development.

In response to a lack of resources, the Western Electricity Coordinating Councils (WECC) developed renewable energy models based on generic models proposed by a renewable energy modelling task force. Since 2010 the WECC has developed models to investigate a wide range of control strategies for wind generation, photovoltaics, and battery energy storage systems. The result was a second-generation generic model presented in 2012 that is well suited to representing a large power park module with multiple components coordinated through the complex remote-controlled plant controller and the provision of frequency response (Ellis et al., 2012).

The modular approach of renewable energy system models, using the second generation WECC model, ensures that individual models for various components are available. They can be combined in different ways to model various renewable energy and non-traditional power sources. The modular structure is represented in Figure 7, and these models consist of three essential components.

1. Renewable Energy Plant Control (REPC)
2. Renewable Energy Eclectic Control (REEC)
3. Renewable Energy Generator/Converter (REGC)

Since this paper is based on sensitivity analysis of active power control systems, this paper will focus on variations of (REPC) components.

3.1.2 REPC_A model for power control at wind farms

The plant controller REPC_A is an essential part of active power control at wind farms as the plant controller allows

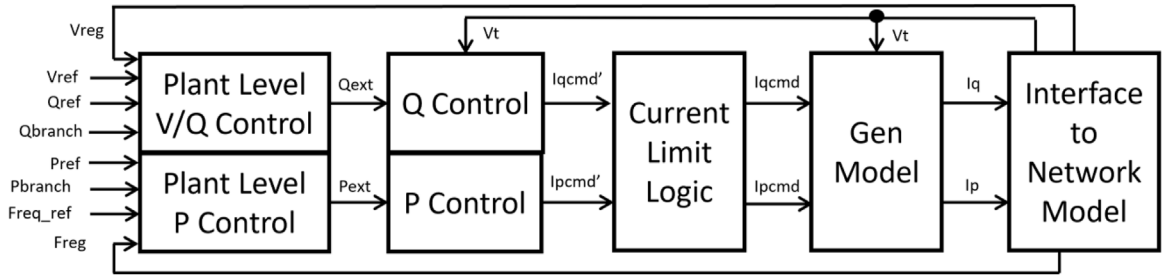

FIGURE 7
Modular representation of System Generation Generic Model.

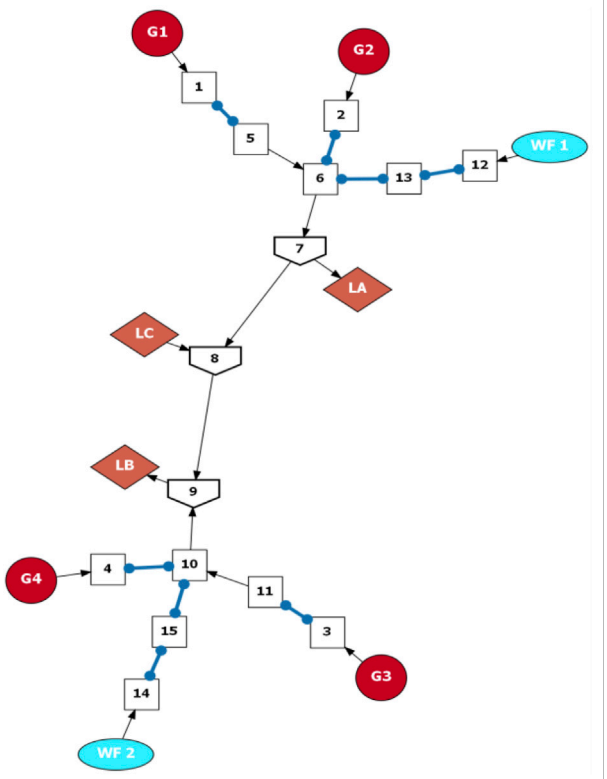

FIGURE 8
Graph Layout of Kundur two Area system. G1, G2 and WF are in area 1. G3 and G4 are in area 2. Blue dotted line signal transformer. Square boxes are transmission buses. Inverse houses are load buses.

frequency control functionality, as shown in Figure 6. The inputs include plant reference for active power set remotely by the TSO and *Pbranch* the measured power output from the wind farm. Likewise, the frequency measurement includes a frequency reference set to nominal frequency and the system frequency measured at the bus terminal of the wind farm. The outputs of this active power control path are then fed into the P control block, shown in Figure 7.

4 Model development and simulations

The Kundur 2-area system (Kundur et al., 1994) shown in Figure 8 is used to conduct sensitivity analysis of APC at a wind farm using a dynamic simulation of VLFOs. Simulations are performed both using the time-domain and small-signal capability within DIgSILENT PowerFactory.

The four synchronous generators are modelled using a detailed sub-transient model with inertia constants of 5 s. All generators are equipped with an IEESGO governor (IEEE standard turbine-governor model), SEXS (Simplified excitation system) automatic voltage regulator and PSS2A (IEEE Dual-Input Stabilizer Model) Power System Stabilizer (Kundur et al., 1994).

The wind farms are composed of type 4, 2 MW wind turbines. The wind farms are added to transmission buses 6 and 15 with APC control functionality. The presence of wind generation is offset by an increase in demand at LA and LB at busses seven and 9. These loads are adjusted to match wind generation resulting from variations in installed capacity and wind speed. When APC is active, power export from the wind farms is reduced to 85% of the available wind resource, allowing similar symmetric droop provision in this study.

A negative load is attached to Bus eight and is used to initiate a generation load imbalance in the time-domain simulations. This negative or positive load is disconnected using the out of service event in DIgSILENT, simulating a generation loss or loss of load after 10 s. This disturbance is sufficient to trigger the VLF mode that is identified in the small-signal analysis.

The simulations are used for sensitivity analysis of the following parameters.

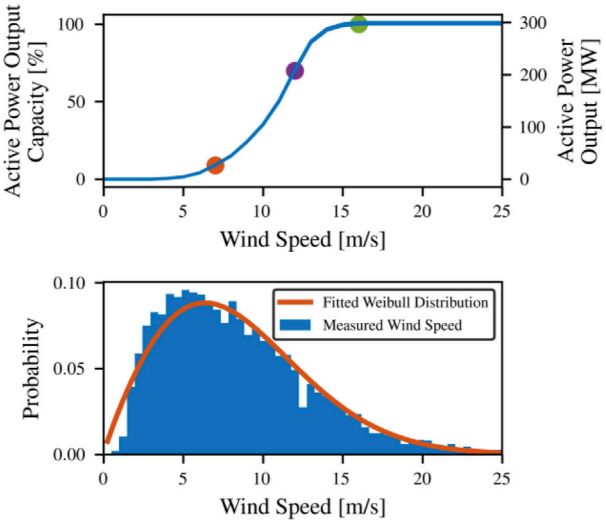

FIGURE 9
(A) Wind Power curve used in study **(B)** Cumulative frequency graph with the average of four wind sites recorded over the calendar year of 2015 with a fitted Weibull distribution.

1. Gain/droop delay time
2. Gain/droop setting
3. wind speed
4. wind farm capacity (number of turbines)

4.1 Wind generation modelling

In this paper, multiple real wind farms are simulated by aggregating them into an individual large wind farm; like the APC control groups employed on the Irish system. Figure 9, shows the power curve used for the wind farm. Three wind speeds of 7 ms-1 (9% of total installed capacity), 12 ms-1 (70%) and 16 ms-1 (100%) are used to simulate the effect different wind speeds have on damping. These speeds are chosen to reflect the damping at low and maximum wind speeds on the real power system, as faced by power system operators.

The wind turbines that are added to the model have a curtailment setpoint of 85% of maximum potential wind power dispatch; therefore, each turbine will dispatch 1.7 MW at full output, reduced from 2MW, it will then provide 300 kW of under frequency response and effectively unconstrained over frequency response. As wind speed drops the under-frequency oscillation response of the turbines will drop to a minimum of 27 kW per turbine, with an output of 153 kW. This change in power response magnitude will contribute to a general improvement in oscillation damping at high wind speeds but can be overcome with increased generation capacity.

TABLE 1 Base case.

Oscillation mode	Damping Ratio [%]	Frequency [Hz]
VLF Mode	−6.70	0.0729
Inter-Area	5.73	0.507
Local I	9.90	1.10
Local II	10.50	1.11

4.2 Small-signal analysis

For small-signal analysis, the deadband on the controllers that provide frequency response was set to zero. A deadband of zero accurately models VLFO damping outside the deadband, as demonstrated in Section 5 with PMU data from wind sites on the Irish power system. At present a deadband of ±15 mHz is employed on the Irish power system (also demonstrated in Section 5), which is sufficiently small to be relatively well approximated by a deadband of zero, especially when dealing with high amplitude VLFO. It is argued that operators should minimize deadbands for VLFO damping based on the simulation work in this section and the PMU data.

Three different scenarios are examined to determine the effect of parameters within the APC model on VLF mode damping.

4.3 Base case

This base case is used as a benchmark for changes in damping resulting from APC at the wind sites.

No wind generation is added for the base case, and the standard load profile is employed. Table 1 shows the damping of the critical modes. The damping ratio describes how oscillations in a system decay after a disturbance. A negative damping ratio means it is not damping but driving oscillations. The VLF mode has negative damping of -6.70%, meaning the system is sensitized to an oscillation of 0.0729 Hz or an oscillation with a period of 13.7 s. In the time domain simulations this VLF mode is triggered with a generation/load imbalance, after which it is self-sustaining.

The electromechanical modes, such as the inter-area and local mode, show relatively good damping of 5.13, 9.90 and 10.50%, respectively. Although these modes are not investigated further, it was noted that APC consistently increased the damping of these modes.

4.4 Scenario 1—Time lag

The *sTlag* time constant, shown in Figure 6, is varied at different wind speeds to determine its sensitivity within the control system. The droop settings for Dbn and Dup are set

TABLE 2 Variation in delay time.

Wind Speed [m/s]	Lag [s]	Damping Ratio [%]	Frequency [Hz]
7	0.02	2.04	0.079
	0.1	2.11	0.079
	0.2	2.21	0.079
12	0.02	2.84	0.078
	0.1	2.92	0.078
	0.2	3.02	0.078
16	0.02	2.96	0.078
	0.1	3.04	0.078
	0.2	3.13	0.078

to 25 to be consistent with the frequency response gain of 25 (4% droop) that is standard on the Irish grid. Each conventional generator in the Irish system has a governor droop setting of 4%, meaning that a frequency deviation from 50 Hz of 4% (i.e. 48 Hz or 52 Hz) would lead the generator to increase or decrease its power output by 100% of its rated power. The number of turbines at WF1 and WF2 was set at 50, operating at 85% of available output for APC.

It can be inferred from Table 2 that VLF mode damping is not sensitive to changes within the time lag (sTlag) parameter in the control system. There is a small improvement in damping as the time lag increases, but the improvement is minor and counter-intuitive.

The damping times considered, 20–200 m s, covers the spectrum of possible real-world delay times in APC systems. However, these times are small compared to the period of the specific VLFO (0.078 Hz or 12.8 s) or general VLFO that may have a period in the region of 5–40 s. Consequently, the effect of delay time is minor and has only been included in the analysis to demonstrate that it is not a significant factor for the oscillations under investigation. Moving forward a time delay of 0.1s is employed for the forthcoming scenarios.

4.5 Scenario 2—Droop setting sensitivities

Table 3 summarizes the results for droop settings of 10–50 (equivalent to a 10–2% droop). The time lag was set at 0.1s with 50 wind turbines in total placed at WF1 and WF2, wind speeds of 7, 12 and 16 m/s are investigated, with curtailment of 15% for APC. Substantial improvements in VLFO damping are observed for increased gain; however, even a weak frequency response gain of 10 (10% droop) still improves the damping ratio from -6.7% to between -3.7% and -3.0%. A gain of 20 (5% droop) was sufficient to achieve positive damping of the VLFO for all the wind speeds considered. At a gain of 50 (2% droop), the VLF mode was no longer apparent in the small-signal studies as it was so well damped.

Increases in wind speed, resulting in increased wind generation and therefore available power response, provides a small improvement in damping. Damping VLFOs does not require substantial amounts of power; consequently, even at a low wind speed of 7 ms-1 (9% of capacity), sufficient droop response is available. In this circumstance, only ±1.35 MW of symmetric APC control was available. Judging from the relative sensitivity to gain and insensitivity to wind speed, much less than ±1.35 MW was required to achieve substantial damping of the VLF modes.

It is noteworthy that improvements in damping observed in Table 3 were also observed in all electromechanical modes; this is consistent with previous studies on the frequency response provided by wind generation.

4.6 Scenario 3—Number of turbines

Dup and *Ddn* shown in Figure 6 are set to (4% droop) for this analysis, partially because it is in concordance with settings on the Irish power system, making the results comparable to the PMU data from APC enabled wind farms on the Irish power system. As with wind speed variation, the loads LA and LB were varied to match wind generation at WF1 and WF2, this prevents generation dispatch from affecting the VLF mode.

The dampening power from the wind farms increases linearly with the number of wind turbines with active APC; therefore, a significant increase in dampening ratio is observed as the number of turbines increases, as shown in Table 4. The incremental increase in damping is not quite linear as the active wind turbines reduce the VLF mode when positive damping in excess of 10% is achieved.

These results are similar to observations from sensitivity analysis for gain, whereby wind speed was not a significant factor in mode dampening. A similar interpretation is made, that even at low wind speeds sufficient power is available to achieve substantial dampening. The damping improvement from more wind turbines is evident; therefore, reductions in gain can

TABLE 3 Variation in grain/droop, delay time of 100 m s.

Wind Speed [m/s]	Gain of *Ddn* and *Dup*	Damping Ratio [%]	Frequency [Hz]
7	10	-3.714	0.078
	20	0.192	0.079
	30	4.016	0.079
	40	7.745	0.079
	50	11.353	0.079
12	10	-3.087	0.078
	20	0.950	0.078
	30	4.853	0.078
	40	8.602	0.078
	50	12.171	0.078
16	10	-2.998	0.078
	20	1.059	0.078
	30	4.975	0.078
	40	8.727	0.078
	50	12.289	0.078

TABLE 4 Variation in number of turbines, delay time of 100 m s, gain of 25.

Wind Speed [m/s]	No. Turbines	Damping Ratio [%]	Frequency [Hz]
7	50	2.115	0.079
	100	11.320	0.079
	150	19.535	0.077
	200	26.374	0.075
12	50	2.920	0.078
	100	12.651	0.077
	150	20.824	0.074
	200	28.147	0.071
16	50	3.036	0.078
	100	12.851	0.077
	150	21.236	0.074
	200	28.451	0.071

easily be offset by increases in the number of turbines participating in APC. This type of operation may be more acceptable to asset owners and system operators while achieving the same VLF mode dampening.

4.7 Time domain analysis

Figure 10. shows time-domain simulations for a generation load imbalance at load LC. A positive and negative 40 MW load is disconnected at t = 10s, initiating the VLFO that the system is sensitive to (Table 1, 0.0729 Hz, 13.7 s). As the load is positively damped, it will grow if not sufficiently damped by the APC. A total of 100 wind turbines were deployed at WF1 and WF2, the time lag (sTlag) is set to 0.1s, and the gain is varied between 10 (10% droop) and 50 (2%). The results in this section can be compared to the damping coefficients in Table 3 for a wind speed of 16 ms-1.

The disconnection of negative load results in a VLFO below nominal frequency (plots on the left, Figures 10A, C, E while the disconnection of positive load results in a VLFO above nominal frequency (plots on the right, Figures 9D, F. Curtailment is required to provide under frequency response and dampen oscillations below nominal frequency. Three curtailment settings are investigated, no curtailment (Figures 10A, B), 1.5% curtailment (Figures 10B, C) and 15% curtailment

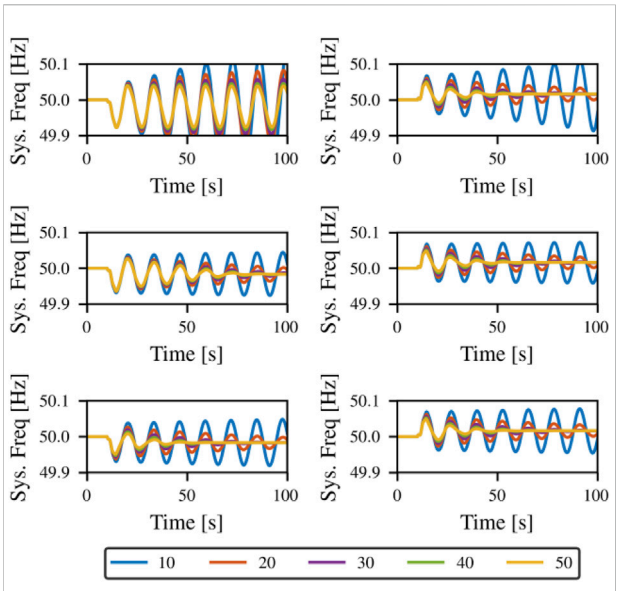

FIGURE 10
(A) Curtailment is 0% and loss of generation **(B)** Curtailment is 0% and loss of load **(C)** Curtailment is 1.5% and loss of generation **(D)** Curtailment is 1.5% and loss of load **(E)** Curtailment is 15% and loss of generation **(F)** Curtailment is 15% and loss of load.

(Figures 10D, E). A curtailment of 15%, or 85% of potential generation, is standard on the Irish system when APC is active, in this scenario, 60 MW are provisioned for droop response. A curtailment of 1.5% provisions 6 MW of power for damping, as such a power response from such a large resource (200 MW) can hardly be considered a droop response.

Figures 10A, B demonstrate that zero curtailments seriously reduces damping potential, particularly in VLFO below nominal frequency. In Figure 10A, APC cannot remove the VLFO as a substantial proportion of the oscillation occurs below the nominal frequency. Therefore APC can only reduce the VLFO damping ratio to zero in this generation scenario, a frequency response gain of greater than 30 (3.33% droop) is required. Although APC does not eliminate the VLFO, the APC response would still provide an incredibly valuable service to system operators, preventing the onset of a catastrophic VLFO or buying time for remedial action. Figure 10B demonstrates that the same control strategy will move the system into positive damping with a frequency response gain between 10 and 20 (10 and 5% droop).

Curtailment of power at renewable sites is undesirable as it represents wasted energy, therefore a minimal curtailment of 1.5% was investigated. It can be noted from Figures 10A, D that the VLFO is moved out of negative damping, even with the lowest frequency gain investigated. Low gain settings of 10 and 20 appear to perform similarly in under and over frequency VLFO scenarios. VLFO damping is more effective at higher gains in over frequency conditions; this is because, under frequency conditions, the power response is clipped as the availability from curtailed power is used up. When APC is activated on the Irish power system, a curtailment of 15% is initiated. Figures 10D, F demonstrate little to no difference between APC performance above or below the nominal frequency when damping VLFO. It can be noted that even at a low gain setting of 10, the system is moved from negative to positive dampening. The results in this section demonstrate that a small provision of curtailed power is sufficient to damp VLFO above and below nominal frequency actively. It is also demonstrated that relatively modest frequency response gains (>20 or >5%) are sufficient to achieve appreciable VLFO damping. It is argued that curtailment for an under-frequency APC droop response and curtailment for an APC VLFO service could be separated. It would be anticipated that the VLFO damping service could be in continual operation and droop response enabled when necessary. This problem could be overcome through centralized or local adjustment of frequency setpoint, whereby the minimum frequency recorded over a period of perhaps 100 s was targeted. This would provide a full VLFO response, regardless of curtailment or ambient frequency conditions.

5 Very low-frequency oscillations and active power control on Ireland's power system

Wind farm APC is used on Ireland's power system for frequency regulation. The details of when APC is enabled are not public and seem to be decided in the control room, however some tendencies can be inferred. As a general guide, APC is on when Ireland is exporting more than 300 MW to Great Britain, and this provides additional security in the event of an over frequency transient. Currently, there is no automated system in place, and APC is turned on manually from the control center.

Three oscillatory events are presented in this section. Measurements are from PMU data, this data is used to qualitatively assess the damping effect of wind farms with active APC. Damping is provided when the MW output of a wind farm is in anti-phase to the system frequency. PMU data is available from five wind farms with APC, data from two wind farms are presented. APC response is remarkably consistent between sites, and general performance can be inferred from specific sites.

5.1 Variability of wind generation possibly exciting VLFOs

In our research, CIG infrastructure has not been implicated as a source for VLFO; however it can strongly influence system parameters that appear to sensitize the power systems to VLF modes, these parameters include generator dispatch, active

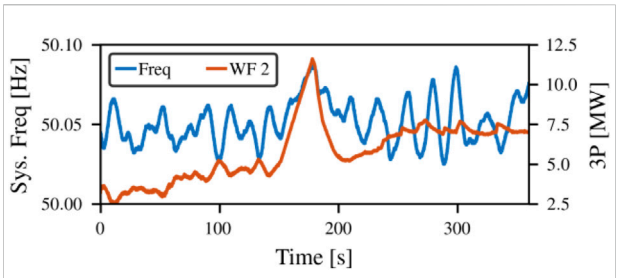

FIGURE 11
VLF Oscillation corresponding to 7.5 MW perturbation at a wind farm on Ireland's power system.

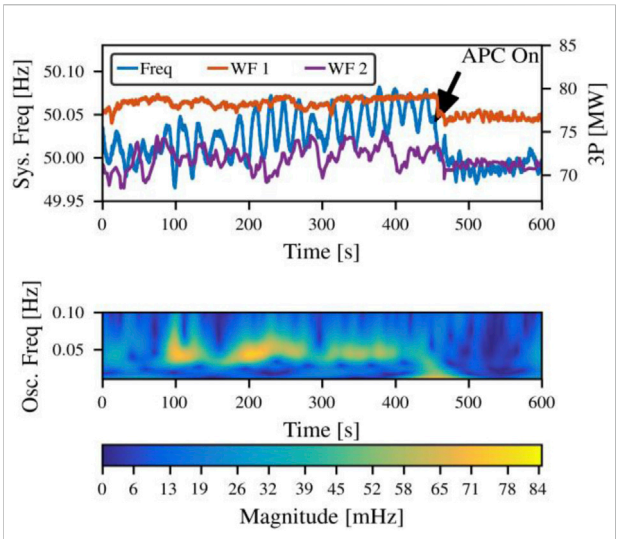

FIGURE 12
(A) System frequency and active power output from WF1 and WF2 when APC is switched on after 450 s **(B)** continuous wavelet transform showing the reduction in oscillation magnitude in system frequency for oscillation frequencies between 0.02 and 0.1 Hz.

governor control systems, system configuration and line flows. The purpose of installing renewable generation is to displace conventional generators, which reduces synchronous inertia on a power system, changing VLF modes and making the system more sensitive to perturbations such as transient generation/load imbalances and short circuits. Stochastic generation can also be a trigger that exposes sensitized oscillatory modes (Adeen and Milano, 2021).

Displayed in Figure 11 is a fluctuation that moved the system frequency. While the observed 7.5 MW power perturbation was small, a similar fluctuation at wind farms within the region could have contributed to the deflection of system frequency. The exact cause of the variation is unknown and may arise from wind gusts or the control room releasing curtailments before turning them back on. Similar frequency deviations in the following analysis are observed due to curtailment being added or released as APC is switched into and out of service.

Due to the lack of PMU measurements, it is hard to discount possible causes and consequences of the minor transient event in Figure 11. Whatever the cause, the wind farm fluctuation coincides with an increase in the VLF mode magnitude to 50mHz, before being damped. Due to governors providing the majority of pseudo steady-state frequency regulation, interactions between governors and wind farms likely caused an increase in mode magnitude.

5.2 APC activation to decrease oscillation magnitude

Figure 12 captures the effect of activation of APC at wind farms. Shown in Figure 12A is PMU data that recorded the 60-70 mHz oscillation that took place as system frequency transitions above 50 Hz, this persisted for approximately 250 s. The activation of APC controls reduced power output from multiple wind sites, reducing the power system frequency by approximately 50 mHz. This curtailed power was then employed by the APC to successfully dampen the oscillation to below 10 mHz. The dampening effect is seen in the continuous wavelet transform in Figure 12B, with a clear generalized oscillation pre-450s. Once APC is initiated, the period of the VLFO increases as its magnitude drops to zero.

These data demonstrate that APC can be used in an emergency control situation or ambient conditions to reduce background oscillations. It is worth noting that the oscillation magnitude of the power response at the wind farm will be proportional to the oscillation magnitude of the system frequency and that only a small proportion of the curtailed power was required to dampen the VLFO. This observation supports the findings in Section 4 that small power provision and low droop settings can quickly and effectively move the power system into positive damping. Therefore, TSOs may not need to employ costly curtailment to achieve significant dampening of VLFOs.

5.3 APC turned off and increase in oscillation magnitude

Figure 13A shows the active power output of WF1, alongside system frequency. Wind curtailment for APC was possibly discontinued to increase system frequency. Switching off curtailment resulted in a 15 MW rise in output from WF1; presumably, similar increases would be observed at other wind farms with active APC. The additional power resulted in a frequency increase of approximately 12 mHz. The removal of APC control also coincides with an immediate onset of a VLFO apparent in the frequency trace in Figure 13A. The magnitude of

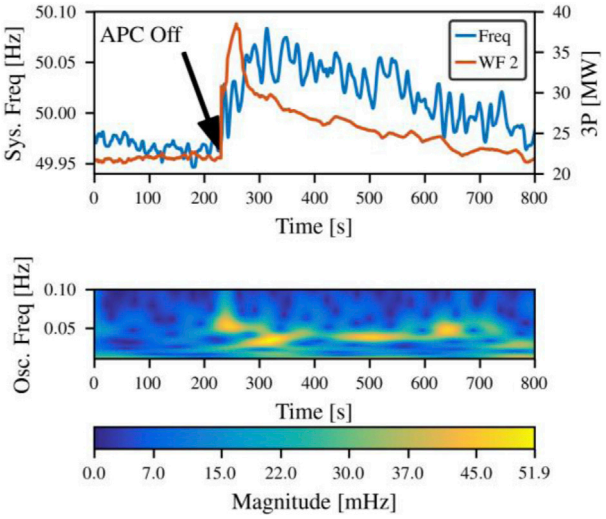

FIGURE 13
(A) System frequency and active power output fromWF2 when APC is switched off after 200 s **(B)** continuous wavelet transform showing the increase in oscillation magnitude in system frequency for oscillation frequencies between 0.02 and 0.1 Hz.

background oscillations increased from approximately 10–50 mHz. The continuous wavelet transform plot of the frequency data is presented in Figure 13B and decomposes the VLFO into its constituent parts. It is noteworthy that VLFOs operate across multiple bands and emerge and dissipate multiple times. It is probable that the sources of the VLFO were active while the APC was on but that they were so well damped that they were virtually undetectable due to positive dampening. This supposition is supported by the observation from small-signal analysis in Section 4, where high positive dampening made the study of VLFO almost impossible as they did not emerge.

5.4 APC interaction with deadband

Figure 14 shows the active power output from WF1 as the system frequency passes through the ±15 mHz APC deadband typically set on the Irish power system.

During the time 0-200 s, the frequency is above the deadband, and WF1 modulates its power output in anti-phase to frequency oscillations. Similarly, from 650 s onwards, system frequency is below the deadband, and the windfarm responds with a similar anti-phase power/frequency response. However, while the frequency is within the deadband the power output from the wind farm remains relatively constant, with perturbations in power output arising primarily from infringements of the deadband. It is noteworthy that the magnitude of background frequency oscillations are markedly higher while system frequency is in the deadband and wide-area APC is effectively discontinued. In the simulations in Section 4 a deadband of zero was employed, this allowed for analysis of fundamental oscillatory interactions but also demonstrated the maximum potential for oscillation damping. A deadband was historically employed in control systems for a synchronous generator to reduce wear, hunting and undesirable interactions between electromechanical systems; however, CIG does not suffer as much from these issues.

Consequently, a deadband of zero might reduce wear, hunting and oscillatory coupling on power systems. That said, a deadband ±15 mHz is relatively small and VLFO magnitudes of 30 mHz are tolerated on the Irish power system. Finally, a not insignificant drop in power system frequency is observed around the 650 s point in Figure 14, this results in an appreciable droop response of 2 MW from WF1. This 2 MW power response indicates the extent of the curtailment on WF1, which may be carrying a reserve of 9.7 MW. Such a droop response is desirable for frequency stability resulting from generation/load imbalance but is unnecessary for VLFO dampening. Therefore, as demonstrated in Section 3 a VLFO dampening service would require vastly less curtailment than is currently implemented in the APC control scheme.

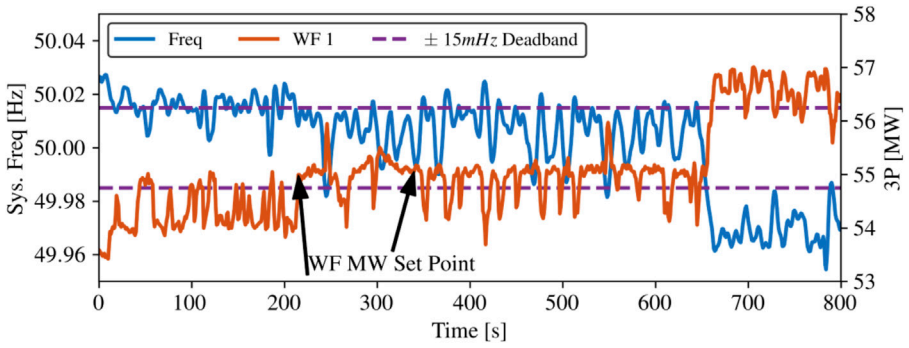

FIGURE 14
Wind Farm power response and interaction with reduced ±15 mHz deadband.

6 Conclusion

This work investigated the damping provided by APC controls for VLFOs using small-signal and time-domain simulations and PMU data from the Irish power system. It is demonstrated that APC control is incredibly effective for increasing the damping of VLFOs, often mitigating them beyond the point of observation or study. APC time delays were found to have minimal effect on APC performance; while increased droop settings, wind speed, curtailment and resource capacity can have a substantial impact when damping the VLF mode. Simulations demonstrated that even very conservative APC settings move the power system model from negatively damped VLFO to positive damping. PMU data from wind farms engaging in APC were investigated, and the ameliorating effect of APC is particularly apparent when APC is switched in or out of service or when power response stops while in the deadband. While APC was damping VLFO, beyond the point of observation, only a tiny proportion of the curtailed power was being utilized. A major cost of APC operation is the curtailment of active power generation from wind sites. Observations from PMU data and simulations indicate that very little curtailment is required for VLFO dampening. On the Irish system, curtailment of 15% is initiated once APC is activated, from the observations in this paper, curtailment of 1.5% should be sufficient for dampening VLFO. Alternatively, adjusting the target frequency for APC would more efficiently damp VLF modes. APC is observed to be inhibited by deadbands. The deadband on the Irish power system is small, at ±15 mHz, but an objective of zero for improving performance should be sought. There is no indication from power system models or available PMU data that this would result in deleterious system effects. While APC successfully eliminated VLFO in simulations and from PMU data, it is not suspected that CIG was the cause. Rather, it mitigated undesirable operation on conventional assets, particularly poorly tuned governors at synchronous generators. To summarize, effective VLFO damping can be achieved with low curtailment, low droop, and low wind speeds; system operators should continuously employ less aggressive APC at CIG to dampen VLFO.

Data availability statement

All simulated data created during this research is openly available from Zenodo open data repository at DOI: 10.5281/zenodo.6805574. PMU Data supporting this study cannot be made available due to NDA agreement.

Author contributions

CD contributed to conception and design of the study, performed analysis, wrote the first draft of the manuscript. XL, RB, and JM contributed to supervision, all authors contributed to manuscript revision, read, and approved the submitted version.

Acknowledgments

The authors would like to thank SONI/EirGrid for providing PMU data. The authors would also like to thank DIgSILENT for granting a thesis license to continue research off-campus during COVID-19. The authors would like to acknowledge the financial support from the SPIRE2 project (Storage Platform for the integration of Renewable Energy). The SPIRE two project is supported by the European Union's INTERREG VA Programme, managed by the Special EU Programmes Body (SEUPB). The views and opinions expressed in this paper do not necessarily reflect those of SEUPB. This work is alo supported by EPSRC Supergen Networks Hub (EP/S00078X/2) - SEN Hub Sub-Project Award for a project entitled "Challenges and Opportunities of Machine Learning and BESS for Oscillations Mitigation in Low Inertia Power Networks'. All simulated data created during this research is openly available. The names of the repository and accession number can be found in the article upon publication.

Conflict of interest

The authors declare that the research was conducted in the absence of any commercial or financial relationships that could be construed as a potential conflict of interest.

Publisher's note

References

Adeen, M., and Milano, F. (2021). On the impact of auto-correlation of stochastic processes on the transient behavior of power systems. *IEEE Trans. Power Syst.* 36 (5), 4832–4835. doi:10.1109/tpwrs.2021.3068038

AEMO (2017). *Review of frequency control performance in the NEM under normal operating conditions*. Brisbane: DIgSILENT Pacific.

Arango, O. J., and Sanchez, H. M. (2010). Low frequency oscillations in the Colombian power system – identification and remedial actions. *CIGRE 2010 Paris*, 1–12.

Chen, G., Tang, F., Shi, H., Yu, R., Wang, G., Ding, L., et al. (2018). Optimization strategy of hydrogovernors for eliminating ultralow-frequency oscillations in hydrodominant power systems. *IEEE J. Emerg. Sel. Top. Power Electron.* 6 (3), 1086–1094. doi:10.1109/jestpe.2017.2788004

Chen, L., Min, Y., and Hu, W. (2013). An energy-based method for location of power system oscillation source. *IEEE Trans. Power Syst.* 28 (2), 828–836. doi:10.1109/tpwrs.2012.2211627

Chen, L., Min, Y., Lu, X., Xu, X., Li, Y., Zhang, Y., et al. (2017). Online emergency control to suppress frequency oscillations based on damping evaluation using dissipation energy flow. *Int. J. Electr. Power & Energy Syst.* 103, 414–420. doi:10.1016/j.ijepes.2018.06.022

Clark, S., Wilson, D., Al-Ashwal, N., Macleod, F., Mohapatra, P., Yu, J., et al. (2016). "Addressing emerging network management needs with enhanced WAMS in the GB VISOR project," in 19th 2016 Power Systems Computation Conference (PSCC), Genoa, Italy, 20-24 June 2016. doi:10.1109/PSCC.2016.7540948

De Marco, F., Martins, N., Pellanda, P. C., and E Silva, A. S. (2018). Simulating sustained oscillations and ambient data in a large nonlinear power system model. *IEEE Power Energy Soc. Gen. Meet.*, 1–5. doi:10.1109/PESGM.2017.8274268

Duggan, C., Brogan, P., Liu, X., Best, R., and Morrow, J. (2021). "Synchronisation control action for very low-frequency oscillations," in 2021 32nd Irish Signals and Systems Conference (ISSC), Athlone, Ireland, 10-11 June 2021, 1–7. doi:10.1109/ISSC52156.2021.9467843

Ellis, A., Behnke, M., and Elliott, R. (2012). Generic solar photovoltaic system dynamic simulation model specification*Electr. Coord. Counc. Model. Valid. Work Group, Sandia Contract*, 1–32. doi:10.2172/1177082

Grondin, R., Kamwa, G., Trudel, J., Taborda, R., Lenstroem, H., Baumberger, L., et al. (2000). The multi-band PSS: A flexible technology designed to meet opening markets. *CIGRE 2000 Paris Pap.* (September), 1–12.

Homan, S., and Brown, S. (2021). The future of frequency response in Great Britain. *Energy Rep.* 7, 56–62. doi:10.1016/j.egyr.2021.02.055

Kundur, P., Balu, N. J., and Lauby, M. G. (1994). *Power system stability and control*, 7. New York: McGraw-Hill.

Lin Zhou, K. G., Yu, Xirui, Li, Bin, Zheng, Chen, Liu, Jinhong, and Liu, Qiang (2017). Damping inter-area oscillations with large-scale PV plant by modified multiple-model adaptive control strategy. *Ieee Trans. Sustain. Energy* 8 (4), 1629–1636. doi:10.1109/tste.2017.2697905

Mele, F. M., Wall, P., Qazi, H., Cunniffe, N., Keane, A., and Osullivan, J. (2020). Mitigating extreme over-frequency events using dynamic response from wind farms. *IEEE Trans. Power Syst.* 8950 (c), 1. doi:10.1109/TPWRS.2020.3011268

Milano, F., Dorfler, F., Hug, G., Hill, D. J., and Verbič, G. (2018). "Foundations and challenges of low-inertia systems," in 2018 Power Systems Computation Conference (PSCC), Dublin, Ireland, 11-15 June 2018, 1–25. doi:10.23919/PSCC.2018.8450880

National Grid (2019). Technical report on the events of 9 august 2019. Available at: https://www.ofgem.gov.uk/system/files/docs/2019/09/eso_technical_report_-_final.pdf (Accessed Apr. 25, 2021).

Ruttledge, L., and Flynn, D. (2012). System-wide contribution to frequency response from variable speed wind turbines. *IEEE Power Energy Soc. Gen. Meet.* (09), 1–8. doi:10.1109/PESGM.2012.6345684

Saadatmand, M., Gharehpetian, G. B., Member, S., and Siano, P. (2021). PMU-Based FOPID controller of large-scale wind-PV farms for LFO damping in Smart grid. *IEEE Access*, 1. doi:10.1109/ACCESS.2021.3094170

SEMO (2020). Active power control groups. Available at: https://www.semo.com/documents/general-publications/Active_Power_Control_Groups_Information_Note (Accessed Mar. 11, 2021).

Singh, M., Allen, A. J., Muljadi, E., Gevorgian, V., Zhang, Y., Santoso, S., et al. (2015). Interarea oscillation damping controls for wind power plants. *IEEE Trans. Sustain. Energy* 6 (3), 967–975. doi:10.1109/tste.2014.2348491

Wall, P., Bowen, A., Geaney, C., and O'Connell, B. (2019). Common mode oscillations on the power system of Ireland and northern Ireland. *18th Int'l Wind Integr. Work*.

Wall, P., Bowen, A., O'Connell, B., Cunniffe, N., Geaney, C., Doyle, R., et al. (2020). Analysis, monitoring and mitigation of the common mode oscillations on the power systems of Ireland and northern Ireland. *CIGRE 2020 Paris*, 1–14.

Wilches-Bernal, F., Chow, J. H., and Sanchez-Gasca, J. J. (2016). A fundamental study of applying wind turbines for power system frequency control. *IEEE Trans. Power Syst.* 31 (2), 1496–1505. doi:10.1109/tpwrs.2015.2433932

Xie, R., Kamwa, I., and Chung, C. Y. (2020). A novel wide-area control strategy for damping of critical frequency oscillations via modulation of active power injections. *IEEE Trans. Power Syst*, 485–494. doi:10.1109/TPWRS.2020.3006438

Xie, R., Kamwa, I., Rimorov, D., and Moeini, A. (2018). Fundamental study of common mode small-signal frequency oscillations in power systems. *Int. J. Electr. Power & Energy Syst.* 106, 201–209. doi:10.1016/j.ijepes.2018.09.042

Zhu, Y., Liu, C., Wang, B., and Sun, K. (2018). Damping control for a target oscillation mode using battery energy storage. *J. Mod. Power Syst. Clean. Energy* 6 (4), 833–845. doi:10.1007/s40565-017-0371-3

frontiers | Frontiers in Energy Research

ORIGINAL RESEARCH
published: 11 August 2022
doi: 10.3389/fenrg.2022.927453

Coordinated Control of a Wind Turbine and Battery Storage System in Providing Fast-Frequency Regulation and Extending the Cycle Life of Battery

Yuan Tang[1], *Conghuan Yang*[2], *Zuanhong Yan*[3]*, *Ying Xue*[1] *and Yi He*[4]

[1]School of Electric Power Engineering, South China University of Technology, Guangzhou, China, [2]Department of Electronic, Electrical and System Engineering, University of Birmingham, Birmingham, United Kingdom, [3]Quant-Cloud Energy Co, Ltd., Shenzhen, China, [4]Department of Electrical Engineering, The Hong Kong Polytechnic University, Kowloon, China

Fast-frequency regulation (FFR) is becoming a key measure to enhance the frequency stability of power systems as the penetration of renewables and power electronics continues to grow and the system inertia declines. Although different control methods have been proposed to provide a wind turbine generator (WTG) with a limited capability of virtual inertia and frequency support, the coordination between the WTG and a battery energy storage system (BESS), as well as the potential optimization benefits, have not been fully studied. This study proposes a coordinated control of WTG and BESS that provides FFR to the AC system and at the same time extends the cycle life of the battery. First, a cost effective and SOC-based FFR strategy of BESS alone was proposed. Then, a coordinated FFR method for the WTG–BESS hybrid system under all wind speeds was proposed by analyzing the operational characteristics of WTG. The proposed coordinated strategy improves the FFR performance with a longer cycle life and lower cost of battery under different operating conditions. Simulation results based on varying wind speeds indicate that the proposed FFR strategy raises the frequency nadir and avoids the frequency secondary dip.

Keywords: fast-frequency regulation, wind turbine generator, battery energy storage, cycle life, frequency nadir, frequency secondary dip

OPEN ACCESS

Edited by:
Xue Lyu,
University of Wisconsin-Madison, United States

Reviewed by:
Yue Wang,
Xi'an Jiaotong University, China
Shuang Zhao,
Hefei University of Technology, China

***Correspondence:**
Zuanhong Yan
themichaelyan@outlook.com

Specialty section:
This article was submitted to Smart Grids, a section of the journal Frontiers in Energy Research.

Received: *24 April 2022*
Accepted: *14 June 2022*
Published: *11 August 2022*

Citation:
Tang Y, Yang C, Yan Z, Xue Y and He Y (2022) Coordinated Control of a Wind Turbine and Battery Storage System in Providing Fast-Frequency Regulation and Extending the Cycle Life of Battery. Front. Energy Res. 10:927453. doi: 10.3389/fenrg.2022.927453

1 INTRODUCTION

A rapid development of renewable energy is becoming a global consensus. Over 10 countries have set targets to increase the installed capacity of renewable energy to meet 50% of total energy demands (Kurbatova and Perederii, 2020). At the same time, the increasing penetration of converter-interfaced renewable power causes issues regarding frequency stability. Variable-speed wind turbine generators (WTGs) normally operate under the maximum power point tracking (MPPT) mode to obtain the maximum output at a certain wind speed; thus, their power output is decoupled from the system frequency. As the WTGs gradually replace the conventional synchronous generators (SG), the inertia reserve of the power system is further reduced, and the frequency-regulation capability is thus weakened (Lin and Wu, 2020).

Nowadays, many countries have regulations in place for grid-connected WTG to provide frequency regulation to the system. For instance, the United Kingdom National Grid

requires onshore wind farms to provide short-term frequency support and automatic generation control ability (Dallmer-Zerbe et al., 2017). Hence, the methods of frequency support have been proposed and can be divided into two categories: power reserve control and kinetic energy control (Attya and Dominguez-García, 2018). For kinetic energy control, WTGs release the kinetic energy of the rotor to provide frequency support. However, this method works only a very short period of time (<5 s) and suffers the drawback of frequency secondary dip (FSD) when the rotor speed recovers, especially under low-speed conditions (Jin et al., 2018). For power reserve control, overspeeding and pitch deloading methods allow WTGs to leave a margin of active power to meet the frequency support requirements (Li et al., 2016; Wang et al., 2018; Datta et al., 2020). However, the significant cost of wind power curtailment reduces the financial benefits and usually makes this method infeasible (Motamed et al., 2013).

In the past few years, the development of battery energy storage systems (BESSs) has also driven research on frequency support (Zhang et al., 2014). The fast response and precise power-tracking characteristics of BESSs make them attractive solutions considering the technical difficulties encountered by the frequency support using WTG, as discussed above (Sun et al., 2020). Studies have discussed the inertia control and frequency regulation based on WTG and BESS together (Xu et al., 2013; Gao, 2014; Wu et al., 2015; Sato et al., 2020). However, none of them considered potential benefits of coordinated operations. The high cost of BESS investment remains an obstacle to large-scale application. Considering the economic feasibility of wind-storage hybrid systems, studies by Dang et al. (2012) and Miao et al. (2015) proposed coordinated frequency-regulation strategies based on the state of charge (SOC) feedback to improve the battery efficiency and smooth the frequency variations. However, simply setting the upper and lower SOC limits cannot achieve desired performances under changing network and wind conditions. Hao et al. (2015) discussed a hybrid frequency-regulation strategy using adaptive fuzzy control, which improves the frequency regulation accuracy of wind farm and supercapacitor, while optimizing the capacity of supercapacitor to reduce the investment cost. Zhang et al. (2018) optimized the battery capacity based on the frequency droop control with a fixed droop coefficient to maintain a constant BESS power output. A coordinated virtual synchronous generator control of photovoltaic and battery systems for grid support was also studied by Liu et al. (2022). Xiong et al. (2021) discussed a frequency response strategy based on fast power compensation in low-inertia power systems.

In this study, the coordination and optimal operation of a hybrid system of WTG and BESS were examined to 1) provide high-performance fast-frequency regulation (FFR) at all wind speeds, and 2) optimize the SOC management to extend the cycle life of battery, thus further decreasing the lifecycle investment cost. The main contributions of this study are as follows

1) Compared to the conventional method, the frequency nadir is further raised under the proposed coordinated control of the WTG–BESS hybrid system.
2) Compared to controlling the BESS alone, the proposed SOC-based control optimizes the SOC management and extends the cycle life of battery.
3) The technoeconomic feasibility of using BESS to support the system frequency was analyzed and improved, with either better performance of frequency regulation or lower cost of BESS.
4) The proposed SOC-feedback droop control integrates real-time battery SOC and conventional droop control to maintain SOC, reducing the additional penalty costs and eliminating the FSD.

The rest of this study is organized as follows. **Section 2** discusses the selection of battery, BESS capacity dimensioning, and the impacts of battery SOC on its cycle life. **Section 3** proposes the SOC-based droop control of BESS and the coordinated FFR method of the WTG–BESS hybrid system. **Section 4** presents case studies based on time domain simulations to demonstrate the proposed method. At last, **Section 5** cconcludes the study.

2 TECHNOECONOMIC FEASIBILITY STUDY OF BATTERY ENERGY STORAGE SYSTEM

In order to clarify the technical and economic benefits of the proposed coordinated control method, it is necessary to analyze the economic feasibility of using BESS to provide FFR under certain technical conditions. Three aspects were discussed:

1) Technical characteristics of different types of battery
2) Dimensioning of the BESS capacity
3) Impacts of SOC on the cycle life of battery

Different Types of Battery

As for different types of battery, key factors of considerations were investment cost, energy density, response time, cycle life, efficiency, and safety. So far, the applications of battery storage have been dominated by lithium-ion batteries. **Table 1** shows the dominant types of battery and their technical characteristics (Wang and Liu, 2017; Zhao et al., 2019).

The investment costs of lead–acid and lead–carbon batteries are low, but these batteries are being phased out due to low energy density and pollution. Lithium-ion batteries dominate all performance indicators, including high-energy density and long cycle life. In particular, lithium–iron–phosphate has a cycle efficiency of about 95%. Therefore, the rest of analysis in this study is based on the lithium–iron–phosphate battery, for its good balance between technical features, cost, and safety. With the latest technical and craftsmanship progresses of the lithium–iron–phosphate battery, it is believed that it makes a

TABLE 1 | Technical characteristics of different types of battery.

Type	Energy Density (Wh/kg)	Cost ($/kWh)	Cycle Life	Cycle Efficiency (%)
Lead-acid	30–200	10–150	500–1,500	65
Lead-carbon	30–200	10–200	2000–5,000	80
Sodium-sulphur	150	200–400	<2,500	70
Lithium iron phosphate	120–190	400–800	2000–5,000	95
Lithium iron titanate	100	400–700	10,000	90
Ternary lithium	200	250–400	2000–10,000	90

better option than ternary lithium for grid-connected applications owing to upgraded energy density and superior safety.

Dimensioning of the Battery Energy Storage System Capacity

Overdimensioned capacity of BESS leads to a higher investment cost, while underdimensioned capacity leads to worse frequency-regulation performance and FSD due to frequency support interruptions. It is important to precisely design the BESS capacity and make the best use of it.

So far, there is no consensus on how to dimension the capacity for the purpose of FFR. One idea is to view the role played by FFR as that similar to the inertia response of conventional SG. Both share the same purpose to prevent the frequency nadir from being too low before the primary frequency regulation kicks in. On this basis, the principle of BESS dimensioning is to assume that it releases the same energy as that released by an SG from a rated grid frequency to the lower limit in a certain period of time.

As an example, in a severe underfrequency event, the system frequency could drop from 50 to 48 Hz, and the corresponding SG rotor speed ranges from 1.0 p. u. to 0.96 p. u. The maximum kinetic energy released by the SG can be calculated as

$$\Delta E_k = \frac{1}{2}J(1\omega_n)^2 - \frac{1}{2}J(0.96\omega_n)^2 = 0.0392J\omega_n^2, \tag{1}$$

where ω_n is the rotor angular speed, and J is the rotational inertia. When the generator is at the rated speed, the kinetic energy of the rotor is

$$E_k = \frac{1}{2}J\omega_n^2 = P_nH, \tag{2}$$

where P_n is the rated power of the SG, and H is the inertia time constant. Assuming the energy released by the BESS in time t_1 equals the maximum kinetic energy released by the SG as calculated in **(1)**, the power of BESS would be

$$E_{BESS} = \Delta E_{kmax}. \tag{3}$$

The left side is $E_{BESS} = P_{BESS}t_1$. As to the right side, from **(1)** and **(2)**, $\triangle E_k = 0.0784\cdot(1/2)J\omega_n^2 = 0.0784P_nH$. Therefore, we have

$$P_{BESS}t_1 = 0.0784P_nH. \tag{4}$$

It is reasonable to assume $t_1 = H$. Although the per unit rotor speed does not drop to zero, the net power applied on the rotor is not the rated power, but the additional load disturbance, which is much smaller. Assuming $t_1 = H$ and leaving a margin for the battery SOC, the BESS capacity is dimensioned as

$$\frac{P_{BESS}}{P_n} = 7.84\% \approx 8\%. \tag{5}$$

The above calculation shows the dimensioning of BESS for the requirements of FFR and its relationship with the lower limit of the system frequency. Note that the calculated result of 8% P_n is for a rather severe underfrequency situation. In practice, the dimensioning of the BESS capacity would depend on the network requirement. In reality, the system frequency can hardly drop <49.5 Hz; therefore, the required battery capacity could be even smaller.

Impacts of State of Charge to the Cycle Life of Battery

SOC is the ratio of the real-time charge and the total charge in a fully charged state. When participating in the frequency regulation, BESS needs to consider not only the target power demand, but also the frequency-regulation capacity that its own SOC can provide. In addition, the penalty cost of SOC to be beyond its upper and lower limits is also considered in the economic impact of SOC on the battery life.

In practical applications, the more energy a battery exchanges with the network before reaching the cycle life, the higher efficiency is achieved and the more financial benefits it brings. However, the rate of battery aging is closely related to the operating conditions. One key factor is the depth of discharge (DOD). The DOD of a complete discharge is 100%. **Figure 1** shows the attenuation relationship between the DOD of a lithium–iron–phosphate battery and its cycle life (Li et al., 2019).

As shown in **Figure 1**, the increasing DOD accelerates the rate of battery aging, reaching a minimum cycle life at a DOD of 1.0. The reduced cycle life of the battery increases its economic investment. Therefore, discharging the battery at its maximum DOD depth in every cycle is undesirable. From the above analysis, the energy management of BESS first requires an analysis of the SOC interval model.

As an electrochemical energy storage, the structure of the lithium-ion battery shows that overcharging or discharging would reduce the available capacity and shorten the cycle life (Yan et al., 2020). More serious problems could happen when the battery releases too much energy for frequency regulation and the SOC drops to a very low level close to zero. Therefore, the BESS

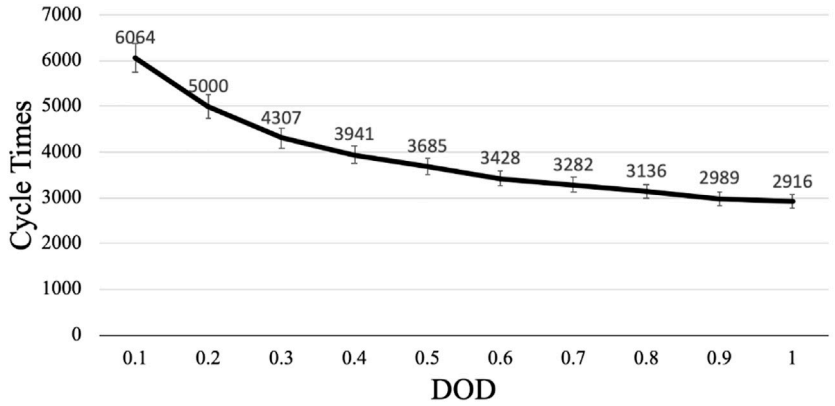

FIGURE 1 | Relationship between the battery depth of discharge and its cycle life.

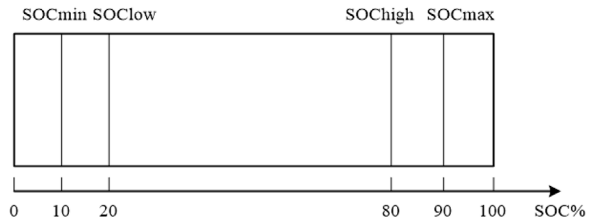

FIGURE 2 | State of charge (SOC) interval model.

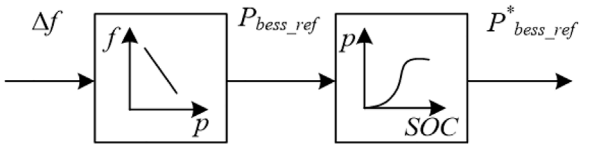

FIGURE 3 | SOC-based frequency droop control for battery energy storage system (BESS).

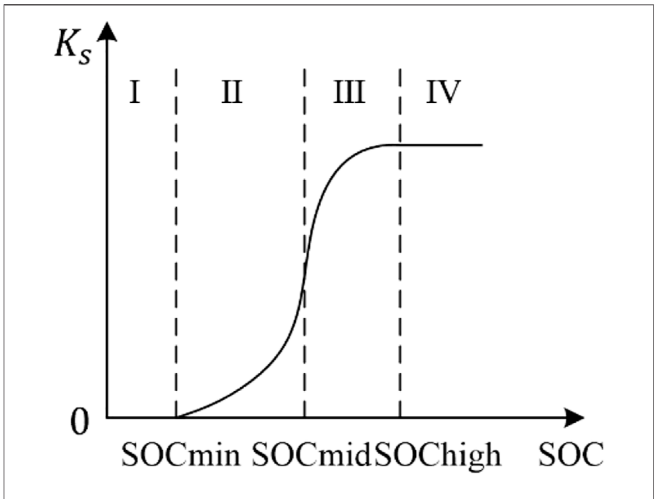

FIGURE 4 | Schematic for constraint.

needs to regulate the charge and discharge power based on real-time SOC feedback. A reasonable upper and lower SOC limit for the operation of BESS hence becomes significant in ensuring satisfactory BESS participation in the frequency regulation. The established SOC interval model is presented in **Figure 2**.

SOC is divided into four intervals by four thresholds: overdischarge threshold SOC_{min}, critical overdischarge threshold SOC_{low}, critical overcharge threshold SOC_{high} and overcharge threshold SOC_{max}.

1) When $SOC \in [0, SOC_{min}]$, BESS is in overdischarge state.
2) When $SOC \in [SOC_{min}, SOC_{low}]$, BESS is in critical overdischarge state.
3) When $SOC \in [SOC_{low}, SOC_{high}]$, BESS is in critical overcharge state.
4) When $SOC \in [SOC_{max}, 1]$, BESS is in critical overdischarge state.

The above four intervals will be used for the proposed control of BESS, allowing batteries to adjust their output power according to SOC in a timely manner, which helps to extend the cycle life of battery.

3 STATE OF CHARGE–BASED DROOP CONTROL AND COORDINATED FAST-FREQUENCY REGULATION METHOD

State of Charge–Based Droop Control for Battery Energy Storage System

Based on the conventional frequency droop control and the technical–economic feasibility analysis of BESS in **Section 2**, **Figure 3** shows the proposed SOC-based droop control. The control scheme consists of two modules: the p–f frequency droop and SOC–p constraint.

The conventional *p–f* droop control does not consider battery SOC, and it has a fixed droop coefficient. When BESS is charged and discharged to SOC limit, it shortens the BESS lifecycle and brings FSD, hence increasing economic costs.

To avoid BESS being charged and discharged to the SOC limit, the BESS SOC has been proposed as an input variable to constrain the power reference $P^*_{bess\_ref}$ for a BESS, by scaling the output from the droop block P_{bess_ref} using a coefficient K_s.

Hence, it has $P^*_{bess\_ref} = K_s(SOC) * P_{bess\_ref}$, as shown in **Figure 3**. The shape of $K_s(SOC)$ is presented in **Figure 4**.

In **Figure 4**, the *x*- and *y*-axis are the BESS SOC and Ks. Based on the SOC interval model in **Figure 2**,**Section 2.3**, design of the constraint coefficient K_s can be divided into the following four zones: very low (Zone I), low (Zone II), high (Zone III), and very high (Zone IV). It is based on the principles of providing a sufficient FFR when SOC is high, and protecting the battery when SOC is low.

1) Zone I (0–10%):

When $0 \le SOC \le 10\%$ in Zone I, BESS is in overdischarge state. Discharging BESS in this zone to provide frequency regulation will shorten the battery cycle life and increase the penalty costs. In addition, there is risk of FSD due to low SOC. Therefore, when entering Zone I, BESS terminates its power output, and the constraint coefficient decreases to 0, i.e., $K_{s1} = 0$.

2) Zone II (10–50%):

In Zone II, $10\% \le SOC \le 50\%$, and BESS presents a moderately sufficient capability to provide frequency regulation. To avoid entering the overdischarging Zone I (to slow down battery aging), in Zone II the power output of BESS decreases with SOC at a progressively slower rate. Hence the constraint coefficient is designed as

$$K_{s2} = \frac{1}{1 + e^{\frac{SOC - SOC_{mid}}{SOC_{min} - SOC_{mid}} \cdot 10}}. \tag{6}$$

3) Zone III (50–80%):

In Zone III, $50\% \le SOC \le 80\%$, and BESS has sufficient capacity to provide frequency support. Therefore, a BESS provides a large power output when SOC is close to 80%, and it decreases slowly when SOC decreases. When SOC reduces closer to 50%, the decrease rate of BESS power output becomes larger, which aligns with the power provision in Zone II. In Zone III, BESS regulates the output power based on the following constraint coefficient

$$K_{s3} = \frac{1}{1 + e^{\frac{SOC - SOC_{mid}}{SOC_{max} - SOC_{mid}} \cdot 10}}. \tag{7}$$

4) Zone IV (80–100%)

In Zone IV, $SOC \ge 80\%$SOC > 80%, and BESS has large a capacity to provide frequency regulation. Hence, the BESS power output remains maximum, and the constraint coefficient is designed as 1.0:

$$K_{s4} = 1 \tag{8}$$

Equations 6 and **7** jointly were designed based on the following principles: 1) Ks = 1 under SOC_max; 2) Ks = 0 under SOC_min; 3) Ks(SOC) should be a continuous function; and 4) Ks should be larger than a linear selection in Zone III when SOC is relatively high to effectively provide FFR, while being smaller than a linear selection in Zone II when SOC is relatively low to protect the battery. **Equations 6** and **7** were designed so that it meets these four principles. Other higher-level function designs are possible as long as these principles are met, yet the functions of Ks presented as above are straightforward in math given the same principles. In **Equations 6** and **7**, the coefficient 10 is simply an integer large enough to make Ks− > 0 when SOC = SOC_min and Ks− > 1 when SOC = SOC_high, while simultaneously not too large to avoid making Ks(SOC) close to a step function. In a power system, the frequency is not regulated only by one device, but a great number of different devices together, and each has a different real-time SOC. The power deficit from devices with low SOC would be compensated by other devices with high SOC.

TABLE 2 | Coordinated frequency support strategy.

Wind Speed	Turbine	BESS
Low (6–9 m/s)	FFR off (MPPT only)	SOC-based droop control
Medium (9–12 m/s)	FFR on	Priority in FFR
High (over 12 m/s)		

Coordinated Fast-Frequency Regulation Method of the Hybrid System

The WTG has different levels of kinetic energy reserves that can be provided at varying wind speeds. Therefore, the WTG–BESS hybrid system needs to be coordinated to provide frequency regulation under the following three wind speed conditions.

Low wind speed (6–9 m/s): The WTG operates in the MPPT mode in this wind speed range with insufficient kinetic energy reserves. When a WTG releases its kinetic energy causing a fall of its rotor speed to be below the lower speed limit (0.8 p. u.), the FSD will happen when restoring the rotor speed. To eliminate FSD, BESS will participate in frequency regulation when the wind speed is low.

Medium wind speed (9–12 m/s): The WTG has sufficient kinetic energy to support the system frequency. Under this condition, the WTG and the BESS provide FFR jointly.

High wind speed (above 12 m/s): The WTG maintains its maximum power output at rated values at high wind speeds by regulating the pitch angle. If the WTG provides extra power to regulate the system frequency drop, its power output will exceed the rated value. Therefore, at high wind speeds, only BESS participates in frequency regulation.

The above coordinated FFR method is summarized in **Table 2**. The FFR control of the turbine alone is the classical proportional

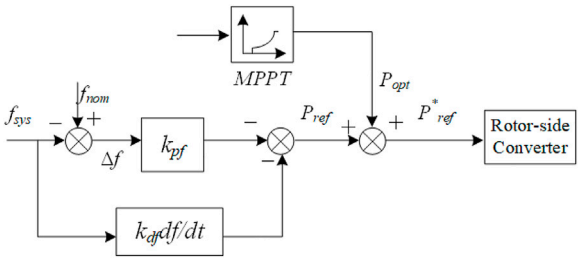

FIGURE 5 | Virtual inertia control scheme for doubly-fed induction generator–based wind turbines.

and differential frequency-feedback control, as shown in **Figure 5**, which is not repeated in this study.

4 CASE STUDIES

To verify the effectiveness of the proposed method, a WTG–BESS hybrid system was modeled in MATLAB/Simulink. The single-line diagram of the system is presented in **Figure 6**.

The WTG is based on a turbine model with a rated power of 1.5 MW. It is connected to a 40-km 35–kV transmission line parallel with a 12.5 kWh BESS. The SG is 30 MW. The load 1 in the system is a constant power load with a rated power of 10 MW. The rated system frequency is 50 Hz. **Appendix Table A1** shows the parameters of the overall system. **Appendix Tables A2** and **A3** show the parameters of the WTG (doubly-fed induction generator [DFIG] in this case) and the transmission line, respectively.

For the case studies, a step load change of 1.5 MW was considered. Given the proposed method in this study, we are particularly interested in how it works under different wind speeds and SOC levels. In Cases 1–3, three different wind speeds of 7, 11, and 13 m/s are simulated to verify and compare the control performance of the coordinated FFR method under low, medium, and high wind speed conditions. The initial battery SOC is set as 85%. Case 4 is simulated under different levels of battery SOC to verify the impacts.

Case 1: Low Wind Speed

The wind speed is set to 7 m/s, and an extra load of 1.5 MW is added at 20 s. When the frequency drops, only BESS provides frequency regulation. **Figure 7** presents the simulation results.

Figure 7A shows that the frequency nadir is raised from 49.83 to 49.86 Hz with FFR provided by BESS. In the low wind speed condition, the turbine does not participate in the frequency regulation, and it follows the MPPT control only. **Figure 7D** shows that the BESS releases energy to support frequency with a response time of <20 ms. **Figure 7C** shows the rotor speed of the WTG is 0.79 p. u. below the lower limit of 0.8 p. u. It validates the necessity and feasibility of the coordinated strategy of only allowing BESS to provide frequency support at low wind speeds.

In conclusion, BESS provides the full FFR in this case and has shown good frequency control performances. The dimensioned capacity BESS does not lead to excessive investment costs or the penalty cost of inadequate frequency support. A reasonable distribution of output power between the BESS and WTG reduces wind energy losses and ensures the economic feasibility of the hybrid system.

Case 2: Medium Wind Speed

In this case, the wind speed is set to 11 m/s, and the extra load of 1.5 MW is added at the 20 s. The simulation results are shown in **Figure 8**.

Figure 8A shows the frequency-regulation performance using the proposed method under medium wind speed. The highest frequency nadir is 49.87 Hz, which is 0.05 Hz higher than 49.82 Hz in the without control mode. In the DFIG mode, when only the DFIG-based WTG provides frequency support via virtual inertia control, the nadir is raised by 0.3 Hz compared to that without control. Furthermore, the system frequency suffers less oscillation and reaches the steady state faster due

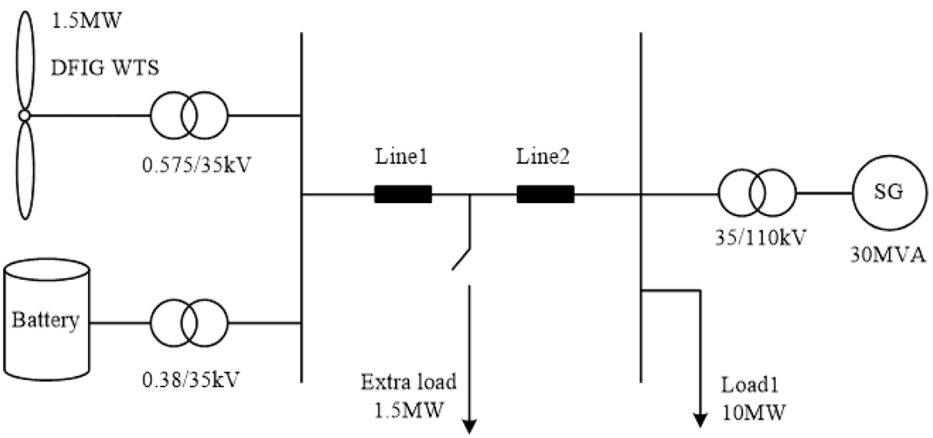

FIGURE 6 | Single-line diagram of the wind turbine generator–BESS hybrid system.

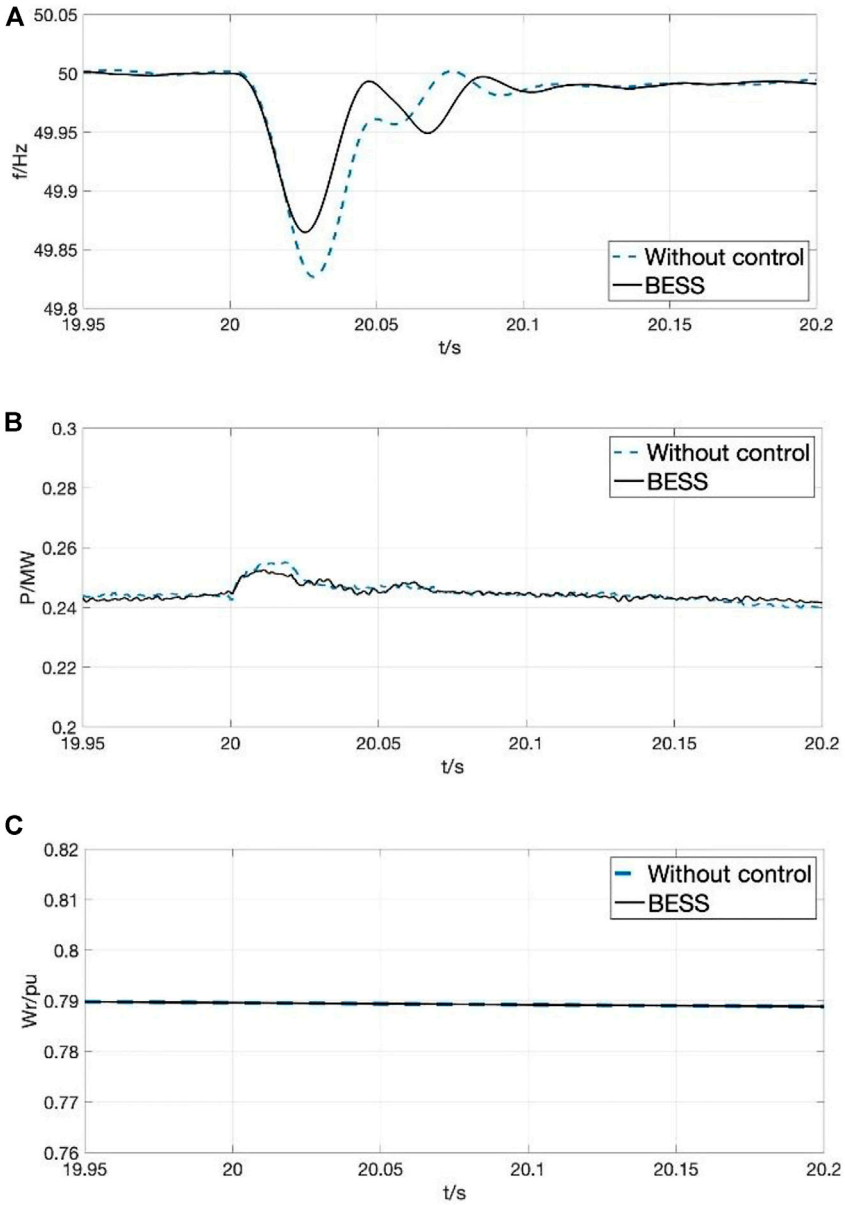

FIGURE 7 | Results for case 1. **(A)** system frequency. **(B)** turbine output power. **(C)** rotor speed of turbine.

to the additional frequency support from BESS. **Figure 8B** shows the output power of the turbine under different controls. It increases to regulate the frequency and decreases to recover the rotating speed of turbine afterwards. The output power of DFIG decreases from 1.09 MW when it supports frequency alone to 1.056 MW when BESS further assists the frequency support. **Figure 8C** shows the rotor-speed variations. The rotor speed drops during the underfrequency event, releasing power to provide frequency support. The rotor-speed variation under the DFIG + BESS mode is smaller than that under the DFIG mode.

In conclusion, the coordinated control provides frequency support improved performances. On the one hand, the hybrid system shares the output energy of the BESS, while making reasonable use of the kinetic energy to provide frequency support. For a set DOD of 0.9, the aging rate of BESS is slowed down, which reduces the operation and maintenance costs of BESS.

Case 3: High Wind Speed

The wind speed is set to 13 m/s and other conditions remain the same as in case 2. **Figure 9** shows the simulation results for different control modes.

Figure 9A shows the raised frequency nadir to a maximum of 49.87 Hz under the proposed FFR method. As shown in **Figures 9B** and **9C**, the rotor speed decreases, releasing kinetic

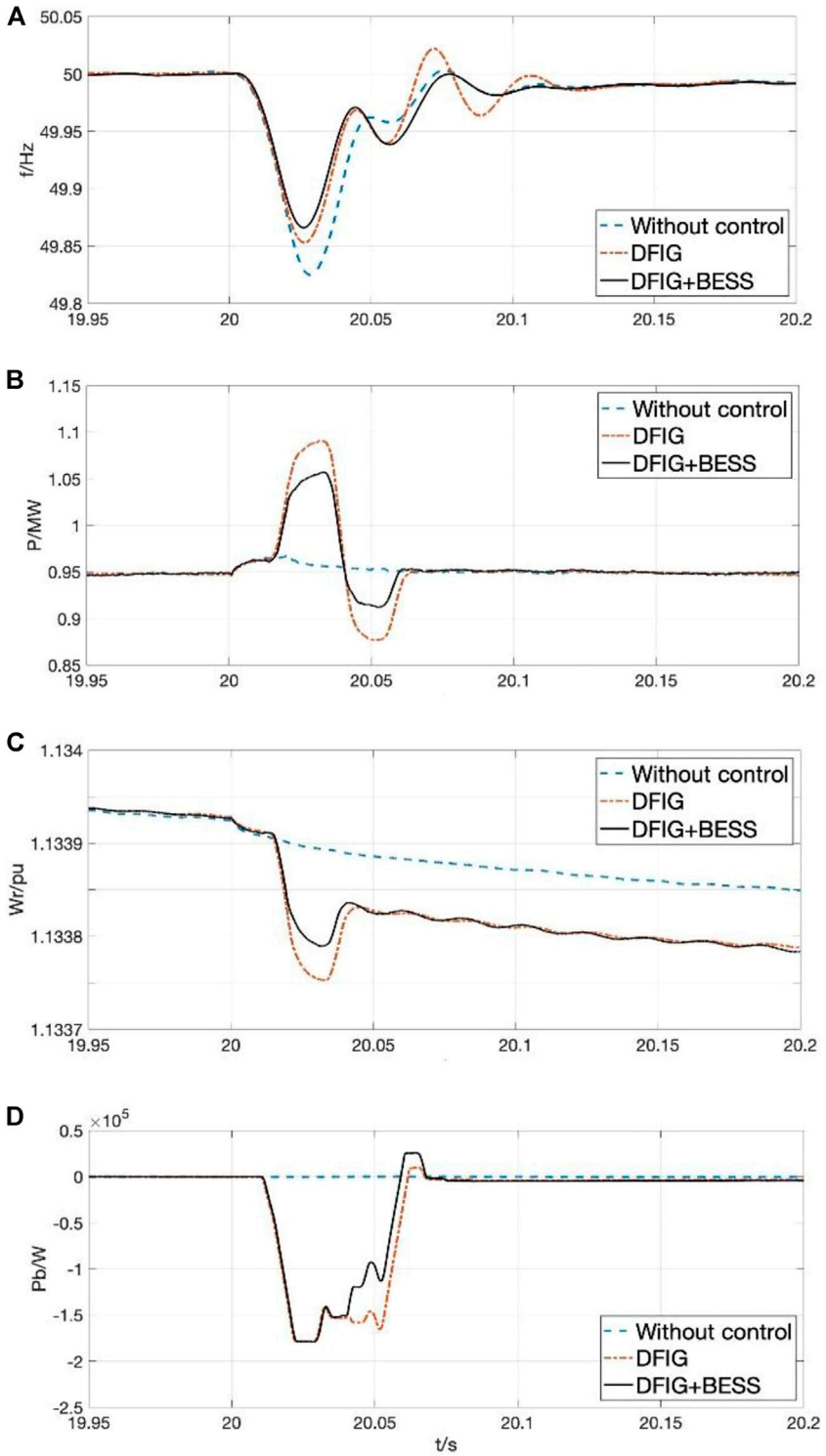

FIGURE 8 | Results for case 2. **(A)** system frequency. **(B)** turbine output power. **(C)** rotor speed. **(D)** output power of the BESS.

energy to provide frequency support to the system. Therefore, the output power is raised accordingly. However, compared to case 2, the difference shown in **Figure 9B** is that the DFIG is capable of increasing its output power by 0.16 MW, which is 0.02 MW greater than that at a medium wind speed in **Figure 8B**. The rotor can store more kinetic energy at higher wind speeds, allowing for better frequency-regulation performance.

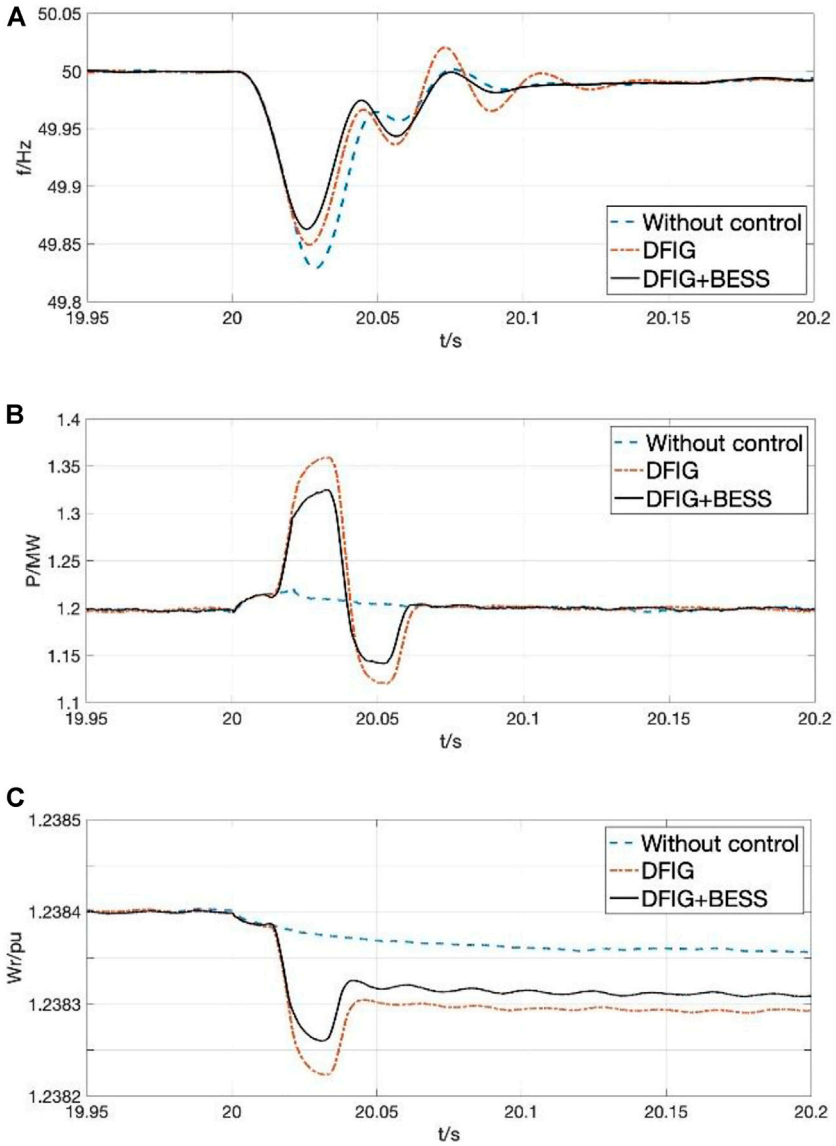

FIGURE 9 | Results for case 3. **(A)** system frequency. **(B)** turbine power output. **(C)** rotor speed.

Case 4: Impacts of State of Charge

In this case, the proposed coordinated control is demonstrated with different levels of the SOC of battery to verify the proposed *SOC–p* constraint.

As shown in **Figures 10A** and **10B**, the BESS reaches a maximum active output of 0.18 MW at 85% SOC, and the frequency nadir is also the highest. When the SOC drops to 40%, the constraint coefficient K_s in the *SOC–p* module constrains the power output of the BESS to 0.15 MW, and when the SOC reaches the lower limit of 10%, the BESS enters the charging state and thus it does not participate in frequency support. Although the frequency-regulation performance weakens as the BESS output decreases, slowing of the SOC decline can further extend the battery life. For operators of the hybrid system, a prolonged period of BESS output power at maximum DOD raises the investment cost of battery. In summary, the simulation results show that the proposed *SOC–p* module can effectively limit the fall of SOC to prevent FSD in the system. In addition, the hybrid system can achieve more financial benefits using this method, balancing the safety of the frequency-regulation service with its economic viability.

However, it is important to point out that batteries will inevitably age over time. When faced with the same frequency-regulation requirement, especially at low wind speeds where the BESS is operating alone, the total number of hours during which BESS provides frequency support is decreased by the reduction in available capacity. In addition, the weakening of the available power output due to battery aging can have a significant impact on control performance, which can threaten the grid safety and stability. Therefore, regular

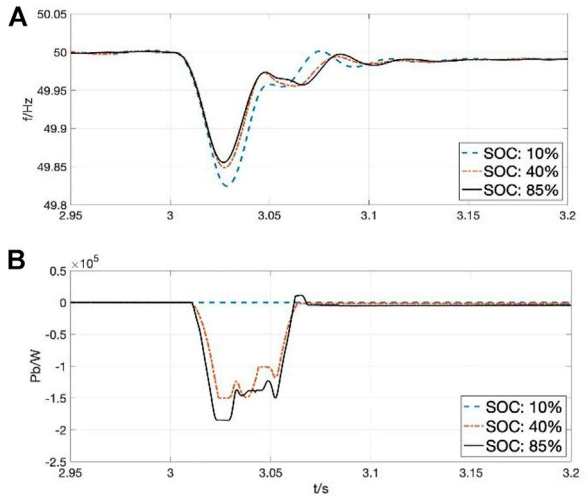

FIGURE 10 | Results for case 4. **(A)** system frequency. **(B)** output power of the BESS.

maintenance and replacement of the battery units is a necessity with BESS. A mix of energy storage devices can also be applied to further reduce the rate of battery aging, for example, by using supercapacitors to compensate for the frequency support of the batteries at low SOC.

5 CONCLUSIONS

This study proposed a SOC-based droop control of BESS and a coordinated FFR method of the WTG–BESS hybrid system. The proposed control strategy can provide FFR to the power system with satisfactory performances.

As to FFR by BESS, the battery type and capacity dimensioning are determined based on the technical and economic analysis of BESS, and a SOC-based droop control is proposed based on the SOC interval model. By constraining the BESS output and maintaining the SOC, the frequency-regulation performance is guaranteed with limited capacity while extending the battery life.

As for the coordinated FFR control of the WTG–BESS hybrid system, the method allocates the output power between the turbine and BESS at different wind speeds. Furthermore, it brings additional frequency support from utilizing the kinetic energy of DFIG.

The proposed control methods were demonstrated using MATLAB/Simulink simulations under different wind speeds and SOC conditions. Our results demonstrate the following advantages:

1) The highest frequency nadir compared to no control, BESS alone, and WTG alone conditions
2) Applicable to all wind speeds
3) Extending the cycle life of battery through SOC management and improving the economic feasibility of the proposed method

DATA AVAILABILITY STATEMENT

The raw data supporting the conclusions of this article will be made available by the authors, without undue reservation.

AUTHOR CONTRIBUTIONS

Conceptualization and formal analysis, YT; investigation, ZY; resources and supervision, YX; validation and writing—original draft preparation, CY; writing—review and editing, YH. All authors have read and agreed to the published version of the manuscript.

FUNDING

This work is funded by China Postdoctoral Science Foundation 2020M682704.

REFERENCES

Attya, A. B. T., and Dominguez-García, J. L. (2018). Insights on the Provision of Frequency Support by Wind Power and the Impact on Energy Systems. *IEEE Trans. Sustain. Energy* 9 (2), 719–728. doi:10.1109/tste.2017.2759503

Dallmer-Zerbe, K., Spahic, E., Kuhn, G., Morgenstern, R., and Beck, G. (2017). "Fast Frequency Response in UK Grid — Challenges and Solution," in 13th IET International Conference on AC and DC Power Transmission (ACDC 2017) (Manchester, UK: IEEE), 1–6.

Dang, J., Seuss, J., Suneja, L., and Harley, R. G. (2012). "SOC Feedback Control for Wind and ESS Hybrid Power System Frequency Regulation," in *2012 IEEE Power Electronics and Machines in Wind Applications* (Denver, CO, USA: IEEE), 1–7. doi:10.1109/pemwa.2012.6316384

Datta, U., Shi, J., Kalam, A., and Li, J. (2020). "DFIG Pitch Angle Control with PID-type Fuzzy Logic Controller in a Microgrid," in 2020 15th IEEE Conference on Industrial Electronics and Applications (ICIEA) (Kristiansand, Norway: IEEE), 258–263. doi:10.1109/iciea48937.2020.9248090

Gao, C. (2014). "An Wind Turbines and Energy Storage Joint Tuning Scheme Applying to High Wind Power Penetration Power Grid," in 2014 International Conference on Power System Technology (Chengdu, China: IEEE), 3046–3051. doi:10.1109/powercon.2014.6993550

Hao, X., Zhou, T., Wang, J., and Yang, X. (2015). "A Hybrid Adaptive Fuzzy Control Strategy for DFIG-Based Wind Turbines with Super-capacitor Energy Storage to Realize Short-Term Grid Frequency Support," in *2015 IEEE Energy Conversion Congress and Exposition (ECCE)* (Montreal, QC, Canada: IEEE), 1914–1918. doi:10.1109/ecce.2015.7309930

Jin, X., Xie, Z., Zhang, X., Niu, L., and Gao, X. (2018). "A Control Strategy for DFIG-Based Wind Turbines Based on the Fulfilment of Virtual Inertia," in 2018 IEEE International Power Electronics and Application Conference and Exposition (PEAC) (Shenzhen, China: IEEE), 1–5. doi:10.1109/peac.2018.8590613

Kurbatova, T., and Perederii, T. (2020). "Global Trends in Renewable Energy Development," in *2020 IEEE KhPI Week on Advanced Technology (KhPIWeek)* (Kharkiv, Ukraine: IEEE), 260–263. doi:10.1109/khpiweek51551.2020.9250098

Li, B., Mo, X., and Chen, B. (2019). Direct Control Strategy of Real-Time Tracking Power Generation Plan for Wind Power and Battery Energy Storage Combined System. *IEEE Access* 7, 147169–147178. doi:10.1109/access.2019.2946453

Li, P., Hu, W., Hu, R., and Chen, Z. (2016). "The Integrated Control Strategy for Primary Frequency Control of DFIGs Based on Virtual Inertia and Pitch Control," in *2016 IEEE Innovative Smart Grid Technologies - Asia (ISGT-Asia)* (Melbourne, VIC, Australia: IEEE), 430–435. doi:10.1109/isgt-asia.2016.7796424

Lin, C.-H., and Wu, Y.-K. (2020). "Overview of Frequency Control Technologies for Wind Power Systems," in *2020 International Symposium on Computer, Consumer and Control (IS3C)* (Taichung City, Taiwan: IEEE), 272–275. doi:10.1109/is3c50286.2020.00077

Liu, Y., Wang, Y., Wang, M., Xu, Z., Peng, Y., and Li, M. (2022). Coordinated VSG Control of Photovoltaic/Battery System for Maximum Power Output and Grid Supporting. *IEEE J. Emerg. Sel. Top. Circuits Syst.* 12 (1), 301–309. doi:10.1109/jetcas.2022.3143716

Miao, L., Wen, J., Xie, H., Yue, C., and Lee, W.-J. (2015). Coordinated Control Strategy of Wind Turbine Generator and Energy Storage Equipment for Frequency Support. *IEEE Trans. Ind. Appl.* 51 (4), 2732–2742. doi:10.1109/tia.2015.2394435

Motamed, B., Chen, P., and Persson, M. (2013). "Comparison of Primary Frequency Support Methods for Wind Turbines," in 2013 IEEE Grenoble Conference (Grenoble, France: IEEE), 1–5. doi:10.1109/ptc.2013.6652357

Sato, T., Asharif, F., Umemura, A., Takahashi, R., and Tamura, J. (2020). "Cooperative Virtual Inertia and Reactive Power Control of PMSG Wind Generator and Battery for Improving Transient Stability of Power System," in 2020 IEEE International Conference on Power and Energy (PECon) (DHAKA, Bangladesh: IEEE), 101–106. doi:10.1109/pecon48942.2020.9314621

Sun, Y., Zhao, Z., Yang, M., Jia, D., Pei, W., and Xu, B. (2020). Overview of Energy Storage in Renewable Energy Power Fluctuation Mitigation. *CSEE J. Power Energy Syst.* 6 (1), 160–173.

Wang, T., Ding, L., Bao, W., and Zheng, J. (2018). "A Novel Deloaded Control Strategy of DFIG Wind Farm," in 2018 13th IEEE Conference on Industrial Electronics and Applications (ICIEA) (Wuhan, China: IEEE), 1681–1685. doi:10.1109/iciea.2018.8397980

Wang, X., and Liu, Y. (2017). "Analysis of Energy Storage Technology and Their Application for Micro Grid," in 2017 International Conference on Computer Technology, Electronics and Communication (ICCTEC) (Dalian, China: IEEE), 972–975. doi:10.1109/icctec.2017.00215

Wu, L., Gao, W., Cui, Z., and Kou, X. (2015). "A Novel Frequency Regulation Strategy with the Application of Energy Storage System for Large Scale Wind Power Integration," in 2015 Seventh Annual IEEE Green Technologies Conference (New Orleans, LA, USA: IEEE), 221–226. doi:10.1109/greentech.2015.34

Xiong, L., Liu, X., Zhang, D., and Liu, Y. (2021). Rapid Power Compensation-Based Frequency Response Strategy for Low-Inertia Power Systems. *IEEE J. Emerg. Sel. Top. Power Electron.* 9 (4), 4500–4513. doi:10.1109/jestpe.2020.3032063

Xu, G., Xu, L., and Morrow, J. (2013). "System Frequency Support Using Wind Turbine Kinetic Energy and Energy Storage System," in 2nd IET Renewable Power Generation Conference (RPG 2013) (Beijing: IEEE), 1–4. doi:10.1049/cp.2013.1812

Yan, N., Li, S., Yan, T., and Ma, S. h. (2020). "Study on the Whole Life Cycle Energy Management Method of Energy Storage System with Risk Correction Control," in 2020 IEEE 4th Conference on Energy Internet and Energy System Integration (EI2) (Wuhan, China: IEEE), 2450–2454. doi:10.1109/ei250167.2020.9346933

Zhang, A. Y., Zhao, C., Low, S., and Tang, W. (2018). "Profit-Maximizing Planning and Control of Battery Energy Storage Systems for Primary Frequency Control," in *2018 IEEE Power & Energy Society General Meeting (PESGM)* (IEEE), 1. doi:10.1109/pesgm.2018.8586290

Zhang, S., Mishra, Y., and Ledwich, G. (2014). "Battery Energy Storage Systems to Improve Power System Frequency Response," in 2014 Australasian Universities Power Engineering Conference (AUPEC) (Perth, WA, Australia: IEEE), 1–5. doi:10.1109/aupec.2014.6966644

Zhao, G., Shi, L., Feng, B., Sun, Y., and Su, Y. (2019). "Development Status and Comprehensive Evaluation Method of Battery Energy Storage Technology in Power System," in 2019 IEEE 3rd Information Technology, Networking, Electronic and Automation Control Conference (ITNEC) (Chengdu, China: IEEE), 2080–2083. doi:10.1109/itnec.2019.8729448

Conflict of Interest: Author ZY was employed by Quant-Cloud Energy Co, Ltd.

The remaining authors declare that the research was conducted in the absence of any commercial or financial relationships that could be construed as a potential conflict of interest.

APPENDIX

TABLE A1 | Parameters of the overall hybrid system.

Parameters	Value	Unit
SG	30	MVA
DFIG-based WTS	1.5	MW
BESS	12.5	kWh
Load1	10	MW
Extra load	1.5	MW
T1	110/35	KV
T2	0.575/35	KV
T3	0.38/35	KV

TABLE A2 | Parameters of the doubly-fed induction generator–based wind turbines.

DFIG-based WTS	Value	Unit
P_n	1.5	MW
V_s	0.575	kV
f_n	50	Hz
Rs	0.023	p.u
L_s	0.18	p.u
R_r	0.016	p.u
L_r	0.16	p.u
L_m	2.9	p.u
H	5.05	s

TABLE A3 | Parameters of the transmission line.

Line	R (Ω/km)	L (H/km)	C (F/km)	Length (km)
Line1	0.1153	0.00105	$11.33*10^{-9}$	20
Line2	0.1153	0.00105	$11.33*10^{-9}$	20

frontiers | Frontiers in Energy Research

TYPE Original Research
PUBLISHED 25 August 2022
DOI 10.3389/fenrg.2022.975319

OPEN ACCESS

EDITED BY
Xue Lyu,
University of Wisconsin-Madison,
United States

REVIEWED BY
Jiayong Li,
Hunan University, China
Kun Wang,
Zhejiang University, China

*CORRESPONDENCE
Bowen Zhou,
zhoubowen@ise.neu.edu.cn

SPECIALTY SECTION
This article was submitted to Smart Grids,
a section of the journal
Frontiers in Energy Research

RECEIVED 22 June 2022
ACCEPTED 01 August 2022
PUBLISHED 25 August 2022

CITATION
Luo Y, Zhang S, Zhou B, Li G, Hu B, Liu Y and Xiao Z (2022), Multi-time scale trading profit model of pumped storage power plant for electricity market. *Front. Energy Res.* 10:975319. doi: 10.3389/fenrg.2022.975319

Multi-time scale trading profit model of pumped storage power plant for electricity market

Yanhong Luo[1,2], Shiwen Zhang[1,2], Bowen Zhou[1,2]*, Guangdi Li[1,2], Bo Hu[3], Yubo Liu[4] and Zhaoxia Xiao[5]

[1]College of Information Science and Engineering, Northeastern University, Shenyang, China, [2]Key Laboratory of Integrated Energy Optimization and Secure Operation of Liaoning Province, (Northeastern University), Shenyang, China, [3]State Grid Liaoning Electric Power Co., Ltd., Shenyang, China, [4]Information and Telecommunication Branch, State Grid Liaoning Electric Power Co., Ltd., Shenyang, China, [5]School of Electrical Engineering, Tiangong University, Tianjin, China

Pumped storage power plant (PSPP) has the upper hand on economy and cleanness. It also has the functions of frequency regulation, phase regulation, and spare, which have been instrumental in maintaining the stability of power system operation. But now the mechanism for PSPP to become involved in electricity market transactions in China is imperfect. How to properly establish a multi-time scale trading profit model and reasonably allocate the capacity of PSPP has been instrumental in realizing the economic operation of the power system. So, this article analyzes the mechanism for PSPP to become involved in electricity market trading by providing combined electricity supply services and ancillary services, and establishes an optimization model with respect to economic optimization. At the same time, considering the volatility of electricity prices in the spot market, the risk of PSPP becoming involved in electricity market trading is measured by conditional Value at Risk (CVaR) to achieve economic optimization while minimizing the risk. The case studies demonstrate that the proposed profit model can enhance the revenue and decrease the risk of PPSP.

KEYWORDS

cost-benefit analysis, power markets, risk analysis, energy storage, multi-time scale

1 Introduction

Since the transitional burning of fossil fuels has led to global warming, reducing greenhouse gas emissions has become an urgent problem (Luka et al., 2017). However, at present, power generation in China's power industry is still dominated by thermal power, it is particularly important to replace traditional thermal power with clean energy power generation. And accelerating the construction of a new type of power system based on clean energy, so as to achieve the objective of carbon peaking and carbon neutrality (Yang et al., 2021). However, on the one hand, the prediction of the amount of clean energy generation is difficult, such as wind power is severely affected by wind and is highly random; on the other hand, when transmission lines are congested or underloaded, excessive clean energy generation will be cut, leading to energy waste and low utilization

(Guo et al., 2021). Therefore, energy storage is particularly important for power systems containing clean energy, energy storage not only can enhance the utilization of clean energy but also increase the dependability of electricity supply (Pang et al., 2021).

PSPP is considered to be a good solution for energy storage units. Firstly, Pumped storage does not emit carbon dioxide when generating electricity as a clean energy source. Secondly, the high flexibility of PSPP dispatch has a significant effect on the constant operation of the power system. Thus, with the further advancement of green energy generation, the role of the PSPP will become more important in the power system (Jahns et al., 2020).

However, because China's electricity market is not mature enough, it is tough for PSPP to recover its costs by making profits only based on the difference between peak and valley electricity prices. Therefore, various scholars have studied the cost recovery and benefits situation of PSPP. Masoumzadeh et al. (2018) pointed out that the current cost of PSPP is comparatively high, but government support and decreasing technology costs could create conditions for full-scale adoption of PSPP in the electricity market. Julian et al. (2020) proposed a combination of long-term and short-term cycles for pumped storage power plants, which greatly reduces the cost of pumped storage power plants, but this combination requires strict requirements for the construction location of pumped storage power plants and the surrounding theoretical environment. Zhao et al., 2021 used the cooperative game approach to share the cost of auxiliary services of pumped storage power plants and develop a compensation mechanism for auxiliary services, but in their study, they mainly focused on peak-shaving auxiliary services only, and the remaining several auxiliary services were not fully considered. Sospiro et al. (2021) mainly consider the environmental and social aspects of pumped storage plants and focus on the environmental aspects of the auxiliary services of pumped storage plants, but do not consider the cost recovery of pumped storage itself. However, the cost reclaim mechanism and revenue mechanism of PSPP studied by most scholars nowadays are not perfect, and most of them only share the cost for a single ancillary service, which cannot give full play to the profitability of each ancillary service of PSPP, making it difficult for PSPP to obtain considerable revenue.

Moreover, the current electricity price mechanism is not sufficient and the fluctuation of electricity price is random, which has a certain impact on the economic, stable and efficient operation of PSPP. Li et al. (2022) proposed a two-part tariff for pumped storage plants to promote wind power consumption, but the pricing mechanism is not very different from the traditional two-part tariff, and the role of the ancillary services market is not considered in the trading process. Lazar et al. (2020) analyze the role of peaking services of pumped storage power plants on the power system and analyze the uncertain relationship between tariff difference and revenue, but only the time-of-use tariff of pumped storage power plants is considered, so the tariff mechanism is single. He et al. (2022) designed a two-part tariff mechanism for different stages of pumped storage power plants to enable pumped storage plants to earn significant revenues, but did not consider pumped storage as an independent trading entity and considered only peaking auxiliary services. AK et al. (2019) propose a situational method to work out the return of PSPP by considering the volatility of electricity prices and using historical electricity prices. And Koko et al. (2018) improved the current time-of-use Pricing (TOU) by dividing the TOU into a weekday TOU and a weekend TOU. By treating weekday TOU and weekend TOU as variables, the consumption cost of residential customers at different times is effectively reduced. However, most of the current studies on pumped storage electricity tariff mechanisms only involve a single unit price, like TOU and double-stage tariff, without combining different tariff mechanisms.

PSPP not only faces the challenge of imperfect tariff mechanisms but also the challenge of the imperfect electricity market. Most studies have been conducted mainly for a single electricity market. Zejneba et al. (2022) compared the benefits between pumped storage plants and battery storage and demonstrated that pumped storage is the most efficient energy storage technology available. However, only energy arbitrage returns were considered when comparing the two, without diversifying to consider returns in other markets. Rodica and Corentin, (2021)analyze the energy and capacity benefits of pumped storage plants and propose the type of contract that mixes capacity and energy, but it can only be applied to competitive electricity markets and does not adequately consider the ancillary service benefits of pumped storage plants. Huang et al. (2022) introduced pumped storage into the Midcontinent Independent System Operator (MISO) day-ahead market in combination with other units to improve the flexibility of MISO day-ahead market dispatch and to improve the system economics through pumped storage. Luo et al. (2020) considered the impact of the pollutant trading market on system economics while considering the optimal economics of multi-energy systems. The pollutant emissions are reduced while achieving the optimal system economy. In addition to studies considering only a single electricity market, some scholars have also studied multiple electricity markets. Mosquera-Lopez and Nursimulu (2019) contrasted the price drivers of the spot and medium- and long-term market (MLTM), concluding that the determinants of the spot market were renewable energy and electricity demand, while the determinants of MLTM are the prices of natural gas as well as coal. Zhu et al. (2021) researched the mixed electricity market, extended the definition of the mixed electricity market, and compared and analyzed two different contract decision models of shared contract and wholesale price contract to study the pricing strategy of clean energy grid connection. Parinaz et al. (2022) transformed the terraced

hydro plants into pumped storage plants to achieve enhanced returns but did not consider the transformation costs and medium- and long-term market transactions in the process. Mou (2019) proposed to use the spot market to make up for the defect of the two-sided market as well as combine different ancillary service trading models to obtain more profitability for PSPP. However, it did not consider the potential revenue of ancillary services, which led to the underestimation of the revenue of PSPP. In a summary, the current research on multiple electricity markets is not sufficient, and most of them only consider the research on the single spot market, and the research on competitive bidding in the multi-time scale electricity market is less. At the same time, there is less research on the ancillary service market of PSPP, which does not effectively leverage the ancillary services of PSPP to increase revenue. Thus, there is a need to further improve the electricity market mechanism to achieve a reasonable allocation of resources for PSPP, to obtain higher revenue.

At the same time, with the gradual opening and improvement of the electricity market, different bidding strategies will bring different levels of risk, and the relationship between the balance of risk and its economic benefits should also be addressed. Li et al. (2021) proposed a p-robust algorithm to calculate the risk caused by the uncertainty of electricity price on the revenue of pumped storage power plants, but it needs to sacrifice part of the profit while reducing the risk of pumped storage revenue. Luo et al. (2021) considered the uncertainty of distributed energy sources and the role of energy storage devices on multiple time scales to optimize the operation of the electric grid. Yang et al. (2020) proposed a demand response model of energy storage operators to take part in the MLTM to reduce the uncertainty risk while lowering the power purchase cost for operators through flexible energy storage systems. Liu et al. (2021) considered the randomness and volatility of wind power in multiple microgrids and established a random planning model, which provided a strategy for the balance of benefits and risks. Tian et al. (2020) put forward a bidding method to avoid risks for PSPP, which reduces the risk of participating in the market through downside risk constraints. Gao et al. (2019) used the conditional value at risk (CVaR) theory to study the uncertainty of virtual power plant (VPP) market prices and proposed a bi-level model to optimize the operating strategies in the day-ahead and real-time markets. Canakoglu and Adiyeke, (2020) proposed a variety of pricing models for power products based on price uncertainty. The portfolio problem of mean-square optimization and conditional Value at Risk was solved by combining price forecasting and risk management. From above discussion, it can be concluded that there are few studies on the balance between return and risk for PSPP, and most of the studies on PSPP only consider the maximization of power plant return and ignore the risk caused by the volatility of electricity prices. Therefore, how to balance the relationship between return and risk is crucial for PSPP.

Considering the above problems, this article improves from the following aspects:

1) In the study of spot market trading of PSPP, the actual called rotating reserve capacity is considered to complement the power revenue and increase the total revenue of PSPP participating in the spot market, and the impact of different called price factors on the revenue of PSPP is analyzed.
2) Combining the electricity supply services and ancillary services, the trading mechanism of PSPP participating in the MLTM and the spot market is proposed, and an optimization model with respect to economic optimality is established, and compared it with the current double-stage tariff mechanism in my country to prove that ancillary services are of great significance to the cost recovery of PSPP.
3) Considering the volatility of electrovalence in the spot market, the risk of PSPP taking part in the electricity market is measured by CVaR to achieve economic optimization while minimizing the risk, and the validity of the model is proved through comparative analysis.

The rest of the article is shown below. Section 2 discusses the tariff mechanism of PSPP. Afterward, Section 3 proposes a profit model for PSPP. Next, Section 4 verifies the validity of the model through example analysis. Finally, Section 5 summarises this article.

2 Electricity price mechanism of pumped storage power plant

At present, the electricity price mechanism of PSPP in China is mainly TOU and double-stage tariff.

2.1 Time-of-use

The TOU refers to the cost of charging electricity for each period according to the average marginal cost of system operation. The periods are from the division of a 24-h day according to the system operation condition (Zhao et al., 2022). Further improving the TOU, especially reasonably widening the price difference between peak and valley tariffs, is conducive to PSPP to obtain higher electric energy returns, and to create more space for the development of PSPP, thus further helping new energy accommodation.

2.2 Double-stage tariff

The double-stage tariff is a method that combines the basic tariff corresponding to the capacity and the electricity

tariff corresponding to the electricity consumption to determine the tariff (Tan et al., 2021). When the double-stage tariff is applied, it can reflect the benefits of PSPP in all aspects. On the one hand, the electricity tariff reflects the basic operation mode of PSPP using the peak-to-valley price difference, and on the other hand, the capacity tariff reflects the multiple values of the ancillary services of PSPP such as peak-shaving and backup, which has an important impact on improving the benefits of PSPP.

3 Profit model of pumped storage power plant

In the electricity market environment, PSPP can provide multiple types of products in MLTM and spot market due to their superior performance. For example, electric energy products and ancillary service products include spinning reserve, black start, and so on. PSPP can reveal the value of its own power and capacity by taking part in the electricity market bidding and gain considerable profits.

3.1 Profit of pumped storage power plant taking part in the spot market

In this article, the profit of PSPP included electric energy spot market profit and spot profit from ancillary services. In the electric energy spot market, PSPP can earn revenue by purchasing and selling electricity at different times using the peak-to-valley difference. In the spot market for ancillary services, PSPP can generate profits through rapid start-up or rapid change in operating conditions and playing a standby role.

The profit model of PSPP taking part in the spot market is as (1).

$$F_1 = \sum_{i=1}^{24} \sum_{\omega=1}^{N_\omega} \pi_\omega \cdot \left(\delta_i p_i^{e,s} q_i^{e,s} - (1-\delta_i) p_i^{buy} q_i^{buy} + \delta_i \left(p_i^{c,s} q_i^{c,s} + p_i^{c,s'} q_i^{c,s'} \right) \right) \tag{1}$$

where, π_ω is the probability of various typical electricity price scenarios; δ_i is the working state of the PSPP, including pumping and power generation, the pumping state is represented by 0, and the power generation state is represented by 1; $p_i^{e,s}$ is the feed-in price of PSPP in the ith time period; $q_i^{e,s}$ is the on-grid energy of PSPP in the ith time period; p_i^{buy} is the purchased price of PSPP in the ith time period, because PSPP purchases electricity from the power grid as a large user, considering the usage fee of the power grid, the purchased price of PSPP in the same period should be higher than the on-grid electricity price, so the purchased price of PSPP is 1.1 times the on-grid electricity price.; q_i^{buy} is the amount of electricity purchased of PSPP in the ith time period; $q_i^{c,s}$ is the spinning reserve capacity; $p_i^{c,s}$ is the electricity price of spinning reserve capacity in the ith time period; $q_i^{c,s'}$ is the actual called spinning reserve capacity in the ith time period; $p_i^{c,s'}$ is the electricity price of the actual called spinning reserve capacity in the ith time period.

3.2 Price uncertainty in pumped storage power plant market based on conditional value at risk

Since the uncertainty of electricity prices in the spot market effect on the bidding strategy of PSPP, this paper measures the risk because of the uncertainty of electrovalence in the spot market by applying the conditional value at risk (CVaR) (do Prado and Chikezie, 2021). The specific expressions are as (2).

$$X_{CVaR} = X_{VaR} - \frac{1}{1-\alpha} \sum_{\omega=1}^{N_\omega} \pi_\omega [F_1 - X_{VaR}]^+ \tag{2}$$

where, X_{VaR} denotes the VaR; $[F_1 - X_{VaR}]^+$ is the difference between the spot market return and the VaR; α is the confidence level.

3.3 Profit of pumped storage participation in medium- and long-term market

The profits of PSPP participating in MLTM are divided into profits of electric energy and profits of ancillary services. PSPP obtain profits of electric energy from signing MLTM contracts for the provision of electricity, and obtain profits of ancillary services from the black-start ancillary service provided.

Since the time scale of MLTM and the spot market are different, it is necessary to decompose MLTM electric energy. In this paper, the daily power decomposition curve is selected from the peak and flat curve model: the day is divided into peak, flat and valley sections, which can be negotiated by the historical load characteristics of PSPP or other ways to determine the peak, flat and valley load power.

The profit model of PSPP taking part in MLTM is as (3).

$$F_2 = \sum_{i=1}^{24} p_i^{e,f} q_i^{e,f} + p_h t_h \Big/ 365 \tag{3}$$

where, $p_i^{e,f}$ is electricity prices of MLTM contracts, $q_i^{e,f}$ is the daily decomposition electricity of PSPP in the ith time period; p_h is the black start service fee provided by PSPP; t_h is the annual black start service time of PSPP.

3.4 Cost model of pumped storage power plant

In addition to considering the power purchase cost of PSPP in the spot market, this paper also considers the start-up and stop-up cost of PSPP and the deviation cost of decomposing electricity in MLTM.

The cost model of the PSPP is as (4).

$$C = C_s + C_o \tag{4}$$

where, C_s is the start-up and shutdown cost; C_o is the deviation cost of decomposing electricity in MLTM.

The start-up and shutdown cost C_s represents the total start-up and shutdown cost of PSPP in 1 day.

$$C_s = \sum_{i=1}^{24} C_{qt} n_i^{qt} \tag{5}$$

where, C_{qt} refers to the start-up and shutdown cost of a single unit; n_i^{qt} is the number of units started/stopped in the ith time period.

The deviation cost C_o refers to the cost caused by the difference between the actual decomposed electricity and the planned decomposed electricity of PSPP.

$$C_o = M \sum_{i=1}^{24} \Delta\omega_i \tag{6}$$

where, $\Delta\omega_i$ is the electricity deviation of MLTM electricity decomposition in the ith time period; M is the electricity deviation penalty factor.

3.5 Profit model of pumped storage power plant

The objective function consists of four terms.

$$F = max\left(F_1 + F_2 - C + \beta \cdot X_{CVaR}\right) \tag{7}$$

where, the first term is the profit of PSPP in the spot market; the second term is the profit of PSPP in MLTM; the third term is the cost model of PSPP; the last term is the product of the conditional VaR X_{CVaR} and the risk preference coefficient β. The risk appetite coefficient β indicates the degree of the risk.

3.6 Constraints

3.6.1 Output constraints

$$q_{min} \le q_i^{e,s} \le q_{max} \tag{8}$$

$$q_{min} \le q_i^{c,s} \le q_{max} \tag{9}$$

$$q_{min} \le q_i^{buy} \le q_{max} \tag{10}$$

$$q_{min} \le q_i^{e,f} \le q_{max} \tag{11}$$

$$q_{min} \le q_i^{e,s} + q_i^{c,s} + q_i^{buy} + q_i^{e,f} \le q_{max} \tag{12}$$

$$q_i^{c,s'} \le q_i^{c,s} \tag{13}$$

where, q_{min} is the minimum allowable generation/pumping power for each time period; q_{max} is the maximum allowable generation/pumping power for each time period.

3.6.2 Maximum continuous pumping and power generation time constraints

$$T_1 \le T_p \tag{14}$$

$$T_2 \le T_g \tag{15}$$

where, T_1 is the continuous pumping time variable and T_2 is the continuous power generation time variable; T_p is the maximum allowable continuous pumping time; and T_g is the maximum allowable continuous power generation time.

3.6.3 Reservoir capacity constraints

$$x_{min} \le x_i \le x_{max} \tag{16}$$

$$x_i = x_{i-1} + \lambda \quad (1 - \delta_i) q_i^{buy} - \delta_i \left(q_i^{e,s} + q_i^{c,s}\right) \tag{17}$$

where, x_i is the reservoir capacity converted to power generation in the ith time period; x_{max} is the equivalent power generation of maximum reservoir capacity; x_{min} is the equivalent generating capacity of minimum reservoir capacity; λ is the total efficiency of PSPP power generation, taken as 75%.

3.6.4 Outbound flow constraints

$$Q_{i,min} \le Q_i \le Q_{i,max} \tag{18}$$

where, $Q_{i,min}$ is the minimum discharge flow allowed in the ith time period of PSPP; Q_i is the average discharge flow in the ith time period of PSPP; $Q_{i,max}$ is the maximum discharge flow allowed in the ith time period of PSPP.

3.6.5 Spinning reserve market constraints

$$q_i^{c,s'} = k_{c,s} q_i^{c,s} \tag{19}$$

$$p_i^{c,s'} = k_i p_i^{e,s} \tag{20}$$

The actual called spinning reserve capacity is only part of the bidded spinning reserve capacity, and because the actually called spinning reserve capacity cannot be accurately predicted. Thus, a factor $k_{c,s}$ is set to indicate the proportion of the actual called capacity to the bidded capacity. k_i is the price factor of the called

TABLE 1 Actual parameters of PSPP.

Parameters	q_{min}	q_{max}	T_1	T_2	x_{min}	x_{max}	x_0	Conversion efficiency	Number of units
Numerical value	0	2400 MW h	8 h	6 h	0	18400 MW h	0	0.75	4

capacity in the spinning reserve market, indicating that the price of the called capacity in the ith time period is k_i times of the on-grid electricity price in the same period.

3.6.6 The conditional value at risk correlation constraints

CVaR represents the profit of PSPP in changes of the electricity market under certain time and confidence conditions. And the higher the value of CVaR, the lower the risk.

$$X_{VaR} - \sum_{i=1}^{I}\sum_{\omega=1}^{N_\omega} \pi_\omega \cdot F_1 \le [F_1 - X_{VaR}]^+ \tag{21}$$

$$[F_1 - X_{VaR}]^+ \ge 0 \tag{22}$$

where, X_{VaR} denotes the VaR; $[F_1 - X_{VaR}]^+$ is the difference between the spot market return and the VaR.

3.6.7 Daily decomposition electricity constraints

$$q_{i,min}^{e,f} \le q_i^{e,f} \le q_{i,max}^{e,f} \tag{23}$$

$$q_i = q_i^{e,f} + q_i^{e,s} + q_i^{c,s} \tag{24}$$

$$C_i = \sum_{x\in X} c_{x,i}, X = \{p, f, v\} \tag{25}$$

$$c_{x,i} = \gamma_x C_i = \sum_{t\in T_x} q_i^c \Delta T \tag{26}$$

where, $q_{i,max}^{e,f}$ and $q_{i,min}^{e,f}$ are the upper and lower limits of daily decomposition electricity of the unit, which are determined according to the technical parameters of the unit, contract completion and maintenance plan; q_i is the total output in the ith time period of PSPP; C_i is the daily contracted electricity of PSPP; p,f and v represent peak, flat, and valley hours, respectively; $c_{x,i}$ is the contracted electricity in the ith time period of PSPP; T_x is the set of time period indicators included in the ith time period; γ_x is the proportion of the decomposition electricity in the ith time period of PSPP to the contracted electricity. ΔT refers to a certain time period in T_x; q_i^c refers to the decomposition electricity of ΔT.

4 Case studies

This paper uses the CPLEX solver on the MATLAB software platform to solve the established multi-time scale profit model and derive the optimization results.

4.1 Pumped storage power plant taking part in the spot electricity energy market only

When PSPP only participates in the spot market bidding, only the spot market part of the profit model is considered, MLTM and ancillary service market parts are not considered, and the offset cost of MLTM power decomposition is not considered. The parameters of a typical PSPP are shown in Table 1.

Two sets of electricity price scenarios are determined to research the profits of PSPP under different electricity tariff scenarios. The different electricity tariff scenarios are shown in Figure 1.

Scenario 1: The market demand for electricity is large, the electricity supply is insufficient, and the price difference between peak and valley is large.
Scenario 2: A small market demand for electricity, with sufficient power supply and a low peak-to-valley price difference.

The profits of PSPP under the two scenarios are shown in Table 2. The operation of PSPP under scenario 1 is shown in Figure 2.

As can be seen in Figure 2, PSPP pump during the low tariff hours of 0:00–8:00 and 13:00–14:00, and sell electricity online during the peak tariff hours of 9:00–11:00, 15:00–16:00, and 21:00–23:00, using the difference between peak and valley tariffs to obtain the power revenue.

From Table 2 it can be obtained that there is a positive correlation between the profit of PSPP and the peak-to-valley electricity price difference. When the peak-to-valley electricity price difference is high, the profit of PSPP is high, and vice versa. This is because PSPP relies on the peak-to-valley electricity price difference to earn the profit, purchasing electricity for pumping at low prices and selling it at high prices.

According to the static investment of PSPP of 4,500 CNY/kW per unit kilowatt and the capital internal rate of return of 8%, the capacity tariff is 685 CNY/kW, which translates into a daily capacity profit of 4,505,100 CNY. Therefore, PSPP cannot rely on the spot market alone to recover costs and gain more profit, but also need to participate in the ancillary service market bidding and MLTM bidding.

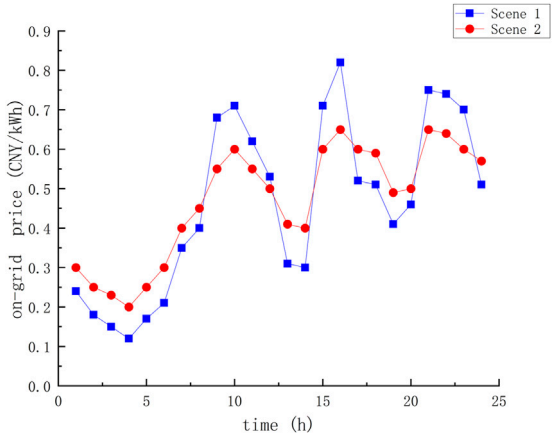

FIGURE 1
Two scenarios of electricity tariff.

4.2 Pumped storage power plant taking part in both the electric energy and ancillary services spot market

The profit obtained when a PSPP taking part in the ancillary services market is related to two aspects. On the one hand, the capacity tariff in the ancillary services market and, on the other hand, the tariff coefficient in the ancillary services market. This section still takes the example of a domestic PSPP in Section 4.1, and the specific parameters remain the same. Take $k_{c,s} = 0.1$, $k_i = 2$, $c_i = 0.15$ CNY/kWh.

Considering the uncertainty of electricity prices, ten typical electricity price scenarios are generated as shown in Figure 3. The corresponding probabilities of each electricity price scenario are shown in Table 3. Scenario 1 and Scenario 2 are typical scenarios in Section 4.1. In this section, three typical electricity price scenarios with the highest probability are selected for comparative analysis. The selected scenarios are scenario 1, scenario 2 and scenario 7, the corresponding optimal daily operation mode is shown in Figures 4, 5, 6.

It can be seen from Figures 4, 5, 6 that PSPP mainly purchases electricity during the early morning valley hours of 1:00–7:00 and sell electricity during the peak hours of 9:00–11:00, 15:00–17:00 and 21:00–23:00 to recover costs through the peak-to-valley tariff difference. Meanwhile, PSPP mainly provide rotating backup services at 8:00–12:00 and 15:00–24:00 to achieve PSPP cost recovery. The total returns of the three typical scenarios were respectively 8,954,200 CNY, 7,635,100CNY and 8,126,410CNY. It can be seen that taking part in both the ancillary service spot market bidding and the electric energy spot market bidding can recover the cost of PSPP and obtain more profits. And through comparison, it can be found that the more PSPP participating in the auxiliary service market, the higher the income will be.

4.3 Comparison with a single double-stage tariff

Combined with the electricity consumption characteristics of the provincial grid where PSPP is located, the peak and valley hours on the power generation side are divided as follows: peak hours: 9:00–16:00, flat hours: 17:00–24:00, valley hours: 0:00–8:00; the tariff for flat hours is 0.44 CNY/kWh, the tariff for valley hours is 0.24 CNY/kWh, and the tariff for peak hours is 0.59 CNY/kWh. The actual capacity profit of PSPP is about 931 million CNY per year, which translates into a capacity tariff of 388.73 CNY/kWh, while the theoretical capacity tariff should reach 685 CNY/kWh based on the capital internal rate of return of 8%. Therefore, the current profit of PSPP is low, and the specific double-stage tariff scheme is shown in Table 4.

The profit of pumped storage under the double-stage tariff is compared with the profit of pumped storage under the multi-electricity market environment in Section 4.2. To ensure the accuracy of the comparison results, the tariff under the electricity market conditions is set according to the TOU in the double-stage tariff case, and the results are shown in Table 5.

As can be seen from Table 5, the market return on electricity energy under the electricity market bidding is lower than the return on electricity under the single double-stage tariff. In contrast, the ancillary service profit under the electricity market tariff is more than twice as high as the capacity profit under the single double-stage tariff, making the total profit higher than the total profit under the single double-stage tariff. The comparison shows that the capacity cost recovery of PSPP in the electricity market environment is not enough to rely on the power profit alone, and the level of profit in the ancillary services market has an important impact on the cost recovery of PSPP.

TABLE 2 Comparison of profit of PSPP under different scenarios.

	Peak and valley tariff difference (CNY/kWh)	Revenue (million CNY)
Scenario 1	0.7	399.5
Scenario 2	0.45	150.13

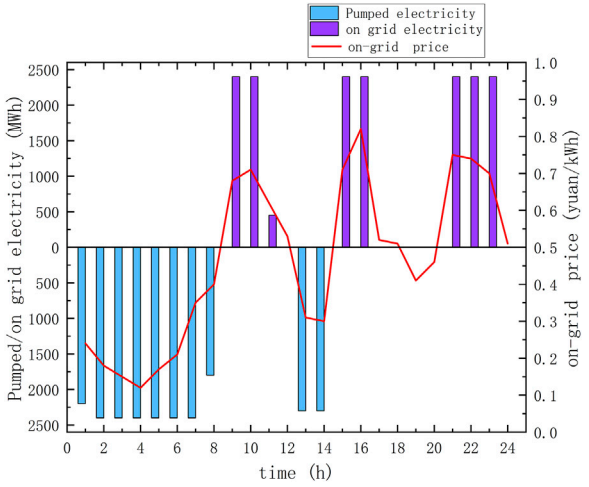

FIGURE 2
Optimal operation of PSPP that only participate in the electric energy spot market in scenario 1.

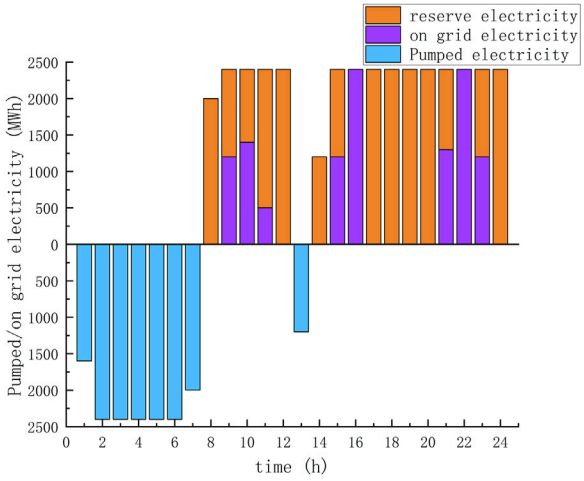

FIGURE 4
Optimal operation of PSPP that both participate in electric energy and ancillary services spot market in scenario 1.

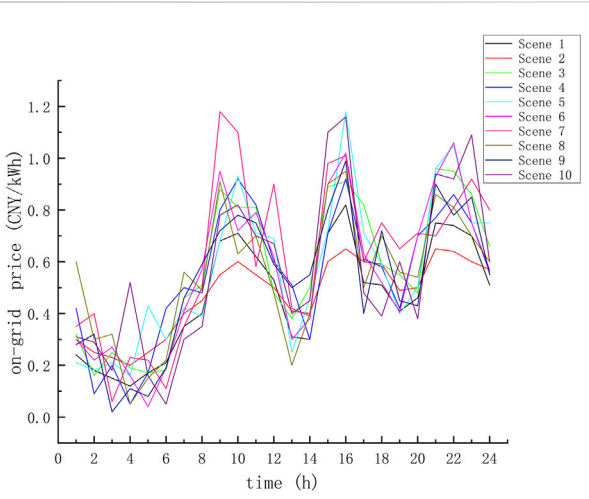

FIGURE 3
Ten typical electricity price scenarios.

4.4 Pumped storage power plant taking part in medium- and long-term market bidding and spot market bidding

When PSPP takes part in both MLTM and the spot market, they need to break down MLTM power into the spot market and reasonably allocate it with the spot market capacity to obtain considerable profit. Firstly, the monthly contract of PSPP is decomposed to each day, and then the 24-h decomposition is adopted day ahead, and the contracted power corresponding to the output in the whole optimization cycle can be provided to the trading center as the result of contract decomposition. Conventional medium- and long-term decomposition curves include the following: Daily average decomposition, Peak-period decomposition, Normal-period decomposition, Valley-period decomposition, and Peak-valley-normal period decomposition (Wu et al., 2022). The pumped storage plant in the example of this paper adopts Peak-valley-normal period decomposition The

TABLE 3 Probability of ten electricity price scenarios.

Scenario	1	2	3	4	5	6	7	8	9	10
probability	0.151	0.127	0.098	0.089	0.067	0.097	0.119	0.070	0.087	0.095

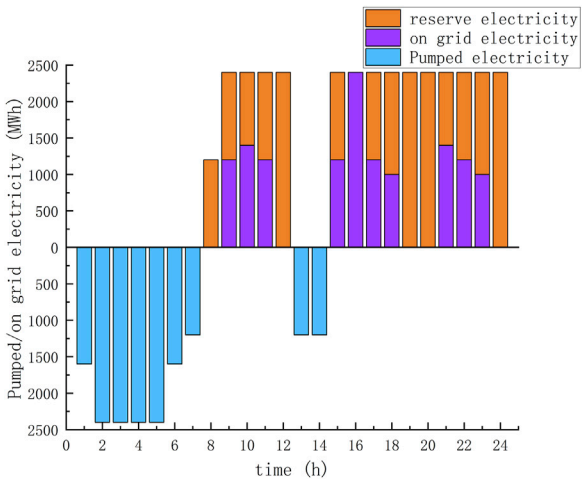

FIGURE 5
Optimal operation of PSPP that both participate in electric energy and ancillary services spot market in scenario 2.

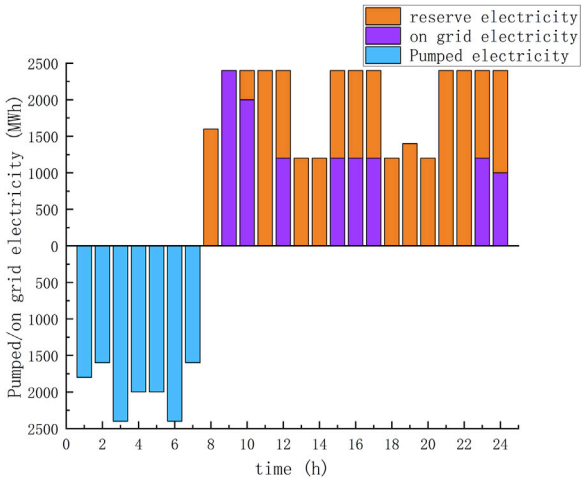

FIGURE 6
Optimal operation of PSPP that both participate in electric energy and ancillary services spot market in scenario 7.

daily power decomposition is carried out by determining the ratio of peak, flat and valley load segments according to the historical load, and its typical daily decomposition curve is shown in Figure 7.

From Figure 7, PSPP suppresses the volatility of spot electricity prices by decomposing medium- and long-term contracted electricity on a time-by-time basis and replacing part of the spot electricity. Meanwhile, the profit of PSPP included three components. The first component is the profit from PSPP taking part in the spot market. The additional profit of MLTM contracts to damp fluctuations in spot electricity prices is expressed through MLTM contracted electricity prices minus the product of the electricity prices for each period in the spot market and MLTM decomposition to spot. The third component is the benefit of PSPP providing black-start services in MLTM. MLTM contract tariff for PSPP is 0.55CNY/kWh, the annual black-start service of PSPP is shown in Table 6, and MLTM decomposition of the power output is shown in Figure 8.

At this point, the total profit of PSPP is 13.625 million CNY, which is significantly improved compared with the profit of participation in the spot market alone, while also smoothing out the risk caused by the randomness of the spot electricity price. The joint bidding strategy of the MLTM and spot market is obtained through the daily contract decomposition curve, which verifies the rationality and effectiveness of the model.

4.5 Impact of risk preference coefficients on returns

Because the risk in this paper only considers the risk caused by the volatility of electricity prices in the spot market, in order to compare the impact of different risk preference coefficient settings on the profit of PSPP, this section only uses the example in Section 4.2 as a reference and does not consider the impact of MLTM on PSPP, and calculates the expected profit and CVaR values of PSPP under different risk preference coefficients. The results are shown in Figure 9.

It can be seen that as the risk preference coefficient increases, the expected total profit gradually decreases and the CVaR gradually increases, at which time a higher capacity price and

TABLE 4 Scheme of double-stage tariff.

Capacity tariff		Amount	Unit
		388.73	CNY/kWh
Energy price	Peak hours	0.59	CNY/kWh
	Flat hours	0.44	CNY/kWh
	Valley hours	0.24	CNY/kWh

TABLE 5 Profit of PSPP under different electricity tariff schemes.

	Double-stage tariff		Electricity market bidding	
	Electricity profit	Capacity profit	Electric energy market profit	Ancillary services market profit
Revenue (million CNY)	201.56	255.95	161.95	463.56
Total revenue (million CNY)	457.51		625.51	

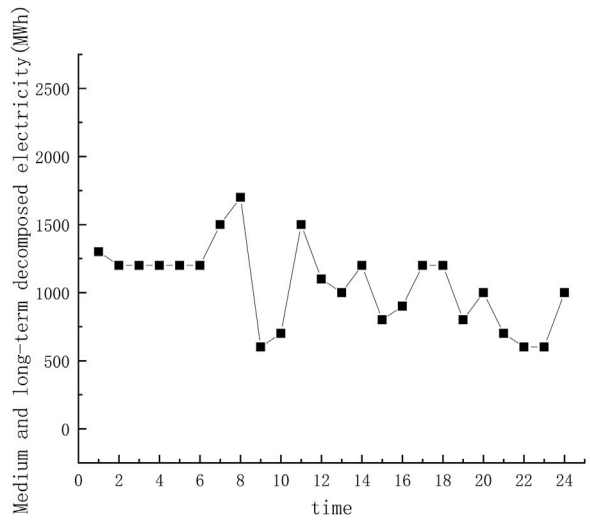

FIGURE 7
Time share power curve for daily contracts.

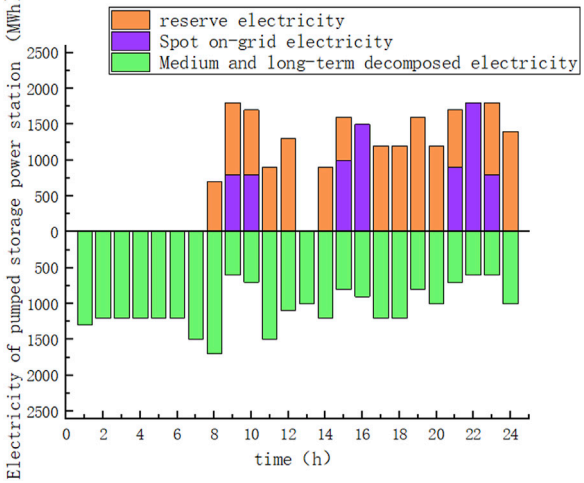

FIGURE 8
MLTM decomposition of PSPP output.

TABLE 6 Black-start service for PSPP.

Annual black-start time of a PSPP (min)	Black start service cost
43200	60000 CNY/h

price coefficient of the called electricity is required to complete the cost-benefit recovery. When the risk preference coefficient is small, the expected total profit decreases slowly with the increase of CVaR. However, when the risk preference coefficient is large, the expected total profit decreases significantly even if the CVaR increases by a small value.

4.5.1 β = 10

When $\beta = 10$, PSPP is extremely risk-averse and will adopt a very conservative strategy at this time, and its most profitable daily operation mode is shown in Figure 10.

Compared with the operation mode at $\beta = 1$, it can be seen that at this time, for the purpose of reducing the risk and increasing the profit expectation of the tail, PSPP tends to take part more in the spinning reserve market to earn capacity profit for the power extracted during the low period, so as to reduce the risk brought by the uncertainty of electrovalence. At this time, the total profit is 8,315,000 CNY, which is slightly lower than that at $\beta = 1$ in Section 4.2. However, the risk is also relatively low. At the same time, reducing the amount and frequency of pumping during the low period reduces the losses of PSPP, which is beneficial to prolong the life of the unit.

4.5.2 β = 0

When $\beta = 0$, PSPP only aims at the maximum expected profit and will adopt a more aggressive strategy, which will have a greater impact on the stable profit of PSPP. At this time, PSPP can participate in the bidding of the day-ahead electricity market and the spinning reserve market, respectively, with a fixed percentage all the time, which can buffer the risk to a certain extent.

Assume that the percentage of pumped storage participating in the day-ahead electricity market is in the range of 10%–90%,

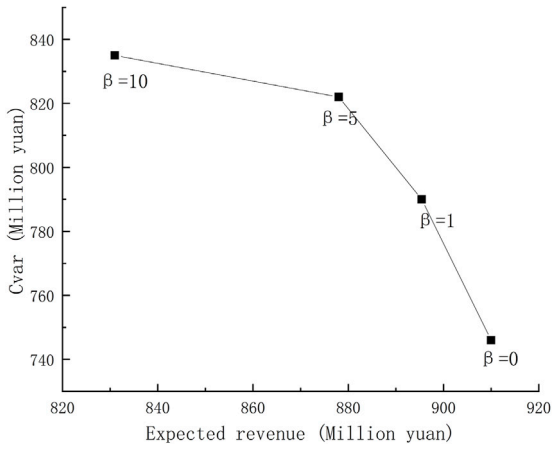

FIGURE 9
Expected profits of PSPP under different risk preferences.

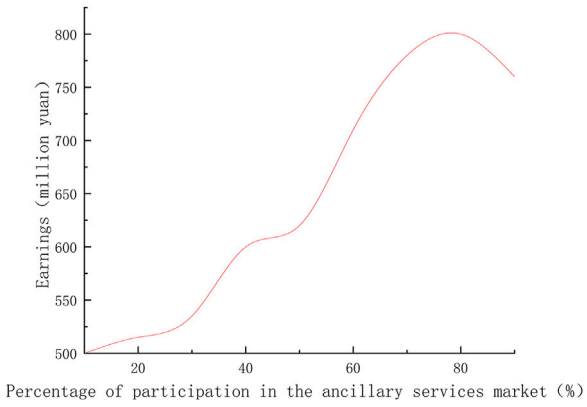

FIGURE 11
The profit of PSPP when the price coefficient of the transferred power is 1.1.

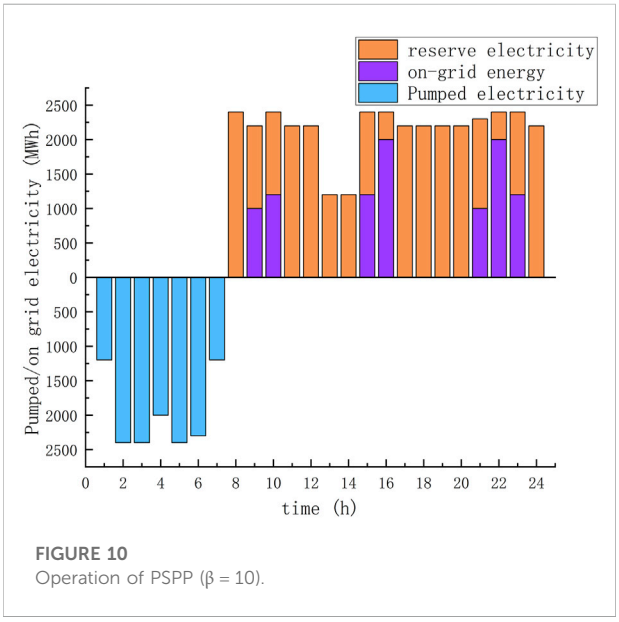

FIGURE 10
Operation of PSPP (β = 10).

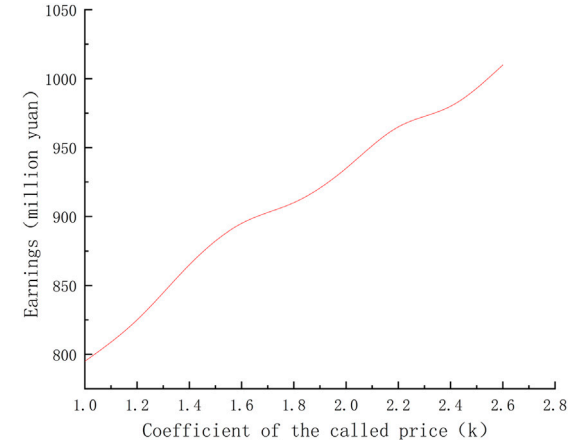

FIGURE 12
PSPP revenue when participating in 80% of the ancillary services market.

and at the same time, assume that the price of the transferred power in the spinning reserve capacity is fixed in the electricity market environment, i.e., k is taken as 1.1. The profit of PSPP at this time is shown in Figure 11.

From Figure 11, it can be seen that when PSPP participates in the ancillary service market with a proportion of 80%, PSPP can obtain a maximum profit. Because the electric energy income obtained by PSPP only through a single peak-to-valley electricity price difference is limited, and the provision of ancillary services is the main way for PSPP to improve its own income. b. In the actual electricity market environment, the price of the transferred power in the spinning reserve capacity will also change with the change of supply and demand. However, it will be greater than the feed-in tariff in the day-ahead electricity market. Thus, the price coefficient of the transferred power in the spinning reserve market is chosen to range from 1 to 3, and the percentage of PSPP participating in the spot market is tentatively set at 80%. The change of PSPP profit with the change of price coefficient is shown in Figure 12.

It can be seen from Figure 12 that theoretically, the greater the price coefficient of the transferred electricity, the more profit of the PSPP. However, in practice, it is necessary to consider the real market situation, when the price of the ancillary services provided by PSPP is higher, the capacity of the ancillary services sold will be lower, and the profit of PSPP will also be lower. Thus, it is necessary to set the price coefficient of the called electricity reasonably.

5 Conclusion

In this paper, the trading mechanism of PSPP in the MLTM and spot market are analyzed. The participation of PSPP in the multi-time scale electricity market is considered, by combining energy and ancillary services. A profit model with respect to optimal economy and lowest risk is established to achieve a reasonable capacity allocation of PSPP in the multi-time scale electricity market.

(1) When PSPP participates in the spot market, it gains energy through the peak-to-valley price difference. The total profit is 3,995,000 CNY when the peak-to-valley price is 0.7 CNY/kWh and 1,501,300 CNY when the peak-to-valley price is 0.45 CNY/kWh. For every 1% decrease in peak-to-valley tariff difference, the total profit from PSPP decreases by 2.5%. When PSPP takes part in both the spot market and the ancillary service market, the total profit is 8,954,200 CNY, which is more profitable than the single participation in the spot market, and the recovery of the cost of PSPP can be achieved through reasonable participation in the ancillary service market.
(2) Since the volatility of real-time electricity prices can have an impact on the profit of pumped storage, different PSPPs have different risk preferences, and the expected total profit of PSPP gradually decreases while the CVaR gradually increases, when the risk preference coefficient increases. The profit of PSPPs under different risk preference coefficients is analyzed to provide a power allocation scheme for PSPPs with different risk preferences.
(3) This paper decomposes MLTM contract power into day-ahead 24-h power, and conducts market trading together with the spot market, so that the volatility of real-time power prices in the spot market can be smoothed out through the stable prices in MLTM. Thus, greater profits can be obtained while reducing the profit risks.

In this paper, the quotas in the ancillary services market decomposition of MLTM contracts to the spot market are not considered, which will be included in future studies.

Data availability statement

The original contributions presented in the study are included in the article/supplementary material, further inquiries can be directed to the corresponding author.

Author contributions

YaL: conceptualization, data curation, writing-original draft, writing—review and editing. SZ: conceptualization, data curation, writing-original draft, writing—review and editing. BZ: conceptualization, data curation, writing-original draft, writing—review and editing. GL: conceptualization, data curation, funding acquisition, writing—review and editing. BH: funding acquisition, methodology, project administration. YuL: conceptualization, data curation, writing—review and editing. ZX: formal analysis, validation, visualization, writing—review and editing.

Funding

This work was partially supported by the National Natural Science Foundation of China (62173082), the Fundamental Research Funds for the Central Universities (N2104014), the Guangdong Basic and Applied Basic Research Foundation (2021A1515110778), the State Key Laboratory of Alternate Electrical Power System with Renewable Energy Sources (LAPS21007), and the Liaoning Revitalization Talents Program (XLYC1902090).

Conflict of interest

Authors BH and YuL were employed by State Grid Liaoning Electric Power Co., Ltd., and Information and Telecommunication Branch, State Grid Liaoning Electric Power Co., Ltd.

The remaining authors declare that the research was conducted in the absence of any commercial or financial relationships that could be construed as a potential conflict of interest.

Publisher's note

References

Ak, M., Kentel, E., and Savasaneril, S. (2019). Quantifying the revenue gain of operating a cascade hydropower plant system as a pumped-storage hydropower system. *Renew. Energy* 139, 739–752. doi:10.1016/j.renene.2019.02.118

Canakoglu, E., and Adiyeke, E. (2020). Comparison of electricity spot price modelling and risk management applications. *Energies* 13 (18), 4698. doi:10.3390/en13184698

do Prado, J. C., and Chikezie, U. (2021). A decision model for an electricity retailer with energy storage and virtual bidding under daily and hourly CVaR assessment. *IEEE Access* 9, 106181–106191. doi:10.1109/ACCESS.2021.3100815

Gao, R., Guo, H., Zhang, R., Mao, T., Xu, Q., Zhou, B., et al. (2019). A two-stage dispatch mechanism for virtual power plant utilizing the CVaR theory in the electricity spot market. *Energies* 12 (17), 3402. doi:10.3390/en12173402

Guo, Z., Wei, W., Chen, L., Dong, Z., and Mei, S. (2021). Impact of energy storage on renewable energy utilization: A geometric description. *IEEE Trans. Sustain. Energy* 12 (2), 874–885. doi:10.1109/TSTE.2020.3023498

He, Y., Liu, Y., Li, M., and Zhang, Y. (2022). Benefit evaluation and mechanism design of pumped storage plants under the background of power market reform - a case study of China. *Renew. Energy* 191, 796–806. doi:10.1016/j.renene.2022.03.070

Huang, B., Chen, Y., and Baldick, R. (2022). A configuration based pumped storage hydro model in the MISO day-ahead market. *IEEE Trans. Power Syst.* 37 (1), 132–141. doi:10.1109/TPWRS.2021.3097270

Jahns, C., Podewski, C., and Weber, C. (2020). Supply curves for hydro reservoirs – estimation and usage in large-scale electricity market models. *Energy Econ.* 87, 104696. doi:10.1016/j.eneco.2020.104696

Julian, D., Behnam, Z., Rafael, L., Paulo, S., Andreas, N., Nivalde, J., et al. (2020). Existing and new arrangements of pumped-hydro storage plants. *Renew. Sustain. Energy Rev.* 129, 109914–110321. doi:10.1016/j.rser.2020.109914

Koko, S. P., Kusakana, K., and Vermaak, H. J. (2018). Optimal power dispatch of a grid-interactive micro-hydrokinetic-pumped hydro storage system. *J. Energy Storage* 17, 63–72. doi:10.1016/j.est.2018.02.013

Lazar, Š., Saša, M., and Vladan, R. (2020). Pumped hydroelectric energy storage as a facilitator of renewable energy in liberalized electricity market. *Energies* 13, 6076. doi:10.3390/en13226076

Li, H., Zheng, H., Zhou, B., Li, G., Yang, B., Hu, Bo., et al. (2022). Two-Part Tariff of pumped storage power plants for wind power accommodation. *Sustainability* 14 (9), 5603. doi:10.3390/su14095603

Li, Z., Zhang, Q., Guo, Q., and Sayyad, N. (2021). Pumped hydro energy storage arbitrage in the day-ahead market in smart grid using stochastic p-robust optimization method. *Sustain. Cities Soc.* 75, 103274. doi:10.1016/j.scs.2021.103274

Liu, Y., Liu, T., and He, S. (2021). Coordination and optimization of CCHP microgrid group game based on the interaction of electric and thermal energy considering conditional value at risk. *IEEE Access* 9, 88664–88673. doi:10.1109/ACCESS.2021.3089591

Luka, P., Hrvoje, M., Luka, P., Xuebin, W., Milan, V., Houzhang, T., et al. (2017). Coupling of cleaner production with a day-ahead electricity market: A hypothetical case study. *J. Clean. Prod.* 143, 1011–1020. doi:10.1016/j.jclepro.2016.12.019

Luo, Y., Nie, Q., Yang, D., and Zhou, B. (2021). Robust optimal operation of active distribution network based on minimum confidence interval of distributed energy beta distribution. *J. Mod. Power Syst. Clean. Energy* 9 (2), 423–430. doi:10.35833/MPCE.2020.000198

Luo, Y., Zhang, X., Yang, D., and Sun, Q. (2020). Emission trading based optimal scheduling strategy of energy hub with energy storage and integrated electric vehicles. *J. Mod. Power Syst. Clean. Energy* 8 (2), 267–275. doi:10.35833/MPCE.2019.000144

Masoumzadeh, A., Nekouei, E., Alpcan, T., and Chattopadhyay, D. (2018). Impact of optimal storage allocation on price volatility in energy-only electricity markets. *IEEE Trans. Power Syst.* 33, 1903–1914. doi:10.1109/TPWRS.2017.2727075

Mosquera-Lopez, S., and Nursimulu, A. (2019). Drivers of electricity price dynamics: Comparative analysis of spot and futures markets. *Energy Policy* 126, 76–87. doi:10.1016/j.enpol.2018.11.020

Mou, D. G. (2019). Pumped storage hydro power's function in the electricity market under the electricity deregulation background in China-A case study of Fujian province. *Energy & Environ.* 30 (6), 951–968. doi:10.1177/0958305X18813727

Pang, N., Meng, Q., and Nan, M. (2021). Multi-criteria evaluation and selection of renewable energy battery energy storage system-A case study of tibet, China. *IEEE Access* 9, 119857–119870. doi:10.1109/ACCESS.2021.3107192

Parinaz, T., Emre, N., and Ayse, S. (2022). Operational benefit of transforming cascade hydropower stations into pumped hydro energy storage systems. *J. Energy Storage* 51, 104444–152X. doi:10.1016/j.est.2022.104444

Rodica, L., and Corentin, S. (2021). Market strategies for large-scale energy storage: Vertical integration versus stand-alone player. *Energy Policy* 151, 112169–114215. doi:10.1016/j.enpol.2021.112169

Sospiro, P., Nibbi, L., Liscio, M. C., and De Lucia, M. (2021). Cost–benefit analysis of pumped hydroelectricity storage investment in China. *Energies* 14 (24), 8322. doi:10.3390/en14248322

Tan, Y., Xiong, Y., Gao, H., Li, X., and Zhao, H. (2021). Less is more? The strategic role of retailer's capacity. *Prod. Oper. Manag.* 30 (10), 3354–3368. doi:10.1111/poms.13438

Tian, M., Yan, S., Tian, X., Nojavan, S., and Jermsittiparsert, K. (2020). Risk and profit-based bidding and offering strategies for pumped hydro storage in the energy market. *J. Clean. Prod.* 256, 120715. doi:10.1016/j.jclepro.2020.120715

Wu, Y., Wu, J., and De, G. (2022). Research on trading optimization model of virtual power plant in medium- and long-term market. *Energies* 15 (3), 759. doi:10.3390/en15030759

Yang, M., Zhang, L., Zhao, Z., and Wang, L. (2021). Comprehensive benefits analysis of electric vehicle charging station integrated photovoltaic and energy storage. *J. Clean. Prod.* 302, 126967. doi:10.1016/j.jclepro.2021.126967

Yang, S., Tan, Z., Liu, Z., Lin, H., Ju, L., Zhou, F., et al. (2020). A multi-objective stochastic optimization model for electricity retailers with energy storage system considering uncertainty and demand response. *J. Clean. Prod.* 277, 124017. doi:10.1016/j.jclepro.2020.124017

Zejneba, T., Reinhard, H., Amela, A., and Albert, H. (2022). Economics of electric energy storage. The case of Western Balkans. *Energy* 238, 121669–125442. doi:10.1016/j.energy.2021.121669

Zhao, D., Wang, H., Huang, J., and Lin, X. (2022). Time-of-Use pricing for energy storage investment. *IEEE Trans. Smart Grid* 13 (2), 1165–1177. doi:10.1109/TSG.2021.3136650

Zhao, J., He, Y., Fang, Y., Weng, Y., Ma, W., Xiao, S., et al. (2021). Multi-source optimal dispatch considering ancillary service cost of pumped storage power station based on cooperative game. *Energy Rep.* 7, 173–186. doi:10.1016/j.egyr.2021.10.040

Zhu, Z., Kong, L., Aisaiti, G., Song, M., and Mi, Z. (2021). Pricing contract design of a multi-supplier-multi-retailer supply chain in hybrid electricity market. *Ind. Manag. Data Syst.* 121 (7), 1522–1551. doi:10.1108/IMDS-09-2020-0543

frontiers | Frontiers in Energy Research

TYPE Original Research
PUBLISHED 31 August 2022
DOI 10.3389/fenrg.2022.957955

OPEN ACCESS

EDITED BY
Xue Lyug,
University of Wisconsin-Madison, United States

REVIEWED BY
Huayi Wu,
Hong Kong Polytechnic University, Hong Kong SAR, China
Zhengmao Li,
Nanyang Technological University, Singapore

*CORRESPONDENCE
Xueqin Liu,
x.liu@qub.ac.uk

SPECIALTY SECTION
This article was submitted to Smart Grids, a section of the journal Frontiers in Energy Research

RECEIVED 31 May 2022
ACCEPTED 20 July 2022
PUBLISHED 31 August 2022

CITATION
Rafferty M, Liu X, Rafferty J, Xie L, Laverty D and McLoone S (2022), Sequential feature selection for power system event classification utilizing wide-area PMU data. *Front. Energy Res.* 10:957955.
doi: 10.3389/fenrg.2022.957955

Sequential feature selection for power system event classification utilizing wide-area PMU data

Mark Rafferty[1], Xueqin Liu[2]*, John Rafferty[3], Lei Xie[4], David Laverty[2] and Seán McLoone[2]

[1]Smarter Grid Solutions, Glasgow, United Kingdom, [2]School of Electronics, Electrical Engineering and Computer Science, Queen's University Belfast, Belfast, United Kingdom, [3]ESB International, Muscat, Oman, [4]State Key Laboratory of Industrial Control Technology, Institute of Cyber-Systems and Control, Zhejiang University, Hangzhou, China

The increasing penetration of intermittent, non-synchronous generation has led to a reduction in total power system inertia. Low inertia systems are more sensitive to sudden changes and more susceptible to secondary issues that can result in large-scale events. Due to the short time frames involved, automatic methods for power system event detection and diagnosis are required. Wide-area monitoring systems (WAMS) can provide the data required to detect and diagnose events. However, due to the increasing quantity of data, it is almost impossible for power system operators to manually process raw data. The important information is required to be extracted and presented to system operators for real/near-time decision-making and control. This study demonstrates an approach for the wide-area classification of many power system events. A mixture of sequential feature selection and linear discriminant analysis (LAD) is adopted to reduce the dimensionality of PMU data. Successful event classification is obtained by employing quadratic discriminant analysis (QDA) on wide-area synchronized frequency, phase angle, and voltage measurements. The reliability of the proposed method is evaluated using simulated case studies and benchmarked against other classification methods.

KEYWORDS

event classification, dimensionality reduction, PMU data, machine learning, power system monitoring

1 Introduction

Globally, electrical power systems are significantly changing, primarily driven by the goal of reducing carbon emissions. In order to achieve renewable energy objectives, generation from traditional synchronous power stations is being replaced with low carbon alternatives. Renewable generation is often viewed as a supplement to traditional generation, but as penetration increases, its effects need to be considered with regard

to power system operation and protection. The renewable generators being installed are typically small and decentralized (compared to conventional plants). This, coupled with a loss of control of dispatchable power (e.g., wind power is considered highly intermittent and non-dispatchable) and system services, means power system dynamics are changing (Mukherjee et al., 2021).

Distributed generators (DG) can benefit power systems (Morozovska et al., 2021). For example, when generating power close to distributed loads, they can reduce transmission losses and congestion and can defer investment in transmission lines and substations. However, significant generation at the peripheries of a network will lead to reverse power flows, meaning traditional control and protection schemes can be less effective. Another concern with the increasing installation of DGs is the reduction of system inertia. The natural inertia contributed by synchronous generators helps maintain system frequency. Therefore, the reduction of synchronous generation yields a system with increased sensitivity to sudden changes. Coupling this with the requirement to operate power systems close to their limit to meet demand increases its susceptibility to the occurrence of system-wide events. Therefore, schemes to detect, diagnose, and contain events in a timely manner are required to minimize potential damage and downtime.

Many countries have invested in smart grid technologies to combat large-scale events, with an emphasis on installing a network of Phasor Measurement Units (PMUs) arranged to form a wide-area monitoring system (WAMS). This improves legacy SCADA systems by providing sub-second analysis of transient behavior, with sub-second latency and granularity, which opens a new window on power system dynamics. PMUs provide precise, time-synchronized local measurements of system frequency and rate of change of frequency (ROCOF) along with voltage and current phasors for each bus bar and line measured. These data are typically streamed to a central server, where it is combined to give a wide-area perspective of the system. At this level, long-standing power system challenges such as system-wide frequency monitoring can quickly be solved (Liu et al., 2013). Our previous work (Liu et al., 2015; Liu et al., 2016; Rafferty et al., 2016; Rafferty et al., 2017) investigated the application of advanced methods for rapid event detection on PMU data. Presently, these methods are demonstrated on the historical and modeled PMU data, but the intention is to utilize live PMU data in a control room environment.

The volume of PMU data is to increase exponentially as the number of PMUs and their reporting rates increase. Even at present data streaming rates, it is a challenge to extract real-time information. Consequently, tools from the field of "Big Data" (Syed et al., 2021) are necessary to condense large amounts of data into information useful to system operators. This motivates the need to develop intelligent, automated techniques for the wide-area monitoring and control (WAMC) of the system in real time.

Building on our previous work (Liu et al., 2015; Liu et al., 2016; Rafferty et al., 2016; Rafferty et al., 2017; Rafferty and Liu, 2020), this study presents a novel method to address the problem of distinguishing between several power system events utilizing wide-area PMU data. A combination of dimensionality reduction techniques is adopted to combat the high-dimensional PMU data and reduce computation time.

To summarize, high event classification accuracy was achieved through the following: 1) the development of a power system event database, which was built on wide-area PMU measurements of known event types; 2) utilizing the database in conjunction with previously developed event detection tools (Rafferty et al., 2016) to identify new events, data encapsulated for analysis; 3) linear discriminant analysis (LDA) utilized as a feature extraction technique to reduce the dimensionality of the database while maximizing the discriminatory information between the different event types; 4) a sequential forward selection (SFS) technique employed to identify the most important features necessary for the classification algorithms, enabling the classifiers to train faster and making it easier to interpret; 5) quadratic discriminant analysis (QDA) employed in the event classification model due to its ability to efficiently handle the nonlinear boundaries in the reduced event training data set; and 6) the approach benchmarked against alternative classification techniques, namely, decision trees (DT), k-nearest neighbor (K-NN), LDA, and SVM.

2 Literature review

In machine learning, classification is the assignment of data sets to categories, distinguished by some metric within the data set or extrapolated from it. Many methods have been investigated for the identification of power system events, including DT (Bykhovsky and Chow, 2003; Dahal and Brahma, 2012; Pandey et al., 2020), k-NN (Gaouda et al., 2002; Biswal et al., 2016a; Biswal et al., 2016b; Brahma et al., 2017), support vector machines (SVM) (Biswal et al., 2016a; Brahma et al., 2017), neural networks (Gaouda et al., 2002; Biswal et al., 2016b), unsupervised clustering methods (Dahal et al., 2014; Klinginsmith et al., 2016), energy similarity measure approach (Yadav et al., 2019), and Best Worth Method (Vosughi et al., 1996).

Some methods focus exclusively on local measurements of system frequency (Bykhovsky and Chow, 2003), whereas others consider local voltage measurements (Gaouda et al., 2002). Focusing on singular measurements is a method of reducing dimensionality; however, using frequency and voltage measurements can refine results (Dahal and Brahma, 2012; Dahal et al., 2014; Biswal et al., 2016a; Biswal et al., 2016b;

Brahma et al., 2017). Often, the use of current or power measurements is avoided as these are either inapplicable to a wide-area study or require very specific connections.

K-NN and SVM methods were compared by Biswal et al. (2016a) and Brahma et al. (2017). This analysis addressed testing accuracy but did not consider training speed and prediction. When considering the suitability of a method for on-line applications, training speed and prediction accuracy are crucial. These studies also employed a strong signal-based approach, which can be problematic during large disturbances. This instability arises due to inaccuracies in PMU measurements during transient conditions, especially those close to the source of the event.

Although the method by Brahma et al. (2017) showed excellent classification accuracy, only two classes were considered; this accuracy dropped with the addition of extra classes. The methods by Biswal et al. (2016a) and Brahma et al. (2017) employed a defined 2 s window, 0.5 before and 1.5 s after event. A predefined event window is not desirable for real-time event detection and classification. Finally, a significant constraint of SVM-based methods is computational inefficiency, leading to long training times (Nalepa and Kawulok, 2018).

Bykhovsky and Chow (2003) used frequency data in a rule-based decision tree to distinguish between different types of events. Firstly, a historical data set was employed to cluster events and determine decision tree rules. Secondly, the decision tree was applied to pseudo-live data to test live event classification performance. The magnitude of frequency change and ROCOF were found to give the best event differentiation. However, this study was limited as only a small selection of disturbances were considered, and events that have a small effect on frequency will go undetected or incorrectly classified. Dahal and Brahma (2012) expanded the decision tree approach to include voltage measurements. It was applied to generation loss, line trip, and line to ground fault events; however, only seven events were tested. Clustering takes a more probabilistic approach than classification. Events can therefore spread across more than one cluster, often occurring during large events with multiple consequences. The clustering methods by Dahal et al. (2014), Klinginsmith et al. (2016), and Gharavi and Hu (2018) observed the generation of unknown clusters. User expertise was required to link a cluster of power system events to the underlying causes and consequences. A further challenge is that dimensionality increases with the number of event clusters. More recently, deep learning-based methods involving long short-term memory neural networks or convolutional neural networks are employed for power system event classification (Ahmed et al., 2021; Li et al., 2021; Ehsani et al., 2022). The deep learning-based neural networks are excellent in dealing with large data sets but suffer from significant computation costs due to the large number of parameters turning at the training stage.

Because there is no theoretical conclusion on which machine learning classifier method is superior, several methods are required to be evaluated to determine which classification algorithm is more appropriate in predicting the event types from the obtained PMU event database. For the construction of an on-line power system event classifier, utilizing a significant number of PMU variables recorded from multiple locations simultaneously, which can be trained (and retrained after successful classification) in a timely manner with a low misclassification rate, dimensionality reduction techniques are required. Techniques for reducing dimensionality have many benefits, such as reducing time and space complexity and allowing more interpretable data by the removal of noise and less important features. An optimal number of variables is required for model construction, and a trade-off between speed and accuracy is required. In contrast to existing literature, the rejection of power system variables is not used as a method to reduce the dimensionality of the problem. Systematic consideration of the frequency, voltage, and phase angle signals and the difference and rate of change to these variables between buses is proposed. The desired computation efficiency is achieved *via* a combination of LAD and sequential forward selection to extract and select the variables contributing most to classification accuracy. Also, in this investigation, the window length is determined by the event detection algorithm in Rafferty et al. (2016). The detection algorithm captures the event data and separates them from those recorded under normal operating conditions, providing a crucial step for event classification.

3 Methodology

3.1 Dimensionality reduction

Construction of an on-line power system event classifier, utilizing a significant number of PMU variables recorded from multiple locations simultaneously, which can be trained rapidly, requires dimensionality reduction techniques to be implemented. Dimensionality reduction (Van Der Maaten et al., 2009) is the process of using statistical techniques to reduce the number of features (or variables) in a data set by transforming the original data set into a lower subspace.

Typical applications of dimensionality reduction include data compression for storage purposes and as a pre-processing step to machine learning algorithms. An optimal number of dimensions is required for model construction; the inclusion of too many can decrease performance with respect to computation efficiency and prediction accuracy. However, the inclusion of too few can also result in lower accuracy.

3.1.1 Feature extraction

LAD is a feature extraction technique whose objective is to find a linear combination of features that preserves as much of the class discriminatory information as possible. The resultant combinations can be utilized for linear classification (this application is presented in Section B) or dimensionality reduction purposes. LDA is a supervised learning technique that reduces the dimensionality in the data set to $C-1$ dimensions, where C = number of classes.

Denote a matrix of PMU data $\mathbf{X}$, where $\mathbf{X} \in \mathrm{IR}^{n\times m}$, consisting of m measurement variables, with each row representing a sample (n = number of samples), which is attributed to one of C-classes of event type, where $C > 2$. The objective of LDA is to obtain $C-1$ projections of y by means of multiple projection vectors w_i, where $i = 1\ldots C-1$:

$$y_i = \mathbf{w}_i^T \mathbf{X}, \tag{1}$$

where $\mathbf{w}_i$ can be arranged by columns into a projection matrix, $\mathbf{W}$. The distance, d, between the projected class means, is a good starting point to maximize the difference between the centers of both classes. However, this measurement does not consider the variance of the data within each class and can cause overlapping between classes.

Therefore, Fisher's proposed method (McLachlan, 2004) maximizes the distance, d, between the classes but also minimizes the variance v within them:

$$J(\mathbf{W}) = \frac{d^2}{v_1 + v_2} = \frac{\mathbf{w}^T S_B \mathbf{w}}{\mathbf{w}^T S_W \mathbf{w}}, \tag{2}$$

when $C = 2$, where S_B and S_W represent the between-class scatter matrix and the within-class scatter matrix, respectively. Therefore, a projection that maximizes S_B while minimizing S_W is sought. When $C > 2$, the projection is now $C-1$ dimensions, and the determinant of the scatter matrices is used to obtain a scalar objective function, transforming **Eq. 2** to

$$J(\mathbf{W}) = \frac{|\,\mathbf{W}^T S_B \mathbf{W}\,|}{|\,\mathbf{W}^T S_W \mathbf{W}\,|}, \tag{3}$$

with S_B and S_W given, respectively, as

$$S_B = \sum_{i=1}^{C} n_i (\mu_i - \mu)(\mu_i - \mu)^T \tag{4}$$

and

$$S_W = \sum_{i=1}^{C} \sum_{i\in C_i} n_i (x_i - \mu_i)(x_i - \mu_i)^T, \tag{5}$$

where n_i represents the total number of samples in the ith class, C the number of classes, μ_i the mean of the samples in the ith class, and μ the overall mean of the data.

The optimal projection matrix $\mathbf{W}^*$ is given as the one whose columns are the eigenvectors that correspond to the largest eigenvalues of the generalized eigenvalue problem:

$$S_W^{-1} S_B \mathbf{w}_i = \lambda_i \mathbf{w}_i \tag{6}$$

or

$$S_W^{-1} S_B \mathbf{W} = \lambda \mathbf{W}, \tag{7}$$

where $\lambda_i = J(\mathbf{w}_i)$ and $i = 1\ldots C-1$. The optimal projection matrix, $\mathbf{W}^*$, is given by

$$\mathbf{W}^* = \arg\max_{\mathbf{W}} J(\mathbf{W}). \tag{8}$$

3.1.2 Feature selection

There are three different types of feature selection techniques: filter methods (e.g., Euclidian distance, t-test), wrapper methods (e.g., SFS, Genetic algorithms), and Embedded methods (e.g., DT and SVM) (Ladha and Deepa, 2011). Sequential forward selection (Ladha and Deepa, 2011) is employed here as the simplest greedy search algorithm compared to machine learning-based methods. This method starts with zero features selected and tests each one individually against an objective function. This process is repeated using the previously selected feature(s) and the remaining unselected features in the data set until a stopping criterion is reached. For this methodology, the stopping criteria are based on the cross-validation error of the classifier. Therefore, features are selected consecutively until the cross-validation error ceases to decrease or increases again.

Cross-validation is a method used to evaluate the accuracy of classifiers by employing the classifier on the training data to allow the misclassification rate, E, to be determined. k-fold cross-validation (Kohavi, 1995) is implemented to assess the generalization performance of different classifier configurations. The K-fold method works by dividing the training data set into K subsets (folds) and uses all, bar 1, of the folds for training the classifier, with the remaining fold used for testing. This process is repeated until all the folds have been used for testing. The cross-validation error, CV_E, is calculated using

$$CV_E = \frac{1}{K} \sum_{k=1}^{K} E_k, \tag{9}$$

where E_k is the misclassification rate for each fold, and K are the total number of folds. This method allows all samples in the data set to be used for both training and validation, with each sample used for validation only once. A common value for the number of folds, K, is 10.

3.2 Classification: discriminant analysis

An on-line, adaptive event classifier consists of three main stages: separation, allocation, and update. In the separation stage, the objective is to find functions that maximize the difference between the event type classes in the labeled training data set, X. The focus of the allocation stage is to assign unclassified samples (from newly detected events) into one of the known classes, C,

based on the functions obtained in the separation stage. Finally, the update stage adds the successfully classified event to the training data set, X, and retrains the classifier for when it is required again.

Discriminant analysis (DA) (Fisher, 1936) is a supervised machine learning technique used to find linear combinations of features in a data set that best discriminates between mutually exclusive groups on the basis of predefined features. A common method for generating the discriminant functions is by using linear methods, such as LDA and QDA, presented in **Section B.1** and **Section B.2**, respectively.

3.2.1 Linear discriminant analysis

The objective of LDA for classification is to determine the maximum posterior probability (denoted as $\hat{G}$) of a sample, x_i, belonging to each event type class, $C = c1, c2, \ldots c_n$ (where n = the number of classes in the data set). Let π_{c1} and π_{c2} denote the prior probability that a randomly selected sample comes from the $c1-th$ and $c2-th$ class, respectively, calculated from $\pi = \frac{No.\ samples\ in\ class}{Total\ No.\ samples}$, and denote $f_C(x_i)$ as the density function of x_i belonging to class $G = c1$. From the Bayes theorem, the following can be stated (Yan and Dai, 2011):

$$Pr(G = c1|X = x_i) = \frac{f_{c1}(x_i)\pi_{c1}}{\sum_{c2=1}^{C} f_{c2}(x_i)\pi_{c2}}, \quad (10)$$

where X is the training data set, which is assumed to follow a multivariate normal distribution (James et al., 2013). The class-conditional density function, $f_{c1}(x_i)$, is given as

$$f_{c1}(x_i) = \frac{1}{(2\pi)^{\frac{p}{2}}|\Sigma_{c1}|^{\frac{1}{2}}} \exp\left(-\frac{1}{2}(x_i - \mu_{c1})^T \Sigma_{c1}^{-1}(x_i - \mu_{c1})\right), \quad (11)$$

where μ_{c1} and Σ_{c1} are the mean vector and covariance matrix for class $c1$, respectively. An underlying assumption of LDA is that all classes share a common covariance matrix, $\Sigma_{c1} = \Sigma \forall_C$. Thus, the linear discriminant function for each class C can be expressed as (James et al., 2013)

$$\delta_C(x_i) = x_i^T \Sigma^{-1} \mu_C - \frac{1}{2}\mu_C^T \Sigma^{-1} \mu_C + \log \pi_C. \quad (12)$$

Sample x_i is determined as the class C, which maximizes $\hat{G}$:

$$\hat{G}(x_i) = \arg\max_C \delta_C(C). \quad (13)$$

3.2.2 Quadratic discriminant analysis

QDA is an extension of LDA and again assumes multivariate data, following a normal distribution. However, unlike LDA, it is assumed that each class, $c1, c2, \ldots, c_n$, has a separate covariance matrix. This yields the quadratic discriminant function for each class C as (James et al., 2013)

$$\delta_C(x_i) = -\frac{1}{2}\log|\Sigma_C| - \frac{1}{2}(x_i - \mu_C)^T \Sigma_C^{-1}(x_i - \mu_C) + \log \pi_C, \quad (14)$$

with classification determined by maximizing $\hat{G}$ (from **Eq. 13**).

3.3 Power system event classifier

The process for the proposed wide-area power system event classifier (PSEC) scheme involves three main stages: off-line classifier construction, on-line wide-area event classification, and classifier retraining. A process flowchart of PSEC is depicted in **Figure 1**. A fourth stage, on-line monitoring (Rafferty et al., 2016; Rafferty et al., 2017), is also included in **Figure 1**.

The off-line construction of the initial event classifier requires a sample of historical data of past events, with corresponding event type label recorded from a wide-area network consisting of n PMUs. The labeled, historical event data are used to train the initial PSEC model by determining the boundaries between each event type class. The trained model is applied to newly detected events to allow the event to be classified. Denoting f_i, ϕ_i, and v_i as the current sample of frequency, phase angle difference, and voltage recorded from a single PMU, respectively, the change in each variable, Δf, $\Delta\phi$, and Δv can be calculated by subtracting the $i-th$ from its corresponding previous sample (f_{i-1}, ϕ_{i-1}, and v_{i-1}). The rate of change (ROC) for each variable over time, $\frac{\Delta f}{\Delta t}$, $\frac{\Delta \phi}{\Delta t}$, and $\frac{\Delta v}{\Delta t}$, respectively, is also calculated. ROC values were calculated over 100 ms and averaged over a 500 ms sliding window, as recommended for ROCOF (Energy, 2013).

In order to compile the training data set, the event database is split into smaller subsets relating to each variable recorded. In the case of this investigation, there are nine subsets, as detailed in the previous paragraph, including all the relevant samples, m, from the n PMUs arranged to form a $m \times n$ matrix. LDA is employed on each subset, reducing the dimensionality from n to a $C-1$ subspace while maximizing separability between each event type. The calculated projection matrix, **W**, for each subset is saved to allow newly detected events to be reduced to the same space. The extracted features from the nine subsets are combined before employing the CV_E-based SFS technique to select the features which best contribute to the accuracy of the classifier. Finally, to conclude the off-line training process for PSEC, QDA is employed on the reduced event training data set to calculate the class boundaries.

Once trained, PSEC can be used to classify newly detected events on the power system. During the on-line monitoring process, the change and rate-of-change values for each measurement variable are continuously calculated. Once an event has been detected on the system, the data from all connected PMUs are isolated from nonevent data and used to classify the event type occurring. During training, the same subset splitting is adhered to before dimensionality reduction is conducted. In order to extract features that will be in the same subspace as before, each subset is reduced using its corresponding projection matrix, **W**. The same selected features, **SF**, are again chosen to classify the end.

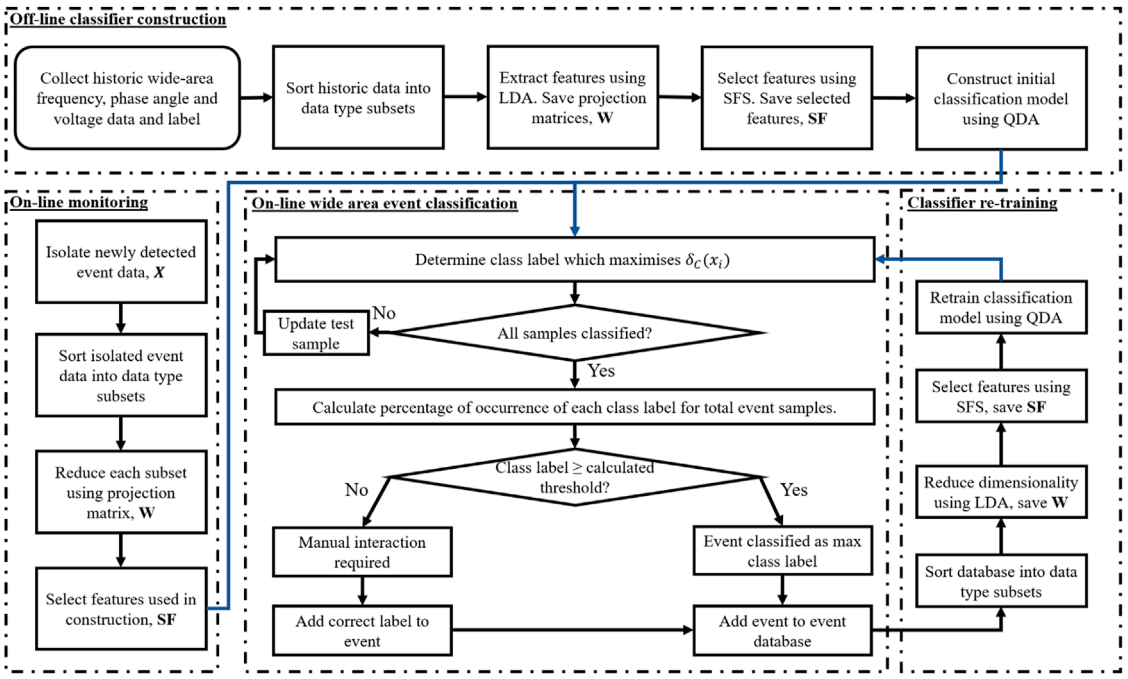

FIGURE 1
Power system event classification (PSEC) process flowchart.

Each sample in the event is classified iteratively by maximizing $\tilde{G}$, from Eq. 13. This process is repeated until each sample in the event has been assigned a class type, with the overall event class determined by calculating the maximum occurrence of each event class type in the event data as a percentage of total event samples.

A confusion matrix is often utilized to evaluate a classification model's performance, which leads to the calculation of many metrics according to the values in the confusion matrix, such as accuracy, precision, recall, Specificity, and F1 score. A more detailed explanation can be found in Singh et al. (2021). Accuracy as a measure of all the correctly identified events is employed due to its simplicity. In order to reduce the likelihood of misclassification, a threshold is implemented based on the accuracy of the current classifier model, with accuracy determined by

$$Accuracy\,(\%) = \frac{TP + TN}{Total} \times 100\%, \tag{15}$$

where *TP*, *TN*, and *Total* represent the true positive, true negative, and the total number of samples in the training data, respectively. The initial threshold is calculated during the off-line classifier construction phase and automatically recalculated during each classifier retraining phase. If an event type achieves ≥ the threshold, the event is automatically added to the database. Otherwise, the event cannot be classified, and manual user interaction is required to add the event to the database before retraining occurs.

4 Evaluation with wide-area PMU data

4.1 Data acquisition

In order to demonstrate the capability of PSEC, several dynamically simulated case studies were conducted on the standard IEEE-39 Bus Test System (Athay et al., 1979) using DigSilent PowerFactory. This test system represents part of the US power system and consists of 10 synchronous generators, 19 loads, and 36 transmission lines. In order to simulate capacitor switching and motor start events, each was connected, *via* a circuit breaker, to each bus in the system. A PMU was placed at each bus in the system not directly connected to a generator, equating to 29 PMUs in total. Each connected PMU has a sampling rate of 100 Hz. For this investigation, it was assumed that all connected PMUs in the system are on-line and do not experience any noise or information loss.

Case studies consisted of 133 generation dip (GD), 114 loss of load (LL), 33 line trip (LT), 78 capacitor switching (CS), and 39 synchronous motor start (MS) events, 397 events in total. Of the simulated events, an 80%–20% split between training

(322 events) and test (75 events) events was implemented for each event type. Typical waveforms for each event type under consideration are illustrated in Figure 2. As event locality dictates severity on system measurements, it is important to include data from each PMU for the duration of the event.

4.2 Construction and evaluation of PSEC

In order to construct the initial PSEC model, 80% of the event database consisting of the six aforementioned event types was utilized as input data. The remaining 20% will be used to test the accuracy of the PSEC model for data it does not have experience with. In this study, the event database contains measurements from each installed PMU, which equates to 261 features (29 installed PMUs × 9 measurement variables per PMU). Following the measurement subset creation procedure described in Section C, each subset consists of 29 features. By employing LDA on each individual subset, the dimensionality will be reduced from 29 to 5 features (equating to C-1, where, in this study, $C = 6$). Therefore, the dimensionality of the event database has been reduced from 261 to 45 features (5 extracted features per subset × 9 subsets).

To further reduce dimensionality, the k-fold cross-validation-based SFS technique was utilized. This technique selected the features that contribute the most information for classification, thus yielding the lowest cross-validation error CV_E. The results for the SFS process are illustrated in Figure 3, which highlights that the optimal number of features from the

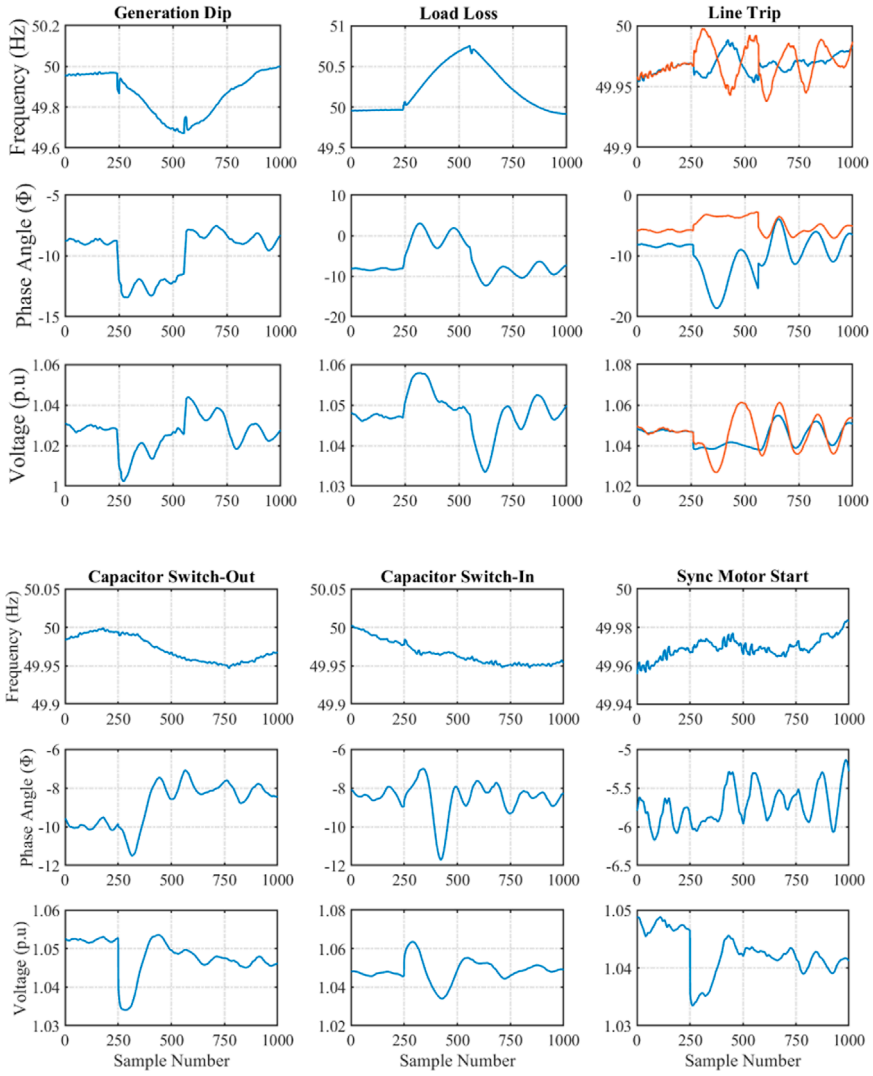

FIGURE 2
PMU recordings for different event types.

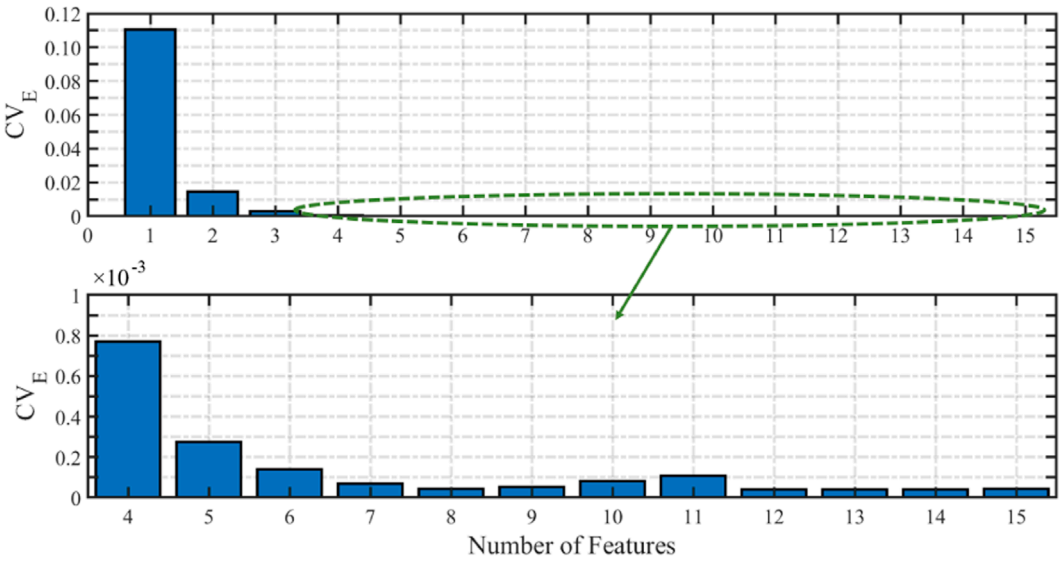

FIGURE 3
Cross-validation error for the number of features included in the classifier.

reduced event database to be used for PSEC training is 8, as, beyond this, CV_E begins to increase. The combined LDA and SFS process reduces the dimensionality of the original event database from 261 features to a smaller event training data set of eight features. The eight selected features, **SF**, are presented in Table 1. The subscript number relates to the feature extracted using LDA for that variable. In other words, f_3 relates to the third feature extracted from the frequency subset. The features were chosen in the following order: f_1, $\Delta\phi_1$, Δf_1, Δf_2, f_3, Δv_5, $\frac{\Delta\phi}{\Delta t}_4$, and $\frac{\Delta f}{\Delta t}_1$. The eight selected features were used as inputs to construct the initial QDA-based PSEC model. To illustrate, conceptually, the output of the initial PSEC model, a two-dimensional scatter plot, is presented in Figure 4. The scatter plot illustrates the reduced event training data set for the first two features selected, f_1 and $\Delta\phi_1$. The calculated event type class boundaries are illustrated by the dashed black lines. It can be observed from Figure 4 that each event type has it is own unique area. However, the three inner event type classes (capacitor switching in/out and motor start) have a small number of samples that overlap between classes because these events have a limited effect on the f_1 and $\Delta\phi_1$ variables and more on voltage variables, as illustrated in Figure 2.

Numerical results for PSEC evaluation with regard to the training time and accuracy are highlighted in bold typeface in Table 2. Additionally, several different configurations of the event training data set are presented, including the proposed combination of LDA and SFS (eight features), the raw event database (261 features), and LDA only (45 features). All simulations were carried out in MATLAB 9.3 (R2017b) on a third-generation Intel Core i5 processor with 12 GB RAM.

TABLE 1 Selected Features (SF) using CV_E-based SFS method for training data consisting of 80% of the data (322 events).

	f	Δf	$\frac{\Delta f}{\Delta t}$	ϕ	$\Delta\phi$	$\frac{\Delta\phi}{\Delta t}$	v	Δv	$\frac{\Delta v}{\Delta t}$
SF	f_1 f_3	Δf_1 Δf_2	$\frac{\Delta f}{\Delta t}_1$		$\Delta\phi_1$	$\frac{\Delta\phi}{\Delta t}_4$		Δv_5	

From the results for the QDA-based PSEC presented in Table 2, it can be observed that training time significantly decreases from 32.8 s, using the raw event database, to 6.12 s, when solely LDA is employed. As expected, the fastest configuration occurs when a combination of LDA and SFS is employed on the event database, which yields a time of 3.06 s. Regarding classification, it can be observed that there is a loss of 0.02% in accuracy between using the raw event database and the proposed combination of LDA and SFS, which is minimal. Accuracy in this investigation is determined by the number of correct classifications as a percentage of the total number of classifications utilizing the training event data set.

As there is no theoretical conclusion on which classification algorithm is superior, many algorithms are required to be evaluated using the training data set. Therefore, Table 2 presents a comparative study of numerical results for several classification algorithms. These algorithms include DT, LDA, SVM, and K-NN.

As the proposed method adopts an adaptive training approach, which involves retraining after a successful classification, the training speed is very important. Therefore, as observed from Table 2, when using the raw event database,

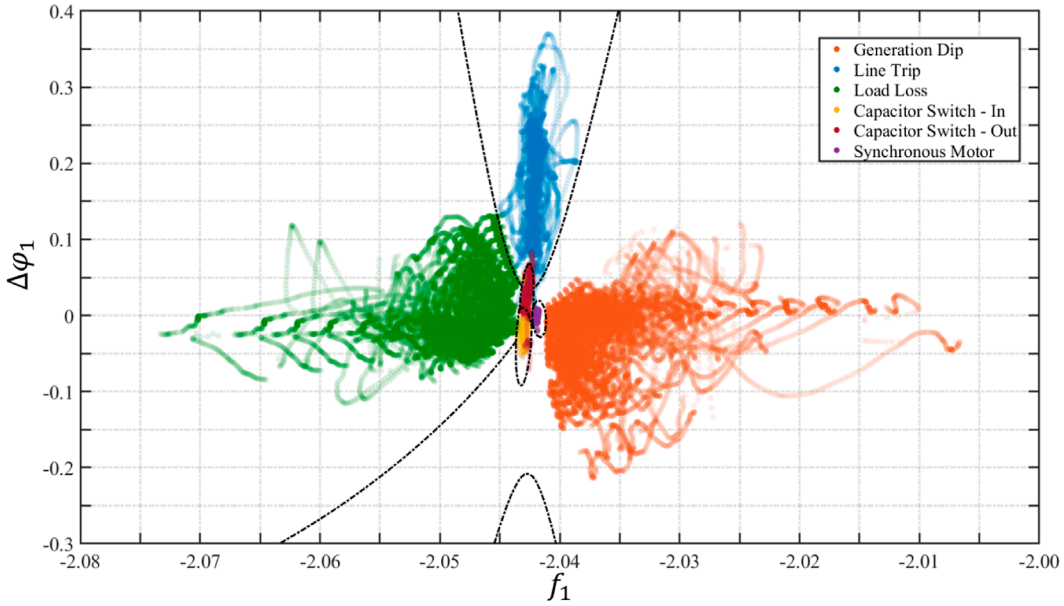

FIGURE 4
Conceptual two-dimensional results for the calculated event type class boundaries for the six event types included in the event database.

TABLE 2 Comparative study, evaluating the speed and accuracy of multiple classification techniques with different dimensionality reduction techniques using 80% of the data (322 events) for training and 20% of the data (75 events) for testing.

Classifier	Training						Testing		
	Time (s)			Accuracy (%)			Accuracy (%)		
	Raw data	LDA	LDA + SFS	Raw data	LDA	LDA + SFS	Raw data	LDA	LDA + SFS
DT-100 Splits	29.62	10.40	5.12	100	99.98	99.96	100	98.67	100
DT-20 Splits	26.85	9.39	3.79	100	99.95	99.66	100	98.67	100
DT-4 Splits	27.86	7.75	3.39	97.8	94.83	94.83	90.67	77.33	77.33
LDA	33.40	6.28	2.96	100	99.95	99.48	100	97.33	97.33
QDA	32.80	6.12	**3.06**	100	99.92	**99.98**	90.67	98.67	**100**
SVM-Linear	235.16	124.61	108.2	99.99	99.99	99.98	100	96.0	97.33
SVM-Quadratic	213.09	118.13	95.3	100	100	100	100	96.0	97.33
1-NN	1568.66	247.42	4.67	100	100	100	97.33	96.0	93.33
10-NN	1559.73	236.63	9.52	99.98	99.95	99.96	97.33	96.0	90.67
100-NN	1388.81	235.21	32.97	98.92	99.23	99.45	96.0	94.67	84.0

The bold values represent the results of the proposed method.

all of the evaluated algorithms are too computationally expensive but return highly accurate models (>97.8%). The DT and DA approaches are comparable in computation speed and accuracy. The computation cost for SVM and k-NN algorithms is very high, greater than 3.5 min for the SVM approaches and substantially over 20 min for each k-NN approach. This reinforces the requirement of dimensionality reduction techniques as a pre-processing step for on-line PSEC.

When LDA was employed on the event database, it can be observed from Table 2 that the computation time for each classifier reduces significantly. However, in the case of the DA and DT, this reduction in computation cost comes with a reduction in accuracy. This loss is minimal (<0.1%) except for a four-split DT (2.97% decrease). It should be noted that the accuracy of the SVM and k-NN either stay the same or increase slightly, but these still experience high computation costs, ≈ 2 and 4 min, respectively, and therefore could not update PSEC in a desirable time frame.

Finally, when a combination of LDA and SFS was implemented, it can be observed that the discriminant analysis techniques, LDA and QDA, are the fastest for model construction, ≈ 3 s. Although these returned slightly lower accuracy (0.02 and 0.52% for QDA and LDA, respectively)

TABLE 3 PSEC results using 80% of the data (322 events) for training and 20% of the data (75 events) for testing.

Event	No. events	Event classification results (%)						
		CS-In	CS-Out	GD	LT	LL	MS	I
CS-In	7	100	0	0	0	0	0	0
CS-Out	7	0	100	0	0	0	0	0
GD	26	0	0	100	0	0	0	0
LT	6	0	0	0	100	0	0	0
LL	22	0	0	0	0	100	0	0
MS	7	0	0	0	0	0	100	0

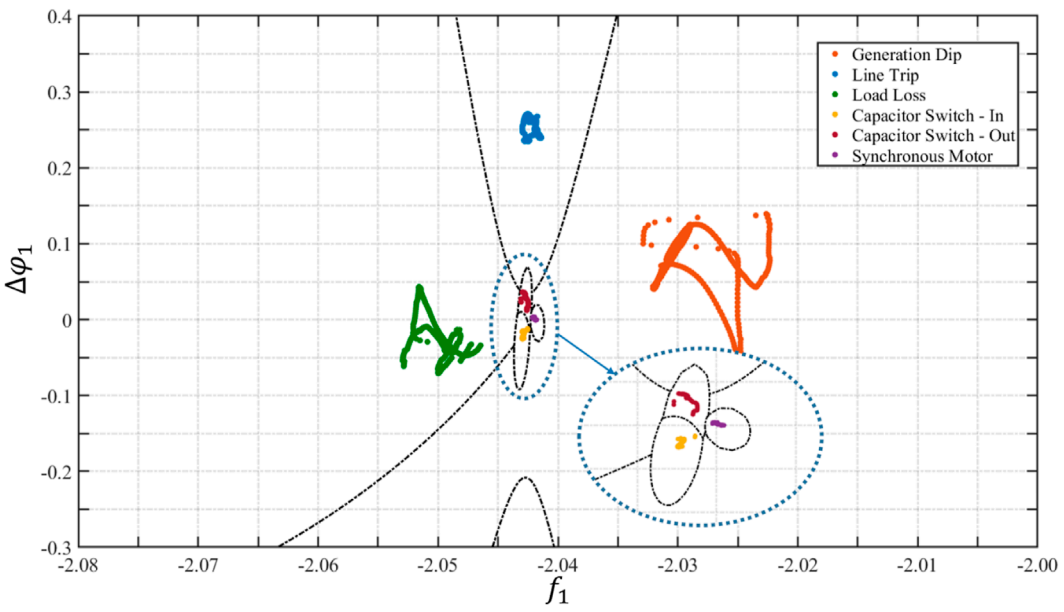

FIGURE 5
PSEC classification results for six simulated case studies.

compared to quadratic SVM and 1-NN, the computation time is less. The DT approaches all offer similar computation costs to QDA and LDA. However, their accuracy has reduced. Finally, although QDA is marginally slower than LDA for training (0.1 s), it has benefits over it with regard to its training accuracy (0.5%) and was, therefore, chosen to be implemented in PSEC.

4.3 Classification of new events

After the construction of the initial PSEC model, it can now be used to classify newly detected events in the power system. Once an event has been detected in the system, the event data are isolated at each PMU in the power system. During the training stage, each sample from the newly detected event for each PMU is arranged into measurement variable subsets. Using the projection matrices, **W**, obtained in the training process, each variable subset is reduced from 29 to 5 features. The features, **SF**, selected in the training process using the SFS technique are selected again and utilized as inputs to PSEC to predict the class of each individual sample, x_i, in the event, with each event sample determined by the event type class which maximizes the function $\hat{G}$. Finally, the overall event is determined by the maximum percentage of occurrence of each event type for the total samples in the event, with a threshold of ≥99%, calculated based on the accuracy of the QDA model, implemented to reduce the chance of misclassification.

Full classification results achieved with PSEC for a number of each simulated event type are displayed in Table 3. A further column (I) has been added to the table to indicate the percentage of events tested that returned inconclusive (i.e., the max percentage of samples is <99% of all samples). Table 3

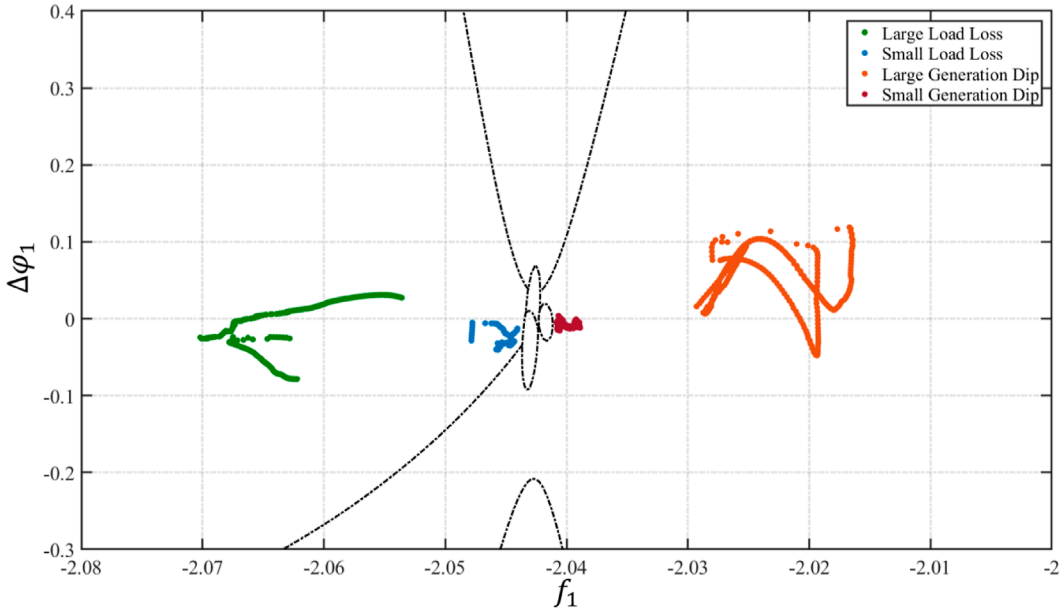

FIGURE 6
PSEC results highlighting the effect of event severity.

concludes that the classification accuracy for each event type implemented in the event database by the QDA-based PSEC method is highly accurate (100%). Conceptual two-dimensional results for an example of each event type considered in PSEC are presented in Figure 5, presenting the previously calculated event type class boundaries, calculated in Section B and depicted in Figure 4. From Figure 5, it can be observed that, for each of the six event types tested, PSEC could successfully be classified, as all event samples are located within their respective regions.

For completeness, the benchmarking evaluations on the classification algorithm and dimensionality reduction techniques conducted in Section B were also conducted to classify newly detected events. This is provided in the testing column of Table 2. As dimensionality is reduced, the accuracy for newly detected events experiences a decrease except for QDA, which experiences an increase (from 90.67 to 98.67%). This rate is further increased when incorporating SFS with LDA for dimensionality reduction. Classification accuracy increases in an SVM, 100 and 20 split decision tree-based approaches, when incorporating SFS with LDA. LDA and a four-split decision tree classification approach remain the same. Finally, as the dimensionality is reduced, all the k-NN-based approaches decrease in accuracy.

The results in Table 2 show that when using a reduced data set, QDA provides the greatest accuracy for testing (100%) and can be trained in 3.06 s. This is 0.1 s slower than the quickest classifier to be trained, LDA, but returns higher accuracy using the training data set (0.5%) and testing data set (2.67%). Considering computation cost and accuracy, QDA has the potential to be improved and implemented in real time on live PMU data.

5 Discussion

The proposed systematic approach for classifying power system events has several advantages; namely, the implementation of an adaptive method that allows the event database to be updated and self-trained after the successful classification of an event occurs. Also, the introduction of dimensionality reduction techniques has been shown to reduce the computational speed during the training of PSEC with a minimal loss in classifier accuracy, 0.02%. It should be noted that a detailed inspection of individual PMU signals would allow the discrimination between each type of event. However, if there are many PMUs to monitor, this becomes cumbersome. Furthermore, determining an accurate threshold between each of the events to allow automatic classification in real time is not an easy task. The proposed automatic approach for event classification has the potential to be used as input knowledge for an intelligent control system to assist real-time decision-making.

As mentioned previously, all PMUs in the system will experience some disruption to power system measurements during an event, with PMUs located closer to the event experiencing greater change. Therefore, by using a representation

of data from the whole system, local inaccuracies are smoothed, making classification independent of PMU locations. Also, the utilization of data from multiple PMUs simultaneously increases the reliability of the method compared to an individual PMU approach. Additionally, as each event sample is determined, PSEC allows automatic classification to begin as received at the PDC, where the data transportation is in the sub-second range. This could be beneficial as an early warning system to predict the type of event occurring in the first number of samples before final determination utilizing full event data.

An investigation into event severity on successful classification is presented in **Figure 6**, where a large load loss represents a loss of 993.6 MW of load; a small load loss represents a loss of 112.4 MW of load; a large generation dip represents a loss of 628 MW of generation; and a small generation dip represents a loss of 98.7 MW of generation. **Figure 6** shows that a small loss leads to the power system measurements varying less and thus being closer to other event-type classes. However, the larger the loss, the easier the classification due to its location in relation to the class boundaries. This makes the classification of smaller events more challenging.

6 Conclusions and future work

This study presents a proposed methodology for classifying wide-area power system events for several regularly occurring power system events. The methodology was based on QDA and utilized a statistically obtained subset of wide-area synchronized measurements collected from a network of PMUs located on a power system. The methodology is extensively tested for a large number of simulated case studies. Results are presented and compared with other classifiers, including SVM, k-NN, DT, and LDA.

The proposed method utilizes a systematic consideration of the frequency, voltage, and phase angle signals, as well as the difference and rate of change to these variables between buses, to achieve successful classification. In order to optimize performance, with respect to speed and accuracy, a combination of LDA (to maximize the discriminatory information between event classes) and SFS (to select variables that contribute the most information) techniques are utilized. By considering the results for accuracy and training speed presented in **Tables 2,3**, the QDA-based PSEC method has the potential to be improved and implemented in real time in future work.

It is worth noting that the sequential forward selection method can identify the most important features and buses (eight features and five buses in this case) that are necessary for the classification algorithms. These simulation results demonstrated that there is no need to have PMU installed in each bus in a practical power system for event classification purposes.

More specifically, future work will look at enhancing some aspects of the classifier. Firstly, the focus should be on improving and expanding the simulated power system event database by including other events, such as transformers energizing, BESS charging/discharging, and the simulation of specific faults in the power system. Secondly, the training time for the construction of the initial PSEC model is presented in **Table 2**, illustrating a training time of ≈3 seconds. However, this will increase dramatically with retraining occurring after each event. One possible solution for reducing this training time is implementing a recursively trained classifier. This will allow the previously trained classifier model to be used in retraining the new classifier instead of beginning from the start each time. Therefore, implementing recursive learning algorithms will be investigated to further optimize PSEC. Finally, the proposed method can be considered moderately theoretical due to its use of off-line simulated PMU data only. Therefore, future work will investigate the response of PSEC to live real-world PMU data.

Data availability statement

All data created during this research is openly available from Zenodo open data repository at DOI: 10.5281/zenodo.6874618.

Author contributions

MR and XL contributed to the conception and design of the study. MR organized the database, performed the statistical analysis, and wrote the first draft of the manuscript. XL and JR wrote sections of the manuscript. XL, DL, SM, and LX contributed to manuscript revision and supervision and read and approved the submitted version.

Funding

This work was supported by EPSRC Supergen Networks Hub (EP/S00078X/2)—SEN Hub Sub-Project Award for a project entitled "Challenges and Opportunities of Machine Learning and BESS for Oscillations Mitigation in Low Inertia Power Networks." All data created during this research are openly available. The

names of the repository and accession number can be found in the article upon publication.

Conflict of interest

The authors declare that the research was conducted in the absence of any commercial or financial relationships that could be construed as a potential conflict of interest.

Publisher's note

References

Ahmed, A., Sajan, K. S., Srivastava, A., and Wu, Y. (2021). Anomaly detection, localization and classification using drifting synchrophasor data streams. *IEEE Trans. Smart Grid* 12 (4), 3570–3580. doi:10.1109/tsg.2021.3054375

Athay, T., Podmore, R., and Virmani, S. (1979). A practical method for the direct analysis of transient stability. *IEEE Trans. Power Apparatus Syst.* (2), 573–584. doi:10.1109/tpas.1979.319407

Biswal, M., Hao, Y., Chen, P., Brahma, S., Cao, H., and De Leon, P. (2016a). "Signal features for classification of power system disturbances using PMU data," in Power Systems Computation Conference (PSCC), 2016 (IEEE), 1–7.

Biswal, M., Brahma, S. M., and Cao, H. (2016b). Supervisory protection and automated event diagnosis using PMU data. *IEEE Trans. Power Deliv.* 31 (4), 1855–1863. doi:10.1109/tpwrd.2016.2520958

Brahma, S., Kavasseri, R., Cao, H., Chaudhuri, N., Alexopoulos, T., and Cui, Y. (2017). Real-time identification of dynamic events in power systems using PMU data, and potential applications—Models, promises, and challenges. *IEEE Trans. Power Deliv.* 32 (1), 294–301. doi:10.1109/tpwrd.2016.2590961

Bykhovsky, A., and Chow, J. H. (2003). Power system disturbance identification from recorded dynamic data at the northfield substation. *Int. J. Electr. Power & Energy Syst.* 25 (10), 787–795. doi:10.1016/s0142-0615(03)00045-0

Dahal, O. P., Brahma, S. M., and Cao, H. (2014). Comprehensive clustering of disturbance events recorded by phasor measurement units. *IEEE Trans. Power Deliv.* 29 (3), 1390–1397. doi:10.1109/tpwrd.2013.2285097

Dahal, O. P., and Brahma, S. M. (2012). "Preliminary work to classify the disturbance events recorded by phasor measurement units," in Power and Energy Society General Meeting, 2012 IEEE. IEEE, 1–8.

Ehsani, N., Aminifar, F., and Mohsenian-Rad, H. (2022). *Convolutional autoencoder anomaly detection and classificationbased on distribution PMU measurements*. IET Gener. Transm. Distrib. 16, 2816–2828. doi:10.1049/gtd2.12424

Energy, P. (2013). *Rate of change of frequency (ROCOF) - review of TSO and generator submissions final report*. Guildford: Commission for Energy Regulation CER.

Fisher, R. A. (1936). The use of multiple measurements in taxonomic problems. *Ann. Eugen.* 7 (2), 179–188. doi:10.1111/j.1469-1809.1936.tb02137.x

Gaouda, A., Kanoun, S., Salama, M., and Chikhani, A. (2002). Pattern recognition applications for power system disturbance classification. *IEEE Trans. Power Deliv.* 17 (3), 677–683. doi:10.1109/tpwrd.2002.1022786

Gharavi, H., and Hu, B. (2018). Space-time approach for disturbance detection and classification. *IEEE Trans. Smart Grid* 9 (5), 5132–5140. doi:10.1109/tsg.2017.2680742

James, G., Witten, D., Hastie, T., and Tibshirani, R. (2013). *An introduction to statistical learning*, 112. New York, NY: Springer.

Klinginsmith, E., Barella, R., Zhao, X., and Wallace, S. (2016). "Unsupervised clustering on PMU data for event characterization on smart grid," in Smart Cities and Green ICT Systems (SMARTGREENS), 2016 5th International Conference on. IEEE, 1–8.

Kohavi, R. (1995). "A study of cross-validation and bootstrap for accuracy estimation and model selection" in Proceedings of the 14th International Joint Conference Artificial Intelligence. Montreal, Canada, 1137–1145.

Ladha, L., and Deepa, T. (2011). Feature selection methods and algorithms. *Int. J. Comput. Sci. Eng.* 3 (5), 1787–1797.

Li, Z., Liu, H., Zhao, J., Bi, T., and Yang, Q. (2021). Fast power system event identification using enhanced lstm network with renewable energy integration. *IEEE Trans. Power Syst.* 5, 4492–4502. doi:10.1109/tpwrs.2021.3064250

Liu, W., Lin, Z., Wen, F., and Ledwich, G. (2013). A wide area monitoring system based load restoration method. *IEEE Trans. Power Syst.* 28 (2), 2025–2034. doi:10.1109/tpwrs.2013.2249595

Liu, X., Kennedy, J. M., Laverty, D. M., Morrow, D. J., and McLoone, S. (2016). Wide-area phase-angle measurements for islanding detection—An adaptive nonlinear approach. *IEEE Trans. Power Deliv.* 31 (4), 1901–1911. doi:10.1109/tpwrd.2016.2518019

Liu, X., Laverty, D., Best, R., Li, K., Morrow, D., and McLoone, S. (2015). Principal component analysis of wide-area phasor measurements for islanding detection-a geometric view. *IEEE Trans. Power Deliv.* 30 (2), 976–985. doi:10.1109/tpwrd.2014.2348557

McLachlan, G. (2004). *Discriminant analysis and statistical pattern recognition*, 544. Hoboken: John Wiley & Sons.

Morozovska, A. V. M. K., Heleno, M., and Hilber, P. (2021). Including dynamic line rating into the optimal planning of distributed energy resources. *IEEE Trans. Smart Grid* 6, 5052–5059. doi:10.1109/tsg.2021.3109130

Mukherjee, S., Chakrabortty, A., and Babaei, S. (2021). Modeling and quantifying the impact of wind penetration on slow coherency of power systems. *IEEE Trans. Power Syst.* 36 (2), 1002–1012. doi:10.1109/tpwrs.2020.3022832

Nalepa, J., and Kawulok, M. (2018). Selecting training sets for support vector machines: A review. *Artif. Intell. Rev.* 52 (2), 857–900. doi:10.1007/s10462-017-9611-1

Pandey, S., Srivastava, A. K., and Amidan, B. G. (2020). A real time event detection, classification and localization using synchrophasor data. *IEEE Trans. Power Syst.* 35 (6), 4421–4431. doi:10.1109/tpwrs.2020.2986019

Rafferty, M., and Liu, X., (2020). "Automatic power system event classification using quadratic discriminant analysis on PMU data," in General Meeting, 2020 IEEE PES, USA.

Rafferty, M., Liu, X., Laverty, D., and McLoone, S. (2016). Real-time multiple event detection and classification using moving window PCA. *IEEE Trans. Smart Grid* 7 (5), 2537–2548. doi:10.1109/tsg.2016.2559444

Rafferty, M., Liu, X., Laverty, D., Xie, L., and McLoone, S., "Adaptive islanding detection using wide area phase angle monitoring," in 7th IEEE International Conference on Innovative Smart Grid Technologies, 2017, pp. pp. 1–6.

Singh, P., Singh, N., Singh, K. K., and Singh, A. (2021). "Chapter 5 - diagnosing of disease using machine learning," in *Machine learning and the internet of medical things in healthcare*. Editors K. K., Singh, M., Elhoseny, A., Singh, and A. A., Elngar (Academic Press), 89–111.

Syed, D., Zainab, A., Ghrayeb, A., Refaat, S., Abu-Rub, H., and Bouhali, O. (2021). Smart grid big data analytics: Survey of technologies, techniques, and applications. *IEEE Access* 9, 59564–59585. doi:10.1109/ACCESS.2020.3041178

Van Der Maaten, L., Postma, E., and Van den Herik, J. (2009). Dimensionality reduction: A comparative review. *J. Mach. Learn Res.* 10, 66–71.

Vosughi, A., Sadanandan, S. K., and Srivastava, A. K. (1996). Synchrophasor-based event detection, classification, and localization using koopman, transient energy matrix, best worth method, and dynamic graph. *IEEE Trans. Power Deliv.* 37 (3), 19862022. doi:10.1109/tpwrd.2021.3102148

Yadav, R., Pradhan, A. K., and Kamwa, I. (2019). Real-time multiple event detection and classification in power system using signal energy transformations. *IEEE Trans. Ind. Inf.* 15 (3), 1521–1531. doi:10.1109/tii.2018.2855428

Yan, H., and Dai, Y. (2011). "The comparison of five discriminant methods," in Management and Service Science (MASS), 2011 International Conference on. IEEE, 1–4.

frontiers | Frontiers in Energy Research

TYPE Original Research
PUBLISHED 01 September 2022
DOI 10.3389/fenrg.2022.987773

OPEN ACCESS

EDITED BY
Minghao Wang,
Hong Kong Polytechnic University,
Hong Kong SAR, China

REVIEWED BY
Hao Fu,
Central Southern China Electric Power Design Institute, China
Tohid Rahimi,
Carleton University, Canada
Jing Li,
State Grid Energy Research Institute (SGCC), China

*CORRESPONDENCE
Conghuan Yang,
conghuanyang@foxmail.com

SPECIALTY SECTION
This article was submitted to Smart Grids,
a section of the journal
Frontiers in Energy Research

RECEIVED 06 July 2022
ACCEPTED 19 July 2022
PUBLISHED 01 September 2022

CITATION
Alashqar M, Xue Y, Yang C and Zhang X-P (2022), Comprehensive economic analysis of PV farm -A case study of Alkarsaah PV farm in qatar. *Front. Energy Res.* 10:987773.
doi: 10.3389/fenrg.2022.987773

Comprehensive economic analysis of PV farm -A case study of Alkarsaah PV farm in qatar

Mohamed Alashqar[1], Ying Xue[3], Conghuan Yang[2]* and Xiao-Ping Zhang[1]

[1]University of Birmingham, Birmingham, United Kingdom, [2]Guangzhou Maritime University, Guangdong, China, [3]South China University of Technology, Guangzhou, China

Countries around the world are rapidly deploying renewable energy generation to reduce carbon emissions. Countries in the Gulf Cooperation Council (GCC) are investing heavily in PV generation due to their rich solar resources. As PV technology becomes more mature, future PV developments will largely depend on the cost of the PV generation but there is currently very limited published work that shows a detailed design and in particular the economic analysis of large-scale PV farms. Therefore, this paper uses the Qatar's first PV farm, the 800MWp Alkarsaah PV farm as a case study to explain the design considerations and especially the economic benefits of large-scale PV farms. Economic comparisons will be made with the most efficient CCGT (combined cycle gas turbine) plants in the network to highlight the economic benefits of PV farms. The results show that the Levelized cost of electricity (LCOE) for this PV farm is 14.03$/MWh, much lower than the LCOE of 39.18$/MWh and 24.6$/MWh from the most efficient CCGTs in the network, highlighting the significant economic benefits of developing PV farms in a low carbon power networks in the future.

KEYWORDS

LCOE, marginal cost, capital cost, fixed cost, PV solar project, renewable energy

Introduction

Reducing energy-related CO_2 emissions is at the heart of the energy transition and developing renewable energy generation is one of the key measures. Moreover, it helps improve the air quality (Akella et al., 2009; Hung, 2010; Petinrin and Petinrin, 2014; IRENA, 2019) and energy security, especially during instability in the energy market (e.g., during sudden changes in the fossil fuel market (Franco et al., 2017; Chen et al., 2022)).

In the last decade, renewable energy (RE) witnessed a dramatic cost decrease. The Levelized Cost of Electricity (LCOE) is commonly used to evaluate the generation assets or the power system as well as to compare the cost of energy gained from different sources. The LCOE estimates the income necessary to develop and run a generator over a particular cost recovery time. The LCOE calculations include different costs: capital costs, decommissioning, fuel costs, fixed and variable operations and maintenance costs, finance costs, and an anticipated utilisation rate (McCulloch and McCulloch, 2017; Wang

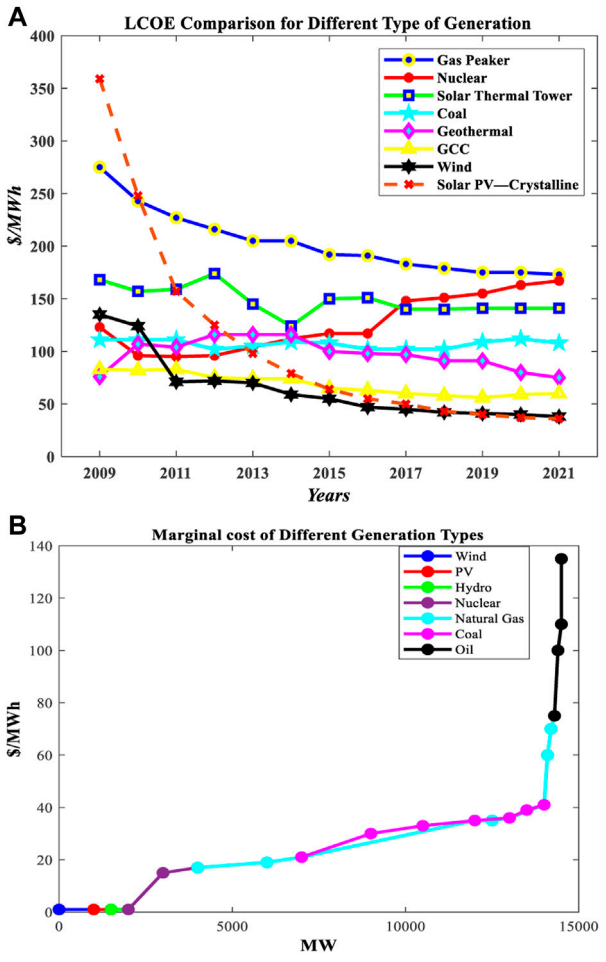

FIGURE 1
Comparison between different types of generation **(A)** LCOE comparison, **(B)** Marginal cost comparison (Hartman, 2016; Ray, 2021).

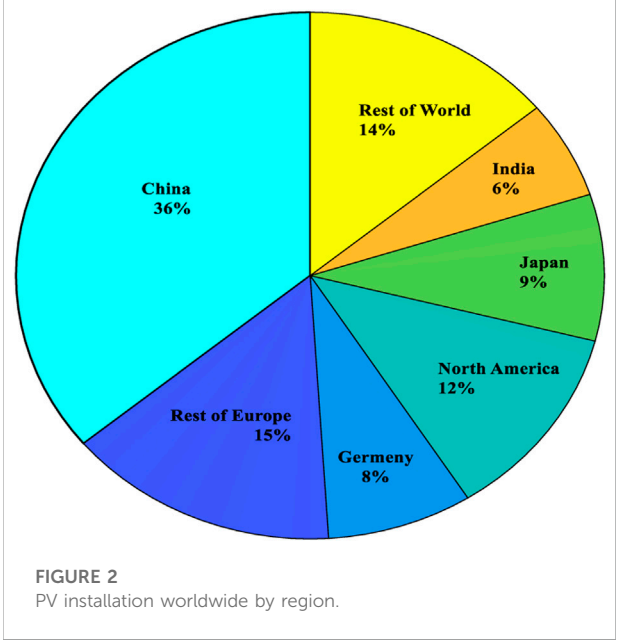

FIGURE 2
PV installation worldwide by region.

et al., 2018a; U.S. Energy Information Administration, 2022; Cucchiella et al., 2017; Kosmadakis et al., 2022; Heidari Yazdi et al., 2022).

Figure 1A shows the LCOE comparison for diverse generation technologies. It illustrates the significant fall in solar power from around 359$/MWh in 2009 to approximate 36$/MWh in 2021, which means a 90% decline in the last decade. In the same period, the LCOE of wind generation decreased from 135$/MWh to 38$/MWh, a 72% reduction. The considerable declines in solar and wind are due to the drop in capital costs (Mcelroy and Chen, 2017).

RE systems need significant upfront financial commitments similar to thermal or nuclear power plants. However, the marginal costs of operating the asset and generating electricity are much lower, as illustrated in Figure 1B (e.g., this includes replacing selected PV modules or inverters for solar PV projects and periodic lubrication and general maintenance for wind turbines (Wang et al., 2018b; Srinivasan, 2019; Tian et al., 2020)). It can be seen from Figure 1B that the marginal cost of wind and solar is almost negligible. In contrast, the marginal cost of other generation types increases with increasing power production. For example, it is around 75$/MWh for natural gas, and around 140$/MWh for oil as shown in Figure 1B. It is mainly because the marginal cost of generation for conventional generators is dominated by fuel costs (coal, oil, and gas). On the other hand, for renewable generation, the fuel from the sun and wind is essentially free, and the operations and maintenance (O&M) costs dominate the marginal costs.

These remarkable changes motivate countries to implement renewable energy resources. For example, Figure 2 illustrates that at the end of 2020, the total cumulative PV installations were at 710GWp (Bett, 2022), where China represents 36% of the PV installations, Europe 23%, North America 12%, Japan 9%, India 6%, and the rest of the world 14%.

Many countries have started utilising deserted areas for installing renewable energy sources (Shah et al., 2019). However, each region around the world has unique challenges. For example, India installed many large-scale PV plants in tropical regions to benefit from the summer sunshine. However, in a tropical climate, the rain caused by monsoon seasons influences the performance of PV plants (gopi et al., 2021). In addition, the paper (Shah et al., 2019) concludes that during the southwest monsoon season, the energy generation dropped by 36% compared to the annual average generation.

In Qatar, the weather plays a factor during summertime due to the dust waves and high humidity. To reduce its impact, at Alkarsaah PV farm, four flees of six robots in each fleet are used to perform cleaning activities at night for 10 hours daily to

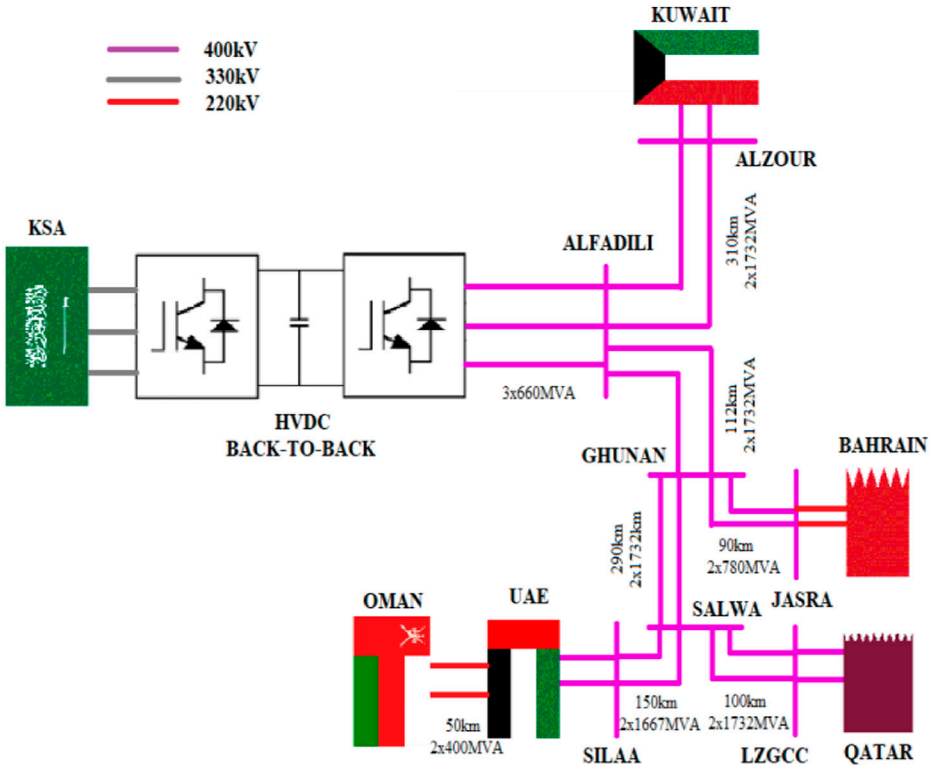

FIGURE 3
SLD of GCC interconnection.

TABLE 1 PV solar projects operated in the GCC region.

Project	Country	Year	Total capacity (MW)
Mohammed bin Rashid Al Maktoum Solar Park	UAE	2018	1,013
Noor Abu Dhabi, Sweihan	UAE	2019	1,177
Sakaka	KSA	2019	300
Askar Landfill	Bahrain	2019	100
PDO Amin PV Plant	Oman	2020	100
Shagaya	Kuwait	2019	10
Ibri	Oman	2021	500

maintain the PV plant's performance. There was a coupling between water and power production in Qatar, which makes a stumbling block in front of renewable integration, but with the reverse osmosis (RO) system, the flexibility of integrating renewable energy increases. Qatar focused on RO technologies to decuple water and power production in the recent water project.

Some research discusses small-scale PV farms with rated capacity within 2 MW (Díez-Mediavilla et al., 2010; Chandel et al., 2014; Shah, 2018; Brodziński et al., 2021). Most of these researches focused on PV farms connected to the distribution network and its techno-economic impacts. Other research concentrated on analysing the economic impact of PV installations at the residential level (Woodhouse et al., 2011), (Kizito, 2017). Other research analysed the RE economy in the electricity market framework (Liu et al., 2020) and showed that a continued support policy is required to make wind and solar energy competitive in the energy market (Okere and Iqbal, 2021). compared various solar PV modules for utility-scale PV installation in California and concluded that the bifacial

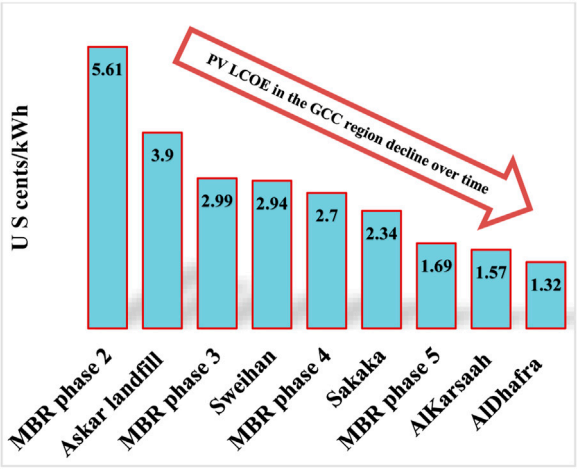

FIGURE 4
The LCOE of the existing solar project in the GCC region.

technology gives the best performance in terms of annual energy production. So far, very limited published work on the development and economic analysis of large-scale PV farms. Therefore, this paper contributes to this aspect by presenting a comprehensive analysis of Alkarsaah PV Farm in Qatar under the context of PV developments in the Gulf Cooperation Council (GCC) regions. The objective is to share the experience and especially the economic rationale of large-scale PV farm development with the research and industry community to promote future PV farms' development further.

Gulf cooperation council overview

This section discusses the motivations that lead GCC countries to move toward renewable energy, the benefits of the GCC interconnection, and the existing and agreed-upon solar energy projects.

Renewable energy motivation

The GCC countries, namely the Kingdom of Saudi Arabia (KSA), Kuwait, Bahrain, Qatar, United Arab Emirates (UAE), and Oman, are in the top 25 globally in CO2 emissions per capita. Concerns about global climate and environmental challenges have been raised in the GCC region, necessitating an integrated plan to take a more proactive approach to ecological modernisation and energy policies. The requirements for forming a strategic partnership focused on the GCC region's sustainability

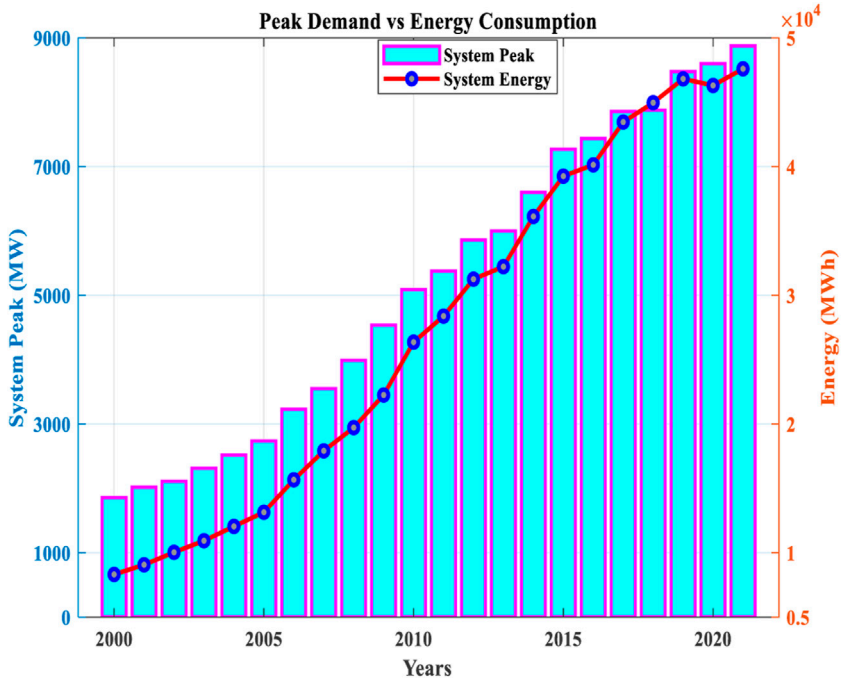

FIGURE 5
Historical peak demand and annual energy consumption from 2000 to 2021.

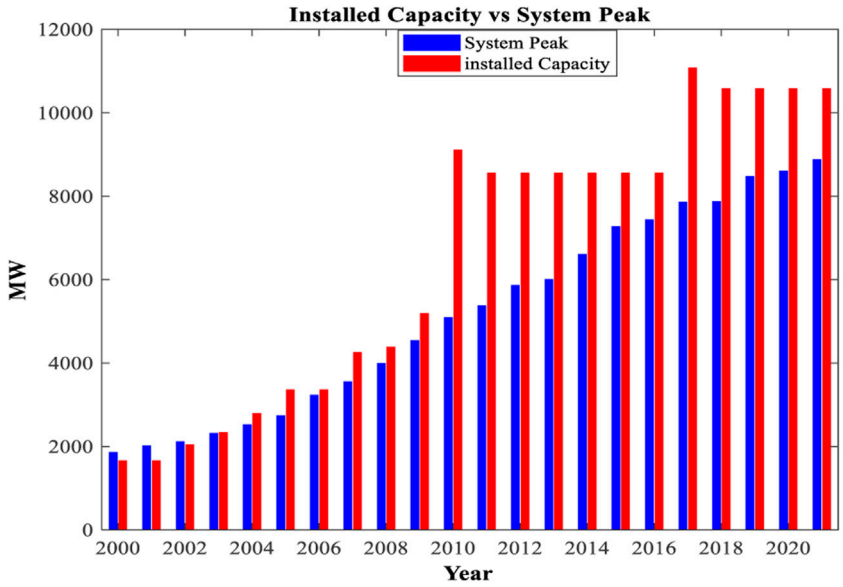

FIGURE 6
The installed capacity and system peak from 2000 up to 2021.

and well-being have been highlighted by regional authorities (Csala and Csala, 2020).

Years ago, it may appear irrational to invest in renewable energy technologies in a location where the oil and gas sectors dominate (Ferroukhi et al., 2013). In addition, such investments do not provide sufficient short-term financial returns and instead create competitors for the region's key exports. However, this perspective has changed due to the enormous opportunities with renewable generation, and the GCC's reliance on oil and gas earnings is decreasing.

Gulf cooperation council interconnection

The GCC Interconnection was established in 2009 by connecting the member states in the GCC (Aljohani and Alzahrani, 2014), (Al-Ebrahim and Jones, 2017). This interconnection aims to share energy during emergencies, reduce the spinning reserves and improve the efficiency of the interconnected power system (Csala and Csala, 2020), (Aljohani and Alzahrani, 2014). Figure 3 shows the GCC interconnection's single line diagram (SLD). It shows that the member states are connected via a 400 kV extra-high voltage (EHV) network, while the KSA (Kingdom of Saudi Arabia, 60 Hz) is connecting to the GCCIA (50 Hz) through a high-voltage direct-current (HVDC) back-to-back converter. The strength and modernity of the Gulf connection encouraged member states to launch renewable energy projects.

PV solar projects in the gulf cooperation council region

The region witnessed a rapid movement with the launch of renewable energy projects, especially photovoltaic energy. For instance, the KSA constructed a 300 MW PV project in Sakaka province in 2019 (Alnaser et al., 2022), (Alharbi and Csala, 2021).

The United Arab Emirates (UAE) started earlier than other GCC member states and built the first phase of the 13 MW Mohammed bin Rashid Al Maktoum (MBR) solar park in 2013, followed by the second phase rated at 200 MW in 2018, then in 2020, the third phase started operation with a rated capacity of 800 MW. The fourth phase combined three technologies of clean energy: 100 MW from a concentrated solar tower, 250 MW from photovoltaic panels, and 600 MW from a parabolic basin complex (Saqib, 2018; Obaideen et al., 2021; Xiao et al., 2022). The fifth phase started in stages from the second quarter of 2021 with a total capacity of 900 MW (Saqib, 2018). These projects align with the plan to reach 5 GW production from clean energy in 2030 with $13.6bn of investments. In addition, in 2019, a 1177 MW Sweihan solar plant was operated in Abu Dhabi (Ramachandran, Mourad, Hamed). Moreover, the 2 GW Al Dhafra solar project is under construction and expected to be operated by 2022 (Apostoleris and Chiesa, 2019; Cheema et al., 2021; Jim, 2021). As a result, these projects placed the UAE at the top of the renewable energy deployment in the GCC region.

Bahrain comes into the picture with a 100 MW Askar landfill solar project in 2019 (Apostoleris et al., 2021).

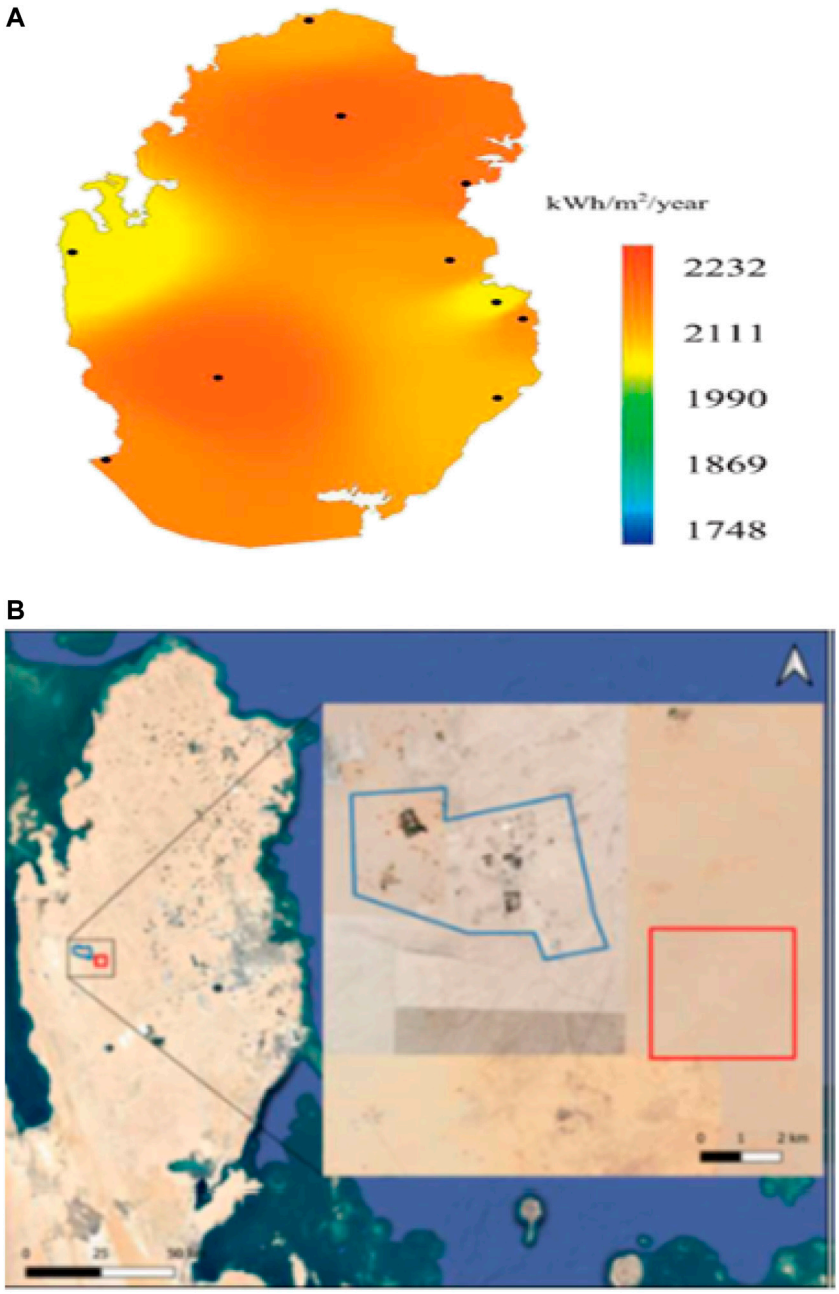

FIGURE 7
(A) Qatar solar GHI (kWh/m2/yr). **(B)** Alkarsaah PV farm location.

Furthermore, in 2019, Kuwait commissioned 10 MW at Shagaya renewable energy park (Wang et al., 2021a). Also, Oman started implementing solar energy with 100 and 500 MW in 2020 and 2021, respectively (Wang et al., 2021b). Likewise, in 2020, Qatar announced an 800 MW AlKarsaah PV farm to be entirely operated in 2022. A detailed economic analysis of this PV farm project will be presented in the rest of this paper.

Table 1 shows the existing solar project in the GCC region, and it can be observed that within 4 years, more than 3 GW generation came from PV only, with more projects in the pipeline. Figure 4 shows the LOCE of the existing solar projects in the GCC member states. It can be seen from Figure 4 that from 2018 to 2020, the LOCE of PV solar project cost is decreased by 76.5%, resulting in more PV farm deployment in the GCC countries.

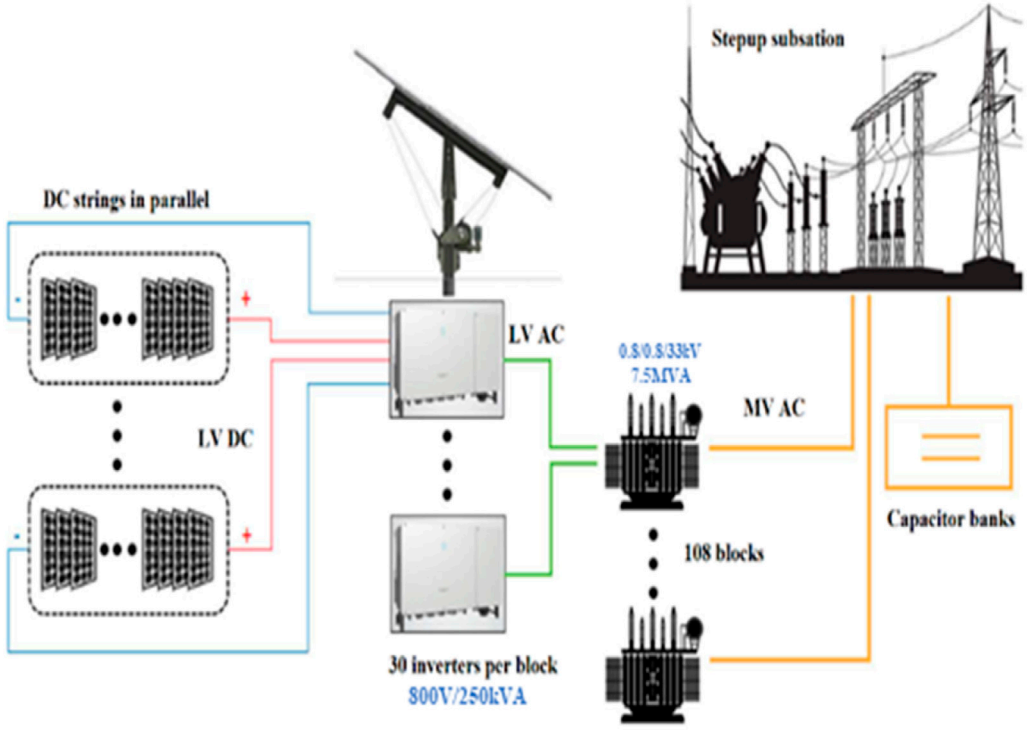

FIGURE 8
PV farm structure.

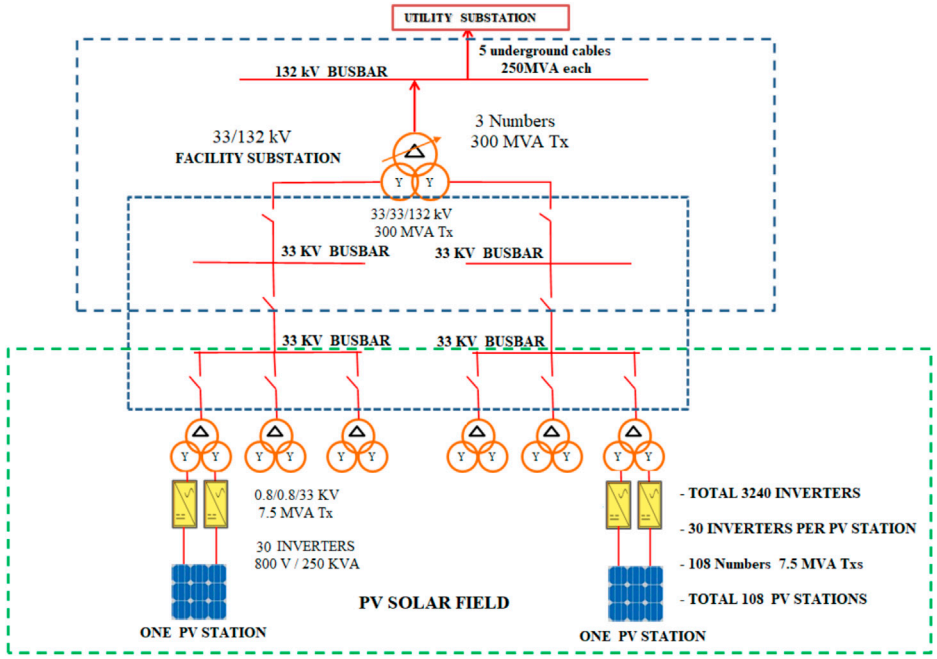

FIGURE 9
PV farm in detail.

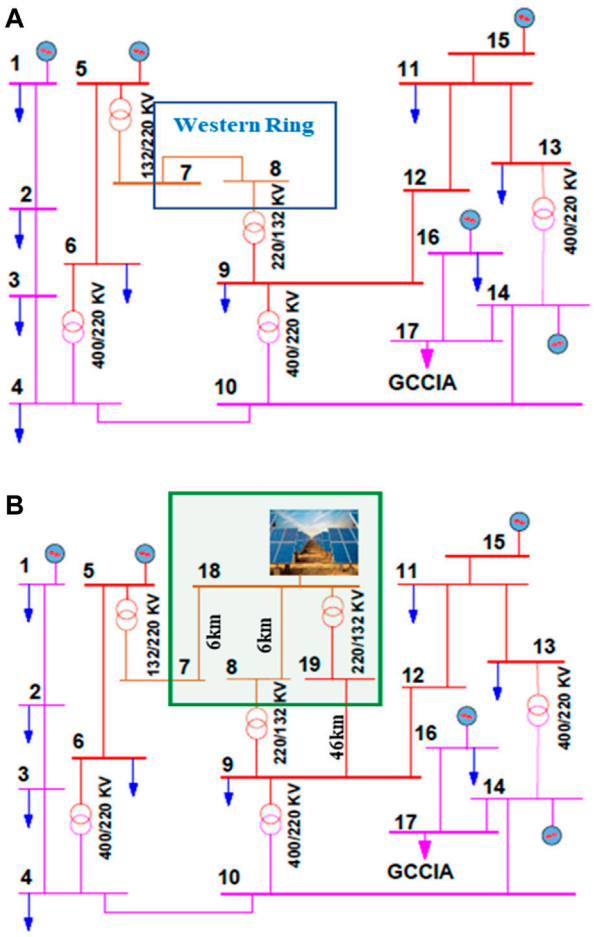

FIGURE 10
Qatar power system SLD **(A)** without PV farm. **(B)** With PV farm.

Qatar power system overview

Generation

Qatar General Electricity and Water Corporation (KAHRAMAA) was established in July 2000 to manage and maintain electricity and water supply to the consumers in Qatar. Since its establishment, the electricity sector has witnessed extraordinary growth due to many factors. For example, the population in Qatar has increased by 378% from 2004 (744029) to 2022 (2811774). This significantly increases peak demand and annual energy consumption, as shown in Figure 5. It can be seen from Figure 5 that in 2000, the maximum demand and energy consumption were 1855 MW and 8332GWH, respectively; in 2021, they increased to 8875 MW (468% increase) and 48683 GWh (584% increase). This gives significant challenges in developing generation capacities in Qatar.

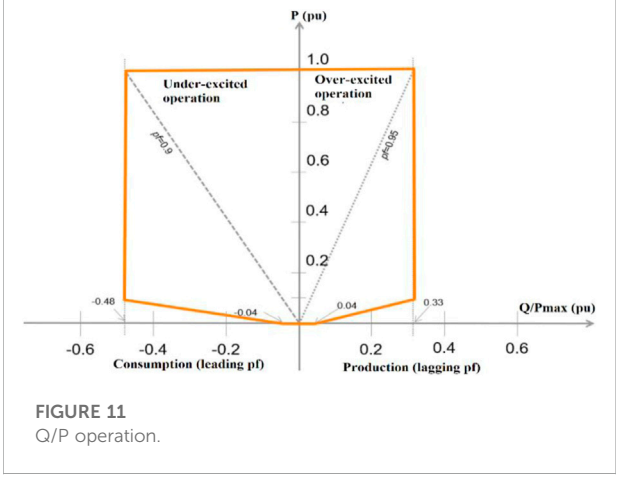

FIGURE 11
Q/P operation.

Transmission and distribution network

To meet high demand growth as described above, KAHRAMAA, in collaboration with Independent Power Producers (IPP), expanded the generation capacity from 4032 MW in 2008–10575 MW by commissioning three large-scale power plants in 2009, 2010 and 2017, with an installed capacity of 1995, 2730, and 2520 MW respectively as shown in Figure 6. All these power plants use natural gas to produce electricity. Furthermore, the electricity demand rise has led to the expansion of the transmission network with the commissioning of a new voltage level at 400 kV. Accordingly, the primary substations are increased from 87 in 2000 to 400 in 2021.

At the same time, the distribution network also witnessed a colossal expansion where the number of substations increased to 18613 in 2020, with a 5% growth compared to 2019. This number is planned to rise further to reach 23400 substations by the end of 2026 to serve the urban development, economic activities and events hosted by Qatar. This expansion paralleled with the specific crucial projects in the country, including but not limited to Lusail City, Metro project, New Port, and 2022 World Cup Stadiums.

AlKarsaah PV farm

The project background

The project is planned to be connected to the grid in two phases. The first phase is 350 MW which will be grid-connected in June 2022, and the second phase is expected to be fully operational in July 2022. The total cost of the project is 448.4$M for 800MWp including connection equipment 220 and 132 kV substations. With this capacity, Alkarsaah PV farm is the third largest project in the GCC region of its kind.

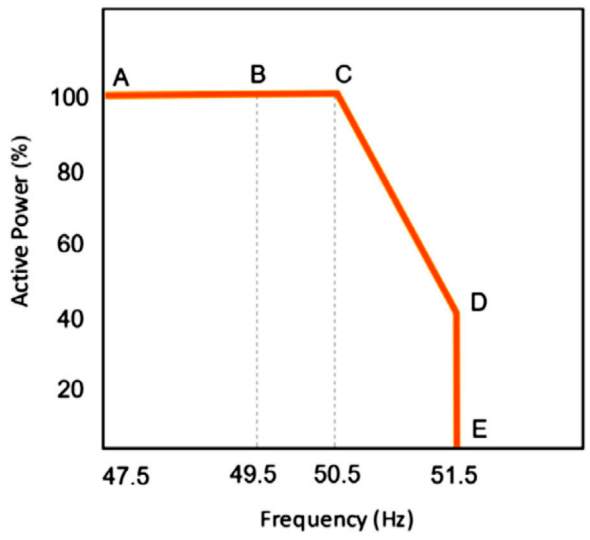

FIGURE 12
Active Power limitation during over frequency.

The project is designed as build, own, operate, and transfer (BOOT) for 25 years, then the ownership will be transferred to KAHRAMAA. Consequently, KAHRAMAA signed a 25-years Power Purchase Agreement (PPA) with Siraj 1 (the purpose company that was established to build, operate and manage the project) in January 2020 to acquire electricity from the power plant. After the agreement of all relevant parties, AlKharsaah area was chosen as the project site, which is located 80 km^2 west of Doha, as shown in Figure 7B. The location was chosen based on several key criteria:

1) The high potential of Global Horizontal Irradiation (GHI) with 2,145 kWh/m2/yr, as shown in Figure 7A, these figures are based on the findings of solar radiation monitoring stations at various locations in Qatar, including AlKharsaah, which were conducted by the Qatar meteorological department (QMD), Qatar Environment and Energy Research Institute (QEERI), Total, Marubeni, and Kahramaa.
2) The local environment impacts because it is located in a desert environment where living creatures are scarce.

PV farm structure

The structure of the PV farm is shown in Figure 8, with the detailed SLD of the system shown in Figure 9. It consists of 1,803,240 modules, where 1,357,920 modules of 445W and 445,320 modules of 440W. There are 108 blocks in the PV plant. Each block is connected to 1 MV substation, and there are 30 inverters connected to 17,280 PV modules that generate 7.5 MW. Hence there are in total 3,240 inverters for the project. Capacitor banks are installed at the AC substation, as shown in Figure 8, to meet the reactive power control requirement as explained subsection D.

TABLE 2 Cost of modificationsin the network.

Items	Cost (M$)
Cost of 220 KV—132 KV GIS s/s	44
Cost of 220 kV OHL [2 CCT's] 35 km	19.2
Cost of 220 kV cables [2 CCT's] 11 km	42.2
Cost of 132kVOHL [4 CCT's] 6 km	5.8
Cost of modification at both ends of the LILO	0.5

Keys benefits of the project

The overall capacity of the solar project will be able to cover 7.5% of the 2022 peak demand. Also, the project will contribute to Qatar's commitment in hosting a carbon-neutral FIFA World Cup in 2022, which is a goal of the Qatar National Vision 2030. In addition, the plant will save 26 million tonnes of CO2 throughout its lifespan, contributing to the ambitious goal of reducing carbon emissions by one million tonnes every year starting from 2022. Furthermore, the project will help achieve sustainable development by reducing the dependency on gas for energy generation. AlKharsaah PV farm uses cutting-edge solar energy technology such as twin panels to conserve space, automated sun-tracking systems, and robotic solar panel cleaning to enhance production efficiency and lower plant operating costs. Additionally, more than two million bifacial solar modules with trackers will maximise efficiency.

Qatar power system and PV connection

The power system of Qatar consists of eight power plants as shown in Figure 10A with a 10.6 GW installed capacity. Three combined cycle power plants with 2730, 2520, and 1992 MW are connected to the 400 kV level, and another two combined cycle power plants with 756 and 1025 MW are connected to the 220 kV level. In addition, three open cycle power plants are connected to the 220 kV level. All power plants use gas as a fuel supply. The GCCIA interconnector is connected to the grid at 400kV, as shown in Figure 10A as well.

The weakest point in the network is the western ring from bus 7 and bus 8 in Figure 10A. This ring has double circuit overhead lines of 205 km in length. Therefore, the ring suffers from voltage stability in case of n-2 contingency, and during normal operation, the voltage profile is poor because there is no reactive power compensation. Consequently, due to the high

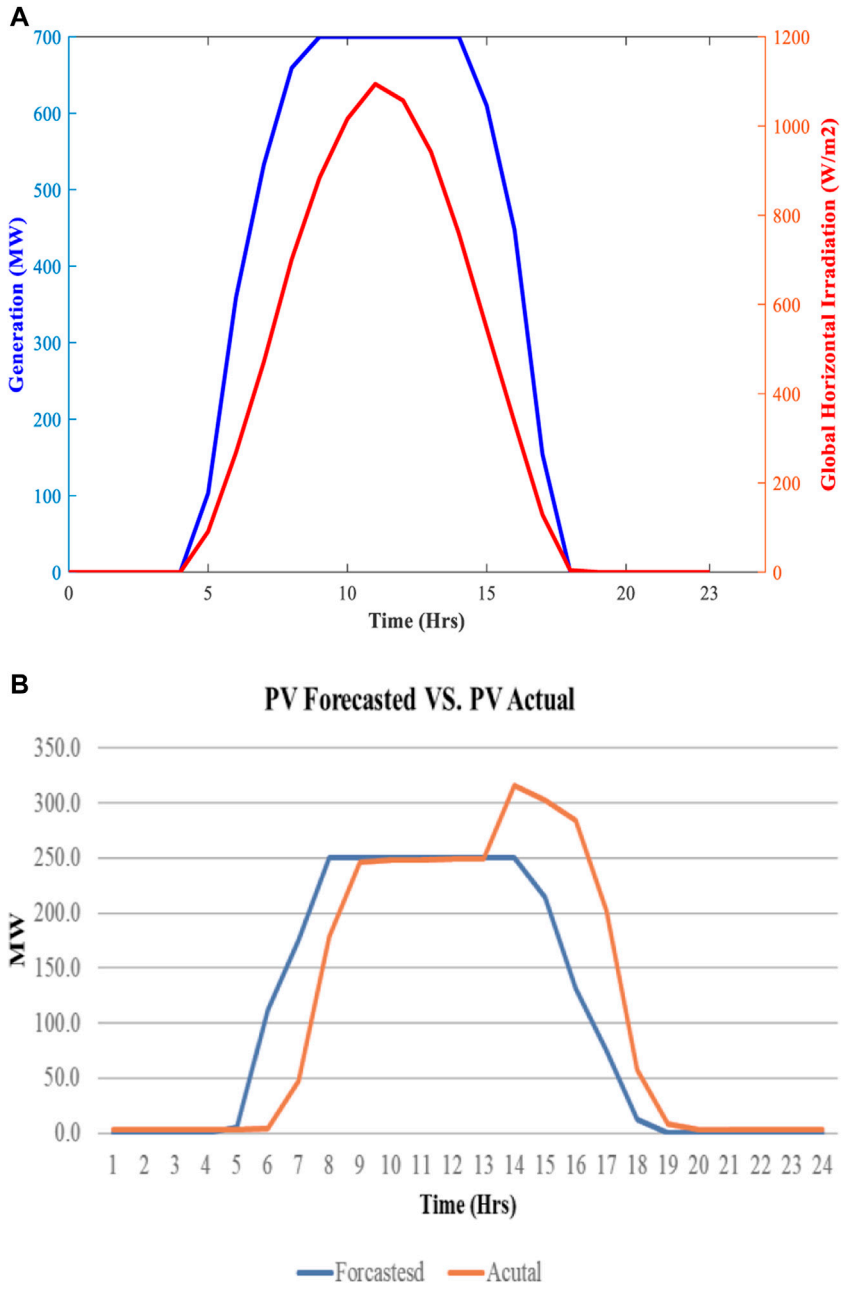

FIGURE 13
(A) Typical daily generation profile. **(B)** Forecasted and actual generation profile for 1 day.

radiation in the Alkarsaah area and reactive power support ability (explained below) from the PV farm, the preferred option is to connect AlKarsaah PV farm to the 132 kV subnetwork as a loop-in-loop-out (bus 18 in Figure 10B) between two existing substations (bus 7 and 8) in the western ring. The length between the existing substation and the PV farm is 6 km as shown in Figure 10B. In addition, the substation will be connected to the new Kahramaa substation (LILO substation), bus 18 in Figure 10B, through five underground cables to meet the n-2 criteria. Moreover, the PV farm will be connected to the 220 kV network via a double circuits overhead line for a 35 km distance, then an 11 km cable portion to the existing substation, bus 9 in the single line diagram (SLD), as shown in Figure 10B.

For reactive power control capability of the PV farm, according to the PPA and the grid code, it must be able to provide reactive power at the Point of interconnection (POI) at

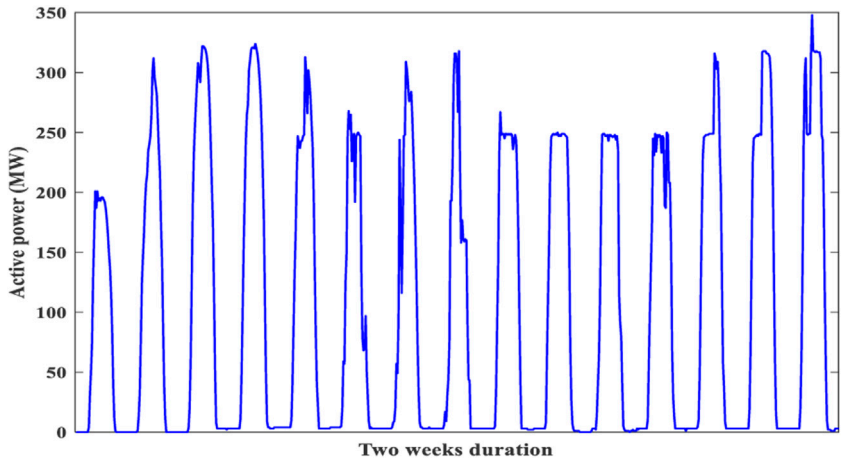

FIGURE 14
Hourly active power generated from PV farm.

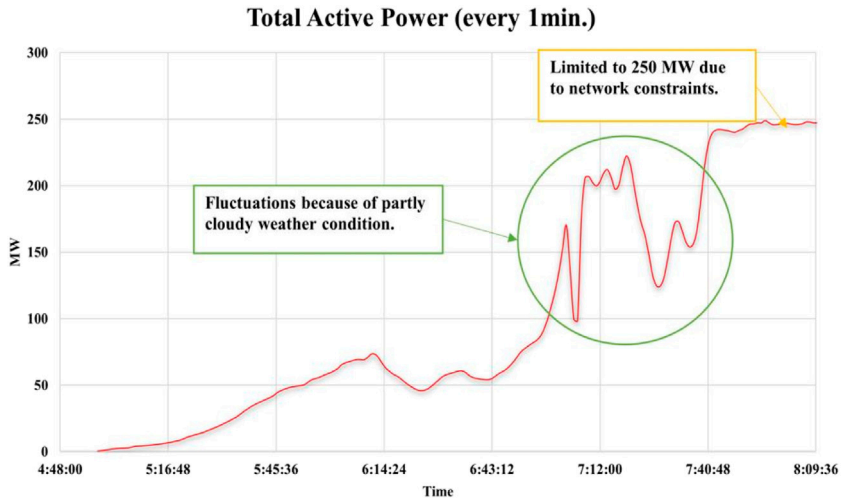

FIGURE 15
PV fluctuation due to partly cloudy weather conditions.

any operating point inside the P-Q/Pmax profile as shown in Figure 11.

To achieve that, the Power Plant Controller (PPC) of Al-Kharsaah PV farm controls the inverters and capacitor banks to change its reactive power generation/absorption to achieve a reactive power setpoint imposed either by the on-site operator or by the grid operator. Consequently, during the daytime, when the load increases, the PV farm will inject up to 462.9MVAR to the network to maintain the voltage at the POI within the operational limits. Therefore, the inverters will operate with a power factor between −0.95 and +0.95 (±252.9MVAr), and capacitor banks (6 × 35MVar) will compensate for the remaining reactive power. On the other hand, during nighttime, when the load decreases, the inverters will absorb reactive power so that the KAHRAMAA grid can deliver to the PV plant 359 MVAr at POI. The reactive power capability analysis concluded that the PV farm with additional reactive power support (capacitor banks 6 × 35 MVA) is capable to meet the reactive power requirements at POI and there is no need for reactors to absorb the reactive power from the network during low load.

In addition, the PV farm will remain at the maximum available power when the frequency range between 47.5≤ f ≤ 50.5, then gradually curtail its output when the frequency hits 50.5 Hz to reach zero at a frequency equal to 51.5 Hz. Figure 12

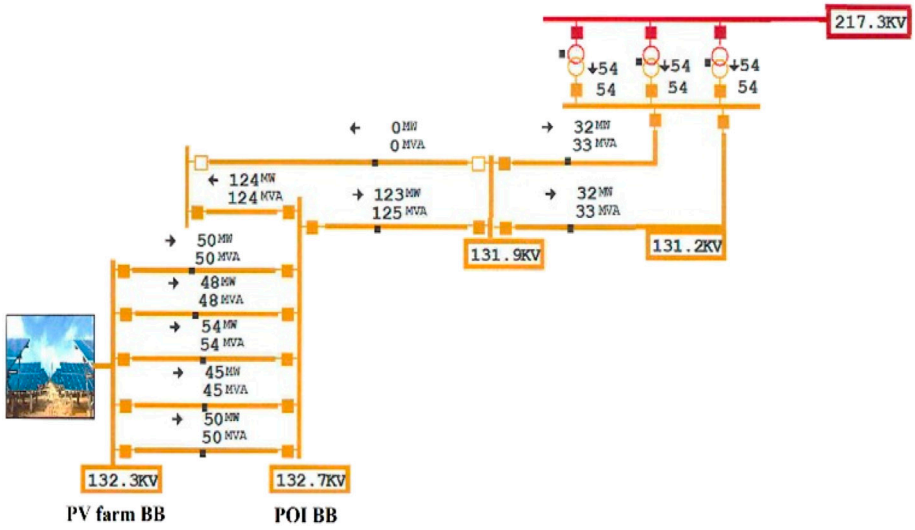

FIGURE 16
Power flow at peak time.

shows This slope is programmed into the Active Power—frequency function of the PPC, taking into consideration the limitation during over frequency.

Table 2 shows the cost of network modifications (as shown in Figure 10B) due to integrating the 800 MW Alkarsaah PV farm. The cost of 220 and 132 kV Gas-insulated substations is 44M$, while the cost of both 220 and 132 kV overhead lines is 67.2M$, and the cost of modification at the existing substations is 0.5M$.

Power generation of the PV farm

The PV farm generates power during the daytime. Due to the stability of weather in summer in Qatar, the generated power from the PV is predictable when there is no cloud. Figure 13A shows a typical daily generation during June when the electricity demand is at its peak. It can be seen that power starts to be injected into the grid at around 4:30 a.m. at sunrise and increases to reach the maximum at 9 a.m. because of the maximum power point tracking. The maximum output power remains for 6 hours, then declines to zero at 6 p.m. (sunset) due to the drop in irradiance. This generation behaviour will allow grid operators to stop the inefficient conventional generation on the system. Figure 13B accentuates the generation forecasted and actual PV generation profile throughout 1 day. It displays the pattern of the PV generation from the sunrise to the sunset, where it jumps in the actual profile because the system operators allow the PV farm to generate more power than the plan during peak to utilise the cheapest available energy instead of synchronising conventional generation to pass the peak time.

Figure 14 illustrates the active power produced from the PV farm for 2 weeks since the date of commissioning and shows only the 1st phase, while the 2nd phase has not yet operated because the network upgrading under commissioning is expected by mid of August.

After the first phase of commissioning, the PV fluctuations occurred due to the partly cloudy weather. It was the first time that system operators experienced this phenomenon, as shown in Figure 15. However, these changes in generation output did not affect the system frequency because it happened early morning when the minimum demand and the spinning reserve were at the highest and the automatic generation control (AGC) took action to maintain the balance.

Figure 16 shows the power flow at the PV farm area and the voltage at different buses during the peak time. In addition, Figure 17A,B represent the voltage at the PV farm and POI buses and the reactive power flow from the PV farm. It can be seen that the inverters operate according to network requirements and within the Q/P operation curve, as shown in Figure 11. It can be seen that the voltage at each bus is close to the nominal value for 132 and 220 kV voltage levels.

The base case forecasted peak demand for summer 2022 is 9300MW, higher than the peak recorded in summer 2021, 8875 MW. However, the high forecast scenario is 9557MW, and the PV farm will contribute positively because of its availability during peak times. Figure 18 illustrates the forecasted peak demand in 2022 and the generation contributions to meet the demand on the designated date. It

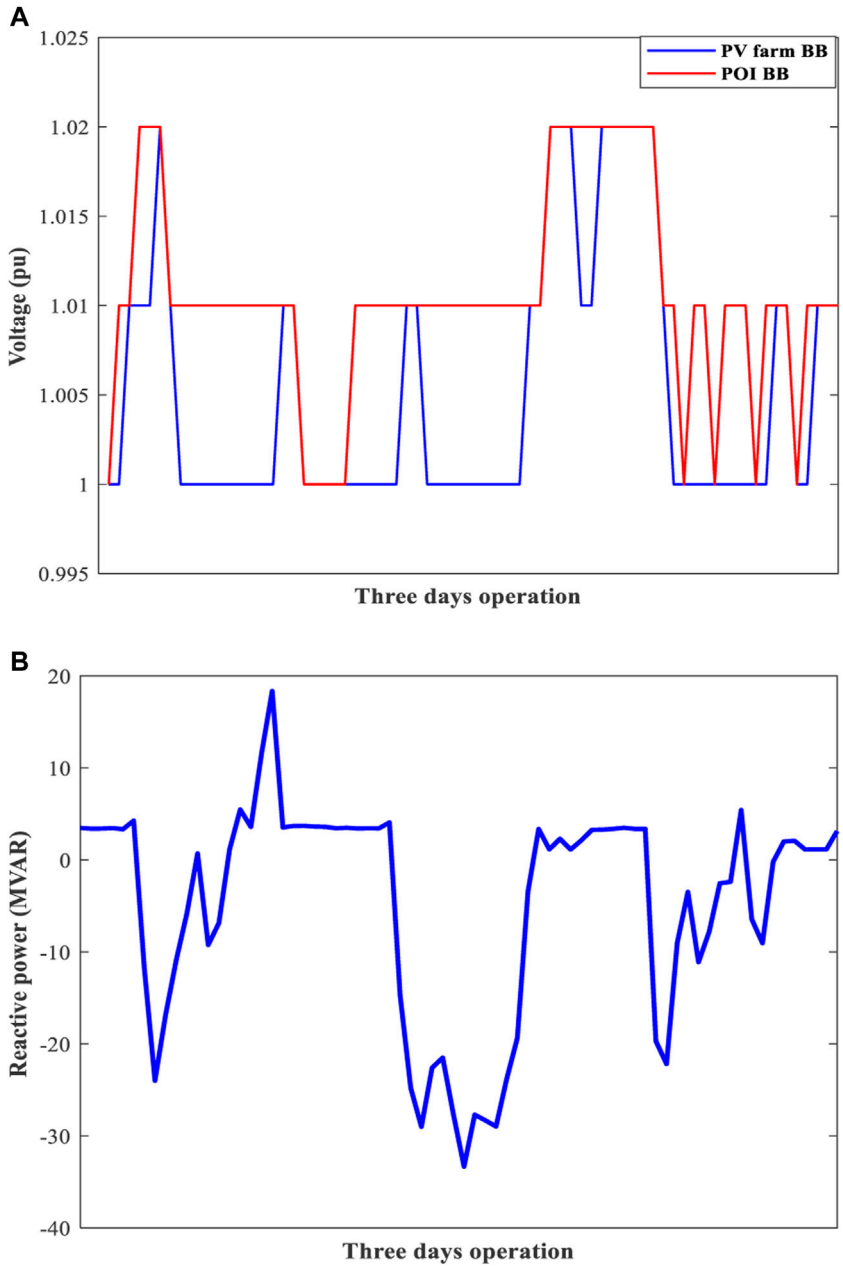

FIGURE 17
(A) Voltage at PV farm and POI buses for 3 days of operation. **(B)** Reactive power flow from the PV farm for 3 days of operation.

is also noticeable that solar power production remains at its peak during the peak demand because of solar tracker usage. Therefore, the thermal units reduce the output power to leave the space for the cheapest energy in the grid. Also, when solar power production decreases due to the low irradiance, the conventional power plant ramps up to maintain the balance between demand and generation.

The FIFA World Cup (FIFA WC) is planned to start on 18th November 2022 and will continue for 1 month; it is considered the most challenging tournament due to the considerable increase in demand. Figure 19 explains the pattern of the electricity demand during the FIFA WC. Also, it shows the peak demand is shifted to the evening peak during winter compared to the afternoon peak during summer in Figure 18; this is due to the considerable change in weather and temperature reduction. In addition, Figure 19 clarifies the PV generation during the WC tournament, which has slight variations that will be covered by the existing thermal units or the GCCIA interconnector.

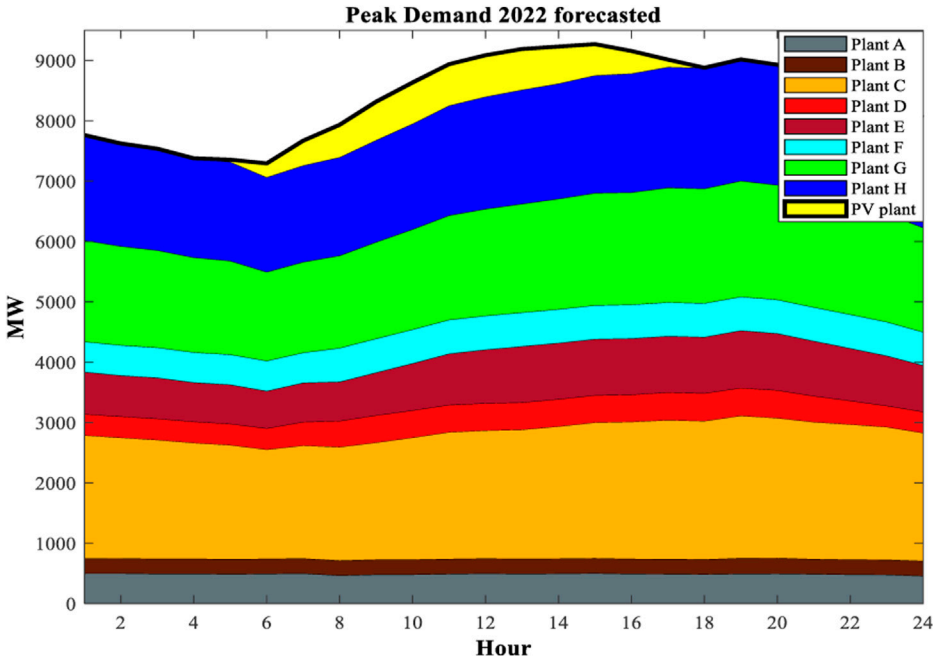

FIGURE 18
The forecasted peak demand in 2022.

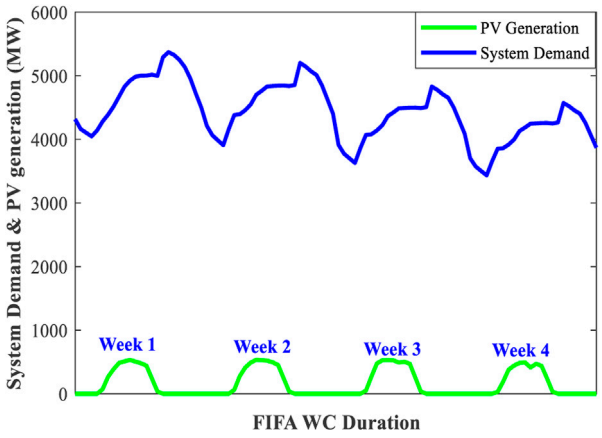

FIGURE 19
System demand and PV generation during the FIFA WC.

TABLE 3 Comparison between two newest conventionalgeneration and PV farm.

Items	Units	Plant D	Plant E	PV Farm
Net Facility Output	MW	2,730	2,520	800.15
Total Capital Cost	$/KW	956.7	673.15	639.45
Fixed O&M	$/KW	1.67	1.22	2.03
Variable O&M	$/MWh	0.096	0.0137	N/A
Heat Rate	MmBtu/MWh	8.82	8.82	N/A
Capacity Factor	%	95.00	95.00	N/A
Fuel Price	$/MMBtu	3.3	3.3	N/A
Construction Time	Months	3	2	2
Facility life	Years	25.00	25.00	25.00
LCOE	$/MWh	39.18	24.6	14.47

Economic analysis

Table 3 shows that the most efficient existing plants in Qatar power system, plant D and plant E, are compared with the PV farm to highlight the economic benefits. These two plants have the biggest generation in the system and use gas as a fuel supply. Plant D has a 2730 MW capacity, and plant E has a 2520 MW capacity. Table 3 shows the detailed comparison of costs between these two plants and the PV farm. First, the total capacity cost of $ per KW of the solar is higher than the total capacity cost of both plant D and plant E, considering the size of all plants. In addition, Solar's fixed operations and maintenance (O&M) costs are higher than others.

However, the variable O&M of plants D and E are 0.096$/MWh and 0.0137$/MWh, respectively, whereas the variable O&M is not applicable for the solar project. Finally, the

TABLE 4 Capacity and output charge rates.

IPP	Contract capacity	Capacity charge rate ($/MW/h)	Output charge rate ($/MWh)
A	567	11.29	30
B	1,025.00	10.39	26.3
C	1995.00	13.9	25.16
D	2,730.00	13.45	22.5
E	2,520	6.18	21.68
PV	800	0	14.03

TABLE 5 Financial comparison between PV solar operation and thermal operation.

Items	Results
2022 Total Energy Forecast (MWH)	51,003,056
Solar Energy Dispatch (MWH)	1,971,542
Av. Gas Ratio (MMBTU/MWH)	9.5
Total Consumed Gas (MMBTU)	484,529,036
Gas Saving (MMBTU)	14,392,253
% Gas Saving	2.88%
Output Unit Cost of Plant E ($/MWH)	22.4
Operation Cost Saving ($)—1 year	44,100,697
Plant E Capacity Charge ($/MWH)	6.315
Plant E Annual Availability (MWH)	21,924,336
Plant E Annual Equivalent to Solar project (MWH)	6,090,093
Plant E 25 years Equivalent Capacity Cost ($)	961,431,232
Total Payment for Solar Project (25 years)—($)	750,000,000
Operation Cost Saving ($)—25 years	4,024,409,103
Total Equivalent Cost for 25 years of thermal Units ($)	2,063,948,656
Total Solar Project Saving Amount ($)	1,313,948,656

LCOE of the solar project is relatively low at 14.03$/MWh, while Plant D is 39.18$/MWh and Plant E is 24.6$/MWh. The calculation of the LCOE is based on the following equations where the system's lifetime, the amount of energy it will produce, and the input costs are considered.

$$TLC = \sum_{t=1}^{n} \frac{I_t + M_t + F_t}{(1+r)^t} \quad (1)$$

$$TLO = \sum_{t=1}^{n} \frac{E_t}{(1+r)^t} \quad (2)$$

$$LCOE = \frac{TLC}{TLO} \quad (3)$$

$$LCOE = \frac{\sum_{t=1}^{n} \frac{I_t + M_t + F_t}{(1+r)^t}}{\sum_{t=1}^{n} \frac{E_t}{(1+r)^t}} \quad (4)$$

where TLC represents the total lifetime cost, TLO represents the total lifetime output, I_t represents the investment and expenditures for the year (t), M_t represents the operational and maintenance expenditures for the year (t), F_t represents the fuel expenditures for the year (t), E_t energy output for the year (t), r represents the discount rate, and n represents the (expected) lifetime of the power system.

The above calculations can be directly applied to other PV farm projects as well by considering subsidies, tax rebates, tax abatements, and other government initiatives that may further decrease the LCOE of PV farm. For example, if the government provides a subsidy for the capital investment in a solar system, the initial cost of establishing the system falls, and the total cost falls proportionally. In addition, the high solar irradiation directly relates to the low LCOE of a project. For example, building an 800 MW PV farm in a different country, e.g., the UK, will require more PV panels to capture more solar irradiation, which leads to an increase in the capital cost of the project and the LCOE. Moreover, the effective daily irradiation time is one of the most critical variables in analysing the total lifetime energy production PV. For example, Qatar has more GHI yearly than the UK, and the weather throughout the year in Qatar is more stable than in the UK. Therefore, increasing the energy production throughout the lifetime of the PV farm will reduce the LCOE.

Another important financial consideration for utility companies and LCOE is the capacity and output charges. For a conventional power plant, the capacity charge is paid based on the availability of the generation in $/MW/h, and the output charge is based on the actual energy output in $/MWh. In Qatar, only the output charge is considered for PV farm, but for thermal units, the utility must pay the capacity charges for the units, as long as they are available but not necessarily running. Table 4 shows the capacity and output charge rates for thermal units and PV. It can be seen from Table 4 that the charges to the utility company for the PV farm is much less than that for thermal units.

From an environmental point of view, the use of RE saves the use of fossil fuels and hence the associated costs. Table 5 shows a detailed financial comparison between the Alkarsaah PV farm

and the most efficient gas power plant (i.e., plant E as mentioned above) to highlight the benefits of PV generation. It can be seen from Table 5 that the total energy forecasted from all generations is around 51 TWh in 2022, and the energy forecasted from Alkarsaah PV farm is around 2 TWh, representing 4% of the total energy. Consequently, the total consumed gas is 484,529,036 MMBTU, and the average amount of gas saved in 2022 is around 14,400,000MMBTU, which saves 44M$. If Alkarsaah PV farm is not installed, the most efficient CCGT will be running with a total equivalent cost of around 2.063B$ for 25 years of operation, including the capacity and operating charges. In contrast, the total payment of the solar project for the 25-years contractual period will be 750M$ as shown in Table 5. As a result; the total savings will be 1.313B$.

Conclusion

Many PV farm projects have been commissioned in the last 5 years in the GCC region due to the high potential of solar irradiance. As a result, some GCC solar projects recorded the lowest LCOE globally at that time. In order to share the experience of large-scale PV farm development in the GCC region and further promote the development of PV farms, the 800MWp Alkarsaah PV Farm in Qatar has been discussed in detail in this paper. Its site selection and structure are explained, and its financial benefits are discussed in detail. In particular, detailed economic analysis has shown that this PV farm can achieve a record low LCOE at 14.03$/MWh, much lower than the 39.18$/MWh and 24.6$/MWh of the most efficient CCGTs in the network. Such analysis can provide useful information for the research community and industry in developing future large-scale PV farms.

As part of our future work, the impact of Alkarsaah PV farm on the practical network operation will be analysed and reported after the system is put into service.

Data Availability statement

The original contributions presented in the study are included in the article/supplementary material, further inquiries can be directed to the corresponding authors.

Author contributions

MA and YX developed the original ideas and prepared the manuscript; CY and X-PZ helped revise the paper.

Conflict of interest

The authors declare that the research was conducted in the absence of any commercial or financial relationships that could be construed as a potential conflict of interest.

Publisher's note

All claims expressed in this article are solely those of the authors and do not necessarily represent those of their affiliated organizations, or those of the publisher, the editors and the reviewers. Any product that may be evaluated in this article, or claim that may be made by its manufacturer, is not guaranteed or endorsed by the publisher.

References

Akella, A. K., Saini, R. P., and Sharma, M. P. (2009). Social, economical and environmental impacts of renewable energy systems. *Renew. Energy* 34 (2), 390–396. doi:10.1016/j.renene.2008.05.002

Al-Ebrahim, A. (2017). "Integrating new and renewable energy in the GCC region," in *Renewable energy integration*. Editor L. E. Jones. Second Edition (Boston: Academic Press), 189–197. doi:10.1016/b978-0-12-809592-8.00014-7

Alharbi, F. R., and Csala, D. (2021). Wind speed and solar irradiance prediction using a bidirectional long short-term memory model based on neural networks. *Energies* 14 (20), 6501. doi:10.3390/en14206501

Aljohani, T. M., and Alzahrani, A. M. (2014). The operation of the GCCIA HVDC project and its potential impacts on the electric power systems of the region. *Int. J. Electron. Electr. Eng.*, 207–213. doi:10.12720/ijeee.2.3.207-213

Alnaser, N. W., Albuflasa, H. M., and Alnaser, W. E. (2022). The transition in solar and wind energy use in Gulf cooperation Council countries (GCCC). *Renew. Energy Environ. Sustain.* 7 (4). doi:10.1051/rees/2021034

Apostoleris, H., Al Ghaferi, A., and Chiesa, M. What is going on with Middle Eastern solar prices, and what does it mean for the rest of us? *Prog. Photovolt. Res. Appl.*, 2021, 29.6: 638–648. doi:10.1002/pip.3414

Apostoleris, H., and Chiesa, M. (2019). "The role of financing in realising ultra-low solar electricity prices in the Middle East," in 2019 IEEE 46th Photovoltaic Specialists Conference (PVSC), 0595–0600.

Bett, A. (2022). *Photovoltaics report*. Freiburg: Fraunhofer Institute for Solar Energy Systems.

Brodziński, Z., Brodzińska, K., and Szadziun, M. Photovoltaic farms—economic efficiency of investments in north-east Poland. *Energies* 14 (8). Art. no. 8, Jan. 2021.

Chandel, M., Agrawal, G. D., Mathur, S., and Mathur, A. (2014). Techno-economic analysis of solar photovoltaic power plant for garment zone of Jaipur city. *Case Stud. Therm. Eng.* 2, 1–7. doi:10.1016/j.csite.2013.10.002

Cheema, A., Shaaban, M. F., Ismail, M. H., and Azzouz, M. A. (2021). "A new approach for long-term optimal scheduling of photovoltaic panels cleaning," in 2021 International Conference on Electromechanical and Energy Systems (SIELMEN), 319–324. doi:10.1109/sielmen53755.2021.9600271

Chen, J., Su, F., Jain, V., Salman, A., Tabash, M. I., Haddad, A. M., et al. (2022). Does renewable energy matter to achieve sustainable development goals? The impact of renewable energy strategies on sustainable economic growth. *Front. Energy Res.* 10. doi:10.3389/fenrg.2022.829252

Csala, F. R., and Csala, D. (2020). GCC countries' renewable energy penetration and the progress of their energy sector projects. *IEEE Access* 8, 211986–212002. doi:10.1109/access.2020.3039936

Cucchiella, F., D'Adamo, I., and Gastaldi, M. (2017). Economic analysis of a photovoltaic system: A resource for residential households. *Energies* 10 (6). Art. no. doi:10.3390/en10060814

Díez-Mediavilla, M., Alonso-Tristán, C., Rodríguez-Amigo, M. C., and García-Calderón, T. (2010). Implementation of PV plants in Spain: A case study. *Renew. Sustain. Energy Rev.* 14 (4), 1342–1346.

Ferroukhi, R., Ghazal-Aswad, N., Androulaki, S., Hawila, D., and Mezher, T. (2013). Renewable energy in the GCC: Status and challenges. *Int J Energy Sect. Man* 7 (1), 84–112. doi:10.1108/17506221311316498

Franco, A., Shaker, M., Kalubi, D., and Hostettler, S. (2017). A review of sustainable energy access and technologies for healthcare facilities in the Global South. *Sustain. Energy Technol. Assessments* 22, 92–105. doi:10.1016/j.seta.2017.02.022

gopi, A., Sudhakar, K., Ngui, W. K., Kirpichnikova, I. M., and cuce, E. (2021). Energy analysis of utility-scale PV plant in the rain-dominated tropical monsoon climates. *Case Stud. Therm. Eng.* 26, 101123. doi:10.1016/j.csite.2021.101123

Hartman, D. (2016). *Economic characteristics of electricity*. Washington, D.C: R STREET'S ELECTRICITY 101 SERIES NO.

Heidari Yazdi, S. S., Rahimi, T., Khadem Haghighian, S., Bagheri, M., and Gharehpetian, G. B. (2022). Over-voltage regulation of distribution networks by coordinated operation of PV inverters and demand side management program. *Front. Energy Res.* 10. doi:10.3389/fenrg.2022.920654

Hung, C. (2010). *Environmental impacts of renewable energy: An overview of life cycle results*. MS thesis. Trondheim: Institutt for energi-og prosessteknikk.

IRENA (2019). Future of solar photovoltaic, Abu Dhabi. IRENA. [Online]. Available media/Files/IRENA/Agency/Publication/2019/Nov/IRENA_Future_of_Solar_PV_2019.pdf (Accessed January 10th, 2022).

Jim, K. (2021). "Pairing coal with solar: The UAE's fragmented electricity policy," in *Low carbon energy in the Middle East and North africa* (Cham: Palgrave Macmillan), 57–91.

Kizito, R. M. (2017). *An economic analysis of residential photovoltaic systems with and without energy storage*. Fayetteville: University of Arkansas.

Kosmadakis, M., and Kosmadakis, G. (2022). "Resource, environmental, and economic aspects of SGHE," in *Salinity gradient heat engines*. Editors A. Tamburini, A. Cipollina, and G. Micale (Sawston: Woodhead Publishing), 319–353. doi:10.1016/b978-0-08-102847-6.00006-1

Liu, W., Zhang, X., Wu, Y., and Feng, S. (2020). Economic analysis of renewable energy in the electricity marketization framework: A case study in guangdong, China. *Front. Energy Res.* 8. doi:10.3389/fenrg.2020.00098

McCulloch, C. S., and McCulloch, M. D. (2017). Levelized cost of electricity for solar photovoltaic and electrical energy storage. *Appl. Energy* 190, 191–203. doi:10.1016/j.apenergy.2016.12.153

Mcelroy, M. B., and Chen, X. (2017). Wind and solar power in the United States: Status and prospects. *Csee Jpes* 3 (1), 1–6. doi:10.17775/cseejpes.2017.0002

Obaideen, K., Nooman AlMallahi, M., Hai Alami, A., Ramadan, M., Abdelkareem, M. A., Shehata, N., et al. (2021). On the contribution of solar energy to sustainable developments goals: Case study on Mohammed bin Rashid Al Maktoum Solar Park. *Int. J. Thermofluids* 12, 100123. doi:10.1016/j.ijft.2021.10012

Okere, A., and Iqbal, M. T. (2021). "Techno-economic comparison of emerging solar PV modules for utility scale PV installation," in 2021 IEEE 12th Annual Information Technology, Electronics and Mobile Communication Conference (IEMCON) (IEEE), 0827–0833. doi:10.1109/iemcon53756.2021.9623086

Petinrin, M., and Petinrin, J. O. (2014). Renewable energy potentials in Nigeria: Meeting rural energy needs. *Renew. Sustain. Energy Rev.* 29, 72–84. doi:10.1016/j.rser.2013.08.078

Ramachandran, T., Mourad, A.-H. I., and Hamed, F. (). A review on solar energy utilization and projects: Development in and around the UAE. *Energies* 15 (10), 3754.

Ray, D. (2021). *Lazard's levelized cost of energy analysis—version 15.0*, 21.

Saqib, S. (2018). "Hybrid steam supply system for saving fuel gas and reducing carbon footprint of the Oil & Gas Industry," in *Research and development petroleum conference and exhibition 2018* (Houten: European Association of Geoscientists & Engineers), 172–174.

Shah, N. (2018). *ANALYSIS OF THE KEY FACTORS AFFECTING LEVELIZED COST OF ELECTRICITY OF SOLAR PV IN INDIA*, 3, 7.

Shah, S. F. A., Khan, I. A., and Khan, H. A. (2019). Performance evaluation of two similar 100MW solar PV plants located in environmentally homogeneous conditions. *IEEE Access* 7, 161697–161707. doi:10.1109/access.2019.2951688

Srinivasan, S. (2019). Power relationships: Marginal cost pricing of electricity and social sustainability of renewable energy projects. *Technol. Econ. Smart Grids Sustain Energy* 4 (1). doi:10.1007/s40866-019-0070-4

Tian, K., Sun, W., Liu, W., and Song, H. (2020). Coordinated RES and ESS planning framework considering financial incentives under centralised electricity market. *CSEE J. Power Energy Syst.*, 1–8.

U.S. Energy Information Administration (2022). Levelized costs of new generation resources in the annual energy outlook 2021, U.S. Energy information administration (EIA). [Online]. Available: https://www.eia.gov/outlooks/aeo/pdf/electricity_generation.pdf (Accessed March 26th, 2022).

Wang, M. -H., He, Y., Xu, Y., and Xu, Z. (2021b). A power-decoupled current-source inverter for PV energy harvest and grid voltage regulation. *IEEE Trans. Ind. Electron.* 68 (10), 9540–9549. doi:10.1109/tie.2020.3026264

Wang, M. -H., Li, S., He, Y., Jia, J., and Jia, Y. (2021a). Leakage current suppression of single-phase power-decoupled current-source inverters. *IEEE J. Emerg. Sel. Top. Power Electron.* 9 (6), 6846–6853. doi:10.1109/jestpe.2021.3085684

Wang, M., Mok, K., Tan, S., and Hui, S. Y. (2018). Multifunctional DC electric springs for improving voltage quality of DC grids. *IEEE Trans. Smart Grid* 9 (3), 2248–2258.

Wang, M., Tan, S., Hui, C., and Hui, S. Y. (2018). A configuration of storage system for DC microgrids. *IEEE Trans. Power Electron.* 33 (5), 3722–3733. doi:10.1109/tpel.2017.2723909

Woodhouse, M., James, T., Margolis, R., Feldman, D., Merkel, T., and Goodrich, A. (2011). "An economic analysis of photovoltaics versus traditional energy sources: Where are we now and where might we be in the near future?," in 2011 37th IEEE Photovoltaic Specialists Conference (Seattle, WA, USA, 002481–002483.

Xiao, J., Ye, D., Xie, X., Yao, Z., Qu, J., and Liu, B. (2022). Numerical simulation of the airflow at the world's largest concentrated solar power plant in a desert region. *Sol. Energy* 232, 421–432. doi:10.1016/j.solener.2022.01.005

frontiers | Frontiers in Energy Research

TYPE Original Research
PUBLISHED 02 September 2022
DOI 10.3389/fenrg.2022.989430

OPEN ACCESS

EDITED BY
Xue Lyu,
University of Wisconsin-Madison,
United States

REVIEWED BY
Shiwei Xia,
North China Electric Power University,
China
Bin Zhou,
Hunan University, China

*CORRESPONDENCE
Yiping Zhang,
nynujekiwa2@outlook.com

SPECIALTY SECTION
This article was submitted to Smart Grids,
a section of the journal
Frontiers in Energy Research

RECEIVED 08 July 2022
ACCEPTED 10 August 2022
PUBLISHED 02 September 2022

CITATION
Zhang Y, Qi F, He Y, Wang B and Yang D (2022), Synchrophasor data-based inertia estimation for regional grids in interconnected power systems.
Front. Energy Res. 10:989430.
doi: 10.3389/fenrg.2022.989430

Synchrophasor data-based inertia estimation for regional grids in interconnected power systems

Yiping Zhang[1]*, Feng Qi[1], Yangdong He[1], Bo Wang[2] and Deyou Yang[2]

[1]State Grid Heilongjiang Electric Power Co, Ltd, Haerbin, China, [2]Department of Electrical Engineering, Northeast Electric Power University, Jilin, China

The inertia level is a significant indicator that guides operators to integrate renewable power generation into the power system for safe operation. In this study, a method that can estimate the effective inertia of power grids located in different regions in the interconnected system is proposed by using the synchronous measurement data. Based on the equivalent swing equation formed as a second-order oscillator, the inertia is expressed as a ratio of the time-evolution solution of this equation. To avoid a meaningless ratio, the Hilbert transformation is leveraged to recast the inertia analytical expression, which is composed of the time-independent characteristic parameters of the oscillation signal. Furthermore, the signal identification technique is employed to extract the characteristic parameters from the synchronized measurements so that the proposed scheme can estimate the regional inertia by using only the outputs measured by the synchorphasor measurement units. A comparison of the simulation results and methods validate the effectiveness and robustness of the proposed method.

KEYWORDS

inertia estimation, regional grid, electromechanical oscillation, synchrophasor measurement, power system

1 Introduction

The increasing integration of converter-control-based renewable power generation into power systems makes the system inertia a focus of widespread concern due to the small amount of inertia they provide (Yang et al., 2022a; He et al., 2021; Lyu et al., 2022). In addition to the perspective of the whole system, regional inertia has also attracted attention because of the spatial distribution characteristics of the integration of renewable power generation into the system (Pulgar-Painemal et al., 2018; Yang et al., 2022b). The significance of regional inertia is that the island power grid formed by the disconnection of tie lines in the interconnected power system can withstand a sudden interruption of the transmission power to prevent the frequency collapse of the island. Similar to the blackout accruing in South Australia in 2016 (Yan et al., 2018), insufficient regional inertia has no

ability to prevent the frequency collapse caused by the disconnection of the tie lies. Nevertheless, this blackout may be foreseen and prevented once the transmission system operator (TSO) can obtain the distance between the minimum requirement inertia and operation inertia of the regional power grids. The former can be determined by the frequency stability constraint of a system (Golpira et al., 2016), while the latter can be obtained by inertia estimation. To summarize, estimating regional inertia can not only assist the TSO in seeking out the low inertia region but also provide guidance for the TSO to integrate renewable power generation into the system from the local perspective.

Access to obtaining regional inertia based on a synchronous measurement can be divided into two categories: online calculation and online estimation. In online calculations, the component inertia is taken as the basic unit to be estimated (Sun et al., 2019), whereas the regional inertia can be obtained by calculating the sum of inertia units in the regional power grids (Arjona et al., 2012; Hajnoroozi et al., 2015; Huang et al., 2018). However, a reduction in the efficiency of online calculations has gradually become prominent with the increasing scale and complexity of power systems.

To adapt to the large-scale interconnected power system, online inertia estimation for regional grid is developed. The regional inertia can be estimated by minimizing the difference between the PMU measured signal and the simulated signal based on the equivalent dynamic model (Sarić et al., 2019; Vahidnia et al., 2013; Chavan et al., 2017). However, the estimation methods based on optimization is model-dependent. Instead of optimization, online estimation based on the analytical expression of the inertia have been developed (Ashton et al., 2017; Wilson et al., 2019; Tuttelberg et al., 2018; Panda et al., 2020). In (Ashton et al., 2017), the regional power grid is aggregated as an equivalent generator so that the regional inertia can be estimated by the ratio of the sudden step power and the rate of change of frequency (RoCoF) at the disturbance moment. Although the accuracy of the RoCoF-based method can be improved by integration calculation (Wilson et al., 2019), the controller response and system damping can also affect the estimation results. In (Tuttelberg et al., 2018), the regional inertia is expressed as a unit impulse response of an equivalent swing equation formed as a first-order transfer function at time zero. The regional inertia estimation based on the step response and impulse response of an equivalent swing equation needs to measure the frequency response trajectory at the moment of disturbance. Recently, the relationship between the inertia and electromechanical oscillation behaviour has been utilized to estimate the equivalent inertia. In (Panda et al., 2020), the inertia of an equivalent generator at the connected bus is expressed based on the maximum point information during oscillation. However, the time corresponding to the extreme point needs to be exactly determined. Overall, these estimation methods highly depend on the measurement of the single point value at the disturbance moment or extreme point, so the robustness to distorted data caused by measurement noise or missing data is poor. Moreover, the estimation accuracy can also disturb by the calculation of RoCoF.

The purpose of this study is to develop a method to estimate the regional inertia of an interconnected power system using wide-area measurements, which has a lower sensitivity to the single point value. An inertia expression based on the swing equation is first developed. Then, an online regional inertia estimation scheme for the interconnected power system is established. Specifically, the contributions of this study are as follows:

1) An inertia explicit expression is developed by using the Hilbert transformation on the time-domain solution of the swing equation formed as a second-order oscillator. The developed inertia expression consists of the characteristic parameters of the oscillation signal with no relation to time, exhibiting prominent differences from the inertia expressions in (Ashton et al., 2017; Wilson et al., 2019; Tuttelberg et al., 2018; Panda et al., 2020).
2) The online estimation scheme for the regional inertia of an interconnected power system is established based on the combination of the developed inertia expression and the adaptive identification algorithm that has been applied in the power system. Unlike the estimation method mentioned above, whose estimation results have a strong sensitivity to single point measurement, the proposed estimation scheme strengthens the robustness of the estimation to noise interference by utilizing the overall information carried by the PMU-measured data.
3) A comparative analysis between the proposed method and commonly used RoCoF-based method is carried out with a large-scale interconnected power system in the simulation circumstance.

The remainder of the paper is structured as follows: Section 2 discusses the power system dynamic response based on the swing equation. In Section 3 the inertia analytical expression is derived. The online estimation scheme for regional inertia is presented in Section 4. Section 5 demonstrates the effectiveness and robustness of the proposed method through simulation data. Section 6 presents the conclusions drawn and discusses future studies.

2 Theoretical basis

The electromechanical dynamic behaviour of a synchronous subsystem in a bulk power system can be equivalent to an aggregated synchronous generator (ASG) (Panda et al., 2020), whose dynamic is modelled as a second-order oscillator, expressed as

$$M\ddot{\delta} + K_D\dot{\delta} + K_s\delta = P_m \tag{1}$$

where $\delta(t)$ is the rotor angle; M and D are the inertia constant and damping coefficient, respectively; K_D is the damping torque coefficient; and K_s is the synchronous torque coefficient. Considering P_m unchanged, and linearizing (1) around the equilibrium point yields

$$M\Delta\ddot{\delta} + K_D\Delta\dot{\delta} + K_s\Delta\delta = 0 \tag{2}$$

where $\Delta(\cdot)$ represents the variable deviation.

If all variables in (Eq. 2) are in p. u, then the relationships $\Delta\omega_r(t) = \Delta\dot{\delta}(t)$ and $\Delta P(t) = K_D\Delta\dot{\delta}(t) + K_S\Delta\delta(t)$ exist (Kundur, 1994), where P and ω represent the electrical power and speed of the ASG, respectively. Then, the homogenous differential Eq. 2 can be rewritten as

$$M\Delta\dot{\omega} = -\Delta P \tag{3}$$

Based on (Eq. 3), it is reasonable to directly express the inertia by the ratio of $\Delta\dot{\omega}(t)$ to $\Delta P(t)$. However, these functions are sinusoidal. In other words, the responses of electric power and speed during the transient period follow the form of an exponentially decaying sinusoidal oscillation (EDSO), which is proven in the Appendix. Thus, a situation in which $\Delta\dot{\omega}(t)$ and $\Delta P(t)$ simultaneously coincide at zero at a certain moment may occur. Although in such a situation, the relationship depicted by (Eq. 3) also exists, the ratio of $\Delta\dot{\omega}(t)$ to $\Delta P(t)$ is meaningless, so it cannot express the inertia. A simple way to solve this problem is to choose a point where $\Delta\dot{\omega}(t)$ and $\Delta Pe(t)$ are simultaneously non-zero, such as the pick point of the oscillation. However, this method has a strong sensitivity to the single point value. Instead of directly utilizing the time evolution, the Hilbert transformation is employed to avoid the meaningless situation.

3 Inertia quantification based on the hilbert transformation

As seen from the comparison of (A.3) and (A.4), the difference between $\Delta\dot{\omega}(t)$ and $\Delta P(t)$ is the phase and amplitude rather than the oscillation frequency and decay coefficient. Since the amplitudes of $\Delta\dot{\omega}(t)$ and $\Delta P(t)$ are not zero, the main reason for the above problem is the periodic feature of the oscillation, which is caused by the phase changing with time. Thus, the Hilbert transformation is employed to separate the phase information in the EDSO signal to derive the analytical expression of the inertia.

3.1 Hilbert transformation

The time-domain response trajectory of a dynamic system contains complex transient information. The Hilbert transform is an advanced technique to analyse dynamic information during the transient period (Michael, 1994). The Hilbert transformation for the time-domain signal $x(t)$ is presented as follows:

$$\mathrm{HT}[x(t)] = \frac{1}{\pi}C\int_{-\infty}^{\infty}\frac{x(\tau)}{t-\tau}d\tau \tag{4}$$

where $\mathrm{HT}[\cdot]$ represents the Hilbert transformation and C is the Cauchy principal value integral.

Then, the analytical expression of $x(t)$, recorded as $X(t)$, can be obtained through the sum of the original signal and the production between imaginary j and the Hilbert transformed signal, expressed as follows:

$$X(t) = x(t) + j\mathrm{HT}[x(t)] = A(t)e^{jk(t)} \tag{5}$$

where $A(t) = \sqrt{x^2(t) + (\mathrm{HT}[x(t)])^2}$ and $\kappa(t) = tan^{-1}(\mathrm{HT}[x(t)]/x(t))$ are the instantaneous amplitude and instantaneous phase, respectively.

The Hilbert transformation can convert a real signal in the one-dimensional axis into a complex signal in the two-dimensional plane by representing the amplitude and phase of the real signal as the module and angle of the complex signal, respectively.

3.2 Analytic expression of inertia

The advantage of the instantaneous information extraction of the Hilbert transformation provides the basis for the separation of the phase information. Since the Hilbert transformation is linear, performing it on (Eq. 3) leads to

$$\mathrm{HT}[M\Delta\omega] = -\mathrm{HT}[\Delta P] \tag{6}$$

Multiplying each term in the Hilbert transformed equation by the unit imaginary j and adding each term in the imaginary equation to each term in (Eq. 6), an analytical expression of (Eq. 3) is obtained; i.e.,

$$MA\ d\omega(t)e^{jk_{d\omega}(t)} = A_P(t)e^{jk_P(t)} \tag{7}$$

where $A_{dw}(t)$ and $A_P(t)$ are the instantaneous amplitudes of $\Delta\dot{\omega}(t)$ and $\Delta P(t)$, respectively; and $k_{dw}(t)$ and $k_p(t)$ are the instantaneous phases of $\Delta\dot{\omega}(t)$ and $\Delta P(t)$, respectively.

Since the inertia is the positive real number, its norm is itself. The analytical term is complex; thus, its norm is equal to the instantaneous amplitude of the analytical signal. Consequently, the phase information can be eliminated by norm calculation on both sides of (Eq. 7).

$$MA_{d\omega}(t) = A_P(t) \tag{8}$$

According to the relationship between the instantaneous amplitude of $\Delta\dot{\omega}(t)$ and $\Delta\omega(t)$, derived in the Appendix, a further derivation of (Eq. 9) is

$$MA_{\omega}(t)\sqrt{\gamma^2+\eta^2}=A_P(t) \tag{9}$$

Since the instantaneous amplitudes of $\Delta\omega(t)$ and $\Delta P(t)$ have no zero points, the inertia calculated based on the ratio of $A_{pe}(t)$ to $A_{dw}(t)$ is meaningful. Specifically, the instantaneous amplitude of the time-evolution signal following the EDSO form is equal to the product of the initial amplitude and the exponential term (Kreyszig et al., 2011); i.e., $A(t) = A_0 e^{-\eta t}$. The inertia thus can be analytically expressed as

$$M = A_{P0}/A_{\omega 0}\sqrt{\gamma^2+\eta^2} \tag{10}$$

In (Eq. 10), the initial amplitude of the oscillation power A_{P0}, the initial amplitude of the oscillation speed $A_{\omega 0}$, the decaying decay coefficient η, and the oscillation frequency γ are the characteristic parameters of the electromechanical oscillation, which are not a function of time. Therefore, the inertia can be quantified once these oscillation characteristic parameters are determined.

4 Scheme for regional inertia estimation

The derived inertia analytical expression provides an important basis for the online inertia estimation. It is feasible to estimate the inertia by extracting these characteristic parameters from the observed electromechanical oscillation response. However, practical applications of the regional inertia estimation for the interconnected power system based on (Eq. 10) need further illustration, namely, the equivalent of the multi-region interconnected system and the extraction of oscillation characteristic parameters.

4.1 Equivalence of a multi-region interconnected power system

The generation of the interconnected power system is motivated by insufficient or excessive generation power in the regional grid. Consequently, the partition of the system consisting of multiple interconnected regional power grids can be achieved by finding the boundary buses of each regional grid, which is geographical in nature. A significant sign of the partition an interconnected system is the tie-line connecting regional power grids. In such partitions, each regional grid can be referred to as an ASG whose electromechanical dynamic behaviour is described by (Eq. 2) (Chavan et al., 2017), while the interconnected structure is preserved. Then, the dynamic behaviour of the interconnected power system can be represented by the multiple ASGs model, expressed as

$$\boldsymbol{M}\Delta\ddot{\boldsymbol{\delta}}+\boldsymbol{K}_D\Delta\dot{\boldsymbol{\delta}}+\boldsymbol{K}_s\Delta\boldsymbol{\delta}=0 \tag{11}$$

where $\boldsymbol{\delta}=([\boldsymbol{\delta}_i]^{\mathrm{T}}, i\in\mathbb{R})$ is the rotor angle vector; $\omega=([\omega_i]^{\mathrm{T}}, i\in\mathbb{R})$ is the rotor speed vector; $M=\mathrm{diag}(\{M_i\}, i\in\mathbb{R})$ is the inertia matrix; $K_D=([K_{Di}]^{\mathrm{T}}, i\in\mathbb{R})$ is the damping matrix; $K_S=([K_{S,ij}]$, and $i, j\in\mathbb{R})$ is the synchronous power coefficient matrix. Simplifying (11) by $\Delta\omega=\Delta\dot{\delta}$ and $\Delta\boldsymbol{P}=\boldsymbol{K}_D\Delta\dot{\boldsymbol{\delta}}+\boldsymbol{K}_S\Delta\boldsymbol{\delta}$ yields

$$\boldsymbol{M}\Delta\dot{\boldsymbol{\omega}}=-\Delta\boldsymbol{P} \tag{12}$$

where $\boldsymbol{P}=([P_i]^{\mathrm{T}}, i\in\mathbb{R})$ is the electric power vector.

It can be seen that (Eq. 11) is the high-order extension of (Eq. 2). Although this extension cannot change the EDSO form that the speed and electric power signals follow, it will make the time-domain response of the speed and power complicated; that is, the speed and power signal contain multiple components with different oscillation frequencies due to increased order. The complicated oscillation creates a barrier to directly calculating the regional inertia by using the proposed inertia quantification methodology because (10) is derived based on the speed and power at a single oscillation frequency. Thus, the decomposition of the signal consisting of the components with different oscillation frequencies should be further considered.

4.2 Extraction of the oscillation characteristic parameter

Considering the above situation, the extraction of the oscillation characteristic parameters contains two phases: decomposition and identification (Yang et al., 2017). Signal processing technology based on intrinsic mode function (IMF) sifting provides an effective way to decompose nonlinear, non-stationary, multi-component coupling signals. An IMF satisfies two conditions: 1) the number of local extreme points and zero-crossing points must be equal or differ by at most one in the whole-time window, and 2) the average of the upper envelope and lower envelope is equal to zero at any time. After IMF sifting, the original signal can be expressed as

$$m(t)=\sum_n y_i(t)+r(t) \tag{13}$$

where $y_i(t)$ is the ith IMF and $r(t)$ is the monotonic residue component.

According to the IMF sifting conditions, the IMF in the EDSO signal with multiple components corresponds to the component with a single oscillation frequency. Fortunately, many methods can be used to extract the IMFs of the multi-component EDSO signal, such as the Prony method, the empirical mode decomposition algorithm, and adaptive local iterative filter decomposition (ALIFD). Among them, ALIFD is utilized here due to its better performance than others and robustness to the strong nonstationary behaviour of the dynamic system.

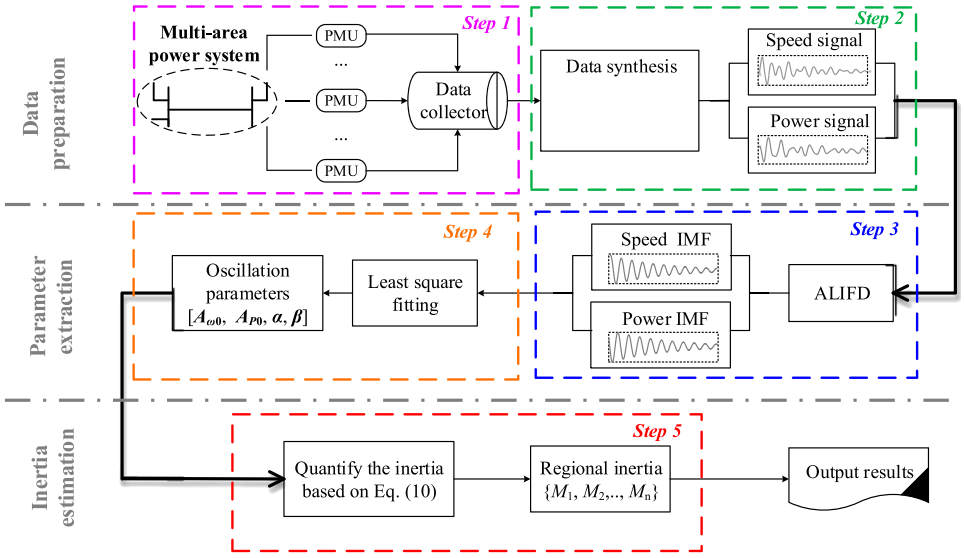

FIGURE 1
Flowchart for the data-driven regional inertia estimation.

After decomposition, the component with a single oscillation frequency is obtained. The amplitude, decay coefficient, and oscillation frequency of each decomposed signal can then be identified by linear fitting, which can be achieved by least squares fitting (LSF).

4.3 Procedure for the online regional inertia estimation

According to the above analysis, the speed and electric power response of each ASG need to be obtained first. In the p. u, the speed of the ASG can be approximately represented by the average frequency of the regional power grid corresponding to the ASG, which can be obtained by the weighted average of the bus frequency captured by the PMU in the region (Tuttelberg et al., 2018). The electrical power of the ASG can be obtained by the sum of the measured transmission power in the tie lines. By integrating the bus frequency and the transmission power captured by the PMU, the data set for the regional inertia estimation is generated.

As shown in Figure 1, the proposed online inertia estimation method for the interconnected power system consists of five steps, where the step 1 and step 2 are to prepare the input data, step 3 and step 4 are to extract the oscillation parameters, and the inertia of each region is finally estimated by step 5. Specifically, the estimation procedure is as follows:

Step 1: Capture the time-domain response of the bus frequency deviation in each regional grid and tie-line power deviation during the electromechanical oscillation process by using synchrophasor measurements.

Step 2: Integrate the PMU-measured response into the speed and electrical power signal of the ASG corresponding to each regional grid.

Step 3: Decompose the integrated speed and electric power signals with multiple intrinsic modes coupled into the signals with a single oscillation mode by using the ALIFD algorithm.

Step 4: Identify the oscillation characteristic parameters of each ALIFD decomposed signal by linear fitting.

Step 5: Estimate the inertia based on (Eq. 10), where the oscillation characteristic parameters have been determined by step 4.

5 Numerical simulation

This section tests the performance of the proposed method based on the IEEE standard system, i.e., the 5-region, 16-machine, 68-bus power system (Canizares et al., 2017). The topology of the system is shown in Figure 2. According to the interconnected structure, the test system is geographically divided into five regional power grids, i.e., the New England power grid (Region I), the New York power grid (Region II), and the remaining three equivalent power grids (Region III, Region IV, and Region V). Region I and Region II include generator G1–G9 and generator G10–G13, respectively. Region III, Region IV, and Region V are represented by three equivalent generators G14, G15, and G16, respectively.

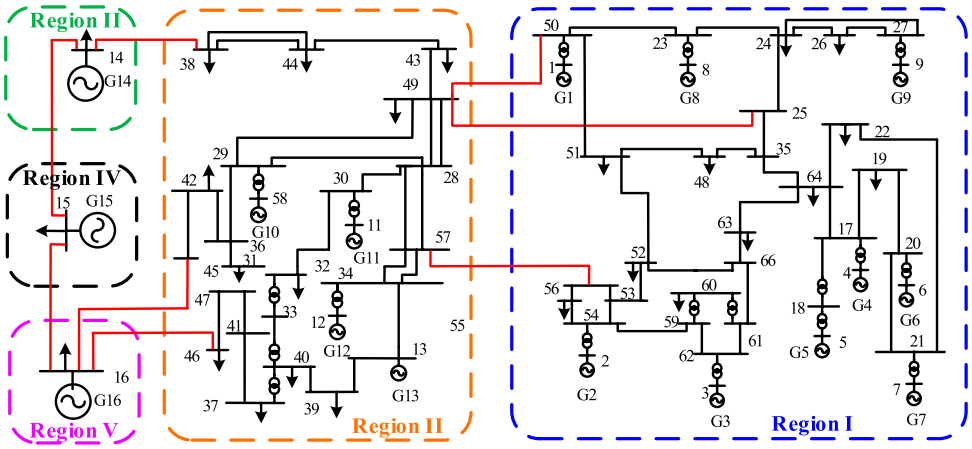

FIGURE 2
Diagram of the IEEE five-region power system.

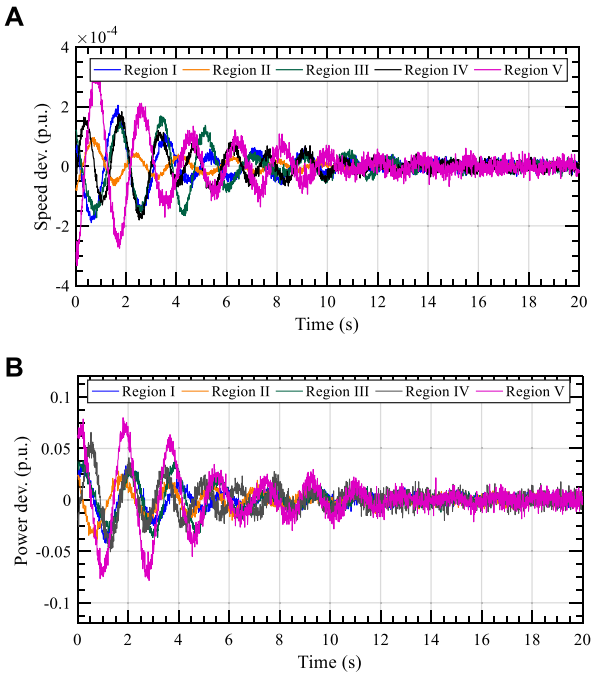

FIGURE 3
Simulated signal: **(A)** speed deviation signal of ASG I to ASG V and **(B)** power deviation signal of ASG I to ASG V.

The test system is established on the DIGSILENT numerical simulation software. The base power, rate frequency, and simulation step are set as 1000 MW, 60 Hz, and 0.01 s, respectively. Moreover, Gaussian noise is added to the simulated signals to imitate the measurement noise.

The proposed regional inertia online estimation method takes the measured signal as input. However, according to the theory in Section 2, the estimation is based on the extraction of oscillation characteristic parameters from the measured signal. Thus, the exact electromechanical oscillation parameters should be extracted before quantifying the inertia by (Eq. 10).

5.1 Oscillation parameter extraction

To stimulate the electromechanical response of the system, a single-phase ground fault with a duration of 0.05 s is carried out at the 31 Bus. Then, the ASG speed and power signals corresponding to the regional grid are generated by the bus frequency and tie-line power, respectively, which exhibit decaying oscillations, as shown in Figure 3.

Meanwhile, a spectrum analysis based on a Fourier transform is performed on the filtered speed and power signals to reveal the oscillating components. Figure 4A shows that the ASG speed signal contains three inherent components with a determined frequency. Figure 4B shows that the WFT spectrum of the ASG power signal also contains three inherent components whose oscillation frequencies are the same as the inherent components in the ASG power signals.

To extract the oscillation parameters of the inherent oscillation components in the speed and power signal, the ALIFD algorithm is performed. The speed and power signal of each ASG is decomposed by the ALIFD algorithm, generating three components with a single oscillation frequency for each signal. Then, the oscillation parameters of decomposed components are identified by LSF. The identified oscillation parameters are shown in Table 1 to Table 3 where Table 1, Table 2 and Table 3 correspond to the oscillation parameters of inherent component 1, inherent component 2, and inherent

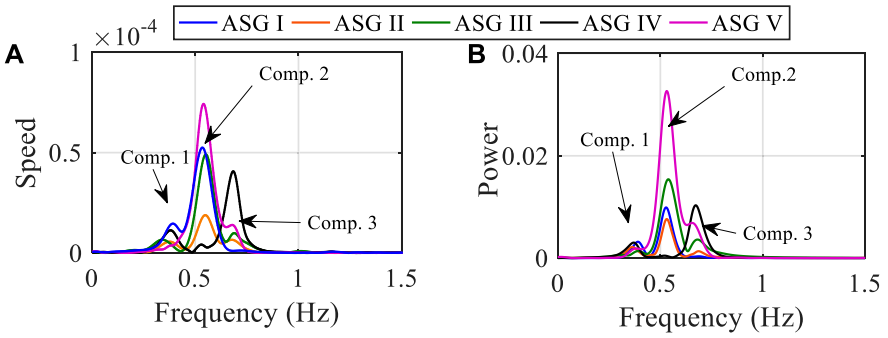

FIGURE 4
Spectrum analysis for the **(A)** speed signals and **(B)** power signals.

TABLE 1 Oscillation characteristic parameters of comp. One.

ASG	f_d (Hz)	α (s)	A_{f0} (10^{-4} p.u.)	A_{pe0} (p.u.)
I	0.384	0.241	0.830	0.012
II	0.382	0.249	0.291	0.009
III	0.381	0.246	0.479	0.007
IV	0.385	0.251	0.767	0.011
V	0.386	0.248	0.269	0.006

TABLE 2 Oscillation characteristic parameters of comp. Two.

ASG	f_d (Hz)	α (s)	A_{f0} (10^{-4} p.u.)	A_{pe0} (p.u.)
I	0.542	0.203	1.717	0.034
II	0.547	0.207	0.747	0.033
III	0.541	0.208	2.417	0.050
IV	0.539	0.205	0.193	0.004
V	0.545	0.204	3.024	0.092

TABLE 3 Oscillation characteristic parameters of comp. Three.

ASG	f_d (Hz)	α (s)	A_{f0} (10^{-4} p.u.)	A_{pe0} (p.u.)
I	0.685	0.182	0.086	0.002
II	0.683	0.180	0.179	0.009
III	0.688	0.179	0.867	0.020
IV	0.687	0.187	1.901	0.045
V	0.682	0.183	0.528	0.018

component 3, respectively, in the power and speed signals. It can be observed that the same inherent components of the different signals have the same oscillation frequency and decay coefficient, while the initial amplitudes are different.

TABLE 4 Inertia Configuration of the test system based on 1000 MVA.

Region	Generator index	Inertia(s)	Normal value (s)
Region I	G1	8.40	58.8
	G2	8.40	
	G3	7.16	
	G4	5.72	
	G5	5.20	
	G6	6.96	
	G7	5.20	
	G8	4.86	
	G9	6.90	
Region II	G10	6.10	129.4
	G11	5.66	
	G12	18.44	
	G13	99.20	
Region III	G14	60.00	60.00
Region IV	G15	60.00	60.00
Region V	G16	90.00	90.00

Based on the identified oscillation parameters, the speed and power signals are reconstructed, as shown in Figure 3. As can be seen from the figure, the reconstructed signals also show the decaying trend and have almost the same oscillation process as the original signals, indicating that the parameters extracted by ALIFD-LSF can quantitively represent the oscillation characteristic.

5.2 Regional inertia estimation

After the oscillation characteristic parameters are extracted, the regional inertia can be obtained by using (Eq. 10). This subsection aims to verify the correctness of the proposed inertia

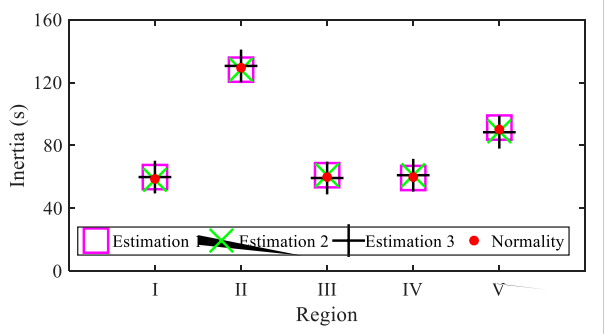

FIGURE 5
Comparison of the estimation results based on the oscillation parameters of the different components.

analytical expression by comparing the estimated inertia and nominal inertia calculated directly from the system data (Kundur, 1994), where the nominal inertia is shown in Table 4.

To quantify the accuracy of the estimation results, the relative error between the inertia obtained by the estimation method and the calculated inertia at the same base power is employed and is expressed as

$$E = \frac{\left|\tilde{M} - M\right|}{M} \times 100\% \tag{14}$$

where $\tilde{M}$ represents the estimated inertia.

According to the extracted oscillation characteristic parameters, three sets of estimation results can be obtained. We first estimate the regional inertia by using the oscillation characteristic parameters in Table 1, which correspond to inherent component 1. The estimated inertia for the five regional power grids in the test system based on inherent component 1 is shown in Figure 5 and Table 5. It can be seen by comparing the estimated inertia marked as a pink square and the real inertia marked as the red points in Figure 5 that the estimated results have a slight deviation from the real inertia. Table 5 shows that the numerical deviation between the estimated inertia and real inertia of Region I to Region V is {-0.8 s, 1.15 s, -0.7 s, 1.01 s, and -1.42 s, respectively}.

The estimated inertia based on inherent component 2 and inherent component 3, i.e., oscillation characteristic parameters in Table 2 and Table 3 are subsequently obtained, which are also presented in Figure 5. The estimation results based on the parameters in Table 3 and Table 4 are marked as the green cross and black cross, respectively. Apparently, both of them also have a small deviation from the real inertia. As seen from Table 5, the numerical deviation between the estimation and reality of Region I to Region V based on the parameters of component 2 and component 3 are {0.76 s, 1.07 s, -0.74 s, -1.06, and 1.32 s} and {-0.73 s, -1.10 s, 0.65 s, -0.97 s, and 1.38 s}, respectively.

Furthermore, the estimation error is calculated based on the estimation results to indicate the accuracy of the proposed method. As shown in Table 5, the relative errors for the estimation results based on these three inherent components are all small, indicating the accuracy of the proposed method. Moreover, an apparent situation can be seen from Figure 5; that is, the estimation results are almost coincident, which means that the estimated inertias based on the oscillation characteristic parameters of the different inherent components have no significant impact on the estimation results. Moreover, such a situation can also be seen by comparing the estimation error based on the different inherent components in Table 5. This feature means that there is no need to extract the oscillation characteristic parameters of all inherent components hiding in the ASG speed and power signal, which makes the proposed method adaptable to large-scale interconnected power systems.

5.3 Comparison with the RoCoF-based method

To demonstrate the outperformance of the proposed method, the RoCoF-based inertia estimation method, which is based on the frequency events caused by sudden power mismatch between generation and consumption, is carried out

TABLE 5 Estimation results and error based on the oscillation parameter of the different components.

Region	Estimation 1		Estimation 2		Estimation 3	
	Result	Error (%)	Result	Error (%)	Result	Error (%)
I	59.60	1.36	58.04	1.29	59.53	1.24
II	128.25	0.89	128.33	0.83	130.50	0.85
III	60.70	1.17	60.74	1.23	59.35	1.08
IV	58.99	1.68	61.06	1.77	60.97	1.62
V	91.42	1.58	88.68	1.47	88.62	1.53

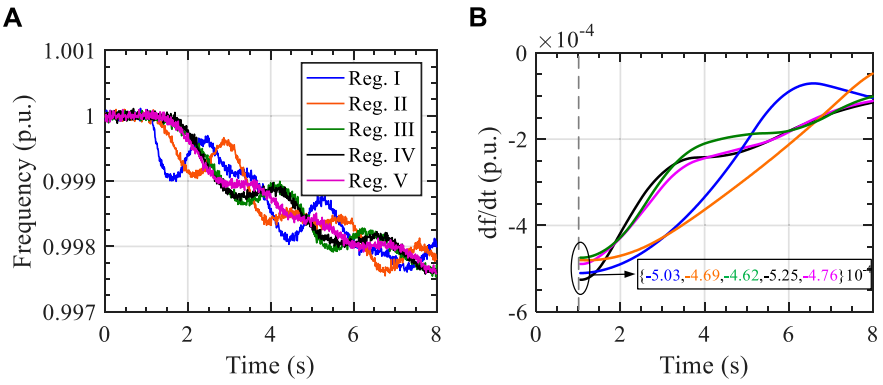

FIGURE 6
Time-domain trajectories caused by a sudden load increase: **(A)** frequency signals and **(B)** RoCoF signals.

TABLE 6 Estimation results of the RoCoF-Based method.

Region	Normality	Estimation	Error (%)
Reg. I	58.8	75.54	28.47
Reg. II	129.4	153.52	18.64
Reg. III	60.00	73.59	22.65
Reg. IV	60.00	64.76	7.93
Reg. V	90.00	105.04	16.71

with the test system. The frequency response trajectory of each regional power grid caused by a sudden 0.228 p. u. load increase at 1 s is shown in Figure 6A. The mismatched power of each regional power grid can be calculated through the deviation of the generation power after disturbance, from Region I to Region V being 0.038 p. u, 0.072 p. u, 0.034 p. u, 0.034 p. u, and 0.05 p. u, respectively.

A lowpass Butterworth filter with a corner frequency of 0.5 Hz is utilized to filter out the slow network modes in the frequency response trajectories, Then, the RoCoF of each regional power grid can be calculated, as shown in Figure 6B. Based on the RoCoF and mismatched power, the inertia can be estimated by the method proposed in (Ashton et al., 2017). The estimation results are shown in Table 6, which is close to the real value. However, the numerical deviation between the estimation and reality of Region I to Region V based on the RoCoF is {-16.74 s, -24.12 s, -13.59 s, -4.76 s, and -15.04 s}, respectively, which is larger than that of the proposed method. Additionally, it can be seen by comparing the ER of different methods that the inertia based on the proposed method is more accurate than that of the RoCoF-based method.

Theoretically, the inertia expression based on frequency events is described as $H = \Delta P / \dot{f}(t)|_{t=t_0}$. According to this, the results of the RoCoF-based method are highly sensitive to the derivative of frequency at the disturbance moment. Although the measurements of the frequency at the disturbance moment can be achieved, the filter process for the noise and slow network modes may distort the frequency derivative at the disturbance moment due to boundary effects, which cause a larger estimation error than the proposed method based on the characteristic parameters of the oscillation signal.

6 Conclusion

This paper presented a synchrophasor data-driven method to estimate the regional inertia for an interconnected power system. The estimation scheme is based on the relationship between the regional inertia and the characteristic parameters of the electromechanical oscillation signal, which is developed by the Hilbert transformation of the equivalent swing equation. Since the developed inertia expression is time-independent, the proposed method can accommodate the measurement data under noise conditions. Additionally, there is no need to determine the disturbance time, and the measured data is directly used rather than further derivative calculation, thereby improving accuracy.

The performance of the proposed method is demonstrated on the simulated data of the five-region power system and then compared with the RoCoF-based method. The simulation results showed the outperformance of the proposed method. The proposed method expands the application of the signal identification technique in power systems. To further explore this issue, our future work will include the application of random signal processing technology to realize the real-time estimation of the regional inertia.

Data availability statement

The raw data supporting the conclusions of this article will be made available by the authors, without undue reservation.

Author contributions

YZ and FQ contributed to the conception and design of the proposed strategy. All authors wrote and edited the manuscript.

Funding

This article is supported by the State Grid Corporation of China Science and Technology Project (SGHL0000DKJS2101550).

Conflict of interest

Authors YZ, FQ, YH were employed by the company State Grid Heilongjiang Electric Power Co, Ltd.

The remaining authors declare that the research was conducted in the absence of any commercial or financial relationships that could be construed as a potential conflict of interest.

Publisher's note

References

Arjona, M. A., Hernandez, C., Cisneros-Gonzalez, M., and Escarela-Perez, R. (2012). Estimation of synchronous generator parameters using the standstill step-voltage test and a hybrid genetic algorithm. *Int. J. Electr. Power & Energy Syst.* 35 (1), 105–111. doi:10.1016/j.ijepes.2011.10.003

Ashton, P. M., Saunders, C. S., Taylor, G., Carter, A., and Bradley, M. E. (2017). Inertia estimation of the GB power system using synchrophasor measurements. *IEEE Trans. Power Syst.* 30 (2), 701–709. doi:10.1109/tpwrs.2014.2333776

Canizares, C., Fernandes, T., Geraldi, E., Gerin-Lajoie, L., Gibbard, M., Hiskens, I., et al. (2017). Benchmark models for the analysis and control of small-signal oscillatory dynamics in power systems. *IEEE Trans. Power Syst.* 32 (1), 715–722. doi:10.1109/tpwrs.2016.2561263

Chavan, G., Weiss, M., Chakrabortty, A., Bhattacharya, S., Salazar, A., and Ashrafi, F. (2017). Identification and predictive analysis of a multi-area WECC power system model using synchrophasors. *IEEE Trans. Smart Grid* 8 (4), 1977–1986. doi:10.1109/tsg.2016.2531637

Golpira, H., Seifi, H., Messina, A. R., and Haghifam, M. R. (2016). Maximum penetration level of micro-grids in large-scale power Systems: Frequency stability viewpoint. *IEEE Trans. Power Syst.* 31 (6), 5163–5171. doi:10.1109/tpwrs.2016.2538083

Hajnoroozi, A. A., Aminifar, F., and Ayoubzadeh, H. (2015). Generating unit model validation and calibration through synchrophasor measurements. *IEEE Trans. Smart Grid* 6 (1), 441–449. doi:10.1109/tsg.2014.2322821

He, T., Li, S., Chen, Y., Wu, S., and Li, C. (2021). Optimal array reconfiguration of a PV power plant for frequency regulation of power systems. *Front. Energy Res.* 9, 698003. doi:10.3389/fenrg.2021.698003

Huang, R., Diao, R., Li, Y., Sanchez-Gasca, J., Huang, Z., Thomas, B., et al. (2018). Calibrating parameters of power system stability models using advanced ensemble Kalman filter. *IEEE Trans. Power Syst.* 33 (3), 2895–2905. doi:10.1109/tpwrs.2017.2760163

Kreyszig, E., Kreyszig, H., and Norminton, E. J. (2011). *Advanced engineering mathematics*, Hoboken, New Jersey, United States: Wiley.

Kundur, P. (1994). *Power system stability and control*. New York, NY, USA: McGraw-Hill.

Lyu, X., Zhao, Y., Grob, D., and Liu, T., (2022). Receding horizon control based secondary frequency regulation for power systems with wind energy integration. *Int. J. Electr. Power & Energy Syst.* 142, 108282. doi:10.1016/j.ijepes.2022.108282

Michael, F. (1994). Non-linear system vibration analysis using Hilbert transform--I. Free vibration analysis method 'Freevib. *Mech. Syst. Signal Process.* 8 (2), 119–127. doi:10.1006/mssp.1994.1011

Panda, R. K., Mohapatra, A., and Srivastava, S. C. (2020). Online estimation of system inertia in a power network utilizing synchrophasor measurements. *IEEE Trans. Power Syst.* 35 (4), 3122–3132. doi:10.1109/tpwrs.2019.2958603

Pulgar-Painemal, H., Wang, Y., and Silva-Saravia, H. (2018). On inertia distribution, inter-area oscillations and location of electronically-interfaced resources. *IEEE Trans. Power Syst.* 33 (1), 995–1003. doi:10.1109/tpwrs.2017.2688921

Sarić, A. T., Transtrum, M. T., and Stanković, A. M. (2019). Data-driven dynamic equivalents for power system areas from Boundary measurements. *IEEE Trans. Power Syst.* 34 (1), 360–370. doi:10.1109/tpwrs.2018.2867791

Sun, M., Feng, Y., Wall, P., Azizi, S., Yu, J., and Terzija, V. (2019). On-line power system inertia calculation using wide area measurements. *Int. J. Electr. Power & Energy Syst.* 109, 325–331. doi:10.1016/j.ijepes.2019.02.013

Tuttelberg, K., Kilter, J., Wilson, D. H., and Uhlen, K. (2018). Estimation of power system inertia from ambient wide area measurements. *IEEE Trans. Power Syst.* 33 (6), 7249–7257. doi:10.1109/tpwrs.2018.2843381

Vahidnia, A., Ledwich, G., Palmer, E., and Ghosh, A. (2013). Dynamic equivalent state estimation for multi-area power systems with synchronized phasor measurement units. *Electr. Power Syst. Res.* 96, 170–176. doi:10.1016/j.epsr.2012.11.006

Wilson, D., Yu, J., Al-Ashwal, N., Heimisson, B., and Terzija, V. (2019). Measuring effective area inertia to determine fast-acting frequency response requirements. *Int. J. Electr. Power & Energy Syst.* 113, 1–8. doi:10.1016/j.ijepes.2019.05.034

Yan, R., Masood, N. A., Saha, T. K., Bai, F., and Gu, H. (2018). The anatomy of the 2016 South Australia blackout: A catastrophic event in a high renewable network. *IEEE Trans. Power Syst.* 33 (5), 5374–5388. doi:10.1109/tpwrs.2018.2820150

Yang, D., Jin, Z., Zheng, T., and Jin, E. (2022). An adaptive droop control strategy with smooth rotor speed recovery capability for type III wind turbine generators. *Int. J. Electr. Power & Energy Syst.* 135, 107532. doi:10.1016/j.ijepes.2021.107532

Yang, D., Wang, B., Cai, G., and Wen, J. (2017). Oscillation mode analysis for power grids using adaptive local iterative filter decomposition. *Int. J. Electr. Power & Energy Syst.* 92, 25–33. doi:10.1016/j.ijepes.2017.04.004

Yang, D., Yan, G.-G., Zheng, T., Zhang, X., and Hua, L. (2022). Fast frequency response of a DFIG based on variable power point tracking control. *IEEE Trans. Ind. Appl.* 58, 5127–5135. early access. doi:10.1109/tia.2022.3177590

frontiers | Frontiers in Energy Research

TYPE Review
PUBLISHED 13 September 2022
DOI 10.3389/fenrg.2022.967220

OPEN ACCESS

EDITED BY
Jiajia Yang,
University of New South Wales, Australia

REVIEWED BY
Wenliang Yin,
Shandong University of Technology, China
Tong Zhang,
Cardiff University, United Kingdom

*CORRESPONDENCE
Weiqing Sun,
sunwq@usst.edu.cn

SPECIALTY SECTION
This article was submitted to Smart Grids, a section of the journal Frontiers in Energy Research

RECEIVED 12 June 2022
ACCEPTED 04 August 2022
PUBLISHED 13 September 2022

CITATION
Yang C, Sun W, Han D and Yin X (2022), Research on power system flexibility considering uncertainties.
Front. Energy Res. 10:967220.
doi: 10.3389/fenrg.2022.967220

Research on power system flexibility considering uncertainties

Ce Yang[1], Weiqing Sun[2]*, Dong Han[2] and Xiangyang Yin[2]

[1]Department of Control Science and Engineering, University of Shanghai for Science and Technology, Shanghai, China, [2]Department of Electrical Engineering, University of Shanghai for Science and Technology, Shanghai, China

In order to help achieve the goal of carbon peak and carbon neutrality, the large-scale development and application of clean renewable energy, like wind generation and solar power, will become an important power source in the future. Large-scale clean renewable energy generation has the uncertain characteristics of intermittency, randomness, and volatility, which brings great challenges to the balance regulation and flexible operation of the power system. In addition, the rapid development of renewable energy has led to strong fluctuations in electricity prices in the power market. To ensure the safe, reliable, and economic operation of the power system, how to improve the power system flexibility in an uncertain environment has become a research hotspot. Considering the uncertainties, this article analyzes and summarizes the research progress related to power system flexibility from the perspective of power system planning, operation, and the electricity market. Aiming at the modeling technology of uncertainty, the related modeling methods including stochastic programming, robust optimization, and distributionally robust optimization are summarized from the perspective of mathematics, and the application of these methods in power system flexibility is discussed.

KEYWORDS

power system flexibility, uncertainty, robust, stochastic, distributionally robust

1 Introduction

In order to deal with energy depletion and environmental problems, many countries have formulated carbon emission strategies. On 22 September 2020, Chairman Xi announced to the world that China will strive to achieve peak carbon dioxide emissions before 2030 and carbon neutrality by 2060. The United States and the European Union have proposed a Zero Carbon Action Plan (ZCAP) and a net zero emission target for 2050, respectively. Canada is expected to commit to a net zero emission target by 2050 and develop a legally binding 5-year carbon budget. Sweden set a net zero emission target in 2017. According to the Paris Agreement, it promised to achieve carbon neutrality by 2045, with at least 85% of the emission reduction to be achieved through domestic policies and the rest to be made up by international emission reduction. Germany promises to "pursue" greenhouse gas neutrality by 2050. Singapore avoided promising a clear decarbonization date but made it the ultimate goal of the long-term

strategy submitted to the United Nations in March 2020. By 2040, diesel locomotives will be phased out and replaced by electric vehicles. Therefore, a high proportion of renewable energy power generation has become a future power system scenario of widespread concern around the world. Under the new scenario, the characteristics of the power system have changed significantly. The randomly fluctuating wind and solar energy have become the main power sources, the "base load" power plants have been basically cancelled, the conventional thermal power units are started and stopped within a day, and the stochastic volatility of renewable energy is complemented through the flexible resource regulation of hydropower plants, gas-fired power plants, energy storage, etc.; flexibility has become the core issue of planning and operation.

In China, guided by the goal of carbon peaking and carbon neutrality, China has put forward the development strategy of building a new power system with new energy as the main body. The goal of "carbon peak and carbon neutrality" is a systematic project, and the power industry shoulders an important historical mission. According to the statistics of the International Energy Agency (IEA) in 2019, the total carbon emission in China was 11.3 billion tons, and the carbon emission in the energy field was 9.8 billion tons, accounting for 87% of the national total. Among them, the carbon emission in the power industry was 4.2 billion tons, accounting for 37% of the national total (United Nations Environment Programme, 2019). At present, China's energy consumption and carbon dioxide emissions per unit of GDP have been reduced by 13.5 and 18%, respectively, which has been written into the main objectives of economic and social development during the 14th Five-Year Plan (Xinhuanet, 2021). According to EIA data, the carbon emission of the United States in 2019 was 6.558 billion tons, down 11.96% from 2007. In 2020, renewable energy accounted for 12.49% of primary energy consumption in the United States. Biomass energy accounts for the highest proportion of renewable energy, accounting for 39%, followed by wind energy (26%), hydropower (22%), light energy (11%), and geothermal energy (2%). In 2020, the carbon emission of the EU was 2.551 billion tons, a decrease of 32.05% compared with 1990.

Therefore, to achieve the goal of carbon peak and carbon neutrality, the power industry has the heaviest task and the greatest responsibility and will play an important role of the main force. Therefore, the intermittent renewable energy power generation represented by wind power and solar energy will enter the fast lane of large-scale development and gradually form a clean and sustainable power supply mode dominated by renewable energy power generation. Also, the power system will change from a high-carbon power system to a deep low-carbon or zero-carbon power system.

However, due to the strong uncertainty and strong fluctuation characteristics of intermittent renewable energy power generation, realizing the status of the power subject and responsibility subject of renewable energy power generation faces complex technical challenges and needs a long-term development process. In addition to continuing to pay attention to safety, reliability, and economy, the flexibility of the power system has become a new focus. Under this background, it has become an urgent problem to explore the flexibility mechanism, planning, and operation theory and method of the new power system in a complex environment and multi-space–time interaction (Xu et al., 2020).

Security, reliability, economy, and flexibility are the internal requirements of modern power systems and are important indexes to measure whether the operation mode of the power system is reasonable or not (Telukunta et al., 2017). There is an extremely close relationship between them. In order to analyze the power system flexibility, we briefly introduce the other three research statuses. The security of the power system represents the ability of the power system to maintain a continuous power supply in case of an accident in a short time. From the perspective of security, aiming at the rapid development of power systems, Shu and Tang (2017) analyzed the main standards of power system security in China and discussed the development direction in the future. Shahidehpour et al. (2005) discussed the important role of security in power system planning and operation, studied the challenges and problems faced by security in different time- and space scales, and put forward the corresponding solutions. Yorino et al. (2018) proposed a bi-level robust optimization model to solve the problem of reserve margin under the environment of uncertain renewable energy output to ensure the safe operation of the whole system. From the economic viewpoint, Wang et al. (2017) described the scheduling problem containing a large amount of random wind power as a chance-constrained economic scheduling problem. The joint probability density function of multiple wind farms was established by using the Gaussian mixture model, and the results verify that the system can achieve a better economy. In order to solve the problem of excess wind power generation, power-to-gas technology was introduced into the integrated electricity and natural gas system, and a stochastic dynamic economic dispatching model based on the conditional value at risk method security risk constraints was established in Chen (2019). From the reliability side, AmandaSteele et al. (2021) discussed the impact of the growth of renewable energy on power system reliability. In order to maintain the safe operation of the system in the short and medium term, considering the uncertainty of wind power, a multi-state model of hybrid power generation and standby suppliers was proposed in Ding et al. (2014), and a time-varying reliability evaluation technology was used for system reliability evaluation.

Under the background of zero-carbon transformation of energy structure, building a new power system with renewable energy as the main body will become an important means to achieve the goals of carbon peaking and carbon neutrality. A high proportion of renewable energy has become the main feature of the power system. Different from conventional thermal power,

renewable energy power generation is affected by meteorological conditions and environmental factors, and its output shows the characteristics of intermittence and fluctuation, which makes the power system change from a deterministic system to a strong uncertain system. The random variation characteristics of high-proportion renewable power will bring unprecedented challenges to the power system. However, due to the lack of flexibility in the power system, it is difficult to absorb renewable energy efficiently. Enhancing flexibility and improving system regulation capacity are inevitable requirements for realizing power zero-carbon transformation. However, the problem of insufficient flexibility in the power system restricting the consumption of renewable energy has not been fundamentally solved. Flexibility has become one of the indispensable indexes of the power system. At present, researchers have made relevant research and summary on the aspects of flexibility resources and flexibility evaluation methods (Brunner et al., 2020; Michael et al., 2020; Semich et al., 2020). Li et al. (2018) summarized the flexibility indicators and evaluation methods. Mohandes et al. (2019) analyzed the concept, indexes, and related economic technologies of power system flexibility in high penetration of the renewable energy environment and focused on the impact of uncertain renewable energy on storage and reserve. Taking the impact of renewable energy growth on power systems as the starting point, Alireza et al. (2019) analyzed the role of various flexibility resources in system flexibility from the point of timescales. The existing review on power system flexibility research mainly focuses on the definitions of power system flexibility, flexibility resources, and power balance mechanism in an uncertain environment, but there is no discussion on the application of the uncertainty modeling method in power system flexibility research. On this basis, this article further discusses the modeling technology of uncertainty factors in detail. Therefore, aiming at the planning flexibility, operation flexibility, and electricity market flexibility of power systems in an uncertain environment, this article summarizes the main modeling methods of uncertainties and analyzes the advantages and disadvantages of various methods.

In the following, Section 2 presents the concept and the characteristics of power system flexibility. Section 3 summarizes the uncertainty modeling methods from the perspective of mathematics. Section 4 summarizes the related research on power system flexibility under an uncertainty environment, and Section 5 narrates the concluding remarks.

2 Power system flexibility

2.1 Definition of power system flexibility

Flexibility is the ability of a power system to use all resources to respond to changes in net demand in a certain environment (Lannoye et al., 2012). At present, the research on power system flexibility is still in its infancy. The North American Electric Reliability Council (NERC) and International Energy Agency (IEA) define flexibility from different perspectives as follows: the NERC believes that power system flexibility is the ability to use system resources to meet load changes, which is mainly reflected in operation flexibility, and it focuses on the methods to improve power system flexibility (Milligan et al., 2010). IEA believes the power system flexibility means that, under its boundary constraints, the power system can quickly respond to large fluctuations in supply or load demand and can quickly respond to predictable changes (International Energy Agency, 2014). Hence, some researchers have declared their views on the definition of power system flexibility from different perspectives. In terms of power capacity and ramp rate, power system flexibility is described as the ability to increase energy production with a certain rate and ramp duration, that is, the ability to sustain ramping for a given duration (Dvorkin et al., 2014). Zhao et al. (2016) defined flexibility as the maximum uncertainty range that the power system can cope with. Generally speaking, the research on power system flexibility focuses more on the dynamic response and adequacy of the generation side and demand side.

2.2 Characteristics of power system flexibility

Power system flexibility has three characteristics: inherent characteristics of the power system, directionality, and spatio-temporal characteristics (Lu et al., 2018).

Flexibility is an inherent characteristic of a power system (Denholm and Hand, 2011). For the power system, it has the ability to resist a certain risk, that is, the power system has an internal tolerance that allows the power system to deviate from the preset operating point to a certain extent without any change. This tolerance is considered as the inherent flexibility of the power system. From the perspective of power system active power balance, the climbing capacity, output range, and load characteristics of units are the inherent characteristics of power system flexibility.

Directionality (Lannoye et al., 2010): the power system is affected by many uncertain factors. The intermittent power sources have changed the traditional power structure and increased the randomness and uncertainty of power system operation from the power generation side, resulting in a power imbalance in the power system in a short time. Under different operating conditions, the power system flexibility is different. In view of this characteristic of flexibility, it can be considered that power system flexibility has two directions: upward and downward, that is, the flexibility is directional. The upregulation ability and downregulation ability reflect the flexibility of the system in different directions.

Spatio-temporal characteristic means the power system flexibility needs to be described on a certain timescale

TABLE 1 Some power system flexibility evaluation indexes.

Evaluation object	Directionality	Probability index	Expected index
Peak-shaving capacity shortage	upward	$p^t_{\mathrm{UPCS},i}$	$E^t_{\mathrm{UPCS},i}$
	downward	$p^t_{\mathrm{DPCS},i}$	$E^t_{\mathrm{DPCS},i}$
Ramp capacity shortage	upward	$p^t_{\mathrm{URCS},i}$	$E^t_{\mathrm{URCS},i}$
	downward	$p^t_{\mathrm{DRCS},i}$	$E^t_{\mathrm{DRCS},i}$
Flexibility shortage	upward	p^t_{UFS}	E^t_{UFS}
	downward	p^t_{DFS}	E^t_{DFS}

(Thatte and Xie, 2016). The power change caused by uncertainty in the power system rarely increases or decreases monotonically, and the change duration is also different. Therefore, the evaluation of power system flexibility is different in different timescales. According to the timescales, it can be divided into the flexibility of frequency modulation and unit climbing. On the spatial scale, due to the influence of resource distribution and transmission conditions, flexible resources cannot be dispatched freely in the system (Chen et al., 2020).

2.3 Evaluation methods of power system flexibility

In the research of power system flexibility, evaluation methods are the key point (Semich et al., 2020). According to the power system flexibility characteristics, many research studies have put forward different flexibility evaluation indexes. Velocity ramps (positive ramp and negative ramp) and load duration (the duration of continuous maximum and minimum loads) were presented as the evaluation indexes to evaluate the flexibility of the system (Martin et al., 2019). From the perspective of the attributes of the five flexible resources (supply, demand, grid, storage, and markets), Papaefthymiou et al. (2018) divided them into 14 flexibility index systems. Similar to Papaefthymiou et al. (2018), the authors also adopt the attribute classification method and put forward four flexibility attribute indexes, namely: positive flexibility, negative flexibility, production flexibility, and time-varying flexibility in Zhou et al. (2021). Some other evaluation indexes, such as upward and downward reserves (Ma et al., 2013), optimal costs, time-dependent flexibility potentials, costs of flexibility provision (Wanapinit et al., 2021), and flexibility metrics (flexibility regulation range increase rate and flexibility promotion cost) (Guo et al., 2020), were presented to evaluate power system flexibility.

We briefly list several commonly used power system flexibility evaluation indexes in Table 1.

3 Modeling methods of uncertainties

Renewable energy generation, load demand forecasting, electricity price fluctuation, and other uncertain factors make the power system in a strong uncertain environment. The traditional deterministic method is no longer appropriate, and it is necessary to consider the influence of uncertain factors. How to optimize the problem under uncertainty becomes important. To solve the problem of uncertainties in the power system, the key is to accurately describe the impact of uncertain factors and how to effectively use the information on uncertain variables to provide theoretical data for power departments to make safe and economic decision-making schemes.

For the traditional deterministic optimization problem, its mathematical expression is generally as follows (Anthony Man, 2011):

$$\begin{aligned} &\min f(x) \\ &s.t. \quad h(x) \le 0, \end{aligned} \tag{1}$$

where x is the decision vector, $f(x)$ is the objective function, and $h(x)$ is the constraint function. In model (1), the corresponding parameters of both constraints and objective function are determined.

However, due to the emergence of various uncertain factors, the problems related to power systems have changed from traditional certainty to uncertainty, and the general expression of the uncertain optimization mathematical model is as follows(Sun et al., 2022):

$$\begin{aligned} &\min f(x,\xi) \\ &s.t. \quad h(x,\xi) \le 0 \\ &\quad \forall \xi \in U, \end{aligned} \tag{2}$$

where ξ is an uncertain parameter, and U is an uncertain set.

According to the different modeling of uncertain factors, the uncertain optimization methods mainly include stochastic programming, robust optimization, and distributionally robust optimization, and the comparisons of these methods are shown in Appendix 1.

3.1 Stochastic programming

In stochastic programming, random variables are often fitted to obtain the probability density distribution through the statistical analysis of historical data (Birge and Dempstert, 1996). The accurate acquisition of probability distribution and the accuracy of sampling calculation optimal solution are the main problems of stochastic programming methods (Jiang and Li, 2021). At present, the common stochastic programming methods mainly include the following.

3.1.1 Stochastic expectation model

In the stochastic expectation model, the distribution function model of uncertain parameters is determined, and the uncertain parameters are described by selecting a discrete or continuous probability distribution function. The stochastic expectation model is described as follows (Zhu et al., 2007):

$$\begin{cases} \max \quad \mathbb{E}[f(x,\xi)], \\ s.t. \quad \mathbb{E}\left[g_j(x,\xi)\right] \le 0, \quad j = 1,2,\ldots,p, \end{cases} \tag{3}$$

where ξ is an uncertain parameter, x is the decision vector, $f(x,\xi)$ is the objective function, and $g_j(x,\xi)$ is the constraint condition function.

If there are random parameters in the objective function and constraints, it is only necessary to take the expected value of the corresponding function, and the uncertain model can be transformed into a deterministic model and be solved.

3.1.2 Chance constrained

Chance constrained programming refers to the situation where constraints contain random variables, and the decisions must be made before the realization of random variables is predicted. However, considering that the decision may not meet the constraints when adverse circumstances occur, the decision needs to meet the constraints to a certain extent, but the decision should make the probability of the establishment of the constraints not less than a certain confidence level (Guo et al., 2021). The generalized chance-constrained programming model is described as follows (Mohanty et al., 2020):

$$\begin{cases} \min \quad \bar{f} \\ s.t. \quad \mathbb{P}\left\{f(x,\xi) \ge \bar{f}\right\} \ge \beta \\ \quad \mathbb{P}\{g_i(x,\xi) \le 0,\ i = 1,2,\cdots,p\} \ge \alpha_i, \end{cases} \tag{4}$$

where $\bar{f}$ is the objective value, x is the decision variable, ξ is the uncertain variable, $\mathbb{P}\{\cdot\}$ is the probability of event occurrence, β is the confidence level that the objective function is not lower than the threshold $\bar{f}$, and α_i is the ith constraint that satisfies the given confidence level.

There are two main solutions to chance-constrained programming. The first one is to transform the chance constrained into deterministic programming and then solve it by the theory of deterministic programming (Huo et al., 2021). The second one is an intelligent algorithm. The optimal value of the objective function and the optimal solution set of decision variables are obtained by stochastic simulation technology and solving them by intelligent algorithms, such as the simulated annealing algorithm (Özcan, 2010), genetic algorithm (Shing Chih and Fu, 2014), and random hill climbing algorithm (Kaur and Dhillon, 2021). The main disadvantage of these intelligent algorithms is their low efficiency.

3.1.3 Conditional value at risk

The theory of conditional value at risk (CVaR) is derived from the value at risk (VaR), which refers to the maximum expected loss at a given confidence level (Fernández, 2016; Belhajjam et al., 2017). The mathematical description of the VaR method is as follows (Crespi and Mastrogiacomo, 2020):

$$VaR_\beta(x) = \min\{\xi \in \mathbb{R} | \varphi(x,\xi) \ge \beta\}, \tag{5}$$

where x is the decision variable, ξ is the uncertain variable, $\varphi(x,\xi)$ is the function of the random variable ξ, andβ is the value of the confidence level. $\varphi(x,\xi)$ can be obtained by the following formula (Belhajjam et al., 2017):

$$\varphi(x,\xi) = \int_{h(x,\xi) \le \alpha} p(\xi) d\xi, \tag{6}$$

where$p(\xi)$ is the probability density function of a random variable, $h(x,\xi)$ is the lost function, and α is the threshold.

The VaR method considers the probability density characteristics of random variables and can describe the minimum value of loss under a given value. However, the defects of VaR, such as lack of convexity and subadditivity, limit its further application in practical optimization problems (Khodabakhsh and Sirouspour, 2016).

In view of the fact that VaR cannot describe the tail risk, CVaR, which reflects the expected value of loss exceeding the VaR threshold at a given confidence level, as an alternative risk measure, is presented to avoid the problems of VaR. The mathematical description of CVaR is as follows (Crespi and Mastrogiacomo, 2020):

$$\begin{aligned} CVaR_\beta(x) &= \mathbb{E}\left[f(x,\xi) | f(x,\xi) \ge VaR_\beta(x)\right] \\ &= \frac{1}{1-\beta} \int_{f(x,\xi) \ge VaR_\beta(x)} f(x,\xi) p(x) d\xi. \end{aligned} \tag{7}$$

To calculate the value of CVaR, Rockafellar and Uryasev (2000) established a linear programming model by using the sample average approximation method to avoid the calculation of the VaR and get the CvaR directly:

$$\begin{aligned} &CVaR_\beta(x) = \min\left\{ z_0 + \frac{1}{n(1-\beta)} \sum_{i=1}^{n} z_i \right\} \\ &s.t. \quad z_i \ge f(x,\xi_i) - z_0 \\ &\quad z_i \ge 0, i = 1,2,\cdots n. \end{aligned} \tag{8}$$

The CVaR method can describe the impact of random variables from the perspective of risk, solve the problem that the VaR method cannot accurately describe the tail risk, and provide rich decision-making information for decision-makers (Ang et al., 2021). This method can use the constraints in the optimization model as the risk index to describe its risk, simplify the constraints in the model, obtain the risk decision information, and has the same good characteristics as the VaR method in mathematics.

3.1.4 Dependent-chance programming

Dependent-chance programming is a programming method generated when decision-makers face multiple events and want to maximize the probability of meeting these events. Dependent-chance programming is a stochastic optimization theory to optimize the chance function of events in an uncertain environment. The general model is given as follows (Liu, 1997):

$$\begin{cases} \max & \mathbb{P}\{h(x_i,\xi)\le 0\} \\ s.t. & g_j(x_i,\xi)\le 0,\ j=1,2,\ldots,p, \end{cases} \tag{9}$$

where x_i is the decision variable, andξ is the uncertain variable. The dependent-chance programming model can be expressed as maximizing the probability of a random event $h(x_i,\xi)\le 0$ under an uncertain environment $g_j(x_i,\xi)\le 0$.

At present, the genetic algorithm is mainly used to solve the dependent-chance programming model. In Zhang and Song (2017), the author proposed a Sugeno measure space-based algorithm to solve the dependent-chance programming model.

3.2 Robust optimization

The stochastic programming method requires the accurate distribution of random variables, but this is very unrealistic in practice. For example, incomplete data may lead to an inaccurate probability distribution, which may affect the decision-making results (Yang et al., 2019). The robust optimization method is different from stochastic programming. When facing uncertain parameters, the robust optimization method does not need to know its accurate distribution but only its uncertain space (Ben-Tal and Nemirovski, 2002). Robust optimization assumed that the range of uncertain parameters is a specific uncertain set. Within the range of the uncertain set, the objective function or constraints in the worst-case scenario are constructed, which can generally be expressed as a min-max-min optimization problem (Gabrel et al., 2014):

$$\begin{aligned} &\min \max_{x\in R,\xi\in\mathcal{U}} \min f(x,\xi) \\ &s.t.\quad g_i(x,\xi)\le 0 \\ &\quad \forall\xi\in\mathcal{U} \\ &\quad i=1,2,\cdots m, \end{aligned} \tag{10}$$

where x is the decision variable, ξ is the uncertain variable, and $\mathcal{U}$ is the uncertain set.

By choosing a different uncertain set to describe the uncertainties, robust optimization models with different modeling characteristics and solving difficulties can be obtained. According to different selection types of uncertainty sets, robust optimization methods can generally be divided into the box robust optimization method, ellipsoid robust optimization method, polyhedron robust optimization method, and budget robust optimization method. There are mainly the following types of robust sets to characterize uncertain variables.

3.2.1 Box robust set

The box uncertainty set is the simplest uncertainty set, also known as an interval set. Because robust optimization is an optimization solution method considering the worst case, it is possible for some models to optimize all uncertain parameters in the upper and lower bounds of the interval set. The generalized box robust optimization model is described as follows (Xiao et al., 2013):

$$\mathcal{U}=\left\{\xi\middle|\xi^0+\hat{\xi},e^T\hat{\xi}=0,\underline{\xi}\le\hat{\xi}\le\bar{\xi}\right\}, \tag{11}$$

where $\boldsymbol{e}$ is the column vector with element 1, and $\underline{\xi}$ and $\bar{\xi}$ are the upper and lower bounds of the given set, respectively.

However, in practice, the probability of this situation may not happen. Therefore, the results are easy to be excessively conservative (Gu et al., 2016).

3.2.2 Ellipsoidal robust set

To reduce the aggressive conservatism in Xiao et al. (2013), the ellipsoidal robust optimization method is presented as follows (Ben-Tal and Nemirovski, 1998):

$$\mathcal{U}=\left\{\xi\middle|\xi^0+A\hat{\xi},e^TA\hat{\xi}=0,\left\|\hat{\xi}\right\|\le 1\right\}, \tag{12}$$

where A is the control matrix of ellipsoidal size. Selecting different matrices can effectively control the distribution of uncertain parameters from the center of the sphere and the radius from the center of the sphere. Different values of A can realize the optimal decision of ellipsoid robust optimization with the coordination of conservatism and optimality (Hanks et al., 2017). Compared with the box robust optimization method, the ellipsoidal robust optimization method can describe uncertain parameters more accurately. However, the ellipsoidal robust optimization method increases the complexity of problem-solving, which limits the application of this method.

3.2.3 Polyhedral robust set

For robust uncertain optimization problems, not only the robustness of the results needs to be considered but also the trade-off between optimization performance and robustness. The

polyhedral robust optimization method can meet such requirements at the same time. The generalized polyhedral robust optimization model is described as follows (Jalilvand-Nejad et al., 2016):

$$\mathcal{U} = \{\xi \| \|\xi\|_1 \le \Gamma, |\xi| \le e\}. \tag{13}$$

The polyhedral uncertain set can be regarded as a special form of the ellipsoidal uncertain set. Although the polyhedral uncertainty set is difficult to characterize the correlation between uncertain parameters, they are widely favored in practical engineering problems because of their linear structure and easy-to-control uncertainty (Saric and Stankovic, 2008).

3.2.4 Budget robust set

The budget robust optimization method builds the uncertainty set based on the relative value of the offset of uncertain parameters, which can more accurately describe the fluctuation of uncertainties and is described as follows (Goerigk et al., 2020):

$$\mathcal{U} = \left\{ \xi \left| \sum \left| \frac{\xi_i - \hat{\xi}_i}{\bar{\xi}_i - \underline{\xi}_i} \right| \le \Gamma, |\xi| \le e \right. \right\}, \tag{14}$$

where $\hat{\xi}_i$ is the forecast value of an uncertain variable, and $\bar{\xi}$ and $\underline{\xi}$ are the upper and lower bounds of the given set, respectively.

3.2.5 Combined robust set

In addition to the aforementioned common uncertain sets, in order to adapt to different situations and describe the uncertainties more accurately, some researchers have also derived many kinds of combined uncertain sets, such as the "box + ellipsoidal" uncertain set and "box + polyhedral" uncertain set (Papadimitriou and Fortz, 2015; Dong et al., 2020).

3.3 Distributionally robust optimization

In recent years, the distributionally robust optimization (DRO) method has been proposed to overcome the shortcomings of stochastic optimization and robust optimization (Goh and Sim, 2010). Considering that in practical problems, some statistical information of random variables is often known, such as expectation and variance, and historical sample data. By establishing the ambiguity set of a random variable probability distribution based on some statistical information, the DRO method seeks the minimum expected value of system operation cost under the worst probability distribution. Therefore, the DRO method not only makes use of the statistical information of random variables but also ensures the reliability of the scheduling scheme to a certain extent (Wiesemann et al., 2014). Constructing the ambiguity set is the basis and key of the DRO method. At present, the ambiguous set construction methods mainly include as followed.

3.3.1 Moment-determination ambiguity set

Although it is impossible to accurately obtain the distribution of random variables through limited historical data, it can determine the mean and variance of random variables. Therefore, the DRO moment-determination method is derived, and the ambiguity set is described as follows (Wei et al., 2016):

$$\mathrm{D} = \left\{ P(\xi) \left| \begin{array}{c} P(\xi \in \Xi) = 1 \\ \mathbb{E}(\xi) = \mu \\ \mathbb{E}\left((\xi - \mu)^2 \right) = \sigma^2 \end{array} \right. \right\}, \tag{15}$$

where D is the ambiguity set, and μ and σ^2 are the mean and variance of random variables, respectively.

The uncertainty of the correlation moment is not considered in the DRO moment-deterministic method, which has a great impact on the decision results.

3.3.2 Moment-uncertainty ambiguity set

In practice, due to many reasons such as limited data and missing data, the moment-determination ambiguity set obtained from historical data statistics is not completely accurate and has certain uncertainty. Therefore, the DRO method considering moment uncertainty is particularly important. The moment-uncertainty ambiguity set can be expressed as follows (Chang et al., 2019):

$$\mathrm{D} = \left\{ \mathbb{P} \in \Omega \left| \begin{array}{c} \mathbb{P}(\xi \in \Xi) = 1 \\ (\mathbb{E}[\xi] - \mu_0)^{\mathrm{T}} \sigma_0^{-1} (\mathbb{E}[\xi] - \mu_0) \le \gamma_1 \\ \mathbb{E}\left[(\xi - \mu_0)(\xi - \mu_0)^{\mathrm{T}} \right] \le \gamma_2 \sigma_0 \\ \gamma_1 \ge 0, \gamma_2 \ge 1 \end{array} \right. \right\}, \tag{16}$$

where the second line assumes that the mean value of the random variable is located in an ellipsoid with μ_0 as the center and γ_1 as the size. The third line describes the possibility that the random variable ξ is close to μ_0 based on the correlation σ_0. The parameters γ_1 and γ_2 quantify the decision-making trust in μ_0 and σ_0, respectively.

3.3.3 Wasserstein distance-based ambiguity set

The Wasserstein distance-based method constructs the initial empirical distribution based on the sampled data and can make full use of the available historical data. Moreover, this method uses the Wasserstein sphere to limit the fluctuation range of probability distribution (Graf and Luschgy, 2009; Zhou et al., 2020). The selection of sphere radius has an important impact on the conservatism of system decision-making results. The ambiguity set is defined as a ball in the probability distribution space, which contains all distributions close to the real distribution or the most likely distribution in terms of probability distance. The decision-maker can control the conservatism of the optimization

problem by adjusting the radius of the ball. If the radius is zero, the ambiguity set will be reduced to a single element set containing only the real distribution. The Wasserstein distance-based ambiguity set can be expressed as follows (Zheng and Chen, 2020):

$$\mathcal{M}_\epsilon\left(\tilde{\mathbb{P}}_S\right) = \left\{\mathbb{P} \in \mathcal{R}(\Xi)\colon W\left(\mathbb{P}, \tilde{\mathbb{P}}_S\right) \le \epsilon\right\}, \tag{17}$$

where $\mathcal{M}_\epsilon(\tilde{\mathbb{P}}_S)$ represents the Wasserstein ball with ϵ as the radius and $\tilde{\mathbb{P}}_S$ as the center of the sphere.

The worst expectation of constructing an ambiguity set based on first-order Wasserstein distance has the following form and theorem (Mohajerin Esfahani and Kuhn, 2018):

$$\mathcal{Z}(x) = \max_{\mathbb{P}} \mathbb{E}_{\mathbb{P}}[Z(x,\xi)]. \tag{18}$$

Through the strong duality theory, we can get the following equation:

$$\mathcal{Z}(x) = \inf_{\lambda \in \mathbb{R}^+} \epsilon\lambda + \frac{1}{I}\sum_{s\in S} \sup Z(x,\xi) - \lambda d\left(\xi, \tilde{\xi}\right). \tag{19}$$

Using Wasserstein distance to construct the ambiguity set has two advantages: 1) the distribution constructed by this method is more reasonable than that constructed by other common methods; 2) the robust problem can be transformed into finite convex programming or even linear programming, which is easy to calculate (Duan et al., 2018).

3.3.4 Kullback–Leibler distance-based ambiguity set

Different from the DRO method based on Wasserstein distance, the DRO method based on the Kullback–Leibler divergence assumes that the probability is discrete, and the Kullback–Leibler divergence is defined as follows (Kullback, 1987):

$$D_{KL}(p|P_0) = \int_\Omega P(\theta)\log\frac{P(\theta)}{P_0(\theta)}d\theta, \tag{20}$$

where p and p_0 are probability distribution functions of the random variable ξ, and $D_{KL}(p|P_0)$ represents the Kullback–Leibler divergence from p to p_0.

The ambiguity set of a probability distribution based on Kullback–Leibler divergence is as follows (Yang et al., 2019):

$$D := \{P \in D | D_{KL}(p|P_0) \le \eta\}, \tag{21}$$

where η is the divergence tolerance to control the size of the ambiguity set.

This kind of model transforms the original problem through simple dual derivation and the discrete probability scene value technique, and the solution is relatively simple. However, although the subproblem can be accelerated by solving each discrete scene separately, the solution time of the whole model is long.

4 Study on power system flexibility considering uncertainties

Uncertainty affects the power system in many ways. The current research mainly includes power system planning, power system operation, electricity market, load forecasting, and supply-demand balance.

The research on the uncertainty of power system load forecasting is mainly divided into two aspects: probabilistic load forecasting and the uncertainty of load forecasting results. There are few studies on the uncertain supply-demand balance of power systems, especially the system balance and operation problems caused by renewable energy. From a certain point of view, the purpose of power system load forecasting and supply-demand balance is mainly to provide a scientific basis for power system planning and operation. Therefore, aiming at the problem of power system flexibility in an uncertain environment, this study mainly summarizes the research progress of power system planning, operation, and electricity market flexibility.

4.1 Planning flexibility

Generally, power system planning consists of generation planning, capacity planning, and reserve planning (Dong and Tong, 2020). In the uncertain environment, the uncertainties increase the need for planning flexibility in electric power systems, and great progress has been made in the research of power system flexibility planning (Sun et al., 2021).

External flexibility resources, such as energy storage and demand response, are exploited in generation expansion planning for coping with renewable energy increases (Dai et al., 2021). Due to variable renewable energy source integration, a power-based unit commitment generation expansion planning model was presented to overcome the problem of overestimating the actual flexibility of the system, and from the perspective of directional characteristics, the indicators of insufficient flexibility of up- and downregulation and their expression forms are defined (Tejada-Arango et al., 2020). In Hua et al. (2018), from the viewpoint of representing system flexibility, a unit commitment generation expansion planning model was presented, and a convex relaxation was used to solve the problem computationally challenging of unit commitment, which is different from the model in Tejada-Arango et al. (2020). Flexibility is rarely fully considered in capacity planning models because of the computational demands of including mixed integer unit commitment within the capacity expansion; considering the carbon emission constraints and the penetration of renewable energy in power systems, the problems of generation of planning flexibility (Palmintier and Webster, 2016) and capacity planning flexibility (Hargreaves et al., 2015; Chen et al., 2018) were discussed, respectively. Based on a computational efficient modeling formulation, the chanced programming (Chen et al., 2018) and

robust method (Hargreaves et al., 2015) were used to present the uncertainty of the wind power output.

A flexible power system should have sufficient ramp capacity and reserve capacity to meet the occurrence of uncertain conditions. Therefore, traditional reserve planning is deemed impeding to the system's flexibility (Khoshjahan et al., 2019). The concept of flexibility envelopes, which can capture reserve requirements, was presented as an alternative approach to the traditional reserve scheduling method (Nosair and Bouffard, 2015a; Nosair and Bouffard, 2015b). In Ghaemi and Salehi (2021) and Yang and Sun (2022), flexibility constraints were considered as a limit to reduce costs of the system, and MILP expansion planning was proposed, where an interval optimization has been utilized to address uncertainties due to the computational efficiency. In Dehghan et al. (2020), (2020), and Pourahmadi et al. (2020a), the problem of generation expansion planning was studied by the robust method, stochastic method, and distributionally robust method, respectively. Through different uncertainty modeling techniques, these literature reports analyzed the flexibility improvement methods from different viewpoints, and the flexibility of the system is evaluated from the time scale.

From the perspective of power system planning flexibility, the aforementioned research considers the uncertain factors including wind, transmission lines, and load demand but rarely considers the correlation between wind power. For power system planning, this is an important factor worthy of consideration. Whether it can effectively improve flexibility is worth discussing.

4.2 Operation flexibility

Compared with the problem of power system planning flexibility, the problem of power system operational flexibility in an uncertain environment, such as unit commitment and economic dispatch, has changed more obviously (Li et al., 2021). Operation flexibility is an important characteristic of the power system. It is an important means to reduce the power supply interruption caused by uncertainties in the power system. Improving the availability of renewable energy is one of the methods to meet the requirements of operational flexibility in power systems (Huo et al., 2020). It is the most important link to accurately model the uncertainties and describe their characteristics with corresponding mathematical methods (Pourahmadi et al., 2019; Pourahmadi et al., 2020b). The robust method, as a mature uncertainty modeling technology, has been widely used. To discuss the flexible unit commitment problem, box-based, ellipsoidal-based and polyhedral-based approaches as the uncertainties' modeling have been used in Li et al. (2015), Angulo Cárdenas et al. (2016), and Cho et al. (2019) to model the uncertainty of renewable power and load demand, and the results showed that a flexible scheduling strategy was obtained which balances the economic and efficiency. From the perspective of the model solving efficiency, these three modeling methods have good performance. Demand response, as a flexible resource, its uncertainty is characterized by the stochastic method, and the role of improving system flexibility in multi-energy systems and unit commitment problems was studied in Good and Mancarella, (2019) and Saeed Poorvaezi et al. (2019). In the research, the difficult solution form of the problem is simplified by applying methods such as random scene reduction.

In the power system, with the rapid development of distributed generation, user-side management has become an important way to improve system flexibility (Rashidizadeh-Kermani et al., 2020). To assess the operational flexibility capacity of the system, a fixed robust uncertainty set and an adjustable uncertainty set were constructed; the wind power model based on a two-stage robust unit commitment was introduced in Pourahmadi et al. (2022), and the author adopts the improved method based on the CCG algorithm to solve the adjustable robust model. Considering energy storage and reserves, Zhang et al. (2016) presented a flexibility-oriented unified scheduling model to study the features required for flexibility assessment.

With the development of energy storage technology, much attention has been paid to the research of power system reserve flexibility from the perspective of the economy (Krad et al., 2017). Flexibility reserve, both with the function of supplying the energy imbalance in real-time operation and determining flexible ramping requirements (Khatami et al., 2020), and a continuous-time stochastic multi-fidelity model for co-optimization of energy and flexibility reserve were proposed by Khatami and Parvania (2020). Compared with these two similar stochastic modeling forms, the solution is more difficult and less efficient when considering the time scale.

4.3 Electricity market flexibility

Flexibility is the key to the operation of a high proportion renewable energy electricity market. Large power abandonment, frequent occurrence of negative electricity prices, and price fluctuation are all manifestations of inflexibility after the power system is connected to a high proportion of renewable energy (Bistline, 2019; Mamounakis et al., 2019; Ordoudis et al., 2020; Zhang et al., 2020). In the uncertain environment, how to improve the flexibility of the power market is worthy of attention for the realization of a new power system and the goal of dual carbon (Muñoz et al., 2021).

The flexibility of the electricity market can be improved by strengthening transmission investment and improving generation side flexibility and mechanism innovation (Papadaskalopoulos and Strbac, 2013; Chen and Jing, 2022; Tu, 2022). In addition, flexible ramping products, such as traditional thermal power units, electric vehicles, energy storage, electricity-gas combined system, and demand response, have made great progress as a method to improve system flexibility in an uncertain environment (Wang and Hodge, 2017; Wang et al., 2021). Considering the spatio-temporal correlations of wind power and demand uncertainties, a

distributionally robust chance constrained multi-interval model was proposed to solve the deliverability issues of flexible ramping products (Fang et al., 2020), and the Wasserstein distance ambiguity set was transformed into a MILP problem. By aggregating demand-side flexibility resources, Di Somma et al. (2019) formulated a stochastic MILP problem, and the uncertainties of day-ahead market price and intermittent renewable energy generation were modeled through a set of scenarios to improve the flexibility operation of the electricity market. For the same MILP model, the difference between the two modeling methods leads to different difficulties and efficiency of the solution. Due to a large number of random scenes, the solution time is obviously long (Di Somma et al., 2019; Fang et al., 2020).

With the increasing proportion of renewable energy, energy storage, and natural gas, the main body of electricity market transactions is both an energy producer and energy consumer (Iria et al., 2019). At the same time, a large number of uncertain factors have challenged the effectiveness of various traditional operation measures. In the multi-energy environment, how to improve the flexibility of operation of the electricity market under uncertainties has attracted great attention (Baringo et al., 2019; Qin et al., 2021; Sayed et al., 2021; Yang et al., 2021). By using a set of inexact distributions based on historical data to portray the volatile market price, an electricity and heat market self-scheduling model was modeled as a distributionally robust problem, and the results validated that a more flexible electricity market can be obtained by this method (Li et al., 2022). For market flexibility, price and load demand are two major sources of uncertainty. The robust method (Velloso et al., 2020; Liu et al., 2022) and stochastic method (Hartwig and Kockar, 2016; Dvorkin, 2020; Jiang et al., 2022) were used to describe the uncertainty of market price and renewable energy generation, respectively. Numerical results showed that these methods have good performance in improving the flexibility of the electricity market in an uncertain environment.

5 Conclusion

This article reviews the concepts and characteristics of power system flexibility. Aiming at the problem of power system flexibility in an uncertain environment, the uncertainty modeling methods, including the robust method, stochastic method, and distributionally robust method, are summarized, and the corresponding mathematical modeling expressions are given. From the perspective of economy and conservatism, the advantages and disadvantages of these methods are compared and analyzed. Furthermore, from the perspective of planning, operation, and electricity market flexibility, the existing literature reports are summarized and analyzed in detail, and the following conclusions are obtained as follows:

1) Deepening the reform of the power system and building a new power system with renewable energy as the main body are important measures to achieve the goal of dual carbon. In this context, various uncertain factors, such as the output randomness and price instability of new energy, have a great impact on the power system flexibility.
2) The research on power system flexibility considering uncertainty factors and the research on using stochastic programming and robust optimization methods to solve such uncertain problems are mature at present. The application of constrained programming, value at risk method, conditional value at risk method, and robust optimization method in the power system will have further development. The new method combining the characteristics of stochastic programming and the robust optimization method can also be a way for subsequent related research. The distributionally robust method is the main research field of power system operation and planning flexibility, considering uncertainties, but there is little application research in electricity market flexibility. In addition, the random variable modeling method of distributionally robust optimization can be deeply studied to describe the uncertainty more accurately.

In recent years, with the improvement of computer computing power and the development of artificial intelligence technology, which has been gradually applied to power system uncertainty modeling, combining probability prediction technology with the optimal method, a decision-making method based on probability prediction has been constructed from mathematical theory so as to improve the flexibility ability of the power system to deal with the actual uncertainty factors in the future. For the research of power system flexibility in an uncertainty environment, the innovation of the modeling method, the efficiency of the solution algorithm, and the accurate combination of application scenarios are worth considering.

Author contributions

CY contributed to manuscript writing. WS contributed to review and editing. DH contributed to the supervision. All authors have read and agreed to the published version of the manuscript.

Funding

This work is supported by the National Natural Science Foundation of China (51777126).

Conflict of interest

The authors declare that the research was conducted in the absence of any commercial or financial relationships that could be construed as a potential conflict of interest.

Publisher's note

References

Alireza, A., Meysam, D., and Farrokh, A. (2019). Power system flexibility: an overview of emergence to evolution[J]. *J. Mod. Power Syst. Clean. Energy* 7 (5), 987–1007.

AmandaSteele, J. H., Wesley Burnett, J., and Bergstrom, J. C. (2021). The impact of variable renewable energy resources on power system reliability. *J. Energy Policy* 151, 111947.

Ang, X., Shen, X., Guo, Q., and Sun, H. (2021). A conditional value-at-risk based planning model for integrated energy system with energy storage and renewables[J]. *Appl. Energy* 294, 116971.

Angulo Cárdenas, A. A., Mancilla-David, F., Palma-Behnke, R. E., and Espinoza, D. G. (2016). A polyhedral-based approach applied to quadratic cost curves in the unit commitment problem. *IEEE Trans. Power Syst.* 31 (5), 3674–3683. doi:10.1109/tpwrs.2015.2499442

Anthony Man, C. S. (2011). Deterministic approximation algorithms for sphere constrained homogeneous polynomial optimization problems. *Math. Program.* 129, 357–382. doi:10.1007/s10107-011-0464-0

Baringo, A., Baringo, L., and Arroyo, J. M. (2019). Day-ahead self-scheduling of a virtual power plant in energy and reserve electricity markets under uncertainty. *IEEE Trans. Power Syst.* 34 (3), 1881–1894. doi:10.1109/tpwrs.2018.2883753

Belhajjam, A., Belbachir, M., and Ouardirhi, S. E. (2017). Robust multivairiate extreme value at risk allocation[J]. *Fina. Res. Lett.*, S1544612316303622.

Ben-Tal, A., and Nemirovski, A. (1998). Robust convex optimization. *Math. OR.* 23 (4), 769–805. doi:10.1287/moor.23.4.769

Ben-Tal, A., and Nemirovski, A. (2002). Robust optimization–methodology and applications[J]. *Math. Program.* 11, 453–480.

Birge, J. R., and Dempstert, M. A. H. (1996). Stochastic programming approaches to stochastic scheduling. *J. Glob. Optim.* 9, 417–451. doi:10.1007/bf00121682

Bistline, J. E. (2019). Turn down for what? The economic value of operational flexibility in electricity markets[J]. *IEEE Trans. Power Syst.* 34 (1), 527–534. doi:10.1109/tpwrs.2018.2856887

Brunner, C., Deac, G., Braun, S., and Zophel, C. (2020). The future need for flexibility and the impact of fluctuating renewable power generation. *Renew. Energy* 149, 1314–1324. doi:10.1016/j.renene.2019.10.128

Chang, Z., Ding, J., and Song, S. (2019). Distributionally robust scheduling on parallel machines under moment uncertainty. *Eur. J. Operational Res.* 272 (13), 832–846. doi:10.1016/j.ejor.2018.07.007

Chen, D., and Jing, Z. (2022). An improved market mechanism for energy storage based on flexible state of energy[J]. *CSEE J. Power Energy Syst.* 8 (3), 838–848.

Chen, X., Dall'Anese, E., Zhao, C., and Li, N. (2020). Aggregate power flexibility in unbalanced distribution systems. *IEEE Trans. Smart Grid* 11 (1), 258–269. doi:10.1109/tsg.2019.2920991

Chen, X., Lv, J., McElroy, M. B., Han, X., Nielsen, C. P., and Wen, J. (2018). Power system capacity expansion under higher penetration of renewables considering flexibility constraints and low carbon policies. *IEEE Trans. Power Syst.* 33 (6), 6240–6253. doi:10.1109/tpwrs.2018.2827003

Chen, Z. (2019). Stochastic dynamic economic dispatch of wind-integrated electricity and natural gas systems considering security risk constraints[J]. *CSEE J. Power Energy Syst.* 5 (3), 324–334.

Cho, Y., Ishizaki, T., Ramdani, N., and Imura, J. (2019). Box-based temporal decomposition of multi-period economic dispatch for two-stage robust unit commitment. *IEEE Trans. Power Syst.* 34 (4), 3109–3118. doi:10.1109/tpwrs.2019.2896349

Crespi, G. P., and Mastrogiacomo, E. (2020). Qualitative robustness of set-valued value-at-risk. *Math. Methods Oper. Res. (Heidelb).* 91, 25–54. doi:10.1007/s00186-020-00707-9

Dai, W., Shi, B., Zhang, D., Goh, H. H., Liu, H., and Li, J. (2021). Incorporating external flexibility in generation expansion planning. *IEEE Trans. Power Syst.* 36 (6), 5959–5962. doi:10.1109/tpwrs.2021.3101700

Dehghan, S., Amjady, N., and Aristidou, P. (2020). A robust coordinated expansion planning model for wind farm-integrated power systems with flexibility sources using affine policies. *IEEE Syst. J.* 14 (3), 4110–4118. doi:10.1109/jsyst.2019.2957045

Denholm, P., and Hand, M. (2011). Grid flexibility and storage required to achieve very high penetration of variable renewable electricity. *Energy Policy* 39 (3), 1817–1830. doi:10.1016/j.enpol.2011.01.019

Di Somma, M., Graditi, G., and Siano, P. (2019). Optimal bidding strategy for a DER aggregator in the day-ahead market in the presence of demand flexibility. *IEEE Trans. Ind. Electron.* 66 (2), 1509–1519. doi:10.1109/tie.2018.2829677

Ding, Y., Singh, C., Goel, L., Østergaard, J., and Wang, P. (2014). Short-term and medium-term reliability evaluation for power systems with high penetration of wind power. *IEEE Trans. Sustain. Energy* 5 (3), 896–906. doi:10.1109/tste.2014.2313017

Dong, H., and Tong, X.-J. (2020). Review of mathematical methodology for electric power optimization problems[J]. *J. Operations Res. Soc. China* 8 (2), 295–309.

Dong, H., Yang, C., and Sun, W. (2020). Modelling the operation of small-scale integrated energy systems based on data-driven robust optimization[J]. *IEEJ Trans Electr. Electron. Eng.* 15 (3), 442–450.

Duan, C., Fang, W., Jiang, L., Yao, L., and Liu, J. (2018). Distributionally robust chance-constrained approximate AC-OPF with Wasserstein metric. *IEEE Trans. Power Syst.* 33 (5), 4924–4936. doi:10.1109/tpwrs.2018.2807623

Dvorkin, Y., Kirschen, D. S., and Ortega-Vazquez, M. A. (2014). Assessing flexibility requirements in power systems. *IET Gener. Transm. &amp. Distrib.* 8 (11), 1820–1830. doi:10.1049/iet-gtd.2013.0720

Dvorkin, Y. (2020). A chance-constrained stochastic electricity market. *IEEE Trans. Power Syst.* 35 (4), 2993–3003. doi:10.1109/tpwrs.2019.2961231

Fang, X., Sedzro, K. S., Yuan, H., Ye, H., and Hodge, B. M. (2020). Deliverable flexible ramping products considering spatiotemporal correlation of wind generation and demand uncertainties. *IEEE Trans. Power Syst.* 35 (4), 2561–2574. doi:10.1109/tpwrs.2019.2958531

Fernández, J. A. (2016). Economic lot sampling inspection from defect counts with minimum conditional value-at-risk[J]. *Eur. J. Oper. Res.*, S0377221716308761.

Gabrel, V., Murat, C., and Thiele, A. (2014). Recent advances in robust optimization: An overview. *Eur. J. Operational Res.* 235 (3), 471–483. doi:10.1016/j.ejor.2013.09.036

Ghaemi, S., and Salehi, J. (2021). Incorporating ramp problem into the expansion planning of distributed energy resources for improving flexibility of renewable-based distribution network using interval optimization. *Electr. Eng.* 103, 341–355. doi:10.1007/s00202-020-01079-3

Goerigk, M., Kurtz, J., and Poss, M. (2020). Min–max–min robustness for combinatorial problems with discrete budgeted uncertainty. *Discrete Appl. Math.* 285, 707–725. doi:10.1016/j.dam.2020.07.011

Goh, J., and Sim, M. (2010). Distributionally robust optimization and its tractable Approximations. *Operations Res.* 58 (4), 902–917. doi:10.1287/opre.1090.0795

Good, N., and Mancarella, P. (2019). Flexibility in multi-energy communities with electrical and thermal storage: A stochastic, robust approach for multi-service demand response. *IEEE Trans. Smart Grid* 10 (1), 503–513. doi:10.1109/tsg.2017.2745559

Graf, S., and Luschgy, H. (2009). Quantization for probability measures in the prokhorov metric. *Theory Probab. Appl.* 53 (2), 216–241. doi:10.1137/s0040585x97983687

Gu, C., Yang, W., Song, Y., and Li, F. (2016). Distribution network pricing for uncertain load growth using fuzzy set theory. *IEEE Trans. Smart Grid* 7 (4), 1932–1940. doi:10.1109/tsg.2016.2518175

Guo, G., Zephyr, L., Morillo, J., Wang, Z., and Lindsay Anderson, C. (2021). Chance constrained unit commitment approximation under stochastic wind energy. *Comput. Operations Res.* 134, 105398. doi:10.1016/j.cor.2021.105398

Guo, Z., Zheng, Y., and Li, G. (2020). Power system flexibility quantitative evaluation based on improved universal generating function method: A case study of zhangjiakou. *Energy* 205, 117963. doi:10.1016/j.energy.2020.117963

Hanks, R. W., Weir, J. D., and Lunday, B. J. (2017). Robust goal programming using different robustness echelons via norm-based and ellipsoidal uncertainty sets [J]. *Eur. J. Operational Res.* 262, 34–39.

Hargreaves, J., Hart, E. K., Jones, R., and Olson, A. (2015). Reflex: An adapted production simulation methodology for flexible capacity planning. *IEEE Trans. Power Syst.* 30 (3), 1306–1315. doi:10.1109/tpwrs.2014.2351235

Hartwig, K., and Kockar, I. (2016). Impact of strategic behavior and ownership of energy storage on provision of flexibility. *IEEE Trans. Sustain. Energy* 7 (2), 744–754. doi:10.1109/tste.2015.2497967

Hua, B., Baldick, R., and Wang, J. (2018). Representing operational flexibility in generation expansion planning through convex relaxation of unit commitment. *IEEE Trans. Power Syst.* 33 (2), 2272–2281. doi:10.1109/tpwrs.2017.2735026

Huo, D., Gu, C., Greenwood, D., Wang, Z., Zhao, P., and Li, J. (2021). Chance-constrained optimization for integrated local energy systems operation considering correlated wind generation. *Int. J. Electr. Power & Energy Syst.* 132, 107153. doi:10.1016/j.ijepes.2021.107153

Huo, Y., Bouffard, F., and Joós, G. (2020). Spatio-temporal flexibility management in low-carbon power systems. *IEEE Trans. Sustain. Energy* 11 (4), 2593–2605. doi:10.1109/tste.2020.2967428

International Energy Agency (2014). The power of transformation: wind, sun and the economics of flexible power systems[J].

Iria, J. P., Soares, F. J., and Matos, M. A. (2019). Trading small prosumers flexibility in the energy and tertiary reserve markets. *IEEE Trans. Smart Grid* 10 (3), 2371–2382. doi:10.1109/tsg.2018.2797001

Jalilvand-Nejad, A., Shafaei, R., and Hamid, S. (2016). Robust optimization under correlated polyhedral uncertainty set. *Comput. Industrial Eng.* 92, 82–94. doi:10.1016/j.cie.2015.12.006

Jiang, J., and Li, S. J. (2021). On complexity of multistage stochastic programs under heavy tailed distributions. *Operations Res. Lett.* 49 (2), 265–269. doi:10.1016/j.orl.2021.01.016

Jiang, T., Yuan, C., Bai, L., Chowdhury, B. H., Zhang, R., and Li, X. (2022). Bi-level strategic bidding model of gas-fired units in interdependent electricity and natural gas markets. *IEEE Trans. Sustain. Energy* 13 (1), 328–340. doi:10.1109/tste.2021.3110864

Kaur, G., and Dhillon, J. S. (2021). Economic power generation scheduling exploiting hill-climbed Sine–Cosine algorithm. *Appl. Soft Comput.* 111, 107690. doi:10.1016/j.asoc.2021.107690

Khatami, R., Parvania, M., and Narayan, A. (2020). Flexibility reserve in power systems: Definition and stochastic multi-fidelity optimization. *IEEE Trans. Smart Grid* 11 (1), 644–654. doi:10.1109/tsg.2019.2927600

Khatami, R., and Parvania, M. (2020). Stochastic multi-fidelity scheduling of flexibility reserve for energy storage. *IEEE Trans. Sustain. Energy* 11 (3), 1438–1450. doi:10.1109/tste.2019.2927598

Khodabakhsh, R., and Sirouspour, S. (2016). Optimal control of energy storage in a microgrid by minimizing conditional value-at-risk. *IEEE Trans. Sustain. Energy* 3 (7), 1264–1273. doi:10.1109/tste.2016.2543024

Khoshjahan, M., Dehghanian, P., Moeini-Aghtaie, M., and Fotuhi-Firuzabad, M. (2019). Harnessing ramp capability of spinning reserve services for enhanced power grid flexibility. *IEEE Trans. Ind. Appl.* 55 (6), 7103–7112. doi:10.1109/tia.2019.2921946

Krad, I., Gao, D. W., and Wu, H. (2017). An assessment of flexibility reserves in stochastic modeling at multiple timescales. *CSEE J. Power Energy Syst.* 3 (1), 84–92. doi:10.17775/cseejpes.2017.0011

Kullback, S. (1987). The kullback-leibler distance[J]. *Am. Statistician* 41 (4), 340–341.

Lannoye, E., Milligan, M., and Adams, J. (2010). Integration of variable generation: capacity value and evaluation of flexibility[J]. *Proc. Power Energy Soc. General Meeting. Minneapolis Minnesota, USA: IEEE*, 25–29.

Lannoye, J. E., Flynn, D., and O'Malley, M. (2012). Evaluation of power system flexibility. *IEEE Trans. Power Syst.* 27 (2), 922–931. doi:10.1109/tpwrs.2011.2177280

Li, H., Lu, Z., Qiao, Y., Zhang, B., and Lin, Y. (2021). The flexibility test system for studies of variable renewable energy resources. *IEEE Trans. Power Syst.* 36 (2), 1526–1536. doi:10.1109/tpwrs.2020.3019983

Li, J., Liu, F., Li, Z., Shao, C., and Liu, X. (2018). Grid-side flexibility of power systems in integrating large-scale renewable generations: A critical review on concepts, formulations and solution approaches. *Renew. Sustain. Energy Rev.* 93, 272–284. doi:10.1016/j.rser.2018.04.109

Li, P., Guan, X., Wu, J., and Zhou, X. (2015). Modeling dynamic spatial correlations of geographically distributed wind farms and constructing ellipsoidal uncertainty sets for optimization-based generation scheduling. *IEEE Trans. Sustain. Energy* 6 (4), 1594–1605. doi:10.1109/tste.2015.2457917

Li, Z., et al. (2020). Probability-Interval-Based optimal planning of integrated energy system with uncertain wind power[J]. *IEEE Trans. Industry Appl.* 56 (1), 4–13.

Li, Z., Chen, L., Wei, W., and Mei, S. (2022). Risk constrained self-scheduling of AA-CAES facility in electricity and heat markets: A distributionally robust optimization approach[J]. *CSEE J. Power Energy Syst.*, 1–9. doi:10.17775/CSEEJPES.2020.06130

Liu, B. (1997). Dependent-chance programming: A class of stochastic optimization. *Comput. Math. Appl.* 34 (12), 89–104. doi:10.1016/s0898-1221(97)00237-x

Liu, F., Wang, X., Xiao, Y., and Bie, Z. (2022). Robust pricing of energy and ancillary services in combined electricity and natural gas markets. *IEEE Trans. Power Syst.* 37 (1), 603–616. doi:10.1109/tpwrs.2021.3091021

Lu, Z., Li, H., and Qiao, Y. (2018). Probabilistic flexibility evaluation for power system planning considering its association with renewable power curtailment. *IEEE Trans. Power Syst.* 33 (3), 3285–3295. doi:10.1109/tpwrs.2018.2810091

Ma, J., Silva, V., Belhomme, R., Kirschen, D. S., and Ochoa, L. F. (2013). Evaluating and planning flexibility in sustainable power systems. *IEEE Trans. Sustain. Energy* 4 (1), 200–209. doi:10.1109/tste.2012.2212471

Mamounakis, I., Efthymiopoulos, N., Vergados, D. J., Tsaousoglou, G., Makris, P., and Varvarigos, E. M. (2019). A pricing scheme for electric utility's participation in day-ahead and real-time flexibility energy markets. *J. Mod. Power Syst. Clean. Energy* 7 (5), 1294–1306. doi:10.1007/s40565-019-0537-2

Martin, D., Pfeiffer, D., Lauer, M., et al. (2019). How to measure flexibility-performance indicators for demand driven power generation from biogas plants[J]. *Renew. Energy* 134, 135–146.

Michael, E., Kate, D., Cakir, B., Markovic, M., and Hodge, B. M. (2020). A review of power system planning and operational models for flexibility assessment in high solar energy penetration scenarios. *Sol. Energy* 210 (1), 169–180. doi:10.1016/j.solener.2020.07.017

Milligan, M., O Malley, M., and Adams, J. M. (2010). Flexibility requirements and potential metrics for variable generation: implications for system planning studies [J]. NERC.

Mohajerin Esfahani, P., and Kuhn, D. (2018). Data-driven distributionally robust optimization using the Wasserstein metric: performance guarantees and tractable reformulations. *Math. Program.* 171, 115–166. doi:10.1007/s10107-017-1172-1

Mohandes, B., Moursi, M. S. E., Hatziargyriou, N., and Khatib, S. E. (2019). A review of power system flexibility with high penetration of renewables. *IEEE Trans. Power Syst.* 34 (4), 3140–3155. doi:10.1109/tpwrs.2019.2897727

Mohanty, D. K., Pradhan, B. M. P., and Biswal, M. P. (2020). Chance constrained programming with some non-normal continuous random variables. *Opsearch* 57, 1281–1298. doi:10.1007/s12597-020-00454-9

Muñoz, F. D., Suazo-Martínez, C., Pereira, E., and Moreno, R. (2021). Electricity market design for low-carbon and flexible systems: Room for improvement in Chile. *Energy Policy* 148, 111997. doi:10.1016/j.enpol.2020.111997

Nosair, H., and Bouffard, F. (2015). Flexibility envelopes for power system operational planning. *IEEE Trans. Sustain. Energy* 6 (3), 800–809. doi:10.1109/tste.2015.2410760

Nosair, H., and Bouffard, F. (2015). Reconstructing operating reserve: Flexibility for sustainable power systems. *IEEE Trans. Sustain. Energy* 6 (4), 1624–1637. doi:10.1109/tste.2015.2462318

Ordoudis, C., Delikaraoglou, S., Kazempour, J., and Pierre, P. (2020). Market-based coordination of integrated electricity and natural gas systems under uncertain supply. *Eur. J. Operational Res.* 287 (3), 1105–1119. doi:10.1016/j.ejor.2020.05.007

Özcan, U. (2010). Balancing stochastic two-sided assembly lines: A chance-constrained, piecewise-linear, mixed integer program and a simulated annealing algorithm. *Eur. J. Operational Res.* 205 (1), 81–97. doi:10.1016/j.ejor.2009.11.033

Palmintier, Bryan S., and Webster, Mort D. (2016). Impact of operational flexibility on electricity generation planning with renewable and carbon targets. *IEEE Trans. Sustain. Energy* 7 (2), 672–684. doi:10.1109/tste.2015.2498640

Papadaskalopoulos, D., and Strbac, G. (2013). Decentralized participation of flexible demand in electricity markets—Part I: Market mechanism. *IEEE Trans. Power Syst.* 28 (4), 3658–3666. doi:10.1109/tpwrs.2013.2245686

Papadimitriou, D., and Fortz, B. (2015). "Robust cooperative monitoring problem [J]," in *7th international workshop on reliable networks design and modeling (RNDM)*, 186–193.

Papaefthymiou, G., Haesen, E., and Sach, T. (2018). Power System Flexibility Tracker: Indicators to track flexibility progress towards high-RES systems. *Renew. Energy* 134, 1026–1035. doi:10.1016/j.renene.2018.04.094

Pourahmadi, F., Heidarabadi, H., Hosseini, S. H., and Dehghanian, P. (2020). Dynamic uncertainty set characterization for bulk power grid flexibility assessment. *IEEE Syst. J.* 14 (1), 718–728. doi:10.1109/jsyst.2019.2901358

Pourahmadi, F., Hosseini, S. H., Dehghanian, P., Shittu, E., and Fotuhi-Firuzabad, M. (2022). Uncertainty cost of stochastic producers: Metrics and impacts on power grid flexibility. *IEEE Trans. Eng. Manag.* 69 (3), 708–719. doi:10.1109/tem.2020.2970729

Pourahmadi, F., Hosseini, S. H., and Fotuhi-Firuzabad, M. (2019). Economically optimal uncertainty set characterization for power system operational flexibility. *IEEE Trans. Ind. Inf.* 15 (10), 5456–5465. doi:10.1109/tii.2019.2906058

Pourahmadi, F., Kazempour, J., Ordoudis, C., Pinson, P., and Hosseini, S. H. (2020). Distributionally robust chance-constrained generation expansion planning. *IEEE Trans. Power Syst.* 35 (4), 2888–2903. doi:10.1109/tpwrs.2019.2958850

Qin, Zhijun, Mo, Yuhong, Liu, Hui, and Zhang, Yihui (2021). Operational flexibility enhancements using mobile energy storage in day-ahead electricity market by game-theoretic approach. *Energy* 232, 121008. doi:10.1016/j.energy.2021.121008

Rashidizadeh-Kermani, H., Vahedipour-Dahraie, M., Shafie-Khah, M., and Siano, P. (2020). A regret-based stochastic Bi-level framework for scheduling of DR aggregator under uncertainties. *IEEE Trans. Smart Grid* 11 (4), 3171–3184. doi:10.1109/tsg.2020.2968963

Rockafellar, R. T., and Uryasev, S. (2000). Optimization of conditional value-at-risk. *J. Risk* 2 (3), 21–41. doi:10.21314/jor.2000.038

Saeed Poorvaezi, R., Abdollahi, Amir, and Rashidinejad, Masoud (2019). Probabilistic-possibilistic flexibility-based unit commitment with uncertain negawatt demand response resources considering Z-number method[J]. *Int. J. Electr. Power & Energy Syst.* 113, 71–89.

Saric, A. T., and Stankovic, A. M. (2008). Applications of ellipsoidal approximations to polyhedral sets in power system optimization. *IEEE Trans. Power Syst.* 23 (3), 956–965. doi:10.1109/tpwrs.2008.926435

Sayed, A. R., Wang, C., Wei, W., Bi, T., and Shahidehpour, M. (2021). Robust operational equilibrium for electricity and gas markets considering bilateral energy and reserve contracts. *IEEE Trans. Power Syst.* 36 (4), 2891–2905. doi:10.1109/tpwrs.2020.3043230

Semich, I., Secil Varbak, N., and Oral, B. (2020). Challenges of renewable energy penetration on power system flexibility: A survey [J]. *Energy Strategy Rev.* 31, 100539.

Shahidehpour, M., Tinney, F., and Fu, Y. (2005). Impact of security on power systems operation. *Proc. IEEE* 93 (11), 2013–2025. doi:10.1109/jproc.2005.857490

Shing Chih, T., and Fu, S. Y. (2014). Genetic-algorithm-based simulation optimization considering a single stochastic constraint[J]. *Eur. J. Operational Res.* 236 (1), 113–125.

Shu, Y., and Tang, Y. (2017). Analysis and recommendations for the adaptability of China's power system security and stability relevant standards. *CSEE J. Power Energy Syst.* 3 (4), 334–339. doi:10.17775/cseejpes.2017.00650

Sun, Q., Wu, Z., Gu, W., Zhu, T., Zhong, L., and Gao, T. (2021). Flexible expansion planning of distribution system integrating multiple renewable energy sources: An approximate dynamic programming approach. *Energy* 226, 120367. doi:10.1016/j.energy.2021.120367

Sun, X., Feng, X., and Teo, K. L. (2022). Robust optimality, duality and saddle points for multiobjective fractional semi-infinite optimization with uncertain data. *Optim. Lett.* 16, 1457–1476. doi:10.1007/s11590-021-01785-2

Tejada-Arango, D. A., Morales-Espana, G., Wogrin, S., and Centeno, E. (2020). Power-based generation expansion planning for flexibility requirements. *IEEE Trans. Power Syst.* 35 (3), 2012–2023. doi:10.1109/tpwrs.2019.2940286

Telukunta, V., Pradhan, J., Agrawal, A., Singh, M., and Srivani, S. G. (2017). Protection challenges under bulk penetration of renewable energy resources in power systems: A review. *CSEE J. Power Energy Syst.* 3 (4), 365–379. doi:10.17775/cseejpes.2017.00030

Thatte, A. A., and Xie, L. (2016). A metric and market construct of inter-temporal flexibility in time-coupled economic dispatch. *IEEE Trans. Power Syst.* 31 (5), 3437–3446. doi:10.1109/tpwrs.2015.2495118

Tu, T. (2022). Collusion potential assessment in electricity markets considering generation flexibility[J]. *CSEE J. Power Energy Syst.*, 1–15. doi:10.17775/CSEEJPES.2020.01550

United Nations Environment Programme (2019). "United Nations environment Programme," in *Emissions gap report 2019* (New York, United States: United Nations.

Velloso, A., Street, A., Pozo, D., Arroyo, J. M., and Cobos, N. G. (2020). Two-stage robust unit commitment for Co-optimized electricity markets: An adaptive data-driven approach for scenario-based uncertainty sets. *IEEE Trans. Sustain. Energy* 11 (2), 958–969. doi:10.1109/tste.2019.2915049

Wanapinit, Natapon, Thomsen, Jessica, Kost, Christoph, and Weidlich, A. (2021). An MILP model for evaluating the optimal operation and flexibility potential of end-users. *Appl. Energy* 282, 116183. doi:10.1016/j.apenergy.2020.116183

Wang, Q., and Hodge, B. (2017). Enhancing power system operational flexibility with flexible ramping products: A review. *IEEE Trans. Ind. Inf.* 13 (4), 1652–1664. doi:10.1109/tii.2016.2637879

Wang, S., Tan, X., Liu, T., and Tsang, D. H. K. (2021). Aggregation of demand-side flexibility in electricity markets: Negative impact analysis and mitigation method. *IEEE Trans. Smart Grid* 12 (1), 774–786. doi:10.1109/tsg.2020.3018227

Wang, Z., Shen, C., Liu, F., Wu, X., Liu, C., and Gao, F. (2017). Chance-constrained economic dispatch with non-Gaussian correlated wind power uncertainty. *IEEE Trans. Power Syst.* 32 (6), 4880–4893. doi:10.1109/tpwrs.2017.2672750

Wei, W., Liu, F., and Mei, S. (2016). Distributionally robust Co-optimization of energy and reserve dispatch. *IEEE Trans. Sustain. Energy* 7 (1), 289–300. doi:10.1109/tste.2015.2494010

Wiesemann, W., Kuhn, D., and Sim, M. (2014). Distributionally robust convex optimization. *Operations Res.* 62 (6), 1358–1376. doi:10.1287/opre.2014.1314

Xiao, Z., Chen, W., and Li, L. (2013). A method based on interval-valued fuzzy soft set for multi-attribute group decision-making problems under uncertain environment. *Knowl. Inf. Syst.* 34, 653–669. doi:10.1007/s10115-012-0496-7

Xinhuanet (2021). Xinhuanet. Available at: http://www.xinhuanet.com/2021-03/13/c1127205642.htm.

Xu, X. Y., Yan, Z., Shahidehpour, M., Li, Z., and Kong, X. (2020). Data-Driven risk-averse two-stage optimal stochastic scheduling of energy and reserve with correlated wind power. *IEEE Trans. Sustain. Energy* 11 (1), 436–447. doi:10.1109/tste.2019.2894693

Yang, Ce, and Sun, W. (2022). Risk-averse two-stage distributionally robust economic dispatch model under uncertain renewable energy[J]. *CSEE J. Power Energy Syst.*, 1–10. doi:10.17775/CSEEJPES.2020.03430

Yang, C., Han, D., Sun, W. Q., and Tian, K. (2019). Distributionally robust model of energy and reserve dispatch based on kullback–leibler divergence. *Electronics* 8 (12), e1454. doi:10.3390/electronics8121454

Yang, J., Liu, C., Mi, Y., Zhang, H., and Terzija, V. (2021). Optimization operation model of electricity market considering renewable energy accommodation and flexibility requirement. *Glob. Energy Interconnect.* 4 (3), 227–238. doi:10.1016/j.gloei.2021.07.007

Yorino, N., Abdillah, M., Sasaki, Y., and Zoka, Y. (2018). Robust power system security assessment under uncertainties using Bi-level optimization. *IEEE Trans. Power Syst.* 33 (1), 352–362. doi:10.1109/tpwrs.2017.2689808

Zhang, H., and Song, J. (2017). Dependent-chance programming on Sugeno measure space. *J. Uncertain. Anal. Appl.* 4, 7. doi:10.1186/s40467-017-0061-8

Zhang, L., Capuder, T., and Mancarella, P. (2016). Unified unit commitment formulation and fast multi-service LP model for flexibility evaluation in sustainable power systems. *IEEE Trans. Sustain. Energy* 7 (2), 658–671. doi:10.1109/tste.2015.2497411

Zhang, Z., Li, R., and Li, F. (2020). A novel peer-to-peer local electricity market for Joint trading of energy and uncertainty. *IEEE Trans. Smart Grid* 11 (2), 1205–1215. doi:10.1109/tsg.2019.2933574

Zhao, J., Zheng, T., and Litvinov, E. (2016). A unified framework for defining and measuring flexibility in power system. *IEEE Trans. Power Syst.* 31 (1), 339–347. doi:10.1109/tpwrs.2015.2390038

Zheng, X., and Chen, H. (2020). Data-Driven distributionally robust unit commitment with Wasserstein metric: Tractable formulation and efficient solution method. *IEEE Trans. Power Syst.* 35 (6), 4940–4943. doi:10.1109/tpwrs.2020.3014808

Zhou, A., Yang, M., Wang, M., and Zhang, Y. (2020). A linear programming approximation of distributionally robust chance-constrained dispatch with Wasserstein distance. *IEEE Trans. Power Syst.* 35 (5), 3366–3377. doi:10.1109/tpwrs.2020.2978934

Zhou, Y., Wang, J., Dong, F., Qin, Y., Ma, Z., Ma, Y., et al. (2021). Novel flexibility evaluation of hybrid combined cooling, heating and power system with an improved operation strategy. *Appl. Energy* 300, 117358. doi:10.1016/j.apenergy.2021.117358

Zhu, H., Gu, M., and Peterson, B. (2007). Maximum likelihood from spatial random effects models via the stochastic approximation expectation maximization algorithm. *Stat. Comput.* 17 (2), 163–177. doi:10.1007/s11222-006-9012-9

10.3389/fenrg.2022.967220

Appendix 1: Comparison of uncertainty modeling methods

	Characteristics of uncertainty modeling	Modeling method	Solution transformation method	Advantage	Disadvantage
Stochastic method	Describing uncertain information based on accurate probability distribution	Stochastic expectation	Analog sampling	There are many constraint functions, which are difficult to solve	Long solution time
		Chance constrained	Equivalent transformation	Good performance	Multiple random variable model is difficult to be solved
		Conditional value at risk	It is generally equivalent to a linear problem	The constraint conditions are simplified and easy to solve	Difficult to characterize the random correlation
Robust method	The uncertainty set is used to represent its variation range	Box robust Ellipsoidal robust Polyhedral robust Budget robust	Dual method transformation and solved by decomposition or CCG	The modeling method is simple and easy to be transformed	The results were conservative
Distributionally robust method	The ambiguity set of the probability distribution is established based on the data to describe the uncertainties	Moment-based	Linear decision rule and dual theory transformation, solved by decomposition or CCG	The statistical moment is easy to obtain	Underutilization of data statistics, and the results are slightly conservative
		Wasserstein distance		Make full use of statistical information and can generally be transformed into a linear problem	The scale of the problem increases with the increase of the amount of data
		Kullback–Leibler divergence		Low requirements for data information, and the performance outside the sample is good	Cannot be used to model continuous random variables

frontiers | Frontiers in Energy Research

TYPE Original Research
PUBLISHED 28 September 2022
DOI 10.3389/fenrg.2022.998902

OPEN ACCESS

EDITED BY
Jiajia Yang,
University of New South Wales, Australia

REVIEWED BY
Pingfeng Ye,
Shandong University of Science and Technology, China
Tianran Li,
Nanjing Normal University, China
Chuan QIN,
Hohai University, China

*CORRESPONDENCE
Lili Hao,
haolili@njtech.edu.cn

SPECIALTY SECTION
This article was submitted to Smart Grids,
a section of the journal
Frontiers in Energy Research

RECEIVED 20 July 2022
ACCEPTED 30 August 2022
PUBLISHED 28 September 2022

CITATION
Shao Y, Hao L, Cai Y, Wang J, Song Z and Wang Z (2022), Day-ahead joint clearing model of electric energy and reserve auxiliary service considering flexible load.
Front. Energy Res. 10:998902.
doi: 10.3389/fenrg.2022.998902

Day-ahead joint clearing model of electric energy and reserve auxiliary service considering flexible load

Yijun Shao[1], Lili Hao[1]*, Yaqi Cai[1], Jiwen Wang[2], Zhiwei Song[2] and Zhengfeng Wang[2]

[1]College of Electrical Engineering and Control Science, Nanjing Tech University, Nanjing, China, [2]State Grid Anhui Electric Power Co Ltd., Hefei, China

With the increasing of renewable energy penetration, adequate reserve capacity is more important to modern power system facing with various uncertain factors. Mobilizing the enthusiasm of units and demand response to participate in reserve auxiliary service can reduce the reserve providing pressure of conventional power supplies, which is conducive to the reliable and economical operation of system. The uncertain factors such as system random failure, prediction error of both load and renewable energy output are considered, and taking unit reserve, demand response such as flexible loads as system reserve resources, this paper establishes the risk cost models to optimize system up and down reserve requirement and make optimal allocation among units and flexible loads. A joint market clearing model of day-ahead electric energy and reserve auxiliary service is established in which both the units and flexible loads participate, and is solved by the robust optimization theory. The joint market clearing model takes the reliability and the economy of the system operation into account, and optimizes the clearing scheme for market decision makers, which can provide a decision reference for the market to resist the risk of uncertainty. Finally, the effectiveness of the model and method proposed in this paper is verified by a modified 10-machine 39-bus simulation example system.

KEYWORDS

renewable energy, electric energy market, reserve ancillary service, demand response, uncertainty factors, joint clearing model

1 Introduction

In order to ensure the safe and reliable operation of the modern power system, it is necessary to remain a certain reserve capacity to deal with uncertain factors such as random system failures, prediction error of load and renewable energy output (Li et al., 2022). The access of a large number of random renewable energy sources puts more pressure on the system reserve. Thermal power units have better response capabilities and usually account for a large proportion of installed capacity, therefore, they are easily

selected as the main source of reserve capacity. However, thermal power units operating at low output level usually have a higher cost per unit electricity (Herranz et al., 2012). It is obviously uneconomical or even unreliable whether generators do not respond to the load demand for keeping reserve capacity during periods of high load, or generators start up and operate at a low load rate to provide reserve capacity for a short period of time during periods of low load (Bompaard et al., 2007).

Flexible load can provide reserve capacity for the system by interrupting or transferring part of the load in time, improve the elastic space of power dispatching and reduce the pressure on thermal power units to provide reserve (Anuj et al., 2018). Wen (Wen et al., 2019) has built a cost model of insufficient flexibility to evaluate the risk cost caused by random fluctuation of load demand and generator output for system reserve optimization. Chen (Chen et al., 2017) has comprehensively considered the wind power forecast error, load fluctuation, unplanned outage of units and other uncertain factors, and has integrated the interruptible load and wind curtailment as upper and lower reserve into the day-ahead dispatching to optimize the reserve capacity (Nikolaos et al., 2015). Has built a two-stage stochastic programming model to obtain the system reserve requirement from generation and load sides under the condition of high proportion of wind power penetration.

With the continuous advancement of the electricity market reform, the electricity market trading mechanism in China has become more flexible (Liu et al., 2019). The trading products have transitioned from a single electric energy market to a multi-type market with parallel electricity energy and auxiliary services (Yang et al., 2017). Trading entities have expanded from single generation side resource to multi-type resources of load and generation, and the operation mode has shifted from independent operation in each market to joint operation in multiple markets (Xun, 2010). Under the premise of transparent market information, independent markets can only achieve the best welfare of their respective markets (Shan, 2021). A reserve ancillary market clearing model for dealing with wind power and load uncertainty is established for system operation reliability by (Reddy et al., 2015). The risk cost of the unit failure and the interruptible load failure to provide system required up reserve is considered in the reserve market, meanwhile, a settlement scheme is proposed to reasonably allocate reserve cost between units and interruptible loads by (Luo and Xue, 2007), but it does not take the risk cost caused by insufficient down reserve into account. The reserve ancillary market can get the rational distribution of reserve resources from both the generation and load sides through flexible market forces (Wang et al., 2015), but it cannot obtain the optimal total benefit of the electric energy and reserve markets.

When the electric energy market and the reserve ancillary market are jointly cleared day-ahead, the generation side can bid the quantity and price based on its own generation cost, start-up cost and reserve dispatch cost (Anthony and Oren, 2014). The flexible load reports the adjustable quantity and price of different time periods day-ahead based on the electricity consumption income and reserve dispatch cost, and the transaction institution will make clearing according to the principle of maximizing social welfare and under certain system constraints (Shi et al., 2019; Chen et al., 2021). The influence of the traditional unit combination model on the utilization efficiency of flexible resources is analyzed (Yang et al., 2020; Li et al., 2021), a joint clearing model of day-ahead electric energy and reserve ancillary market is proposed for system flexibility. Sun (2020) has considered the quantity and price bidding of flexible load to participate in the joint market clearing of electric energy and reserve auxiliary service, but the impact of system uncertainty on the clearing results is not considered. The method of iterative game theory is used to consider the impact of wind power uncertainty on the joint market of electric energy and reserve (Xu et al., 2016). A model of the optimal supply strategy of concentrated solar power plants in the joint market is established, which takes the uncertainty of photovoltaic output into account based on the robust optimization theory (Lazaros et al., 2017). Chen (He et al., 2016) and He (2010) have considered the problem that the generation outage may cause insufficient power supply, and have established a power shortage expectation evaluation model to analyze the impact of interruptible loads on system reliability. Huang (Huang et al., 2019) has proposed a joint operation mode of energy market and multiple ancillary service markets. There are few studies on the joint market of electric energy and reserve auxiliary service with both units and flexible loads involving in system up and down reserve. To sum up, a few studies consider joint clearing model of electric energy and reserve auxiliary service with the participating of both generation and demand response, but most of the existing literatures fail to comprehensively consider the risk caused by insufficient up and down reserve. How to build the risk cost models to optimize the system up and down reserve requirement and make optimal allocation among units and flexible loads during market clearing is crucial. Besides, less joint clearing study of electric energy and auxiliary service has considered the uncertainty of both renewable energy and load. The uncertainty of these forecasting value has a certain impact on market clearing results, and comprehensive consideration of them will greatly enhance the market's ability to resist uncertain risks.

Therefore, in this paper, the flexible load is introduced into the market in the form of bidding quantity and price, and the characteristics of flexible load, the uncertainty of net load and the risk caused by insufficient up and down reserves are comprehensively considered. A day-ahead joint clearing model of electric energy and reserve auxiliary service with the participating of both generation and demand response is established. A robust optimization model considering the uncertainty of net load is

further proposed, which can help market decision makers find out the market clearing scheme under the worst scenario in the system and provide a reference decision for the market to resist the risk of uncertainty. Finally, the effectiveness of the method proposed in this paper is verified by example analyses.

2 Reserve risk model

2.1 Risk model for net load uncertainty

The uncertainty of load demand is an important factor in the analysis of modern power system reserve requirement. Assume that the load prediction errors of each period are independent of each other. It is generally believed that the short-term load prediction error follows the standard normal distribution:

$$\delta_{L,t}: N\left(0, \left(\sigma_{L,t}\right)^2\right) \tag{1}$$

$$\delta_{L,t} = P_{L,t} - P^{F}_{L,t} \tag{2}$$

Where, $\delta_{L,t}$ is the load prediction error at time t, $\sigma_{L,t}$ is the standard deviation, $P_{L,t}$ is the actual load value at time t, $P^{F}_{L,t}$ is the load prediction value at time t.

Assume that the prediction error $\delta_{R,t}$ of renewable energy output at time t also follows the standard normal distribution with standard deviation $\sigma_{R,t}$ (Chen et al., 2017), that is:

$$\delta_{R,t}: N\left(0, \left(\sigma_{R,t}\right)^2\right) \tag{3}$$

$$\delta_{R,t} = P_{R,t} - P^{F}_{R,t} \tag{4}$$

Where, $P_{R,t}$ is the actual output of the renewable energy at time t, and $P^{F}_{R,t}$ is the forecasting output of the renewable energy at time t.

System net load is defined as the difference between system load and renewable energy output. Since the prediction errors of load and renewable energy output are all subject to independent normal distribution, it can be known from the nature of the normal distribution that the net load forecast error $\delta_{D,t}$ also follows the normal distribution with expectation of 0 and standard deviation of $\sigma_{D,t}$ (Chen et al., 2017), that is:

$$\delta_{D,t}: N\left(0, \left(\sigma_{D,t}\right)^2\right) \tag{5}$$

$$\delta_{D,t} = P_{D,t} - P^{F}_{D,t} \tag{6}$$

$$\sigma_{D,t} = \sqrt{\sigma^2_{L,t} + \sigma^2_{R,t}} \tag{7}$$

Where, $P_{D,t}$ is the actual value of the net load at time t, and $P^{F}_{D,t}$ is the forecasting value of the net load at time t.

2.2 Risk model for system failure

In order to ensure the safe and reliable operation of the modern power system, it is necessary to reserve a certain reserve capacity to deal with uncertain factors such as random system failures, the load and renewable energy output forecast error (Fang et al., 2019). Thermal power units have better response capability, therefore, they are easily selected as the main source of reserve capacity. If demand response is considered to provide reserve capacity for the modern power system, it will be a beneficial supplement to the reserve of thermal power units, which will reduce the operation cost of the system. Therefore, this paper considers reserve resources form both units and flexible loads at the same time, and introduce risk cost to optimize the system reserve capacity.

2.2.1 Model of flexible load providing reserve

In this paper, flexible load is considered as interruptible load and transferable load. Considering the constraints of interruption capacity and times, the model of interruptible load providing reserve is as follows:

$$\underline{P}_{IL,j} \le P_{IL,j,t} + r^{U}_{IL,j,t} \le \bar{P}_{IL,j}\ j \in \Omega_{IL} \tag{8}$$

$$\sum_{t \in \Omega_T} u_{IL,j,t} \le N_{IL,j} \tag{9}$$

Where, $P_{IL,j,t}$ is the power of interruptible load j at time t, $r^{U}_{IL,j,t}$ is the winning bid up reserve capacity of interruptible load j at time t, $\underline{P}_{IL,j}$ and $\bar{P}_{IL,j}$ are the minimum and maximum values of interruptible load j respectively, Ω_{IL} is the set of interruptible loads, $u_{IL,j,t}$ is the state variable of the interruptible load j at time t, "1" means that load j at time t can be interrupted, and "0" means that it cannot be interrupted, Ω_T is the set of statistical time, $N_{IL,j}$ is the maximum allowable interruption numbers of interruptible load j in the scheduling period.

The total electricity quantity consumption of transferable load in a dispatching cycle remains fixed, but the electricity quantity in each time interval can be flexibly adjusted. The model is as follows:

$$\underline{P}_{SL,k} \le P_{SL,k,t} \le \bar{P}_{SL,k}\ k \in \Omega_{SL} \tag{10}$$

$$\underline{P}_{SL,k} \le P_{SL,k,t} + u^{U}_{k,t} r^{U}_{SL,k,t} + u^{D}_{k,t} r^{D}_{SL,k,t} \le \bar{P}_{SL,k} \tag{11}$$

$$0 \le u^{U}_{k,t} + u^{D}_{k,t} < 2 \tag{12}$$

Where, $P_{SL,k,t}$ is the power consumption of transferable load k at time t, $\underline{P}_{SL,k}$ and $\bar{P}_{SL,k}$ are the minimum and maximum values of transferable load k respectively, Ω_{SL} is the set of transferable load. $r^{U}_{SL,k,t}$ is the winning bid up reserve capacity of transferable load k at time t, $r^{D}_{SL,k,t}$ is the winning bid down reserve capacity of the transferable load k at time t, $u^{U}_{k,t}$ and $u^{D}_{k,t}$ are the winning bid up and down reserve states of transferable load $k$at time t, respectively, "1" indicates winning the bid, and "0" means not winning the bid.

2.2.2 Risk cost model of up reserve insufficiency

The risk cost caused by system insufficient up reserve is reflected in the cost of load loss caused by unit failure and net load prediction error.

$$A\left(R_t^{\mathrm{U}}\right) = \mathrm{C_L} E_t^{\mathrm{U}} \tag{13}$$

Where, $\mathrm{C_L}$ is the unit loss of load cost. E_t^{U} is the expected value of system up reserve shortage at time t.

Combined with the random failure information of each unit, E_t^{U} of the system under different reserve capacities can be analyzed. The probability of a single unit outage is:

$$PR_{\mathrm{G},i,t} = PR_{i,t} \prod_{y \neq i} \left(1 - PR_{y,t}\right) \quad i, y \in \Omega_{\mathrm{G}} \tag{14}$$

Where, $PR_{\mathrm{G},i,t}$ is the probability that only unit i fails at time t, $PR_{i,t}$ is the probability that unit i fails at time t, and Ω_{G} is the set of all units.

In the above situation, the system reserve shortage $P_{Loss,t}^{\mathrm{U}}$ is:

$$P_{Loss,t}^{\mathrm{U}} = \max\left\{P_{i,t} + \delta_{\mathrm{D},t} - \left(R_t^{\mathrm{U}} - r_{i,t}^{\mathrm{U}}\right), 0\right\} \tag{15}$$

$$\sum_{j \in \Omega_{\mathrm{IL}}} r_{\mathrm{IL},j,t}^{\mathrm{U}} + \sum_{k \in \Omega_{\mathrm{SL}}} r_{\mathrm{SL},k,t}^{\mathrm{U}} + \sum_{i \in \Omega_{\mathrm{G}}} r_{i,t}^{\mathrm{U}} = R_t^{\mathrm{U}} \tag{16}$$

Where, $P_{Loss,t}^{\mathrm{U}}$ is the system power shortage when only unit i is out of service at time t, $P_{i,t}$ is the winning bid output of unit i at time t, R_t^{U} is the system up reserve capacity at time t, $r_{i,t}^{\mathrm{U}}$ is the winning bid up reserve capacity of conventional unit i at time t.

The formula for calculating E_t^{U} is:

$$E_t^{\mathrm{U}} = \sum_{i \in \Omega_{\mathrm{G}}} PR_{\mathrm{G},i,t} P_{Loss,t}^{\mathrm{U}} \tag{17}$$

2.2.3 Risk cost model of down reserve insufficiency

Considering the unplanned out-of-operation of load and the prediction error of net load, it is necessary for the system to remain enough down reserve capacity. Due to the existence of distributed or centralized power supply recovery equipment or control systems, such as automatic reclosing, standby automatic switching, and feeder automation, even if transformers, lines and other equipment fail, the load may still get continuous power supply. To model the loss due to excess power also needs to consider the substitutability of the equipment and the reserve capacity of the replacement system, which can make the model too complex. For a certain power grid, the occurrence time of load unplanned out-of-operation has certain regularity. Therefore, according to the historical information of load unplanned out-of-operation caused by the reasons other than unit failure at each time interval in the historical observation period, then the monthly average probability of load unplanned out-of-operation at each time interval of a day can be obtained to reflect the down reserve requirement of the system when the load is unplanned out.

In this paper, in the historical observation period of the month which time t belongs to, the ratio of cumulative load outage by the reasons other than unit failure to the total load demand is defined as the probability of load unplanned out-of-operation:

$$PR_{\mathrm{L},t} = \frac{q_{\mathrm{C}}}{q_{\mathrm{C}} + q_{\mathrm{L}}} \tag{18}$$

Where, $PR_{\mathrm{L},t}$ is the probability of load unplanned out-of-operation at time t, q_{C} is the accumulated electrical quantity of the outage load in the historical observation period of the month which time t belongs to, q_{L} is the power supply quantity in the historical observation period of the month which time t belongs to.

According to the load unplanned out-of-operation in the historical observation period, when the load unplanned out-of-operation occurs at the time t, the average proportion of the outage load $\varepsilon_{\mathrm{L},t}$ is defined as:

$$\varepsilon_{\mathrm{L},t} = \frac{\sum_{x=1}^{N} P_{\mathrm{L},t,x}^{\mathrm{C}} / P_{\mathrm{L},t,x}}{N} \tag{19}$$

Where, $P_{\mathrm{L},t,x}^{\mathrm{C}}$, $P_{\mathrm{L},t,x}$, and $P_{\mathrm{L},t,x}^{\mathrm{C}}/P_{\mathrm{L},t,x}\,(x = 1, 2, \cdots, N)$ are respectively the load outage power, load demand, and load unplanned outage ratio when the load occurs the x time unplanned outage caused by reasons other than unit failure at time t in the historical observation period, N is the cumulative load outage times at time t in the historical observation period.

If the down reserve is not sufficient, the emergency control or correction control will cut off one or more units to maintain the safe and stable operation of system (Xue, 2002). In this paper, the minimum unit cutting cost caused by the unplanned load outage is used to evaluate the consequences of unplanned load outage, and the risk cost $A(R_t^{\mathrm{D}})$ is defined as:

$$A\left(R_t^{\mathrm{D}}\right) = \mathrm{C_G} E_t^{\mathrm{D}} \tag{20}$$

Where, $\mathrm{C_G}$ is the unit cutting cost per unit capacity, and E_t^{D} is the expected value of the system down reserve shortage at time t.

The system down reserve shortage $P_{\mathrm{Loss},t}^{\mathrm{D}}$ is:

$$P_{\mathrm{Loss},t}^{\mathrm{D}} = \max\left\{P_{\mathrm{L},t}\varepsilon_{\mathrm{L},t} + \delta_{\mathrm{D},t} - \left(R_t^{\mathrm{D}} - \varepsilon_{\mathrm{L},t} r_{\mathrm{SL},k,t}^{\mathrm{D}}\right), 0\right\} \tag{21}$$

$$\sum_{k \in \Omega_{\mathrm{SL}}} r_{\mathrm{SL},k,t}^{\mathrm{D}} + \sum_{i \in \Omega_{\mathrm{G}}} r_{i,t}^{\mathrm{D}} = R_t^{\mathrm{D}} \tag{22}$$

$$\sum_{t \in \Omega_{\mathrm{T}}} \left(P_{\mathrm{SL},k,t} + r_{\mathrm{SL},k,t}^{\mathrm{U}} + r_{\mathrm{SL},k,t}^{\mathrm{D}}\right) \Delta t = q_{\mathrm{SL},k} \tag{23}$$

Where, R_t^{D} is the system down reserve capacity at time t, $r_{i,t}^{\mathrm{D}}$ is the winning bid down reserve capacity of conventional unit i at time t, $\Delta t$is the statistical time interval, $q_{\mathrm{SL},k}$ is the total power demand of transferable load k in the scheduling period.

Combined with the information analysis of load unplanned outage, the expected value of down reserve shortage is:

$$E_t^{\mathrm{D}} = PR_{\mathrm{L},t} P_{\mathrm{Loss},t}^{\mathrm{D}} \tag{24}$$

3 Joint clearing model

3.1 Objective function

In the electric energy market, the income of flexible loads and the generation cost of units are considered. Among them, wind

power and photovoltaic units only participate in the electric energy market, and their costs are ignored to ensure their priority of clearing. In the reserve auxiliary service market, the reserve cost, start-up and shutdown cost of conventional units, and the reserve cost of flexible loads are considered, and the risk cost caused by the shortage of system reserve is also taken into account, a joint clearing model of electric energy and reserve market with the goal of maximizing social welfare is established:

$$\max f = \max \sum_{t\in\Omega_T}\Bigg(\Bigg(\sum_{l\in\Omega_{RL}} F_0\left(P_{RL,l,t}\right) + \sum_{j\in\Omega_{IL}} F_1\left(P_{IL,j,t}\right) + \sum_{k\in\Omega_{SL}} F_2\left(P_{SL,k,t}\right) - \sum_{i\in\Omega_G} C\left(P_{i,t}\right)\Bigg) - \Bigg(\sum_{i\in\Omega_G} u_{i,t}^{U} L_1\left(r_{i,t}^{U}\right) + \sum_{i\in\Omega_G} u_{i,t}^{D} L_2\left(r_{i,t}^{D}\right) + \sum_{j\in\Omega_{IL}} L_3\left(r_{IL,j,t}^{U}\right) + \sum_{k\in\Omega_{SL}} u_{k,t}^{U} L_4\left(r_{SL,k,t}^{U}\right) + \sum_{k\in\Omega_{SL}} u_{k,t}^{D} L_5\left(r_{SL,k,t}^{D}\right) + \sum_{i\in\Omega_G} S_i u_{i,t}^{S}\left(1-u_{i,t-1}^{S}\right)\Bigg) - A\left(R_t\right)\Bigg) \tag{25}$$

Where, $P_{RL,l,t}$ is the power consumption of rigid load l at time t, $F_0\left(P_{RL,l,t}\right)$ is the income function of rigid load l at time t,$l \in \Omega_{RL}$, Ω_{RL} is the set of rigid loads, $F_1\left(P_{IL,j,t}\right)$ is the income bidding function of interruptible load j at time t, $F_2\left(P_{SL,k,t}\right)$ is the income bidding function of transferable load k at time t , $C\left(P_{i,t}\right)$ is the bidding function of power generation cost of conventional unit i at time t, $u_{i,t}^{U}$ and $u_{i,t}^{D}$ are the winning bid state variables of up and down reserve capacity for conventional unit i at time t respectively, "1" indicates winning the bid, and "0" means not winning the bid, $L_1\left(r_{i,t}^{U}\right)$ is the bidding function of conventional unit i in the up reserve market at time t,$L_2\left(r_{i,t}^{D}\right)$ is the bidding function of conventional unit i in the down reserve market at time t, $L_3\left(r_{IL,j,t}^{U}\right)$ is the bidding function of interruptible load j in the up reserve market at time t, $L_4\left(r_{SL,k,t}^{U}\right)$ is the bidding function of transferable load k in the up reserve market at time t, $L_5\left(r_{SL,k,t}^{D}\right)$ is the bidding function of transferable load k in the down reserve market at time t, S_i is the start-up cost of conventional unit i, $u_{i,t}^{S}$ is the start-up and shutdown state variable of conventional unit i at time t, "1" means start-up, and "0" means shutdown.

Conventional units' power generation cost bidding function and up reserve bidding function are:

$$C\left(P_{i,t}\right) = \left(a_{i,1}P_{i,t}^2 + a_{i,2}P_{i,t} + a_{i,3}\right)u_{i,t}^{S} \tag{26}$$

$$L_1\left(r_{i,t}^{U}\right) = \left(m_{i,1}r_{i,t}^2 + m_{i,2}r_{i,t} + m_{i,3}\right)u_{i,t}^{S} \tag{27}$$

Where, $a_{i,1}$, $a_{i,2}$, and $a_{i,3}$ are the bidding coefficients of conventional unit i in the electric energy market respectively, $m_{i,1}$, $m_{i,2}$, and $m_{i,3}$ are the bidding coefficients of conventional unit i in the up reserve market respectively. And the same bidding method is used in down reserve market.

Because the rigid load needs to be cleared and balanced completely, its income function will not affect the clearing results of neither the electricity energy market nor the reserve market, so it is only a part of the overall social welfare in the objective function and can be ignored in the optimization process. Interruptible loads' bidding functions in the electric energy market and the reserve market are:

$$F_1\left(P_{IL,j,t}\right) = d_{j,1}P_{IL,j,t}^2 + d_{j,2}P_{IL,j,t} + d_{j,3} \tag{28}$$

$$L_3\left(r_{IL,j,t}^{U}\right) = g_{j,1}\left(r_{IL,j,t}^{U}\right)^2 + g_{j,2}r_{IL,j,t}^{U} + g_{j,3} \tag{29}$$

Where, $d_{j,1}$, $d_{j,2}$, and $d_{j,3}$ are the bidding coefficients of interruptible load j in the electric energy market respectively, $g_{j,1}$, $g_{j,2}$, and $g_{j,3}$ are the bidding coefficients of interruptible load j in the reserve market respectively. The transferable loads' bidding functions in the electric energy market and the up and down reserve markets are the same as formulas Eq. (28) and (29).

The risk cost $A\left(R_t\right)$ caused by insufficient reserve is:

$$A\left(R_t\right) = A\left(R_t^{D}\right) + A\left(R_t^{U}\right) \tag{30}$$

3.2 Constraint

3.2.1 System power balance constraint

$$\sum_{i\in\Omega_G} P_{i,t} + \sum_{w\in\Omega_W} P_{w,t}^{F} + \sum_{n\in\Omega_{PV}} P_{n,t}^{F} = \sum_{e\in\Omega_E} P_{L,e,t}^{F} + \delta_{D,t} + P_{DC,t} \tag{31}$$

Where, Ω_W is the set of wind turbines, $P_{w,t}^{F}$ is the forecasting output of wind unit w at time t, Ω_{PV} is the set of photovoltaic units, $P_{n,t}^{F}$ is the forecasting output of photovoltaic unit n at time t, Ω_E is the set of system nodes, $P_{L,e,t}^{F}$ is the load forecasting of node e at time t, $P_{DC,t}$ is the total power of all tie lines at time t, the receiving power is negative, and the sending power is positive.

3.2.2 Unit startup and shutdown time constraint

$$\begin{cases} \sum_{m=0}^{T_i^{on}-1} u_{i,t+m}^{S} \geq T_i^{on}\left(u_{i,t}^{S} - u_{i,t-1}^{S}\right) \\ \sum_{m=0}^{T_i^{off}-1} \left(1-u_{i,t+m}^{S}\right) \geq T_i^{off}\left(u_{i,t-1}^{S} - u_{i,t}^{S}\right) \end{cases} \tag{32}$$

Where, T_i^{on} and T_i^{off} are the minimum time needed by conventional unit i after startup and shutdown respectively, m is the time.

3.2.3 Conventional unit reserve capacity constraint

$$r_{i,t}^{\mathrm{U}} \le \min\left[S_i^{\mathrm{up}}\tau, u_{i,t}\bar{P}_i - P_{i,t}\right] \tag{33}$$

$$r_{i,t}^{\mathrm{D}} \le \min\left[S_i^{\mathrm{down}}\tau, P_{i,t} - u_{i,t}\underline{P}_i\right] \tag{34}$$

Where, S_i^{up} is the upward ramp rate of conventional unit i, τ is the response time of the reserve capacity. S_i^{down} is the downward ramp rate of conventional unit i, $\bar{P}_i$ and $\underline{P}_i$ are the upper and lower output limit of conventional unit i, respectively.

3.2.4 Branch safety constraint

$$\left|\left(\boldsymbol{K}_b^{\mathrm{G}}\right)^{\mathrm{T}}\boldsymbol{P}_t - \left(\boldsymbol{K}_b^{\mathrm{L}}\right)^{\mathrm{T}}\boldsymbol{P}_{\mathrm{L},t} - K_b^{\mathrm{DC}}P_{\mathrm{DC},t}\right| \le \bar{P}_b, b \in \Omega_{\mathrm{B}} \tag{35}$$

Where, Ω_{B} is the set of system branches, $(\cdot)^{\mathrm{T}}$ is the matrix transposition operation, $\boldsymbol{K}_b^{\mathrm{G}}$ and $\boldsymbol{K}_b^{\mathrm{L}}$ are the injection and transfer distribution factor vectors of the unit nodes and the load nodes to branch b respectively, K_b^{DC} is the injection and transfer distribution factor of the tie line power exchange nodes to branch b, $\boldsymbol{P}_t$ is the output vector of all units at time t, $\boldsymbol{P}_{\mathrm{L},t}$ is the load vector of all nodes at time t, $\bar{P}_b$ is the upper limit of power transmission of branch b.

3.2.5 Other constraint

At the same time, constraints such as the ramp rate, output limits of all units need to be considered, which is not repeated here.

3.3 Calculation of electricity price

Assuming that the electricity market adopts the locational marginal price, and the reserve market adopts the regional price. According to the Karush-Kuhn-Tucker condition, an extended Lagrangian function is constructed to obtain the dual multipliers of each constraint condition (Wang et al., 2021), and the prices of electric energy market and reserve market at time t are calculated:

$$L_{t,e,1} = l_{t,1} + \sum_{b\in\Omega_{\mathrm{B}}}\left(\bar{\partial}_{t,b} + \partial_{t,b}\right)K_{e,b} \tag{36}$$

$$L_{t,2} = l_{t,2} \tag{37}$$

Where, $L_{t,e,1}$ is the locational marginal price of node e at time t, $L_{t,2}$ is the reserve price at time t, $l_{t,1}$ and $l_{t,2}$ are the dual multipliers of the power balance constraint and the reserve demand constraint respectively, $\bar{\partial}_{t,b}$ and $\partial_{t,b}$ are the dual multipliers of the upper and lower safety constraints of branch respectively, $K_{e,b}$ is the power transfer factor of node e to branch b.

4 Model solving based on robust optimization

4.1 Construction of uncertainty set model

Considering the prediction error of uncertain variables, the uncertainty set model is established. Define the polyhedron uncertain variable set Ω_{U} and the uncertain error set Ω_{U}:

$$\Omega_{\mathrm{U}} = \left\{P_t | P_t = P_t^{\mathrm{F}} + \hat{P_t}z_t, t \in \Omega_{\mathrm{T}}\right\} \tag{38}$$

$$z_t = \frac{P_t - P_t^{\mathrm{F}}}{\hat{P_t}} \in [-1, 1] \tag{39}$$

$$P_t \in \left[P_t^{\mathrm{F}} - \hat{P_t}, P_t^{\mathrm{F}} + \hat{P_t}\right], \hat{P_t} > 0 \tag{40}$$

$$\Omega_Z = \left\{ z_t \middle| \sum_{t\in\Omega_{\mathrm{T}}} |z_t| \le \Gamma \right\} \tag{41}$$

Where, P_t^{F} is the forecasting value of the uncertainty variable at time t, $\hat{P_t}$ is the maximum prediction error of the uncertainty variable at time t, z_t indicates the deviation degree of the actual value of uncertainty variable from the forecasting value, Γ is the uncertainty parameter reflecting the influence of uncertainty on decision making, $\Gamma = 0$ indicates the corresponding robust optimization model is a deterministic model.

4.2 Construction of optimization model

The purpose of robust optimization is to find the scheduling scheme with the best economy when the uncertain variables change towards the worst scenario in the uncertain variable set Ω_{U}, and to find the optimal solution in the worst scenario. Therefore, the day-ahead spot market clearing model is established as formula Eq. 42. The decision variables are the deviation degrees of the actual value of wind power output, photovoltaic output and load demand from their respective predicted values, the winning bid electric energy and reserve capacity of units, and the winning bid reserve capacity of flexible loads, etc.

$$\min\ (\max f) \tag{42}$$

Constraints are as follows:

$$\sum_{t\in\Omega_{\mathrm{T}}}\left|\sum_{w\in\Omega_{\mathrm{W}}} z_{w,t} + \sum_{n\in\Omega_{\mathrm{PV}}} z_{n,t} + \sum_{e\in\Omega_{\mathrm{E}}} z_{\mathrm{L},e,t}\right| \le \Gamma \tag{43}$$

$$\sum_{i\in\Omega_{\mathrm{G}}} P_{i,t} + \sum_{w\in\Omega_{\mathrm{W}}}\left(P_{w,t}^{\mathrm{F}} + z_{w,t}\hat{P_{w,t}}\right) + \sum_{n\in\Omega_{\mathrm{PV}}}\left(P_{n,t}^{\mathrm{F}} + z_{n,t}\hat{P_{n,t}}\right) = \sum_{e\in\Omega_{\mathrm{E}}}\left(P_{\mathrm{L},e,t}^{\mathrm{F}} + z_{\mathrm{L},e,t}\hat{P_{\mathrm{L},e,t}}\right) + P_{\mathrm{DC},t} \tag{44}$$

Where, $z_{w,t}$, $z_{n,t}$ and $z_{\mathrm{L},e,t}$ are the deviation degrees of the actual value of wind power output, photovoltaic output and load demand from their respective predicted values

respectively, $\hat{P}_{w,t}$ is the maximum output prediction error of wind turbine w at time t, $\hat{P}_{n,t}$ is the maximum output prediction error of photovoltaic unit n at time t, $\hat{P}_{L,t}$ is the maximum prediction error of load at time t. See 3.2 for other constraints.

4.3 Model solving process

A bilevel solving process is established for the min-max model of Eq. 42, in which the Genetic Algorithm is used in the upper-level for scenario enumerating with different renewable energy output and load demand, and try to find the worst scenario with the minimum max f. In the lower-level CPLEX is used to solve max f with a fixed scenario. The upper-level and the lower-level iterate until convergence (Ma et al., 2016). The specific process is as follows:

Step 1: set related parameters in the algorithm, such as population size, cross mutation probability, iteration number k, initial power flow, renewable energy output, load and unit parameters, etc.

Step 2: encode and form an initial uncertain set population, randomly generate x uncertain sets of renewable energy output and load, and transmit the uncertain sets to the lower-level.

Step 3: receive an uncertain set at the lower-level, use CPLEX to solve max f to obtain the winning bid quantity of each unit and flexible load, and return the optimized social welfare f^* to the upper-level.

Step 4: in the upper-level replace the current optimal solution with the smallest social benefit to obtain the current worst scenario. If the calculated social welfare f^* converges, save the worst scenario of renewable energy output and load demand and the optimization results in the lower-level problem, end the loop (the convergence basis is that the minimum social welfare difference obtained by two adjacent iterations does not exceed 0.01); otherwise, use the selection and mutation of Genetic Algorithm to generate a new uncertain set, let $k = k + 1$.

Step 5: if the number of iterations reaches the maximum, exit this process, otherwise, return to *Step* 3.

5 Case study

In this paper, a modified IEEE 10-machine 39-node system as shown in Supplementary Appendix Figure SA1 is established, in which the thermal power plant G10 and the load of bus 39 are used as the equivalent sending power grid, and the other receiving power grid get supply through tie line 39-1. Day-ahead clearing simulation of the receiver grid verifies the effectiveness of the proposed method in this paper. The power supply capacity in the receiving power grid is 9610MW, including 4 thermal power plants G1-G4, 2 hydropower plants G5-G6, 1 wind power plant G7 and 2 photovoltaic power plants G8-G9, of which G5 is set as a frequency modulation power plant. It is assumed that 5% of the load capacity of each bus in the receiving grid is flexible load, of which the interruptible and transferable loads are 3% and 2% respectively. See Appendix A for the parameters of unit, line and flexible load. The failure probability of each unit in each period is assumed as 0.5%, the unplanned outage probability of load is 0.5% and the load loss probability is 5%. According to the historical prediction error, the maximum prediction error of load is set to be 10%, the maximum prediction error of renewable energy output is set to be 15%, and the uncertainty parameter is taken as 40. See Appendix A for the forecasting values of tie line exchanging power and load.

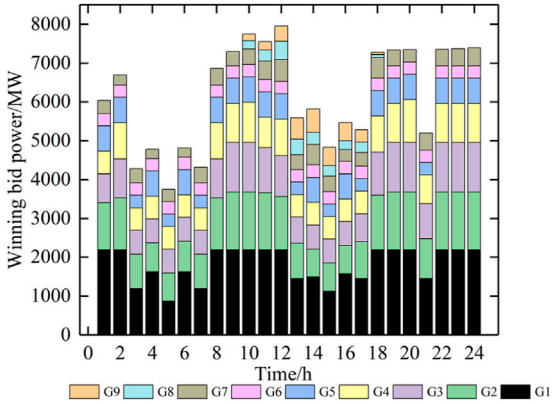

FIGURE 1
Winning bid power of plants in electric energy market.

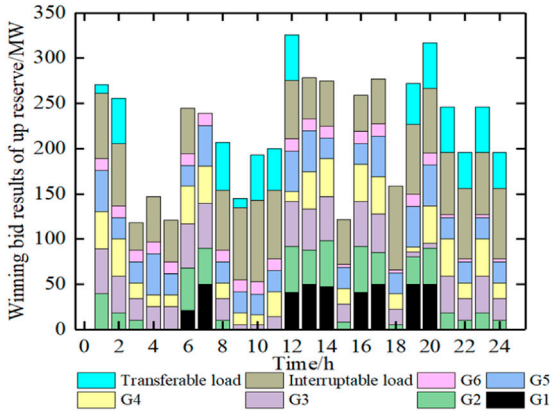

FIGURE 2
Winning bid results of up reserve.

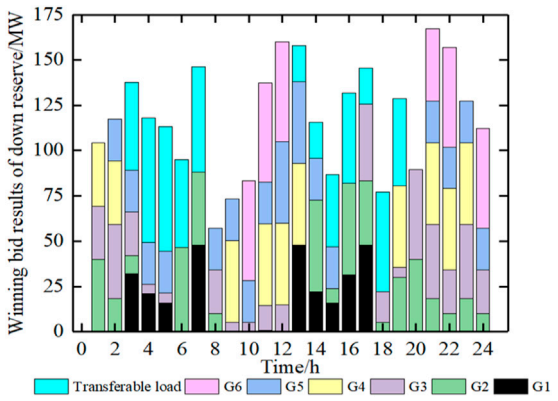

FIGURE 3
Winning bid results of down reserve.

5.1 Example of day-ahead clearing

According to the robust optimization method proposed in this paper, the day-ahead calculation example is cleared, and the electric energy clearing results of the power plant are further obtained, which is shown in Figure 1. It can be seen from the figure that since the operation cost of wind power and photovoltaic is far lower than that of thermal power, and they do not participate in the reserve market. Therefore, all renewable energy units have priority to be cleared in the electric energy market at all times, and the insufficient part is balanced by hydropower and thermal power. The overall output level of thermal power plants G1 and G2 is high, and the output level of G3 and G4 is low. Among them, the power generation cost of thermal power plant G4 is higher than that of thermal power plants G1-G3, so G4 has the smallest winning bid power. Because hydropower has a better price advantage in the reserve market, its clearing result in the electric energy market is far lower than that of thermal power.

Figures 2, 3 show the winning bid power of plants and loads in the reserve ancillary service market for the up and down reserve, respectively. In the example, the equipment failure probability and unplanned load outage probability are both set as constant within a day. Therefore, the reason why the system reserve capacity is large at 12:00 and 20:00 in Figure 2 is that the fault during peak load will cause a larger loss of load, resulting in a high risk of load loss. Because the reserve bidding price of flexible load has certain advantages, flexible loads are cleared as part of the system up reserve at all times. From 8:00 to 11:00 and 22:00 to 24:00, when more thermal power and hydropower are cleared in the electric energy market, the winning bid up reserve capacity of the load is even higher than that of the unit. It can be seen that the participation of interruptible load and transferable load in the reserve auxiliary

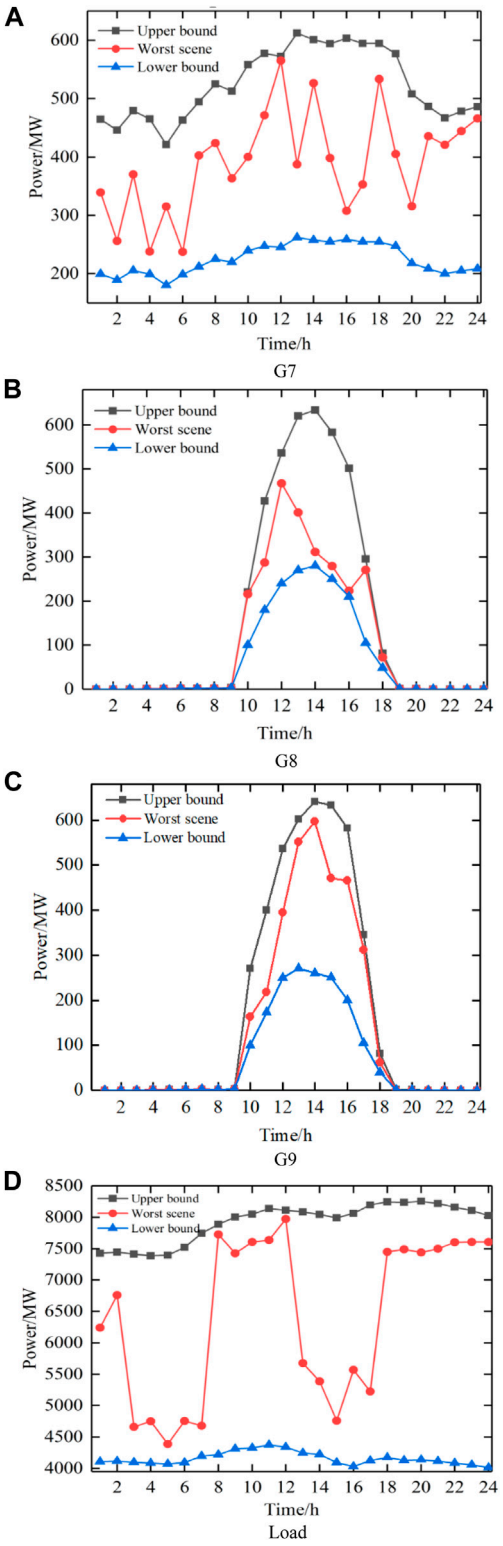

FIGURE 4
Winning bid results of electric energy.

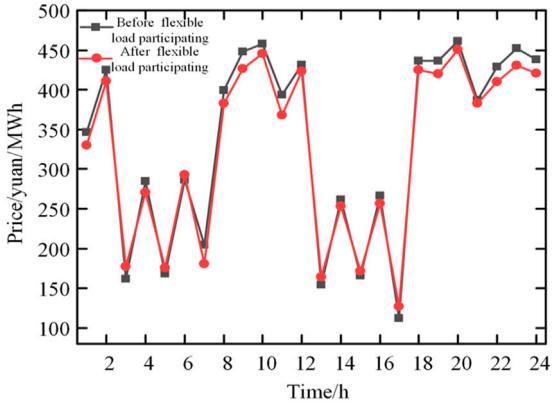

FIGURE 5
Clearing price of electric energy market before and after flexible load participating in joint market.

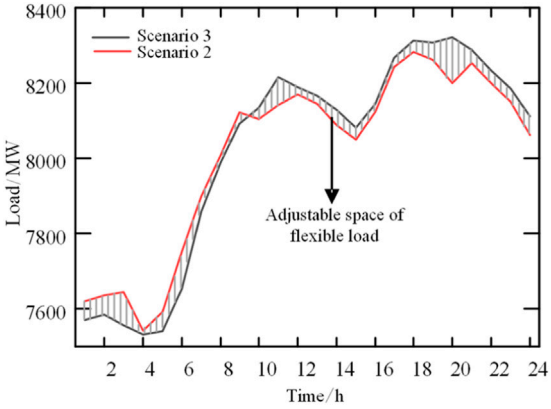

FIGURE 7
Comparison between scenario 2 and scenario 3 for providing load reserve adjustment.

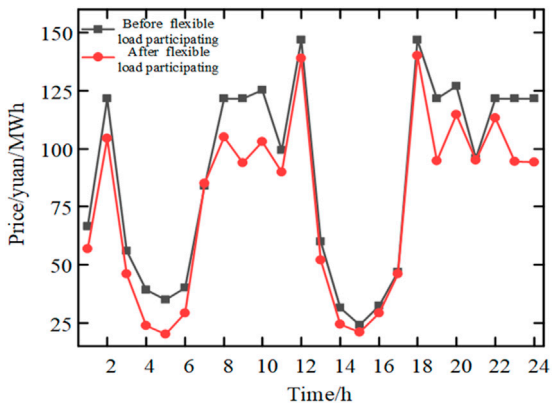

FIGURE 6
Clearing price of reserve market before and after flexible load participating in joint market.

service will reduce the bid-winning capacity of the unit in the reserve market and reduce the pressure on the unit to provide reserve capacity. Because the price of interruptible load set in this paper is lower than that of transferable load in reserve market, the bid-winning capacity of interruptible load in each period is higher than that of transferable load.

It can be seen from Figure 3 that the down reserve capacity cleared in the market at 12:00 and 21:00 is large, the reason is that the load outage during peak load will cause greater risk of unit tripping. The participation of transferable loads effectively supplements the system's demand for down reserve from units. Since the transferable load accounts for a small proportion in the system, the winning bid results of down reserve capacity from the loads is smaller than that of the units.

Through robust optimization, the winning bid results of the wind power plant G7, photovoltaic power plant G8 and total load in the worst scenario are shown in Figure 4. The winning bid results are all between the upper and lower bounds of the prediction error.

After the flexible load participates in the joint market of electric energy and reserve auxiliary service, the clearing prices of electric energy and reserve capacity in each period are shown in Figures 5, 6.

It can be seen from Figure 5 that after the participation of flexible load, the daily average price of electric energy market is reduced from 321.6 yuan/MWh to 313.1 yuan/MWh. Especially from 8:00 to 11:00 and from 18:00 to 24:00, when the load demand is large and the risk of insufficient reserve is high, the clearing of flexible load in the reserve market reduces the load clearing in the electric energy market, which will help to reduce the clearing price of the electric energy market and reduce the fluctuation degree of electricity price throughout the day when the bidding strategy of units and loads remains unchanged. As the flexible loads which have lower prices than thermal power units participate in the reserve market, the average price of reserve market is also reduced from 80.7 yuan/MWh to 67.6 yuan/MWh throughout the day.

In order to discuss the effectiveness of the method proposed in this paper, three comparison scenarios are set up for joint clearing optimization. Scenario 1: the proportion of flexible load is 0, and the joint clearing model is calculated by robust optimization; Scenario 2: the proportion of flexible load is 5%, and the forecasting value of load and renewable energy is determined with 95% confidence; Scenario 3: the proportion of flexible load is 0, the forecasting value of load and renewable energy is determined with 95% confidence. Figures 5, 6 show the clearing prices of electric energy and reserve capacity in each period of scenario 1, respectively. See Appendix B for the optimization results of winning bid capacity, winning bid reserve capacity of units and loads, and clearing electricity

TABLE 1 Clearing results under four scenarios (10^4 yuan).

Clearing results	Proposed method	Scenario 1	Scenario 2	Scenario 3
Unit generating cost	5497.93	5882.52	5688.47	6196.42
Unit reserve cost	1265.98	1505.42	1195.00	1358.32
Flexible load reserve cost	403.33	0	403.33	0
Flexible load income	306.68	0	306.68	0
Risk cost	28.77	38.13	48.71	49.46
Total cost	6889.33	7426.06	7028.83	7604. 20

prices for scenarios 2 and 3. Among them, after the flexible load participates in providing the up and down reserve of the system, the load reserve adjustment capability that scenario 2 can provide compared to scenario 3 is shown in Figure 7, which fully shows the flexibility of interruptible and transferable load to provide up and down reserve for the system. The market clearing results under the four scenarios are shown in Table 1.

According to Table 1, it can be seen that:

1) The participation of flexible load in the provision of up and down reserve of the system can effectively avoid the need for unit to operate in the range with higher production costs in order to ensure system safety, thereby reducing the power generation cost of the unit. Therefore, in the example, the methods considering the flexible load, that are the proposed method and scenario 2, have much lower generation cost than those of scenarios 1 and 3 without considering flexible load, and the proposed method in this paper has the lowest power generation cost.
2) Since the flexible load with price advantage is introduced into the reserve market to provide up and down reserve to the system, the proposed method in this paper and scenario 2 both have lower reserve cost. Since the robust optimization method in this paper considers the worst scenario, the reserve cost is slightly higher than that of scenario 2.
3) Since the price bidding strategy of flexible load of the method in this paper is same as that of scenario 2 and all cleared, the reserve cost and benefit of the flexible load of the two are equal.
4) Since the worst scenario is considered, the risk cost of the proposed method in this paper is lowest.
5) The total operation costs of the proposed method and scenario 2 are lower than that of scenarios 1 and 3, indicating that the participation of flexible load in reserve will reduce the total cost of the system.

In the above example, the failure probability of each unit in each period is assumed as a fixed unit failure probability value 0.5%. Here, assume that the failure probability of G1 increases from 0.5% to 15% during 8:00 to 12:00 and the failure probability of G3 increases from 0.5% to 20% during 15:00 to 20:00, here a variable unit failure probability case is introduced. The clearing results of the cases with fixed probability and variable unit failure probability are shown in Table 2. The winning bid results in electric energy market and reserve market are shown in Figures 8, 9 respectively.

Compared with winning bid results in Figures 1, 2, the risk cost increases due to the increase of unit failure probability of G1 from 8:00 to 12:00, leading to significant increase of winning bid results of up reserve. Among them, the winning bid power of G1 in electric energy market decreases and the winning bid up reserve capacity of G1 increases obviously. When the failure probability of G3 increases from 15:00 to 20:00, the winning bid results of the system also has a similar rule.

In order to cope with the uncertainty of failure probability, the system reserve capacity increases from 872.21 MW to 966.22 MW during 8:00 to 12:00, and increases from 1205.13 to 1254.13 MW during 15:00 to 20:00. The total reserve capacity increases from 4107.79 W M to 4252.79 WM. Unit reserve cost and risk cost have increased. The reserve market price increases during 8:00 to 12:00 and during 15:00 to 20:00. The average daily reserve market price rises to 80.22 yuan/MWh.

5.2 Influence analysis of uncertain parameters in robust optimization

In order to further discuss the influence of the robust optimization model, the sensitivity analysis is carried out on the uncertain parameter Γ, and the relationship between social welfare and Γ in the interval of $\Gamma \in [40, 56]$ is shown in Figure 10. It can be seen from the figure that the social welfare decreases with the increase of the uncertain parameter Γ. The reason is that the increasing of Γ will make the feasible region of the uncertain set continue to increase, and the system optimization result will develop to a worse scenario, therefore, the social welfare will continue to decrease. When Γ is greater than 52, the continuous increase of the feasible range of the uncertain set cannot generate worse scenarios. Therefore, social welfare no longer changes with Γ.

TABLE 2 Total cost and income of system before and after failure probability increasing (10^4 yuan).

Clearing results	Unit generating cost	Unit reserve cost	Risk cost	Flexible load income	Flexible load reserve cost
Fixed failure probability	5497.93	1265.98	28.77	306.68	403.33
Variable failure probability	6596.41	1432.12	76.17	306.68	403.33

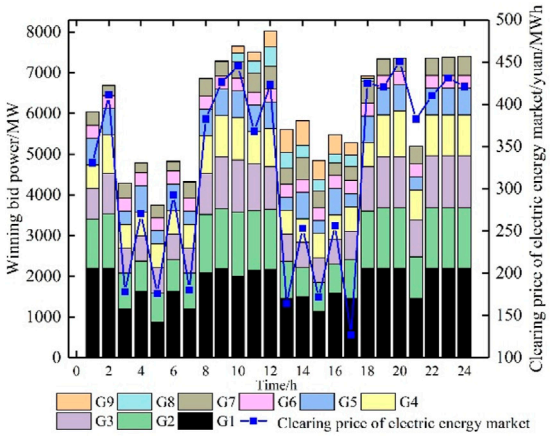

FIGURE 8
Winning bid power of plants in electric energy market and clearing price.

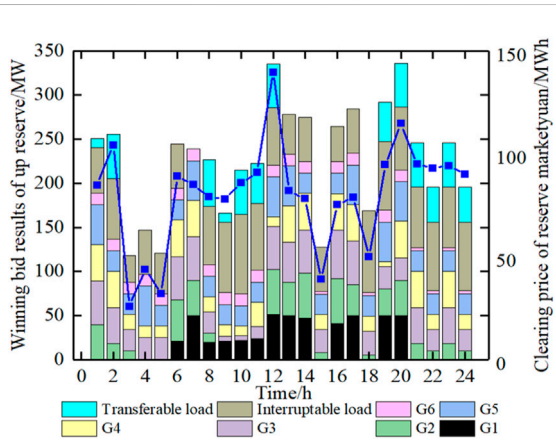

FIGURE 9
Winning bid results of up reserve and clearing price.

5.3 Influence analysis of flexible load bidding

In order to further discuss the influence of flexible load bidding in the joint market, define o_1 and o_2 as the price adjustment coefficients

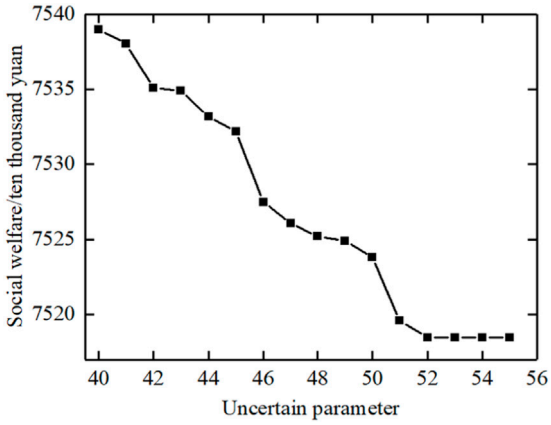

FIGURE 10
Relationship between social welfare and Γ.

of flexible load in the electric energy market and the reserve market, changing the bidding price to $o_1 F_1$ and $o_2 L_3$ respectively. When o_1 and o_2 are fixed to 1, the benchmark bidding is set.

In order to prevent the abuse of market power, it is necessary to limit the bidding range to monitor the behavior of individual bidding. This paper mainly considers the upper and lower limit constraints of the price adjustment coefficients:

$$\underline{o} \le o_1 \le \bar{o} \tag{46}$$

$$\underline{o} \le o_2 \le \bar{o} \tag{47}$$

Where, $\bar{o}$ and $\underline{o}$ are the maximum and minimum values of the price adjustment coefficients respectively. This paper sets $o_1, o_2 \in [0.5, 2]$.

The change of social welfare Δf is defined as the difference between the social welfare f' after changing the bidding and that under the benchmark bidding f. When o_2 is fixed to 1, Δf with o_1 as 0.8, 0.9, 1.0, 1.1, and 1.2 is shown in Table 3. The table shows that when o_1 increases from 0.8 to 1.2, social welfare increases gradually. When o_1 is set to 1.2, the corresponding electric energy bidding can obtain greater social welfare.

When o_1 is fixed to 1, Δf with o_2 as 0.8, 0.9, 1.0, 1.1, and 1.2 is shown in Table 4. The table shows that when o_2 increases from 0.8 to 1.2, social welfare decreases gradually. When o_2 is set to 0.8, the corresponding electric energy bidding can obtain greater social welfare.

TABLE 3 Influence of electric energy market biding to Δf.

o_1	0.8	0.9	1	1.1	1.2
Δf/ten thousand yuan	−633.5	−311.4	0	306.7	613.3

TABLE 4 Influence of reserve market biding to Δf.

o_2	0.8	0.9	1	1.1	1.2
Δf/ten thousand yuan	642.5	422.1	0	−403.3	−613.3

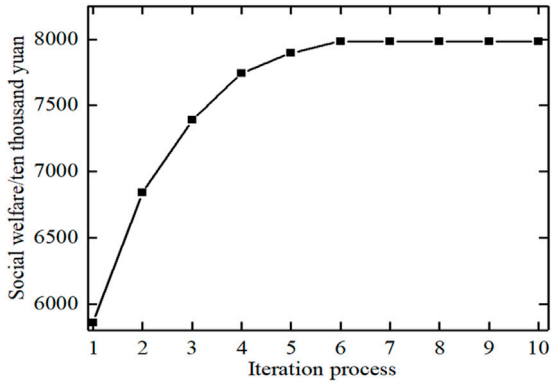

FIGURE 11
Iteration process.

From the above analysis, it can be seen that the bidding of flexible load in the electric energy market and reserve market will affect the optimal distribution of load in the electric energy market and reserve capacity market, thereby affecting social welfare. In this paper, the bidding strategy is optimized based on Genetic Algorithm. The optimization iteration process is shown in Figure 11. It can be seen from the figure that the social welfare reaches the maximum after 6 iterations, and the optimal price adjustment coefficients are 1.61 and 0.57 respectively.

5.4 Influence analysis of flexible load proportion

Based on the optimal price adjustment coefficients of flexible load, o_1=1.61, o_2=0.57, further analyze the impact of flexible load proportion on the market clearing results. All load nodes are set to have a fixed proportion throughout the period, and the impact of different flexible load proportions on social welfare is studied,

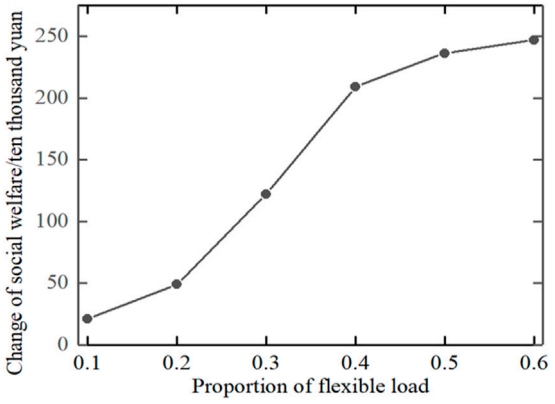

FIGURE 12
Influence of flexible load proportion on social welfare.

as shown in Figure 12. It can be seen from Figure 12 that the social welfare increases with the increase of the proportion of flexible load, because the increase of the proportion of flexible load will increase the flexibility of the system, thereby increasing the social welfare. Because when the flexible load proportion is in the range of 0.3–0.4, the change rate of social welfare is the largest, so considering the efficiency and reliability of power supply, it is reasonable to choose this interval to set flexible load.

6 Conclusion

The demand for system reserve due to uncertain factors such as net load prediction error, random failure of units and unplanned load shedding is considered in this paper, and the risk cost model of insufficient up reserve and down reserve of the system are established respectively. Two reserve resources from demand response and generators are considered, and the reserve capacity of the system is optimized through the risk cost. Aiming at the maximization of social welfare, a joint clearing model of electric energy and auxiliary service in the day-ahead spot market is established. A robust optimization model which takes the uncertainty of net load into account is then put forward, which can help market decision makers find out the market clearing scheme under the worst scenario of the system and provide reference decisions for the market to resist the risk of uncertainty. The research shows that the participation of the flexible load in the joint market can reduce the costs of power generation and reserve, avoiding the operation of units in the high operating cost section, increasing the total welfare of the power market, and improving the distribution of market-clearing electricity prices within a day. By rationally setting the bidding price and proportion of the flexible load, demand response can be guided to use electricity more scientifically and rationally, which can improve social welfare.

Data availability statement

The original contributions presented in the study are included in the article/Supplementary Material, further inquiries can be directed to the corresponding author.

Author contributions

YS: Conceptualization, Methodology, Software, Investigation, Formal Analysis, Writing—Original Draft; LH: Methodology, Writing—Original Draft; YC: Investigation, Formal Analysis; JW: Resources, Supervision; ZS: Data Curation, Validation; ZW: Writing—Review and Editing.

Funding

This work was supported by the project of State Grid Anhui Electric Power Co., Ltd. "Research on optimal allocation of energy storage and participation in power market mode considering coordinated control of load and storage". The funder was not involved in the study design, collection, analysis, interpretation of data, the writing of this article, or the decision to submit it for publication.

Conflict of interest

JW, ZS, and ZW were employed by the State Grid Anhui Electric Power Co Ltd.

The remaining authors declare that the research was conducted in the absence of any commercial or financial relationships that could be construed as a potential conflict of interest.

Publisher's note

Supplementary material

The Supplementary Material for this article can be found online at: https://www.frontiersin.org/articles/10.3389/fenrg.2022.998902/full#supplementary-material

References

Anthony, P., and Oren, S. S. (2014). Large scale integration of deferrable demand and renewable energy sources. *IEEE Trans. Power Syst.* 29 (1), 489–499. doi:10.1109/TPWRS.2013.2238644

Anuj, B., Naveen, K. S., Yog, R. S., and Shrivastava, R. (2018). Market-based participation of energy storage scheme to support renewable energy sources for the procurement of energy and spinning reserve. *Renew. Energy* 135, 326–344. doi:10.1016/j.renene.2018.12.009

Bompaard, E., Ma, Y. C., Napoli, R., and Abrate, G. (2007). The demand elasticity impacts on the strategic bidding behavior of the electricity producers. *IEEE Trans. Power Syst.* 22 (1), 188–197. doi:10.1109/TPWRS.2006.889134

Chen, H. H., Wang, Y., and Zhang, R. F. (2017). Spinning reserve capacity optimization considering coordination between source and load for power system with wind power. *Electr. Power Autom. Equip.* 37 (8), 185–192. doi:10.16081/j.issn.1006-6047.2017.08.025

Chen, Q., Wu, M. X., and Liu, Y. Q. (2021). Joint operation mechanism of spot electric energy and auxiliary service for wind power market-oriented accommodation. *Electr. Power Autom. Equip.* 41 (3), 179–188. doi:10.16081/j.epae.202101026

Fang, X., Brimathiaa, H., Du, E., Kang, C., and Li, F. (2019). Introducing uncertainty components in locational marginal prices for pricing wind power and load uncertainties. *IEEE Trans. Power Syst.* 34 (3), 2013–2024. doi:10.1109/TPWRS.2018.2881131

He, G. N., Chen, Q. X., Kang, C. Q., and Xia, Q. (2016). Optimal offering strategy for concentrating solar power plants in joint energy, reserve and regulation markets. *IEEE Trans. Sustain. Energy* 7 (3), 1245–1254. doi:10.1109/TSTE.2016.2533637

He, Y. (2010). *Research on model of interruptible load participating in reserve ancillary services market open to both supply and demand sides*. Guangdong, China: South China University of Technology. Available at: https://kns.cnki.net/kcms/detail/detail.aspx?dbcode=CMFD&dbname=CMFD2011&filename=2010227822.nh.

Herranz, R., Munoz, S, R, A., Villar, J., and Campos, F. A. (2012). Optimal demand side bidding strategies in electricity spot markets. *IEEE Trans. Power Syst.* 27 (3), 1204–1213. doi:10.1109/TPWRS.2012.2185960

Huang, D. S., Wu, Y. H., and Lv, X. (2019). Optimization model for combined electricity spot and ancillary service markets considering variable generation resources. *Power Demand Side Manage* 21 (6), 30–37. doi:10.3969/j.issn.1009-1831.2019.06.007

Lazaros, E., Jalal, K., Pierre, P., De Greve, Z., and Vallee, F. (2017). Impact of public aggregate wind forecasts on electricity market outcomes. *IEEE Trans. Sustain. Energy* 8 (4), 1394–1405. doi:10.1109/TSTE.2017.2682299

Li, P., Li, F. T., and Song, X. F. (2021). Considering the flexible load new energy access system optimization forSpinning reserve. *Power Syst. Technol.* 45 (4), 1289–1297. doi:10.13335/j.1000-3673.pst.2020.0113a

Li, R., Wang, M. Q., and Yang, M. (2022). Robust-stochastic reserve optimization considering uncertainties ofContingency probability and net load. *Autom. Electr. Power Syst.* 46 (6), 20–29. doi:10.7500/AEPS20210523001

Liu, Z., Lei, S. F., and Wang, Q. L. (2019). Clearing model of regional electricity spot market considering reserve sharing. *Electr. Power Constr.* 42 (11), 64–71. doi:10.12204/j.issn.1000-7229.2021.11.007

Liu, Z. (2019). *Research on the market transaction of reserve ancillary service considering interruptible load*. Xian, China: Xian University of Technology. Available at: https://kns.cnki.net/kcms/detail/detail.aspx.

Luo, Y. H., and Xue, Y. S. (2007). Hybrid optimization of generation capacity adequacy. *Autom. Electr. Power Syst.* 31 (12), 30–35. Available at: https://kns.cnki.net/kcms/detail/detail.aspx=CJFD&dbname=CJFD2007.

Ma, L., Liu, N., Zhang, J. H., Tushar, W., and Yuen, C. (2016). Energy management for joint operation of CHP and PV prosumers inside a grid-connected microgrid:a game theoretic approach. *IEEE Trans. Ind. Inf.* 12 (5), 1930–1942. doi:10.1109/TII.2016.2578184

Nikolaos, G., Ozan, E., Anastasios, G., and Catalao, J. P. S. (2015). Load-following reserves procurement considering flexible demand side resources under high wind power penetration. *IEEE Trans. Power Syst.* 30 (3), 1337–1350. doi:10.1109/TPWRS.2014.2347242

Reddy, S. S., Bijwe, P. R., and Abhyankar, A. R. (2015). Joint energy and spinning reserve market clearing incorporating wind power and load forecast uncertainties. *IEEE Syst. J.* 9 (1), 152–164. doi:10.1109/JSYST.2013.2272236

Shan, Y. (2021). *Research on short-term pricing decisions of thermal power rnterprises in electricity spot market*. Beijing, China: North China Electric Power University. Available at: https://kns.cnki.net/kcms/detail/detail.aspx?dbcode=CMFD&dbname=CMFD202201&filename=1021124929.nh&uniplatform=NZKPT&v=o4vPA8ZnSaOCxvXtw8vYdsey6ug9r6P8BRq89igbN_8VjiBcIHOfdqxlejTW6qz.

Shi, X. H., Zheng, Y. X., and Xue, B. K. (2019). Effect analysis of unit operation constraints on locational marginal price of unit nodes. *Power Syst. Technol.* 43 (8), 2659–2664. doi:10.13335/j.1000-3673.pst.2019.0540

Sun, G. X. (2020). *Research on flexible load participating in the joint market of electricitiy and reserves under the bilateral bidding model*. Guangdong, China: South China University of Technology. Available at: https://kns.cnki.net/kcms/detail/detail.aspx?dbcode=CMFD&dbname=CMFD202101&filename=1020330782.nh.

Wang, B. B., Li, Y. R., and Li, Y. (2015). Optimal coordination between system reserve and interruptible loads with response uncertainty. *Electr. Power Autom. Equip.* 35 (11), 82–89. doi:10.16081/j.issn.1006-6047.2015.11.013

Wang, Y., Yang, Z. F., and Yu, J. (2021). Analysis and extension of internal relationship between locational marginal price and dual multiplier. *Autom. Electr. Power Syst.* 45 (6), 82–91. doi:10.7500/AEPS20200718001

Wen, F. R., Li, H. Q., and Wen, X. Y. (2019). Optimal allocation of energy storage systems considering flexibility deficiency risk in active distribution network. *Power Syst. Technol.* 43 (11), 3952–3962. doi:10.13335/j.1000-3673.pst.2018.2528

Xu, Q. Y., Zhang, N., Kang, C. Q., Xia, Q., He, D., Liu, C., et al. (2016). A game theoretical pricing mechanism for multi-area spinning reserve trading considering wind power uncertainty. *IEEE Trans. Power Syst.* 31 (2), 1084–1095. doi:10.1109/TPWRS.2015.2422826

Xue, Y. S. (2002). Coordinations of preventive control and emergency control for transient stability. *Autom. Electr. Power Syst.* 25 (04), 1–4. Available at: https://kns.cnki.net/kcms/detail/detail.aspxDLXT200204000.

Xun, W. (2010). *The study of reserve ancillary service rrading and pricing considering interruptible load*. Beijing, China: Beijing Jiaotong University. Available at: https://kns.cnki.net/kcms/detail/detail.aspx.

Yang, M., Zhang, L. Z., and Lv, J. H. (2020). Flexibility-oriented day-ahead market clearing model for electrical energy and ancillary services. *Electr. Power* 53 (8), 182–192. doi:10.11930/j.issn.1004-9649.202006277

Yang, W., Zeng, Z. J., and Chen, H. Y. (2017). Research on demand response trading mechanism in guangdong electricity market. *Guangdong Electr. Power* 30 (5), 25–34+68. doi:10.3969/j.issn.1007-290X.2017.05.006

frontiers | Frontiers in Energy Research

TYPE Original Research
PUBLISHED 05 January 2023
DOI 10.3389/fenrg.2022.1022060

OPEN ACCESS

EDITED BY
Siqi Bu,
Hong Kong Polytechnic University,
Hong Kong SAR, China

REVIEWED BY
Qiang Fu,
Sichuan University, China
Jun Cao,
Luxembourg Institute of Science and Technology (LIST), Luxembourg
Bowen Zhou,
Northeastern University, China

*CORRESPONDENCE
Yi Zhou,
zhouyi@tbea.com

SPECIALTY SECTION
This article was submitted to Smart Grids,
a section of the journal
Frontiers in Energy Research

RECEIVED 18 August 2022
ACCEPTED 12 September 2022
PUBLISHED 05 January 2023

CITATION
Zhou Y, Cao J and Zhao J (2023), Small-signal oscillatory stability of a grid-connected PV power generation farm affected by the increasing number of inverters in daisy-chain connection. *Front. Energy Res.* 10:1022060. doi: 10.3389/fenrg.2022.1022060

Small-signal oscillatory stability of a grid-connected PV power generation farm affected by the increasing number of inverters in daisy-chain connection

Yi Zhou*, Junzheng Cao and Jing Zhao

Central Research Institute, TBEA Science and Technology Investment Co., Ltd., Tianjin, China

The daisy-chain connection of inverters is one of the basic configurations of the power collecting network in a grid-connected photovoltaic (PV) power generation farm. In this study, the total impact of a cluster of M similar inverters in daisy-chain connection in the PV farm is examined in the following two aspects: 1) aggregated representation of the cluster of inverters is derived for stability study based on the dynamic equivalence. The derivation confirms the rationality of representing the cluster of inverters by an aggregated inverter connected to the external system *via* an equivalent reactance, which is the maximum eigenvalue of the matrix of daisy-chain connection defined in the article. 2) Analysis is conducted to indicate that the risk of oscillatory instability may be collectively induced by all the inverters in the daisy-chain connection in the cluster. This explains why the increasing number of inverters may imply the possible instability risk of a PV farm. An example of a power system with a grid-connected PV power generation farm is presented in the article to demonstrate and evaluate the analytical conclusion obtained.

KEYWORDS

small-signal stability, photovoltaic power generation farm, dynamic equivalence, linearized state-space model, modal analysis

Abbreviations: $V_{ix}+jV_{iy}$, terminal voltage of PVi; $I_{ix}+jI_{iy}$, output current of PVi; $V_{PCCx}+jV_{PCCy}$, voltage of the PCC; *M*, number of PVs in the PV farm; *Xi*, Te reactance of the cable linking the i^{th} and $(i\text{-}1)^{th}$ PV; M_M, network reactance matrix of the grid-connected PV; Xw, network reactance matrix of the power collecting network; X_L, network reactance matrix of the PV transmission line; ρ_i, i^{th} eigenvalue of the network reactance matrix M_M; v_i, the right eigenvector of M_M corresponding to ρ_i; w_i, the left eigenvectors of M_M corresponding to ρ_i; λ, complex conjugate eigenvalue of $\boldsymbol{A}_p+\rho\boldsymbol{A}_n$; ρ_{min}, the minimum eigenvalues of $\boldsymbol{M}_M$; ρ_{max}, the maximum eigenvalues of $\boldsymbol{M}_M$; I_{cx}, *X*-axis current output of the inverter; I_{cy}, *Y*-axis current output of the inverter; $x_{G_{id}}$, output of the integrator of d-axis CCIL of the inverter; $x_{G_{iq}}$, output of the integrator of q-axis CCIL of the inverter; V_{dc}, voltage across the DC capacitor; x_{dc}, output of integrator of VDC of the inverter; x_{PLL}, output of integrator of the terminal voltage tracked by the PLL; θ_{PLL}, output of integrator of the terminal voltage tracked by the PLL; MPPT, maximum power point tracking; SI, sensitivity index; PLL, phase-locked loop; CWMV, aggregated model derived by using the capacity-weighted mean value method; CCIL, current control inner loop of inverter; VDC, DC voltage control outer loop of inverter.

1 Introduction

In recent years, renewable power generation, such as wind and photovoltaic (PV), has developed rapidly (Wang, 2020). In contrast to traditional thermal and hydraulic power generation, wind and PV power generation are connected to the grid through power electronic devices such as inverters (Shah et al., 2021), which affect the operation of an AC power system in a different way than traditional generation.

PV power generation has attracted the attention of many researchers, and a lot of studies have been carried out about its maximum power point tracking (MPPT) strategy, inverter control, stability analysis, and control. In order to eliminate inter-harmonics in a PV generation system, Sangwongwanich and Blaabjerg (2019) proposed an MPPT algorithm of a random selection of sampling rate, and Pan et al. (2020) developed a phase-shifting MPPT method. Ali et al. (2021) advocated an efficient fuzzy logic-based variant-step incremental conductance MPPT method to improve the efficiency of maximum power tracking, which improves the static and dynamic response. As one of the most important components of PV power generation, the inverter directly affects the external dynamic characteristics of PV power generation. Callegaro et al. (2022) proposed a feedback linearization-based controller that eliminates the instability of photovoltaic voltage. In order to reduce the leakage current of a PV inverter, a five-level transformer-less inverter and a three-phase Z-source three-level four-leg inverter were developed (Zhu et al., 2020; Guo et al., 2018), respectively.

A grid-connected inverter may behave as an RLC circuit with negative resistance in various frequency regions, thus destabilizing the system (Harnefors, 2007; Harnefors et al., 2007; Du et al., 2020a). Moradi-Shahrbabak and Tabesh (2018) found that the damping of the oscillation mode may decrease when the capacitance and reactance corresponding to the DC link and the front-end inverter increase, bringing about the instability risk. By using the eigenvalue analysis, Zhao et al. (2017) found that the parameters of inverter control systems, tie line length, and other factors in a grid-connected inverter system may affect the damping of mid-low frequency oscillation mode. The line length directly affected the power grid strength such that the decrease in power grid strength would destabilize the system (Huang et al., 2015; Xia et al., 2018; Du et al., 2019; Malik et al., 2019; Du et al., 2021a).

Studies so far in the literature have indicated that the number of inverters is an important factor affecting the oscillatory stability of a grid-connected PV generation system. The increase in the number of inverters may lead to system instability (Agorreta et al., 2011; Majumder and Bag, 2014; Shahnia, 2016; Du et al., 2020a; Fu et al., 2020; Du et al., 2021b). Shahnia (2016) found that when the total power generation capacity of a microgrid remained constant and the number of converter-interfaced distributed energy resources increased, the system stability decreased. A study by Majumder and Bag (2014) indicated that if the control gains of converters remained unchanged, the increase in the number of parallel back-to-back converters may induce system instability. However, the study about the impact of an increasing number of grid-connected inverters relied on the results of numerical computation/simulation of study cases.

Du et al. (2020b) analytically examined the impact of the increasing number of parallel-connected PV generating units on system stability and came to the conclusion that the increase in the number can reduce system stability. The mechanism of growing oscillations caused by the increased number of the PV generating units in parallel connection was analytically revealed by Du et al. (2020c). A study by Du et al. (2020a) is the extension of their pioneering investigation of the oscillatory stability of a grid-connected wind power generation system (Du et al., 2019). Possible small-signal instability of a grid-connected wind farm as being caused collectively by M similar wind turbine generators in parallel connection was found and examined analytically. The effect of the increasing number of wind turbine generators in parallel connection to destabilize the grid-connected wind farm was reported for the first time in the literature, which is an important innovative contribution to the field (Du et al., 2019).

The general topology of the power collecting network of a PV farm is radial, which is the combination of two basic configurations, that is, inverters in parallel connection and inverters in daisy-chain connection (Wang et al., 2009; Liu et al., 2016). Du only studied the basic configuration of PV generating units in parallel connection. Investigation of the second basic configuration of PV generating units in daisy-chain connection is important for revealing the full picture of the impact of the increasing number of inverters on the small-signal stability of the grid-connected PV power generation form. This has motivated the study in this article.

The article examines the total impact of a cluster of M similar inverters in daisy-chain connection on the small-signal oscillatory stability of a grid-connected PV power generation farm. The organization of the article is as follows.

In the next section, the full-order model of a cluster of M similar inverters in daisy-chain connection is derived first. Afterward, state transformation is applied to the state matrix of the full-order model. The result of state transformation proves that the state matrix of the full-order model is approximately similar to a block diagonal matrix with M elementary matrices. Hence, the cluster of inverters in daisy-chain connection is approximately equivalent to M dynamically independent subsystems. Finally, analysis is carried out in the section to indicate that for studying the instability risk, the cluster of similar inverters in a daisy-chain connection can be represented by an inverter being connected to the external system *via* a lumped reactance, which is the maximum eigenvalue of the matrix of daisy-chain connection defined in the article. Hence, it is rational to represent the cluster of similar

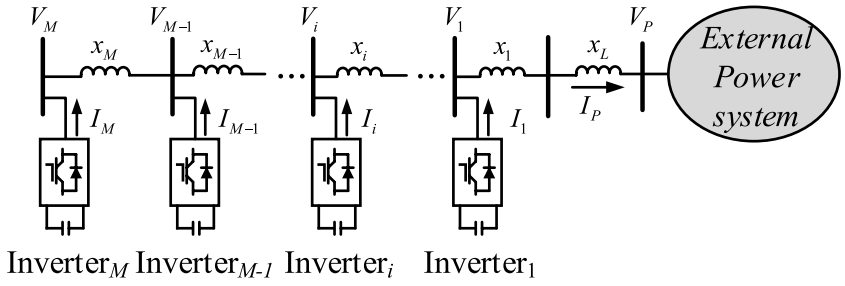

FIGURE 1
Cluster of *M* inverters in daisy-chain connection.

inverters in a daisy-chain connection by an aggregated inverter. In addition, when the number of similar inverters in daisy-chain connection increases, the possible instability risk may increase. This confirms that similar inverters may collectively induce poorly damped or even growing oscillations, and the risk of the oscillation increases when the number of the inverters in the cluster increases.

In Section 3, an example power system with a grid-connected PV power generation farm is presented. In the PV farm, there is a cluster of inverters in the daisy-chain connection. Analysis and conclusions made in Section 2 are demonstrated and evaluated. In the demonstration and evaluation, two study cases are presented when the dynamics of inverters in daisy-chain connection are either similar or considerably different. The final section summarizes the main conclusions of the article and future work.

The main contributions of the article, particularly as compared with previous work by Du et al. (2020b), are as follows:

(1) Analysis is conducted to conclude that it is rational to represent a cluster of similar inverters in daisy-chain connection as an aggregated inverter for the stability study. This extended the innovative work by Du et al. (2020c) from the case of parallel connected inverters to the case of the inverters in daisy-chain connection.
(2) Investigation reveals the mechanism of why and how similar inverters in daisy-chain connection may collectively induce the oscillations, that is, the increasing number of inverters may likely increase the instability risk.

2 Impact analysis

2.1 Full-order model of a cluster of inverters in daisy-chain connection

The structure of a cluster of M inverters in a daisy-chain connection being connected to an external power system is shown in Figure 1. The cluster of inverters can be a portion of a PV power farm. Thus, the external system includes the AC grid and the remainder of the grid-connected PV power generation farm. Alternatively, the cluster of inverters can constitute the complete PV power generation farm, and thus the external system is the AC grid. In this study, analysis is conducted and presented on the former case as the analytical conclusions obtained are applicable to the latter case. In Figure 1, x_L denotes the reactance of the cable between the cluster of inverters and the remainder of the grid-connected PV generation power farm. The model of PV is shown in Supplementary Appendix S1A.

The linearized state-space model of the i^{th} inverter is

$$\begin{aligned} \frac{d}{dt}\Delta \boldsymbol{X}_{wi} &= \boldsymbol{A}_i \Delta \boldsymbol{X}_{wi} + \boldsymbol{B}_i \Delta \boldsymbol{V}_i \\ \Delta \boldsymbol{I}_i &= \boldsymbol{C}_i \Delta \boldsymbol{X}_{wi}, \quad i = 1, 2, \cdots, M \end{aligned}, \tag{1}$$

where Δ denotes the small increment of a vector of variables, ΔX_{wi} is the state variable vector of the i^{th} inverter, $\Delta I_i = [\,\Delta I_{ix} \;\; \Delta I_{iy}\,]^T$, and $\Delta V_i = [\,\Delta V_{ix} \;\; \Delta V_{iy}\,]^T$. $I_{ix} + jI_{iy}$ and $V_{ix} + jV_{iy}$ are the output current and terminal voltage of the i^{th} inverter, respectively, expressed in the common $x - y$ coordinate. In this article, the linearized model of the i^{th} inverter described by Eq. 1 is denoted simply as (A_i, B_i, C_i).

Ignoring the resistance of the cable, linearized voltage equations for each section of the cable connecting the inverters are

$$\begin{aligned} \Delta \boldsymbol{V}_i &= \boldsymbol{x}_i \sum_{k=i}^{M} \Delta \boldsymbol{I}_k + \Delta \boldsymbol{V}_{i-1}, i = 2, \cdots, M \\ \Delta \boldsymbol{V}_1 &= (\boldsymbol{x}_1 + \boldsymbol{x}_L) \sum_{k=1}^{M} \Delta \boldsymbol{I}_k + \Delta \boldsymbol{V}_p \end{aligned}, \tag{2}$$

where $\Delta \boldsymbol{V}_p = [\,\Delta V_{px} \;\; \Delta V_{py}\,]^T$, $V_{px} + jV_{py}$ is the voltage at the terminal of the remainder of the PV power generation farm; $\boldsymbol{x}_i = x_i \begin{bmatrix} 0 & -1 \\ 1 & 0 \end{bmatrix}$ and $\boldsymbol{x}_L = x_L \begin{bmatrix} 0 & -1 \\ 1 & 0 \end{bmatrix}$, and x_i is the reactance of the cable linking the i^{th} and $(i\text{-}1)^{\text{th}}$ inverter. It should be noted that the

dynamics of the cable affect are in the range of frequency much higher than those of inverters and hence are neglected in Eq. 2.

Substituting Eq. 2 into Eq. 1, a linearized model of the cluster of inverters can be gained as follows:

$$\begin{aligned} \frac{d}{dt}\Delta \boldsymbol{X} &= \boldsymbol{A}_X \Delta \boldsymbol{X} + \boldsymbol{B}_X \Delta \boldsymbol{V}_p \\ \Delta \boldsymbol{I}_p &= \boldsymbol{C}_X \Delta \boldsymbol{X} \end{aligned}, \tag{3}$$

where $\Delta X = [\,\Delta X_{w1}^T \;\; \Delta X_{w2}^T \;\; \cdots \;\; \Delta X_{wM}^T\,]^T$;

$A_X = \begin{bmatrix} A_1 + A_{t11} & A_{t12} & \cdots & A_{t1M} \\ A_{t21} & A_2 + A_{t22} & \cdots & A_{t2M} \\ \vdots & \vdots & \ddots & \vdots \\ A_{tM1} & A_{tM2} & \cdots & A_M + A_{tMM} \end{bmatrix}$, when $j \le i$,

$A_{tij} = B_i\left(x_L + \sum_{k=1}^{j} x_k\right)C_j$ and when $j > i$, $A_{tij} = B_i\left(x_L + \sum_{k=1}^{i} x_k\right)C_j$, $(i, j = 1, 2, \ldots, M)$; $B_X = [\,B_1^T \;\; B_2^T \;\; \ldots \;\; B_M^T\,]^T$; $C_X = [\,C_1 \;\; C_2 \;\; \cdots \;\; C_M\,]$.

Equation 3 is referred to as the full-order model of the cluster of inverters in a daisy-chain connection.

2.2 State transformation

In practice, similar inverters in daisy-chain connection being clustered in one group may often be in one area of the PV power generation farm over which the illumination intensity does not vary considerably. Often, similar inverters in the cluster are often supplied by one manufacturer, who sets the parameters of inverters with the same default values. Subsequently, the dynamics (dynamic models) of similar inverters in the cluster are similar. It is reasonable to assume that identical models of inverters are the approximate description of the case where the dynamics of inverters in daisy-chain connection, that is,

$$(\boldsymbol{A}_i, \boldsymbol{B}_i, \boldsymbol{C}_i) = \left(\boldsymbol{A}_p, \boldsymbol{B}_p, \boldsymbol{C}_p\right);\; i = 1, 2, \cdots, M, \tag{4}$$

where $A_p \in R^{N\times N}, B_p \in R^{N\times 2}, C_p \in R^{2\times N}$; N is the order of the linearized state-space model of a single inverter. Equation 4 is an approximate description of similar dynamics of inverters in daisy-chain connection.

Substituting Eq. 4 into Eq. 3, the state matrix of the cluster of inverters to be aggregated is obtained as follows:

$$\boldsymbol{A}_X = diag\left[\boldsymbol{A}_p\right] + \boldsymbol{A}_{XL}, \tag{5}$$

where $diag[\boldsymbol{A}_p]$ denotes a diagonal block matrix;

$$\boldsymbol{A}_{XL} = \begin{bmatrix} (x_L + x_1)\boldsymbol{A}_n & (x_L + x_1)\boldsymbol{A}_n & \cdots & (x_L + x_1)\boldsymbol{A}_n \\ (x_L + x_1)\boldsymbol{A}_n & \left(x_L + \sum_{i=1}^{2} x_i\right)\boldsymbol{A}_n & \cdots & \left(x_L + \sum_{i=1}^{2} x_i\right)\boldsymbol{A}_n \\ \vdots & \vdots & \ddots & \vdots \\ (x_L + x_1)\boldsymbol{A}_n & \left(x_L + \sum_{i=1}^{2} x_i\right)\boldsymbol{A}_n & \cdots & \left(x_L + \sum_{i=1}^{M} x_i\right)\boldsymbol{A}_n \end{bmatrix};$$

$$\boldsymbol{A}_n = \boldsymbol{B}_p \begin{bmatrix} 0 & -1 \\ 1 & 0 \end{bmatrix} \boldsymbol{C}_p \in R^{N\times N}.$$

The state matrix of a grid-connected PV power generation farm with inverters in parallel connection is derived from Du et al. (2020a). Due to the special structure of the state matrix derived, a simple transformation of state variables is proposed and applied to decompose the state matrix. State matrix of inverters in daisy-chain connected as given in Eq. 5 is much more complicated than and different to that derived from Du et al. (2020b) because the configuration of a daisy-chain connection is completely different to that of a parallel connection.

Two main factors affecting the small-signal stability of PV power generation farms are the dynamics of inverters and dynamic interactions of inverters. The latter affecting factor is determined partially by the configuration of the connecting network of inverters. The difference of state matrix given in Eq. 5 for the daisy-chain connection with that given in Du et al. (2020c) for parallel connection indicates the impact of the configuration of the connecting network of inverters on the small-signal stability. Hence, it is expected that stability analysis based on Eq. 5 is entirely different and more complex than that conducted in Du et al. (2020a). To start with the analysis, a new state transformation needs to be invented to decompose the state matrix given in Eq. 5. For that, the following matrix of daisy-chain connections is defined:

$$\boldsymbol{M}_M = \begin{bmatrix} x_L + x_1 & x_L + x_1 & x_L + x_1 & \cdots & x_L + x_1 \\ x_L + x_1 & x_L + \sum_{i=1}^{2} x_i & x_L + \sum_{i=1}^{2} x_i & \cdots & x_L + \sum_{i=1}^{2} x_i \\ \vdots & \vdots & \vdots & \ddots & \vdots \\ x_L + x_1 & x_L + \sum_{i=1}^{2} x_i & x_L + \sum_{i=1}^{3} x_i & \cdots & x_L + \sum_{i=1}^{M} x_i \end{bmatrix}, \tag{6}$$

where $\boldsymbol{M}_M \in R^{M\times M}$.

Denote the i^{th} eigenvalue and corresponding eigenvector of $\boldsymbol{M}_M$ to be ρ_i and $\boldsymbol{v}_i = [\,v_{1i} \;\; v_{2i} \;\; \cdots \;\; v_{Mi}\,]^T$ $(i = 1, 2, \cdots, M)$, respectively. It can be proved that the following state transformation can be applied (for details, see Du et al., 2021c):

$$\Delta \boldsymbol{X} = \boldsymbol{T}\Delta \boldsymbol{Z}. \tag{7}$$

After the state transformation, the following equivalent state-space representation of the cluster of inverters in the daisy-chain connection is obtained:

$$\begin{aligned} \frac{d}{dt}\Delta \boldsymbol{Z} &= \boldsymbol{A}_Z \Delta \boldsymbol{Z} + \boldsymbol{B}_Z \Delta \boldsymbol{V}_p \\ \Delta \boldsymbol{I}_p &= \boldsymbol{C}_Z \Delta \boldsymbol{Z} \end{aligned}, \tag{8}$$

where $\boldsymbol{A}_Z = diag[\boldsymbol{A}_p + \rho_i \boldsymbol{A}_n]$,

$$\boldsymbol{B}_Z = \left[\, v_1 \boldsymbol{B}_p^T \;\; v_2 \boldsymbol{B}_p^T \;\; \ldots \;\; v_M \boldsymbol{B}_p^T \,\right]^T,$$

$$\boldsymbol{C}_Z = [\, v_1 \boldsymbol{C}_p \;\; v_2 \boldsymbol{C}_p \;\; \cdots \;\; v_M \boldsymbol{C}_p \,], \text{ and } v_i = \sum_{k=1}^{M} v_{ki}, i = 1, 2, \cdots, M.$$

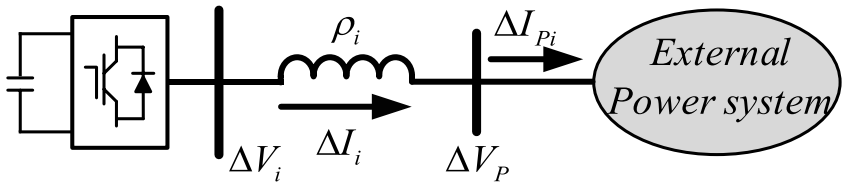

FIGURE 2
Configuration of the *i*th subsystem.

The state-space representation in Eq. 8 can be seen as comprising M subsystems, and the state-space model of the *i*th subsystem is

$$\begin{aligned} \frac{d}{dt}\Delta \boldsymbol{Z}_i &= \left(\boldsymbol{A}_p + \rho_i \boldsymbol{A}_n\right)\Delta \boldsymbol{Z}_i + \nu_i \boldsymbol{B}_p \Delta \boldsymbol{V}_p \\ \Delta \boldsymbol{I}_{pi} &= \nu_i \boldsymbol{C}_p \Delta \boldsymbol{Z}_i \end{aligned}. \tag{9}$$

Equations 8 and 9 indicate that under the assumed condition of identical models of the inverters, the cluster of inverters can be equivalently transformed to M dynamically independent subsystems. Each subsystem consists of a grid-connected inverter. The state-space model of the inverter in the subsystem is the same as that described by Eq. 1 and Eq. 4, that is,

$$\begin{aligned} \frac{d}{dt}\Delta \boldsymbol{Z}_i &= \boldsymbol{A}_p \Delta \boldsymbol{Z}_i + \boldsymbol{B}_p \Delta \boldsymbol{V}_i \\ \Delta \boldsymbol{I}_i &= \boldsymbol{C}_p \Delta \boldsymbol{Z}_i,\ i = 1, 2, \cdots, M \end{aligned}. \tag{10a}$$

Connection of the inverter in the subsystem with the external system is depicted by the following equations:

$$\begin{aligned} \Delta \boldsymbol{V}_i &= \rho_i \begin{bmatrix} 0 & -1 \\ 1 & 0 \end{bmatrix} \Delta \boldsymbol{I}_i + \nu_i \Delta \boldsymbol{V}_p \\ \Delta \boldsymbol{I}_{pi} &= \nu_i \Delta \boldsymbol{I}_i,\ i = 1, 2, \cdots, M \end{aligned}. \tag{10b}$$

From Eqs 9 and 10, the configuration of the subsystems is established, as shown in Figure 2. The linearized model of the subsystem, as described by Eqs 9 and 10, is denoted as (A_p, B_p, C_p, ρ_i).

2.3 Aggregated representation

State transformation conducted in the previous subsection indicates that the cluster of M similar inverters in daisy-chain connection is approximately equivalent to M dynamically independent subsystems. In each independent subsystem, an inverter is connected to the external system *via* an equivalent reactance, which is an eigenvalue of matrix daisy-chain connection, ρ_i, as shown in Figure 2.

For the case of M similar inverters in parallel connection studied in Du et al. (2020b), M dynamically independent subsystems are obtained after state transformation. Each of the first $(M-1)$ subsystems is a standalone inverter. The M^{th} subsystem comprised an inverter being connected to the external system *via* an equivalent reactance, which is equal to the product of the number of inverters and x_L, that is, Mx_L. Subsequently, the M^{th} subsystem can be used as the model of aggregated inverter for stability study (Du et al., 2020c). However, in the current case of inverters in daisy-chain connection, each of the M subsystems comprised an inverter being connected to the external system after state transformation. Hence, further analysis is needed to determine which subsystem can be used as the aggregated inverter to represent the cluster of inverters in a daisy-chain connection for stability study as follows.

Denote $\lambda_i, i = 1, 2.\cdots M$ as the oscillation modes of the cluster of similar inverters in daisy-chain connection, that is, the conjugate complex eigenvalues of state matrix, $\boldsymbol{A}_p + \rho_i \boldsymbol{A}_n, i = 1, 2, \cdots M$. A matrix with a variable ρ can be defined as $\boldsymbol{A}_p + \rho \boldsymbol{A}_n$. Denote λ as a complex conjugate eigenvalue of $\boldsymbol{A}_p + \rho \boldsymbol{A}_n$. Furthermore, the following sensitivity index (SI) is defined:

$$SI_i = \left.\frac{\partial \lambda}{\partial \rho}\right|_{\substack{\lambda=\lambda_i \\ \rho=\rho_i}} = \frac{\boldsymbol{w}_i^T \boldsymbol{A}_n \boldsymbol{v}_i}{\boldsymbol{w}_i^T \boldsymbol{v}_i}. \tag{11}$$

where $\boldsymbol{w}_i$ and $\boldsymbol{v}_i$ are, respectively, the left and right eigenvectors of the matrix $\boldsymbol{A}_p + \rho_i \boldsymbol{A}_n, i = 1, 2, \cdots M$ for λ_i.

From Eq. 6, it can be seen that $\boldsymbol{M}_M$ is a symmetrical real matrix with positive elements. Thus, the eigenvalues of $\boldsymbol{M}_M$ are all real positive numbers. Denote $\rho_{\min}$ and $\rho_{\max}$ as the minimum and maximum eigenvalues of $\boldsymbol{M}_M$. Denote $\lambda_{\min}$ and $\lambda_{\max}$ to be the oscillation mode calculated from $\boldsymbol{A}_p + \rho_{\min} \boldsymbol{A}_n$ and $\boldsymbol{A}_p + \rho_{\max} \boldsymbol{A}_n$, respectively. From Eq. 11, it can be seen that if the real part of SI_i is negative for $\rho = \rho_i; \rho_{\min} \le \rho_i \le \rho_{\max}$, real part of eigenvalue of $\boldsymbol{A}_p + \rho \boldsymbol{A}_n$ increases when ρ decreases. Thus, when ρ is the smallest (i.e., $\rho = \rho_{\min}$), the real part of the corresponding eigenvalue of $\boldsymbol{A}_p + \rho \boldsymbol{A}_n$, that is, $\lambda_{\min}$) is of the least damping among $\lambda_i, i = 1, 2.\cdots M$. The possible smallest value of ρ_i is zero, that is, $\rho_{\min} = 0$. Hence, the damping of $\lambda_{\min}$ could be equal to the damping of the same type of oscillation mode of the standalone inverter, that is, the conjugate complex eigenvalue of the matrix $\boldsymbol{A}_p$. Because the standalone inverter is

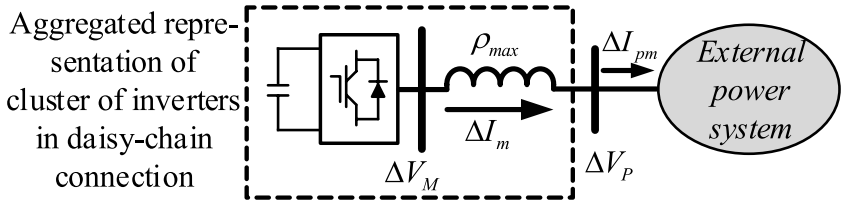

FIGURE 3
Aggregated representation for studying oscillatory stability of a cluster of similar inverters in a daisy-chain connection.

stable, $\lambda_{\min}$ should be of sufficient damping and is thus not a concern for oscillation stability analysis. Hence, if the real part of SI_i is negative, there is no instability risk of the cluster of inverters in the daisy-chain connection.

However, if the real part of SI_i is positive, $\lambda_{\max}$ is of the poorest damping among $\lambda_i, i = 1, 2.\cdots M$. Hence, for detecting the instability risk of the cluster of inverters in daisy-chain connection, only the complex conjugate eigenvalues of $\boldsymbol{A}_p + \rho_{\max}\boldsymbol{A}_n$ need to be calculated. This implies that if and only if the subsystem displayed in Figure 2 with the state matrix of $\boldsymbol{A}_p + \rho_{\max}\boldsymbol{A}_n$ is stable, the cluster of inverters in the daisy-chain connection is stable. Hence, the subsystem with the state matrix $\boldsymbol{A}_p + \rho_{\max}\boldsymbol{A}_n$ should be used as the aggregated representation for the stability study. The subsystem is the aggregated inverter of the cluster of similar inverters in the daisy-chain connection, as shown in Figure 3. This aggregated inverter in Figure 3 is referred to as the aggregated representation of the cluster of similar inverters in daisy-chain connection for studying the risk of oscillatory instability.

From Eqs 9 and 10 and Figure 3, the linearized model of the proposed aggregated representation can be written as follows:

$$\begin{aligned} \frac{d}{dt}\Delta\boldsymbol{Z}_m &= \left(\boldsymbol{A}_p + \rho_{\max}\boldsymbol{A}_n\right)\Delta\boldsymbol{Z}_m + v_m\boldsymbol{B}_p\Delta\boldsymbol{V}_p \\ \Delta\boldsymbol{I}_{pm} &= v_m\boldsymbol{C}_p\Delta\boldsymbol{Z}_m \end{aligned}, \tag{12}$$

where v_m is the sum of the eigenvector of $\boldsymbol{M}_M$ for $\rho_{\max}$.

The linearized model of the external system can be expressed as follows:

$$\begin{aligned} \frac{d}{dt}\Delta\boldsymbol{Z}_e &= \boldsymbol{A}_e\Delta\boldsymbol{Z}_e + \boldsymbol{B}_e\Delta\boldsymbol{I}_{pm} \\ \Delta\boldsymbol{V}_p &= \boldsymbol{C}_e\Delta\boldsymbol{Z}_e + \boldsymbol{D}_e\Delta\boldsymbol{I}_{pm} \end{aligned}. \tag{13}$$

Thus, from Eqs 12 and 13, the linearized model of the entire power system in Figure 1 can be established as

$$\frac{d}{dt}\Delta\boldsymbol{Z} = \boldsymbol{A}\Delta\boldsymbol{Z}, \tag{14}$$

where $\boldsymbol{A} = \begin{bmatrix} \boldsymbol{A}_p + \rho_{\max}\boldsymbol{A}_n + v_m^2\boldsymbol{B}_p\boldsymbol{D}_e\boldsymbol{C}_p & v_m\boldsymbol{B}_p\boldsymbol{C}_e \\ v_m\boldsymbol{B}_e\boldsymbol{C}_p & \boldsymbol{A}_e \end{bmatrix}$.

The aggregated inverter in the case of inverters in daisy-chain connection is different to that derived from Du et al. (2020a) for the case of inverters in parallel connection as the lumped reactance for the two cases is different. The difference is due to the fact that two different forms of state transformation are applied for two different cases of inverters' connection. A further examination of the difference is conducted as follows.

Assume that the cable that connects the cluster of inverters in the daisy-chain connection to the external system in Figure 1 is much longer than the cables inside the cluster, that is, $x_L \gg \sum_{i=1}^{N} x_i$ in Eq. 6. In this case, x_i is ignored such that the inverters in the daisy-chain connection become approximately parallel connections as all the inverters are connected to a common point at the terminal of a cluster in Figure 1. With ignorance of x_i, it can be seen from Eq. 6 that the matrix of daisy-chain connection approximately becomes,

$$\boldsymbol{M}_M \approx \begin{bmatrix} x_L & x_L & \cdots & x_L \\ x_L & x_L & \cdots & x_L \\ \vdots & \cdots & \ddots & \vdots \\ x_L & x_L & \cdots & x_L \end{bmatrix} \tag{15}$$

.

It is easy to prove that $\rho_i = 0$, $(i = 1, 2, ..., M-1)$ and $\rho_M = Mx_L$ which is $\rho_{\max}$. Subsequently, the lumped reactance in the aggregated inverter shown in Figure 3 is that for the inverters in parallel connection.

Therefore, the analysis above indicates that the state transformation and the aggregated inverter derived from Du et al. (2020b) are just a special example of those in the current study about similar inverters in daisy-chain connection. Analysis and conclusions obtained from the special example in Du et al. (2020c) cannot be simply extended to the case of inverters in daisy-chain connection. Hence, the total impact of inverters in daisy-chain connection about how the inverters may collectively cause instability risk needs to be investigated as to be presented in the following subsection.

2.4 Impact of increasing number of inverters

First, the following theorem is introduced:

the Cauchy interlace theorem (Mercer and Mercer, 2000). Let $\boldsymbol{M}_{M+1}$ be a Hermitian matrix of order $M+1$, and $\boldsymbol{M}_M$ be a

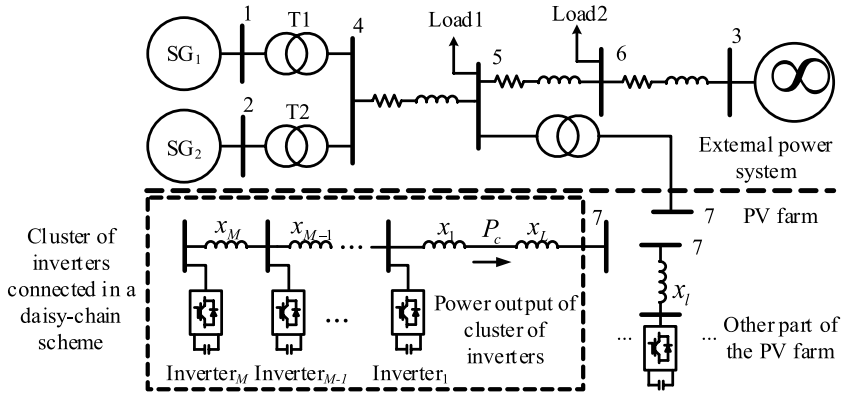

FIGURE 4
An example power system with a grid-connected PV power generation farm.

TABLE 1 Oscillation modes of the cluster of five inverters in daisy-chain connection (case study 1).

Type of mode	Aggregated representation	Full-order model	CWMV model
d-axis CCIL	−14.24 + 723.12j	−14.25 + 723.11j	−15.87 + 723.50j
q-axis CCIL	−20.04 + 580.31j	−20.04 + 580.29j	−20.04 + 579.84j
VDC	−9.37 + 232.78j	−9.37 + 232.74j	−10.57 + 236.62j
PLL	−6.94 + 199.69j	−6.94 + 199.64j	−6.95 + 198.27j

(CCIL, current control inner loop of inverter; VDC, DC voltage control outer loop of inverter; PLL, phase-locked loop; CWMV model, aggregated model derived by using the capacity-weighted mean value method).

principal submatrix of $\boldsymbol{M}_{M+1}$ of order M. If $\mu_1 \le \mu_2 \le \cdots \le \mu_M \le \mu_{M+1}$ are the eigenvalues of $\boldsymbol{M}_{M+1}$ and $\rho_1 \le \rho_2 \le \cdots \le \rho_{M-1} \le \rho_M$ are the eigenvalues of $\boldsymbol{M}_M$, then

$$\mu_1 \le \rho_1 \le \mu_2 \le \rho_2 \le \cdots \le \rho_{M-1} \le \mu_M \le \rho_M \le \mu_{M+1}. \tag{16}$$

Second, consider that one more inverter is connected at the end of the daisy chain in Figure 1. According to the definition of the matrix of daisy-chain connection given in Eq. 6,

$$\boldsymbol{M}_{M+1} = \begin{bmatrix} \boldsymbol{M}_M & \boldsymbol{b}^T \\ \boldsymbol{b} & x_L + \sum_{i=1}^{M+1} x_i \end{bmatrix}, \tag{17}$$

where $\boldsymbol{b} = [\, x_L + x_1 \;\; x_L + \sum_{i=1}^{2} x_i \;\; \cdots \;\; x_L + \sum_{i=1}^{M} x_i \,]$.

From Eqs 6 and 17, it can be seen that the matrix $\boldsymbol{M}_M$ defined in Eq. 6 is a principal submatrix of $\boldsymbol{M}_{M+1}$ in Eq. 17. In addition, $\boldsymbol{M}_{M+1}$ is symmetrical and is thus a Hermitian matrix. Hence, according to the Cauchy interlace theorem, the maximum eigenvalue of the matrix of daisy-chain connections increases when one more inverter is connected in the daisy chain in Figure 1.

Finally, according to the analysis conducted in the previous subsection, it is known that when $\rho_{\max}$ increases, possible instability risk as caused by the cluster of similar inverters in a daisy-chain connection also increases. Hence, it can be concluded that in the case of inverters in a daisy-chain connection, it is possible that the oscillatory instability may be induced collectively by the inverters.

3 An example power system with a grid-connected photovoltaic power generation farm

Figure 4 shows the configuration of an example power system with a grid-connected PV power generation farm. In the PV farm, a cluster of inverters is in a daisy-chain connection. The AC power system consists of two synchronous generators (SG_1 and SG_2) connected to an infinite busbar. The 20th-order model recommended for subsynchronous oscillation studies in Padiyar (1996) is adopted for SG_1 and SG_2, with the parameters adjusted in line with their capacities. On the basis of previous work (Du et al., 2020a), the inverter adopts an 8th-order model, including DC capacitance voltage (1-order), control system (3-order), filter reactance (2-order), and PLL (2-order). The relevant parameters are shown in Supplementary Appendix S1B. P_c denotes the active power output from the cluster of inverters.

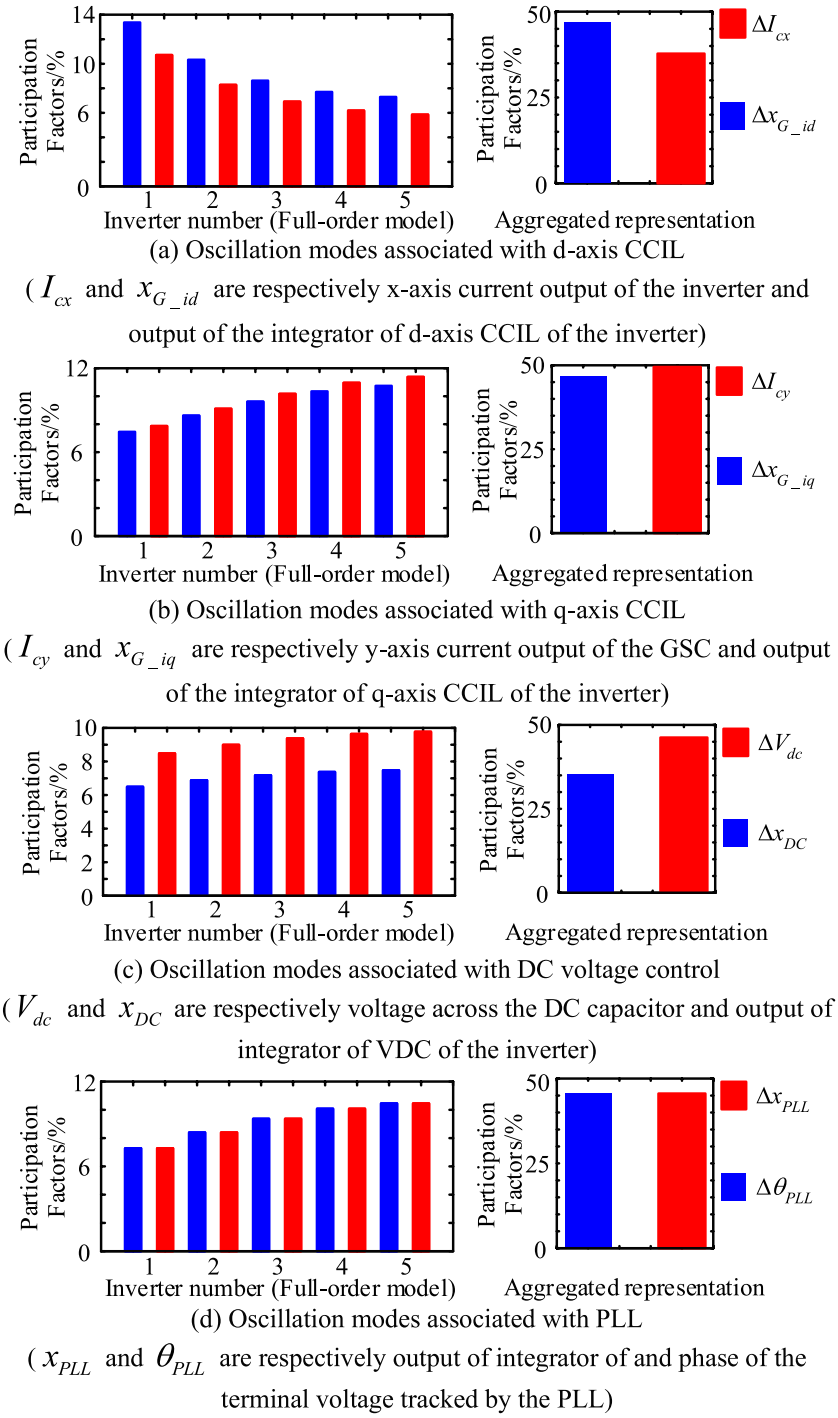

FIGURE 5
Computational results of participation factors (case study 1). **(A)** Oscillation modes associated with d-axis CCIL (I_{cx} and x_{G_id} are, respectively, the *x*-axis current output of the inverter and output of the integrator of d-axis CCIL of the inverter). **(B)** Oscillation modes associated with q-axis CCIL (I_{cy} and x_{G_iq} are, respectively, the *y*-axis current output of the GSC and output of the integrator of q-axis CCIL of the inverter). **(C)** Oscillation modes associated with DC voltage control (V_{dc} and x_{DC} are, respectively, the voltage across the DC capacitor and output of integrator of VDC of the inverter). **(D)** Oscillation modes associated with PLL (x_{PLL} and θ_{PLL} are, respectively, the output of integrator and phase of the terminal voltage tracked by the PLL).

TABLE 2 Computational results of sensitivity index.

ρ_i	PLL mode	DC mode
1.5	0.52–2.00j	−0.26 + 1.35j
3.5	2.94–25.12j	−2.15 + 10.13j
5.5	5.15–57.42j	−3.72 + 22.41j

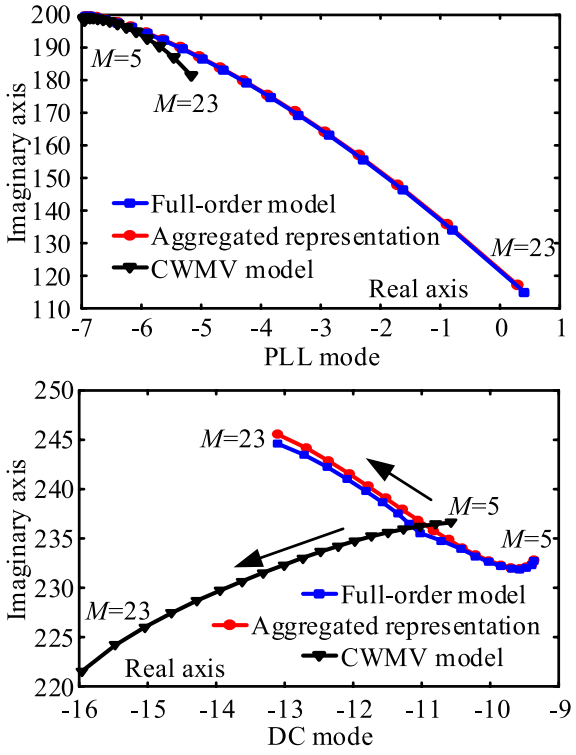

FIGURE 6
Trajectories of oscillation modes as M increased (case study 2, CWMV model, aggregated model derived by using the capacity-weighted mean value method).

3.1 Case study 1: Aggregated representation

Initially, there are five inverters in the cluster of daisy-chain connections, that is, $M = 5$. At steady state, the power factor of each inverter is 0.98 with the active power output being 0.1 p.u. The parameters of the inverters and the converter control systems are the same. However, steady-state terminal voltages of the inverters are different (otherwise, there will be no load flow in the cluster). Hence, linearized models of five inverters in the cluster are slightly different instead of being identical. Analysis of the aggregated representation of a cluster of inverters in a daisy-chain connection is evaluated as follows.

First, the fifth inverter in the cluster, that is, inverter$_5$ is selected to represent the other four inverters in the cluster, that is,

$$(\boldsymbol{A}_i, \boldsymbol{B}_i, \boldsymbol{C}_i) = \left(\boldsymbol{A}_p, \boldsymbol{B}_p, \boldsymbol{C}_p\right) = (\boldsymbol{A}_5, \boldsymbol{B}_5, \boldsymbol{C}_5), i = 1, 2, 3, 4.$$

Second, the matrix of daisy-chain connections defined by Eq. 6 is derived, and its eigenvalues are calculated to be $\rho_1 = 0.0028$, $\rho_2 = 0.0038$, $\rho_3 = 0.0072$, $\rho_4 = 0.025$, and $\rho_5 = \rho_{\max} = 1.1112$.

Thus, the aggregated representation of the cluster of five inverters, shown in Figure 3, is obtained to be $(\boldsymbol{A}_p, \boldsymbol{B}_p, \boldsymbol{C}_p, \rho_{\max})$. Oscillation modes are computed from the state matrices of the aggregated representation, $\boldsymbol{A}_p + \rho_{\max}\boldsymbol{A}_n$. The 12th-order model of inverter is used, that is, $N = 12$, and hence there are twelve state variables in the aggregated representation. According to the results of the study reported in the literature, oscillatory instability of inverter is often related to the oscillation modes of the control system of the inverter and the PLL (Kroutikova et al., 2007; Wen et al., 2015; Peng and Yang, 2020). Hence, in the 2nd column of Table 1, only four oscillation modes are listed, which are associated with the *d*-axis and *q*-axis current control inner loops, the DC voltage control outer loop of the inverter, and the PLL of the inverter in the aggregated representation, respectively. Those associations, referred to as the type of oscillation mode in Table 1, can be identified by calculating the participation factors of the oscillation modes. Hence, from the right and left eigenvectors of $\boldsymbol{A}_p + \rho_{\max}\boldsymbol{A}_n$ (state matrix of aggregated representation) corresponding to the oscillation modes, participation factors of each of the oscillation modes are calculated to identify the types of oscillation modes. For example, if the participation factors of state variables of the PLL corresponding to one particular oscillation mode are the largest, the oscillation mode is identified as being associated with the PLL.

Third, for validation, a full-order model of the cluster of five inverters, as described in Eq. 3, is established, in which linearized models of the inverters are similar but slightly different. Oscillation modes are computed from the state matrix of the full-order model, $\boldsymbol{A}_X$ given in Eq. 5. Of all the computational results, the modes with the poorest damping for each type of oscillation mode are identified and are listed in the 3rd column of Table 1. Again, types of oscillation modes are identified by calculating the participation factors of oscillation modes being computed by using $\boldsymbol{A}_X$. By comparing the computational results in the 2nd and 3rd columns, it can be seen that the aggregated representation obtained provides a good approximation of the cluster of five inverters in the daisy-chain connection in the example power system for stability study, thus confirming the correctness of the analysis and derivation of aggregated representation presented in the previous section.

Participation factors of the oscillation modes are presented in Figure 5.

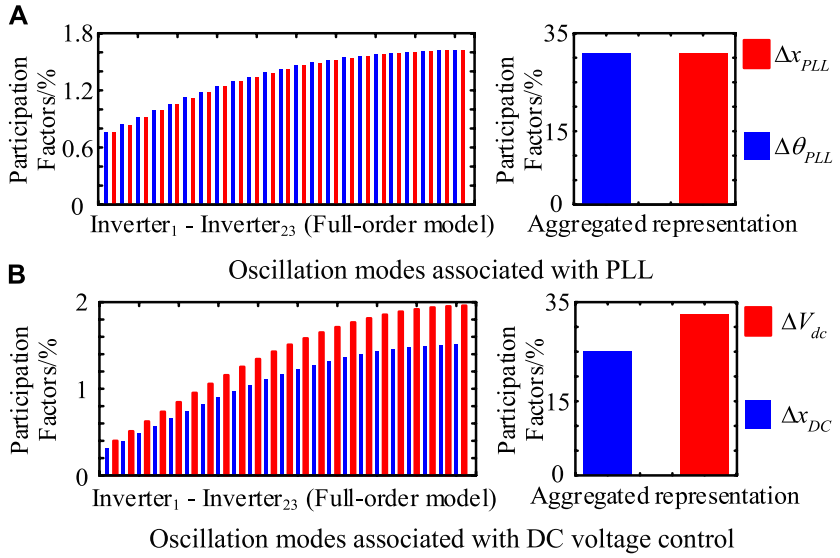

FIGURE 7
Computational results of participation factors (case study 2, M = 23). **(A)** Oscillation modes associated with PLL. **(B)** Oscillation modes associated with DC voltage control.

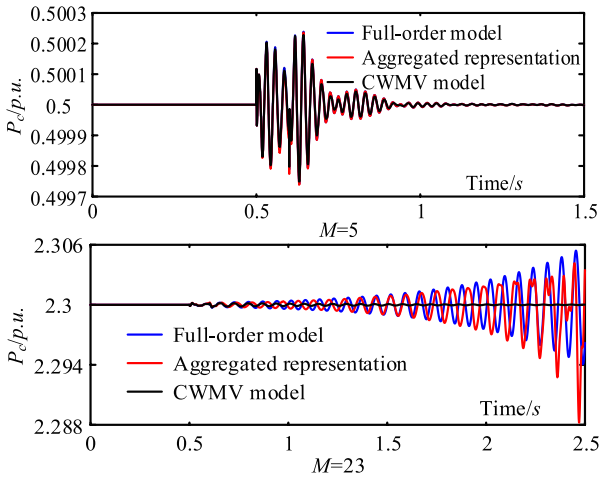

FIGURE 8
Non-linear simulation results (case study 2, CWMV model, aggregated model derived by using the capacity-weighted mean value method).

Finally, for comparison, the capacity-weighted mean value method (Zou et al., 2015; Zhou et al., 2018) is applied to derive an aggregated model of the cluster of five inverters in the daisy-chain connection in the example power system. Oscillation modes are computed by using the aggregated model derived by using the capacity-weighted mean value method. Computational results are listed in the 4th column of Table 1. From Table 1, it is obvious that the aggregated representation proposed in the previous section gives more accurate results in stability assessment than the aggregated model derived by using the capacity-weighted mean value method.

3.2 Case study 2: Increasing number of inverters

By using the aggregated representation obtained earlier, the sensitivity index defined by Eq. 11 is computed for the oscillation modes with variation in the value of ρ_i. Due to the limitation of space, only the computational results for the oscillation modes associated with the PLLs (PLL mode) and DC voltage control outer loops (DC mode) are given in Table 2. According to the analysis described in the previous section and Table 2, it is expected that with an increase in the number of inverters in the daisy-chain connection, the PLL mode would move to the right on the complex plane with reduced damping, and the DC mode would move to the left with enhanced damping.

To evaluate this prediction, oscillation modes are computed by using the aggregated representation shown in Figure 3, the full-order model of Eq. 3, and the aggregated model derived by using the capacity-weighted mean value method. Results of modal computation with variation of the number of inverters in daisy-chain connection in the example power system give the trajectories of the PLL mode and DC mode presented in Figure 6. When more inverters are connected in the daisy chain in the PV farm, the same number of inverters in the other part of the PV

TABLE 3 Oscillation modes of the cluster of five inverters in daisy-chain connection (case study 3).

Type of mode	Aggregated representation	Full-order model	CWMV model
d-axis CCIL	−14.24 + 723.12j	−13.19 + 695.99j	−15.87 + 723.50j
q-axis CCIL	−20.04 + 580.31j	−17.76 + 547.30j	−20.04 + 579.84j
VDC	−9.37 + 232.78j	−8.48 + 221.02j	−10.57 + 236.62j
PLL	−6.94 + 199.69j	−6.26 + 188.14j	−6.95 + 198.27j

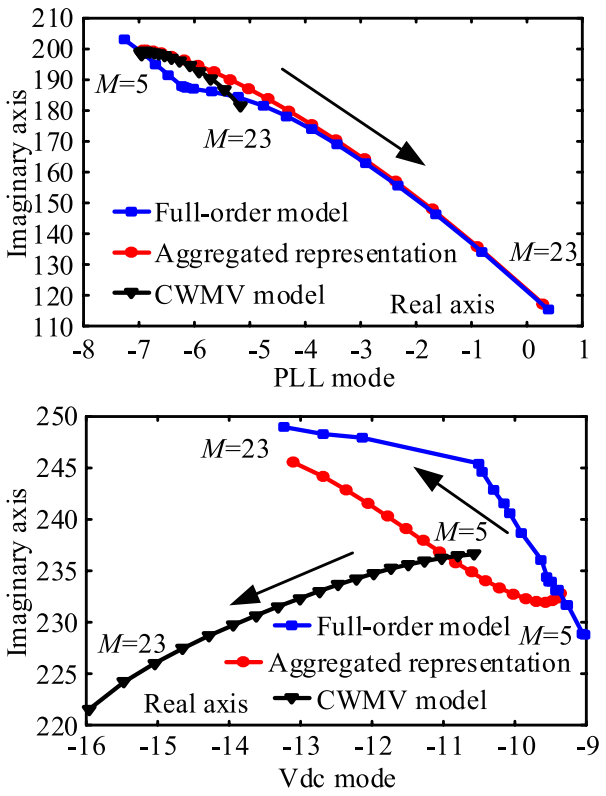

FIGURE 9
Trajectories of oscillation modes as M increases (case study 3).

farm is withdrawn from the operation. In order to exclude the impact of dynamics of the PVs in the other part of the PV farm, the PVs in the other part are modeled as constant power sources. Subsequently, the impact of a varied number of PVs is that dynamic interactions between the PVs and the steady-state power generation from the PV farm remain unchanged. The following observations can be made from Figure 6.

1) The PLL mode moves toward the right on the complex plane as the number of inverters in the daisy-chain connection increases. When 23 inverters are in daisy-chain connection, ρ_{max} = 6.5821; the PLL mode moves into the right half of the complex plane, resulting in oscillatory instability. Damping of the DC mode is improved when the number of inverters in the daisy-chain connection increases. This confirms the abovementioned prediction and the correctness of the analytical conclusion drawn in the previous section: instability risk can be induced collectively by all the inverters in the daisy-chain connection.
2) The computational results obtained using aggregated representation are more accurate than those using the aggregated model from the capacity-weighted mean value method. The latter in fact fails to identify the oscillatory instability when the number of inverters in the daisy-chain connection is increased, indicating that the aggregated model derived by using the capacity-weighted mean value method is not applicable for the stability assessment in this case study.

Participation factors of the oscillation modes are presented in Figure 7.

Validation by non-linear simulation is given in Figure 8. At 0.5 s of simulation, the active power output over other parts of the PV farm in the example power system decreases by 5% for 0.1 s. From Figure 8, it can be seen that when 23 inverters are in a daisy-chain connection, growing oscillations occur, confirming the conclusion that inverters in a daisy-chain connection may collectively cause oscillatory instability and the effectiveness of the aggregated representation.

3.3 Case study 3: Dynamic models of the inverters are different

In the two study cases presented earlier, the parameters of inverters in daisy-chain connection are the same such that dynamic models of inverters are similar. In this study case, the parameters of inverters in daisy-chain connection are different. Consequently, the dynamic models of inverters in daisy-chain connection in the example power system are different. Evaluation of the analysis and conclusions made in the previous section is carried out as follows.

First, parameters of inverter$_5$ are used as a base. Parameters of the control systems and the PLLs of other

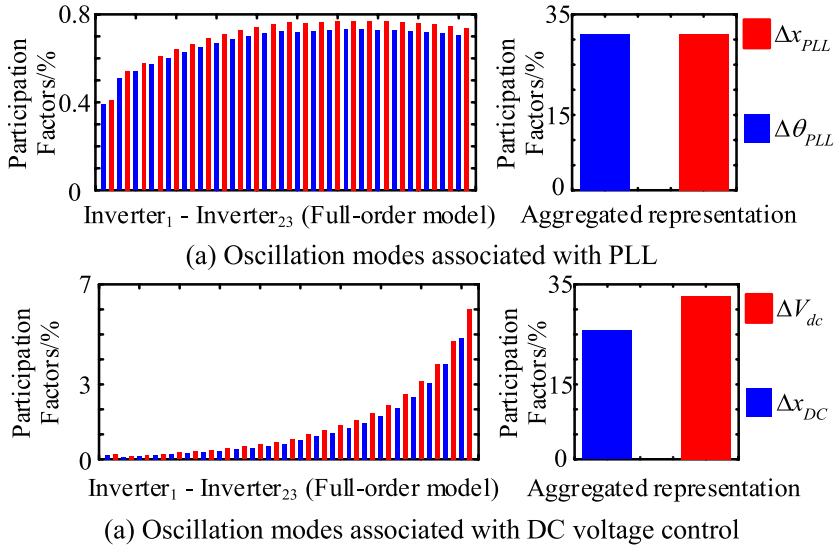

FIGURE 10
Computational results of participation factors (case study 1, M = 23). **(A)** Oscillation modes associated with PLL. **(A)** Oscillation modes associated with DC voltage control.

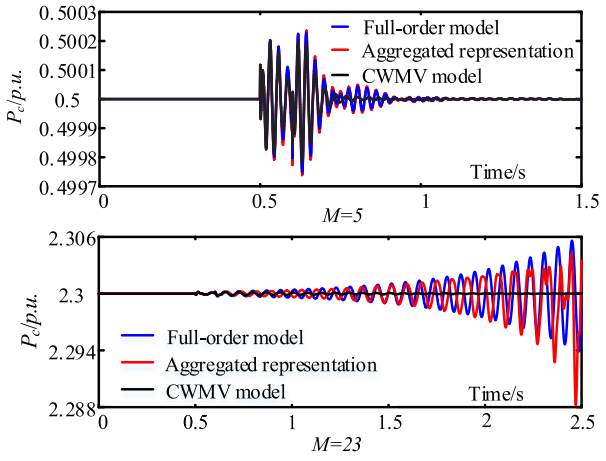

FIGURE 11
Non-linear simulation results (case study 3 similar parameters).

inverters in the daisy-chain connection in the example power system are varied from the base within the limit of ±10%. Subsequently, linearized models of the inverters in the daisy-chain connection are different. Results of modal computation are listed in Table 3. From Table 3, it can be noted that the results from modal computation using the aggregated representation are more accurate than those obtained using the aggregated model derived using the capacity-weighted mean value method, as compared with the results obtained using the full-order model.

Second, the impact of the increasing number of inverters in the daisy-chain connection is evaluated. Because the dynamic model of inverter$_5$ is the same as that in case studies 1 and 2, computational results of the sensitivity index are the same as those given in Table 2. Hence, it is expected that when the number of inverters in the daisy-chain connection increases, damping of PLL mode would decrease and damping of the DC model would increase. Evaluation from modal computation and non-linear simulation are presented in Figures 9, 10, and 11, respectively. The results indicate that although the linearized models of the inverters in the daisy-chain connection are different in this case study, the analysis made under the condition that the linearized models of the inverters are similar is still valid. The small-signal oscillatory stability can be approximately assessed by using the aggregated representation. The increasing number of inverters in daisy-chain connection results in oscillatory instability. This confirms that multiple inverters in a daisy-chain connection may collectively induce instability risk. In addition, the aggregated representation proposed in the article provides more accurate results in stability assessment than the aggregated model derived by using the capacity-weighted mean value method.

Third, when the dynamics of the PVs are similar, the model of any PV in the PV farm can be used as the aggregated model of the PV farm. However, when the dynamics of the PVS are considerably different, the error in assessing the stability by using the aggregated model of the PV farm may be large. This is demonstrated by the following study case.

Parameters of inverter$_5$ remain unchanged. Deviation of values of parameters of other inverters in daisy-chain connection in the

TABLE 4 Oscillation modes of the cluster of five inverters in daisy-chain connection with different parameter settings.

Parameter difference	VDC	Error (%)	PLL	Error (%)
±10%	−9.02 + 228.98j	1.67	−7.32 + 203.01j	1.65
±20%	−7.21 + 203.90j	14.19	−5.57 + 177.51j	12.51
±30%	−6.12 + 186.88j	24.61	−4.88 + 166.19j	20.19
±40%	−4.97 + 167.96j	38.66	−4.19 + 154.08j	29.64
±50%	−3.90 + 147.47j	57.95	−3.51 + 141.24j	41.44

(VDC mode and PLL mode using the aggregated representation, respectively, are −9.37 + 232.78j and −6.94 + 199.69j).

TABLE 5 Oscillation modes of the cluster of twenty-three inverters in daisy-chain connection with different parameter settings.

Parameter difference	VDC	Error (%)	PLL	Error (%)
±10%	−13.23 + 248.98j	1.54	0.39 + 115.25j	1.87
±20%	−12.28 + 256.90j	4.60	0.36 + 110.94j	5.82
±30%	−12.49 + 265.33j	7.61	0.32 + 110.70j	6.05
±40%	−13.19 + 276.76j	11.42	0.24 + 110.15j	6.58
±50%	−14.13 + 287.88j	14.84	0.15 + 106.30j	10.44

(VDC mode and PLL mode using the aggregated representation, respectively, are −13.05 + 245.12j and 0.32 + 117.40j).

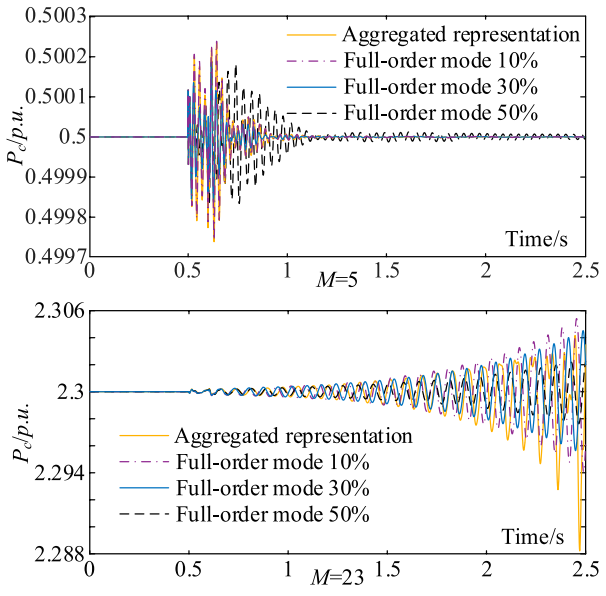

FIGURE 12
Non-linear simulation results (case study 3 different parameters).

example power system from those of inverter$_5$ increases above the limit of ±10%. Since inverter$_5$ is used as the representative of inverters to establish the aggregated model of the example power system. Hence, the results of modal computation and simulation using the aggregated representation of the inverters in the daisy-chain connection are the same as those presented in the second column of Table 3 and Figure 11. When the deviation of parameters of inverters from those of inverter$_5$ is ±20%, ±30%, ±40%, and ±50%, respectively, results of modal computation using the full-order model are presented in Tables 4 and 5, where the error of modal computation is

$$error = \frac{|\lambda_1 - \lambda_2|}{|\lambda_1|}, \tag{18}$$

where λ_1 and λ_2 are, respectively, the oscillation mode obtained from the full-order model and the aggregated representation. VDC and PLL are, respectively, the DC mode and PLL mode.

Results of the simulation are given in Figure 12.

From Tables 4 and 5 and Figure 12, it can be seen that when the deviation of parameters of inverters is within ±10%, the error to assess the stability between using the aggregated representation and using the full-order model is 1%~2%, which is acceptable. However, when the deviation is over ±20% or more, the error is more than 5%, when the aggregated representation might not be acceptable.

3.4 Case study 4: External oscillation stability

In the study cases presented earlier, oscillatory stability of the cluster of inverters in a daisy-chain connection is examined. In the examination, the cluster of inverters is not connected to the external system. Hence, the

TABLE 6 External oscillation modes of the example power system (case study 4).

	Aggregated representation	Full-order model	CWMV model
Torsional modes of SG_1	−2.44 + 324.62j	−2.44 + 324.62j	−2.44 + 324.62j
	−2.30 + 309.96j	−2.30 + 309.96j	−2.30 + 309.96j
	−1.85 + 208.75j	−1.85 + 208.75j	−1.85 + 208.75j
	1.12 + 158.13j	**1.03 + 157.89j**	**0.35 + 156.99j**
	−1.59 + 111.95j	−1.59 + 111.95j	−1.58 + 111.96j
Torsional modes of SG_2	−1.33 + 276.86j	−1.33 + 276.86j	−1.33 + 276.86j
	−1.06 + 294.55j	−1.06 + 294.55j	−1.06 + 294.55j
	−1.50 + 188.03j	−1.50 + 188.03j	−1.49 + 188.03j
	−0.73 + 142.28j	−0.73 + 142.28j	−0.74 + 142.28j
	−0.94 + 98.41j	−0.94 + 98.41j	−0.94 + 98.41j
Oscillation modes of inverters in daisy-chain connection	−19.67 + 719.06j	−14.84 + 725.20j	−25.31 + 719.95j
	−22.40 + 585.00j	−21.23 + 593.56j	−22.50 + 583.11j
	−8.72 + 235.76j	−9.08 + 230.04j	−11.55 + 235.47j
	−3.72 + 159.49j	−3.77 + 159.00j	−3.50 + 157.18j

Aggregated representation, model using the aggregated representation state matrices. Full-order model, model using a full-order state-space. CWMV model, aggregated model derived by using the capacity-weighted mean value method.

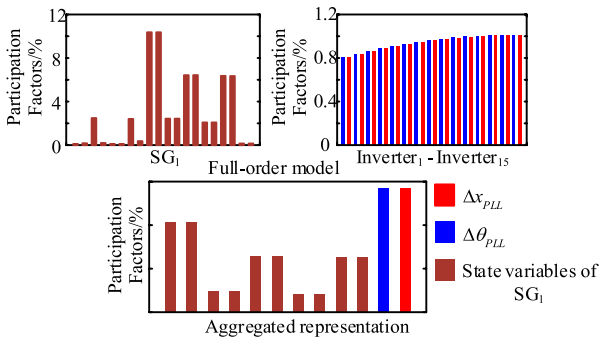

FIGURE 13
Computational results of participation factors (case study 4).

examination is about the stability of the cluster of inverters as an open-loop subsystem. The examination is important because the instability of the cluster of the inverters shall cause the entire system to become unstable when the inverters are connected to the external system.

In this subsection, oscillatory stability with the cluster of inverters in the daisy-chain connection being connected to the external system is assessed. The assessment is about the stability of the entire system integrated with the cluster of the inverters. For the assessment, aggregated representation proposed in the previous section, the full-order model, and the aggregated model derived by using the capacity-weighted mean value method for the cluster of inverters in the daisy-chain connection are compared.

When the number of cluster of inverters in the cluster is 15, the cluster of inverters in the daisy-chain connection is stable before being connected to the external system, as being indicated by previous study cases. After the cluster of 15 inverters is connected to the external system, the aggregated representation of the cluster of inverters shown in Figure 3 is used to establish the state-space model of the entire example power system depicted by Eq. 14. Afterward, from the state matrix, $\boldsymbol{A}$, oscillation modes of the example power system are calculated. In Table 6, selected oscillation modes of the example power system are presented in the 2nd column of Table 6. It can be seen that one oscillation mode associated with the torsional system of SG_1 is unstable. Hence, growing subsynchronous oscillations are expected to occur in the example power system.

For confirmation, the full-order model of a cluster of 15 inverters in a daisy-chain connection is derived and

TABLE 7 Torsional oscillation mode of SG_1 when M decreases (case study 4).

M	Aggregated representation	Full-order model	CWMV model
15	1.12 + 158.13j	1.03 + 157.89j	0.35 + 156.99j
14	0.43 + j158.88	0.43 + j158.88	−0.31 + j158.66
13	−0.08 + j158.87	−0.08 + j158.88	−0.36 + j158.64

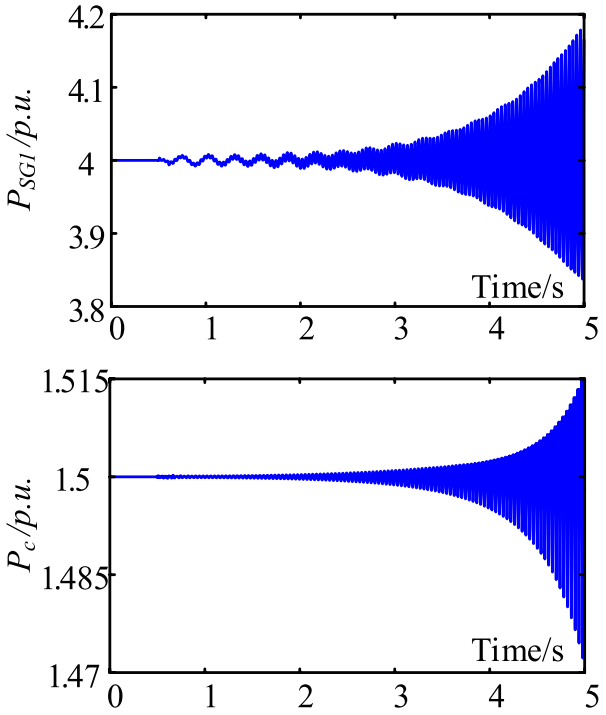

FIGURE 14
Non-linear simulation results (case study 4, full-order model used).

integrated with the model of the external system. Subsequently, a full-order model of the entire example power system with the PV power generation farm is established. Results of modal computation are presented in the 3rd column of Table 6. It can be seen that the example power system is unstable, confirming the correctness of the assessment made by using the aggregated representation proposed.

Furthermore, the participation factors of the unstable torsional oscillation mode of SG_1, 1.12 + 158.13j, are computed. Computational results are presented in Figure 13. It can be seen that the unstable torsional oscillation mode is associated with all 15 inverters in the daisy-chain connection. This confirms that the oscillatory instability is caused collectively by the cluster of inverters in the daisy-chain connection.

For confirmation, the full-order model of a cluster of 15 inverters in a daisy-chain connection is derived and integrated with the model of the external system. Subsequently, a full-order model of the entire example power system with the PV power generation farm is established. Results of modal computation are presented in the 3rd column of Table 4. It can be seen that the example power system is unstable, confirming the correctness of the assessment made by using the aggregated representation proposed.

Furthermore, the participation factors of the unstable torsional oscillation mode of SG_1, 1.12 + 158.13j, are computed. Computational results are presented in Figure 12. It can be seen that the unstable torsional oscillation mode is associated with all 15 inverters in the daisy-chain connection. This confirms that the oscillatory instability is caused collectively by the cluster of inverters in the daisy-chain connection.

Computational results of the unstable torsional oscillation mode of SG_1 with the change in the number of inverters in daisy-chain connection (M) are presented in Table 7. It can be seen that when M is reduced to 13, the example power system is stable. However, when $M = 14$, the example power system is unstable. The CWMV model fails to identify the danger of oscillation instability of the example power system in this case.

Results of validation by non-linear simulation using the full-order model are given in Figure 14.

4 Conclusion

This study examines the total impact of a cluster of similar inverters in a daisy-chain connection, which is one of the most common basic configurations of PV power collecting network on the small-signal stability of a grid-connected PV power generation farm. The main conclusions and contributions made by the study are as follows:

1) An aggregated representation of the cluster of similar inverters in daisy-chain connection is derived for the stability study based on the dynamic equivalence. Hence, the derivation confirms the rationality of representing the cluster of similar inverters in daisy-chain connection by an aggregated inverter connected to the external grid *via* a lumped reactance.
2) Analysis is carried out to indicate that the cluster of similar inverters in the daisy-chain connection may collectively induce the growing oscillations in the PV farm. The analysis is carried out to indicate that the cluster of similar inverters in the daisy-chain connection may collectively induce the growing oscillations in the PV farm. Subsequently, an increasing number of inverters in the daisy-chain connection may increase the instability risk, although the total steady-state active power output from the grid-connected PV farm remains unchanged.
3) General topology of the power collecting network of a grid-connected PV farm is radial, with a combination of two basic configurations: daisy-chain connection and parallel connection. The article extends the pioneering study by Du et al. (2020c), which was about the total impact of inverters in a parallel connection.

Further study on the total impact of the increasing number of inverters on the small-signal stability of PV farms in the near future may be in two folds. First, it is the extension of stability analysis to the case of the general radial topology of the PV power collecting network. Second, it is the total impact when the dynamics of inverters are different.

There are two kinds of methods to tackle the instability risk. The first one is to tune the parameters of the PVs in the PV farm. The second is to assign damping controllers on the PVs or/and the PV farm. Both methods have been investigated in the literature. Hence, following-on work to be carried out in the near future will be the examination of applying those two methods to mitigate the instability risk brought about by the daisy-chain connection of PVs in the PV farm.

Data availability statement

The original contributions presented in the study are included in the article/Supplementary Material; further inquiries can be directed to the corresponding author.

Author contributions

YZ proposed this research direction and assigned the work. JC determined the research method and completed the main work. The rest of the work was carried out by JZ.

Funding

This work is supported by TBEA Science and Technology Investment Co., Ltd. "Research on modeling and broadband oscillation suppression of large-scale renewable energy bases (including pure photovoltaics) (TBEA-KJTZ-ZYYJ-2022-019)."

Conflict of interest

Authors YZ, JC, and JZ were employed by TBEA Science and Technology Investment Co., Ltd.

Publisher's note

All claims expressed in this article are solely those of the authors and do not necessarily represent those of their affiliated organizations, or those of the publisher, the editors, and the reviewers. Any product that may be evaluated in this article, or claim that may be made by its manufacturer, is not guaranteed or endorsed by the publisher.

References

Agorreta, J. L., Borrega, M., López, J., and Marroyo, L. (2011). Modeling and control of *N*-paralleled grid-connected inverters with LCL filter coupled due to grid impedance in PV plants. *IEEE Trans. Power Electron.* 26 (3), 770–785. doi:10.1109/TPEL.2010.2095429

Ali, M. N., Mahmoud, K., Lehtonen, M., and Darwish, M. M. (2021). An efficient fuzzy-logic based variable-step incremental conductance MPPT method for grid-connected PV systems. *IEEE Access* 9, 26420–26430. doi:10.1109/ACCESS.2021.3058052

Callegaro, L., Rojas, C. A., Ciobotaru, M., and Fletcher, J. E. (2022). A controller improving photovoltaic voltage regulation in the single-stage single-phase inverter. *IEEE Trans. Power Electron.* 37 (1), 354–363. doi:10.1109/TPEL.2021.3100530

Du, W., Dong, W. K., Wang, H., and Cao, J. (2019). Dynamic aggregation of same wind turbine generators in parallel connection for studying oscillation stability of a wind farm. *IEEE Trans. Power Syst.* 34 (6), 4694–4705. doi:10.1109/TPWRS.2019.2920413

Du, W., Zheng, K. Y., and Wang, H. F. (2020a). Instability of a DC microgrid with constant power loads caused by modal proximity. *IET Generation, Transm. Distribution* 14 (5), 774–785. doi:10.1049/iet-gtd.2019.0696gtd.2018.6940

Du, W., Fu, Q., and Wang, H. F. (2020b). Stability of small-gain closed-loop system and its applications in VSC-based DC/AC power systems. *Electr. Power Components Syst.* 47 (18), 1610–1622. doi:10.1080/15325008.2019.1689455

Du, W., Ma, Z., Wang, Y., and Wang, H. F. (2020c). Harmonic oscillations in a grid-connected PV generation farm caused by increased number of parallel-connected PV generating units and damping control. *CSEE JPES.* 1–9. doi:10.17775/CSEEJPES.2020.02790

Du, W., Dong, W. K., Wang, Y., and Wang, H. F. (2021a). Small-disturbance stability of a wind farm with virtual synchronous generators under the condition of weak grid connection. *IEEE Trans. Power Syst.* 36 (6), 5500–5511. doi:10.1109/TPWRS.2021.3080700

Du, W., Wang, Y., Wang, H. F., Yu, J., and Xiao, X. Y. (2021b). Collective impact of multiple doubly fed induction generators with similar dynamics on the oscillation stability of a grid-connected wind farm. *IEEE Trans. Power Deliv.* 36 (5), 2942–2954. doi:10.1109/TPWRD.2020.3030645

Du, W., Wang, Y., Wang, H. F., and Xiao, X. Y. (2021c). Reduced-order method for detecting the risk and tracing the sources of small-signal oscillatory instability in a power system with a large number of wind farms. *IEEE Trans. Power Syst.* 36 (2), 1563–1582. doi:10.1109/TPWRS.2020.3020041

Fu, Q., Du, W., and Wang, H. F. (2020). Planning of the DC system considering restrictions on the small-signal stability of EV charging stations and comparison between series and parallel connections. *IEEE Trans. Veh. Technol.* 69 (10), 10724–10735. doi:10.1109/TVT.2020.3006480

Guo, X., Yang, Y., Wang, B., and Blaabjerg, F. (2018). Leakage current reduction of three-phase Z-source three-level four-leg inverter for transformerless PV system. *IEEE Trans. Power Electron.* 34 (7), 6299–6308. doi:10.1109/TPEL.2018.2873223

Harnefors, L., Bongiorno, M., and Lundberg, S. (2007). Input-admittance calculation and shaping for controlled voltage-source converters. *IEEE Trans. Ind. Electron.* 54 (6), 3323–3334. doi:10.1109/TIE.2007.904022

Harnefors, L. (2007). Analysis of subsynchronous torsional interaction with power electronic converters. *IEEE Trans. Power Syst.* 22 (1), 305–313. doi:10.1109/TPWRS.2006.889038

Huang, Y., Yuan, X., Hu, J., and Zhou, P. (2015). Modeling of VSC connected to weak grid for stability analysis of DC-link voltage control. *IEEE J. Emerg. Sel. Top. Power Electron.* 3 (4), 1193–1204. doi:10.1109/JESTPE.2015.2423494

Kroutikova, N., Hernandez-Aramburo, C. A., and Green, T. C. (2007). State-space model of grid-connected inverters under current control mode. *IET Electr. Power Appl.* 1 (3), 329–338. doi:10.1049/iet-epa:20060276

Liu, S., Liu, P. X., and Wang, X. (2016). Stability analysis of grid-interfacing inverter control in distribution systems with multiple photovoltaic-based distributed generators. *IEEE Trans. Ind. Electron.* 63 (12), 7339–7348. doi:10.1109/TIE.2016.2592864

Majumder, R., and Bag, G. (2014). Parallel operation of converter interfaced multiple microgrids. *Int. J. Electr. Power & Energy Syst.* 55, 486–496. doi:10.1016/j.ijepes.2013.09.008

Malik, S. M., Sun, Y., Ai, X., Chen, Z., and Wang, K. (2019). Small-signal analysis of a hybrid microgrid with high PV penetration. *IEEE Access* 7, 119631–119643. doi:10.1109/ACCESS.2019.2937123

Mercer, A. M., and Mercer, P. R. (2000). Cauchy's interlace theorem and lower bounds for the spectral radius. *Int. J. Math. Math. Sci.* 23 (8), 563–566. doi:10.1155/s016117120000257x

Moradi-Shahrbabak, Z., and Tabesh, A. (2018). Effects of front-end converter and DC-link of a utility-scale PV energy system on dynamic stability of a power system. *IEEE Trans. Ind. Electron.* 65 (1), 403–411. doi:10.1109/TIE.2017.2721902

Padiyar, K. R. (1996). *Power system dynamics stability and control*. New York, NY, USA: Wiley.

Pan, Y., Sangwongwanich, A., Yang, Y., and Blaabjerg, F. (2020). A phase-shifting MPPT to mitigate interharmonics from cascaded H-bridge PV inverters. *IEEE Trans. Ind. Appl.* 57 (3), 3052–3063. doi:10.1109/TIA.2020.3000969

Peng, X., and Yang, H. (2020). Impedance-based stability criterion for the stability evaluation of grid-connected inverter systems with distributed parameter lines. *CSEE JPES*. 1–13. doi:10.17775/CSEEJPES.2019.02250

Sangwongwanich, A., and Blaabjerg, F. (2019). Mitigation of interharmonics in PV systems with maximum power point tracking modification. *IEEE Trans. Power Electron.* 34 (9), 8279–8282. doi:10.1109/TPEL.2019.2902880

Shah, C., Vasquez-Plaza, J. D., Campo-Ossa, D. D., Patarroyo-Montenegro, J. F., Guruwacharya, N., Bhujel, N., et al. (2021). Review of dynamic and transient modeling of power electronic converters for converter dominated power systems. *IEEE Access* 9, 82094–82117. doi:10.1109/ACCESS.2021.3086420

Shahnia, F. (2016). Stability and eigenanalysis of a sustainable remote area microgrid with a transforming structure. *Sustain. Energy Grids Netw.* 8, 37–50. doi:10.1016/j.segan.2016.09.005

Tan, Y. T., Kirschen, D. S., and Jenkins, N. (2004). A model of PV generation suitable for stability analysis. *IEEE Trans. Energy Convers.* 19, 748–755. doi:10.1109/TEC.2004.827707

Wang, X., Freitas, W., Dinavahi, V., and Xu, W. (2009). Investigation of positive feedback anti-islanding control for multiple inverter-based distributed generators. *IEEE Trans. Power Syst.* 24 (2), 785–795. doi:10.1109/TPWRS.2008.2007002

Wang, S. (2020). Current status of PV in China and its future forecast. *CSEE JPES* 6 (1), 72–82. doi:10.17775/CSEEJPES.2019.03170

Wen, B., Boroyevich, D., Burgos, R., Mattavelli, P., and Shen, Z. (2015). Small-signal stability analysis of three-phase AC systems in the presence of constant power loads based on measured d-q frame impedances. *IEEE Trans. Power Electron.* 30 (10), 5952–5963. doi:10.1109/TPEL.2014.2378731

Xia, Y., Yu, M., Wang, X., and Wei, W. (2018). Describing function method based power oscillation analysis of LCL-filtered single-stage PV generators connected to weak grid. *IEEE Trans. Power Electron.* 34 (9), 8724–8738. doi:10.1109/TPEL.2018.2887295

Zhao, Z., Yang, P., Wang, Y., Xu, Z., and Guerrero, J. M. (2017). Dynamic characteristics analysis and stabilization of PV-based multiple microgrid clusters. *IEEE Trans. Smart Grid* 10 (1), 805–818. doi:10.1109/TSG.2017.2752640

Zhou, Y., Zhao, L., and Lee, W. J. (2018). Robustness analysis of dynamic equivalent model of DFIG wind farm for stability study. *IEEE Trans. Ind. Appl.* 54 (6), 5682–5690. doi:10.1109/TIA.2018.2858738

Zhou, B., Shi, P., Xu, Y., and Zeng, Z. (2022). Impact of electrical connection distance on the open loop modal resonance of grid connected photovoltaic farms. *Front. Energy Res.* 10, 872143. doi:10.3389/fenrg.2022.872143

Zhu, X., Wang, H., Zhang, W., Wang, H., Deng, X., and Yue, X. (2020). A novel single-phase five-level transformer-less photovoltaic (PV) inverter. *Trans. Electr. Mach. Syst.* 4 (4), 329–338. doi:10.30941/CESTEMS.2020.00040

Zou, J., Peng, C., Xu, H., and Yan, Y. (2015). A fuzzy clustering algorithm-based dynamic equivalent modeling method for wind farm with DFIG. *IEEE Trans. Energy Convers.* 30 (4), 1329–1337. doi:10.1109/TEC.2015.2431258

frontiers | Frontiers in Energy Research

TYPE Methods
PUBLISHED 05 January 2023
DOI 10.3389/fenrg.2022.998543

OPEN ACCESS

EDITED BY
Xue Lyu,
University of Wisconsin-Madison,
United States

REVIEWED BY
Meng Chen,
Aalborg University, Denmark
Jiaxin Wen,
Hong Kong Polytechnic University,
Hong Kong SAR, China

*CORRESPONDENCE
Lixin Wang,
wanglxnedu@163.com

SPECIALTY SECTION
This article was submitted to Smart Grids,
a section of the journal
Frontiers in Energy Research

RECEIVED 20 July 2022
ACCEPTED 25 July 2022
PUBLISHED 05 January 2023

CITATION
Wang Z, Lyu X, Li D, Zhang H and Wang L (2023), Oscillation mode analysis for multi-mode coupling power systems with high renewables penetration using improved blind source separation. *Front. Energy Res.* 10:998543. doi: 10.3389/fenrg.2022.998543

Oscillation mode analysis for multi-mode coupling power systems with high renewables penetration using improved blind source separation

Zhiwei Wang[1], Xiangyu Lyu[2], Dexin Li[2], Haifeng Zhang[2] and Lixin Wang[3]*

[1]State Grid Jilinsheng Electric Power Supply Company, Changchun, China, [2]State Grid Jilinsheng Electric Power Supply Company Electric Power Institute, Changchun, China, [3]Northeast Electric Power University, Jilin, China

The extensive application of power electronic equipment and the increasing penetration of renewable energy generation gradually strengthen the nonlinear and modal-coupling characteristics of electromechanical oscillation of modern power systems. In this study, a data-driven method based on improved blind source separation (IBSS) combined with sparse component analysis (SCA) is proposed to extract electromechanical mode (oscillation frequency, damping ratio and mode shape) from synchrophasor measurements. First, short time Fourier transform is used to convert the modal-coupling oscillation signal to sparse domain, then, on the basis of time-frequency point clustering characteristics of source signals, the mixture matrix ***A*** is estimated by frequency energy peak point algorithm, and L1 norm is utilized to separate each mode from mixture matrix ***A***. Finally, the Hilbert identification algorithm is applied to extract the oscillation parameters. The performance of the proposed IBSS method for the mode extraction is verified using the test signal, the simulation signal, and the measured data.

KEYWORDS

modal-coupling electromechanical oscillation, improved blind source separation, sparse component analysis, synchrophasor measurement, mode extraction

1 Introduction

With the acceleration of power grid interconnection across the country and the increasing scale of renewable energy, the power systems are being operated closer to their limits and even reach the collapse point, resulting in obvious coupling and non-stationary characteristics after a power system is disturbed. Low-frequency oscillation has become one of the important factors affecting the stability of power system (Yang et al., 2020; Lv et al., 2021; Xue et al., 2022). Therefore, accurate and timely extraction of

electromechanical modal parame-ters after disturbance is important for ensuring the stability and security of the power system (Feng et al., 2019).

Traditionally, the power system oscillation modes can be obtained through a model-based approach by linearizing the non-linear differential algebraic equations of a power system at the current operating point. However, this kind of approach is highly dependent on the complete system structure and accurate component parameters. The advent and deployment of phasor measurement units (PMUs) builds a reliable data platform for real-time monitoring, analysis and control of power systems, which provides a new approach for low-frequency oscillation mode identification (Khosravi-Charmi and Amraee, 2018)– (Kopse et al., 2015). Therefore, the measurement-based approaches are alternatives to complement the model-based approaches. In the early days, the single measurement channel was used to extract electromechanical modal parameters, using the advanced identification technique, such as Prony (Hauer, 2015) and its improved algorithm (Wadduwage et al., 2015), Hilbert Huang transform (HHT) algorithm (Lauria and Pisani, 2014), etc., This kind of algorithm can identify oscillation frequency, damping ratio and other oscillation characteristic parameters by directly processing and analyzing the synchrophasor measurement collected by PMUs. Recently, with the advances in PMU configuration, dynamic feature extraction methods based on multi-channel sources were introduced to analyze the dynamic behavior and estimate the dominant modes from the global perspective, among which the representative algorithms include stochastic subspace identification (SSI) (Jiang et al., 2015), multivariate empirical mode decomposition (MEMD) (You et al., 2016), etc. This kind of modal parameters extraction method can analyze the dynamic behavior of each generator from a global perspective, and the identification accuracy is high. However, due to the large amount of input measurements, the calculation is time-consuming and the analysis efficiency is low.

Moreover, the extensive application of power electronic equipment gradually strengthens the nonlinear and coupling characteristics of electromechanical oscillation of modern power systems. Fast and effective identification of modal-coupling oscillation is the focus of power system operators. Traditional measurement-based methods are difficult to meet the needs of security analysis of multi-modal coupled power systems. Blind source separation method was first developed to extract the modal parameters of the structures such as voice and image processing, and the application of the method in the signal processing field shows that it has good attribute of separating the independent source signals, however, until so far, we have not seen much application in electromechanical modal parameters in power systems (Yi et al., 2017; Ye et al., 2018).

To address the deficiencies listed above, first, the measurement input signals are filtered according to the rational inertia, which effectively reduce the dimensionality of original data, then an improved blind source separation method based on sparse component analysis is introduced to extract the power system oscillation modal parameters. Compared with the traditional low-frequency oscillation mode identification method, the improved blind source separation algorithm can accurately separate the stationary source signal with single frequency from the nonlinear and nonstationary multi-modal coupled oscillation signals, and accurately extract the oscillation modal parameters such as mode frequency and damping ratio. The case studies of test signal, the simulation signal and the measured data confirm the superior characteristics of the proposed IBSS based multi-modal coupled modal parameter extraction.

The remainder of this paper is organized as follows: Section 2 introduces the theoretical foundation of the traditional BSS. Section 3 develops the IBSS method based on sparse component analysis. Section 4 expands the IBSS to extract the oscillation modal parameters. Section 5 presents three cases to evaluate the performance of the proposed method. Section 6 concludes the paper.

2 Blind source separation

The term blind source separation (BSS) refers to a wide class of problems in signal and image processing, in which one needs to extract the underlying sources from a set of mixtures. The mathematical model of BSS can be expressed as (Ye et al., 2018):

$$\boldsymbol{X}(t) = \boldsymbol{A}\boldsymbol{S}(t) = \sum_{i=1}^{n} \boldsymbol{a}_i s_i(t) \tag{1}$$

where $\boldsymbol{S}(t) = [s_1(t), \cdots, s_n(t)]^{\mathrm{T}}$ is an n-dimension unknown source signals. $\boldsymbol{X}(t) = [x_1(t), \cdots, x_m(t)]^{\mathrm{T}}$ is an m-dimension observed vector. $\boldsymbol{A}$ is an unknown $m \times n$ mixing matrix, in which a_i is the mixing parameter of the source signal; $s_i(t)$ is discrete signals.

BSS algorithm is usually suitable for solving positive definite problems, that is, the mixing matrix $\boldsymbol{A}$ is full rank, in which the number of observed signals (m) is greater than or equal to the number of source signals (n). The core of BSS is to solve the mixture matrix $\boldsymbol{A}$ and its inverse matrix $\boldsymbol{W}$, which is called the separation matrix, moreover, the source signal can be separated simultaneously, satisfying (Yang et al., 2018):

$$S(t) = WX(t) \tag{2}$$

3 Improved blind source separation

3.1 Sparse component analysis

An attractive advantage of sparse component analysis (SCA) is that it can transform the time-domain signal into the frequency domain through appropriate linear transformation method, such as short-time Fourier transform, wavelet transform, etc., making

the observed measurement signals sparse in the frequency domain. The sparsity of observation signal means that most time-frequency points are zero, and only a few time-frequency points have large values in the time-frequency domain (Ye et al., 2018). In this paper, one-dimensional time-domain signal is transformed into two-dimensional time-frequency-domain signal by short-time Fourier transform, and the rectangular window function is selected. And 1) could be further expressed as (Yi et al., 2017):

$$\begin{bmatrix} x_1(t,f) \\ x_2(t,f) \\ \vdots \\ x_p(t,f) \end{bmatrix} = \begin{bmatrix} \boldsymbol{a}_1 & \boldsymbol{a}_2 & \cdots & \boldsymbol{a}_Q \end{bmatrix} \begin{bmatrix} s_1(t,f) \\ s_2(t,f) \\ \vdots \\ s_Q(t,f) \end{bmatrix} = \begin{bmatrix} a_{11} & \cdots & a_{1Q} \\ a_{22} & \cdots & a_{2Q} \\ \vdots & \ddots & \vdots \\ a_{P1} & \cdots & a_{PQ} \end{bmatrix} \begin{bmatrix} s_1(t,f) \\ s_2(t,f) \\ \vdots \\ s_Q(t,f) \end{bmatrix} \tag{3}$$

where $[\boldsymbol{a}_1 \quad \boldsymbol{a}_2 \quad \cdots \quad \boldsymbol{a}_Q]$ is the column vector of mixing matrix $\boldsymbol{A}$. a_{PQ} is the attenuation factor for the *Q-th* source signal reaching the *P-th* observation point.

When each source signal is sparse and disjoint, the observed signal has at most one source signal at a certain time-frequency point. Assuming that only the source signal $s_j(t_v, f_v)$ exists at the time-frequency point (t_v, f_v), 3) can be expressed as:

$$\begin{bmatrix} x_1(t_v,f_v) \\ x_2(t_v,f_v) \\ \vdots \\ x_p(t_v,f_v) \end{bmatrix} = \begin{bmatrix} \boldsymbol{a}_1 & \boldsymbol{a}_2 & \cdots & \boldsymbol{a}_Q \end{bmatrix} \begin{bmatrix} 0 \\ \vdots \\ s_j(t_v,f_v) \\ \vdots \\ 0 \end{bmatrix} = \begin{bmatrix} a_{11} & \cdots & a_{1Q} \\ a_{22} & \cdots & a_{2Q} \\ \vdots & \ddots & \vdots \\ a_{p1} & \cdots & a_{PQ} \end{bmatrix} \begin{bmatrix} 0 \\ \vdots \\ s_j(t_v,f_v) \\ \vdots \\ 0 \end{bmatrix} \tag{4}$$

Then, (4) can be simplified as:

$$\frac{x_1(t_v,f_v)}{a_{1j}} = \frac{x_2(t_v,f_v)}{a_{2j}} = \cdots = \frac{x_P(t_v,f_v)}{a_{Pj}} = s_j(t_v,f_v) \tag{5}$$

From a geometrical point of view, if the real part or imaginary part of $x_1(t,f), x_2(t,f)$ is used as the horizontal axis and vertical axis to draw a scatter plot, $x_1(t_v,f_v)/x_2(t_v,f_v) = a_{1j}/a_{2j}$ is constant for the sampling times belonging to the source signal s_j. That is, the time-frequency points belonging to the source signal s_j will determine a straight line. Similarly, the time-frequency points of different source signals will be clustered into corresponding clustering lines. The direction vector of these clustering lines is the attenuation coefficient ratio of each source signal mixed to the observation point, which is the column vector a_Q of the mixing matrix $\boldsymbol{A}$. And the mixing matrix $\boldsymbol{A}$ can be estimated by the direction of each clustering line in the scatter diagram.

Based on the obtained mixing matrix $\boldsymbol{A}$, the L1 norm is used to solve the underdetermined equation, then the system source signal is extracted.

3.2 Mixing matrix estimation

The premise of estimating the mixing matrix $\boldsymbol{A}$ is that the time-frequency points of the mixed signal can form a clustering line with certain directionality in the real or imaginary part scatter diagram. In this paper, the fuzzy C-means method is used to estimate the mixing matrix $\boldsymbol{A}$ by calculating the clustering center of the clustering line, which is suitable for the blind source decomposition problem with any number of measurement signal channels. However, when there are too many time-frequency points, the clustering direction in the scatter diagram is complicated, resulting in much calculation time and poor identification accuracy.

The source signal propagates outward in the energy form, however, the energy will be attenuated during the propagation process, the final energy of the same source signal reaching each observation is a little different. Therefore, an algorithm combing the frequency energy peak point method (Jin et al., 2021) and the fuzzy C-means method is proposed to estimate the mixing matrix $\boldsymbol{A}$.

The main principle of the proposed method to estimate the mixture matrix $\boldsymbol{A}$ is: since the energy of each source signal is the largest near its own frequency point, the frequency value of each source can be determined by using the frequency peak method. The clustering straight line direction of the corresponding time-frequency point at the maximum energy is the clustering direction of each source signal. Then, the real part or imaginary part time-frequency dispersion points corresponding to each peak frequency point are normalized and mapped to the unit circle. Finally, the clustering center is calculated by using the fuzzy C-means algorithm, so as to obtain the mixing matrix $\boldsymbol{A}$.

In the time-frequency domain, the energy distribution of a single measurement signal is firstly calculated, and then the energy of multiple channels at the same frequency point is added, which is:

$$E(f) = \sum_{i=1}^{m} \int_{t_1}^{t_2} \left(\left(\mathrm{Re}(x_i(t,f)) \right)^2 + \left(\mathrm{Im}(x_i(t,f)) \right)^2 \right) dt \tag{6}$$

where $E(f)$ is the sum of the energy of all observation signals at each frequency point; x_i is the i-th time-frequency point; $\mathrm{Re}(x_i(t,f))$ and $\mathrm{Im}(x_i(t,f))$ are the real part and imaginary part of the time-frequency point respectively; m is the number of the observation signals.

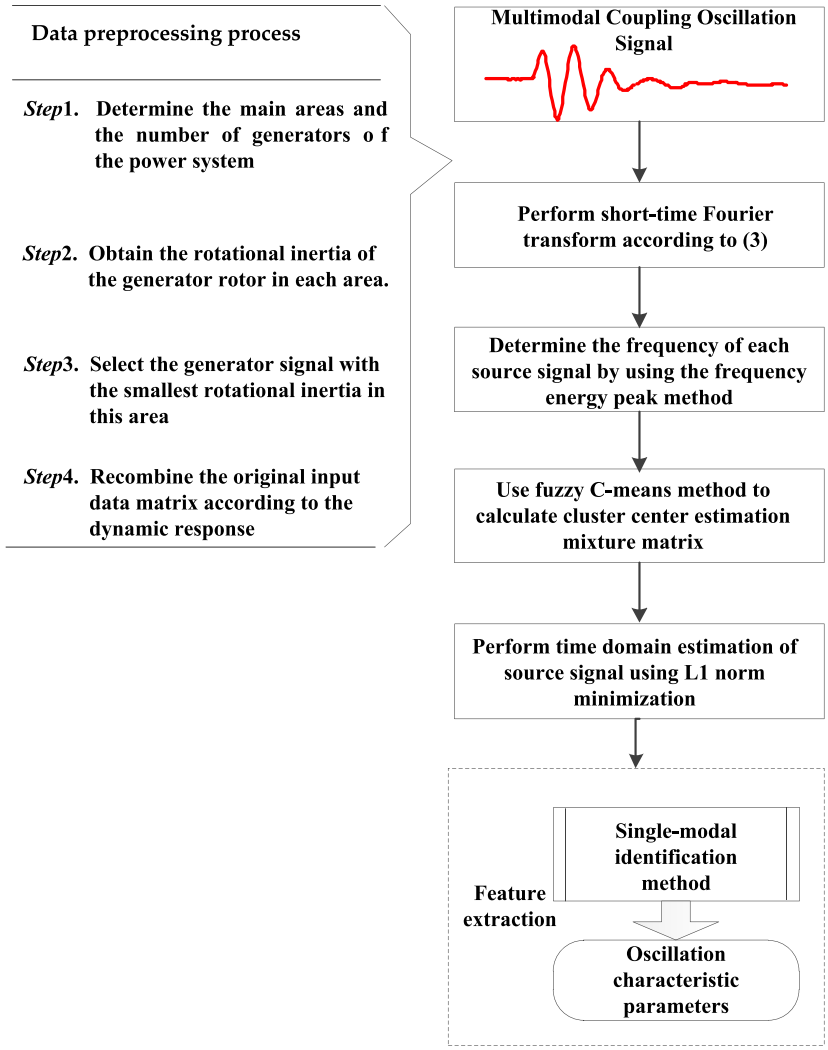

FIGURE 1
Flow chart of SCA and the modal parameter identification.

3.3 Source signal recovery

SCA algorithm utilizes the sparsity of the source signal in time-frequency domain to recover the source signal. The sparse solution is obtained by establishing and solving the optimization problem (P_1) in (7):

$$(P_1): \begin{cases} \tilde{s}(t,f) = \min\left|s(t,f)\right|_{l_1} \\ subject \quad to \quad \boldsymbol{A}s(t,f) = x(t,f) \end{cases} \tag{7}$$

where $\tilde{s}(t,f)$ is the estimation of the source signal $s(t,f)$; (P_1) is a convex optimization problem. The solution of the optimization problem is the L1 norm minimum solution (Donoho, 2006).

4 Oscillation modal parameter identification

4.1 Rotational inertia-based input measurement selection

The power system requires accurate generator parameters and mathematical models when performing small-signal stability calculation and analysis. The kinetic energy of the generator is an important parameter of the generator, which is determined by the rotational inertia of the generator rotor. The rotational inertia refers to the inertia of the generator rotor during the rotation process, which affects the electromechanical transient process of each

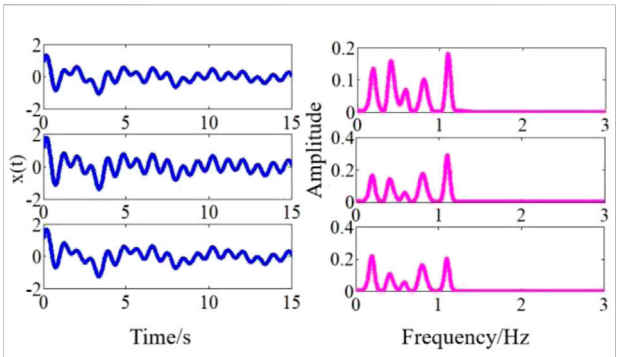

FIGURE 2
Test signal waveforms and their WFT spectrum.

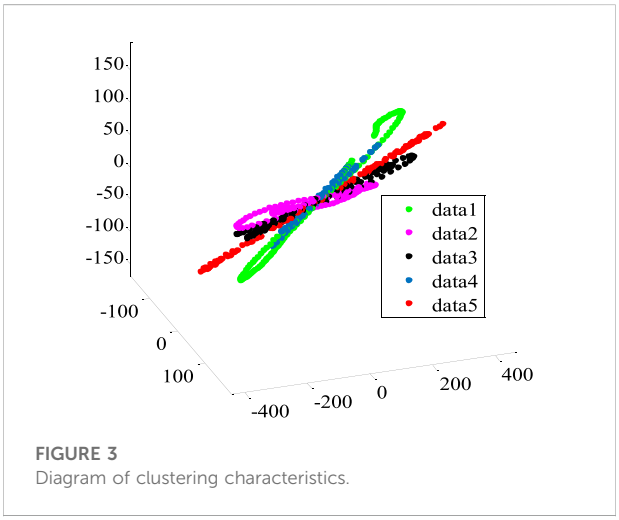

FIGURE 3
Diagram of clustering characteristics.

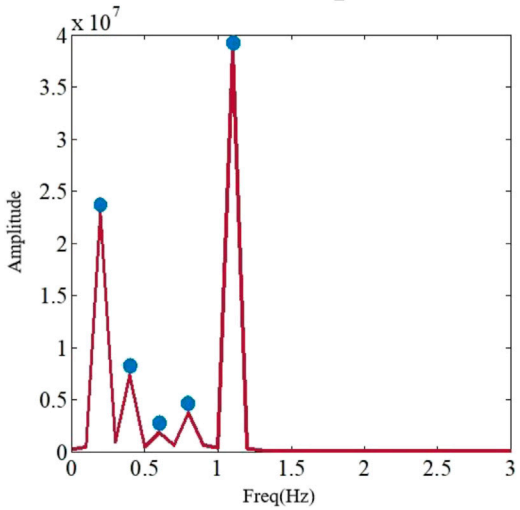

FIGURE 4
The peak plot in frequency domain.

generator and is of great significance to the stability and safety of the power system. When the system is disturbed, the generator rotor will accelerate or decelerate due to the unbalanced torque, and the rotational inertia can be expressed as the ability of the system to return to the original stable operation. The smaller the rotational inertia, the worse the generator's resistance to disturbance. When the proposed method is applied to the actual system, it is necessary to use the rotational inertia of the generator in each region as a quantitative index, and select the measurement signals of the generator with the smallest rotational inertias as the input signals of SCA algorithm, which can greatly reduce the number of the input signals and effectively improve the calculation speed.

4.2 Estimation of modal matrix

The low-frequency oscillation signal of power system is essentially the multimodal coupling response, which can be expressed by (8). The oscillation frequency has a large deviation in a period of time, which shows obvious nonlinear characteristics:

$$x(t) = \boldsymbol{\Phi} q(t) = \sum_{i=1}^{n} \boldsymbol{\varphi}_i q_i(t) \tag{8}$$

where $\boldsymbol{\Phi} = [\boldsymbol{\varphi}_1, \boldsymbol{\varphi}_2, \cdots \boldsymbol{\varphi}_n]$ is the mode shape matrix, the mode shape of the *i-th* column $\boldsymbol{\varphi}_i$ is related to the *i*-th modal response vector $q_i(t)$, and can also be transformed into the form of (9) (Yang and Satish, 2013):

$$q(t) = \boldsymbol{\Phi}^{-1} x(t) \tag{9}$$

Comparing (1) and (8), the viewpoints of characteristic parameter identification of electromechanical oscillation mode and blind source separation are consistent, that is, the perturbed dynamic response of multi-modal coupling is regarded as a linear group of multiple single-modal responses. The single-modal response $q(t)$ is equivalent to a special form of the source signal $s(t)$, and the mixing matrix $\boldsymbol{A}$ contains the information of the modal matrix, satisfying $\boldsymbol{\Phi} = \boldsymbol{A}$.

4.3 Oscillation frequency and damping ratio identification based on hilbert transform

In this paper, Hilbert transform (HT) is used to extract the oscillation frequency and damping ratio (Gibbard and Vowles, 2010). Performing the HT on a single-mode oscillation component $q_i(t)$, we can obtain:

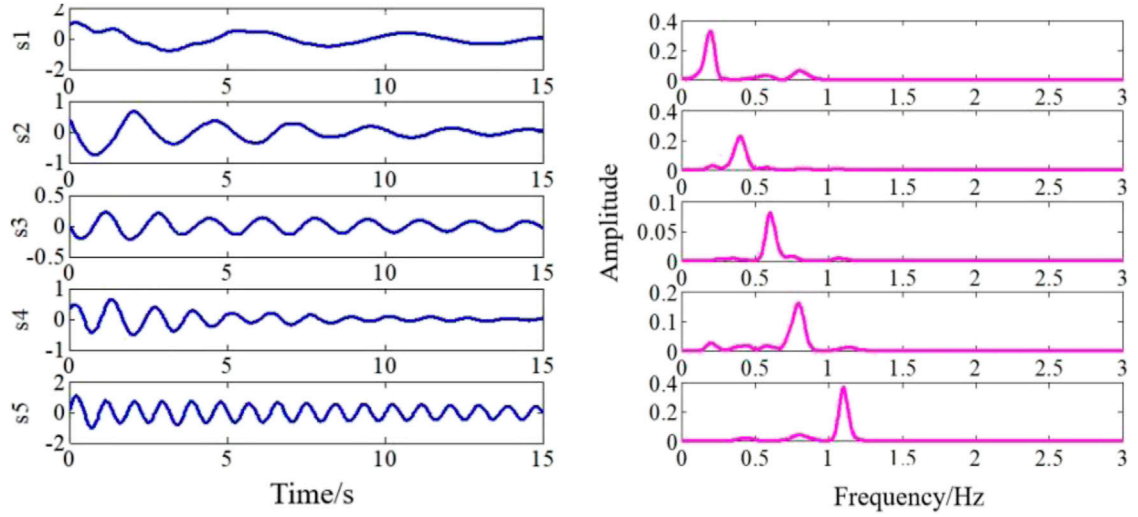

FIGURE 5
The separated source signals and their WFT spectrum.

TABLE 1 Extracted modal parameters of test signal.

Mode	Frequency (Hz)		Damping ratio (%)	
	Identified value	Theoretical value	Identified value	Theoretical value
1	0.1960	0.2	8.3913	6.3662
2	0.3972	0.4	8.1498	5.9683
3	0.6033	0.6	2.3319	2.6526
4	0.7699	0.8	3.8385	4.9736
5	1.0995	1.1	0.9751	0.7234

$$h(t) = \frac{1}{\pi}\int_{-\infty}^{+\infty}\frac{q(t)}{t-\tau}dt \tag{10}$$

Where τ is the integral variable.

Introduce an analytic function consisting of $q(t)$ and $h(t)$:

$$Z(t) = q(t) + jh(t) = A(t)e^{-j\varphi(t)} \tag{11}$$

Where A(t) is the envelope of the signal after Hilbert transform and $\varphi(t)$ is the instantaneous phase, namely:

$$\begin{cases} A(t) = \left[q^2(t) + h^2(t)\right]^{1/2} \\ \varphi(t) = \tan^{-1}\left[\dfrac{h(t)}{q(t)}\right] \end{cases} \tag{12}$$

The instantaneous frequency can be obtained:

$$f(t) = \frac{1}{2\pi} \times \frac{\mathrm{d}A(t)}{\mathrm{d}t} \tag{13}$$

The system oscillation signal can be deduced from the generator swing equation, which can be expressed as:

$$x(t) == \sum_{i=1}^{\mathrm{n}}\varphi_i q_i(t) = \sum_{i=1}^{n}\varphi_i u_i e^{-\lambda_i t}\cos(\omega_{di}t + \theta_i) \tag{14}$$

Where $q_i(t)$ is a cosine curve that decays exponentially; u_i and θ_i are the amplitude and phase respectively, which are determined by the initial conditions; λ_i is the decay coefficient; ω_{di} is the oscillation frequency.

For a damped oscillaion, the single-modal response signal $q_i(t)$ can be expressed as:

$$q_i(t) = u_i e^{-\xi\omega_0 t}\cos\left(\omega_0\sqrt{1-\xi^2}t + \theta_i\right) \tag{15}$$

By comparing 14) and (15), we can obtain:

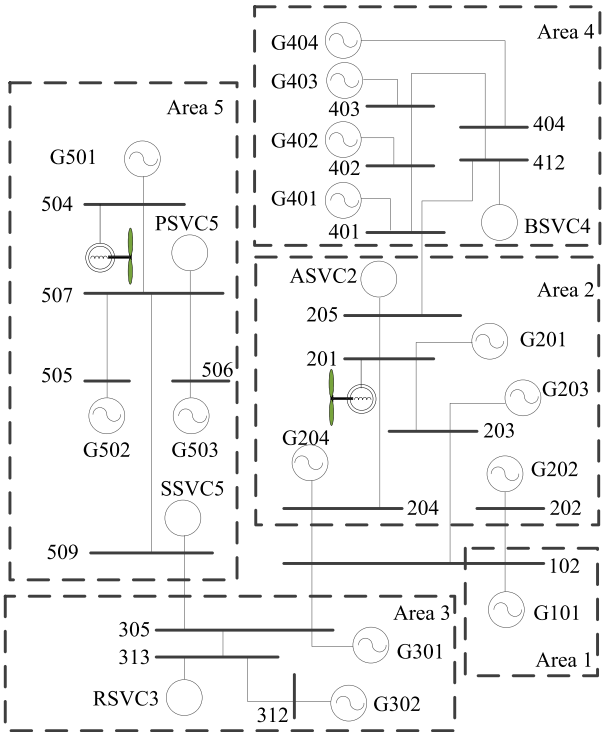

FIGURE 6
Single line diagram of simplified 14-generator system.

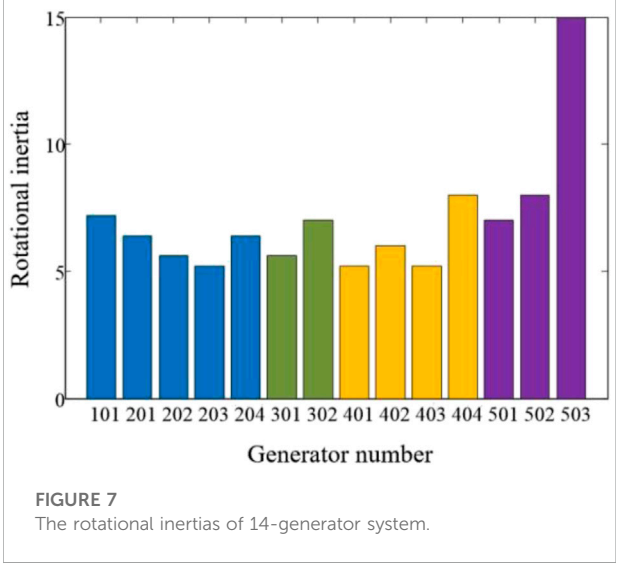

FIGURE 7
The rotational inertias of 14-generator system.

$$\begin{cases} \xi\omega_0 = \lambda_i \\ \omega_{di} = \omega_0\sqrt{1-\xi^2} \end{cases} \tag{16}$$

The damping ratio of the signal is calculated as:

$$\xi = -\frac{\lambda_i}{\sqrt{\omega_{di}^2 + \lambda_i^2}} \tag{17}$$

The modal parameter extraction of an electromechanical oscillation based on the SCA algorithm is shown in Figure 1:

5 Case studies

The proposed method has been tested on test signal, test system and real measurements. In this section, the experiments are carried out on an Intel Core i7 3.7 GHz computer with 16 GB of RAM. Additionally, our proposed method is coded by MATLAB.

5.1 Test signal analysis

The five single-mode oscillation signals shown in Eq. 18 are constructed with frequencies of 0.6 Hz, 1.1 Hz, 0.4 Hz, 0.8 Hz, and 0.2 Hz, in that order:

$$\begin{cases} S_1 = e^{-0.1t}\sin\left(2\pi \times 0.6t + \pi/6\right) \\ S_2 = e^{-0.05t}\sin\left(2\pi \times 1.1t + 0\right) \\ S_3 = e^{-0.15t}\cos\left(2\pi \times 0.4t + \pi/3\right) \\ S_4 = e^{-0.25t}\sin\left(2\pi \times 0.8t + \pi/4\right) \\ S_5 = e^{-0.08t}\sin\left(2\pi \times 0.2t + \pi/5\right) \end{cases} \tag{18}$$

TABLE 2 The characteristic results of simplified 14-generator system.

Mode	Real	Imaginary	Frequency (Hz)	Damping ratio (%)
1	−0.589	2.513	0.399	22.8
2	−0.563	3.322	0.529	16.7
3	−1.080	4.581	0.729	22.9

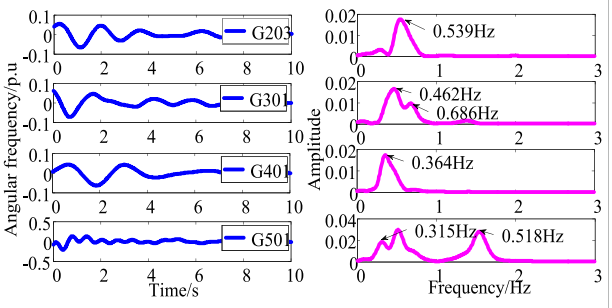

FIGURE 8
The waveforms of rotor speed of generators and their frequency domain.

Using a three-dimensional random mixing matrix $A = \begin{bmatrix} 0.6 & 0.4 & 0.53 & 0.45 & 0.41 \\ 0.44 & 0.65 & 0.5 & 0.68 & 0.48 \\ 0.5 & 0.45 & 0.35 & 0.67 & 0.61 \end{bmatrix}$, it is mixed into three coupled oscillating signals with non-smooth characteristics as the test signals. The three test signals are sampled separately with the sampling frequency of 0.01Hz, and the sampling time is 15s. The spectrum analysis of the three test signals is performed using window Fourier transform (WFT), as shown in Figure 2.

Short time Fourier transform (STFT) is used to transform the three groups of test signals into time-frequency domain, and the window function is chosen to be a rectangular window of length 10s, and the window was shifted by four points each time. Figure 3 shows the scatter plot of the real part of the test signal x. From Figure 3, we can know that there are five obvious clustered straight lines, indicating that there are five source signals in the test signal x.

According to (6), the total energy of the three groups of test signals at each frequency point is calculated, and the frequency corresponding to each energy peak is detected using the frequency energy peak point method, as shown in Figure 4. The normalized clustering center of the five straight lines is calculated using the fuzzy C-mean algorithm, and the mixing matrix $\boldsymbol{A}$ can finally be accurately estimated as:

$$A = \begin{bmatrix} 0.4826 & 0.6458 & 0.6662 & -0.4350 & 0.4478 \\ 0.5492 & 0.6030 & 0.4770 & -0.6257 & 0.7329 \\ 0.6777 & 0.4243 & 0.5484 & -0.6230 & 0.5040 \end{bmatrix}.$$

The L1 norm minimization method was used to separate the five source signal components, and the time domain and frequency domain distribution of the five source signals is shown in Figure 5. As shown in Figure5, each component has the characteristics of periodic oscillation, and the calculated frequencies are basically the same as the actual frequencies. Meanwhile, the proposed algorithm decomposes the multi-modal coupled oscillation signal into multiple source signals with the single frequency, without modal aliasing. The detected frequencies are arranged in the order from low to high, which effectively solves the problem of uncertainty in the order of source signals.

Hilbert transform was utilized to extract modal parameters of the separated components, and the oscillation frequencies and damping ratios are obtained, as shown in Table 1. It can be seen from Table 1 that the results of the extracted modal parameters are quite close to their true values, indicating the effectiveness of the proposed method.

5.2 Modified IEEE 14-genertor 5-area test system

In this section, the modified IEEE 14-generater 5-area simplified system is used as an example (Ding et al., 2019), as shown in Figure 6. There are five areas in this system, but since area one is strongly coupled with area 2, the system can be considered to have four main areas, which are defined as Area 1, Area 2, Area 3, and Area 4, respectively. Area one contains five generators, namely G101, G201, G202, G203, and G204; Area2 contains two generators, G301, G302; Area3 contains four generators, namely G401, G402, G403, G404; Area4 contains G501, G502, G503. And two aggregated PMSG-based wind farms are connected to Buses 504 and 201, respectively in Figure 6. Furthermore, the parameters of the two wind farms are configured in accordance with Literature (Dejian et al., 2022a; Dejian et al., 2022b). Moreover, the active outputs of the SGs in the same area are reduced accordingly to keep the operating point the same as that before the SG reduction.

Inter-area mode is more likely to excite a poorly damped oscillation, which involves more generators and has a wide range of influence, so it is usually considered the mode of most interest. The 14-generator test system was linearized around an operating point, and small-signal stability analysis (SSSA) results show that the system has three inter-area modes. as shown in Table 2.

In this paper, the rotational inertia of the generators in each area of the system is used as a quantitative index, and the angular frequency of the generator with the smallest rotational inertia in each area is selected as the input signal. Figure 7 shows the rotational inertia of each generator. According to the signal selection principle and the inertia results in Figure 7, generator G203 is selected as the representative of Area1, in which its inertia is lower than the other generators in the same area. Similarly, the signal of generator G301 is selected as representative of Area2, generator G401 is se-lected as representative of Area3, and generator G501 is selected as representative of Area4.

In order to verify the effectiveness of the proposed method for identifying the interarea modes, a representative two-phase grounded short circuit is applied at bus 506, the sampling frequency of 100 Hz and the sampling time is 50 s. And the simulation was carried out using power system toolbox (PST).

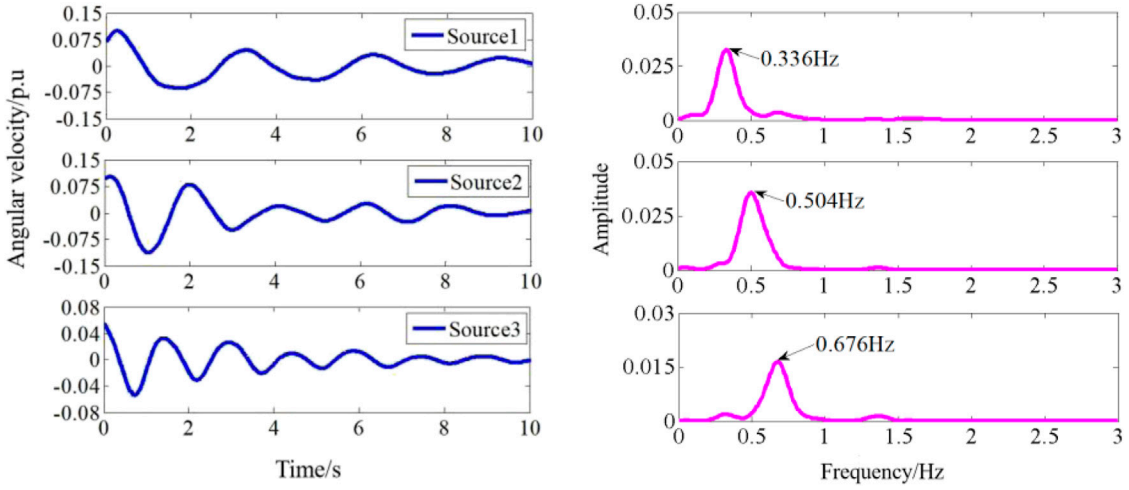

FIGURE 9
The separated single-mode components and their WFT spectrum.

TABLE 3 Identified results with three different methods of simplified 14-generaror system.

Mode	Frequency (Hz)			Damping ratio (%)	
	Identified value	WFT	SSSA	Identified value	SSSA
1	0.336	0.34	0.399	12.22	22.8
2	0.504	0.51	0.529	9.09	16.7
3	0.679	0.68	0.729	6.19	22.9

The angular frequency of each generator within 10s after the fault is used as the input signal in this paper. The input signals of generator G203, generator G301, generator G401, and generator G501 were first detrended, and the time domain angular frequencies of these four generators were transformed into the frequency domain using WFT. Three interarea oscillation modes could be identified, with frequencies of 0.34 Hz, 0.51 Hz, and 0.68 Hz, respectively. Figure 8 shows the time-domain distributions and the corresponding frequency-domain distributions of the angular frequencies of the four generators.

The four input signals are decomposed using SCA algorithm, and three single-mode oscillation components can be obtained. The time-domain and frequency-domain distributions of each single-mode component are shown in Figure 9. HT was used to calculate the oscillation frequency and damping ratio, and the obtained modal parameter results were compared with WFT results and SSSA results, as shown in Table 3. From Figure3, we can know that all the three inter-area modal parameters can be extracted by using only four input signals of generator G203, G301, G401 and G501, which effectively saves calculation time.

While identifying the oscillation frequency and damping ratio of the system, SCA algorithm can also estimate the modal matrix utilizing the clustering characteristics.

The modal matrix is estimated as:

$$\begin{bmatrix} 0.1902 & 0.4766 & -0.6595 & -0.0357 \\ -0.1971 & 0.451 & 0.7167 & -0.0124 \\ 0.5477 & -0.4067 & -0.0325 & -0.0364 \\ -0.7905 & -0.6355 & -0.2221 & -0.9985 \end{bmatrix}$$

The mode shape corresponding to the three inter-area oscillation modes are shown in Figure 10. For Mode 1, generator 401 oscillates against generator 501. In this paper, the input signal is the representative of each region, so it can also be considered that mode one is the inter-area oscillation mode, with generator 401 in Area3 oscillates against generator 501 in Area4. By the same token, the oscillation area clusters of mode two is Area two and Area three against Area 4, the oscillation area clusters of mode three is Area two against Area 3. The estimated oscillation frequencies, damping ratios and mode shapes using the proposed method in this paper are summarized in Table 4.

10.3389/fenrg.2022.998543

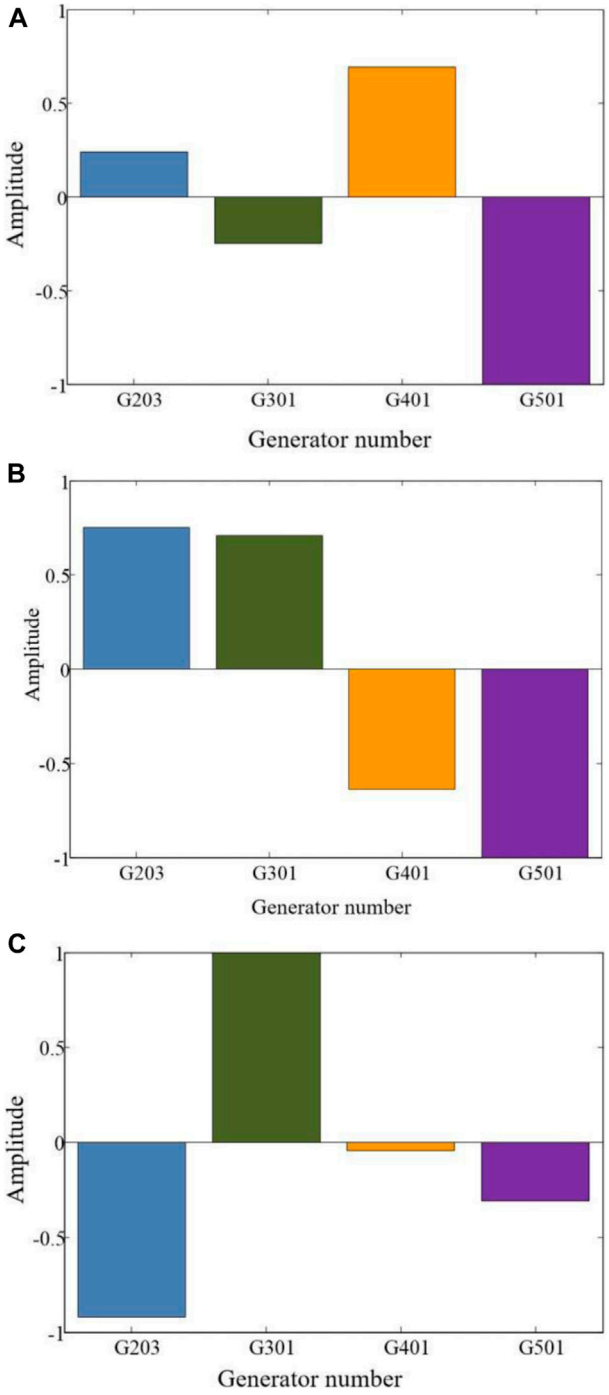

FIGURE 10
Normalized mode shapes.

TABLE 4 Identified results of the simplified 14-generator system.

Mode	Frequency (Hz)	Damping ratio (%)	Mode shape
1	−0.589	0.399	22.8
2	−0.563	0.529	16.7
3	−1.080	0.729	22.9

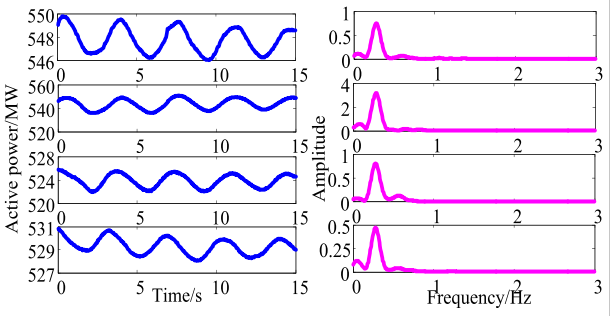

FIGURE 11
Active power oscillation signal in time and frequency domain.

5.3 Test on the real measurements

In this section, a set of real PMU measurements from north power grid of China was used to further illustrate the adaptability of the algorithm in practical system. The system comprises two major areas connected through four 500-kV transmission lines. When the maintenance schedule requires, heavy power is delivered between the two areas, the electromechanical oscillation is one of the major threats to the power grid stability. The data are collected from four PMUs located in the two areas. The input signals were recorded for a duration of 15 s with the sampling frequency of 30 Hz. The time-domain oscillation waveforms and the corresponding frequency-domain distributions are shown in Figure 11. As can be seen from Figure 11, the practical power grid contains an inter-area oscillation mode with the frequency of 0.28 Hz.

The SCA algorithm was used to extract oscillation features from PMU measurement data, the decomposed time-domain source signals and their spectrum are shown in Figure 12. Then the HT algorithm was applied to the decomposed source signals to extract oscillation frequencies and damping ratios, as shown in Table 5. As can be seen from Table 5, the proposed method identified the oscillation mode with the frequency of 0.28 Hz, which is consistent with the spectrum analysis, and the corresponding mode shape is shown in Figure 13. From Figure 13, it can be seen that PMU2 is mainly involved in the oscillation of this mode.

To sum up, it can be seen that the proposed algorithm in this paper can not only effectively extract the modal parameters from the test signal and the simulated signal, but also has good applicability to the real measured signal.

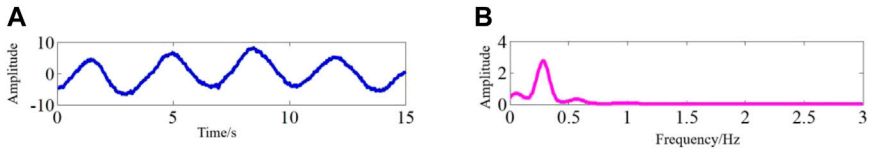

FIGURE 12
The decomposed waveform of active power and its spectrum. **(A)** The decomposed source signal **(B)** Spectrum of the source signal.

TABLE 5 Identified oscillation mode of active power oscillation signal.

Mode	Frequency (Hz)	Damping ratio (%)
1	0.2653	0.3323

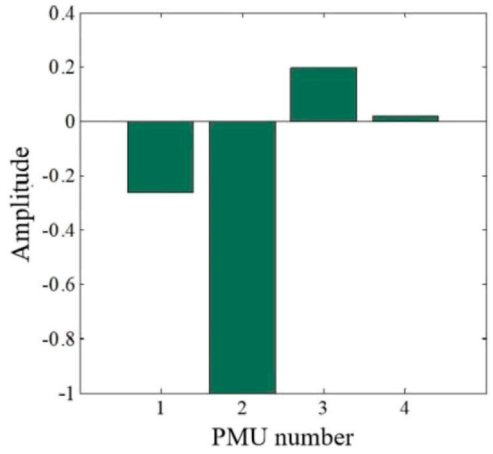

FIGURE 13
The identified mode shape of the actual power grid.

6 Conclusion

In this paper, an improved blind source separation algorithm based on sparse component analysis is proposed to extract electromechanical modal parameters in power systems. Test cases of simulation studies and PMU measured data can obtain the following conclusions:

First, the proposed algorithm decomposes the multi-modal coupled nonstationary oscillation signal into source signals with single frequencies, and the source signals are arranged in the order of oscillation frequency from small to large, which effectively avoids the problem of modal aliasing.

Second, the SCA algorithm reduces the original input measurement data by using the rotational inertia of the generator rotor in each area of the system as a quantitative index, which effectively reduces the calculation time and improves the analysis efficiency.

Third, the proposed method can extract the modal parameters from the multi-mode coupled oscillation signal, which can accurately reflect the inherent electromechanical characteristics of power systems, and provide a new idea for the analysis of the electromechanical oscillation.

The proposed algorithm is suitable for analyzing the mode-coupled oscillation signal of the interconnected power system, and provides a new idea for the extraction of electromechanical oscillation parameters.

Data availability statement

The raw data supporting the conclusions of this article will be made available by the authors, without undue reservation.

Author contributions

ZW and XL contributed to the conception and design of the proposed strategy. All authors wrote and edited the manuscript.

Funding

This project is funded by State Grid Jilin Company's science and technology project "Weak inertia supports the research and application of key technologies for dynamic frequency security defense of sending-end power grids" (52234221000A).

Conflict of interest

ZW, XL, DL, and HZ were employed by State Grid Jilinsheng Electric Power Supply Company.

The remaining author declares that the research was conducted in the absence of any commercial or financial relationships that could be construed as a potential conflict of interest.

Publisher's note

References

Dejian, Y., Gan-gui, Y., and Taiying, Z. (2022). *Fast frequency response of a DFIG based on variable power point tracking control*. Jilin: IEEE Transactions on Industry Applications. early access.

Dejian, Y., Zhaoyang, J., Taiying, Z., and Jin, E. (2022). An adaptive droop control strategy with smooth rotor speed recovery capability for type III wind turbine generators. *Int. J. Electr. Power & Energy Syst.* 135, 107532. doi:10.1016/j.ijepes.2021.107532

Ding, H., Wang, Y., Yang, Z., and Pfeiffer, O. (2019). Nonlinear blind source separation and fault feature extraction method for mining machine diagnosis. *Appl. Sci. (Basel).* 9 (9), 1852–1905. doi:10.3390/app9091852

Donoho, D. (2006). For most large underdetermined systems of linear equations the minimal 1-norm solution is also the sparsest solution. *Commun. Pure Appl. Math.* 59 (4), 797–829. doi:10.1002/cpa.20132

Feng, S., Chen, J., and Tang, Y. (2019). Identification of low frequency oscillations based on multidimensional features and ReliefF-mRMR. *Energies* 12, 2762. doi:10.3390/en12142762

Gibbard, M., and Vowles, D. (2010). *Simplidied 14-generator model of the SE Australian power system*. Australia: The University of Adelaide.

Hauer, J. (2015). Application of Prony analysis to the determination of modal content and equivalent models for measured power system response. *IEEE Trans. Power Syst.* 6 (3), 1062–1068. doi:10.1109/59.119247

Jiang, T., Yuan, H., Jia, H., Zhou, N., and Li, F. (2015). Stochastic subspace identification-based approach for tracking inter-area oscillatory modes in bulk power system utilising synchrophasor measurements. *IET Gener. Transm. &amp. Distrib.* 9 (15), 2409–2418. doi:10.1049/iet-gtd.2015.0184

Jin, S. S., Jeong, S., Sim, S. H., Seo, D. W., and Park, Y. S. (2021). Fully automated peak-picking method for an autonomous stay-cable monitoring system in cable-stayed bridges. *Automation Constr.* 126, 103628–103638. doi:10.1016/j.autcon.2021.103628

Khosravi-Charmi, M., and Amraee, T. (2018). Wide area damping of electromechanical low frequency oscillations using phasor measurement data. *Int. J. Electr. Power & Energy Syst.* 99, 183–191. doi:10.1016/j.ijepes.2018.01.014

Kopse, D., Rudez, U., and Mihalic, R. (2015). Applying a wide-area measurement system to validate the dynamic model of a part of European power system. *Electr. Power Syst. Res.* 119, 1–10. doi:10.1016/j.epsr.2014.08.024

Lauria, D., and Pisani, C. (2014). On Hilbert transform methods for low frequency oscillations detection. *IET Gener. Transm. and Distrib.* 8 (6), 1061–1074. doi:10.1049/iet-gtd.2013.0545

Lv, H., Abuduwayiti, X., Meng, L., and Shi, C. (2021). Rapid power compensation-based VSC-hvdc control strategy for low-frequency oscillation suppression of the island power system. *Front. Energy Res.* 9, 768340. doi:10.3389/fenrg.2021.768340

Wadduwage, D., Annakkage, U., and Narendra, K. (2015). Identification of dominant low-frequency modes in ring-down oscillations using multiple Prony models. *IET Gener. Transm. Distrib.* 9 (15), 2206–2214. doi:10.1049/iet-gtd.2014.0947

Xue, L., Yunzheng, Z., Dominic, G., and Tao, L. (2022). Receding horizon control based secondary frequency regulation for power systems with wind energy integration. *Int. J. Electr. Power and Energy Syst.* 142, 108282. doi:10.1016/j.ijepes.2022.108282

Yang, D., Zhang, Y., Ge, M., Yi, C., and Liu, C. (2018). Improved tensor-based singular spectrum analysis based on single channel blind source separation algorithm and its application to fault diagnosis. *Appl. Sci. (Basel).* 7, 418. doi:10.3390/app7040418

Yang, D., Wang, B., Cai, G., Jin, M., and Sun, Z. (2020). Ambient-data-driven modal-identification-based approach to estimate the inertia of an interconnected power system. *IEEE Access* 8, 118799–118807. doi:10.1109/access.2020.3004335

Yang, Y., and Satish, N. (2013). Blind modal identification of output-only structures in time-domain based on complexity pursuit. *Earthq. Eng. Struct. Dyn.* 42 (13), 1885–1905. doi:10.1002/eqe.2302

Ye, F., Chen, J., Gao, L., Nie, W., and Sun, Q. (2018). A mixing matrix estimation algorithm for the time-delayed mixing model of the underdetermined blind source separation problem. *Circuits Syst. Signal Process.* 38 (4), 1889–1906. doi:10.1007/s00034-018-0930-5

Yi, C., Lv, Y., Dang, Z., Xiao, H., You, G., and Dang, Z. (2017). Research on the blind source separation method based on regenerated phase-shifted sinusoid-assisted EMD and its application in diagnosing rolling-bearing faults. *Appl. Sci. (Basel).* 7, 414. doi:10.3390/app7040414

You, S., Guo, J., Kou, G., Liu, Y., and Liu, Y. (2016). Oscillation mode identification based on wide-area ambient measurements using multivariate empirical mode decomposition. *Electr. Power Syst. Res.* 134, 158–166. doi:10.1016/j.epsr.2016.01.012

frontiers | Frontiers in Energy Research

TYPE Original Research
PUBLISHED 25 January 2023
DOI 10.3389/fenrg.2022.1047624

OPEN ACCESS

EDITED BY
Siqi Bu,
Hong Kong Polytechnic University,
Hong Kong SAR, China

REVIEWED BY
Bowen Zhou,
Northeastern University, China
Gao Bf,
NCEPU, China

*CORRESPONDENCE
Bixing Ren,
renbixing@126.com

SPECIALTY SECTION
This article was submitted to Smart Grids, a section of the journal Frontiers in Energy Research

RECEIVED 18 September 2022
ACCEPTED 12 December 2022
PUBLISHED 25 January 2023

CITATION
Ren B, Li Q, Jia Y, Zhou Q, Wang C and Zou X (2023), A machine learning method for locating subsynchronous oscillation source of VSCs in wind farm induced by open-loop modal resonance based on measurement. *Front. Energy Res.* 10:1047624. doi: 10.3389/fenrg.2022.1047624

A machine learning method for locating subsynchronous oscillation source of VSCs in wind farm induced by open-loop modal resonance based on measurement

Bixing Ren[1,2]*, Qiang Li[1,2], Yongyong Jia[1,2], Qian Zhou[1,2], Chenggen Wang[1,2] and Xiaoming Zou[1,2]

[1]Jiangsu Electric Power Test Research Institute Co., Ltd., Nanjing, China, [2]State Grid Jiangsu Electric Power Company Ltd. Research Institute, Nanjing, China

In recent years, sub-synchronous oscillation incidents have been reported to happen globally, which seriously threatens the safe and stable operation of the power system. It is difficult to locate the oscillation source in practice using the parameterized model of open-loop modal resonance. Therefore, this paper aims at the problem of oscillation instability caused by the interaction between the multiple voltage source converters in the wind farm grid-connected system, proposes a method for locating the oscillation source of a wind farm using measurement data based on the transfer learning algorithm of transfer component analysis. At the same time, in order to solve the problem of the lack of oscillation data and the inability to label in the real system, a simplified simulation system was proposed to generate large batches of labeled training samples. Then, the common features of the samples from simulation system and the real system were learned through the transfer component analysis algorithm. Afterward, a classifier was trained to classify samples with common features. Finally, two grid-connected wind farms with VSC access are used to verify that the proposed method has good locating performance. This has important reference value for the practical application of power grid dispatching and operation using measurement to identify oscillation sources.

KEYWORDS

machine Learning, transfer component analysis (TCA), voltage source converter (VSC), oscillation source localization, mode resonance

1 Introduction

In recent years, as renewable energy has become more and more dominant in the power grid, various new Flexible Alternative Current Transmission Systems (FACTS) devices including Voltage Sourced Converter (VSC) have been continuously connected. Through flexible power flow, voltage regulation and reactive power compensation technology, the optimal allocation of resources in a wider range can be realized (CHEN and JIANG, 2017; GAO et al., 2020; MA et al., 2020).

However, some studies have shown that the interaction between VSCs or between VSCs and the synchronous generator shafting is easy to cause oscillation instability (SONG et al., 2017; Chen et al., 2018). For example, in (ZHOU et al., 2018), the static synchronous compensator (STATCOM) is prone to strong dynamic interactions with the control loop of the wind generator. (REN et al., 2020). discusses the possible interaction between the Unified Power Flow Controller (UPFC) and the synchronous generator shafting. It can be found that the internal structures of UPFC and STATCOM are both VSC-controlled devices. Therefore, when wind farms use such VSC-controlled power conversion devices to connect to the power grid, there is a risk of oscillation and instability due to dynamic interaction. It has become a hot research issue to locate the wind farm with improper control parameters (the accidental wind farm, also known as the oscillation source) and take targeted suppression measures in time.

The research on the localization of oscillation sources mainly based on mechanism analysis and damping control has been fully developed in the past 10 years, but most of them are aimed at the localization of low-frequency oscillation sources (WANG and SUN, 2017; WU et al., 2018). However, in recent years, there have been many reports on sub-synchronous oscillation (SSO) of wind farms (WANG et al., 2020; XUE et al., 2020). In order to quickly locate the SSO oscillation source, measurement-based methods led by the energy method and the impedance method have emerged (ZHENG et al., 2016; XU, 2018). Calculate the total energy and amplitude of the system, and then judge the contribution of the energy-consuming components to the oscillation attenuation, so as to realize the method of locating the SSO oscillation source; (Ma et al., 2021); adopts the method of combining real-time monitoring data and aggregated impedance model, and proposes sub-synchronization Oscillation stability evaluation index and oscillation traceability method. Obviously, the above methods are either numerical algorithms based on parametric models, or nested numerical methods based on signal parameter identification algorithms. The common point is that they all need to derive numerical calculation models for specific problems. Therefore, there will inevitably be time delays when these methods are applied online. In addition, because the concept of energy is not clearly defined in many components, and the impedance method is greatly affected by noise, if the resonant frequency point is inaccurate, the equivalent impedance calculation will be inaccurate, which will further affect the positioning accuracy of the model.

In recent years, artificial intelligence technology has become an emerging effective method by virtue of the advantages of data sample-based and weakened mechanism modeling (Zhu et al., 2017; HUANG et al., 2019; YANG B et al., 2020), but the research on the localization method of sub-synchronous oscillation sources in wind farms is still insufficient (Yao et al., 2021). For example, (Shuang et al., 2020), once proposed the method of model transfer to transfer the VGG16 grid to the localization of the forced power oscillation source, and obtained high localization accuracy. Limited to the VGG16 model and training samples, this model is not necessarily more suitable for the SSO sub-synchronous oscillation source localization problem. Therefore, the adaptability of the proposed method and the generalization from the training system to the actual system are still insufficient. However, based on the feature transfer method in (CHEN et al., 2021), the characteristics of the simulation system are transferred to the actual system, and the sub-synchronous oscillation source induced by the resonance of a single synchronous machine and a single fan in the wind-fire baling system is located. However, considering that this method requires measurement at the port of each wind turbine, and the actual wind farm has hundreds or thousands of wind turbines, the coverage of the measurement points is very high, and the possibility of practical application needs to be further verified. In addition, in engineering practice, the computer used for computing usually does not have a computing GPU, so it is difficult to meet the hardware conditions required for building a complex deep learning grid.

In order to solve the above problems based on deep learning methods, this paper proposes a method for locating sub-synchronous oscillation sources of wind farms based on transfer component analysis (TCA) based on the engineering practice of wind farms. In this method, TCA is used to extract the features of the measurement data, and a simple classifier is used to locate the oscillation source. Compared with other deep learning methods, this method has fast calculation speed, high positioning accuracy, and low requirements on computer hardware, which is more suitable for practical applications in wind farm engineering.

2 Principle of interaction between wind farm and FACTS

FACTS devices are often installed in the grid-connected system of wind farms to adjust the system power flow or provide reactive power compensation. However, studies have demonstrated (ZHOU et al., 2018; REN et al., 2020) that such VSC-type FACTS devices can interact dynamically with wind

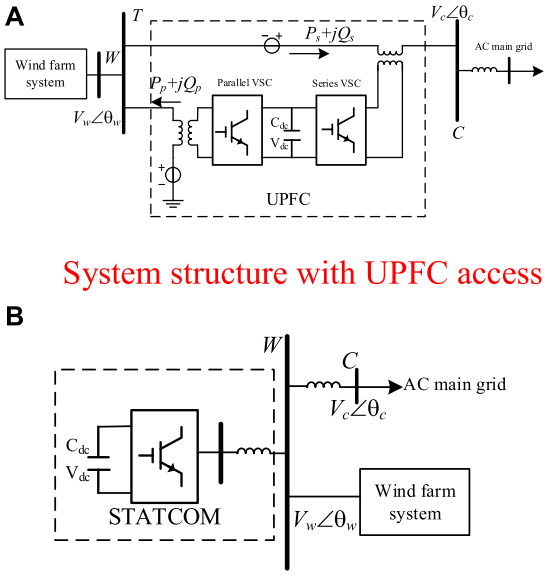

FIGURE 1
Schematic of hybrid power system with VSC. **(A)** System structure with UPFC access .**(B)** System structure with STATCOM access

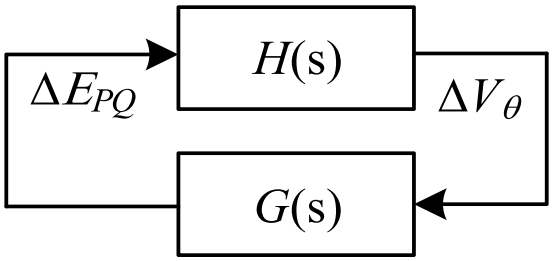

FIGURE 2
Closed-loop interconnected linearized models of multi-wind-turbine power system with VSC.

farms. In order to study the oscillation source in the actual wind farm, as shown in Figure 1, two typical wind farm grid-connected systems equipped with FACTS devices are given. Among them, Figure 1A is a system equipped with a series-parallel combined UPFC; Figure 1B is a system equipped with STATCOM, its structure contains a single-ended VSC, so the connection method is usually connected in parallel; among them, the system of wind farm is formed by the aggregation of N_1 wind farms, through the bus W Assemble and send.

The open-loop mode resonance modeling method (REN et al., 2020) is to take the output power of the wind farm as a node at a certain operating point, and divide the system in Figure 1 into the open-loop subsystem of the wind farm to be studied and the remaining systems (including other VSC-type devices and All components of the AC main grid) are two parts, and the transfer function can be expressed as:

$$\Delta \boldsymbol{V}_\theta = \boldsymbol{H}(s)\Delta \boldsymbol{E}_{PQ} \quad (1)$$

$$\Delta \boldsymbol{E}_{PQ} = \boldsymbol{G}(s)\Delta \boldsymbol{V}_\theta \quad (2)$$

Among them, $\boldsymbol{H}_{2\times2}(s)$ represents the feedforward subsystem transfer function of the wind farm, $\boldsymbol{G}_{2\times2}(s)$ represents the feedback subsystem transfer function matrix of the remaining system, $\boldsymbol{E}_{PQ} = [P_p, \Delta Q_p]^T$ represents the exchange power between the wind farm and the system; $V_\theta = [V_w, \theta_w]^T$ represents the node voltage amplitude and phase angle at the connection point between the wind farm and the system. The grid-connected system of the wind farm is represented as a closed-loop interconnection model, as shown in Figure 2.

The wind farm system and the remaining system constitute an interconnected system. According to the open-loop mode resonance theory (WANG et al., 2019), the influence of the wind farm on the system is mainly caused by the interaction between its control system and the remaining control system, which causes the mode change of the closed-loop system, that is, The mode of $\boldsymbol{H}(s)$ interacts with the mode of $\boldsymbol{G}(s)$, which will affect the changes of input and output variables $\boldsymbol{E}_{PQ}$ and $\boldsymbol{V}_\theta$. At the same time, since $\boldsymbol{E}_{PQ}$ and $\boldsymbol{V}_\theta$ can be measured, the above-mentioned system state equation can be fitted by quantitative measurement, and the relationship can be expressed as:

$$(\Delta \boldsymbol{E}_{PQ}, \Delta \boldsymbol{V}_\theta) \leftrightarrow (\boldsymbol{H}, \boldsymbol{G}) \leftrightarrow \boldsymbol{A}_S \quad (3)$$

The steps of calculating the system oscillation source according to the parametric model can be summarized as follows: first, calculate the oscillation mode l_i of the state matrix $\boldsymbol{A}_s$ of the system, and the corresponding participation factor PF_{ki}; secondly, calculate the element corresponding to the mode with the largest participation factor $|PF_{ki}|$, which is the participation interaction element to determine the element as an oscillation source. Due to engineering practice, it is difficult to measure at the grid-connected location of each wind turbine. Usually, monitoring is performed in units of a line or a wind farm. Therefore, the wind farm is used as a unit here, and a wind farm is regarded as an element. Denote the oscillation source y_n as the number of the wind farm participating in the dynamic interaction of the system, then there is a function g between the oscillation source y_n and the state matrix $\boldsymbol{A}_s$ of the system, that is, Eq. 3 can be further expressed as:

$$(\Delta \boldsymbol{E}_{PQ}, \Delta \boldsymbol{V}_\theta) \leftrightarrow (\boldsymbol{H}, \boldsymbol{G}) \leftrightarrow \boldsymbol{A}_S \rightarrow g(y_n) \quad (4)$$

From this, it can be seen that the relationship between the measurable measurement $\Delta \boldsymbol{E}_{PQ}$ and ΔV_θ and the label of the oscillation source can be expressed as:

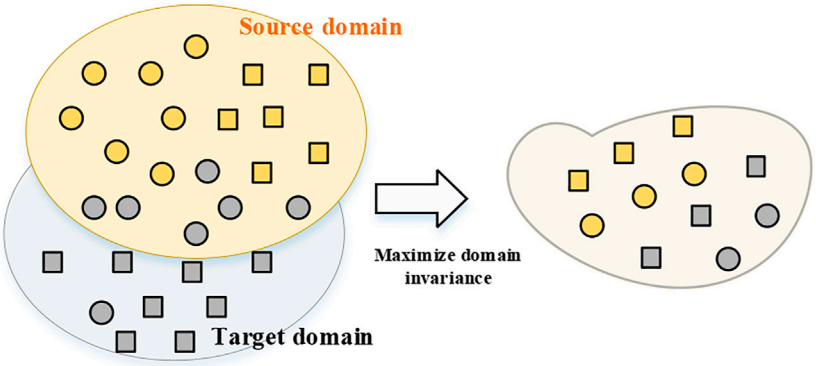

FIGURE 3
Schematic of feature-based transfer learning.

$$(\Delta \boldsymbol{E}_{PQ}, \Delta \boldsymbol{V}_{\theta}) \rightarrow g(y_n) \tag{5}$$

Therefore, the relational modeling of Eq. 5 can be extended to machine learning problems, where the function $g(\cdot)$ is the relational expression of the oscillation source localization model, the input of the machine learning function $g(\cdot)$ is the measurement data sample, and the output is the oscillation source tag.

At the same time, based on the open-loop mode resonance theory, it is easy to obtain the measurement data of the grid-connected port of the wind farm under different operating conditions by offline simulation. The nth sample measurement data obtained is recorded as $X_n = (E_{PQ}, V_{\varnothing}) = (P, Q, V, V_{\varnothing})$, and calculate the participation factor and oscillation source label of the sample according to the parametric model, recorded as $\boldsymbol{Y} = \{y_n\}$, where $y_n = 0$ indicates that the nth sample system is stable, and $y_n = 1$ indicates that wind farm one is an oscillation source, thus constructing a labeled sample.

3 Oscillation source localization method based on TCA

3.1 Introduction to TCA

The TCA method belongs to a feature-based transfer learning method (Yang Q et al., 2020), which learns a pair of mapping functions from the source domain and the target domain. The classifier is retrained, and finally the prediction of the classifier is performed. Therefore, measures of data distribution can be used to narrow the distribution differences between different data domains, enabling transfer learning, as shown in Figure 3.

In the power system, the data samples obtained by the simulated system and the actual system are quite different because their distributions are not the same. Therefore, the most critical step in transfer learning is to reduce the distribution difference of the data samples obtained by the simulated system and the actual system. Let the simulation system be the source domain and the actual system be the target domain, where the source domain is a labeled system, denoted as $\boldsymbol{D}_s = \{(\boldsymbol{X}_1, \boldsymbol{Y}_1), \ldots, (\boldsymbol{X}_n, \boldsymbol{Y}_n)\}$; and the target domain is an unlabeled system, Denoted as $\boldsymbol{D}_t = \{\boldsymbol{X}_{n+1}, \ldots, \boldsymbol{X}_{n+m}\}$. Currently, the most widely used measure of domain distribution discrepancy is the Maximum Mean Discrepancy (MMD) (Yang Q et al., 2020) measure. MMD is a non-parametric measure used to measure the distance between distributions based on kernel embeddings in the regenerated kernel HilBert space, the MMD distance formula is as follows:

$$MMD(P_s, P_t) = \left\| \frac{1}{n_s} \sum_{i=1}^{n} \phi(x_i) - \frac{1}{n_t} \sum_{j=1}^{n_s+n_t} \phi\left(x_j\right) \right\|_H^2 \tag{6}$$

Where, $\phi: \boldsymbol{x} \rightarrow \boldsymbol{H}$ represents the infinite order non-linear feature map in the kernel space, n_s and n_t represent the sample length respectively; By using the kernel function, Eq. 6 can be simplified as:

$$MMD = tr(\boldsymbol{KL}) \tag{7}$$

Among them, $\boldsymbol{K}$ is a composite kernel matrix composed of kernel matrices in the source domain, target domain and intersection domain, and k in each domain is the kernel function corresponding to ϕ, satisfying $< \phi(\boldsymbol{x}_i), \phi(\boldsymbol{x}_j) \geq k(\boldsymbol{x}_i, \boldsymbol{x}_j)$, $<\cdot>$ represents the inner product of two functions. $\boldsymbol{L}$ represents the sample size matrix, see (Yang B et al., 2020) for the detailed definition.

Since the kernel function k in Eq. 7 may be a highly non-linear form of the mapping function, and the function $\phi(\boldsymbol{x})$ is also unknown, the TCA method decomposes the kernel matrix in the equation to obtain the following optimization problem:

$$\begin{aligned} &\min_{w} \; tr\left(\tilde{\boldsymbol{K}} \boldsymbol{W} \boldsymbol{W}^T \tilde{\boldsymbol{K}} \boldsymbol{L}\right) + \lambda tr\left(\boldsymbol{W}^T \boldsymbol{W}\right) \\ &s.t. \; \boldsymbol{W}^T \tilde{\boldsymbol{K}} \boldsymbol{H} \tilde{\boldsymbol{K}} \boldsymbol{W} = I \end{aligned} \tag{8}$$

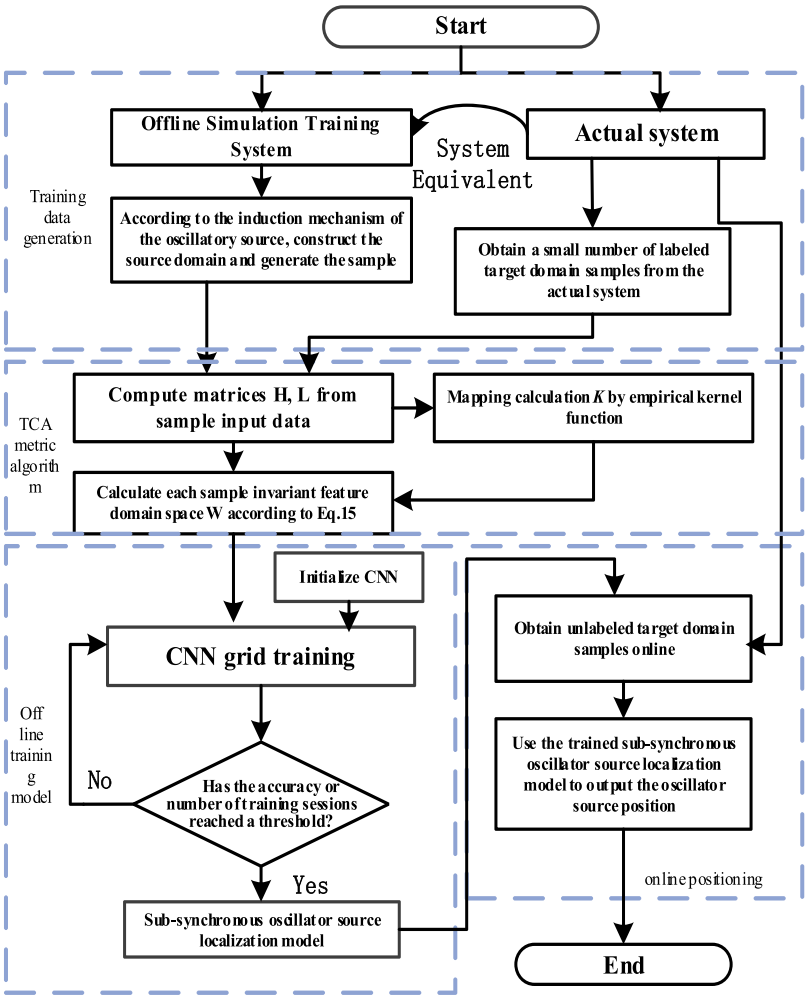

FIGURE 4
Single-machine equivalent model of the grid-connected wind farm.

Among them, H is a centering matrix, the first term of the objective function is to minimize the MMD distance between the mapped source and target domain data, the second term is the regularization term for $\boldsymbol{W}$, and the constraint is to maximize the variance of the data after mapping.

The $\boldsymbol{W}$ obtained by the final calculation contains the m main feature vectors of $(\tilde{K}L\tilde{K}+\lambda I)^{-1}$, that is, the extracted public domain feature space. The above process can be obtained by direct numerical calculation.

3.2 Oscillation source localization model and implementation process based on TCA

According to the above TCA algorithm, the data-driven wind farm sub-synchronous oscillation source localization model in the actual system is established, that is, the relationship between the common features and the classification labels is fitted.

In this paper, the Softmax classifier is combined with the transfer learning algorithm to construct a deep transfer learning framework to establish a sub-synchronous oscillation source localization model. Applying the Softmax classifier on the obtained new source domain feature space realizes the relational modeling of Eq. 5. To sum up, the transfer model learning framework form based on TCA metric can be expressed as:

$$g_{soft} = \underset{f \epsilon H}{\arg\min} \sum_{i=1}^{n} L\left(g_{soft}\left(W_i\right), y_i\right) \tag{9}$$

where $g_{soft} = w^T\phi$ represents the predicted output classifier function. In order to facilitate the function training, the CNN structure is used for the classification and identification of the common feature space, that is, the above g_{soft} representation

function is replaced by a CNN grid with weight parameters, and the final location model of the wind farm sub-synchronous oscillation source is a CNN grid model.

The specific scheme of model construction is mainly divided into three parts: system construction and data sample acquisition, offline model training, and online application testing, as shown in Figure 4.

The details are as follows:

1) Simulation system construction and data sample generation:

The source domain training data required for offline learning can be obtained from the following two aspects: First, based on the power system equivalence theory (DONG et al., 2021), a simulation system is built (the equivalent system is used to generate source domain training samples). According to the open-loop mode resonance theory, the control parameters of the open-loop subsystem are set so that the system may have open-loop mode resonance in the target range. Combined with various possible topological structures, operation modes, fault types, fault locations and disturbance accidents of the system, time-domain simulation is carried out, and the power on the grid-connected connection lines of all wind farms and the node voltage composition data of the grid-connected ports of the wind farm are collected as sample $\boldsymbol{X}_s$, and according to the system parameterized state matrix, the label set $\boldsymbol{Y}_s$ is constructed by calculating the participation factor labeling samples, and finally the source domain training sample $\boldsymbol{D}_s$ is formed. Since the transfer learning training data not only comes from the source domain, but also includes part of the data in the target domain. Therefore, the measured data $\boldsymbol{X}_t$ of the actual operation case records of the system in the past period of time are widely collected from the historical operation records of the system, and the data target domain is constructed as training sample $\boldsymbol{D}_t$.

2) Feature extraction and localization learning of sub-synchronous oscillation source:

The obtained time series datasets $\boldsymbol{X}_s$ and $\boldsymbol{X}_t$ of the source and target domains are used as input, and the aforementioned TCA-based transfer learning method is used to extract the common features of the source and target domains. On this basis, a simple CNN with Softmax classifier is built. The grid is trained to perform classification learning on the extracted common features. Among them, the dimension of the input layer of the CNN model is determined by the number of columns of common features, the convolution pooling layer is set with two modules, the size of the convolution kernel is 5×5, and the size of the pooling kernel is set to 2×2. Connected to the Softmax classifier, the dimension of the output layer is determined by the label type. The model can combine the comprehensive statistical characteristics of the representative data samples to quickly establish a practical model for the location of oscillation sources through CNN.

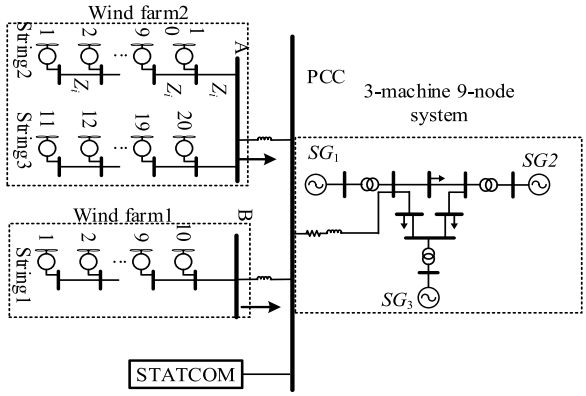

FIGURE 5
Real system structure of numerical example one.

3) Online application test:

During the online monitoring process, when the system has the risk of sub-synchronous oscillation, the measurement information in the 2s time window is collected in real time by the wind farm port of the system to form the target domain test sample. The sub-synchronous oscillation source location model is obtained through the above learning, and the feature extraction and corresponding oscillation source location are performed on the sample, and the current possible oscillation source wind farm number is quickly given. If the number is 0, it is determined that the system is stable, and the next monitoring is performed through the sliding time window; otherwise, an early warning signal is issued to facilitate the dispatcher to take control measures in time to prevent further deterioration of the oscillation. Considering that when the actual system is running, the operating state of the system is constantly changing. In order to improve the reliability of the model, in practical application, new target domain samples can be collected and constructed periodically, so as to repeat the above two steps of offline learning, so as to update Maintain a sub-synchronous oscillator source localization model.

4 Example 1—UPFC and wind turbine resonance

This example analyzes the rationality of the training process of the method in this paper by designing a simulation case of open-loop mode resonance between the fan and the UPFC. The computer hardware configuration used in the experiment is: Intel core-i5-4570 CPU, 128G memory. Among them, the simulation system construction and data preprocessing were completed on Matlab 2019a, and the TCA and classifier models were built in the CPU version of *Python* 3.7 using the CNN architecture.

4.1 Example system and test scenarios

A wind farm grid-connected system with UPFC, its system structure is shown in Figure 5. Two of the wind farms each contain 20 direct-drive fans of the same type, which are collected through the bus W, and the power of the adjacent thermal power units is collected on the PCC bus. A 3-machine 9-node system is used to replace the AC main grid).

As shown in Figure 5, take the wind farm grid connected system with UPFC system as an example, in which the SG4 model of direct drive wind turbine and the model of synchronous machine adopts the 15th order model and six mass block model given in document (Ren, 2019), and the 3-machine 9-node system adopts IEEE typical parameter settings.

Assuming that the wind turbine s in the wind farm 1 may interact dynamically with the UPFC, according to the open-loop mode resonance theory, the control parameters of the UPFC and the wind farm one in the actual system are adjusted to a state that is prone to interaction. Considering that different operating point conditions will affect the stability of the system, set the rated output of the wind farm and 80%–110% load to simulate the typical power flow mode of steady-state operation; simulate the disturbance with the sudden change of the wind turbine output and load, and set the disturbance amount to the rated value 80%–110% of the value/initial value, the duration of the disturbance is 100 m. The sampling window length and frequency are 2s and 1,000 Hz, respectively. Record the *U*/*P*/*Q* on the wind farm one and wind farm two port lines. On the basis of these simulation settings, Matlab is used for batch simulation, 200 cases are generated, and unlabeled training samples in the target domain are formed.

4.2 Training sample generation and model training process

4.2.1 Training sample generation

According to the implementation process of the sub-synchronous oscillation source location method introduced in 1.2, for the actual system in Figure 5, based on the system equivalence theory, the wind farm is equivalent to a wind turbine, and the AC power grid is equivalent to a single-machine infinite system, and then a simulation system is built.

The open-loop mode resonance theory is used to analyze the stability of the system under actual operating conditions in the simulation system. The specific method is: according to the operation mode in the actual system, set the operation point in the simulation system as ± 20% of the actual system operation point: The rated power of each unit is increased or decreased by 0–20%, and the load on the line is 80%–120% of the actual system operation. Then, according to the disturbance and frequency settings in the actual system, the time domain simulation is performed, and the measurement data $\boldsymbol{X}_s$ of the wind farm port is recorded. The state space equation of the parametric model of the simulation system is used to calculate the participation factor, and the sample data obtained by each simulation is marked to form the real label set $\boldsymbol{Y}_s$ of the simulation system. Thus, training samples with labels are generated in large batches in the simulation system. Therefore, some unlabeled samples obtained in the above-mentioned actual system and the labeled samples obtained in the simulation system are unified to form training samples, and finally, 2,464 training samples of calculation example one are obtained. Figure 6 presents the system training sample feature representation obtained by t-SNE dimensionality reduction.

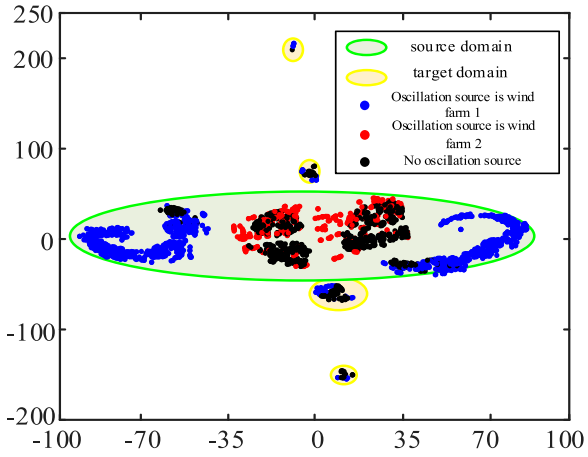

FIGURE 6
Features representation of training samples.

From the characteristic roots of the system generated under different oscillation sources in the example of Figure 6, the different oscillation sources are non-linear, and it is difficult to distinguish them by traditional methods.

4.2.2 Model training process

In order to establish a localization model with better performance, it is hoped to clearly distinguish different oscillation source samples in the same domain. The source domain and the target domain are as similar as possible. Therefore, the TCA algorithm is used to perform feature learning on the training samples, so as to learn the common features of the source domain and the target domain. Figure 7 presents the t-SNE feature representation of the training samples after training using the TCA algorithm.

By comparing with Figure 6, it can be seen that the original training sample source domain and target domain are clearly demarcated, and different oscillation sources in the same domain are non-linear and inseparable. After TCA transformation, the source domain and the target domain appear common feature

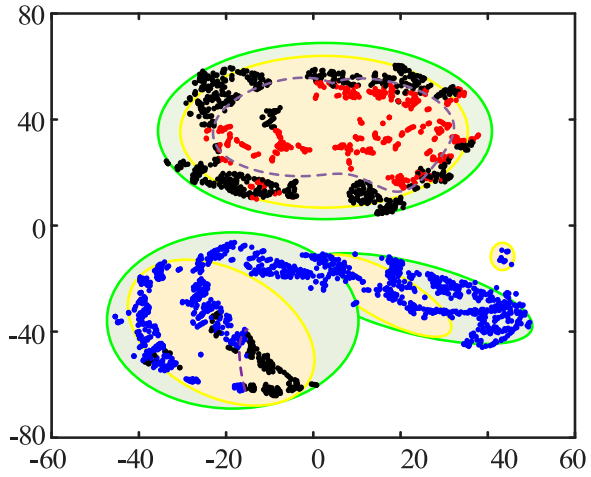

FIGURE 7
Membership function of each variable.

areas, and the boundaries of different oscillation sources in the same domain are gradually clear. This shows that TCA can realize feature learning for the training samples of oscillation source localization.

Considering that the TCA-transformed training samples are separable between different oscillation sources, as shown by the purple dotted line (the periphery of oscillation source in wind farm 2, shown as red dot in Figure 6) in Figure 7, the classification boundary line shows that the relationship between different oscillation sources is still non-linear, and the traditional linear Classifiers are still intractable. Therefore, a simple CNN grid with Softmax classifier needs to be adopted to achieve non-linear classification.

In the training process, in order to evaluate the performance of the model, the method of cross-validation is adopted, the training data is divided into training set and validation set for training, and the positioning accuracy index LAI is defined to evaluate the oscillating source positioning performance of the model:

$$LAI = \frac{TN_1 + TN_2 + \cdots + TN_n}{TO + TS + FO + FS} \tag{10}$$

Among them, the number of samples of the true prediction of wind farm 1 as an oscillation source is denoted as TN_1; similarly, the number of samples of true prediction of wind farm n as an oscillation source is denoted as TN_n. *TO,FO,TS, FS* represent the number of samples in the classification confusion matrix, respectively.

For the oscillation stability of the power system, both "misjudgment stability" and "missing judgment instability" will have a serious impact on the system. Therefore, this paper defines the precision rate (PR) and recall rate (RR) from the perspective of sample stability and instability. The classification discriminant index SCAI expressed comprehensively to evaluate the classification performance of the model for unstable samples:

$$SCAI = \frac{2PR \cdot RR}{PR + RR} \tag{11}$$

$$PR_{rate} = \frac{TN1 + TN2}{TO + FO}, RR_{rate} = \frac{TO}{TO + FS} \tag{12}$$

Taking the above positioning accuracy index and classification discrimination index as the statistical indexes of model performance, Table.1 summarizes the training results of the model in the training process.

It can be seen from the results in Table.1 that because the model is relatively simple, high positioning accuracy can be achieved after 100 times of training. If the number of training times is increased, the accuracy index of the model does not change much, which indicates that the model is stable and can be used for model migration testing. After 500 times of training, the accuracy index of the model has reached about 95%. When the training times continue to increase, the model accuracy index does not increase but decreases, which indicates that the model training has already reached saturation. Increasing the training times may make the model over fit. Therefore, a model trained 500 times is selected for saving.

5 Example 2 - Wind farm system with STATCOM

The computer hardware and software configuration used in example one are the same. This example is simplified and generated by an actual offshore wind power system, and is mainly used to test the applicability of the method in this paper in different scenarios.

5.1 Example system and test scenario

The structure of the example system is shown in Figure 8, which includes 30 direct drive fans belonging to two wind farms. Wind farm one is collected through bus B, and wind farm two is collected through bus A. finally, it is connected to the AC main grid with STATCOM through PCC bus. It is assumed that in the system shown in Figure 8, there is a risk of dynamic interaction between the wind turbines in the wind farm two and STATCOM.

5.2 Simulation setup and training sample generation

Same as Example 1, in the actual system shown in Figure 8, the possible operating conditions in the system

TABLE 1 Training results with different epochs.

Training times	LAI (%)	SCAI (%)	Total training time/s
50	86.97	89.54	96.74
100	90.45	92.37	229.14
500	96.36	97.74	961.57
1,000	95.32	96.69	1928.15

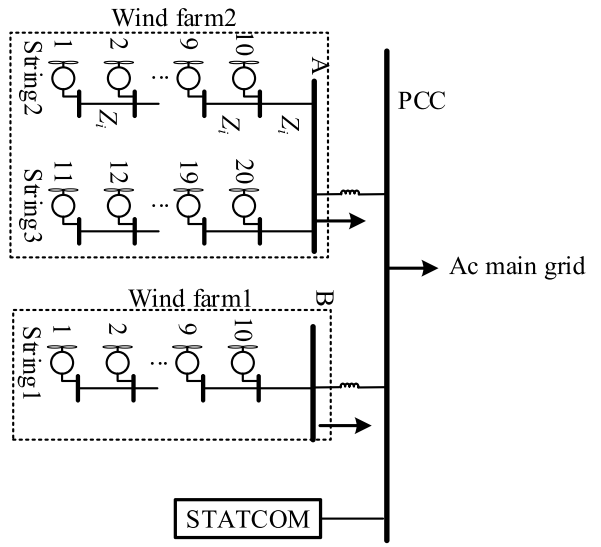

FIGURE 8
Real system structure of numerical example two.

are comprehensively considered, and the output and load level of the wind farm under typical power flow mode are used as the basis for steady-state operation according to the operation mode provided by the system operator. Data; take the sudden change of the fan output and load as the disturbance, also set the duration of the small disturbance to 100 m, the sampling window length and frequency are 2s and 1000 Hz respectively. Based on the above simulation settings, time-domain simulations were performed at different operating points, and measurements were made at the grid-connected ports of two wind farms to generate 200 cases, which were recorded as unlabeled training samples.

Then, according to the training process in 3.2, the simplified simulation system of Figure 8 is used to generate a large batch of labeled training samples, and TCA is used to extract and transform the training samples, and train the classifier. Finally, save the positioning model of Example 2.

5.3 Model comparison test analysis

In order to verify the generalization of the model established by the method proposed in this paper, two sets of scenarios are designed according to the following rules in the actual system of the two examples to generate test samples:

Scenario 1: Simulate the measurement samples with noise in the actual system. The measurement data sampled in the actual system randomly increases the noise with the signal-to-noise ratio SNR = 10dB, and generates 200 samples for testing.

Scenario 2: Using the open-loop mode resonance theory, adjust the control parameters of the wind farm in the two examples (different from the parameters in the target domain training sample generation process), so that the system resonates between the wind farm and the UPFC (or STATCOM). A total of 200 samples are also obtained for testing.

In order to facilitate the calculation of the test accuracy of the model, the linearization equation of the actual system is used to label the samples in the process of generating the above test set. During the test, the measurement data of the grid-connected port of the wind farm is collected from each case by the method of active time window to simulate the online evaluation. For the models saved in the two examples, four groups of test sets were used for testing, and the test results are shown in Table.2.

It can be seen from Table.2 that the trained model can still achieve high positioning accuracy in different scenarios in the same system, indicating that the model has a certain generalization. However, from the perspective of the positioning accuracy of the model for different systems, although the model has a certain generalization ability, the extracted common features cannot be well applied between different systems, indicating that there are still differences in the characteristics of wind farm oscillation sources between different systems.

The test accuracy of samples containing noise decreases slightly, but the positioning accuracy can also be above 95% in the same system. It can be seen that even in the serious measurement error, the method in this paper still has strong robustness. Judging from the test time, the use of TCA algorithm for preprocessing does not have a great impact on the test time. The computing speed under the

TABLE 2 Test results with two models.

Model	Test scenario	LAI (%)	SCAI (%)	Test time/s
Example1	Example 1—scenario 1	95.78	96.45	12
	Example 1—scenario 2	96.22	96.67	12
	Example2—scenario 1	86.38	87.50	13
	Example 2—scenario 1	89.26	90.86	12
Example2	Example 1—scenario 1	81.08	84.47	12
	Example 1—scenario 2	83.54	85.32	12
	Example 2—scenario 1	96.66	96.88	11
	Example 2—scenario 2	98.24	98.63	11

CPU can complete the discriminative positioning of any sample within 0.5 m, which proves that the method meets the requirements of online applications.

6 Conclusion and outlook

Quickly locating the sub-synchronous oscillation source of wind farm is very important to ensure the stability of wind farm grid-connected system. Compared with the traditional positioning method, the wind farm sub-synchronous oscillation source positioning method has higher requirements for rapidity and adaptability to different induced scenarios, and for the positioning accuracy, positioning to the wind farm is easier to operate in engineering practice. It can also meet the control requirements of the load during operation. Therefore, this paper presents a method for locating the oscillation source of wind farms under open-loop mode resonance conditions based on TCA transfer learning.

In this paper, the detailed implementation process of applying the method in a practical system is given, and the feasibility and applicability of the proposed method are analyzed from the aspects of training process and comparative test using two simplified wind farm system examples. The results show that the method in this paper can realize feature extraction and classification according to the measurement of wind farm ports, and shows high positioning accuracy and anti-noise ability when locating the oscillation source of the grid-connected system of multiple wind farms.

With the widespread access of new energy sources to the power grid and the large-scale application of power electronic devices in the power grid, the problem of sub-synchronous oscillation of wind farms has been paid more and more attention. The research results of this paper will lay the foundation for the grid monitoring and location analysis technology adapted to the stability of wind farms.

Data availability statement

The original contributions presented in the study are included in the article/supplementary material, further inquiries can be directed to the corresponding author.

Author contributions

BR: Conceptualization, Funding acquisition, Methodology,Writing, Software, Validation QL: Project administration, Validation YJ: Investigation, Supervision QZ: Validation, Resources CW: Data Curation, Software XZ: Software, Investigation.

Funding

This work was supported by the Natural Science Foundation of Jiangsu Province (No. BK20210057).

Conflict of interest

Authors BR, QL, YJ, QZ, CW, and XZ were employed by the company Jiangsu Electric Power Test Research Institute Co., Ltd. Authors BR, QL, YJ, QZ, CW, and XZ were employed by the company State Grid Jiangsu Electric Power Company Ltd, Research Institute

Publisher's note

References

Chen, C., Du, W., Wang, H., et al. (2018). An examination of SSOs induced by grid-connected wind farms in power systems under near strong open-loop modal resonance [J]. *Power Syst. Technol.* 42 (09), 2778–2788.

Chen, J., Du, W., and Wang, H. (2021). A method of locating the power system sub-synchronous oscilla-tion source unit with grid-connected PMSG using deep transfer learning[J]. *Trans. China Electrotech. Soc.* 36 (01), 179–190.

Chen, Q., and Jiang, P. (2017). Mechanism and impact evaluation of strong dynamic interaction between UPFC and generator shaft [J]. *Electr. Power Engineering Technol.* 36 (02), 56–60.

Dong, W., Wang, Y., and Wang, H. (2021). Sin-gle-machine equivalent model of a group of wind turbine generators for small-signal stability analysis[J]. *Power Syst. Technol.* 45 (04), 1241–1250.

Gao, B., Wang, F., Yu, H., et al. (2020). The suppression method of wind power sub-synchronous oscillation using static synchronous series compensator [J]. *Trans. China Electrotech. Soc.* 35 (06), 1346–1356.

Huang, R., Du, W., and Wang, H. (2019). Short-term prediction of wind power considering turbulence intensity[J]. *Power Syst. Technol.* 43 (06), 1907–1914.

Ma, N., Xie, X., and He, J. (2020). "Review of wide-band oscillation in renewable and power elec-tronics highly integrated power systems[J]," in Proceedings of the CSEE, 4721–4731.4015

Ma, N., Xie, X., and Kang, P. (2021). Wide-area monitoring and analysis of sub-synchronous oscillation in power systems with high-penetration of wind power [J]. *Proc. CSEE* 41 (01), 65–74.

Pan, S. J., Tsang, I. W., Kwok, J. T., and Yang, Q. (2011). Domain adaptation via transfer component analysis. *IEEE Trans. neural grids* 22 (2), 199–210. doi:10.1109/tnn.2010.2091281

Ren, B., Du, W., and Wang, H. (2020). Mechanism and impact evaluation of strong dynamic interaction between UPFC and generator shaft [J]. *Proc. CSEE* 40 (04), 1117–1129+1404.

Ren, B. (2019). *Impact of voltage source converter controlled power devices on power system dynamic interaction [D]*. Beijing: North China Electric Power University.

Shuang, F., Chen, J., and Tang, Y. (2020). Location method of forced oscillation source based on SPWVD image and deep transfer learning[J]. *Automation Electr. Power Syst.* 44 (17), 78–91.

Song, R., Guo, J., and Li, B. (2017). Mecha-nism and characteristics of sub-synchronous oscillation in direct-drive wind power generation system based on input-admittance analysis [J]. *Proc. CSEE* 37 (16), 4662–4670+4891.

Wang, B., and Sun, K. (2017). Location methods of oscillation sources in power systems: A survey. *J. Mod. Power Syst. Clean Energy* 5 (2), 151–159. doi:10.1007/s40565-016-0216-5

Wang, Lichao, Yu, Yongjun, Zhang, Mingyuan, et al. (2020). Impedance model and analysis of sub-synchronous os-cillation influence factors for grid-connected full-converter wind turbines [J]. *Electr. Power Engi-neering Technol.* 39 (01), 170–177.

Wang, Y., Du, W., and Wang, H. (2019). Compar-ative analysis of negative-resistance effect and open-loop modal coupling in sub-synchronous control interaction problem[J]. *Proc. CSEE* 39 (S1), 225–234.

Wu, S., Xu, Y., Zhang, S., et al. (2018). Research on propagation characteristics and locating method of low frequency oscillations induced by turbine generator unit [J]. *Power Syst. Technol.* 42 (06), 1917–1921.

Xu, P. (2018). *Study on sub-synchronous components PropagationPath and disturbance source location of wind power collection areas [D]*. Beijing: North China Electric Power University.

Xue, A., Fu, X., and Qiao, D. (2020). Review and prospect of research on sub-synchronous oscillation mechanism for power system with wind power participation[J]. *Electr. Power Autom. Equip.* 40 (09), 118–128.

Yang, B., Du, W., and Wang, H. (2020). Equivalent modeling of virtual synchronous generator based on data-driven method[J]. *Power Syst. Technol.* 44 (01), 35–43.

Yang, Q., Zhang, Y., Dai, W., et al. (2020). *Transfer learning[M]*. Cambridge: United Kingdom:Cambridge University Press, 29–38.

Yao, M., Yu, Z., Lu, N., and Shi, D. (2021). Time series classification for locating forced oscillation sources. *IEEE Trans. Smart Grid* 12 (2), 1712–1721. doi:10.1109/tsg.2020.3028188

Yap, K. Y., Beh, C. M., and Sarimuthu, C. R. (2021). Fuzzy logic controller-based synchronverter in grid-connected solar power system with adaptive damping factor. *Chin. J. Electr. Eng.* 7 (2), 37–49. doi:10.23919/CJEE.2021.000014

Zheng, B., Shuang, F., and Wu, X. (2016). Localizing disturbance source of power system forced oscillation caused by wind power fluctuation[J]. *Electr. Power Eng. Technol.* 35 (05), 32–34+43.

Zhou, P., Guangfan, L., Song, R., et al. (2018). Sub-synchronous oscillation characteristics and interac-tions of direct drive permanent magnet synchronous generator and static var generator[J]. *Proc. CSEE* 38 (15), 4369–4378+4637.

Zhu, L., Lu, C., Dong, Z. Y., and Hong, C. (2017). Imbalance learning machine-based power system short-term voltage stability assessment. *IEEE Trans. Ind. Inf.* 13 (5), 2533–2543. doi:10.1109/tii.2017.2696534

Frontiers in
Energy Research

Advances and innovation in sustainable, reliable and affordable energy

Explores sustainable and environmental developments in energy. It focuses on technological advances supporting Sustainable Development Goal 7: access to affordable, reliable, sustainable and modern energy for all.

Discover the latest Research Topics

See more →

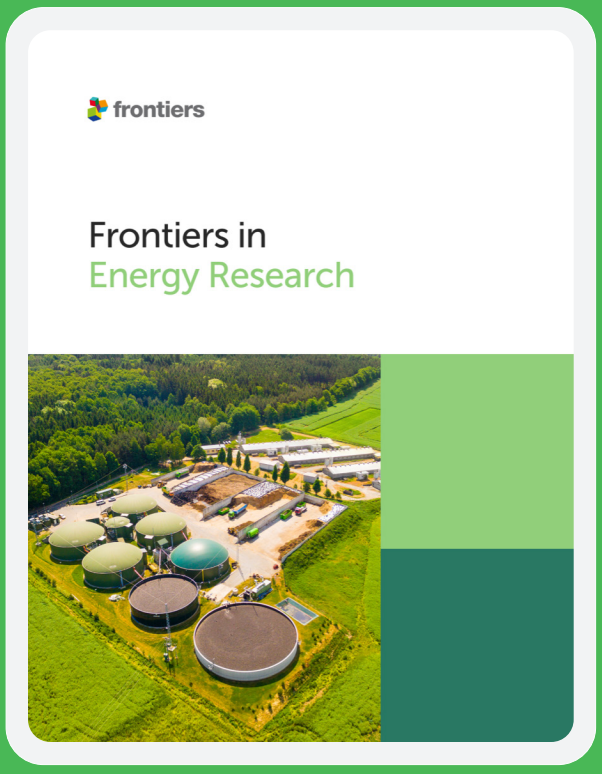

Frontiers

Avenue du Tribunal-Fédéral 34
1005 Lausanne, Switzerland
frontiersin.org

Contact us

+41 (0)21 510 17 00
frontiersin.org/about/contact